Abstract

Title of Dissertation: Turbulence in Star Formation:
Tracing the Velocity Fields of Dense Cores

Nikolaus H. Volgenau, Doctor of Philosophy, 2004

Dissertation directed by: Professor Lee G. Mundy
Department of Astronomy

The theory of star formation that has developed over the past several decades supposes that dense cores are quiescent and isolated from energetic events. However, observations of star-forming regions show that cores develop in active environments. Thus, although the "standard" theory is quantitatively rigorous, it can only explain a fraction of real star-forming events.

The point of departure for this work is the hypothesis that turbulence is a fundamental component of the star formation process. In a turbulent star formation theory, the effects of random gas motions extend from molecular cloud scales down to scales of thousands or hundreds of AU. Dense cores form rapidly at the collision interfaces of turbulent flows and evolve according to the specific physical conditions at those interfaces. Star formation is dynamic and interactive, rather than quasi-static and isolated.

This work presents evidence for turbulent motions in dense cores. The evidence comes from observations of cores in the Perseus cloud made with the BIMA interferometer and the FCRAO 14 m antenna. The cores were mapped in $C^{18}O$ $J = 1 \rightarrow 0$ emission with resolutions of $\sim$44, 10, 5, and 3 arc-seconds. The higher angular resolutions correspond to physical scales within the characteristic core radius ($\sim$0.1 pc) identified in previous studies. In general, the range of velocities traced by the $C^{18}O$,

as well as the complexity of the fields, increases with resolution. No core resembles a quiescent condensation undergoing simple systematic rotation.

The cores are analyzed by applying a gridding technique developed by Ostriker, Stone, & Gammie (2001) to quantify the properties of model clouds. Spectra taken through the datacubes over a wide range of sizes are used to construct correlations between line widths and spatial scale, which show a broad range of line widths even at the smallest measurable scales. The narrowest lines must have a turbulent component at least as great as the thermal component, and for nearly all lines, the turbulent component makes the dominant contribution. A statistical analysis of the variations in line properties as a function of spatial separation across a core shows that the means and variances of the central velocity ($\overline{\Delta}_{V_C}$, $\sigma^2_{\Delta V_C}$) and line width ($\overline{\Delta}_{\rm FWHM}$, $\sigma^2_{\Delta_{\rm FWHM}}$) *difference* distributions exhibit properties characteristic of a hierarchy of turbulent gas motions (Miesch & Bally 1994). The high resolution BIMA data reveal that these turbulent motions persist on sub-core scales.

Turbulence in Star Formation: Tracing the Velocity Fields of Dense Cores

by

Nikolaus H. Volgenau

Dissertation submitted to the Faculty of the Graduate School of the
University of Maryland at College Park in partial fulfillment
of the requirements for the degree of

Doctor of Philosophy

2004

Advisory Committee:

Professor Lee G. Mundy, advisor
Professor Alyssa Goodman
Professor Eve Ostriker
Professor Stuart Vogel
Professor Richard Walker

Beyond the bright cartoons
Are darker spaces where
Small cloudy nests of stars
Seem to float on the air.

These have no proper names:
Men out alone at night
Never look up at them
For guidance or delight,

For such evasive dust
Can make so little clear:
Much less is known than not,
More far than near.

Philip Larkin
Far Out

Acknowledgments

I received a Bachelor's degree in Physics from Northwestern Unversity in 1992. Following graduation, I embarked on a career as a professional musician. I sang with a group called Blind Man's Bluff, and the experience was one of the happiest of my entire life. We performed at colleges and music festivals across the Eastern half of the U.S., from Vermilion, South Dakota to Pensacola, Florida, and from Arlington, Texas to Durham, New Hampshire. We made a lot of music, and we made a lot of people happy, and we had a blast doing it. Throughout all of the performances and rehearsals and the time spent in studio, I learned something that I'd often suspected but could never articulate. In the music world, very few people have the combination of training and talent and desire to become "experts" and create truly great music. There are many more people who are at the opposite end of the spectrum; these are the hack musicians. They may have the desire, but they lack the talent or the work ethic. They want to succeed more than they want to create great music, and sometimes, with luck or good looks, they do. Most musicians fall in between these two extremes. What I learned, time and time again, was that I was more of a hack than an expert. I had a decent singing voice and the willingness

to work hard, but I lacked some of the fundamentals: vocal training, a good ear, the ability to improvise. I came to realize that what I really wanted, more than a career in music, was to be an expert at something. I wanted to be truly *good* at something, and I felt that, with my untrained voice and my uncertain talent, I would never be truly good in the music world. At some point, I decided that the keys to becoming an expert were my intelligence and creativity and love for science.

During one of our stays at home in Chicago, I visited the Northwestern campus and knocked on the door of David Meyer. He had taught a class in optical spectroscopy that I had taken during my last semester. He remembered me (although not by name), and he was visibly startled to see me. I told him some stories about my life on the road, but I concluded by telling him that I had decided I wanted to go to graduate school to study astronomy. An exaggerated look of surprise spread over his face, then he smiled broadly and laughed out loud. He said, "You sing in a band! You drive around the country, you work only a couple of night a week, and you make good money. *Why the Hell do you want to go to grad school?*"

Now, after spending a total of ten years at three different institutions, I ask myself that question in the past tense. Why the Hell *did* I want to go to grad school? If I refer back to my original reason for going, then I'm a failure, because I know I'm still not an expert. I'm not an expert in astronomy or interferometry or star formation or even velocity fields in dense cores, for that matter. In many ways, I'm still a hack: just a hack astronomer rather than a hack musician. I have the desire to do something great. I can work hard and I have a love for science, but now I doubt my intelligence and creativity, the two qualities in which I once had such confidence. Hard work and a love for science won't make you an expert in astronomy; they just enable you to get enough work done to survive graduate school.

Although I'm not an expert, I've gained an enormous amount of knowledge during my graduate school adventure. I've also gained a little bit of wisdom, and on the whole, I've had a good time. When I first made the decision to study astronomy, getting a PhD degree was the summit of my personal mountain of aspirations. Now that I've reached this summit, however, I find that this adventure was only preparation for an assent on an even grander peak, on the higher slopes of which the aspirations of many others rest.

My career in astronomy began in 1994, when I volunteered as a research assistant to Ed Guinan at Villanova University. He introduced me to binary star astronomy and paid me for work that I would have gladly done for free. When I submitted my first AAS abstract, he punctuated my accomplishment by saying, "These are your first steps on the road to Hell." I am also grateful to Brian Abbott, Kunegunde Belle, and Larry DeWarf, who made me feel welcome during my first year back in an academic environment.

My enthusiasm for astronomy really gained momentum while I was a student at San Diego State University, where I got an intellectual kick-in-the-pants from Paul Etzel. He is a diligent scientist, an inspiring teacher, and a fountain of encouragement, and I am indebted to him for getting me to think about the question, "Where do binary stars come from?" My grad student role models at SDSU were Mark Lane, Jeff Mader, and Deron Pease, and my life both in and out of the office was enriched tremendously by the friendship of Anil Dosaj, Jiyune "Blinky" Lee, Grant Miller, Quyen (Nguyen) Hart, and John Whitmer.

At the University of Maryland, I owe the greatest debt of gratitude to Lee Mundy. He has endured my long, contemplative silences with fatherly patience. He has given serious consideration to my often inelegant questions. Most importantly, he has encouraged me to be a good scientist; he has challenged me to think on my feet,

to figure out the right questions to ask, and to not be afraid to state (supportable!) conclusions with conviction. I hope that I can continue to practice what he preaches when I no longer have him looking out for me.

The BIMA Embedded Cores Key Project would not have been successful without the support of Stuart Vogel. I am grateful to him, and to the rest of the BIMA Board, for insuring that the Project was granted sufficient observing time. I would also like to acknowledge Neal Evans, the principal investigator of the Spitzer c2d Legacy Project, who championed the BIMA Key Project from its beginning. I thank Andy Harris, Eve Ostriker, and Virginia Trimble for asking some of the most penetrating questions during the development of this dissertation. Mercifully, not all of their questions were focused directly at me, and sometimes, they answered their questions themselves. I am also grateful for the many helpful additions to this work suggested by Alyssa Goodman and Rich Walker, who served as committee members. I thank Mark Heyer for obtaining $C^{18}O$ observations (in support of this work) at FCRAO in May 2000, as well as for his assistance during my own FCRAO observing runs. I am also obliged to Friedrich Wyrowski, whose wizardry with CLASS software aided this work considerably. Dick Plambeck and Mel Wright taught me most of what I know about the nuts and bolts of interferometry, both during the BIMA summer school and after. All the things that I subsequently forgot, I learned again from Rick Forster, who may have the most saintly temperament of any man I've ever met.

Leslie Looney has been a long distance mentor throughout my grad school years. It was Leslie who first explained to me what an interferometer does, what u,v-visibilities are, and how to reduce data with MIRIAD. I am also indebted to Marc Pound, Peter Teuben, and Stephen White for their answers to my innumerable scientific and technical questions. These three are my "go to" guys in the Department; I hope that I haven't become the "go away" guy for them. I have benefitted im-

measurably from the friendship and intellectual camaraderie of many of my fellow graduate students, especially Yan Fernandez, Neil Nagar, Kartik Sheth, Sally Watt, Woong-Tae Kim, and the gang in the LMA Observatory Room who push me so hard to be smart: Nicholas Chapman, Rahul Shetty, Misty LaVigne, Elyse Casper, and Meredith McCarthy. I'm also particularly grateful for the companionship of Raquel "Biene" Fraga Encinas, who lets me pretend I'm much younger than I am.

I thank my parents, Lewis and Hella Volgenau, for their love and support, even if they didn't think that grad school was a healthy choice for me: physically, socially, or financially. I believe that they are partly responsible for my decision to study astronomy. My mother saw to it that "Guter Mond, du gehst so stille" was one of the first songs I ever heard, and my father pointed out the constellations to me from the end of our driveway. I also credit my father for showing me that science could be "cool" by dazzling my elementary school classmates with beakers full of "witch water" and "black liquor." I thank my sister, Teresa Ruth, for unknowingly pushing me to achieve. It's hard to be a big brother when your little sister is smarter, cleverer, and more resolute than you. I've been competing with her my entire life, even though she hasn't been competing with me. She will always be the person I most want to impress.

Finally, I acknowledge **the people who know that I'm not an expert and have aided or supported or encouraged or cheered or loved me anyway.** These are the people who have, in great and small ways, inspired me. These are the people who make me happy to be alive, and I wish that I could be more like them. I wish that I could list them all first. They are Tiffanie Heben, Jennifer Mulqueen, and Liz Danielian. They are Burr Hitchcock, Geoffrey Benjamin, and Elissa Knights. They are Jonathan Minkoff, Bryan Chadima, and Marc Lionetti, three truly "expert" musicians who let me sing with them for four years. The long

road to grad school was much more fun because of them. Alison (Hill) Tanner sent care packages, but knowing that she was proud of me gave me more energy than any candy bar. Rebecca Springer picked me up and set me on my feet more times than she'll ever know. Laura Amodei showed me how to live boldly and always saw the "scientist-poet" who dwelled inside me. And finally, there's Rachel Anne Lane. If I've ever had a muse, she's it. So much of what I do, I do for her. I hope that someday, she'll read this.

Contents

List of Tables

List of Figures

Chapter 1

Introduction

Stars emerge from cold, dense material in molecular clouds. Gravity compels the gas and dust to coalesce, but the clouds are supported against global collapse by a combination of agents, including thermal pressure, magnetic repulsion, and turbulent motion. In regions where gravity dominates, the clouds ultimately form stars; in regions where gravity is overcome, clouds remain dark. The details of the competition between gravity and the repulsive forces, however, are not yet thoroughly understood, and these details create the rich variety of observed star formation regions. The rate of Galactic star formation, the emergent distribution of stellar masses (the Initial Mass Function), and the prevalence of stellar multiplicity are all synthesized from the outcomes of individual star formation events. The goal of a complete star formation theory is to develop an analytical framework for these events that is illustrative, quantitative, and above all, predictive.

1.1 Dense Cores in Star Formation Theory

Molecular cloud cores represent the transitional step in the evolution from cloud to star. Cores are compact substructures that arise from temperature and density inhomogeneities within molecular clouds. They are typically elongated in shape (Myers *et al.* 1991), with dimensions on the order of 0.1 pc, and contain from one to a few solar masses of gas and dust. They have mean densities of 10^4-10^5 cm^{-3} and temperatures of $\sim$10 K (Myers & Benson 1983; Benson & Myers 1989). Although most cores are somewhat centrally condensed, their central densities must increase by many orders of magnitude in order to form stars.

Modern star formation theory is, essentially, a description of how this redistribution of mass is achieved. A point of departure for a modern theory is the work of Jeans (1902, 1928), who investigated the evolution of gravitational instabilities in an infinite, homogeneous, nonturbulent medium. Jeans determined that, for a particular density and temperature, the medium has a characteristic size at which a perturbation will induce a gravitational instability. This characteristic size, known as the Jeans length, is:

$$\lambda_J = c_s \sqrt{\frac{\pi}{G\rho_0}}, \tag{1.1}$$

where G is the gravitational constant, ρ_0 is the density of the medium, c_s is the sound speed. If the perturbation is spherical, then a sphere with a diameter of λ_J encloses a characteristic mass, known as a Jeans mass:

$$M_J = \rho_0 \left[\frac{4\pi}{3}\left(\frac{\lambda_J}{2}\right)^3\right] = \frac{\pi}{6}\left(\frac{\pi}{G}\right)^{\frac{3}{2}}\left(\frac{1}{\rho_0}\right)^{\frac{1}{2}} c_s^3. \tag{1.2}$$

Masses greater than M_J contained within a Jeans length will undergo spontaneous gravitational collapse. Although a universally homogeneous medium is an unrealistic description of the molecular cloud environment, the Jeans length and Jeans mass

nevertheless provide practical reference points for the scales at which gravitational collapse is likely to occur. For the density ($n = 10^4$ cm^{-3}) and temperature ($T =$ 10 K) of a typical core, the Jeans length is $\lambda_J = 0.2$ pc and the corresponding Jeans mass is $M_J = 2.8$ M$\odot$.

Another simple model for the initial conditions of star formation is an isothermal sphere of gas in hydrostatic equilibrium. The sphere resists collapse because gravity is offset by a pressure gradient. Ebert (1955) and Bonnor (1956) studied, independently, the effect of a sudden compression on an initially stable configuration. They found that hydrostatically balanced spheres become unstable to collapse if their mass-to-size ratio exceed a critical threshold. In the formulation of Bonnor (1956), the critical ratio is:

$$\left(\frac{M}{r}\right)_{crit} = 2.4\frac{kT}{mG} = 2.4\frac{c_s^2}{G}. \tag{1.3}$$

Thus, the critical mass within a sphere of radius r_{crit} is:

$$M_{crit} = 2.4\left[0.49\left(\frac{kT}{mG\rho_{crit}}\right)^{\frac{1}{2}}\right]\frac{kT}{mG} = 1.2c_s^3\frac{1}{G^{\frac{3}{2}}}\frac{1}{\rho_{crit}^{\frac{1}{2}}} = 1.2\frac{c_s^4}{G^{\frac{3}{2}}P_{crit}^{\frac{1}{2}}}, \tag{1.4}$$

where ρ_{crit} and P_{crit} are the density and pressure, respectively, at the surface of the sphere. Using a characteristic core density ($n = 10^4$ cm^{-3}) and temperature ($T = 10$ K) to calculate typical values, the critical radius is $r_{crit} = 0.2$ pc and the critical mass is $M_{crit} = 3.6$ M$\odot$.

Gas spheres that maintain hydrostatic equilibrium are now referred to as Bonnor-Ebert spheres in the vocabulary of star formation theory. Because gravity must be opposed by an internal pressure gradient, Bonnor-Ebert spheres have higher densities toward their centers. Higher mass Bonnor-Ebert spheres are more centrally condensed than lower mass spheres. At their innermost radii, the density is constant, and for most of their volume, the density profile is approximately proportional to r^{-2}. A perturbation that pushes the sphere beyond the critical mass-to-size ratio disrupts

the equilibrium, and the sphere succumbs to gravity. During the collapse, the sphere evolves on a free-fall timescale. Because free-fall time is inversely proportional to the square-root of the density (Spitzer 1978), the collapse accelerates near the center, and the sphere becomes highly centrally condensed. The collapse continues until the medium becomes optically thick (*i.e.* the sphere is no longer isothermal).

The problem of deriving a quantitative description of the collapse of an isothermal sphere has been the focus of thorough study over the past several decades. The "collapse problem" has been shown to have a continuum of analytical solutions (Whitworth & Summers 1985). The two best known and most widely applied solutions lie at extreme ends of this continuum. In the solution derived by Larson (1969) and Penston (1969), the initial configuration is a homogeneous sphere with a well-defined radius. Collapse begins simultaneously at all radii. Material falls inward at supersonic velocities that are 3.3 times the local sound speed. Before the formation of a central protostar, the density profile approaches a $\rho \propto r^{-2}$ dependence. After a central protostar has formed, the density profile at small radii evolves toward a $\rho \propto r^{-\frac{3}{2}}$ dependence (Hunter 1977). One signature of the Larson-Penston collapse solution is the decline in the mass accretion rate onto the protostar. The accretion rate begins at a maximum, when the high density material near the center falls onto the protostar, and diminishes as lower density material from larger radii reach the center.

The other extreme solution to the collapse problem was derived by Shu (1977). In this case, the initial configuration is a singular isothermal sphere, *i.e.* a sphere with $\rho \propto r^{-2}$ at all radii, and the collapse propagates outward from the center. Material at small radii freely fall inward, but material at larger radii remain suspended until the expanding "collapse wave" passes and pressure support drops out. Interior to the collapse wave, the density profile approaches a $\rho \propto r^{-\frac{3}{2}}$ dependence. Because of

the steep density gradient of the singular isothermal sphere, the mass accretion rate is intermediate to the Larson-Penston solution and constant in time ($\dot{\mathrm{M}}= 0.975\frac{c_s^3}{G}$).

The Larson-Penston and Shu collapse solutions are both predicated on unphysical initial conditions. In the former case, the isothermal sphere is homogeneous; in the latter case, the sphere has a central singularity and no fixed outer radius (and therefore infinite mass). Despite these shortcomings, both solutions provide a complete (*i.e.* instantaneous) description of the collapse evolution, and both solutions make quantitative predictions that can (in principle) be compared with observations.

Star formation theory acquires an additional dimension of complexity if the diverse magnetic fields that permeate molecular clouds are taken into account. Ions and charged dust grains respond to magnetic fields, and if the ionization fraction of a cloud is sufficiently high, then the field may be effectively "frozen" in the cloud. Because magnetic field lines resist compression, the ions bound to the field "push" against the neutral particles, mitigating the force of gravity. Thus, the presence of a magnetic field supplements hydrostatic pressure in opposing cloud collapse.

Magnetic fields also break the isotropy of the spherical collapse model. The field lines are inherently polar, but the resistance to field compression operates only in the transverse direction, *i.e.* across the field lines. Consequently, material motions in the sphere are affected by the magnetic field only along the velocity component perpendicular to the field lines. In the direction parallel to the field lines, material motion is unimpeded. For simple, straight field lines, the asymmetrical magnetic pressure and tension concentrate more material into a plane perpendicular to the polar field. The equilibrium geometry of a magnetized pre-collapse cloud, rather than being spherical, is more like an oblate spheroid with a large ($\frac{a}{b}$) axial ratio.

The introduction of magnetic fields creates a division between clouds in which the magnetic flux ($\Phi = \pi R^2 B$) is sufficient to withstand gravity and clouds in

which the magnetic flux is insufficient and collapse is inevitable. In the taxonomy of the standard star formation theory, the former case is a *subcritical* cloud, and the latter case is a *supercritical* cloud. At the boundary between the subcritical and supercritical cases, the magnetic pressure exactly balances the gravitational contraction. The mass-to-magnetic-flux ratio in the cloud is

$$\left(\frac{M}{\Phi}\right)_{crit} = \frac{\epsilon}{\sqrt{G}}, \tag{1.5}$$

where ϵ is a small number (< 1) with an exact value that depends on the geometry of the cloud. For a magnetic field strength of $B = 30$ μG, the critical ratio supports approximately 40 M$\odot$ within a cloud of diameter 0.4 pc.

In a supercritical cloud, the surge toward star formation proceeds on a free-fall timescale. In a subcritical cloud, gravity is held in check, but the cloud is not permanently immune to collapse. Star formation is still possible because a subcritical cloud can evolve toward a supercritical configuration through the quasi-static process of ambipolar diffusion. Neutral particles in the cloud respond to gravity and gradually accumulate in the center by slipping past the ions suspended in the magnetic field. Thus, ambipolar diffusion makes the cloud more centrally condensed without increasing the magnetic flux density. The timescale for redistributing the mass and pushing the cloud over the critical mass-to-flux ratio is a function of both the magnetic field strength and the ionization fraction. For reasonable values of these parameters ($B = 30$ μG, $X = 1.58 \times 10^{-7}$ Elmegreen (1979)), the ambipolar diffusion timescale is roughly an order of magnitude greater than the free-fall timescale.

Finally, introducing magnetic fields into star formation theory also provides an essential mechanism for the redistribution of angular momentum. Without a mechanism for transporting angular momentum during star formation, the conservation of angular momentum requires that, as a cloud condenses, its angular velocity must

increase by many orders of magnitude. As the collapsing material approaches stellar densities, the centrifugal force becomes strong enough to overcome gravity; material cannot continue to feed the forming star. Magnetic fields help solve the "angular momentum problem" by bridging the gap between the initial and final angular momentum distributions seen in visible stars. Because the field lines are frozen in the cloud by the ions, the lines share in both the radial and rotational motions of the collapsing envelope. These motions are oriented in the transverse direction, but they stimulate Alfvén waves that propagate *along* the field lines. The outgoing Alfvén waves provide an energy sink and retard the rotation. Moreover, if there is sufficient mass outside of the collapsing envelope, the angular momentum can be regulated by magnetic braking (Basu & Mouschovias 1994). The rotation decelerates because the frozen field lines couple the internal motion to the motion of the larger embedding cloud.

The current models of dense cores are the inheritors of all of the developments in star formation theory since Jeans. Fundamentally, cores begin as quiescent overdensities in molecular clouds; they are upheld by hydrostatic pressure and threaded by the Galactic magnetic field. Supercritical cores lack adequate support against gravity and collapse on a free-fall timescale to form high mass stars. Subcritical cores, in contrast, undergo a long period of quasi-static evolution while ambipolar diffusion gradually redistributes mass toward the center. When cores become sufficiently centrally condensed that the mass-to-flux ratio exceeds the critical limit, they collapse.

The object formed at the center of the core by the accumulation of infalling material is the nascent protostar. Because of the conservation of angular momentum and the magnetic field geometry, the infalling material rapidly forms a circumstellar disk around the accreting protostar. The subsequent evolution of the core is

measured by the development of these three structures: envelope, disk, and protostar. The spheroidal envelope rarefies as it deposits mass into the disk; the rotating disk expands (in radius) and flattens (in elevation) as it regulates the accretion rate; the protostar continues to grow until the mass reservoir is exhausted or the accretion flow is disrupted. This progression has been codified into a series of observationally defined stages. In the period immediately following the onset of collapse ($t \lesssim 10^4$ yr after collapse), the mass of the protostar is dwarfed by the mass in the envelope, which obscures all optical and near-infrared radiation at wavelengths less than 10 μm. At this stage, the protostar and its attendant envelope are called "Class 0" (André, Ward-Thompson, & Barsony 1993) or "extreme Class I" (Lada 1991) young stellar objects (YSOs). As the infall proceeds, the stages of protostar development are identified by their observed spectral index (a) in the near-infrared ($2 \lesssim \lambda \lesssim 20$ μm). In the formulation of Lada (1987), the spectral index is

$$a = \frac{d \log(\lambda F_\lambda)}{d \log \lambda}. \tag{1.6}$$

A "Class I" YSO has a positive spectral index ($0 < a < 3$), indicating that the slope of its spectral energy distribution (SED) rises toward longer wavelengths. A Class I protostar is an embedded object, and its SED is dominated by emission from the envelope. Protostars at later stages of evolution have negative spectral indices at near-infrared wavelengths and are called Class II and Class III YSOs. In these objects, the SED of the protostar is directly detected, and the longer wavelength radiation from the exposed disk is regarded as an "infrared excess" on a blackbody spectrum.

1.2 Comparing Star Formation Theory with Observations

The beauty of the star formation theory that has developed over the past several decades lies in its quantitative rigor and its predictive power. For a set of initial cloud parameters (mass, volume, temperature, magnetic field strength, ionization fraction, *etc.*), the theory gives a complete description of the cloud's evolution. It specifies *if* the cloud will collapse, *when* collapse will begin, and *how* the collapse will proceed.

Unfortunately, several assumptions upon which the theory rests are not justified by observations of Galactic star forming regions. Perhaps the most problematic assumption is that cores are isolated and immune to external influences throughout the star formation process. In the standard theory, low mass stars materialize from subcritical cores that undergo quasi-static, unperturbed ambipolar diffusion. Although this may be true for some stars, a preponderance of observational evidence shows that most stars form in environments that are neither isolated nor quiescent (Mac Low & Klessen 2004). Young stars are primarily found in clusters, not alone (Clarke, Bonnell, & Hillenbrand 2000; Lada & Lada 2003). The prevalence of clustered protostars strongly suggests that star formation in molecular clouds is a group event. This suggestion is further supported by the narrow age range of protostars in clusters (*e.g.* Bally, Devine, & Reipurth (1996); Lada, Alves, & Lada (1996); Hartmann (2001); Hillenbrand (1997)). The typical range ($t < 10^6$ yr) is considerably smaller than the characteristic timescale for ambipolar diffusion ($t \lesssim 10^7$ yr) (Shu, Adams, & Lizano 1987; McKee *et al.* 1993). If clusters form from the congregation of quiescent cores within a localized portion of a cloud, then the cores should join the cluster at different points in their pre-collapse evolution, and the age range of the en-

suing protostars should be several times the ambipolar diffusion timescale. In these "accidental" clusters, most cores should be in the starless, pre-collapse phase; only a fraction should contain accreting protostars. However, observations find roughly equal populations of pre-collapse and post-collapse cores (Ward-Thompson *et al.* 1994; Ward-Thompson, Motte, & André 1999).

In addition to sharing the same formative event, clustered protostars are near enough to affect each others' evolution. Such interaction clearly violates the standard theory's condition of isolation. High resolution observations reveal that cores do not have the expected density profiles (Looney, Mundy, & Welch 2000; Wilner *et al.* 2000); they are neither homogeneous spheres nor singular isothermal spheres. Most cores have elongated morphologies as well as complex emission features that cannot be satisfactorily explained by an axisymmetric model and projection effects (Myers *et al.* 1991).

The internal substructure of cores is clearly complicated by the effects of protostellar outflows. Embedded protostars produce high-velocity, bipolar outflows that disturb the surrounding core material (Snell, Loren, & Plambeck 1980; Shu 1997). These outflows, traced in the emission from CO and other molecular lines, are a natural consequence of the conservation of angular momentum in a collapsing core. Magnetic field lines, anchored in the ions of the rotating accretion disk, transfer angular momentum from the infalling material to a collimated, outflowing protostellar wind (Richer *et al.* 2000). Although the generation of outflows is accomodated by the standard theory, the effect of an outflow on other protostars in a cluster is not. Many outflows are several times longer than the dimensions of the core from which they originate (Bally & Devine 1994), and some clearly intersect with nearby cores (Bachiller *et al.* 1990). Outflow strength is correlated with the evolutionary stage of the generating protostar (Bontemps *et al.* 1996). Class 0 objects have outflows that

are powerful and well-collimated; Class I objects have weaker, poorly-collimated outflows (Hogerheijde *et al.* 1998). If the strength of an outflow depends upon the accretion rate, the diminishing power of an outflow implies that accretion is also declining (Richer *et al.* 2000; Hartigan, Edwards, & Ghandour 1995; Hartigan, Morse, & Raymond 1994).

Another manifestation of complex core substructure is the high rate of occurrence of multiple protostars within cores. The standard theory does not account for the formation of multiple stars, even though most stars are born into binary or multiple stellar systems (Mathieu *et al.* 2000). The most viable process for creating multiple stellar systems is core fragmentation (Larson 1995; Bodenheimer *et al.* 2000). In this scenario, multiple protostars originate from instabilities that disrupt the core before it becomes significantly centrally condensed. Numerical simulations indicate that cores with relatively flat ($\rho \propto r^{-1}$) density profiles are more likely to fragment than cores with steeper ($\rho \propto r^{-2}$) density profiles (Burkert, Bate, & Bodenheimer 1997). Therefore, fragmentation must occur early in a core's evolution, well before a density distribution resembling a singular isothermal sphere can be achieved by ambipolar diffusion. The observed multiplicity fraction in embedded (Class 0) YSOs confirms that multiplicity must originate very early in the star formation process (Looney, Mundy, & Welch 2000; White & Ghez 1997; Fuller, Ladd, & Hodapp 1996; Ghez, Neugebauer, & Matthews 1993).

1.3 Turbulent Star Formation Theory

In light of the discrepancies between the predictions of the standard theory and observations of star forming regions, a recent wave of theoretical work has reinvigorated the hypothesis that *turbulence* is an essential component of the star formation

process (Ostriker, Stone, & Gammie 2001; Burkert & Bodenheimer 2000; Klessen, Heitsch, & Mac Low 2000; Klessen & Burkert 2001). The idea of turbulence affecting star formation is not new (Chandrasekhar 1949), but it has undergone a renaissance in recent years because of the increasing resolution of millimeter and submillimeter observations and the increasing sophistication of numerical models. To be clear, the term "turbulence" refers simply to random motions in gas flows. Traditionally, turbulence is included in the standard theory only in the microturbulent approximation. In *microturbulence*, the size scale of turbulent motions is significantly smaller than the size scale for significant changes in density or the gravitational field. Consequently, microturbulence is treated like the thermal pressure: a process that solely contributes to the overall resistance of gravitational contraction.

The new theory includes both microturbulence and macroturbulent motions on a wide range of scales. *Macroturbulence* refers to motions on scales up to that of the entire core, and the aggregate effect of many individually turbulent cells. The gas in each cell emits a line profile characteristic of its particular environment, and each cell moves with a peculiar velocity. The observed line profile from a macroturbulent cloud is then the convolution of the emitted line profiles with all of the peculiar velocities of the cells along the line of sight.

The ubiquity of turbulence in the interstellar medium is inferred from the fractal structure of molecular clouds as well as the widths of molecular emission lines. Observed line widths exceed the thermal velocity dispersion,

$$\sigma_T = \sqrt{\frac{kT_k}{m_{obs}}}, \tag{1.7}$$

at kinetic temperatures appropriate for molecular clouds ($T_k \sim 10$ K), implying that the additional contribution to the line widths arises from macroturbulent motion. In large clouds ($\sim$100 pc), the dominant contribution to the line width is the turbulent component (Larson 1981). In cores, thermal and turbulent broadening are

comparable (Fuller & Myers 1992).

One of the remarkable innovations of the turbulent star formation theory, and also one of the crucial ways in which it differs from the standard theory, is that the effects of turbulence on all size scales are considered. Furthermore, turbulence is treated not merely as an inhibitive force (*e.g.* microturbulence), but as a force that can *both retard and accelerate* star formation. Turbulence is the fundamental factor that regulates the rate and the result of the star formation process. In the new theory, the entire range of interstellar clouds, from giant molecular clouds down to individual star-forming globules, arises from a background of multi-scaled turbulence. Molecular clouds are created not only by self-gravity, but also by compression where turbulent flows collide. In addition, such large-scale turbulence supports the clouds against catastrophic gravitational contraction. Numerical models of molecular clouds have demonstrated that although turbulence dissipates rapidly (Stone, Ostriker, & Gammie 1998; Gammie & Ostriker 1996), support for the clouds can be sustained with periodic injections of turbulent energy (Klessen & Burkert 2001).

Sustained, multi-scale turbulence creates within a molecular cloud a network of high-density, filamentary structures that form at the collision interfaces of turbulent flows. Because the turbulent energy cascades through a range of scales (Kolmogorov 1941), the filamentary network develops a self-similar pattern. In filaments where the density enhancements are sufficiently great to exceed the Jeans criterion, the material becomes unstable to gravitational collapse. The network is constantly changing, because not all filaments exceed this threshold, and the density enhancements may disperse again (Mac Low *et al.* 1994). If the interval between shock events (*e.g.* collisions of turbulent flows) is short, then a filament that was created by the first event may be disrupted by the second event. However, if the interval between events is longer, then the material in the filament may have time to become self-coherent and

withstand the passage of the second shock. These self-coherent objects, decoupled from the surrounding gas and sufficiently dense to undergo gravitational collapse, are protostellar cores. Because they are the products of interacting turbulent flows, their physical properties are expected to vary. Their emergence from filamentary structures provides a logical explanation for their observed elongations (Myers *et al.* 1991).

In numerical simulations of collapse conditions stimulated by turbulent interactions, dense cores that form stars resemble Bonnor-Ebert spheres (Ballesteros-Paredes, Klessen, & Vázquez-Semadeni 2003). They have flattened density distributions at their inner radii and distributions that decline according to a power law at large radii. However, unlike Bonnor-Ebert spheres, turbulence-generated cores are *not* in quasi-static configurations. This is another signature of the turbulent formation theory: the ambient medium is never static; dense cores are interactive and transient phenomena. The collapse of a gravitationally unstable core occurs on a dynamical timescale, *i.e.* star formation, when the conditions are right for it to occur, always occurs quickly. Moreover, the velocity field of gas within a core, the accretion rate of star formation events, and the mass distribution of the emergent stars are all critically dependent upon the local conditions at the collision interface. And the details of the collision, in turn, depend upon the driving strength and size of the generating turbulence.

Unlike the standard theory, in which the star formation rate is regulated by the balance between magnetostatic and pressure support and gravity, the new theory opposes gravity with supersonic turbulence. It is the balance between the wavelength of turbulent support and the local density of the cloud that regulates the star formation rate. In regions where turbulent support is lacking, collapse is rapid, star formation is efficient, and formation events tend to form a distribution of clus-

tered stars. Regions with abundant turbulent support are not, however, completely barren of protostars. Instead, numerical simulations (Klessen, Heitsch, & Mac Low 2000; Padoan *et al.* 2001) show that, although regions supported by large-scale turbulence are robust against catastrophic collapse, to entirely prevent collapse, the turbulence must support not only the *mean* density of the medium but also the isolated pockets of high density material (Mac Low & Klessen 2004). Thus, globally supported clouds may still produce isolated stars.

Aside from the central role of turbulence in both promoting and prohibiting star formation, the other fundamental difference between the new theory and the standard theory is that it is probabilistic, rather than deterministic. Given the physical parameters of an isolated cloud (density distribution, magnetic field strength, *etc.*), the standard theory can determine whether the cloud will collapse to form a star, and if so, what the structure of the cloud will look like throughout the collapse. Because the new theory describes star formation against a backdrop of randomly re-energized turbulence, the physical parameters of clouds are constantly changing. Thus, using a static cloud as a starting point is incongruous with the assumptions of the new theory. Instead, the theory describes the evolution of a *distribution* of initial conditions (*e.g.* a distribution of cloud densities, a power law cascade of turbulent perturbations) into a distribution of final states (*e.g.* an ensemble of stars) *without* specifying the details of individual collapse events. These events are assumed to occur rapidly (on a free-fall timescale), but the details of which cores condense to form stars and which do not are governed by a probability function.

1.4 The Role of Millimeter-wave Astronomy in Understanding Star Formation

This work seeks to determine whether the assertion that turbulence is central to the star formation process is justified by the velocity fields observed in dense cores. The investigation of core velocity fields is based upon observations of millimeter-wave continuum and line emission from cores in the Perseus molecular cloud complex. The observations were made with the Berkeley-Illinois-Maryland Association (BIMA) millimeter-wave interferometer (Welch *et al.* 1996) in Hat Creek, California and the Five Colleges Radio Astronomy Observatory (FCRAO) 14-meter antenna in the Quabbin Reservoir near Amherst, Massachusetts. Detailed descriptions of the data acquisition are given in Chapter 2. The observations are used to examine some of the basic physical properties of the cores. The continuum emission reveals the morphology of the envelope structure. The line emission traces the kinematics of the non-interacting gas, *i.e.* gas not associated with outflows. The motivation for this investigation is to define a diagnostic of the velocity data that measures the presence and scale of turbulence in cores.

Each core included in this study already has a forming young star (or multiple system) that is deeply embedded, *i.e.* a Class 0 object. The majority of the mass is contained in the envelope, rather than in the protostar. Although the dominant source of luminosity is the accretion onto the protostar, the density of the envelope absorbs the radiation at shorter (ultraviolet, optical, near-infrared) wavelengths. Observations at longer wavelengths (far-infrared, millimeter, radio) do not suffer from extinction and enable the envelope to be probed directly. The following subsections present the background needed to understand how millimeter emission arises from cores and how that emission is used as a diagnostic.

1.4.1 Millimeter Continuum Emission from Cores

The primary source of continuum emission from cores at millimeter wavelengths is the thermal emission from heated dust grains. Near the center of a core, grains are heated directly by radiation emitted from the accreting protostars. At larger radii, grains are heated by radiation that has been reprocessed by the interior dust grains. Thus, the envelope acts like a radiation filter: high-frequency radiation is absorbed by the grains, which then heat up and re-emit at lower frequencies. The radiation is released once it has been reprocessed down to frequencies at which the core material is optically thin. The global spectrum emitted by the dust is approximately a blackbody spectrum weighted by a dust opacity function that decreases as the frequency decreases according to a power law

$$\kappa_\nu = \kappa_0 \left(\frac{\nu}{\nu_0} \right)^\beta , \tag{1.8}$$

where κ_0 is the mass opacity (in $\mathrm{cm^2 g^{-1}}$) at a fiducial frequency ν_0 (Beckwith & Sargent 1991). This opacity function is not universal; it applies only to the range of frequencies where the core transmits radiation.

Beyond the opacity of the dust, the physical properties that contribute to the observed spectrum are parametrized by the dust temperature (T_d) and the density (ρ_d) distributions through the core. As introduced in §1.1, the density is typically simplified by using a power law dependence on radius,

$$\rho_d = \rho_0 \left(\frac{r}{r_0} \right)^{-p} , \tag{1.9}$$

with an exponent between $p = 1$ and $p = 2$. (The latter exponent is the case of the singular isothermal sphere.) The temperature distribution is also typically approximated by a power law that depends upon both the radial distance and the

luminosity of the central source:

$$T_d(r) = T_0 \left(\frac{L}{L_0}\right)^{\frac{q}{2}} \left(\frac{r}{r_0}\right)^{-q} \tag{1.10}$$

(Wilner, Welch, & Forster 1995; Wolfire & Cassinelli 1986). Because the temperature is coupled to the opacity of the dust, the power law index, q, is a function of the index of the opacity function: $q = \frac{2}{\beta+4}$.

All three parameters contributing to the core SED (ρ_d, T_d, κ_ν) are affected by the compositions and sizes of the individual grains. Grain compositions have been approximately determined from models that match the features of observed extinction curves with the absorption/emission features of grains constructed from metals commonly found in the dense ISM (Mathis, Rumpl, & Nordsieck 1977; Draine & Lee 1984). Results from these studies generally agree that the major constituents of interstellar dust are graphite, amorphous carbon, silicates, and more complex compounds that include elements like magnesium and iron. Fortunately, the rich variety of grain compositions has only modest effect upon the dust transmission properties at millimeter wavelengths (Wolfire & Churchwell 1994). Grain sizes, on the other hand, strongly influence the millimeter wavelength emission (Miyake & Nakagawa 1993). The distribution of grain sizes is commonly described by a steep power law (index$\geq$ 3); the smallest grains are the most abundant. (The plenitude of small grains, $0.01 > d > 0.1$ μm, is inferred from the sharp rise in extinction curves at optical and ultraviolet wavelengths.) The radiation at millimeter wavelengths is much larger than the typical grain size. If the grains are spherical, then the theoretical expectation is that the index of the opacity function will be $\beta = 2$. Observations indicate values in the range $1 < \beta < 2$ in the dense ISM, with $\beta \rightarrow 2$ for the diffuse ISM and $\beta \rightarrow 1$ for denser regions like circumstellar disks (Beckwith & Sargent 1991). Detailed modeling of the millimeter continuum emission is *not* a major component of this work. The purpose of introducing the complexities of the

origin of millimeter continuum emission is to acknowledge that there is a plurality in the physical properties that can generate the observed flux from a particular core. For this work, the overarching assumption is that the millimeter continuum emission is a reliable indicator of the column density of a core. Moreover, the column density is assumed to be an accurate tracer of the true distribution of mass in a core.

1.4.2 Molecular Line Emission from Cores

The majority of this work comprises the presentation and analysis of maps of molecular line emission from cores. Because of the high degree of extinction at optical and near-infrared wavelengths, molecular spectroscopy is one of the best methods for investigating dense core environments (van Dishoeck & Blake 1998; Blake 1997). Many molecules commonly found in the dense ISM undergo transitions between rotational states at energies that correspond to millimeter wavelength radiation. The rotational energy levels can be collisionally or radiatively excited at the densities and temperatures that prevail in cores.

The most abundant molecule in dense cores is diatomic hydrogen (H_2). Because H_2 is a homonuclear molecule, it has no electric dipole moment and thus it does not make simple (dipole) rotational transitions. (H_2 can cascade through *quadrupole* rotational transitions from an excited vibrational state.) Consequently, the emission from less abundant molecules must be used to trace the conditions of core gas. The most commonly employed gas tracer is carbon monoxide (CO), which is a diatomic, heteronuclear molecule with well-determined rotational energy levels. CO is abundant, relative to other molecules, and it is a chemically robust species with a high dissociation energy.

CO line fluxes are routinely used to infer column densities. Although the calculation of column density is subject to certain assumptions, the CO lines at millimeter

wavelengths ($J = 1 \rightarrow 0$,$J = 2 \rightarrow 1$) are generally accepted tracers of intermediate cloud densities (Evans 1999). One crucial assumption concerns the optical depth of the line: the flux accurately traces the column density only insofar as the line is optically thin. If the line becomes optically thick, then some of the emitting molecules are "hidden" by absorption along the line of sight. For this reason, the abundance of CO becomes a liability for observations of high density regions in molecular clouds. In these regions, tracing the column density requires the observations of emission from rarer CO isotopomers (^{13}CO, C^{18}O, and C^{17}O) whose lines remain optically thin. The goal is to observe a molecule that is sufficiently abundant for a line to be bright, but not *so* abundant that it becomes an unreliable column density tracer.

Of course, the purpose of observing molecular lines is not merely to determine column densities but to determine the actual physical conditions in the region where the molecules are emitting. Gas temperatures and densities can be estimated by examining the flux ratio of two transitions from the *same* molecular species. (Assuming that the lines are optically thin, then the emission traces the same molecules along the same lines of sight. Thus, the line ratio reflects changes in the environments generating the individual lines, rather than changes in spatial distribution or abundance.) For this work, observations were made of emission lines with frequencies $\nu \approx 100$ GHz (the $J = 1 \rightarrow 0$ transitions of three different molecules), so line ratios from the same species cannot be calculated.

For a core to produce a detectable rotational line, a significant fraction of the resident molecules must occupy the excited rotational energy state (in this case, $J = 1$). Molecules can be conveyed into the upper state either by collisional excitation, when they collide with other molecules in the medium, or by radiative excitation, when they absorb a photon of the appropriate frequency. *If* cores are sufficiently dense that the dominant source of rotational excitation is collisions with

H_2 molecules and He, and *if* the molecules are radiatively de-excited back to their ground rotational states, then the observed line flux can constrain estimates of the true core density. At a minimum, the density of the emitting region should be comparable to the critical density of the observed line. The *critical density* (n_{crit}) of a line is the density at which the collisional excitation rate (γ_{01}) and the radiative de-excitation rate (A_{10}) are equal, so this is also the density at which the population of molecules in the upper rotational state becomes significant. Following similar logic, the emitting region also has a maximum possible density.

For the maps of molecular line emission presented in the following chapters, the lines are assumed to be reliable tracers of the molecular distributions in the cores. Moreover, the lines are assumed to be emitted from regions with total particle densities that are on the order of the critical densities of the lines.

Characteristics of $C^{18}O$, $H^{13}CO^+$, and N_2H^+ Line Emission.

The principal molecular tracer observed for this work was the $C^{18}O$ $J = 1 \rightarrow 0$ transition at frequency $\nu = 109.782$ GHz. This line has a critical density of $n_{crit} \approx 4 \times 10^3$ cm^{-3}; it is an optically thin probe of core structure on all but the most opaque lines of sight (Alves, Lada, & Lada 1999; Kramer *et al.* 1999). The $C^{18}O$ abundance is not particularly affected by outflow activity or other energetic phenomena (like H_2CO, *etc.*), so the expectation is that all components of core kinematics (*e.g.* infall, rotation, turbulence) contribute to the observed line profiles.

A subset of the Perseus cores was also observed in the emission from two other molecular tracers: the $H^{13}CO^+$ $J = 1 \rightarrow 0$ line at $\nu = 86.754$ GHz, and the N_2H^+ $J = 1 \rightarrow 0$ line at $\nu = 93.176$ GHz. These lines have critical densities of $n_{crit} \approx 6 \times 10^5$ cm^{-3} and $n_{crit} \approx 7 \times 10^5$ cm^{-3}, respectively. Both of these lines are expected to be optically thin throughout the cores and trace material motions at even greater

densities than those probed by the $C^{18}O$ line. Several recent multi-line studies (Caselli *et al.* 2002a,b,c) indicate that N_2H^+ emission may be the most reliable tracer of structure in deeply embedded objects. The $H^{13}CO^+$ and N_2H^+ emission maps serve as important tests of the core structure and kinematics seen in the $C^{18}O$ data.

Because of the asymmetry of their nuclei, nitrogen atoms have permanent electric quadrupole moments, which interact with the orbiting electrons and affect the energies of N_2H^+ lines. Thus, the N_2H^+ $J = 1 \rightarrow 0$ rotational transition is split into seven hyperfine (hf) components. With the spectral resolution of our observations, six of the hf components are blended into two clusters of three lines. Because determining the characteristics of the core velocity fields is of paramount importance to this work, only the "isolated" hf component ($\nu(1_{01} \rightarrow 0_{12}) = 93.176310$ GHz) was mapped. Thus, the emission maps show lower intensities than would result from integrating over all seven hf components, but the velocity information is free of corruption from line blending.

Molecular Line Emission as a Tracer of Core Kinematics.

The observed emission is generated by gas-phase molecules embedded in the core material, and therefore, the characteristics of the line profiles offer "direct access" to the core motions. Unfortunately, only the velocity component along the line of sight, revealed by the Doppler shifting of line frequencies, can be detected. (The cores in the Perseus clouds are too distant to discern proper motions, except, perhaps, in extremely high-velocity outflows, see Girart & Acord (2001)). As the emission is optically thin, it traces velocities throughout the core volumes, but interpreting the observed lines is complicated by the fact that the profiles are integrated along the line of sight. The line profiles are further confused by the finite resolution of

the observations; the profile from a particular line of sight represents an average of the emitting components over the area of the beam. Disentangling the multiple contributions to a particular line profile is a tricky business.

The intensity of an emission line is a function of, essentially, three things: the number of emitting molecules along the line of sight, the temperature distribution of those molecules, and the filling fraction of the beam. Velocity information is encoded in the line by the Doppler shift, which affects the shape of the line and also displaces the center of the line from the rest frequency of the transition. The Doppler line broadening mechanisms on *microscopic* scales include thermal broadening and microturbulent broadening. In thermal broadening, the emitting molecules are assumed to have a Maxwellian velocity distribution that is described by a characteristic temperature. The thermal motion of the molecules affects the distribution of photon frequencies. Microturbulent broadening is a similar process, in that the turbulent motions of the molecules are often assumed to follow a Maxwellian distribution, but the characteristic velocity of the turbulence is different from the thermal velocity dispersion, and it is not dependent on the mass of the molecule. On *macroscopic* scales, the line broadening mechanisms may be either systematic (rotation, contraction, expansion) or unsystematic (macroturbulence). The signatures of these macroscopic broadening mechanisms in observed line profiles are described in the paragraphs below.

The topography of an observed line profile may be further complicated by absorption. The absorption signature may be isolated from the emission profile if the local standard of rest of the absorbing medium differs substantially from the local standard of rest of the emitting core. If, however, the absorption arises from material in the emitting core, the effects upon the observed profile can be both detrimental and beneficial. Self-absorption is clearly detrimental when it obfuscates

velocity information, *e.g.* an absorption dip at the center of a line mimics blended emission lines from two different sources. However, self-absorption is beneficial when it reveals velocity information, *e.g.* the inverse P Cygni profile that signifies infall (see below). Self-absorption is, of course, only relevant for lines with some degree of optical thickness, and therefore less important for the three lines considered in this work. For the $C^{18}O$ molecule, the abundance may be significantly great in the densest regions to induce a small amount of self-absorption.

Uniform Rotation. Pursuant to the standard theory of star formation, magnetic braking couples the motion of a core to the large-scale motion of the surrounding cloud. Numerical simulations (Basu & Mouschovias 1994) of idealized clouds under the influence of ambipolar diffusion and magnetic braking have shown that as a core becomes more centrally condensed, most of the volume and mass undergoes uniform rotation. Such core-wide rotation can be detected in the emission profiles of quiescent gas from variations in the central velocities (V_C) across the cores. A rotating core is distinguished by a velocity gradient centered on a position moving at the local standard of rest (V_{LSR}). The continuity of a gradient is the key to determining the nature of the motion: the velocity field of a uniformly rotating core shows a smooth gradient, whereas the velocity field of (for example) two contiguous gas clumps with different line-of-sight velocities shows a discontinuity at the clump interface.

Infall. Whether the collapse of a supercritical core more closely resembles the Larson-Penston or the inside-out model, the infalling material leaves its fingerprint on the emission profiles of moderately optically thick lines. Emission from the far side of the core (where material falls *toward* the observer) will be blueshifted, and emission from the near side (falling *away* from the observer) will be redshifted. The breadth of the (optically thin) extreme line wings is determined by the material infalling with the greatest velocity, near the central protostar. The (optically thick) line center arises from quiescent material in the outer envelope. Because the strongest redshifted emission lies *behind* the bulk of redshifted gas, whereas the strongest blueshifted emission lies *in front of* the bulk of blueshifted gas, the redshifted line is reduced by self-absorption. The resultant line shape is called an inverse P Cygni profile; it features a blueshifted emission peak and a redshifted absorption trough. To corroborate a diagnosis of infall motion, both optically thick and optically thin lines should be observed. The optically thin emission should peak at precisely the velocities where the optically thick emission is self-absorbed.

Outflow. As with core rotation, the detection of outflows from cores typically requires the combination of spatial and spectral information. Outflows burst out of the quiescent core material, and if they are fortuitously directed near the plane of the sky, then the emitting regions are well-separated from the core center. The emitting regions are also collimated, especially in outflows from the youngest, most deeply embedded objects (Bachiller 1996). Unless the outflows are exactly in the sky plane, the emission should also be well-separated from the core in *velocity* space. Line profiles from outflows have extremely blue- or redshifted wings. Outflows are preferentially detected by emission from molecular species that are abundant (*e.g.* CO) or are energized in the shocked regions where high-velocity gas strikes

the ambient medium. Some typical tracers of outflow-shocked material are SiO, CH_3OH, H_2CO, and HCN (Bachiller 1997). Although many of the cores observed for this work have associated outflows, the $C^{18}O$, $H^{13}CO^+$, and N_2H^+ molecules are tracers of quiescent gas and are not typically enhanced by outflow activity.

Turbulence. Identifying the effects of rotation, infall, and outflow upon a line profile is difficult. The three emission lines observed for this work minimize the "contamination" by infall and outflow motions. Because the lines are optically thin, infall motions shouldn't generate inverse P Cygni profiles. Because the lines are tracers of quiescent gas, outflows shouldn't generate high-velocity line wings. The lines should, however, trace rotation and infall motion of a core. Unlike infall, outflow, and rotation, turbulent motions in cores are unsystematic. Consequently, the velocity fields generated by turbulence should be stochastic. Unless the dominant scale of the turbulence is at the right wavelength to mimic core rotation (*c.f.* Burkert & Bodenheimer (2000)), the two processes should leave different signatures on the observed velocity fields. The fields may be complicated, however, by the degeneracy between turbulent motions within the core material itself and contributions to the emission from multiple regions with fractal structure along the same line of sight.

1.5 Outline

This investigation of turbulence in dense cores unfolds over five chapters. In Chapter 2, three cores (L1448 IRS3, NGC1333 IRAS2, and NGC1333 IRAS4) are presented as representatives of the BIMA Survey of the Perseus cloud complex. These cores are the most thoroughly studied objects in the survey, and they are used as a vehicle for introducing the observations that generated the reservoir of survey data. The types of maps created from these data, and the methods of analyzing the ve-

locity fields, are the same for all of the survey objects. Because the observed $C^{18}O$ emission may be affected by molecular depletion, Chapter 3 presents a study of depletion based upon radiative transfer models. Chapter 4 shows the results of the BIMA survey observations; intensity and velocity maps constructed from the $C^{18}O$ emission are presented for all of the survey targets. In Chapter 5, measurements of the $C^{18}O$ spectra are used to test for the presence of turbulence in the cores. Both the correlations between line width and spatial scale and the spatial variations of line properties (central velocities and line widths) are used to probe the presence and scale of turbulent motions in the cores. Chapter 6 provides a summary of the results and lists the conclusions.

Chapter 2

A Multiple Emission Line Study of L1448 IRS3, NGC1333 IRAS2, and NGC1333 IRAS4

2.1 Background and Motivation

From the Spring 1996 through the Winter 1998 observing seasons, a number of bright, nearby YSOs were surveyed with the Berkeley-Illinois-Maryland Association (BIMA) millimeter-wave interferometer as part of a Key Project to study the evolution of protostellar envelopes. The survey comprised a total of 24 Class 0, Class I, and Class II objects in the Perseus, Taurus, and Ophiuchus clouds. The observations were made of the $\lambda = 2.7$ mm continuum with the A, B, and C configurations of the array. (The observations are described in greater detail in §2.2 below). Looney (1998) analyzed these data in both the u,v and the image planes. The results of these analyses formed the basis for his thesis work, as well as two subsequent papers (Looney, Mundy, & Welch (2000, 2003), hereafter LMW00 and LMW03, respectively).

The $\lambda = 2.7$ mm continuum data revealed the plenitude of protostellar multiplic-

ity in the sub-sample of embedded (Class 0) systems. *All* of the embedded objects in the survey harbored multiple protostars. Furthermore, Looney found that the bulk of the emission from the embedded systems was produced by material in extended envelopes, far from the accreting protostars. On average, 85% or more of the $\lambda = 2.7$ mm continuum emission arises from extended structures, rather than embedded circumstellar disks. This discovery led to the conclusion that disk masses in Class 0 objects cannot be greater than the amount of circumstellar material implied by the power law density distribution of the envelope extrapolated into the center.

Because a high rate of stellar multiplicity is a prediction of a turbulent star formation theory, the results from the BIMA continuum data provide a natural stepping stone to an investigation of turbulence in embedded systems. Multiplicity suggests the turbulent fragmentation of a core, and the extended reservoir of envelope material revealed by the continuum emission suggests that there is sufficient mass (*not* associated with individual protostars) to trace the turbulence. The three objects featured in this chapter (L1448 IRS3, NGC1333 IRAS2, and NGC1333 IRAS4) represent the intersection of the protostar survey examined by LMW00 and LMW03 and the later survey of Perseus cores (described in Chapter 4). All three objects are dense cores within the Perseus cloud. They have all been observed in a wide range of wavelengths, and they are all bright in $\lambda = 2.7$ mm continuum emission. Furthermore, many of the $C^{18}O$ $J = 1 \rightarrow 0$ line observations that are the foundation of the velocity field study presented here were made simultaneously with the continuum observations.

Following descriptions of the observations (§2.2) and the data reduction and mapping procedure (§2.3), the three representative cores are presented in turn (§§2.4-2.6). A summary of the results from the LMW00 and LMW03 continuum studies is given prior to the presentation of the (new) molecular line data.

2.2 Observations

The embedded protostellar cores L1448 IRS3, NGC1333 IRAS2, and NGC1333 IRAS4 were observed with the Berkeley-Illinois-Maryland Association (BIMA) millimeter wave interferometer (Welch *et al.* 1996) in the $\lambda = 2.7$ mm continuum emission and in emission from several low excitation molecular lines. To obtain "zero-spacing" data, the line emission was also observed with the Five College Radio Astronomy Observatory (FCRAO) 14 m antenna. The results presented here are based upon the emission data from the $C^{18}O$ $J = 1 \rightarrow 0$ ($\nu = 109.782$ GHz), $H^{13}CO^+$ $J = 1 \rightarrow 0$ ($\nu = 86.754$ GHz), and N_2H^+ $J = 1 \rightarrow 0$ ($\nu = 93.176$ GHz) lines.

2.2.1 BIMA Observations

The BIMA observations of L1448 IRS3, NGC1333 IRAS2, and NGC1333 IRAS4 were made with the ten element array over several observing seasons. The observations of the $C^{18}O$ $J = 1 \rightarrow 0$ line and $\lambda = 2.7$ mm continuum were made with the A, B, and C configurations of the array during the Fall 1996 and Spring 1997 seasons. With good observing conditions, these configurations provide angular resolutions of approximately $0.6''$, $2''$, and $6''$, respectively. Observations with the D array configuration ($\sim 14''$ resolution) were made in the Spring 2000 observing season. Combining all array configurations, the longest available baseline is 1.9 km and the shortest baseline is set by the 6.1 m antenna diameter.

Coherent integration times on the target objects varied from 11.5 s (in A array) to 30 s (in D array), with observations of the calibrators interspersed every 70 s (A array) to 24 m (D array). The primary phase calibrator was 3C111. During the 1996/1997 observing seasons, its flux followed a well-monitored decline from 6.0 Jy to 3.7 Jy. By the 2000 observing season, its flux stabilized near 2.9 Jy. A secondary

phase calibrator, 0336+323, was also used in some observations. It has a more stable flux history. During the 1996/1997 seasons, its flux was 1.5 Jy; in the 2000 season, its flux reached a nadir at 0.9 Jy. The observing times for the calibrators varied from 23 s (A array) to 180 s (D array). The flux calibrators used were 3C273 in the A & B array and Mars in the C & D arrays.

The correlator spectrometer was configured to place the $C^{18}O$ line in an upper sideband window with 256 channels over a 25 MHz bandwidth, yielding a channel width of 0.27 km s^{-1}. The $\lambda = 2.7$ mm continuum was observed in the upper sideband with six 100 MHz windows; the continuum at $\lambda = 2.8$ mm was observed simultaneously in the lower sideband.

The observations in the $H^{13}CO^+$ and N_2H^+ emission lines were obtained with the B, C, and D configurations of the array during the Fall 2001 and Spring 2002 seasons. Additional B array observations of IRAS4 were obtained in Spring 2003. Coherent integration times were 11.5 s in B array and 23 s in the C & D arrays; phase calibration observations were interspersed every 12 m in B array and 24 m in the C & D arrays. The phase calibrator for these observations was 0336+323. During the 2001/2002 season, its flux gradually increased from 1.7 Jy to 2.0 Jy. By the time of the 2003 observations, the flux had declined to 1.5 Jy. Various flux calibrators were used, including 3C84, W3OH, Uranus, and Mars.

For the $H^{13}CO^+$ observations, the correlator was set to place the line in the lower sideband in a 256 channel window with 12.5 MHz bandwidth, yielding a channel width of 0.17 km s^{-1}. The continuum in each sideband was observed with four 100 MHz windows. The number of spectral windows and the bandwidths were the same for the N_2H^+ observations; the N_2H^+ line was observed in the upper sideband.

2.2.2 FCRAO Observations

Because the interferometer data are restricted to probing emission at specific spatial frequencies, maps constructed from these data alone naturally filter out emission from the larger cloud from which the cores condensed. Consequently, without information from broader spatial frequencies, the large-scale motions of the cloud would be masked out. To provide information on the larger scale emission surrounding the L1448 IRS3, NGC1333 IRAS2, and NGC1333 IRAS4 cores, single-dish observations were made with the FCRAO 14 m antenna. Maps of the $C^{18}O$ $J = 1 \rightarrow 0$ emission were obtained during the Summer 2000 observing season using the SEQUOIA 16-element receiver array in its "footprint" observing mode. The footprint is a 4×4 grid with individual receivers separated by one beamwidth ($44''$ for $\nu = 109.782$ GHz). A $6' \times 6'$ map was filled by shifting the footprint at 300 s intervals to provide half-beamwidth spatial sampling. Each field was observed only once, under good observing conditions with typical system temperatures of 250 K. The background was subtracted by frequency switching by 5 MHz. The $C^{18}O$ line was placed in the single sideband spectral window with a 20 MHz bandwidth and a channel width of 20 kHz. These channels were smoothed to 100 kHz to yield a velocity resolution of approximately 0.25 km s^{-1}. The pointing of the telescope was checked with observations of the IK Tau and Orion SiO masers before and after, respectively, the target observations.

The maps of the $H^{13}CO^+$ and N_2H^+ emission lines were acquired during the Winter 2002 observing season using the upgraded SEQUOIA receiver array in on-the-fly (OTF) observing mode. The new SEQUOIA features a dual IF capability that allowed the $H^{13}CO^+$ and N_2H^+ lines to be observed simultaneously. The OTF maps were acquired by first scanning the receiver array the length of the field in

Right Ascension, then shifting in Declination by half the beamwidth and scanning again. By including a full beamwidth (56.5″ and 52″ at the $H^{13}CO^+$ and N_2H^+ line frequencies, respectively) outside of the map area, the entire map gains half-beam sampling. For the L1448 cloud, the map area was $10' \times 8'$ (in Right Ascension and Declination, respectively). The area was observed three times, and each map required approximately 40 m to acquire. The entire NGC1333 region was mapped in a single $10' \times 24'$ area. This region was also observed three times, and each map was acquired in approximately 140 m. Background subtraction was achieved by position switching to emission-free regions beyond the edge of the Perseus cloud at $\Delta\alpha = -40', \Delta\delta = +20'$ for L1448, and $\Delta\alpha = -40', \Delta\delta = +20'$ for NGC1333. The $H^{13}CO^+$ and N_2H^+ lines were observed in spectral windows with channel widths of 25 kHz. The telescope pointing was checked with observations of the IK Tau and Orion SiO masers.

2.3 Data Reduction and Mapping

The BIMA data were reduced using the MIRIAD software package. Data from each observing track were calibrated independently, then all of the *u,v*-visibilities were combined and inverted simultaneously for mapping. Prior to inverting the line data, clean-component maps of the continuum data were subtracted from the *u,v* data. Maps were created with three different resolutions by weighting the visibilities by adjusting three different parameters: the cell size of the map, the FWHM of a 2D Gaussian function applied in the *u,v* plane, and a "robust" weighting parameter (Briggs, Schwab, & Sramek 1999). The dirty maps of the line data were cleaned down to the rms levels that yielded the lowest noise in the restored data cubes. Final maps were produced with resolutions of 10″, 5″, and 3″.

Maps were created from the FCRAO $C^{18}O$ observations by using the CLASS software package. The beam efficiency at 110 GHz was estimated to be $\eta_B(110\ \mathrm{GHz}) = 0.50$, yielding a temperature-to-flux conversion factor of 35.90 Jy/K. The $H^{13}CO^+$ and N_2H^+ observations were made in OTF mode; these maps were assembled with FCRAO's OTFTOOL. For these observations, the beam efficiencies were estimated to be $\eta_B(87\ \mathrm{GHz}) = 0.47$ and $\eta_B(93\ \mathrm{GHz}) = 0.49$, yielding temperature-to-flux conversion factors of 38.19 Jy/K and 36.63 Jy/K, respectively.

Four different methods of combining the BIMA and FCRAO data were tested: (1) the MIRIAD task `immerge`, (2) the MIRIAD task `mosmem`, (3) the linear combination method described by Stanimirović *et al.* (1999), as modified by Helfer *et al.* (2003), and (4) the AIPS task `VTESS`. For the tests, simple emission models (*e.g.* blackbodies at known distances) were created with the spatial and spectral resolutions of the BIMA and FCRAO data. Although each method had strengths and weaknesses, we elected to use the `VTESS` method for two primary reasons. `VTESS` accommodated the edge of the BIMA primary beam, and the `VTESS`-combined maps had the greatest flux fidelity in the full range of spatial scales present in the sources.

`VTESS` uses a maximum entropy algorithm to jointly deconvolve the BIMA and FCRAO datasets and form a single image of the field. There are three key input parameters: the number of iterations, the total flux in the map, and the target rms residuals for each input map. The number of iterations must be large enough to yield a consistent peak flux. The flux of the FCRAO map was chosen as an initial estimate for the total flux in the combined map; `VTESS` then refined this estimate. The rms noise levels in the individual maps were used as initial estimates for the target residuals, but the final residuals were consistently smaller than these values (see Figure 2.1*c,f,i*). The quality of the output maps was most dependent on this parameter. Because the `VTESS` algorithm is sensitive to abrupt flux changes

("sharp edges"), the boundaries of the FCRAO maps were tapered to gradually decline to zero flux. A boxcar smoothing algorithm was applied to extend the map to unobserved pixels; pixels representing observed emission were not affected.

The quality of a particular `VTESS` solution was assessed by comparing the output map with both input maps. For a comparison with the FCRAO map (Figure 2.1*d*), the combined map (Figure 2.1*e*) was convolved to the FCRAO resolution and then subtracted from the FCRAO map to create a residual map (Figure 2.1*f*). For a comparison with the BIMA map (Figure 2.1*g*), the combined map (Figure 2.1*h*) was weighted by the BIMA primary beam and "re-observed" with the BIMA *u,v*-spacings. The new *u,v*-data were then inverted and subtracted from the original BIMA map to create a residual map (Figure 2.1*i*). High-quality combined maps yielded small, uniformly-distributed residuals. When the best set of input parameters was determined, final maps (Figure 2.1*a*) were created by adding residuals (Figure 2.1*c*) to the `VTESS`-combined maps convolved with the BIMA synthesized beam (Figure 2.1*b*). Only the BIMA maps with resolutions of $10''$ and $5''$ were combined with the FCRAO data; the maps with $3''$ resolution were made with the BIMA data alone using the standard MIRIAD tasks.

2.4 L1448 IRS3

2.4.1 Background

Wide-field maps of the visual extinction (Cernicharo & Bachiller 1984; Cernicharo, Bachiller, & Duvert 1985) and CO emission (Bachiller & Cernicharo 1986a) of the Perseus molecular cloud complex show the L1448 dark cloud (Lynds 1962) near its western extreme. As defined by its NH_3 $(1,1)$ emission (Bachiller & Cernicharo 1986a), L1448 is roughly $11.5' \times 5'$ in size, elongated in the east-west direction. Based

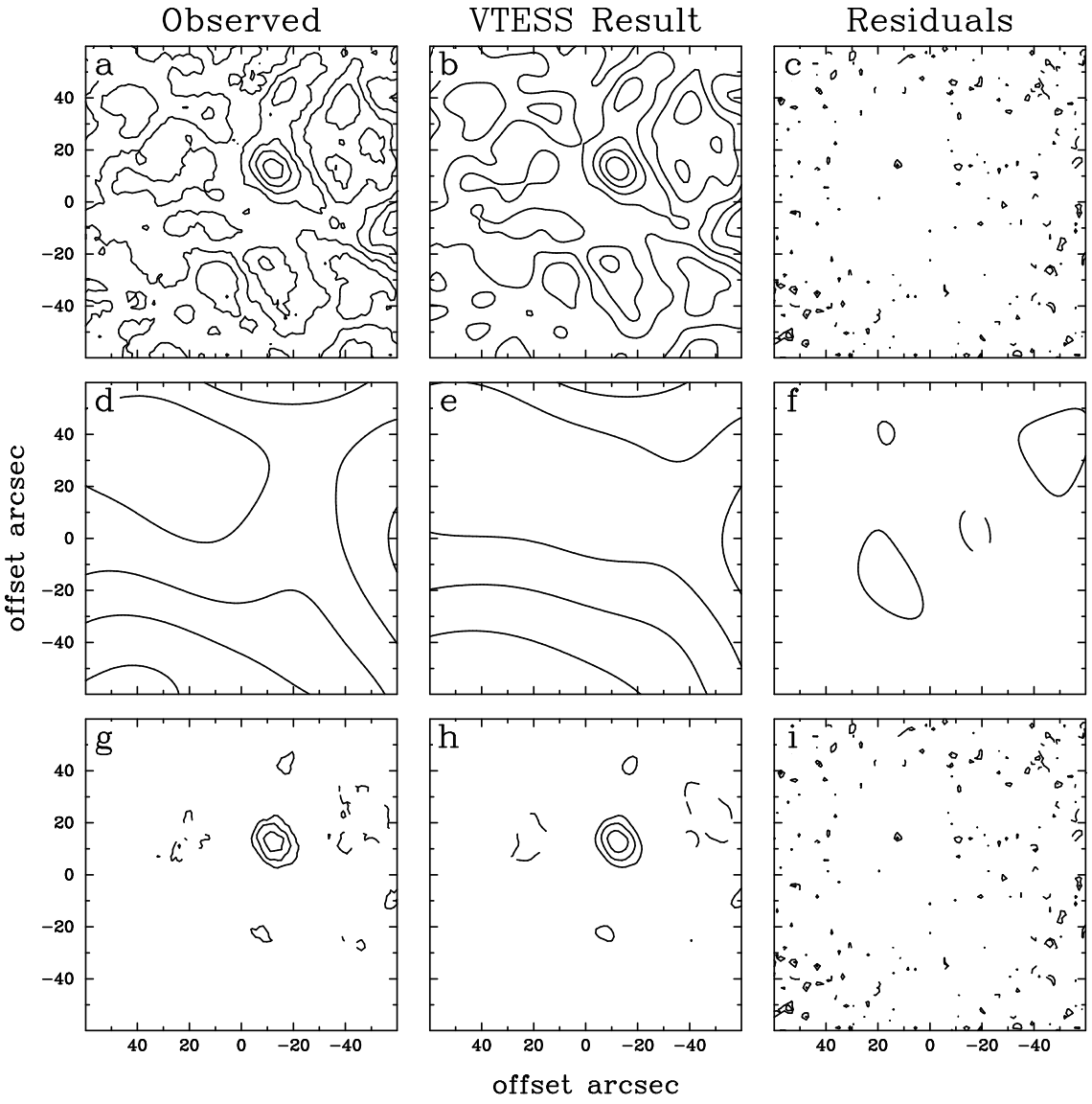

Figure 2.1: The panels show different steps in combining a single plane of the BIMA and FCRAO $C^{18}O$ datacubes with the `VTESS` algorithm. In each figure, the area shown is approximately the area of the BIMA primary beam. (a) Final restored map showing combined BIMA and FCRAO data at $10''$ resolution. Contours are $(2, 3, 4, 5, 6, 7) \times \sigma = 0.53$ Jy beam^{-1}. (b) `VTESS` map showing combined BIMA and FCRAO data at $10''$ resolution. Contours are $(2, 3, 4, 5, 6, 7) \times \sigma = 0.51$ Jy beam^{-1}. (c) Residual map of combined BIMA and FCRAO data at $10''$ resolution. Contours are $(-3, -2, 2, 3) \times \sigma = 0.061$ Jy beam^{-1}. (d) FCRAO dirty map at $55''$ resolution. Contours are $(7, 8, 9, 10, 11) \times \sigma = 5.70$ Jy beam^{-1}. (e) `VTESS` map convolved to FCRAO ($55''$) resolution. Contours are $(8, 9, 10, 11) \times \sigma = 5.47$ Jy beam^{-1}. (f) Residual map of FCRAO data at $55''$ resolution. Contours are $(-2, 2) \times \sigma = 1.03$ Jy beam^{-1}. (g) BIMA dirty map at $10''$ resolution. Contours are $(-2, 2, 3, 4) \times \sigma = 0.42$ Jy beam^{-1}. (h) `VTESS` map "re-observed" with BIMA u,v-spacings. Contours are $(-2, 2, 3, 4) \times \sigma = 0.40$ Jy beam^{-1}. (i) Residual map of BIMA data at $10''$ resolution. Contours are $(-3, -2, 2, 3) \times \sigma = 0.061$ Jy beam^{-1}.

on its NH_3 column density, the mass of the L1448 core is estimated at 50-60 $M\odot$ (Bachiller & Cernicharo 1986a; Anglada *et al.* 1989). Estimates of the distance to L1448 range from 220 pc (Černis 1990) to 350 pc (Herbig & Jones 1983). To remain consistent with the work of LMW00, a distance of 300 pc is adopted; this value is based upon the extinction mapping of Cernicharo, Bachiller, & Duvert (1985).

The L1448 cloud hosts three IRAS point sources. L1448 IRS1 (IRAS 03220+3035) lies on the perimeter of the NH_3 core to the west. IRS1 is observable at visible wavelengths ($m_V = 19.5$, Cohen & Kuhi (1979)) and appears at the vertex of the wedge-shaped reflection nebula RNO13 (Cohen 1980). IRS1 may be the driving source of an east-west outflow that generates a band of H_2 $1 \rightarrow 0$ $S(1)$ emission knots $\sim 30''$ to the east (Eislöffel 2000) and HH194 approximately $2'$ to the west (Bally *et al.* 1997). Its Spectral Energy Distribution (SED) (Ladd, Lada, & Myers 1993) identifies it as either a Class 1 (Wolf-Chase, Barsony, & O'Linger 2000) or Class 2 (Bally *et al.* 1997) YSO. L1448 IRS2 (IRAS 03222+3034) lies about $3'$ west of the density peak of the NH_3 core (Anglada *et al.* 1989). [L1448 IRS2 is a source included in the BIMA survey of Perseus cores, and it is described in greater detail in Chapter 4.]

L1448 IRS3 (IRAS 03225+3034), the brightest of the three in the IRAS bands, lies in the center of the NH_3 cloud (Bachiller & Cernicharo 1986b). IRS3, also dubbed L1448N, is now known to comprise three separate sources (Reipurth *et al.* 2002), all likely Class 0 YSOs (Barsony *et al.* 1998). L1448N(A) was first detected at $\lambda = 2,6$ cm by Curiel *et al.* (1990), coincident with the position of a $\lambda = 6$ cm source seen in a lower resolution map by Anglada *et al.* (1989) and also a strong H_2O maser (Anglada *et al.* 1989; Persi, Palagi, & Felli 1994). L1448N(B), located $6''$ southwest of L1448N(A) (Terebey & Padgett 1997), is a weaker source at centimeter wavelengths (Curiel *et al.* 1990), but dominates the emission at millimeter

wavelengths (Terebey & Padgett 1997). The combined flux from the A-B pair at $\lambda = 2.7$ mm is 185 mJy (in a $7\farcs5 \times 6\farcs6$ beam); the combined bolometric luminosity is estimated to be $\sim$10 L$\odot$ (Terebey, Chandler, & André 1993; Barsony *et al.* 1998). Although their SEDs differ, the proximity of A and B suggests that they are a proto-binary system. Both Barsony *et al.* (1998) and LMW00 speculate that they may be contained in a common envelope; the former study estimates a circumbinary structure containing 1.4 M$\odot$ of material. Interferometric observations at $\lambda = 2.7$ mm led to the detection of L1448NW, which lies approximately $20''$ northwest of the A-B pair (Terebey & Padgett 1997). The separation from the putative binary is sufficient to allow Barsony *et al.* (1998) to isolate the source in their sub-millimeter and millimeter observations and independently fit its SED. They estimated a bolometric luminosity of 2.7 L$\odot$ and an envelope mass of $\sim$0.8 M$\odot$.

The L1448 IRS3 region is permeated by a network of outflows, and all three cores have been identified as outflow sources. L1448N(A) displays an outflow in CO $J = 1 \rightarrow 0$ emission (Bachiller *et al.* 1995) with a redshifted lobe that extends southward for $\sim 7'$ (Wolf-Chase, Barsony, & O'Linger 2000) along a position angle of 150°. This outflow is believed to activate the H_2 emission knots T-Z (Barsony *et al.* 1998). The blueshifted lobe of L1448N(A), which was expected northward of the core, was not detected in the wide-field maps of Wolf-Chase, Barsony, & O'Linger (2000), suggesting that L1448N(A) may be near the edge of the L1448 cloud. The L1448N(B) outflow displays both redshifted and blueshifted lobes along a position angle of $\sim$129°. The redshifted lobe was first detected in CO maps by Bachiller *et al.* (1990). The opposing blueshifted lobe was suggested by the CO maps of Bontemps *et al.* (1996). The full extent of red and blue lobes was demarcated in the wide-field CO maps of Wolf-Chase, Barsony, & O'Linger (2000), who gave a "conservative" estimate of $12'$. On the blueshifted (north) side, the outflow jet intersects the HH196

emission knots (Bally *et al.* 1997), and its suspected interaction with one of the IRS2 outflows may be responsible for the bulges of CO emission observed just south of HH193 (Wolf-Chase, Barsony, & O'Linger 2000). The outflow from L1448NW is less conspicuous. Deep H_2 $1 \rightarrow 0$ $S(1)$ images by Eislöffel (2000) suggest that the outflow may be oriented at P.A.$\sim$90°, stimulating the emission knots "O", $1'$ to the east, and "P", $1'$ to the west.

In the discussions and analyses in this chapter, the nomenclature is as follows. L1448 refers to the entire emitting region included in the FCRAO maps; this region is also identified as the L1448 "cloud." The designation L1448 IRS3 refers to the central part of the cloud, which includes the three continuum sources L1448N(A), L1448N(B), and L1448NW. The region encompassing these three objects is also referred to as the "core." In contrast, the term "clump" is used to indicate any localized emitting region, whether or not it includes a continuum source. Finally, the narrowly separated objects L1448N(A) and L1448N(B) are often designated by the compound L1448N(AB).

2.4.2 Millimeter Continuum Emission.

Maps of the $\lambda = 2.7$ mm continuum emission from L1448 IRS3 are shown in Figure 2.2. (This is Figure 7 from LMW00.) The panels zoom in on L1448N(B), the strongest of the three continuum sources. In the high-resolution images, L1448N(B) displays a complex morphology and appears extended in the NE-SW direction, roughly perpendicular to the direction of its CO outflow. Based upon the observed morphology of the $\lambda = 2.7$ mm emission and the projected separation ($6.87''$(D=300 pc)=2060 AU) of L1448N(A) and L1448N(B), LMW00 consider the L1448N(AB) pair a "common envelope" system. Using a simple, isothermal model of optically thin emission with a uniform dust opacity, they estimate the individ-

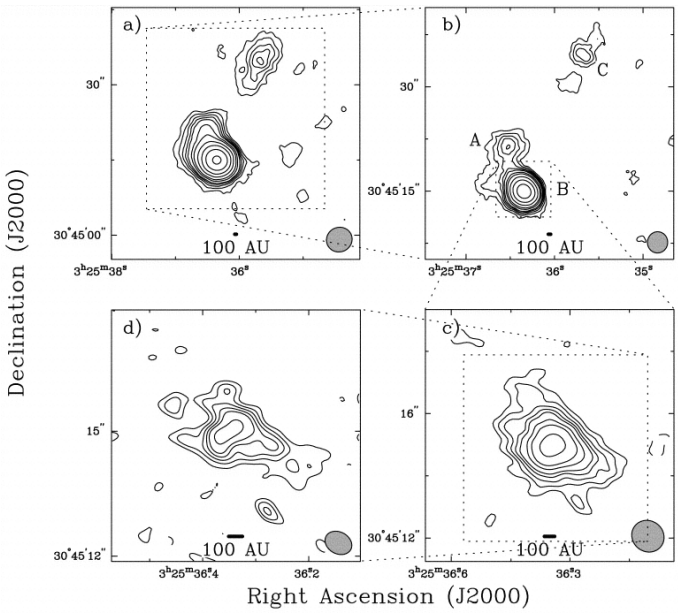

Figure 2.2: Maps of the $\lambda = 2.7$ mm continuum emission from L1448N(B). (Figure 7 from LMW00.) The panels indicate contours in steps of $(-4, -3, -2, 2, 3, 4, 5, 6, 8, 10, 14.14, 20, 28.28, 40, 56.56) \times \sigma$ in mJy beam^{-1}. (a) $\sigma = 1.6$ mJy beam^{-1}; beam is $5.22'' \times 4.89''$, P.A.$= -71°$. (b) $\sigma = 1.5$ mJy beam^{-1}; beam is $3.06'' \times 2.95''$, P.A.$= -61°$. (c) $\sigma = 1.6$ mJy beam^{-1}; beam is $1.08'' \times 0.99''$, P.A.$= 56°$. (d) $\sigma = 2.3$ mJy beam^{-1}; beam is $0.68'' \times 0.52''$, P.A.$= 63°$.

ual masses of the A and B envelopes to be 0.09 M$\odot$ and 0.52 M$\odot$, respectively. L1448NW, although a weaker emitter, is also detected down to sub-arcsecond resolutions. The same isothermal, optically thin model for the continuum emission leads to an estimated envelope mass of 0.12 M$\odot$.

2.4.3 Molecular Line Emission

Integrated intensity, line-of-sight velocity, and velocity dispersion maps of the $C^{18}O$, N_2H^+, and $H^{13}CO^+$ emission from L1448 IRS3 are displayed in Figures 2.3, 2.4, and 2.5, respectively. All three figures are organized identically. The panels in the left columns show the integrated intensity (0^{th} moment) evaluated over all channels in the line profile with signal greater than 3σ. The panels in the center columns show

the line-of-sight velocity fields (1^{st} moment). For all of the velocity maps presented in this and subsequent sections, the clip level for the calculation of the first moment was set at twice the noise level of a single channel. The panels in the right columns show the velocity dispersions (2^{nd} moment). Pixels in the velocity and dispersion maps at which the integrated intensity is less than 3σ are masked. The full range of velocities is indicated by the blue-to-red colorscale; the full range of dispersion is indicated by the grayscale. The ranges for both are reproduced in each row. The contours from the integrated intensity maps are superimposed on both the velocity and dispersion maps. The panels in the top rows (*a,b,c*) show the maps made from only the FCRAO data; the size of the field is approximately $6' \times 6'$. In the $C^{18}O$ maps (Figure 2.3), the resolution is $44''$; in the $H^{13}CO^+$ maps (Figure 2.4), the resolution is $56.5''$; in the N_2H^+ maps (Figure 2.5), the resolution is $52''$. The panels in the second row (*d,e,f*) show the combined BIMA and FCRAO data at $10''$ resolution. The panels in the third row (*g,h,i*) show the combined BIMA and FCRAO data at $5''$ resolution. The panels in the last row of Figure 2.3 (*j,k,l*) show only the BIMA data at $3''$ resolution.

$C^{18}O$ Maps

The FCRAO map (Figure 2.3*a*), encompasses nearly the entire L1448 cloud. The integrated intensity reaches a peak of 68.34 Jy beam^{-1}·km s^{-1} at $3^h25^m35\overset{s}{.}0$, $+30°45'22''$, less than half a beamwidth west of the L1448 IRS3 sources. The velocity map of the same region (Figure 2.3*b*) shows a smooth velocity gradient that runs from velocities near 4.0 km s^{-1} at the northern and western edges of the map to velocities near 5.0 km s^{-1} at the southern edge. The velocities across the area of the BIMA primary beam also vary smoothly in a northwest-to-southeast direction. The range of velocities for all of the $C^{18}O$ velocity maps (*b,e,h,k*) runs from 2.7 to 5.7 km s^{-1}.

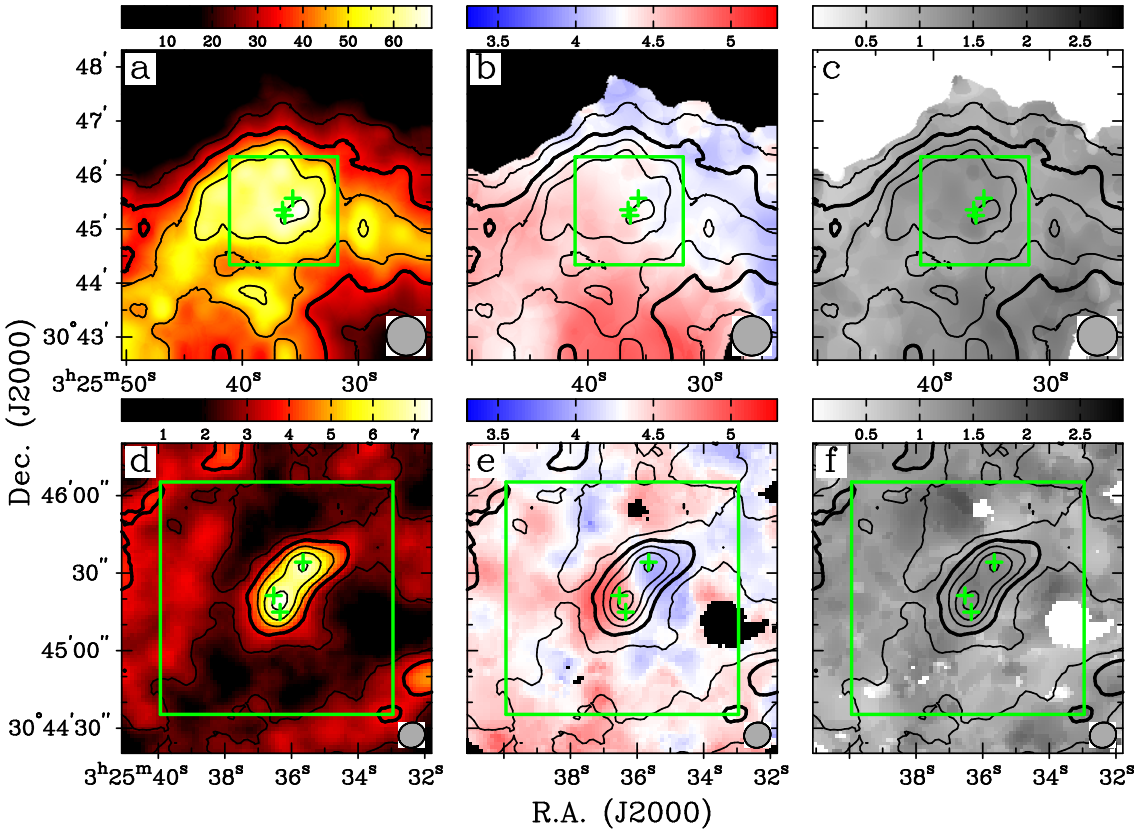

Figure 2.3: $C^{18}O$ $J = 1 \rightarrow 0$ integrated intensity, line-of-sight velocity, and velocity dispersion of L1448 IRS3. Panels *a,d,g,j* show integrated intensity in both contours and colorscale. Contour levels are 35%, 50%, 65%, 80%, and 95% of peak flux density; bold contour is 50% level. Panels *b,e,h,k* show integrated intensity contours and line-of-sight velocity in colorscale. Velocity range is 3.3-5.3 km s^{-1} in all panels. Panels *c,f,i,l* show integrated intensity contours and velocity dispersion in grayscale. Dispersion range is 0.0-2.85 km s^{-1} in all panels. Square regions delineated by green lines indicate areas in the next higher resolution maps. Plus symbols indicate positions of continuum sources from LMW00. (a,b,c) $I_\nu^{peak} = 68.34$ Jy beam^{-1}·km s^{-1}; $\sigma = 6.1$ Jy beam^{-1}·km s^{-1}; beam is $44'' \times 44''$. (d,e,f) $I_\nu^{peak} = 7.39$ Jy beam^{-1}·km s^{-1}; $\sigma = 0.53$ Jy beam^{-1}·km s^{-1}; beam is $10.39'' \times 9.61''$, P.A.$= -61.8°$.

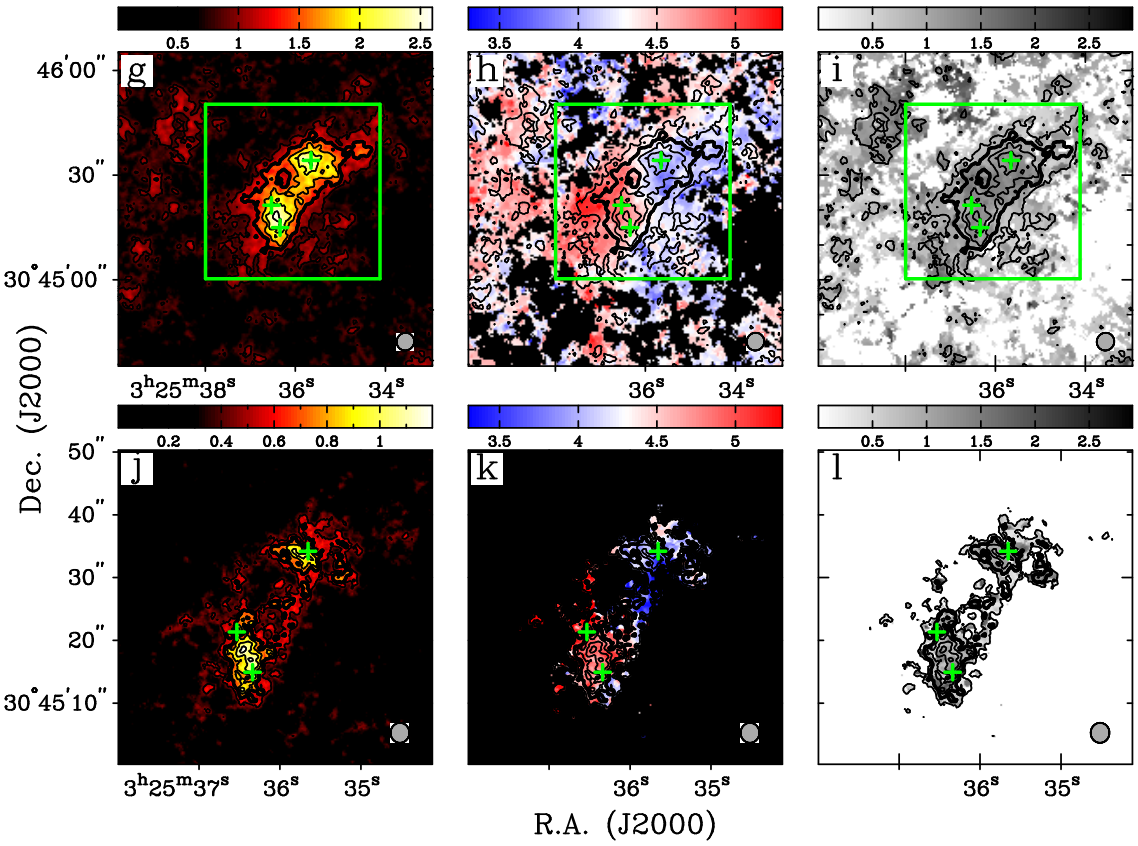

Figure 2.3: *Continued.* (g,h,i) I_ν^{peak} = 2.60 Jy beam^{-1}·km s^{-1}; σ = 0.20 Jy beam^{-1}·km s^{-1}; beam is 5.13″ × 4.97″, P.A.= −32.9°. (j,k,l) I_ν^{peak} = 1.17 Jy beam^{-1}·km s^{-1}; σ = 0.13 Jy beam^{-1}·km s^{-1}; beam is 3.18″ × 2.98″, P.A.= −2.0°.

The most prominent feature in the 10″ resolution intensity map (Figure 2.3*d*), is the oblong shape of the high emission contours surrounding the continuum sources. The peak intensity of the map, 7.4 Jy beam^{-1}·km s^{-1}, appears in between L1448N(A) and L1448N(B). The emission region surrounding the L1448N(AB) pair is slightly extended toward the southwest of L1448N(B). A second, separate emission peak, 7.2 Jy beam^{-1}·km s^{-1}, appears near the position of L1448NW. This emission region is also extended, jutting west-northwest of L1448NW. In the velocity map of the same area (Figure 2.3*e*), the corners of the map show the gradual blueshifted (northwest) to redshifted (southeast) gradient that is apparent in the FCRAO map. The most pronounced contrast in the velocity field is nearly coincident with the elongated

emission region around the IRS3 sources. The blueshifted extreme, 4.0 km s^{-1}, appears 9″ southwest of L1448NW; the redshifted extreme, 5.0 km s^{-1}, appears 10″ east of L1448N(A). The line connecting the velocity extremes (P.A.∼102°) does *not* coincide with the line connecting the $C^{18}O$ emission peaks (P.A.∼149°).

At 5″ resolution (Figure 2.3*g*), the peak emission region surrounding L1448N(AB) is extended in the north-south direction along the line connecting the continuum sources (P.A.∼18°). Between the L1448N(A) and L1448N(B), the emission peak is 2.6 Jy $beam^{-1}$·km s^{-1}. A region of extended lower-level emission stretches in a northeast-southwest direction (P.A.∼62°). At the position of L1448NW, the emission peak is 2.5 Jy $beam^{-1}$·km s^{-1}, and lower-level emission stretches to the west-northwest. The velocity map (Figure 2.3*h*) emphasizes the features that were revealed at 10″ resolution: the extreme velocities range from 3.7 km s^{-1} to 5.3 km s^{-1}, and the locations of these extremes are offset from the emission peaks. The blueshifted extreme is 5″ southwest of L1448NW, and the redshifted extreme is 13″ east of L1448N(A). The position of a line connection these positions (P.A.∼97°) remains offset from the L1448N(AB)-L1448NW axis.

The $C^{18}O$ intensity map with 3″ resolution (Figure 2.3*j*) shows a narrow (∼1 beamwidth) bridge of emission between L1448NW and L1448N(AB). The emission region surrounding the L1448N(AB) pair is greater than three beamwidths in length, but separate envelopes remain unresolved. The peak intensity between L1448N(A) and L1448N(B) is 1.2 Jy $beam^{-1}$·km s^{-1}. At L1448NW, which is also surrounded by an elongated emission region, the peak intensity is 1.0 Jy $beam^{-1}$·km s^{-1}. In the velocity map (Figure 1*k*), the emission region surrounding L1448N(AB) shows a smooth gradient from values < 3.9 km s^{-1} at the southern edge to > 5.4 km s^{-1} at the northern edge. The region surrounding L1448NW also exhibits gradients across the position of the continuum source, with bluer velocities (< 3.0 km s^{-1}) at the

southern and western edges, and redder velocities (> 4.6 km s^{-1}) at the northern and eastern edges.

$H^{13}CO^+$ Maps

The FCRAO map of the $H^{13}CO^+$ emission is shown in Figure 2.4*a*. The $H^{13}CO^+$ emission is clearly more compact than the $C^{18}O$ emission. The overall shape of the cloud is the same, but the emission drops off more steeply outside of the BIMA primary beam area (green square). The emission peak, 52.0 Jy beam^{-1}·km s^{-1}, lies in the midst of the L1448N sources. The velocity map of the area (Figure 2.4*b*) shows the same characteristics as the $C^{18}O$ velocity map at a comparable resolution. The range of velocities in the map is 1.5 km s^{-1}: the bluest velocity (3.9 km s^{-1}) appears at the western edge of the map, and the reddest velocity (5.4 km s^{-1}) appears in the southern part of the cloud. Within the primary beam area, the velocity gradient is in the northwest-southeast direction.

In the $10''$ resolution intensity map (Figure 2.4*d*), the $H^{13}CO^+$ emission contours reveal several elongated structures. As in the $C^{18}O$ maps at this resolution, the emission peaks are centered near L1448N(AB) and L1448NW; the peak intensities are 3.5 Jy beam^{-1}·km s^{-1} and 3.4 Jy beam^{-1}·km s^{-1}, respectively. However, unlike the oblong shape of the high $C^{18}O$ emission contours, the $H^{13}CO^+$ emission region appears more distorted. L1448N(AB) appear near the vertex of two elongated regions of emission, one extending to the east and the other extending to the southwest. Lower-level $H^{13}CO^+$ emission also extends away from L1448NW to the north and west. The most conspicuous feature of the velocity map (Figure 2.4*e*) is the clear division between the blueshifted western half and the redshifted eastern half. L1448N(B) lies near the V_{LSR} velocity at 4.7 km s^{-1}, and L1448N(A) is clearly redshifted (5.0 km s^{-1}), although the maximum redshift lies more than a

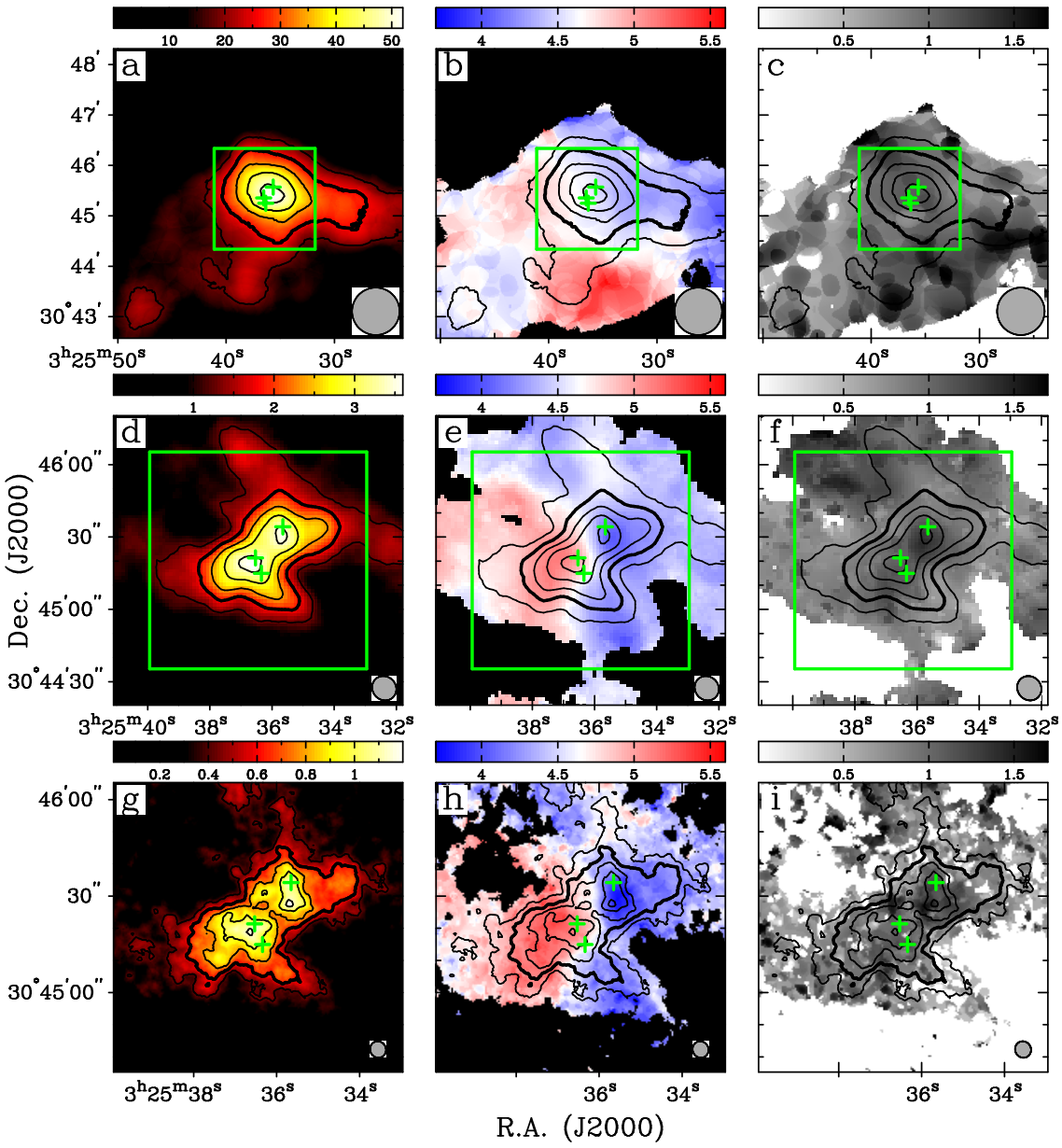

Figure 2.4: $H^{13}CO^+$ $J = 1 \rightarrow 0$ integrated intensity, line-of-sight velocity, and velocity dispersion of L1448 IRS3. Panels *a,d,g* show integrated intensity in both contours and colorscale. Contour levels are 35%, 50%, 65%, 80%, and 95% of peak flux density; bold contour is 50% level. Panels *b,e,h* show integrated intensity contours and line-of-sight velocity in colorscale. Velocity range is 3.7-5.6 km s^{-1} in all panels. Panels *c,f,i* show integrated intensity contours and velocity dispersion in grayscale. Dispersion range is 0.0-1.64 km s^{-1} in all panels. Square regions delineated by green lines indicate areas of the maps in the row immediately below. Plus symbols indicate positions of continuum sources from LMW00. (a,b,c) I_ν^{peak} = 51.96 Jy beam^{-1}·km s^{-1}; σ = 2.3 Jy beam^{-1}·km s^{-1}; beam is 56.5″×56.5″. (d,e,f) I_ν^{peak} = 3.51 Jy beam^{-1}·km s^{-1}; σ = 0.21 Jy beam^{-1}·km s^{-1}; beam is 10.49″ × 9.66″, P.A.= 43.5°. (g,h,i) I_ν^{peak} = 1.18 Jy beam^{-1}·km s^{-1}; σ = 0.08 Jy beam^{-1}·km s^{-1}; beam is 5.19″ × 4.91″, P.A.= 29.2°.

beamwidth ($\sim$11″) further east. L1448NW is clearly blueshifted (4.2 km s^{-1}), but the local maximum blueshifted velocity lies about half a beamwidth ($\sim$4″) to the southwest. Another blueshifted region is $\sim$43″ south of this point, coincident with the emission region extending southwest of L1448N(B).

The emission regions surrounding L1448N(AB) and L1448NW are more clearly separated in the 5″ resolution map (Figure 2.4*g*), although the components of the L1448N(AB) pair are still unresolved. The L1448N(AB) peak is 1.1 Jy beam^{-1}·km s^{-1}, and the L1448NW peak is 1.2 Jy beam^{-1}·km s^{-1}. The morphology of the extended regions of lower-level emission in the 10″ map persist at this resolution. Emission extends to the east and southwest of L1448N(AB) and west and north of L1448NW. In the corresponding velocity map (Figure 2.4*h*), the division into blueshifted (west) and redshifted (east) halves is apparent. The intermediate velocity, in between L1448N(A) and L1448NW is $\sim$4.7 km s^{-1}. The velocity at L1448N(B) is $\sim$4.8 km s^{-1}. In the redshifted half of the map, the positions of maximum velocity ($\gtrsim$ 5.2 km s^{-1}) are all at least one beamwidth eastward of L1448N(AB). The maximum blueshift ($\sim$3.8 km s^{-1}) appears approximately one beamwidth south of the position of the L1448NW. The emission region extending southwest of L1448N(B) is blueshifted at a velocity of $\sim$4.1 km s^{-1}.

Maps showing the integrated intensity and velocity of the $H^{13}CO^+$ emission at 3″ resolution are not included in Figure 2.4. The emission consists of a number of unresolved emission peaks spread out over the core. The noise level in the intensity map is $\sigma = 0.07$ Jy beam^{-1}·km s^{-1}. The highest emission peaks occur in the vicinity of L1448N(B) at $\gtrsim 5\sigma$.

N_2H^+ Maps

The N_2H^+ observations of L1448 IRS3 are presented in Figure 2.5. The integrated intensity map of the FCRAO data alone (Figure 2.5*a*) shows that the N_2H^+ emission from the L1448 cloud is, like the $H^{13}CO^+$, more compact than the $C^{18}O$ emission. The intensity peak, 34.6 Jy beam^{-1}·km s^{-1}, is near the center of the cloud, just west of the position of L1448NW. In the velocity map (Figure 2.5*b*), the extreme blueshifted velocities (4.1 km s^{-1}) are at the western edge of the map, and the extreme redshifted velocities (5.6 km s^{-1}) are at the southern end. Within the area of the BIMA primary beam, the bluer velocities appear in the northwest corner, the redder velocities appear in the southeast corner, and the gradient between these extremes is smooth.

In the 10″ resolution map (Figure 2.5*d*), the N_2H^+ emission peak in the northern half of the core, 2.6 Jy beam^{-1}·km s^{-1}, is offset from the position of L1448NW. Instead, the peak appears in an elongated zone approximately two beamwidths to the west. In the southern half of the core, the peak emission, 3.8 Jy beam^{-1}·km s^{-1}, appears near the L1448N(AB) pair. In general, the regions of extended emission that were suggested in the 10″ $H^{13}CO^+$ maps are more crisply delineated in the N_2H^+ map. The lower emission contours (35%, 50%) in Figure 2.5*d* have a "butterfly wing" morphology: L1448NW is at the vertex of elongated emission regions that extend to the north and west, and L1448N(AB) is at the vertex of regions that extend to the east and southwest. In the velocity map of the same area (Figure 2.5*e*), the western half of the map is blueshifted and the eastern half is redshifted. The maximum redshifted velocity, 5.2 km s^{-1}, is about one beamwidth east of L1448N(A). The emission regions that extend to the north and southwest are near the central core velocity (4.5-4.6 km s^{-1}); the region west of L1448NW is slightly bluer. The maximum blueshifted velocity, 4.3 km s^{-1}, is located one beamwidth southwest of

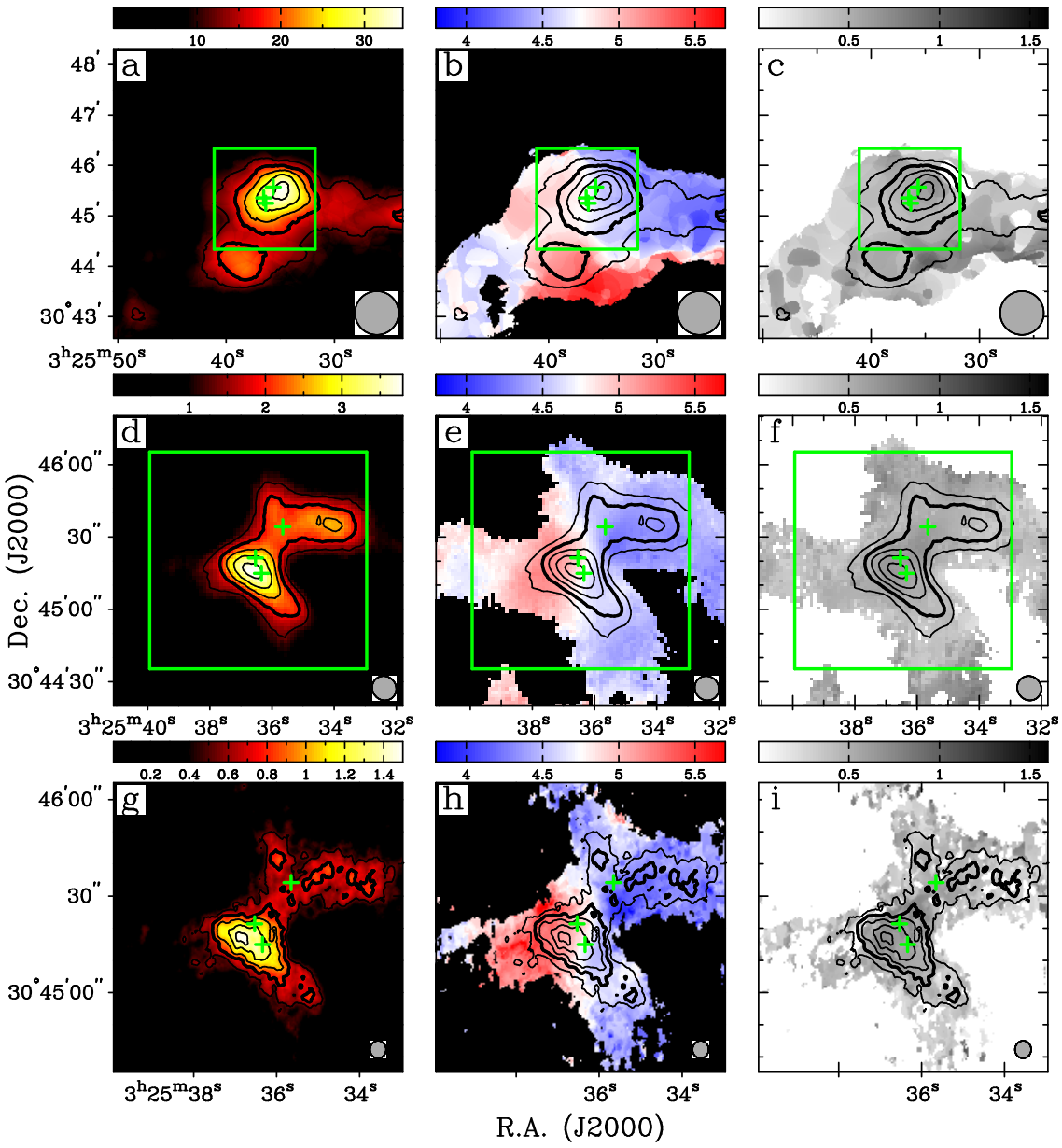

Figure 2.5: N_2H^+ $J = 1 \rightarrow 0$ integrated intensity, line-of-sight velocity, and velocity dispersion of L1448 IRS3. Panels *a,d,g* show integrated intensity in both contours and colorscale. Contour levels are 35%, 50%, 65%, 80%, and 95% of peak flux density; bold contour is 50% level. Panels *b,e,h* show integrated intensity contours and line-of-sight velocity field in colorscale. Velocity range is 3.8-5.7 km s^{-1} in all panels. Panels *c,f,i* show integrated intensity contours and velocity dispersion in grayscale. Dispersion range is 0.0-1.58 km s^{-1} in all panels. Square regions delineated by green lines indicate areas of the maps in the row immediately below. Plus symbols indicate positions of continuum sources from LMW00. (a,b,c) I_ν^{peak} = 34.59 Jy beam^{-1}·km s^{-1}; σ = 1.9 Jy beam^{-1}·km s^{-1}; beam is $52'' \times 52''$. (d,e,f) I_ν^{peak} = 3.79 Jy beam^{-1}·km s^{-1}; σ = 0.16 Jy beam^{-1}·km s^{-1}; beam is $10.37'' \times 9.78''$, P.A.= 39.3°. (g,h,i) I_ν^{peak} = 1.18 Jy beam^{-1}·km s^{-1}; σ = 0.08 Jy beam^{-1}·km s^{-1}; beam is $5.45'' \times 5.02''$, P.A.= −2.8°.

L1448NW.

The butterfly-wing morphology of the N_2H^+ emission persists in the intensity map with 5″ resolution (Figure 2.5*g*). Also, the higher resolution reveals that there is no intensity peak at L1448NW; the N_2H^+ emission contours in the elongated regions to the north and west. The extend emission to the east and southwest of the L1448N(AB) peak (1.4 Jy beam^{-1}·km s^{-1}) are more robust at higher resolution. The velocity map of the region (Figure 2.5*h*) reinforces the characteristics of the velocity field seen at 10″ resolution. Only the emission region eastward of L1448N(A) exhibits a redshift; the maximum velocity is ∼5.7 km s^{-1} about 20″ east of the continuum source. The position of the most extreme blueshift, ∼3.8 km s^{-1}, is 11″ southwest of L1448NW.

Maps of the N_2H^+ emission at 3″ resolution have been omitted from Figure 2.5. Significant N_2H^+ emission is detected at this resolution, but the peaks do not form coherent structures. The highest emission peaks ($> 6\sigma$, $\sigma = 0.08$ Jy beam^{-1}·km s^{-1}) appear near L1448N(B).

$C^{18}O/H^{13}CO^+/N_2H^+$ Line Comparison

Examining the ensemble of maps presented in Figures 2.3, 2.4, and 2.5 shows that the $C^{18}O$ emission is stronger at all resolutions than either the $H^{13}CO^+$ or N_2H^+ emission. In the FCRAO maps and the combined maps with 10″ resolution, the $C^{18}O$ emission is spread out over the entire area of the maps, whereas in the maps with 5″ and 3″ resolution, the $C^{18}O$ emission is primarily concentrated near the continuum sources. The $H^{13}CO^+$ and N_2H^+ data show a contrary behavior as the resolution increases. In the FCRAO data, the $H^{13}CO^+$ and N_2H^+ emitting regions are more compact than the $C^{18}O$ emitting region. Both $H^{13}CO^+$ and N_2H^+ reveal similar extended emission structures: extensions to the east and southwest of

L1448N(AB) and extensions to the north and west of L1448NW. In $C^{18}O$, the emitting region around L1448N(AB) is elongated along the line connecting the binary sources' north-south direction. In the $H^{13}CO^+$ and N_2H^+ maps, the extended emission to the east and southwest give the emitting region a long, flattened appearance. The emission surrounding L1448NW is elongated toward the west-northwest in all three tracers, but whereas the $C^{18}O$ emission peaks near the continuum source, the N_2H^+ emission peak appears displaced westward of the continuum source by approximately 25″ at 10″ resolution and disappears at higher resolution. These extensions persist in the 5″ maps in both $H^{13}CO^+$ and N_2H^+, although the N_2H^+ emission in the vicinity of L1448NW breaks up into smaller emission knots. In the higher resolution (5″ and 3″) maps, the $C^{18}O$ emission appears extended along the axis between L1448N(A) and L1448N(B), and extended in the E-W direction around L1448NW.

The most significant result from the collective velocity maps in Figures 2.3, 2.4 and 2.5 is that, even though the molecules trace material of different density, the trends in the velocities are consistent. The blueshifted/redshifted division between the western and eastern halves of the maps is evident in each of the molecular lines and at all resolutions. Another important observation from the velocity data is that the range of velocities in the maps increases as the resolution increases. In the 10″ resolution maps, the range of velocities across the primary beam area is 1.2 km s^{-1} in the $C^{18}O$ data, 1.3 km s^{-1} in the $H^{13}CO^+$ data, and 1.3 km s^{-1} in the N_2H^+ data. In the 5″ maps, the velocity ranges are 1.6, 1.7, and 1.8 km s^{-1}, respectively. In the $C^{18}O$ maps at 3″, the velocity range increases still further to 1.9 km s^{-1}. At this resolution, the extended structures around L1448N(AB) and L1448NW both show pronounced gradients in their velocities. Around L1448N(AB), the velocities change from blueshifted (4.2 km s^{-1}) south of L1448N(B) to redshifted (5.1 km s^{-1})

north of L1448N(A). Around L1448NW, the velocities are blueshifted to the west and south of the continuum source, and redshifted to the north and east of the source.

2.4.4 Spectra

A sample of spectra taken through the L1448 datacubes are displayed in Figure 2.6. The top row shows spectra taken through the FCRAO datacubes. The spectra labeled "A & B" are taken from a position between L1448N(A) and L1448N(B) (R.A.= $3^h25^m36\overset{s}{.}44$, Dec. = $30°45'18\overset{''}{.}15$) because the individual sources are not resolved in the FCRAO beam. In fact, the position of L1448NW is also included in the beam. Spectra centered at L1448NW are also displayed, and the same molecules at the two positions have similar fluxes. The lines from L1448N(AB) and L1448NW are all well fit by Gaussian functions, with the greatest difference appearing in the double-peaked N_2H^+ line centered at L1448NW. (A summary of the line peaks (I_ν^{peak}), central velocities (V_C), and line widths (ΔV) determined from Gaussian functions fit to the line profiles are given in Tables 2.1, 2.2, and 2.3.)

The positions α, β, γ, and δ in Figure 2.6*a* were chosen to show representative spectra from the larger L1448 cloud. These positions are offset by $90''$ in the four cardinal directions from the field center. At position α ($90''$ east), the height of the $C^{18}O$ line is about the same as in the center of the core (panels A&B, NW), indicating that the slightly lower emission seen at this location in the intensity map arises from a narrower line. All three line profiles are well fit by Gaussian functions. At position β ($90''$ north), the heights of both the $C^{18}O$ and $H^{13}CO^+$ lines are reduced, appropriate for the steep fall-off in emission along the northern edge of the cloud. These lines are both noticably skewed toward the blue. Neither line is particularly well fit by a Gaussian function. The N_2H^+ line here is imperceptable.

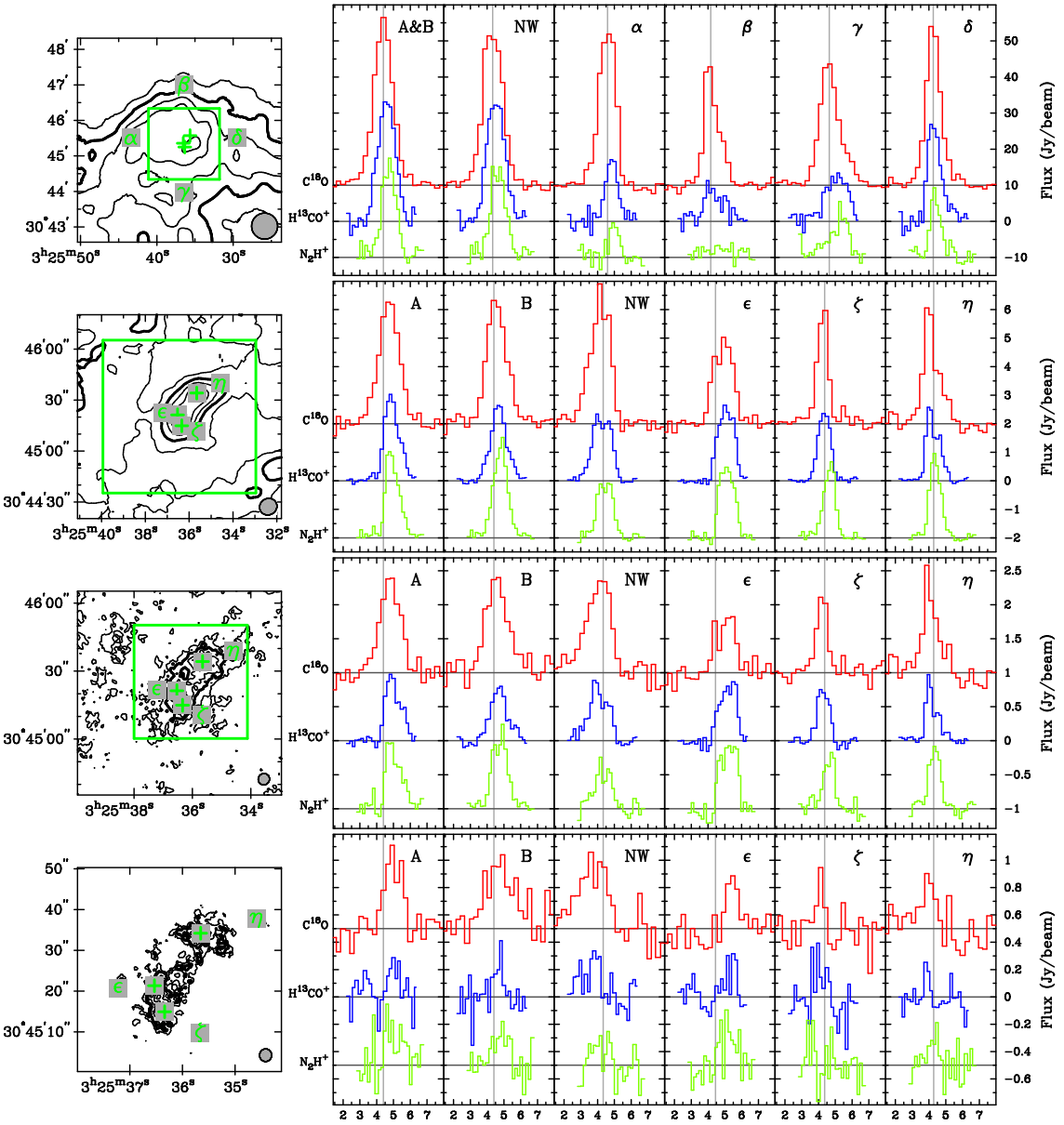

Figure 2.6: L1448 IRS3 spectra. The plots at left show integrated intensity contours from the $C^{18}O$ data, as in Figure 2.3. To the right of each plot are spectra from the $C^{18}O$ (red), $H^{13}CO^+$ (blue), and N_2H^+ (lt. green) datacubes. The positions where spectra were taken are indicated in the plots: plus symbols identify the positions of continuum sources; other positions are identified by letters α through η. All spectra display the mean flux in Jy beam^{-1} taken over a beam area. For clarity, the $C^{18}O$ spectra are given positive offsets, and the N_2H^+ spectra are given negative offsets. In the FCRAO data (top row), the offsets are ± 10 Jy beam^{-1}; in the $10''$ data (second row), the offsets are ± 2 Jy beam^{-1}; in the $5''$ data (third row), the offsets are ± 1 Jy beam^{-1}; in the $3''$ data (bottom row), the offsets are ± 0.5 Jy beam^{-1}. In all rows, the gray vertical lines show central velocities of Gaussian functions fitted to the $C^{18}O$ profile from the FCRAO map (top row). For positions ϵ, ζ, and η, the central velocities are from FCRAO spectra *not* shown in the top row.

Table 2.1. L1448 IRS3 $C^{18}O$ Spectra

ID	Beam (arcsec)	I_ν^{peak} (Jy beam^{-1})	V_C (km s^{-1})	ΔV (km s^{-1})
A	44/56.5/52[a]	45.54 ± 1.18	4.4 ± 0.1	1.3 ± 0.1
	10	4.31 ± 0.13	4.7 ± 0.1	1.4 ± 0.1
	5	1.39 ± 0.11	4.8 ± 0.2	1.4 ± 0.3
	3	0.56 ± 0.11	5.0 ± 0.4	1.2 ± 0.6
B	44/56.5/52[a]	45.54 ± 1.18	4.4 ± 0.1	1.3 ± 0.1
	10	4.31 ± 0.13	4.6 ± 0.1	1.4 ± 0.1
	5	1.36 ± 0.11	4.6 ± 0.2	1.5 ± 0.3
	3	0.45 ± 0.08	4.8 ± 0.7	2.1 ± 1.0
NW	44/56.5/52	44.17 ± 1.16	4.3 ± 0.1	1.4 ± 0.1
	10	4.47 ± 0.13	4.2 ± 0.1	1.4 ± 0.1
	5	1.37 ± 0.10	4.1 ± 0.2	1.6 ± 0.3
	3	0.47 ± 0.08	3.7 ± 0.7	2.0 ± 0.9
α	44/56.5/52	45.06 ± 1.27	4.6 ± 0.1	1.1 ± 0.1
β	44/56.5/52	31.64 ± 1.34	4.2 ± 0.1	1.0 ± 0.1
γ	44/56.5/52	32.83 ± 1.16	4.6 ± 0.1	1.4 ± 0.1
δ	44/56.5/52	43.97 ± 1.35	4.3 ± 0.1	1.0 ± 0.1
ϵ	10	2.95 ± 0.13	4.9 ± 0.1	1.4 ± 0.2
	5	0.79 ± 0.11	5.1 ± 0.4	1.4 ± 0.5
	3	0.41 ± 0.14	5.5 ± 0.5	
ζ	10	4.08 ± 0.17	4.3 ± 0.1	0.7 ± 0.1
	5	1.17 ± 0.16	4.2 ± 0.2	0.7 ± 0.3
	3	0.45 ± 0.16	4.1 ± 0.3	
η	10	3.78 ± 0.15	4.1 ± 0.1	1.0 ± 0.1
	5	1.31 ± 0.14	4.0 ± 0.2	1.0 ± 0.3
	3	0.38 ± 0.13	4.0 ± 0.5	

[a]Spectra of L1448N(A) and L1448N(B) from FCRAO data are identical.

Position γ (90″ south), is also just 34″ from the L1448C core, a known source of strong outflows. The $C^{18}O$ and $H^{13}CO^+$ lines here are well fit by Gaussian functions, although their central velocities are displaced by several channels. The N_2H^+ line profile at γ is the most unusual of the three spectra; the Gaussian fit to the obviously red-skewed profile is poor. The δ position (90″ west) is roughly halfway between L1448N and L1448 IRS2. All three profiles are fairly strong, and all three are fit well by Gaussian functions.

Comparing the spectra in the top row of Figure 2.6 with the velocity maps

Table 2.2. L1448 IRS3 $H^{13}CO^+$ Spectra

ID	Beam (arcsec)	I_ν^{peak} (Jy beam^{-1})	V_C (km s^{-1})	ΔV (km s^{-1})
A	44/56.5/52[a]	33.80 ± 1.33	4.6 ± 0.1	1.2 ± 0.2
	10	2.92 ± 0.04	4.9 ± 0.0	1.0 ± 0.1
	5	0.91 ± 0.04	5.0 ± 0.1	1.1 ± 0.2
	3	0.26 ± 0.09	5.0 ± 0.7	
B	44/56.5/52[a]	33.80 ± 1.33	4.6 ± 0.1	1.2 ± 0.2
	10	2.57 ± 0.04	4.7 ± 0.1	1.1 ± 0.1
	5	0.76 ± 0.04	4.7 ± 0.2	1.1 ± 0.2
	3	0.33 ± 0.11	4.7 ± 0.4	
NW	44/56.5/52	34.44 ± 1.32	4.5 ± 0.1	1.2 ± 0.2
	10	2.31 ± 0.04	4.3 ± 0.1	1.3 ± 0.1
	5	0.77 ± 0.04	4.0 ± 0.2	1.3 ± 0.2
	3	0.24 ± 0.06	3.6 ± 1.1	
α	44/56.5/52	17.73 ± 1.61	4.8 ± 0.2	0.8 ± 0.3
β	44/56.5/52	8.28 ± 1.23	4.3 ± 0.6	1.4 ± 0.9
γ	44/56.5/52	12.93 ± 1.19	5.1 ± 0.4	1.5 ± 0.6
δ	44/56.5/52	27.43 ± 1.55	4.3 ± 0.1	0.9 ± 0.2
ϵ	10	2.66 ± 0.04	5.1 ± 0.1	1.1 ± 0.1
	5	0.86 ± 0.04	5.2 ± 0.1	1.2 ± 0.2
	3	0.23 ± 0.08	5.4 ± 0.8	
ζ	10	2.47 ± 0.05	4.3 ± 0.0	0.8 ± 0.1
	5	0.79 ± 0.05	4.3 ± 0.1	0.8 ± 0.2
	3	0.25 ± 0.09	4.0 ± 0.7	
η	10	2.28 ± 0.05	4.2 ± 0.1	0.9 ± 0.1
	5	0.85 ± 0.05	4.1 ± 0.1	0.7 ± 0.2
	3	0.32 ± 0.32	3.9 ± 0.3	

[a]Spectra of L1448N(A) and L1448N(B) from FCRAO data are identical.

(Figures 2.3*b*, 2.4*b*, and 2.5*b*), the first moment is generally a trustworthy indicator of the dominant velocity along the line of sight. Even spectra that are poorly fit by Gaussian functions have central velocities similar to the velocities in the first moment map. The median difference between the fit central velocities and the velocities in the first moment map is +0.02 km s^{-1}. The mode is only +0.01 km s^{-1}. Given the channel width of 0.17 km s^{-1}, these differences are not significant. The one exception to the second conclusion is the skewed N_2H^+ spectrum at the γ position. The central velocity of the Gaussian function is 0.12 km s^{-1} (*i.e.* one channel)

Table 2.3. L1448 IRS3 N_2H^+ Spectra

ID	Beam (arcsec)	I_ν^{peak} (Jy beam^{-1})	V_C (km s^{-1})	ΔV (km s^{-1})
A	44/56.5/52[a]	26.36 ± 1.80	4.7 ± 0.1	1.0 ± 0.2
	10	2.98 ± 0.06	4.9 ± 0.1	0.9 ± 0.1
	5	0.92 ± 0.06	5.0 ± 0.2	1.1 ± 0.3
	3	0.25 ± 0.08	5.0 ± 1.4	
B	44/56.5/52[a]	26.36 ± 1.80	4.7 ± 0.1	1.0 ± 0.2
	10	3.26 ± 0.06	4.8 ± 0.1	1.0 ± 0.1
	5	1.07 ± 0.06	4.8 ± 0.2	1.1 ± 0.3
	3	0.25 ± 0.10	4.8 ± 1.2	
NW	44/56.5/52	25.13 ± 1.74	4.7 ± 0.2	1.1 ± 0.3
	10	2.03 ± 0.06	4.5 ± 0.1	1.1 ± 0.1
	5	0.57 ± 0.06	4.3 ± 0.4	1.2 ± 0.5
	3	0.26 ± 0.18	4.7 ± 0.6	
α	44/56.5/52	9.60 ± 2.26	5.0 ± 0.5	0.6 ± 0.6
β	44/56.5/52	1.98 ± 1.18	4.6 ± 4.6	2.4 ± 7.3
γ	44/56.5/52	11.29 ± 1.63	5.3 ± 0.5	1.2 ± 0.8
δ	44/56.5/52	17.93 ± 2.11	4.4 ± 0.3	0.7 ± 0.4
ϵ	10	2.61 ± 0.06	5.1 ± 0.1	1.0 ± 0.1
	5	0.99 ± 0.06	5.3 ± 0.2	1.1 ± 0.3
	3	0.24 ± 0.09	5.2 ± 1.3	
ζ	10	2.63 ± 0.07	4.7 ± 0.1	0.8 ± 0.1
	5	0.79 ± 0.07	4.7 ± 0.2	0.8 ± 0.3
	3	0.21 ± 0.13	3.5 ± 1.0	
η	10	2.91 ± 0.07	4.4 ± 0.1	0.8 ± 0.1
	5	0.93 ± 0.07	4.4 ± 0.2	0.8 ± 0.2
	3	0.24 ± 0.13	4.3 ± 0.9	

[a]Spectra of L1448N(A) and L1448N(B) from FCRAO data are identical.

blueward of the velocity in the first moment map.

The second, third, and fourth rows of Figure 2.6 show additional spectra from the positions of the continuum sources. At $10''$ resolution, the spectra from L1448NW are isolated from those of the L1448N(AB) pair, which still overlap by approximately half of a beam. In the $5''$ and $3''$ resolution maps, all spectra are independent. In each spectrum plot, the gray vertical line marks the center of the Gaussian function fit to the $C^{18}O$ line *from the FCRAO data* (top row), allowing the velocity shifts as a function of resolution to be assessed.

Figure 2.6 and the data in Tables 2.1, 2.2, and 2.3 show that, as the spatial resolution of the maps increases, the spectra of L1448N(A) gradually shift toward the red. The center of the $C^{18}O$ line at L1448N(AB) is 4.4 ± 0.1 in the FCRAO data. In the $10''$ map, the center shifts to 4.7 ± 0.1. In the $5''$ map, it shifts again to 4.8 ± 0.2, and in the $3''$ map, where the integrity of a Gaussian fit becomes suspect, the shift is 5.0 ± 0.4. The $H^{13}CO^+$ and N_2H^+ line centers also follow this trend as the resolution of the maps increases. For the $H^{13}CO^+$ line, the line centers are 4.6 ± 0.1 ($56.5''$), 4.9 ± 0.0 ($10''$), and 5.0 ± 0.1 ($5''$). For the N_2H^+ line, the line centers are 4.7 ± 0.1 ($52''$), 4.9 ± 0.1 ($10''$), and 5.0 ± 0.2 ($5''$).

This redward trend is also apparent in the profiles of L1448N(B). The shift is not as stark as with L1448N(A), conforming with what's observed in the velocity maps. For the $C^{18}O$ line, the central velocities are: 4.4 ± 0.1 ($44''$), 4.6 ± 0.1 ($10''$), 4.6 ± 0.2 ($5''$), and 4.8 ± 0.7 ($3''$). For the $H^{13}CO^+$ line: 4.6 ± 0.1 ($56.5''$), 4.7 ± 0.1 ($10''$), and 4.7 ± 0.2 ($5''$). For the N_2H^+ line: 4.7 ± 0.1 ($52''$), 4.8 ± 0.1 ($10''$), and 4.8 ± 0.2 ($5''$). In the N_2H^+ profiles in particular, as the resolution increases and more weight is given to the interferometer data, the peak skews toward the red. In the spectrum taken from the $5''$ resolution map, the line profile is double-peaked, with the stronger peak on the redward side.

The remaining plots in the second, third and fourth rows of Figure 2.6 show spectra taken from the positions labeled ϵ, ζ, and η in the maps. Position ϵ (R.A.= $3^h25^m37\overset{s}{.}22$, Dec. = $30°45'20\overset{''}{.}04$) is located in the region of redshifted emission east of L1448N(A). Position ζ (R.A.= $3^h25^m35\overset{s}{.}67$, Dec. = $30°45'09\overset{''}{.}04$) is located in the blueshifted emission lobe southwest of L1448N(B). Position η (R.A.= $3^h25^m34\overset{s}{.}58$, Dec. = $30°45'37\overset{''}{.}04$) lies in the blueshifted lobe west of L1448NW, near the N_2H^+ emission peak. The central velocities of the FCRAO spectra taken at these positions are indicated by the vertical lines, even though the spectra are not shown in Fig-

ure 2.6*a*. In the FCRAO maps, all of the spectra taken near the center of the core overlap substantially. The central velocities at the positions ϵ, ζ, and η are 4.4 ± 0.1, 4.4 ± 0.1, and 4.3 ± 0.1, respectively. At higher resolution, the $C^{18}O$ spectra from ϵ have a similar height and width as the $H^{13}CO^+$ and N_2H^+ spectra, and all of the lines are obviously redshifted. At the ζ position, the $C^{18}O$ lines are stronger than either the $H^{13}CO^+$ or N_2H^+ lines, which show a separation in their peaks. The centers of the $H^{13}CO^+$ lines remain aligned with $C^{18}O$ velocities (near the velocity from the FCRAO data), but the N_2H^+ lines are shifted toward the red by $\sim$0.3 km s^{-1}. A separation is also detectable, although not as apparent, in the $H^{13}CO^+$ and N_2H^+ spectra from position η. The N_2H^+ lines are again slightly redshifted ($\sim$0.1 km s^{-1}) from the FCRAO map velocity. The centers of the $C^{18}O$ and $H^{13}CO^+$ lines remain aligned and are slightly blueshifted from the FCRAO map velocity.

Overall, the emission profiles remain approximately Gaussian at higher resolutions, except in the 3″ maps. Even for the spectral lines that are not shaped like Gaussian functions (*e.g.* double-peaked profiles), the central velocities provide a satisfactory match to the velocities displayed in the first moment map.

2.5 NGC1333 IRAS2

2.5.1 Background

NGC1333 is a reflection nebula illuminated primarily by the visible stars BD+30°549 (m_V = 10.5) and SVS3 (m_V = 14.5) (Černis 1990; Harvey, Wilking, & Joy 1984; Strom, Vrba, & Strom 1976). The nebula is on the near surface of the L1450 dark cloud (Lynds 1962); the bulk of the cloud extends behind and southward of the nebula. The pervasiveness of L1450 is substantiated by the large number of reddened objects in the vicinity (*e.g.* Strom, Vrba, & Strom (1976); Aspin, Sandell,

& Russell (1994); Lada, Alves, & Lada (1996)). The cloud has long been recognized as a region of active star formation: optical and near-infrared observations reveal an embedded population of emission line stars and Herbig-Haro objects (*e.g.* Herbig & Rao (1972); Strom, Grasdalen, & Strom (1974); Cohen & Schwartz (1980, 1983); Ho & Barrett (1980); Herbig & Jones (1983)), and radio observations of collisionally-excited H_2O masers trace outflow-shocked material (*e.g.* Lo *et al.* (1976); Haschick *et al.* (1980, 1983); Henkel, Haschick, & Güsten (1986)).

A $25' \times 25'$ field including NGC1333 was observed at $\lambda = 50\mu$m and 100μm with the infrared satellite IRAS (Jennings *et al.* 1987). The 50μm flux map showed *nine* emission peaks within the area of the L1450 cloud. The emission peaks identified as IRAS2 and IRAS4 are located at the southern boundary of the emission region and are also prominent emission peaks in the 100μm map. Subsequent observations of the NGC1333 region in CO and ^{13}CO $J = 1 \rightarrow 0$ emission (Liseau, Sandell, & Knee 1988) revealed that five of the IRAS sources, including IRAS2 and IRAS4, power molecular outflows, a common indicator of star formation activity.

IRAS2 lies $\sim 11'$ south-southwest of the center of the NGC1333 reflection nebula. IRAS4 (see §2.6) also lies $\sim 11'$ from the nebula, although due south. Both cores are embedded within the southern arc of a shell of compressed gas that is traced in $100''$-resolution maps of C^{18}O $J = 1 \rightarrow 0$ emission (Warin *et al.* 1996) and in $16''$-resolution maps of CS $J = 3 \rightarrow 2$ emission (Langer, Castets, & Lefloch 1996). The shell surrounds a rarefied cavity that exposes a cluster of pre-Main Sequence (PMS) stars with near-infrared excesses (Aspin, Sandell, & Russell 1994; Lada, Alves, & Lada 1996). The protostars within the IRAS2 core, and any PMS stars in its vicinity, are shrouded by the opacity of the surrounding shell material.

IRAS2 marks the vertex of a pair of nearly-perpendicular outflows that imply the presence of deeply embedded star formation activity (Sandell *et al.* 1994).

The north-south outflow (P.A.$\sim$25°) was first discovered in CO emission by Liseau, Sandell, & Knee (1988). The blueshifted lobe extends southward at least 70″, where it energizes a pair of H_2 $1 \rightarrow 0$ S(1) emission knots (ASR49, ASR71) (Hodapp & Ladd 1995; Aspin, Sandell, & Russell 1994). The axis of the blueshifted lobe if also conspicuously aligned with two bow-shaped Herbig-Haro objects, HH342 ($\sim$4′ away) and HH341 ($> 5.5'$ away) (Bally, Devine, & Reipurth 1996). The redshifted lobe of the outflow extends northward and, in symmetry with the southern lobe, appears to stimulate a pair of H_2 emission knots (ASR 15, ASR16), also $\sim$70″ from the center of the core (Hodapp & Ladd 1995; Aspin, Sandell, & Russell 1994), although the outflow may be confused with redshifted emission from the nearby embedded source SVS13 (Sandell *et al.* 1994; Warin *et al.* 1996; Knee & Sandell 2000). In both directions, the north-south outflow is poorly collimated (Knee & Sandell 2000), suggesting that, even though it must be powered by a relatively young object, it cannot be a new outflow. Sandell *et al.* (1994) derive a dynamical age of $t_{dyn} = 2.5 \times 10^4$ yr. In contrast, the east-west outflow (PA$\sim$104°) is highly collimated (opening angle $< 10°$) and presumably younger. Sandell *et al.* (1994) derive an age of 6×10^3 yr from maps of the CO $J = 3 \rightarrow 2$ and CS $J = 5 \rightarrow 4$ emission, and Bachiller *et al.* (1998) estimate $2 - 5 \times 10^3$ yr from observations of "bullets" of shock-stimulated CH_3OH emission along the outflow axis. The symmetry of the CH_3OH "bullets" suggests periods of episodic mass loss and indicates a collimation factor of $\sim$20. The blueshifted lobe extends $\sim$100″ to the west and terminates in a large bow shock that is marked by strong emission from various CS transitions (Langer, Castets, & Lefloch 1996). The redshifted outflow lobe extends eastward $\sim$85″; it also exhibits bright CS emission (Lefloch *et al.* 1998a; Langer, Castets, & Lefloch 1996). In the high-resolution interferometer observations by Blake (1997), highly-collimated SiO emission appears to distort a ribbon of CS emission into a

bow shape.

From observations of the $\lambda = 1.25$ mm continuum emission with the IRAM 30 m telescope ($11''$ beam), Lefloch *et al.* (1998a) estimated a total core mass of 4.2 M$\odot$. Models of various molecular line profiles (HCO^+,$H^{13}CO^+$,CS) (Ward-Thompson *et al.* 1996; Ward-Thompson & Buckley 2001) suggest that the core gas is infalling. A best fit model estimated an outer radius of 10000 AU (assuming a distance of 220 pc) and a total mass of 3.7 M$\odot$. The HCO^+ and CS maps indicate a velocity gradient in the north-south direction (redshifted north, blueshifted south), suggesting rotation around an east-west axis, although Ward-Thompson & Buckley (2001) propose that the gradient is more likely the result of an interaction with the north-south outflow.

The IRAS2 core comprises at least three condensations (Sandell & Knee 2001). IRAS2A, near the center of the core, is the strongest emitter at millimeter and submillimeter wavelengths. Lefloch *et al.* (1998a) found a flux density of 380 mJy (at $\lambda = 1.25$ mm) within a (barely resolved) diameter of $12''$, and derived a mass of 0.8 M$\odot$ for the IRAS2A condensation. IRAS2B, approximately $30''$ southeast of IRAS2A, was discovered in 2.7 mm continuum and CS $J = 2 \rightarrow 1$ line emission from interferometric observations (Blake 1997), although its existence is suggested in earlier (single-dish) maps (*c.f.* (Lefloch *et al.* 1998a)) by the obvious southeast-northwest extension of the continuum emission. At centimeter wavelengths, IRAS2B is stronger than IRAS2A, although both sources have spectral indices that are characteristic of extremely young embedded objects. IRAS2B may drive its own outflow. The CO $J = 3 \rightarrow 2$ maps of Knee & Sandell (2000) suggest a blueshifted lobe that extends $\sim 1'$ south of IRAS2B; a redshifted lobe is not detected, but may be confused with the redshifted lobe of the main IRAS2 outflow. The origin of the main north-south outflow is uncertain. Knee & Sandell (2000) propose that it is driven by the third continuum source. IRAS2C, the weakest of the three continuum sources,

is located $\sim 30''$ northwest of IRAS2A. However, the axis of the north-south outflow appears to pass closer to IRAS2A, leading several authors (*c.f.* (Sandell *et al.* 1994)) to speculate that IRAS2A is a binary with an unresolved companion.

2.5.2 Millimeter Continuum Emission.

Figure 2.7*a* shows the map (originally Figure 8 of LMW00) of the $\lambda = 2.7$ mm continuum emission from IRAS2; Figures 2.7*b,c,d* show higher-resolution maps of IRAS2A. Most of the continuum emission from IRAS2A arises from an extended envelope, and at the highest resolution, the emitting region is unresolved. LMW00 estimate that IRAS2A is a $\sim$30 L$\odot$ source enshrouded by a 0.44 M$\odot$ envelope. In contrast, most of the continuum emission from IRAS2B is compact, and LMW00 speculate that it originates from either a compact envelope or a circumstellar disk surrounded by a relatively weak envelope. The estimated mass of the circumstellar material around IRAS2B is 0.14 M$\odot$.

2.5.3 Molecular Line Emission

Results from the line observations of NGC1333 IRAS2 are displayed in Figures 2.8, 2.9, and 2.10. In each figure, the panels in the left column show the integrated intensity (0^{th} moment) calculated over all channels with signal $> 3\sigma$. The panels in the center column show the weighted velocity field (1^{st} moment) over the same areas as the intensities in the left columns. The panels in the right column show the velocity dispersion (2^{nd} moment) over these areas. The first and second moments are calculated after exempting pixels with fluxes below 2*times* the single channel noise level, and regions in the integrated intensity maps with flux $< 3\sigma$ are masked in the velocity and dispersion maps. The format of the maps is identical to the L1448 IRS3 maps presented in the previous section, *e.g.* the velocity and dispersion ranges

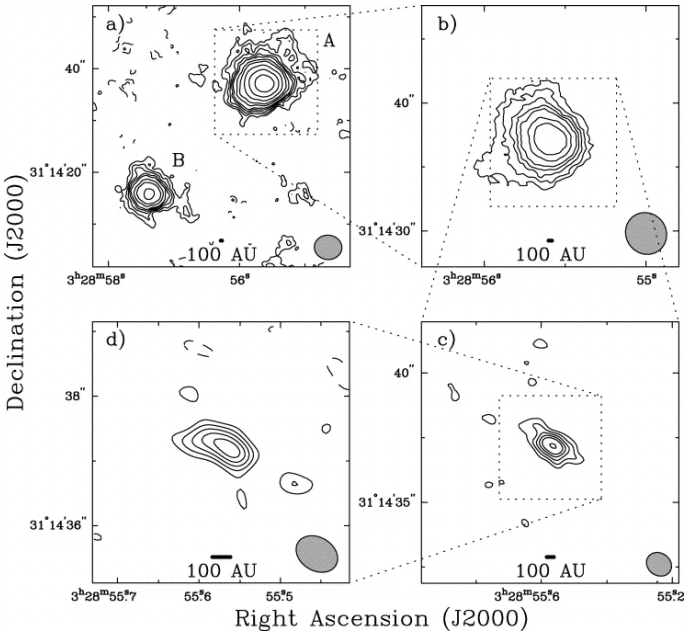

Figure 2.7: Maps of the $\lambda = 2.7$ mm continuum emission from NGC1333 IRAS2A. (Figure 8 from LMW00.) The panels indicate contours in steps of $(-4, -3, -2, 2, 3, 4, 5, 6, 8, 10, 14.14, 20, 28.28, 40, 56.56) \times \sigma$ in mJy beam^{-1}. (a) $\sigma = 1.3$ mJy beam^{-1}; beam is $5.40'' \times 4.70''$, P.A.$= 86°$. (b) $\sigma = 1.2$ mJy beam^{-1}; beam is $3.36'' \times 3.16''$, P.A.$= 45°$. (c) $\sigma = 1.7$ mJy beam^{-1}; beam is $1.02'' \times 0.87''$, P.A.$= 57°$. (d) $\sigma = 2.7$ mJy beam^{-1}; beam is $0.69'' \times 0.52''$, P.A.$= 63°$.

are the same in each row, and the integrated intensity contours are superimposed upon the velocities. The maps in the top rows of Figures 2.8, 2.9, and 2.10 were created solely from the FCRAO observations. The maps in the second and third rows combine the BIMA and FCRAO observations at $10''$ and $5''$ resolutions, respectively, and Figure 2.8 includes a fourth row that shows only BIMA observations at $3''$ resolution.

$C^{18}O$ Maps

The full size of the map in Figure 2.8*a* is approximately $6' \times 6'$, and $C^{18}O$ emission is detected throughout. (The pixels in the northwest corner of the map are masked out because of a defective receiver element.) A ridge of strong emission descends from the direction of SVS13 in the northeast corner. The point of peak

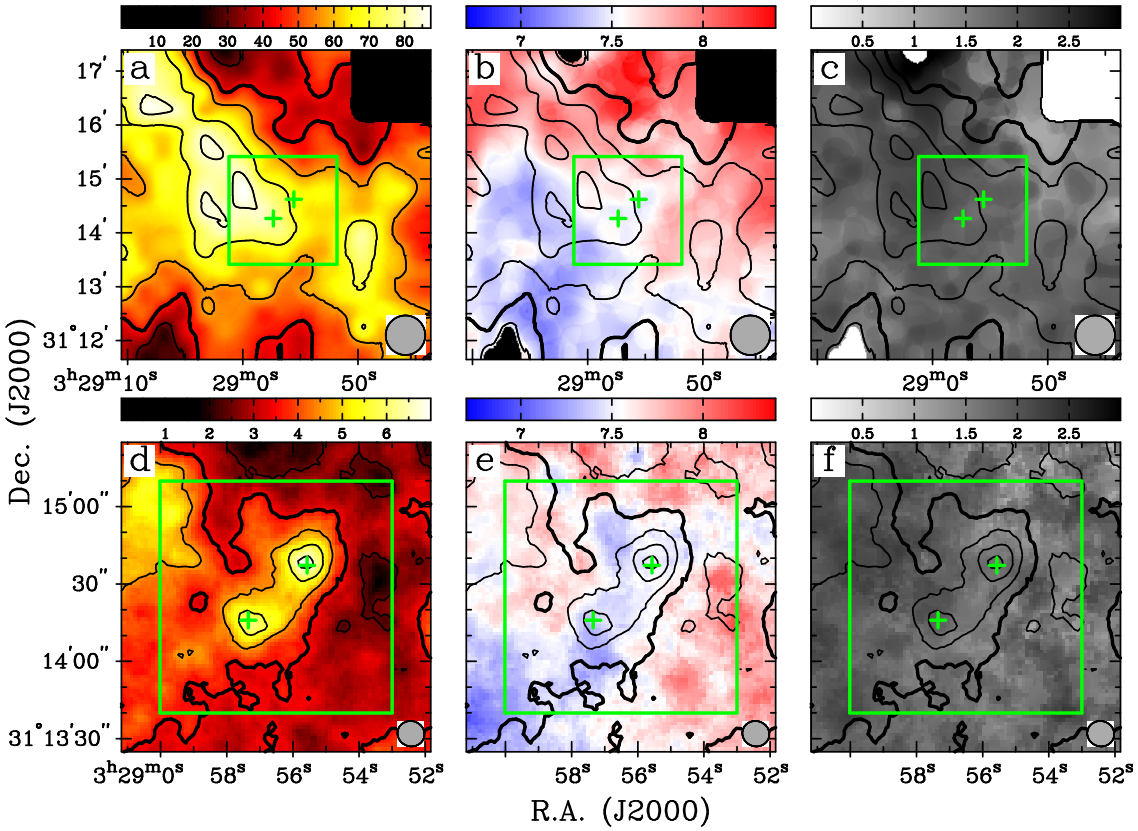

Figure 2.8: Integrated intensity, line-of-sight velocity, and velocity dispersion of NGC1333 IRAS2 traced by $C^{18}O$ $J = 1 \rightarrow 0$ emission. Panels in left column (*a,d,g,j*) show integrated intensity in both contours and colorscale. Contour levels are 35%, 50%, 65%, 80%, and 95% the peak flux density; bold contour is 50% level. Panels in center column (*b,e,h,k*) show velocity in colorscale; contours show the integrated intensities from the left panels. Velocity range is 6.7-8.4 km s^{-1} in all panels. Panels in right column (*c,f,i,l*) show dispersion in grayscale; contours show the integrated intensities from the left panels. Dispersion range is 0.0-2.97 km s^{-1} in all panels. Squares indicate full areas of the maps in the row immediately below. Plus symbols indicate positions of continuum sources from LMW00. (a,b,c) $I_\nu^{peak} = 87.37$ Jy beam^{-1}·km s^{-1}; $\sigma = 9.6$ Jy beam^{-1}·km s^{-1}; beam is $44'' \times 44''$. (d,e,f) $I_\nu^{peak} = 6.98$ Jy beam^{-1}·km s^{-1}; $\sigma = 0.48$ Jy beam^{-1}·km s^{-1}; beam is $10.52'' \times 9.79''$, P.A.$= 72.5°$.

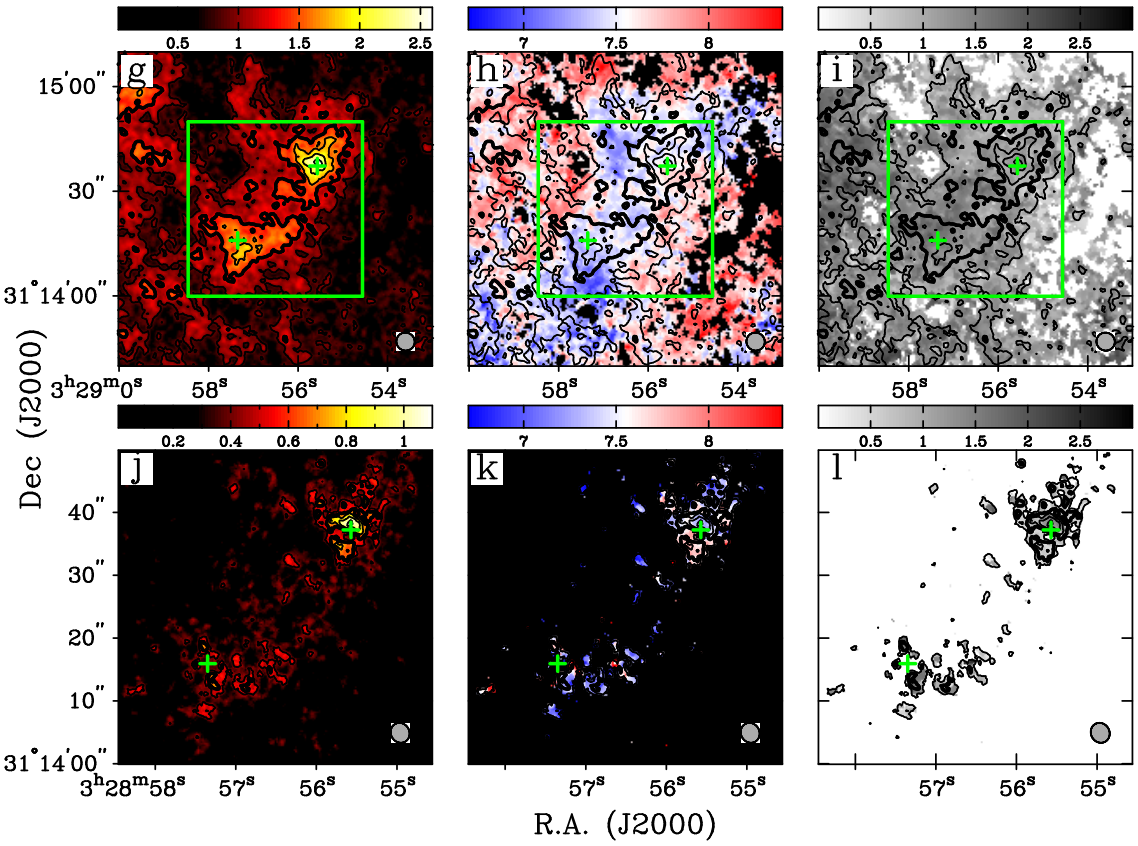

Figure 2.8: *Continued.* (g,h,i) I_ν^{peak} = 2.58 Jy beam^{-1}·km s^{-1}; σ = 0.21 Jy beam^{-1}·km s^{-1}; beam is 5.3″ × 5.1″, P.A.= 66.2°. (j,k,l) I_ν^{peak} = 1.06 Jy beam^{-1}·km s^{-1}; σ = 0.12 Jy beam^{-1}·km s^{-1}; beam is 3.24″ × 2.94″, P.A.= 29.3°.

emission (87.4 Jy beam^{-1}·km s^{-1}) is located at $3^h29^m00\overset{s}{.}0$, +31°14′47″, just inside of the BIMA primary beam area (indicated by the square). The continuum sources, indicated by the plus symbols, are not detected at this resolution. In the velocity map (Figure 2.8*b*), the northern half is redshifted relative to the southern half. The reddest velocities (∼8.4 km s^{-1}) appear along the northern edge where the C^{18}O emission weakens, and the northeast corner toward the SVS13 core is also redder than much of the map. The bluest velocities (∼7.1 km s^{-1}) appear in the region of reduced emission in the southeast corner. Within the primary beam area, the velocities are fairly uniform, with a range between 7.2 and 7.9 km s^{-1} and a mode of ∼7.5 km s^{-1}.

In the maps with 10″ resolution (Figure 2.8*d*), the clump of gas around the IRAS2A and IRAS2B continuum sources is brought into sharp relief by the intensity contours. The peak intensity at IRAS2A is 7.0 Jy beam^{-1}·km s^{-1}, and the peak intensity near IRAS2B (less than half of a beam width to the southwest) is 6.0 Jy beam^{-1}·km s^{-1}. The high emission zone forms a bridge between the continuum objects, and another region of extended emission juts northeast of IRAS2A. To the west of IRAS2B, the C^{18}O emission surrounding the continuum sources blends with the emission from the larger ridge seen in the FCRAO data; the point of peak emission in the northeast corner of the map roughly coincides with the peak emission in the FCRAO map. The velocity field (Figure 2.8*e*) of the center of the core is fairly flat. Most velocities within the half-peak contour remain within a few tenths km s^{-1} of a mean value of 7.5 km s^{-1}. At IRAS2A and IRAS2B, the velocities are 7.5 and 7.4 km s^{-1}, respectively. The emission bulge northeast of IRAS2A is slightly bluer at ∼7.3 km s^{-1}, and another patch of blueshifted emission (∼7.2 km s^{-1}) lies roughly 20″ south of IRAS2B. The most highly redshifted velocities, ∼8.1 km s^{-1}, are along the northern edge of the map and 40″-45″ west of the field center, roughly coincident with regions of lower intensity. On the whole, the center of the IRAS2 core appears blueshifted relative to the background material.

The connections between the IRAS2 core and the larger ridge of emission have nearly dissolved in the maps with 5″ resolution. There is a clump of C^{18}O emission in the northeast corner of Figure 2.8*g*, but the high emission contours around the continuum sources are separate from it. The peak intensity at IRAS2A is 2.6 Jy beam^{-1}·km s^{-1}, and the peak just southwest of IRAS2B is 1.9 Jy beam^{-1}·km s^{-1}. The half-peak contour shows irregularly-shaped splashes of emission jutting out from both continuum sources, but it is unclear whether these are signatures of outflow activity or a consequence of the inherent lumpiness of the cloud. In the velocity map

(Figure 2.8*h*), the dissolution of the embedding cloud obscures large-scale trends in the velocity, creating the map's mottled appearance. The velocities at IRAS2A and IRAS2B are both 7.5 km s^{-1}. Regions with blueshifted velocities appear northeast of IRAS2A ($\sim$7.1 km s^{-1}) and also $\sim$15″ south of IRAS2B ($\sim$6.9 km s^{-1}), in the southeast corner of the map. The extreme redshifted velocities appear along all other edges and avoid the areas occupied by the high-intensity contours around the continuum sources. As in the 10″ resolution map, the IRAS2 core appears offset in velocity space from the background material.

At 3″ resolution (Figure 2.8*j*), most of the detectable $C^{18}O$ gathers around the continuum sources; only a few wisps of 3σ emission, barely discernable in the map, occupy the space in between. The $C^{18}O$ emission peaks are, however, significantly offset from the continuum positions. In the vicinity of IRAS2A, the emission is divided into northern and southern lobes; the larger northern lobe is greater than two beamwidths in length and at least one beamwidth wide. The peak intensity, 1.1 Jy $beam^{-1}$·km s^{-1}, is in the northern lobe, roughly half of a beamwidth from the position of IRAS2A. A channel of reduced emission runs in between the two lobes at a position angle of $\sim$65°. Around IRAS2B, the $C^{18}O$ emission is also divided into two lobes. These emitting regions each have peak intensities of 0.7 Jy $beam^{-1}$·km s^{-1}, and they are aligned along a northeast-southwest axis (P.A.$\sim$18°). IRAS2B itself is located roughly one beamwidth from either lobe within a conspicuous emission-free zone. In the velocity map (Figure 2.8*k*), the motions of the IRAS2A and IRAS2B envelopes are not readily discernable. Around IRAS2A, the northern lobe includes primarily velocities < 7.5 km s^{-1}, and the southern lobe has velocities > 7.5 km s^{-1}. Both of the emission lobes around IRAS2B show similar behavior: velocity gradients that change from blueshifted velocities ($\sim$6.8 km s^{-1}) along the southern edges to redshifted velocities ($\sim$8.2 km s^{-1}) along the northern edges.

$H^{13}CO^+$ Maps

The $H^{13}CO^+$ observations of IRAS2 are displayed in Figure 2.9. As in the $C^{18}O$ maps, the panels in the top row show only the data from the FCRAO observations. In the integrated intensity map (Figure 2.9*a*), the strongest emission arises from the location of the SVS13 core, outside of the BIMA primary beam area (white square). The IRAS2 core occupies the center of the map and is elongated in the east-west direction; its eastern end blends with the SVS13 core. The region of $H^{13}CO^+$ emission is considerably more compact than the northeast-southwest ridge of emission traced by the $C^{18}O$ in Figure 2.8*a*. The peak intensity within the IRAS2 core, 26.76 Jy beam^{-1}·km s^{-1}, lies in between the two continuum sources. In the first moment map (Figure 2.9*b*), the extreme blueshifted velocities, < 6.9 km s^{-1}, arise from the lower intensity region at the southern extent of the cloud. The extreme redshifted velocities, > 8.5 km s^{-1}, are near the northern edge of the SVS13 cloud. The change in velocities across the area of the clouds is uniform; there are no discontinuities at the IRAS2/SVS13 interface. The prevalent velocity in the IRAS2 core is 7.6 km s^{-1}. The velocities at IRAS2A and IRAS2B are 7.6 and 7.5 km s^{-1}, respectively.

In the map with 10″ resolution (Figure 2.9*d*), the outstanding feature is the elongated emission feature that peaks at the position of IRAS2A. The peak intensity is 2.3 Jy beam^{-1}·km s^{-1}, and the intensity contours stretch toward the southeast to create a vaguely "ear-shaped" region, with an "earlobe" just *below* IRAS2B. The emission peak in the "earlobe" is 1.6 Jy beam^{-1}·km s^{-1}; this peak is ∼8″ southwest of IRAS2B. In the northeast corner of the map, a bridge of emission links the IRAS2 core to the edge of the SVS13 core. In the velocity map of the region (Figure 2.9*e*), the velocity field of the "ear-shaped" emission region that surrounds IRAS2A appears nearly uniform; the dominant velocity within 15″ of IRAS2A is 7.4 km s^{-1}.

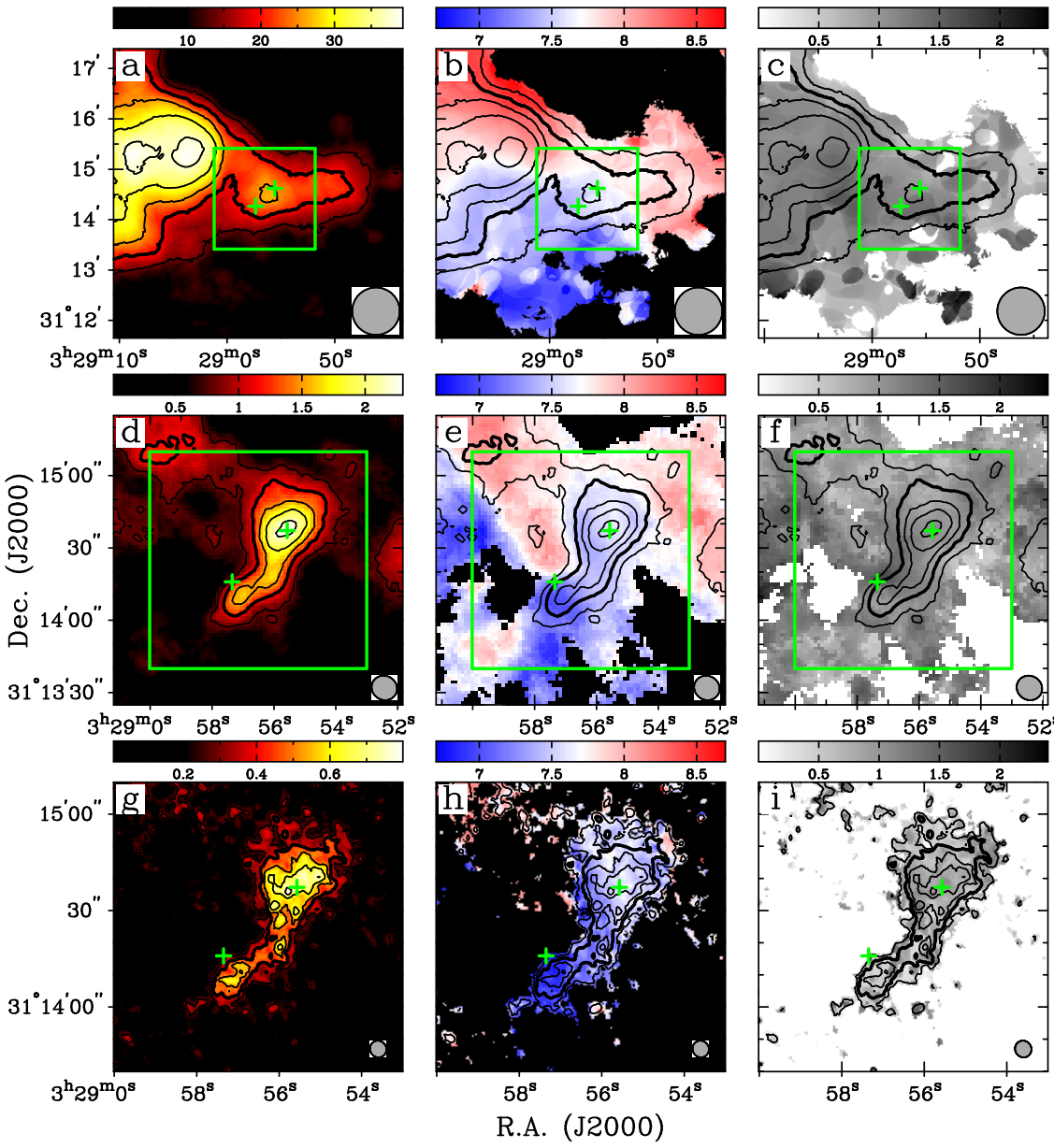

Figure 2.9: $H^{13}CO^+$ $J = 1 \rightarrow 0$ integrated intensity, line-of-sight velocity, and velocity dispersion of NGC1333 IRAS2. Panels *a,d,g* show integrated intensity in both contours and colorscale. Contour levels are 35%, 50%, 65%, 80%, and 95% of peak flux density; bold contour is 50% level. Panels *b,e,h* show integrated intensity contours and line-of-sight velocity field in colorscale. Velocity range is 6.7-8.7 km s^{-1} in all panels. Panels *c,f,i* show integrated intensity contours and velocity dispersion in grayscale. Dispersion range is 0.0-2.34 km s^{-1} in all panels. Square regions delineated by green lines indicate areas of the maps in the row immediately below. Plus symbols indicate positions of continuum sources from LMW00. (a,b,c) I_ν^{peak} = 39.26 Jy beam^{-1}·km s^{-1}; σ = 2.9 Jy beam^{-1}·km s^{-1}; beam is 56.5″ × 56.5″. (d,e,f) I_ν^{peak} = 2.29 Jy beam^{-1}·km s^{-1}; σ = 0.14 Jy beam^{-1}·km s^{-1}; beam is 10.76″ × 9.98″, P.A.= 60.5°. (g,h,i) I_ν^{peak} = 0.74 Jy beam^{-1}·km s^{-1}; σ = 0.07 Jy beam^{-1}·km s^{-1}; beam is 5.29″ × 5.04″, P.A.= 34.6°.

This feature reinforces the assertion that IRAS2 moves independently from a background cloud. As in the $C^{18}O$ velocity field with 10″ resolution (Figure 2.8*e*), the core appears blueshifted relative to the material that surrounds it. Another striking feature of the $H^{13}CO^+$ velocity field is the convergence of two wedges of strongly contrasting velocity at IRAS2B. To the south, the blueshifted wedge ($\sim$7.2 km s^{-1}) culminates at the "earlobe" just below the continuum source. To the north, the redshifted velocity wedge ($\sim$8.0 km s^{-1}) extends all the way to the northeast corner of the map. At the position of IRAS2B, the blue-to-red velocity change is 1.1 km s^{-1} in only 16″.

At 5″ resolution (Figure 2.9*g*), no substantial $H^{13}CO^+$ emission is detected in the northeast corner of the map. IRAS2A is near the strongest peak, 0.7 Jy beam^{-1}·km s^{-1}, where the high emission contours are elongated in an east-west direction. IRAS2B is near the edge of an emission clump that has a maximum, 0.6 km s^{-1}, roughly 8″ to the south. A bridge of emission connects the two local maxima. The most conspicuous characteristic of the velocity map (Figure 2.9*h*) is that the entire emitting region around IRAS2A and IRAS2B occupies only the blueshifted end of the velocity range. Redshifted velocities are contributed almost exclusively by the scattered blobs of emission near the northeast corner of the map. Within the IRAS2A envelope, there is a velocity gradient along the direction of elongation. The velocities shift from $\sim$7.8 km s^{-1} at the western edge to $\sim$7.0 km s^{-1} in the bridge that extends toward IRAS2B. The clump below IRAS2B is blueshifted relative to the IRAS2A envelope, with velocities that range from 6.8 km s^{-1} at the northern edge to 7.2 km s^{-1} at the southern edge. The presence of a systematic velocity gradient across the clump is not clear.

Maps of the $H^{13}CO^+$ emission at 3″ resolution are omitted from Figure 2.9. The noise of the integrated intensity map is 0.08 Jy beam^{-1}·km s^{-1}, and only two small

blobs of $> 4\sigma$ emission in the vicinity of IRAS2A are the only significant features.

N_2H^+ Maps

As with the N_2H^+ maps of L1448 IRS3 (§2.4.3), the intensity maps displayed in Figure 2.10 are integrated over only the "isolated" hyperfine line at $\nu = 93.176310$ GHz. The panels in the top row display the results from the FCRAO observations.

The morphology of the N_2H^+ emission in the $6' \times 6'$ field shown in Figure 2.10*a* is very similar to the morphology of the $H^{13}CO^+$ emission seen in Figure 2.9*a*. The dominant source of emission in the map is the cloud surrounding the SVS13 core in the northeast corner; the intensity peak there is 29.2 Jy beam^{-1}·km s^{-1}. A bridge of emission connects the SVS13 core to the IRAS2 core in the center of the field. The IRAS2 core, with a peak intensity of 20.1 Jy beam^{-1}·km s^{-1} northwest of IRAS2A, is more compact than the $H^{13}CO^+$ emission from the same area. In the velocity map (Figure 2.10*b*), the characteristics of the velocity field that were traced by the $H^{13}CO^+$ emission persist in the N_2H^+ emission. The most highly redshifted velocities ($\sim$8.7 km s^{-1}) occur at the northern edge of SVS13, and the most highly blueshifted velocities ($\sim$7.2 km s^{-1}) appear at the southern edge of IRAS2 and in a separate clump near the southern edge of the map. The velocity gradient across the IRAS2 cloud has approximately the same magnitude and orientation as the gradient seen in the $H^{13}CO^+$ emission. The velocities at IRAS2A and IRAS2B are 7.8 and 7.6 km s^{-1}, respectively.

The N_2H^+ emission maps with $10''$ resolution (Figure 2.10*d*) show no hint of the presence of IRAS2B. Although diffuse 3σ emission appears south and west of the IRAS2B location, the morphology of the emission shows no connection with IRAS2B. In contrast, IRAS2A is bracketed by two clumps of emission. The weaker emission peak ($\sim$2.1 Jy beam^{-1}·km s^{-1}) is less than half of a beamwidth southeast

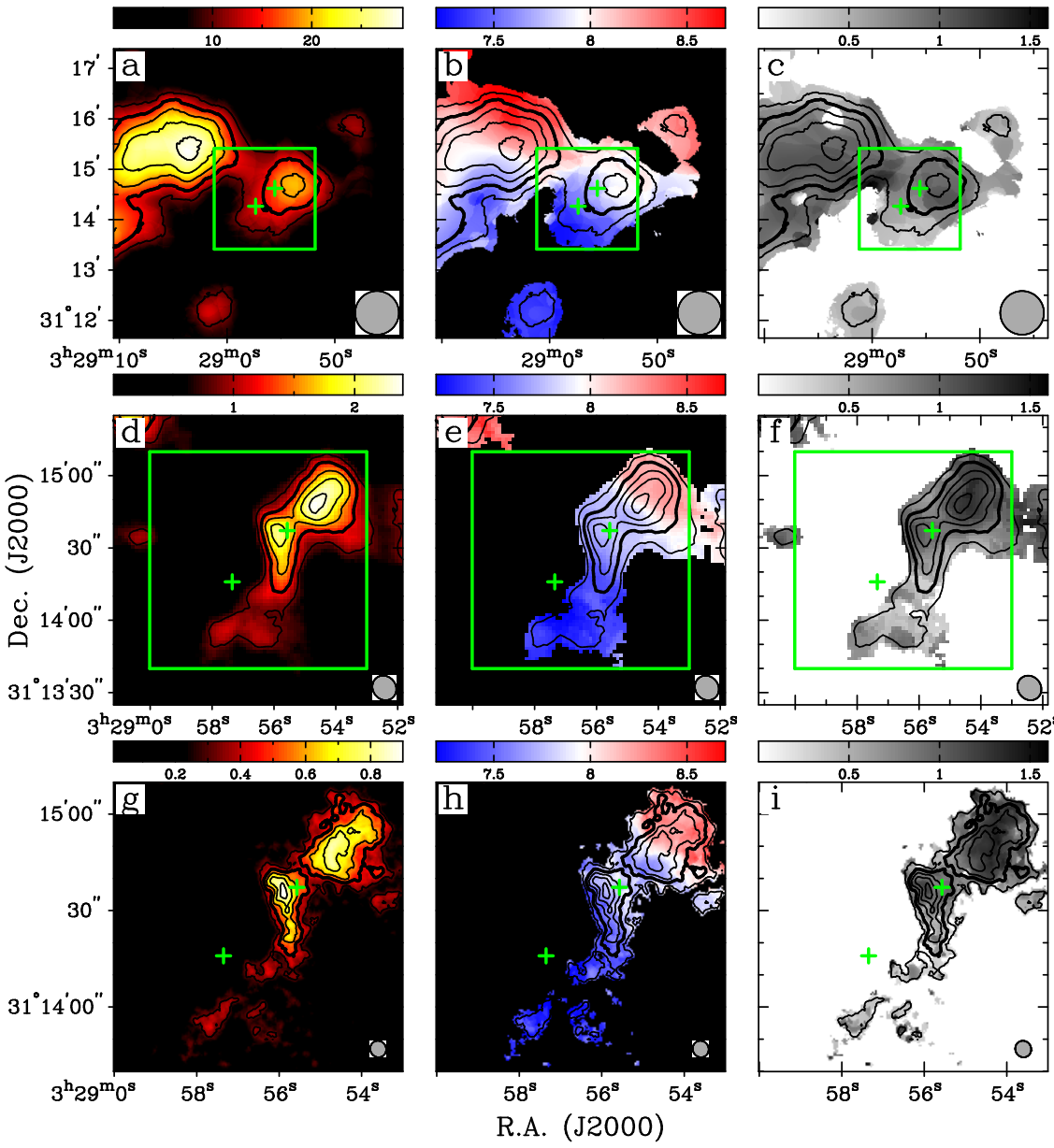

Figure 2.10: N_2H^+ $J = 1 \rightarrow 0$ integrated intensity, line-of-sight velocity, and velocity dispersion of NGC1333 IRAS2. Panels *a, d, g* show integrated intensity in both contours and colorscale. Contour levels are 35%, 50%, 65%, 80%, and 95% of peak flux density; bold contour is 50% level. Panels *b, e, h* show integrated intensity contours and line-of-sight velocity field in colorscale. Velocity range is 7.2-8.7 km s^{-1} in all panels. Panels *c, f, i* show integrated intensity contours and velocity dispersion in grayscale. Dispersion range is 0.0-1.56 km s^{-1} in all panels. Square regions delineated by green lines indicate areas of the maps in the row immediately below. Plus symbols indicate positions of continuum sources from LMW00. (a,b,c) I_ν^{peak} = 29.19 Jy beam^{-1}·km s^{-1}; σ = 2.4 Jy beam^{-1}·km s^{-1}; beam is $52'' \times 52''$. (d,e,f) I_ν^{peak} = 2.35 Jy beam^{-1}·km s^{-1}; σ = 0.22 Jy beam^{-1}·km s^{-1}; beam is $10.60'' \times 9.49''$, P.A.= 38.0°. (g,h,i) I_ν^{peak} = 0.90 Jy beam^{-1}·km s^{-1}; σ = 0.09 Jy beam^{-1}·km s^{-1}; beam is $5.20'' \times 4.91''$, P.A.= 27.9°.

of the continuum source; the stronger emission peak ($\sim$2.3 Jy beam^{-1}·km s^{-1}) is 1.5 beamwidths to the northwest. The southeastern clump is elongated north-south; the northwestern clump is elongated northwest-southeast, on a direct line between IRAS2A and IRAS2C. (The position of IRAS2C is not indicated in Figure 2.10, as it was not detected in the $\lambda = 2.7$ mm continuum observations by LMW00. It is located inside the half-power contour, on the opposite side of the emission peak from IRAS2A.) In the velocity map (Figure 2.10*e*), the regions of low level emission south of IRAS2B are shifted blueward to $\sim$7.2 km s^{-1}. The emission regions surrounding IRAS2A show a velocity gradient along the direction of elongation. The blueshifted extremes at the southeastern tip are $\sim$7.4 km s^{-1}, and the redshifted extremes at the northwestern edge near IRAS2C are $\sim$8.3 km s^{-1}. The change across the region is remarkably uniform.

The intensity map with 5″ resolution (Figure 2.10*g*), like the 10″ map, shows no evidence for N_2H^+ emission at IRAS2B. The emission south and west of the continuum position is scattered and feeble. Around IRAS2A, the emission region maintains its bilateral morphology, and each lobe maintains its orientation, with the southeastern lobe elongated in the north-south direction, and the northwestern lobe is elongated in the northwest-southeast direction. At this resolution, the southeast clump is stronger (0.90 Jy beam^{-1}·km s^{-1}) than the northwestern clump (0.84 Jy beam^{-1}·km s^{-1}). The velocity map at 5″ resolution (Figure 2.10*h*) shows essentially the same behavior that is seen with 10″ resolution. A velocity gradient remains fairly uniform in magnitude and direction across the IRAS2A continuum position. Redshifted velocities ($\sim$8.5 km s^{-1}) occur at the northwest edge of the emitting region, and blueshifted velocities ($\sim$7.4 km s^{-1}) occur south and east of IRAS2A. The extreme blueshifted velocities ($\sim$7.0 km s^{-1}) appear in the diffuse emission south of IRAS2B.

Higher resolution maps of the N_2H^+ emission are not included in Figure 2.10. As with the 3″ $H^{13}CO^+$ maps, only a few bright patches of emission are seen in the vicinity of IRAS2A. The emission peak ($\sim$0.38 Jy beam^{-1}·km s^{-1}) appears > 1 beamwidth southeast of the position of the continuum source.

$C^{18}O/H^{13}CO^+/N_2H^+$ Line Comparison

A comparison of Figures 2.8, 2.9, and 2.10 shows that the emission from the $C^{18}O$ $J = 1 \rightarrow 0$ line, the lower density gas tracer, is consistently stronger and consistently more spread out than the emission from either the $H^{13}CO^+$ or the N_2H^+ line. All of the $C^{18}O$ intensity maps that include FCRAO data (Figures 2.8*a,d,g*) have significant emission throughout the BIMA primary beam area. In contrast, the intensity maps of the $H^{13}CO^+$ and N_2H^+ lines, which are tracers of higher densities, are consistently compact. Another striking difference between the low and high density tracers is the distribution of the emitting gas in the vicinity of IRAS2B. In the $C^{18}O$ line, the emission peak is very close to the continuum source position at all resolutions. The maximum displacement from the continuum position is $\sim$3″ in the high resolution maps. The $H^{13}CO^+$ and N_2H^+ intensity maps, on the other hand, reveal that the emission conspicuously avoids IRAS2B. In the $H^{13}CO^+$ maps, a secondary emission peak is evident $\sim$8″ southwest of the continuum position, but no secondary peak can be detected in the N_2H^+ maps.

In the vicinity of IRAS2A, it is the N_2H^+ distribution that differs from the distribution traced by the other lines. In both the $C^{18}O$ and $H^{13}CO^+$ maps, IRAS2A coincides with the center of a single emission peak. The N_2H^+ emission shows, instead, a bilateral distribution. One lobe peaks southwest of IRAS2A and is elongated in a north-south direction; the other lobe peaks northwest of IRAS2A and extends further to the northwest, almost to the position of IRAS2C.

At least three major conclusions may be drawn from the velocity fields traced by the molecular lines. First, the velocities of all three molecules suggest that the IRAS2 core is shifted in velocity from the background cloud that's detected along the edges of the maps. In the 10″ and 5″ $C^{18}O$ maps, the entire area within the half-peak contour around IRAS2A is blueshifted relative to the surrounding field. The velocity field traced by the $H^{13}CO^+$ line bolsters this finding: the area within the half-peak contour in the $H^{13}CO^+$ maps is blueshifted from the background emission. Second, the higher density tracers detect a pronounced gradient in the velocities surrounding IRAS2A. The 5″ resolution $H^{13}CO^+$ map shows blueshifted velocities southeast of IRAS2A and redshifted velocities to the northwest. The gradient is even more dramatic in the N_2H^+ velocity maps. Third, as observed in the velocity fields around L1448 IRS3, the velocity maps of IRAS2 demonstrate that higher resolution observations probe a greater range of velocities. In the 10″ resolution maps, the range of velocities across the primary beam area is 0.7 km s^{-1} in the $C^{18}O$ data, 1.0 km s^{-1} in the $H^{13}CO^+$ data, and 0.9 km s^{-1} in the N_2H^+ data. In the 5″ maps, the velocity ranges are 1.5, 1.4, and 1.2 km s^{-1}, respectively. In the $C^{18}O$ maps at 3″, the velocity range decreases slightly to 1.1 km s^{-1}, but this may result from the 3σ noise cutoff, which permits fewer pixels to be included in the calculation of the first moment.

2.5.4 Spectra

Representative spectra from the IRAS2 datacubes are presented in Figure 2.11. The strengths, central velocities, and widths of the spectra are listed in Tables 2.4, 2.5, and 2.6 and are determined by fitting single Gaussian functions to the emission line profiles. Spectra taken from the FCRAO data alone are shown in the top row. The positions α, β, γ, and δ are chosen to sample regions of the cloud that may be far

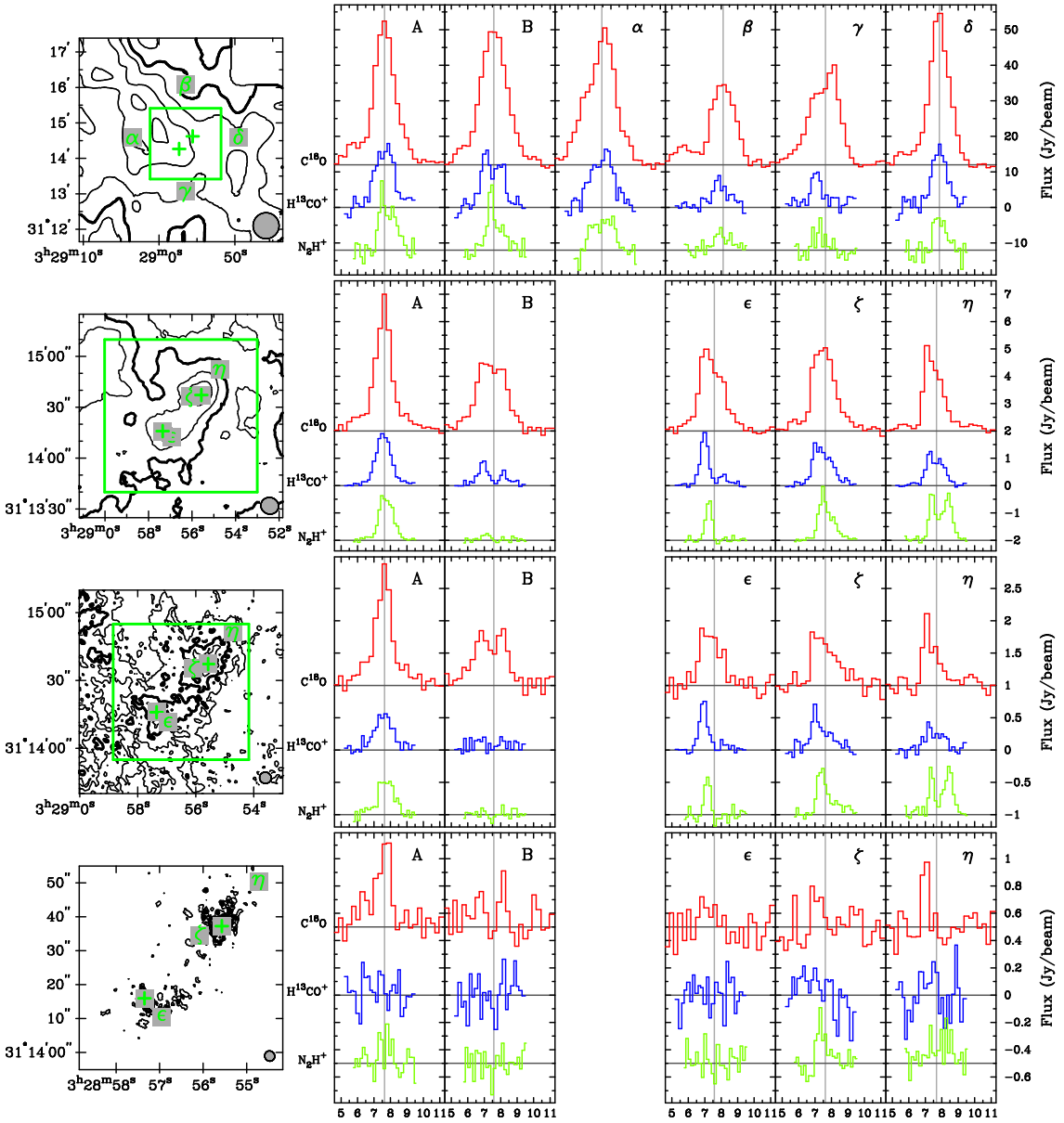

Figure 2.11: NGC1333 IRAS2 spectra. The plots at left show the $C^{18}O$ integrated intensity contours from Figure 2.8. To the right of each plot are spectra from the $C^{18}O$ (red), $H^{13}CO^+$ (blue), and N_2H^+ (lt. green) datacubes. Spectra were taken at the positions of the continuum sources, indicated by plus symbols, and the positions indicated by the letters α through η. All spectra display the mean flux in Jy beam^{-1} taken over a beam area. For clarity, the $C^{18}O$ spectra are given positive offsets, and the N_2H^+ spectra are given negative offsets. In the FCRAO data (top row), the offsets are ± 12 Jy beam^{-1}; in the $10''$ maps (second row), the offsets are ± 2 Jy beam^{-1}; in the $5''$ maps (third row), the offsets are ± 1 Jy beam^{-1}; in the $3''$ maps (bottom row), the offsets are ± 0.5 Jy beam^{-1}. In all rows, the gray vertical lines show central velocities of Gaussian function fitted to the $C^{18}O$ profile from the FCRAO map (top row). For positions ϵ, ζ, and η, the central velocities are from FCRAO spectra *not* shown on the top row.

enough away to be isolated from the IRAS2 core. The four positions are located in the cardinal directions (east, north, south, and west, respectively) exactly 90″ offset from the center of the map. The α position probes the ridge of emission that descends from the northeast corner of the map. This position is also at the edge of the SVS13 cloud in the $H^{13}CO^+$ and N_2H^+ maps, so the spectrum includes primarily emission from the SVS13 region. The α spectrum exhibits a shallow slope on the blue side of the $C^{18}O$ line, which is strong enough to be incorporated in the Gaussian fit and bring its central velocity (7.4 km s^{-1}) in accord with the velocity of the first moment map. This value is distinctly bluer than much of the first moment map (Figure 2.8*b*). The $H^{13}CO^+$ and N_2H^+ line profiles at α also have shallow blueward slopes. In both cases, the enhanced blueward emission results in measured mean velocities that are bluer than the $C^{18}O$ line. The $C^{18}O$ profile from position β is weaker and more symmetrical than the profile from α, but a second hump of emission, centered at 5.8 km s^{-1}, rises on the blueward side. This second hump is not included in the calculation of the first moment. The $H^{13}CO^+$ and N_2H^+ lines are also weaker at β than at α; the integrated intensity falls below the 3σ threshold. At the γ position, the $C^{18}O$ line has an asymmetrical profile. As with the spectrum from α, the relative strength of the emission on the blueward side of the $C^{18}O$ peak at γ results in a Gaussian function with the same mean velocity (7.6 km s^{-1}) as the first moment map. The $H^{13}CO^+$ and N_2H^+ lines at γ are quite different from those at α. These lines have only a single component, centered under the blue shoulder of the $C^{18}O$ profile. The $C^{18}O$ line at position δ is strong, narrow, and nearly symmetrical. A Gaussian function fits the profile very well, and the central velocity is 7.9 km s^{-1}. The $H^{13}CO^+$ profile is also adequately fit by a Gaussian function. The central velocity of the weak N_2H^+ line, 7.9 km s^{-1}, is consistent with the velocities of the $C^{18}O$ and $H^{13}CO^+$ lines, although there is insufficient flux at δ

Table 2.4. NGC1333 IRAS2 $C^{18}O$ Spectra

ID	Beam (arcsec)	I_ν^{peak} (Jy beam^{-1})	V_C (km s^{-1})	ΔV (km s^{-1})
A	44/56.5/52	38.44 ± 1.15	7.6 ± 0.1	1.6 ± 0.1
	10	4.49 ± 0.09	7.6 ± 0.0	1.2 ± 0.1
	5	1.67 ± 0.10	7.6 ± 0.1	1.2 ± 0.2
	3	0.60 ± 0.11	7.6 ± 0.3	1.0 ± 0.5
B	44/56.5/52	37.75 ± 1.04	7.6 ± 0.1	1.9 ± 0.1
	10	2.58 ± 0.07	7.4 ± 0.1	2.1 ± 0.2
	5	0.76 ± 0.07	7.4 ± 0.4	2.4 ± 0.6
	3	0.31 ± 4.30	8.2 ± 9.9	
α	44/56.5/52	34.62 ± 0.98	7.4 ± 0.1	2.1 ± 0.2
β	44/56.5/52	23.00 ± 1.10	8.1 ± 0.2	1.7 ± 0.2
γ	44/56.5/52	25.23 ± 0.99	7.6 ± 0.2	2.1 ± 0.2
δ	44/56.5/52	40.69 ± 1.20	7.9 ± 0.1	1.4 ± 0.1
ϵ	10	2.80 ± 0.08	7.3 ± 0.1	1.7 ± 0.1
	5	0.84 ± 0.09	7.3 ± 0.3	1.5 ± 0.4
	3	0.16 ± 0.11	7.1 ± 1.3	
ζ	10	3.12 ± 0.08	7.5 ± 0.1	1.6 ± 0.1
	5	0.74 ± 0.09	7.5 ± 0.4	1.7 ± 0.5
	3	0.15 ± 0.11	7.2 ± 1.5	
η	10	2.77 ± 0.09	7.4 ± 0.1	1.3 ± 0.1
	5	0.88 ± 0.12	7.2 ± 0.2	0.9 ± 0.3
	3		7.0 ± 5.9	

to calculate the first moment.

The peak in the $C^{18}O$ spectrum at IRAS2A is nearly as strong as the peak at δ. Low-level flux in the channels on the blue side of the line peak pull the first moment blueward to 7.5 km s^{-1}. The central velocity of the Gaussian function fit to the line is slightly redder at 7.6 km s^{-1}. The $H^{13}CO^+$ line shows two peaks. The secondary peak, blueward of the primary, is only fractionally lower in intensity. Consequently, the first moment at IRAS2A is 7.6 km s^{-1}, but the central velocity of the Gaussian function, 7.7 km s^{-1}, is slightly redder. Unlike the $C^{18}O$ and $H^{13}CO^+$ lines, the N_2H^+ line has a secondary peak on the red side of the primary peak. Here, the relative strength of the secondary peak reduces the quality of the Gaussian fit to the spectrum. The mean velocity of the Guassian is 7.8 km s^{-1}, identical to the first

Table 2.5. NGC1333 IRAS2 $H^{13}CO^+$ Spectra

ID	Beam (arcsec)	I_ν^{peak} (Jy beam^{-1})	V_C (km s^{-1})	ΔV (km s^{-1})
A	44/56.5/52	16.86 ± 1.36	7.7 ± 0.3	1.3 ± 0.4
	10	1.88 ± 0.05	7.6 ± 0.1	1.1 ± 0.1
	5	0.54 ± 0.06	7.6 ± 0.4	1.3 ± 0.5
	3		6.6 ± 2.8	
B	44/56.5/52	13.61 ± 1.27	7.5 ± 0.4	1.5 ± 0.6
	10	0.81 ± 0.06	7.0 ± 0.2	0.8 ± 0.2
	5	0.10 ± 0.04	7.6 ± 4.8	4.0 ± 9.9
	3		8.2 ± 1.3	
α	44/56.5/52	14.50 ± 1.23	7.5 ± 0.4	1.6 ± 0.6
β	44/56.5/52	6.56 ± 1.42	7.9 ± 0.8	1.2 ± 1.1
γ	44/56.5/52	9.99 ± 1.79	7.1 ± 0.4	0.8 ± 0.6
δ	44/56.5/52	16.44 ± 1.53	7.9 ± 0.3	1.1 ± 0.4
ϵ	10	1.91 ± 0.07	7.0 ± 0.1	0.6 ± 0.1
	5	0.75 ± 0.08	6.9 ± 0.2	0.6 ± 0.3
	3		8.4 ± 3.3	
ζ	10	1.38 ± 0.05	7.4 ± 0.1	1.4 ± 0.2
	5	0.45 ± 0.06	7.2 ± 0.5	1.3 ± 0.6
	3	0.14 ± 0.10	6.6 ± 3.1	
η	10	1.08 ± 0.05	7.6 ± 0.2	1.2 ± 0.2
	5	0.31 ± 0.05	7.5 ± 0.7	1.3 ± 1.0
	3			

moment velocity.

As the map resolution increases, the IRAS2A spectra provide evidence of a single dominant emission source at this position. Looking down the column of IRAS2A spectra, the peak intensity declines as the resolution increases, but the shape of the profile remains fairly consistent. At all resolutions, low-level flux occupies the blueward sides of the line peaks. Gaussian functions fit to the $C^{18}O$ spectra yield a consistent central velocity of 7.6 km s^{-1}. The value of the first moment at IRAS2A is consistent in the 10″ and 5″ maps (7.5 km s^{-1}), but in the 3″ map, when the blueward channels are not included in the calculation, the first moment increases to 7.6 km s^{-1}. The mean velocities of the $H^{13}CO^+$ and N_2H^+ profiles remain consistent at all resolutions.

Table 2.6. NGC1333 IRAS2 N_2H^+ Spectra

ID	Beam (arcsec)	I_ν^{peak} (Jy beam^{-1})	V_C (km s^{-1})	ΔV (km s^{-1})
A	44/56.5/52	13.69 ± 1.57	7.8 ± 0.4	1.1 ± 0.6
	10	1.61 ± 0.05	7.7 ± 0.1	1.0 ± 0.1
	5	0.54 ± 0.05	7.8 ± 0.3	1.1 ± 0.4
	3	0.15 ± 0.09	7.7 ± 1.5	
B	44/56.5/52	14.54 ± 1.91	7.5 ± 0.3	0.8 ± 0.4
	10	0.24 ± 0.06	7.1 ± 0.5	
	5		8.2 ± 1.2	
	3		8.1 ± 0.0	
α	44/56.5/52	7.95 ± 1.31	7.6 ± 0.8	1.6 ± 1.2
β	44/56.5/52	4.45 ± 1.54	8.1 ± 1.3	
γ	44/56.5/52	5.81 ± 2.03	7.3 ± 0.7	
δ	44/56.5/52	9.26 ± 1.84	7.9 ± 0.5	0.8 ± 0.7
ϵ	10	1.53 ± 0.07	7.3 ± 0.1	0.4 ± 0.1
	5	0.63 ± 0.08	7.2 ± 0.2	0.4 ± 0.2
	3		7.0 ± 1.6	
ζ	10	1.55 ± 0.05	7.6 ± 0.1	0.9 ± 0.1
	5	0.70 ± 0.06	7.4 ± 0.2	0.7 ± 0.3
	3	0.33 ± 0.11	7.4 ± 0.6	
η	10	1.38 ± 0.04	8.0 ± 0.1	1.5 ± 0.2
	5	0.49 ± 0.04	8.1 ± 0.4	1.7 ± 0.6
	3	0.16 ± 0.06	8.0 ± 2.1	

At IRAS2B, the $C^{18}O$ line is wider than at IRAS2A, but like the IRAS2A spectrum, it shows enhanced emission in the blueshifted wing. The line is well fit by a Gaussian function with a central velocity of 7.6 km s^{-1}. The value of the first moment at IRAS2B is 7.5 km s^{-1}. The $H^{13}CO^+$ and N_2H^+ lines are both double-peaked, with the stronger peak on the blueward side. In the $H^{13}CO^+$ profile, the secondary peak is comparable in strength to the primary peak, but in the N_2H^+ profile, the primary peak dominates the secondary. The mean velocity of the $H^{13}CO^+$ profile splits the two peaks at 7.5 km s^{-1}. The mean velocity of the N_2H^+ line favors the primary peak when fit by a Gaussian function (7.5 km s^{-1}) but is slightly redder in the first moment map (7.6 km s^{-1}).

The behavior of the IRAS2B spectral lines at higher resolutions is completely

different from the behavior seen in the IRAS2A spectra. Whereas the IRAS2A spectra are consistently strong and single-peaked, the IRAS2B spectra are weaker and show two peaks of comparable height and width. The doubling is most apparent in the $C^{18}O$ profiles. At $10''$ resolution, the two lines are almost completely blended together Both the Gaussian function fit to the profile and the first moment find the same central velocity: 7.4 km s^{-1}. At $5''$ resolution, the two lines are separated at the half-maximum point. The Gaussian function with a central velocity of 7.3 km s^{-1} fits primarily the blueshifted component. The first moment map, on the other hand, gives more weight to the redshifted component and has a velocity of 7.5 km s^{-1}. At $3''$ resolution, two narrow emission spikes remain in the spectrum. The peak velocities are 6.8 and 8.2 km s^{-1}, but neither spike is satisfactorily fit by a Gaussian function. The $H^{13}CO^+$ and N_2H^+ lines in the higher resolution ($5''$ and $3''$) spectra are impossible to discern. Even at $10''$ resolution, the lines are significantly smaller than the $C^{18}O$ line. Gaussian functions fit to the spectra only match the bluer peak and find central velocities of 7.0 and 7.1 km s^{-1} for $H^{13}CO^+$ and N_2H^+, respectively.

The other spectra in the second, third, and fourth rows of Figure 2.11 correspond to the positions ϵ, ζ, and η on the contour maps. These three positions were chosen to coincide with specific features in the intensity maps. In the case of ϵ (R.A.$= 3^h28^m56\overset{s}{.}95$, Dec. $= 31°14'09\overset{''}{.}51$), the position coincides with the peak in the $H^{13}CO^+$ intensity map (Figure 2.9) roughly $8''$ south of IRAS2B. The $C^{18}O$ spectra at ϵ have strengths comparable with the spectra at IRAS2B, but the ϵ profiles have only a single peak. The blue edges of the lines dominate, and redder emission is smeared over several channels. In both the $10''$ and $5''$ spectra, the mean velocities of Gaussian functions fit to the spectra are 7.3 km s^{-1}; the first moment at ϵ is 7.4 km s^{-1}. The peak of the $H^{13}CO^+$ spectrum at ϵ is, as expected, prominently stronger than the $H^{13}CO^+$ peak at IRAS2B. The secondary (redshifted) line

($\sim$8.2 km s^{-1}) is smaller than the IRAS2B secondary, so the mean velocity of the line is shifted blueward. The center of the Gaussian function fit to the line is 7.0 km s^{-1} in the 10″ spectrum, and the first moment is 7.1 km s^{-1}. In the 5″ spectra, the mean velocity is 6.9 km s^{-1} by either method. The N_2H^+ line is also stronger at ϵ than at IRAS2B, although not as strong as the $H^{13}CO^+$ line. At 10″ resolution, the mean velocity of the N_2H^+ line is 7.3 km s^{-1}; at 5″ resolution, the mean velocity is 7.2 km s^{-1}. The position of ζ (R.A.= $3^h28^m56\overset{s}{.}07$, Dec. = $31°14'33\overset{''}{.}31$) coincides with the peak in the N_2H^+ intensity that lies $\sim$5″ southeast of IRAS2A. The most intriguing features of the spectra at ζ are the shallow declines on the redward sides of the line peaks. In general, these lines are poorly fit by Gaussian functions. At 10″ resolution, a Gaussian function fit to the $C^{18}O$ spectrum has a central velocity of 7.5 km s^{-1}. The value of the first moment is 7.6 km s^{-1}. The mean velocity of the $H^{13}CO^+$ spectrum at 10″ resolution is 7.4 km s^{-1} for both the Gaussian function and first moment. The mean velocity of the N_2H^+ spectrum, on the other hand, is 7.6 and 7.7 km s^{-1} for the Gaussian function and first moment, respectively. At 5″ resolution, the mean velocities in both of these lines are blueshifted even further. The values are 7.2 and 7.3 km s^{-1} for the $H^{13}CO^+$ line and 7.4 and 7.5 km s^{-1} for the N_2H^+ line. For all three lines, the discrepancy in the mean velocities determined by the two methods manifests in the expected systematic way: the first moment values are influenced more strongly by the low-level flux in the redward channels.

The η position (R.A.= $3^h28^m54\overset{s}{.}76$, Dec. = $31°14'48\overset{''}{.}71$) coincides with the N_2H^+ peak on the northwestern side of IRAS2A. The $C^{18}O$ and $H^{13}CO^+$ lines show blueward asymmetries similar to the spectra from ζ. However, the lines are slightly narrower, so the effect on the calculation of the first moment is reduced. For the $C^{18}O$ lines at 10″ resolution, both the Gaussian function fit and the first moment find the same central velocity: 7.4 km s^{-1}. In the 5″ spectra, these values converge

on 7.3 km s^{-1}. The mean velocities of the $H^{13}CO^+$ spectra are generally redder. At 10″ resolution, both methods yield a mean velocity of 7.6 km s^{-1}. At 5″ resolution, a Gaussian fit has a slightly bluer central velocity at 7.5 km s^{-1}, but the first moment map shows an incongruous 7.2 km s^{-1}. The profiles of the N_2H^+ lines contrast sharply with those of the $C^{18}O$ and $H^{13}CO^+$. All of the N_2H^+ spectra show a strong double-peaked profile, similar to the $C^{18}O$ spectra at IRAS2B, but with less line blending. The two components in the profiles are similar in height and width. In both the 10″ and 5″ spectra, both methods for determining the mean velocity split the lines at 8.0 km s^{-1}.

2.6 NGC1333 IRAS4

2.6.1 Background

The IRAS4 core is one of the most thoroughly studied examples of low mass star formation in the embedded phase. It is also among the youngest cores yet discovered. At optical wavelengths, IRAS4 is an unremarkable region $\sim 2'$ south of the bright trail of Herbig-Haro objects HH 7-11 (*c.f.* Strom, Vrba, & Strom (1976); Bally, Devine, & Reipurth (1996)). Attention was drawn to this region as a possible site of active star formation by the detection of two water masers, H_2O(C) (Haschick *et al.* 1980, 1983) and H_2O(D) (Ho *et al.* 1982; Moran 1983), separated by $\sim 1'$. The 50/100 μm emission peak identified by the IRAS satellite as IRAS4 (Jennings *et al.* 1987) is halfway between these masers. The fluxes measured by IRAS indicated a dust temperature of 33 K and a luminosity of 21 $L_\odot$ for an assumed distance of 350 pc.

Observations of the CO $J = 1 \rightarrow 0$ emission from the core (Liseau, Sandell, & Knee 1988) detected a large-scale outflow with a blueshifted southern lobe and a

redshifted northern lobe. Subsequent observations have revealed that the structure of the ambient gas in the IRAS4 core may be quite complex. The emission from various CS transitions observed with the IRAM 30 m telescope indicates the presence of (at least) two different layers of ambient gas permeating the core (Langer, Castets, & Lefloch 1996). In addition, observations of narrow SiO lines (Lefloch *et al.* 1998b) suggest another thin layer of shocked gas located just southwest of the core center.

Maps of the $\lambda = 450/800$ μm continuum emission by Sandell *et al.* (1991) resolved IRAS4 into three components. The two brightest sources at these wavelengths, IRAS4A and IRAS4B, are separated by $\sim 30''$ along a northwest-southeast line. Under the assumption that the dust condensations were homogeneous, Sandell *et al.* (1991) estimated the total masses of IRAS4A and IRAS4B to be 9.2 M$\odot$ and 4.0 M$\odot$, respectively. The third source, IRAS4C, is considerably fainter than the other two and lies $\sim 45''$ above the IRAS4AB plane. Its mass was estimated to be 0.6 M$\odot$.

The IRAS4 core is now known to comprise a small cluster of protostellar objects within a radius of $\sim 30''$. IRAS4A is a binary source. Although it appears only as an elongated source in SCUBA/JCMT maps at $\lambda = 450/850$ μm (Sandell & Knee 2001), its binarity was deduced by Lay, Carlstrom, & Hills (1995) by modeling visibility data at $\lambda = 0.84$ mm. Their prediction that IRAS4A consisted of two components separated by $1.8''$ at a position angle of $\sim 130^\circ$ was emphatically confirmed by sub-arcsecond observations of the $\lambda = 2.7$ mm continuum emission with the BIMA interferometer (LMW00, see Figure 2.12) and the $\lambda = 3.6$ cm continuum with the A-array configuration of the VLA (Reipurth *et al.* 2002).

The IRAS4A pair are surrounded by an envelope of circumbinary material that has been detected from submillimeter (Sandell *et al.* 1991) to centimeter (Mundy *et al.* 1993) wavelengths. Estimates of the dust mass of the envelope have varied as

a function of the observed wavelength; observations of shorter wavelengths produce higher mass estimates. From observations of the $\lambda = 450$ μm continuum, Smith *et al.* (2000) estimated a total dust mass of $M_d = 11.5 \pm 0.5$ M$\odot$; their estimate based upon the $\lambda = 850$ μm continuum is $M_d = 10.9 \pm 1.0$ M$\odot$. From observations of the $\lambda = 1.25$ mm continuum, Lefloch *et al.* (1998a) estimate the dust mass to be $M_{dust} = 6.2$ M$\odot$. And, from observations of the $\lambda = 1.4/2.8$ mm continuum combined with $\lambda = 1.3/2.0/3.6$ cm data from Mundy *et al.* (1993), Blake *et al.* (1995) estimated the dust mass of IRAS4A to be $M_{dust} = 3.5$ M$\odot$. Choi (2001) assumes that the distance to IRAS4 is 220 pc and calculates a dust mass of $M_d = 0.9 \pm 0.3$ M$\odot$ based upon BIMA observations of the $\lambda = 2.7/3.4$ mm continuum, but if IRAS4 were removed to 350 pc, the mass estimate would increase to 2.3 M$\odot$, a value in keeping with the longer wavelength - lower mass trend.

The most extended outflow in the IRAS4 core emanates from the IRAS4A binary (Blake *et al.* 1995; Knee & Sandell 2000). When mapped in CO $J = 3 \rightarrow 2$ emission, the outflow stretches symmetrically over roughly $4'$. The blueshifted lobe extends toward the southwest, where it can be traced by the H_2 $1 \rightarrow 0$ S(1) emission features HL3, HL5, and HL6 (Hodapp & Ladd 1995). Toward the northeast, the redshifted lobe is marked by the emission features HL10, HL11, and ASR57 (Hodapp & Ladd 1995; Aspin, Sandell, & Russell 1994) until it appears to terminate at the Herbig-Haro object HH347 (Bally, Devine, & Reipurth 1996). The CO emission displays a peculiar "bent" morphology; in the inner arcminute, the position angle of the outflow is $\sim 0°$, but at larger radii, the angle changes to $\sim 45°$.

Higher density lines trace the outflow only within $1'$ of the continuum objects (Blake *et al.* 1995) and reveal the presence of dense gas concentrated in an envelope along the IRAS4A-IRAS4B axis (Choi, Panis, & Evans 1999). The most strongly blueshifted emission from the HCO^+ $J = 1 \rightarrow 0$ and HCN $J = 1 \rightarrow 0$

lines lies immediately south of IRAS4A. In fact, interferometer spectra from both of these transitions show *only* blushifted components, and the HCN lines even suggest absorption on the redshifted side (Choi, Panis, & Evans 1999). These spectral features constitute an inverse P-Cygni profile and are signatures of accretion. Inverse P-Cygni profiles are also detected from the position of IRAS4A in high resolution (interferometer) H_2CO, CS, and N_2H^+ spectra (DiFrancesco *et al.* 2001). The N_2H^+ emission (with $< 3''$ resolution) displays a peculiar morphology: elongated lobes of emission bracket the IRAS4A pair on the northwest and southeast sides, but the pair itself lies within an emission-free channel with a position angle of $\sim 45°$.

IRAS4B, roughly $30''$ southeast of the IRAS4A pair, also consists of at least two components. Its multiplicity was predicted from the same $\lambda = 0.84$ mm visibility data that uncovered the binarity of IRAS4A (Lay, Carlstrom, & Hills 1995), although the degree of multiplicity could not be exactly determined. Single-dish observations at millimeter wavelengths (*e.g.* $\lambda = 1.25$ mm, Lefloch *et al.* (1998a)) showed the continuum emission extended in the east-west direction, but IRAS4B was first split into two objects with $\sim 10''$ separation in the $\lambda = 2.7$ mm continuum BIMA observations by Looney (1998), who estimated dust masses of 0.65 $M_\odot$ and 0.18 $M_\odot$ for the west and east sources, respectively. Smith *et al.* (2000) derived separate estimates for the dust masses of the pair by deconvolving the blended 450 μm emission from a SCUBA/JCMT map. They found masses of 5.8 $M_\odot$ for IRAS4B1 and 1.5 $M_\odot$ for IRAS4B2. From their 850 μm observations, the dust mass of both objects combined is estimated to be 6.9 $M_\odot$. As with estimates of the mass of IRAS4A, determinations of the mass of IRAS4B are also a function of observed wavelength. So, based upon observations at $\lambda = 1.25$mm, Lefloch *et al.* (1998a) estimate the dust mass of IRAS4B at 2.1 $M_\odot$, and Blake *et al.* (1995), using observation at $\lambda = 1.4/2.8$ mm combined with centimeter data from Mundy *et al.*

(1993), find a dust mass of 1.5 M$\odot$.

Despite their apparent proximity, IRAS4B1 and IRAS4B2 appear to be at different stages in their evolution. IRAS4B1 is consistently brighter than its companion at millimeter and submillimeter wavelengths. At longer wavelengths, it has been detected at 1.3 (Mundy *et al.* 1993), 3.6 (Reipurth *et al.* 2002), and 6.0 cm (Rodríguez, Anglada, & Curiel 1999), but IRAS4B2 has not. The failure to detect IRAS4B2 beyond the 3 mm window has led to the hypothesis that it may either be a Class I (infrared excess) YSO (Looney, Mundy, & Welch 2000; Choi 2001), or an episodic radio continuum emitter (Reipurth *et al.* 2002).

IRAS4B1 is the point of origin of molecular outflow. In low resolution maps of the CO $J = 3 \rightarrow 2$ and CS $J = 7 \rightarrow 6$ transitions, both blueshifted and redshifted lobes appear roughly coincident with the continuum source (Blake *et al.* 1995), but in higher resolution BIMA observations of the HCN $J = 1 \rightarrow 0$ line, the emission extends $\sim 20''$ along a north-south axis (Choi 2001). The two emission lobes are roughly symmetrical in shape and intensity. The blueshifted lobe extends south, stimulating the double 2.12 μm emission feature HL9 (Hodapp & Ladd 1995), and the redshifted lobe extends north. Maps of the HCO^+ $J = 1 \rightarrow 0$ and HCN $J = 1 \rightarrow 0$ lines show both IRAS4B1 and IRAS4B2 surrounded by a common envelope, elongated in a northwest-southeast direction (Choi, Panis, & Evans 1999). The spectra of these lines only show emission blueward of the cloud velocity, suggesting that IRAS4B is also undergoing material infall onto a central protostar. This suggestion is reinforced by the interferometer observations of the H_2CO $3_{12} - 2_{11}$ and CS $J = 3 \rightarrow 2$ lines (DiFrancesco *et al.* 2001), which show putative inverse P-Cygni profiles from regions of strong emission immediately north and south of IRAS4B1. Interferometric observations of the N_2H^+ $J = 1 \rightarrow 0$ line from IRAS4B1 (DiFrancesco *et al.* 2001) reveal an elongated emission region that extends $\sim 15''$ over the position of the continuum

source in the north-south direction. The N_2H^+ spectra do not exhibit the inverse P-Cygni signature of infall.

IRAS4C lies $\sim 50''$ north and east of IRAS4B. Although undetected in the $\lambda =$ 2.7 mm continuum survey of (Looney, Mundy, & Welch 2000), it is clearly present in the lower contours of the $\lambda = 1.25$ mm emission maps of Lefloch *et al.* (1998a). From maps of the $\lambda = 450/850$ μm continuum emission (Smith *et al.* 2000), the dust mass of IRAS4C is estimated to be $\sim$2.8 M$\odot$. It is detected at radio wavelengths ($\lambda = 3.6/6.0$cm) (Rodríguez, Anglada, & Curiel 1999), although it remains unresolved even when mapped on sub-arcsecond scales (Reipurth *et al.* 2002). From the behavior of its SED, IRAS4C is most likely a deeply embedded protostellar object (Sandell & Knee 2001).

2.6.2 Millimeter Continuum Emission.

Figure 2.12 shows the $\lambda = 2.7$ mm continuum emission maps of NGC1333 IRAS4 that confirmed the source's binarity, first predicted by Lay, Carlstrom, & Hills (1995). IRAS4A1 and IRAS4A2 are a common envelope system (separation = $1.72'' = 600$ AU at D=350 pc) with a total luminosity of 16 L$\odot$ (LMW03) within an envelope of 2.88 M$\odot$ (LMW00). The high resolution observations of IRAS4B1 (see LMW00) reveal tertiary clumps of 4σ emission to the north and southwest of the central object, suggesting that it may also host additional protostellar companions. IRAS4B1 has a luminosity of approximately 5 M$\odot$ embedded within an envelope mass of 0.96 M$\odot$. The weaker emitter IRAS4B2 contains only approximately 0.26 M$\odot$ of material.

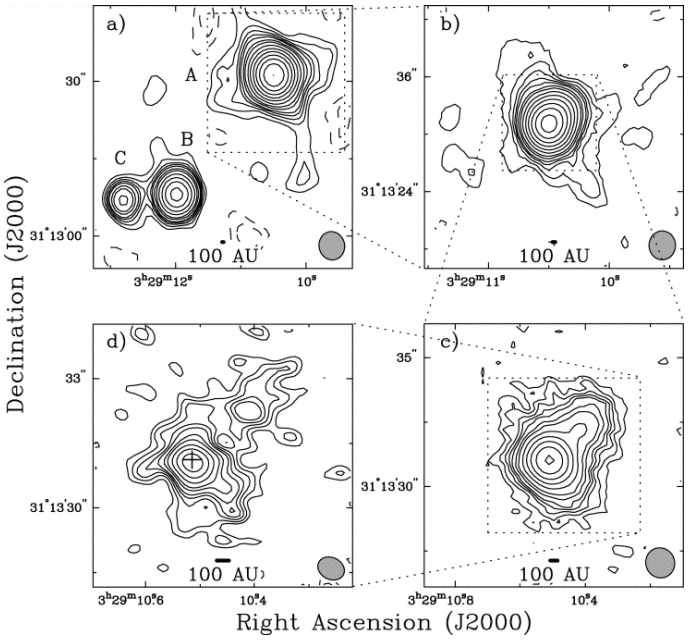

Figure 2.12: Maps of the $\lambda = 2.7$ mm continuum emission from NGC1333 IRAS4A. (Figure 12 from LMW00.) The panels indicate contours in steps of $(-4, -3, -2, 2, 3, 4, 5, 6, 8, 10, 14.14, 20, 28.28, 40, 56.56) \times \sigma$ in mJy beam^{-1}. (a) $\sigma = 3.1$ mJy beam^{-1}; beam is $5.52'' \times 5.02''$, P.A.$= 12°$. (b) $\sigma = 1.9$ mJy beam^{-1}; beam is $3.02'' \times 2.81''$, P.A.$= 1°$. (c) $\sigma = 2.1$ mJy beam^{-1}; beam is $1.18'' \times 1.13''$, P.A.$= 30°$. (d) $\sigma = 2.9$ mJy beam^{-1}; beam is $0.65'' \times 0.51''$, P.A.$= 65°$.

2.6.3 Molecular Line Emission

The $C^{18}O$, $H^{13}CO^+$, and N_2H^+ maps of NGC1333 IRAS4 are displayed in Figures 2.13, 2.14, and 2.15, respectively. The left columns in each figure show the integrated intensities (0^{th} moment) of the lines; the intensities are evaluated over all channels in the datacube where the line strength is greater than $3\times$ the single channel noise. The center columns in each figure show the velocity fields (1^{st} moment), and the right columns show the velocity dispersions (2^{nd} moment), over the same region as the adjacent intensity maps. The first and second moments are calculated for all pixels where the signal is greater than $2\times$ the single-channel noise, and pixels below 3σ in the integrated intensity map are masked out. In the top row of each figure, only maps created from the FCRAO data are displayed. In the second and

third rows of each figure, the BIMA and FCRAO data are combined and tuned to resolutions of 10″ and 5″, respectively. Figure 2.13 also includes a fourth row, which shows IRAS4 at 3″ resolution using only the BIMA data.

$C^{18}O$ Maps

The full size of the FCRAO $C^{18}O$ map (Figure 2.13*a*) is $6' \times 6'$, an area that includes more of the NGC1333 star-forming region than just the IRAS4 core. The peak intensity of the map (82.9 Jy beam^{-1}·km s^{-1}) lies northwest of the map center, in the region of NGC1333 containing the SVS13 core. (The bad pixels in the northwest corner of the map result from a defective receiver element and have been masked out.) In the vicinity of the IRAS4 core, *i.e.* within the area of the BIMA primary beam, the intensity peak (74.1 Jy beam^{-1}·km s^{-1}) is only 4″ from the position of IRAS4C (Reipurth *et al.* 2002), along the ridge of emission that descends from the northwest corner of the map. The IRAS4A-IRAS4B axis is also oriented in the northwest-southeast direction, less than 1′ south of the crest of the emission ridge. The velocity field (Figure 2.13*b*) shows a gradient that runs roughly perpendicular to the ridge; the velocities change from southwest to northeast. The most highly blueshifted velocities (∼7.1 km s^{-1}) appear at the western and southern edges of the map. The most highly redshifted velocities (∼8.2 km s^{-1}) appear near the top. Within the region of the BIMA primary beam, the velocity range is half as wide (7.2-7.8 km s^{-1}). The dominant velocity in the western half of the map (7.5-7.6 km s^{-1}) is only slightly bluer than the dominant velocity in the eastern half (7.3-7.4 km s^{-1}).

The $C^{18}O$ emission in the integrated intensity map with 10″ resolution (Figure 2.13*d*) peaks conspicuously at the position of IRAS4A; the peak intensity is 5.9 Jy beam^{-1}·km s^{-1}. At IRAS4B1 and IRAS4B2, the flux densities are 3.9 and 3.4 Jy beam^{-1}·km s^{-1}, respectively. The morphology of the high-level emission fol-

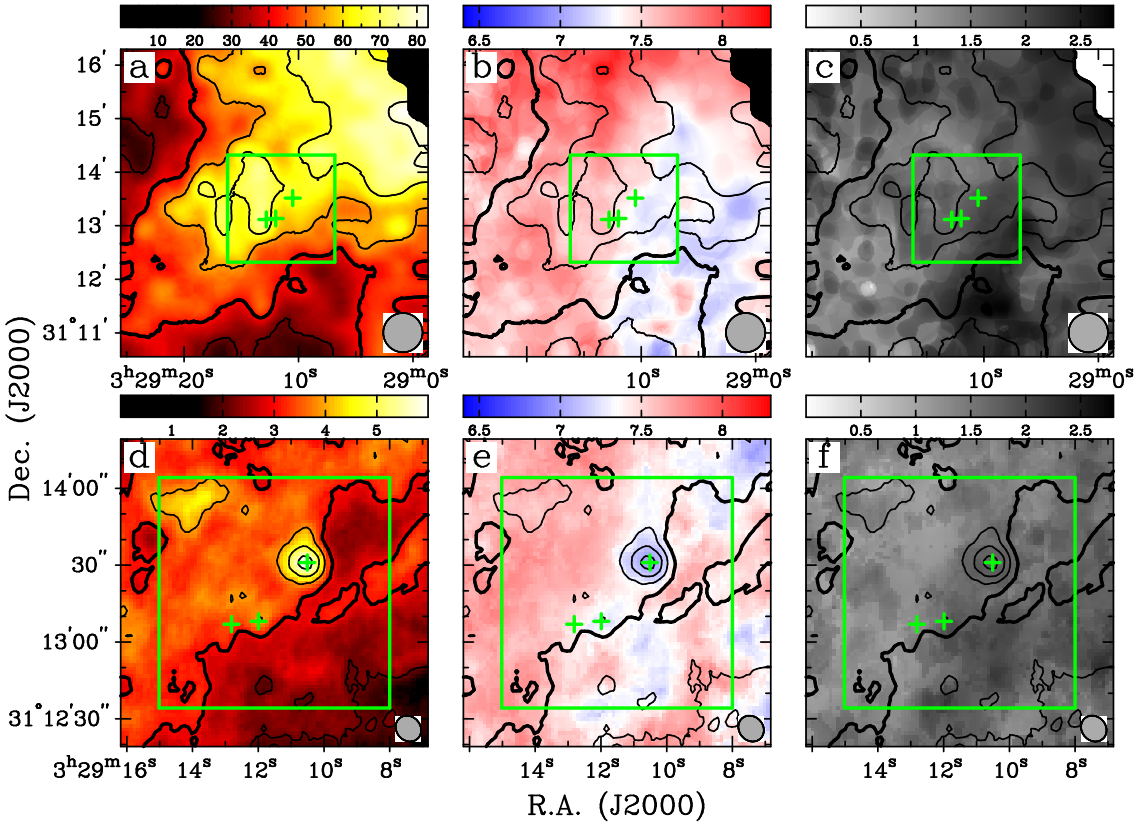

Figure 2.13: Integrated intensity, line-of-sight velocity, and velocity dispersion of NGC1333 IRAS4 traced by $C^{18}O$ $J = 1 \rightarrow 0$ emission. Panels in left column (a,d,g,j) show integrated intensity in both contours and colorscale. Contour levels are 35%, 50%, 65%, 80%, and 95% of peak flux density; bold contour is 50% level. Panels in center column (b,e,h,k) show velocities in colorscale; contours show integrated intensity from left panels. The range of velocities is 6.4-8.3 km s^{-1} in all panels. Panels in right column (c,f,i,l) show dispersions in grayscale; contours show integrated intensity from left panels. The range of dispersions is 0.0-2.71 km s^{-1} in all panels. Plus symbols indicate positions of continuum sources. Squares indicate the area displayed in the panel immediately below. (a,b,c) I_ν^{peak} = 82.93 Jy beam^{-1}·km s^{-1}; σ = 6.6 Jy beam^{-1}·km s^{-1}; beam is $44'' \times 44''$. (d,e,f) I_ν^{peak} = 5.92 Jy beam^{-1}·km s^{-1}; σ = 0.35 Jy beam^{-1}·km s^{-1}; beam is $10.66'' \times 9.33''$, P.A.= 41.6°.

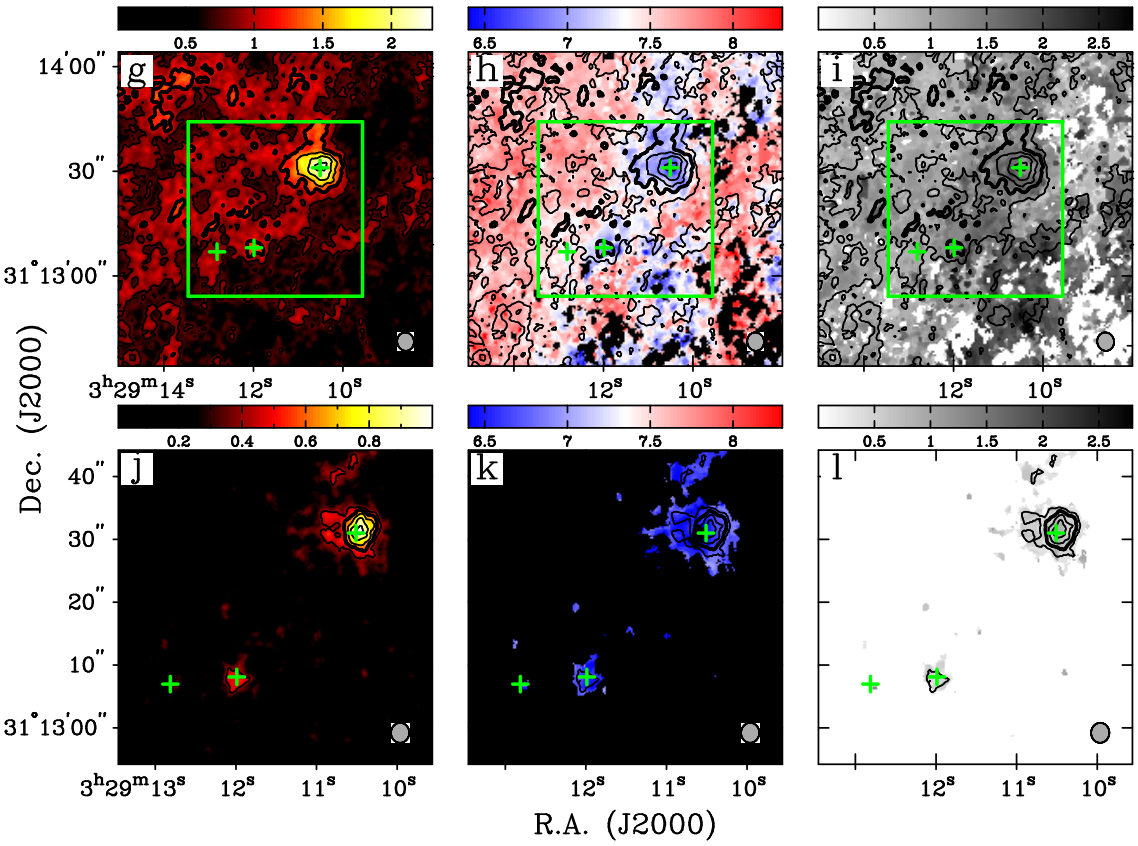

Figure 2.13: *Continued.* (g,h,i) I_ν^{peak} = 2.23 Jy beam^{-1}·km s^{-1}; σ = 0.16 Jy beam^{-1}·km s^{-1}; beam is 5.3″ × 4.8″, P.A.= 12.2°. (j,k,l) I_ν^{peak} = 0.98 Jy beam^{-1}·km s^{-1}; σ = 0.08 Jy beam^{-1}·km s^{-1}; beam is 3.18″ × 2.90″, P.A.= −2.0°.

lows the northwest-southeast ridge seen in the FCRAO data. The contrasts in the velocity map of the same region (Figure 2.13*e*) reveal the complexity that underlies the shallow gradient in the center of the lower resolution velocity map. Although the eastern half of the map is generally redshifted relative to the western half, there is no categorical trend. Some of the higher-emission regions in the northeast show slightly blueshifted velocities; some of the lower-emission regions in the southwest show slightly redshifted velocities. The most remarkable feature is the coincidence of IRAS4A with the bluest velocity (7.0 km s^{-1}) in the map.

In the C^{18}O intensity map with 5″ resolution (Figure 2.13*g*), the most prominent feature is still IRAS4A. The peak intensity is 2.2 Jy beam^{-1}·km s^{-1}, and the half-

peak contour delineates a region greater than three beamwidths across. IRAS4B1 is at the center of another local emission peak (1.4 Jy beam^{-1}·km s^{-1}), but the emission at IRAS4B2 is unremarkable (0.8 Jy beam^{-1}·km s^{-1}). A blotchy region of scattered emission in the northeast corner hints at the presence of IRAS4C. Throughout most of the area of the map, the $C^{18}O$ emission level is still $> 3\sigma$. In the velocity map with the same resolution (Figure 2.13*h*), large-scale trends in the velocity field are obscured by small-scale variations. With the exception of the areas around IRAS4A and IRAS4B1, the velocity field appears random. The velocities at IRAS4A (6.7 km s^{-1}) and IRAS4B1 (7.0 km s^{-1}) are blueshifted relative to the majority of the velocities (> 7.2 km s^{-1}) in the map.

The emission peaks sharply at IRAS4A (1.0 Jy beam^{-1}·km s^{-1}) in the integrated intensity map with $3''$ resolution (Figure 2.13*j*). Within the half-peak contour, the emission extends greater than two beamwidths in the north-south direction. A compact peak of emission centers on IRAS4B1 (0.5 Jy beam^{-1}·km s^{-1}), but IRAS4B2 is not detected. The velocity map (Figure 2.13*k*) only contains reliable information in the regions immediately surrounding the continuum sources. The velocities around IRAS4A and IRAS4B1 are bluer than the velocities of the embedding material seen in the lower resolution maps. The emission highlights slight changes in velocity across the emitting regions. The western end of the IRAS4A envelope is redshifted ($\sim$6.9 km s^{-1}) relative to the eastern end ($\sim$6.4 km s^{-1}). The change in velocity across IRAS4B runs in the opposite direction: the western end is blueshifted ($\sim$6.4 km s^{-1}) relative to the eastern end ($\sim$6.9 km s^{-1}).

$H^{13}CO^+$ Maps

The $H^{13}CO^+$ intensity map made with the FCRAO data (Figure 2.14*a*) shows strong emission (>39 Jy beam^{-1}·km s^{-1}) from the SVS13 core in the northwest corner of the map. The emission extends southeast into the IRAS4 region in a ridge similar to that seen in the $C^{18}O$ emission. Within the area of the BIMA primary beam, the intensity map clearly shows the abrupt fall-off in emission on either side of the ridge. IRAS4A, IRAS4B1, and IRAS4B2 lie on the southern edge of this slope. The gradient in velocity in the ridge of emission runs perpendicular to its long axis (Figure 2.14*b*). As in the $C^{18}O$ velocity map at this resolution, blueshifted velocities are generally on the southwestern side of the ridge, and redshifted velocities are on the northeastern side. The three continuum sources all appear within a large region of intermediate ($\sim$7.5 km s^{-1}) velocity.

At 10″ resolution (Figure 2.14*d*), the regions of high $H^{13}CO^+$ intensity span across the map from the northwest to the southeast corner. The point of peak intensity, 1.7 Jy beam^{-1}·km s^{-1}, is located approximately 8″ from IRAS4A, where the intensity is 1.5 Jy beam^{-1}·km s^{-1}. Neither IRAS4B1 nor IRAS4B2 show disctinctive $H^{13}CO^+$ emission. In contrast, an emission clump surrounds IRAS4C, about 40″ to the northeast of the field center. The peak intensity there is 1.2 Jy beam^{-1}·km s^{-1}. The first moment map of the region (Figure 2.14*e*) brings the characteristics of the lower resolution velocity map into sharper focus. The ridge of emission that extends from northwest to southeast has a velocity gradient along its minor axis: the southwestern side of the ridge is blueshifted relative to the northeastern side. The velocity along the spine of the ridge is $\sim$7.6 km s^{-1}. Above the ridge, the velocities are redshifted to $\sim$8.0 km s^{-1}. The blueshifted velocities ($\sim$6.8 km s^{-1}) arise from the southern edge of the ridge, where the intensity steeply declines. Like the $C^{18}O$ velocity map at this resolution, IRAS4A is shifted blueward (7.0 km s^{-1}) of the

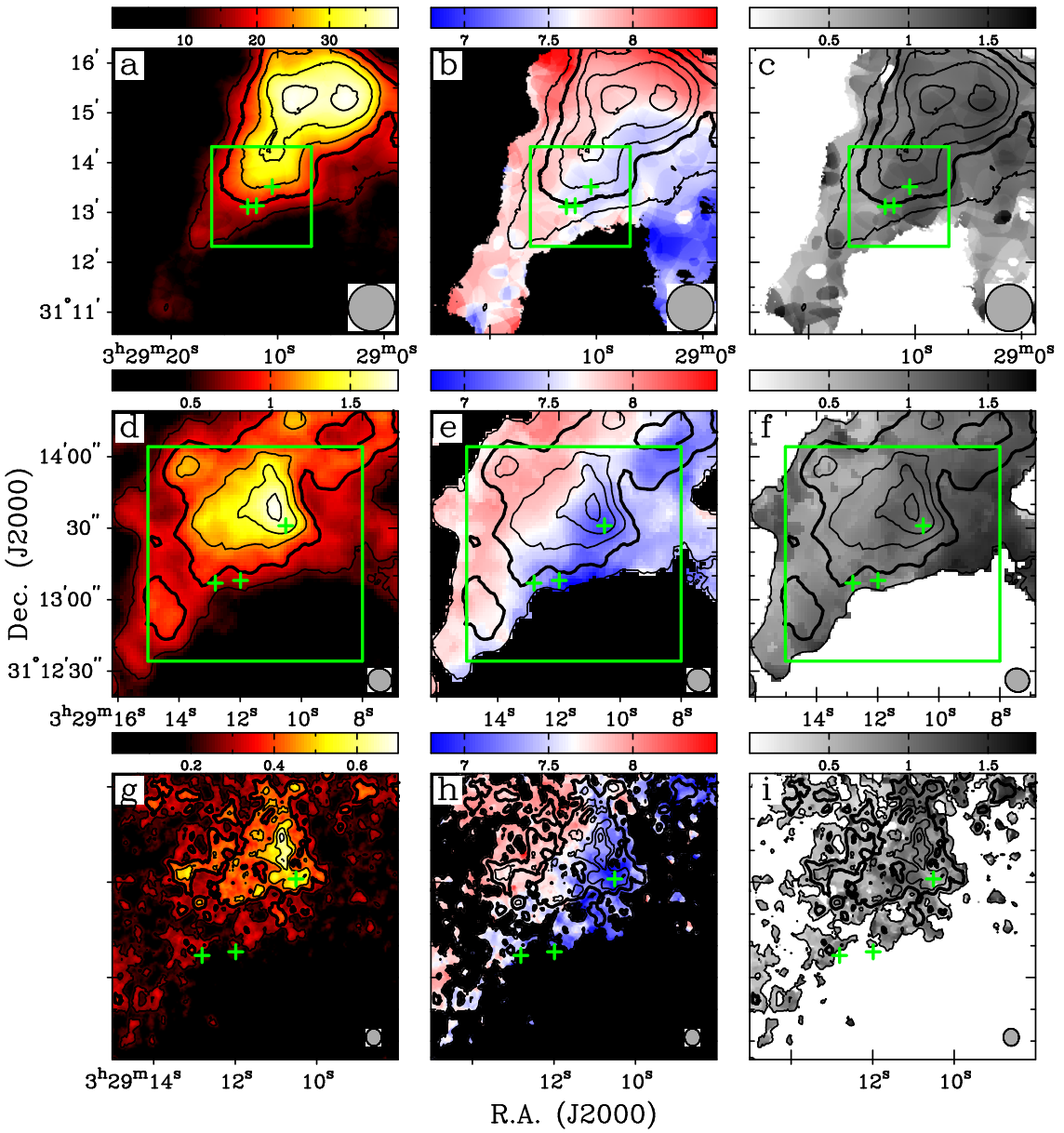

Figure 2.14: $H^{13}CO^+$ $J = 1 \rightarrow 0$ integrated intensity, line-of-sight velocity, and velocity dispersion of NGC1333 IRAS4. Panels *a,d,g* show integrated intensity in both contours and colorscale. Contour levels are 35%, 50%, 65%, 80%, and 95% of peak flux density; bold contour is 50% level. Panels *b,e,h* show integrated intensity contours and velocity in colorscale. Velocity range is 6.8-8.5 km s^{-1} in all panels. Panels *c,f,i* show integrated intensity contours and velocity dispersion in grayscale. Dispersion range is 0.0-1.80 km s^{-1} in all panels. Square regions delineated by green lines indicate areas of the maps in the row immediately below. Plus symbols indicate positions of continuum sources from LMW00. (a,b,c) I_ν^{peak} = 39.47 Jy beam^{-1}·km s^{-1}; σ = 2.5 Jy beam^{-1}·km s^{-1}; beam is 56.5″×56.5″. (d,e,f) I_ν^{peak} = 1.74 Jy beam^{-1}·km s^{-1}; σ = 0.19 Jy beam^{-1}·km s^{-1}; beam is 10.30″ × 9.73″, P.A.= 54.6°. (g,h,i) I_ν^{peak} = 0.63 Jy beam^{-1}·km s^{-1}; σ = 0.07 Jy beam^{-1}·km s^{-1}; beam is 5.44″ × 4.89″, P.A.= 4.5°.

material surrounding it.

The $H^{13}CO^+$ emission ridge begins to break up at 5″ resolution (Figure 2.14*g*). The strongest feature in the map is the finger of emission ($\sim$0.6 Jy beam^{-1}·km s^{-1}) that points north from IRAS4A. The intensity at IRAS4A itself is 0.5 Jy beam^{-1}·km s^{-1}, and the emission quickly drops off to the south and west. The emission at IRAS4B1 and IRAS4B2 is unremarkable. At the location of IRAS4C (near the northern edge of the map), emission is detectable in a small cluster of emission peaks. In the velocity map (Figure 2.14*h*), the velocities around IRAS4C exhibit the highest redshifts ($\sim$8.1 km s^{-1}) in the field. The extreme blueshifted velocities ($\sim$6.9 km s^{-1}) are conspicuously concentrated around IRAS4A. The general orientation of the velocity field remains consistent: the gradient is still from southwest (blueshift) to northeast (redshift). The point of highest intensity, at the tip of the finger of emission, is at the ridge velocity of $\sim$7.4 km s^{-1}.

The $H^{13}CO^+$ emission structure is too weak to be mapped with 3″ resolution; only a few bright spots ($\sim$0.3 Jy beam^{-1}·km s^{-1}) persist in the vicinity of IRAS4A. These maps are omitted.

N_2H^+ Maps

The general features of the $H^{13}CO^+$ intensity and velocity maps are preserved in the N_2H^+ maps presented in Figure 2.15. The emission around the IRAS4 core is weaker than the emission from SVS13. A ridge of emission descends from the northwest corner of the map. The IRAS4 continuum sources are marked by blueward shifts in the velocity maps. At each resolution, however, some notable differences appear.

In the large-scale intensity map (Figure 2.15*a*), the N_2H^+ emission from the IRAS4 core looks more like a contiguous cloud than a ridge extending from SVS13. The core has a local emission maximum ($\sim$21.6 Jy beam^{-1}·km s^{-1}) located within

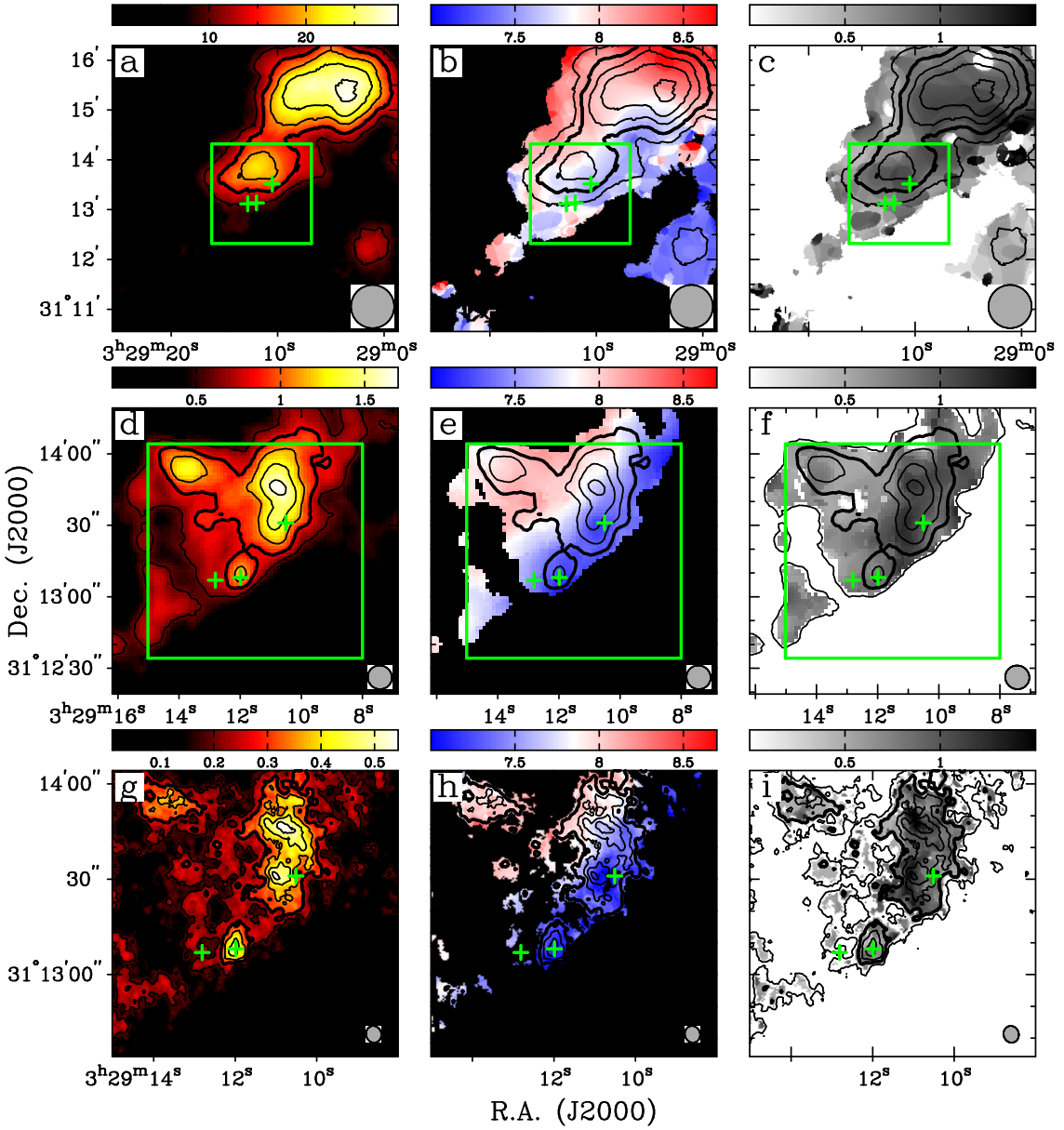

Figure 2.15: N_2H^+ $J = 1 \rightarrow 0$ integrated intensity, line-of-sight velocity, and velocity dispersion maps of NGC1333 IRAS4. Panels *a,d,g* show integrated intensity in both contours and colorscale. Contour levels are 35%, 50%, 65%, 80%, and 95% of peak flux density; bold contour is 50% level. Panels *b,e,h* show integrated intensity contours and velocity field in colorscale. Velocity range is 7.0-8.7 km s^{-1} in all panels. Panels *c,f,i* show integrated intensity contours and velocity dispersion in grayscale. Dispersion range is 0.0-1.44 km s^{-1} in all panels. Square regions delineated by green lines indicate areas of the maps in the row immediately below. Plus symbols indicate positions of continuum sources from LMW00. (a,b,c) I_ν^{peak} = 29.40 Jy beam^{-1}·km s^{-1}; σ = 1.9 Jy beam^{-1}·km s^{-1}; beam is $52'' \times 52''$. (d,e,f) I_ν^{peak} = 1.64 Jy beam^{-1}·km s^{-1}; σ = 0.21 Jy beam^{-1}·km s^{-1}; beam is $10.19'' \times 9.88''$, P.A.= 63.1°. (g,h,i) I_ν^{peak} = 0.54 Jy beam^{-1}·km s^{-1}; σ = 0.08 Jy beam^{-1}·km s^{-1}; beam is $5.31'' \times 4.78''$, P.A.= 17.3°.

the BIMA primary beam area and offset from IRAS4A by $\sim$30″. IRAS4B1 and IRAS4B2 are at the southern edge of the emission region. In the velocity map (Figure 2.15*b*), all three sources occupy a velocity plateau at $\sim$7.6 km s^{-1}. The northern edge of the SVS13 cloud shows the most highly redshifted velocities ($\sim$8.6 km s^{-1}); the extreme blueshifted velocities ($<$ 7.3 km s^{-1}) are from the clump of gas along the western edge of the map.

At 10″ resolution (Figure 2.15*d*), the N_2H^+ emission resembles the emission structure observed in the $H^{13}CO^+$ map. The contours enclosing the regions of high intensity are more compact than the corresponding $H^{13}CO^+$ contours, and the intensity peak (1.6 Jy beam^{-1}·km s^{-1}) is nearly the same. IRAS4A (1.2 Jy beam^{-1}·km s^{-1}) is offset from this peak by $\sim$16″. A second local maximum (1.3 Jy beam^{-1}·km s^{-1}) surrounds the position of IRAS4C to the northeast. Unlike the $H^{13}CO^+$ map, however, there is also a local maximum (1.1 Jy beam^{-1}·km s^{-1}) at the position of IRAS4B1. In the velocity map of the region (Figure 2.15*e*), both IRAS4A and IRAS4B1 leave blueshifted footprints in the general velocity field. The velocity at both continuum sources is 7.2 km s^{-1}, which contrasts slightly with the prevailing with the prevailing 7.3-7.4 km s^{-1} along the southwestern edge of the emission region. The extreme blueshifted velocities ($\sim$7.1 km s^{-1}) appear just south of IRAS2B1/B2. Redshifted velocities ($\sim$8.1 km s^{-1}) appear closer to the position of IRAS4C.

The N_2H^+ emission structure breaks up into a number of smaller clumps in the 5″ map (Figure 2.15*g*). Two irregularly-shaped emission peaks (both greater than 0.5 Jy beam^{-1}·km s^{-1}) are located 15″ north and 7″ east of IRAS4A. The peaks conspicuously eschew the location of IRAS4A. In contrast, IRAS4B1 is at the center of an emission peak (0.5 Jy beam^{-1}·km s^{-1}), and IRAS4C is also surrounded by a broad emission clump. In the velocity map with 5″ resolution (Figure 2.15*h*), the velocities resemble those in the 10″ map. Strips of constant velocity run in

the northwest-southeast direction. Blushifted velocities are along the southwest edge, and redshifted velocities are toward the northeast and the IRAS4C clump. The velocities at IRAS4A and IRAS4B1 (7.1 km s^{-1}) are among the most highly blueshifted in the map.

The N_2H^+ maps with $3''$ resolution have been omitted. The intensity map shows two clumps of $> 3\sigma$ emission. One clump is $\sim 3''$ east of IRAS4A; the other is coincident with IRAS4B1.

$C^{18}O/H^{13}CO^+/N_2H^+$ Line Comparison

In the FCRAO maps, all three molecular tracers show roughly the same large scale morphology. The strongest source of emission in the southern portion of NGC1333 is in the direction of the SVS13 core, and the IRAS4 core lies within a ridge of gas that appears to extend to the southeast. As with the intensity maps of L1448 IRS3 and NGC1333 IRAS2, $C^{18}O$ line is strong and widely distributed; emission is detected throughout the map area. The distribution of $H^{13}CO^+$ and N_2H^+ is more compact; the $H^{13}CO^+$ and N_2H^+ lines trace the higher density region along the center of the ridge as it extends from the northwest toward the southeast corner. In the higher resolution maps, the $C^{18}O$ emission is concentrated on the positions of the IRAS4A and IRAS4B1 continuum sources, which appear along the southwestern edge of the emitting region. IRAS4B1 is also the site of a peak in the N_2H^+ emission, but IRAS4A is not. In both the N_2H^+ and $H^{13}CO^+$ lines, the peak emission in the vicinity of IRAS4A is displaced $\sim 10''$ north of the continuum object. The position of IRAS4B2 is not distinguished in any of the molecular lines.

The velocity fields mapped by the three lines all exhibit the same general characteristics. The lines show a velocity gradient perpendicular to the long axis of the emission ridge. Blueshifted velocities are detected from along the southwestern

edge of the ridge, and redshifted velocities are detected along the northeastern edge. Except for perhaps the 5″ resolution $C^{18}O$ map, the velocities vary smoothly from one edge of the ridge to the other. With this smooth gradient as a backdrop, the emission from IRAS4A and IRAS4B1 appears blueshifted relative to the ridge velocities. Moreover, the amount of blueshift increases at finer map resolutions as the BIMA data are given greater emphasis. In the $C^{18}O$ data, the difference between the first moment at IRAS4A from the FCRAO map and from the BIMA map with 3″ resolution is 0.9 km s^{-1}. At IRAS4B1, the change in the first moment is 0.8 km s^{-1}. In the $H^{13}CO^+$ data, the change in first moment is 0.6 km s^{-1} at IRAS4A; the first moment cannot be calculated at IRAS4B1 in the 3″ map. In the N_2H^+ data, the changes in the first moment are 0.5 km s^{-1} at both IRAS4A and IRAS4B1.

2.6.4 Spectra

A sample of spectra from the IRAS4 core, taken from various positions in the intensity maps, is presented in Figure 2.16. In each row, the panel adjacent to the contour plot shows the spectra taken at the position of IRAS4A. In the $C^{18}O$ spectrum from the FCRAO data (top row), the line is strong and skewed toward the red. The Gaussian function fitted to the line has a central velocity of 7.6 km s^{-1}. (The peak intensities (I_ν^{peak}), central velocities (V_C), and line widths (ΔV) determined from Gaussian functions fit to the spectra are summarized in Tables 2.7, 2.8, and 2.9.) The $C^{18}O$ spectrum also shows a smaller peak at 5.2 km s^{-1}. This peak is detected at several other positions in the map (see below), but it is not included in the calculation of the integrated intensities. The profile of the $H^{13}CO^+$ line is weakly double-peaked, with the secondary peak at 6.8 km s^{-1} on the blue wing of the primary, and the N_2H^+ line also appears to have enhanced emission on the blueward side of the line peak.

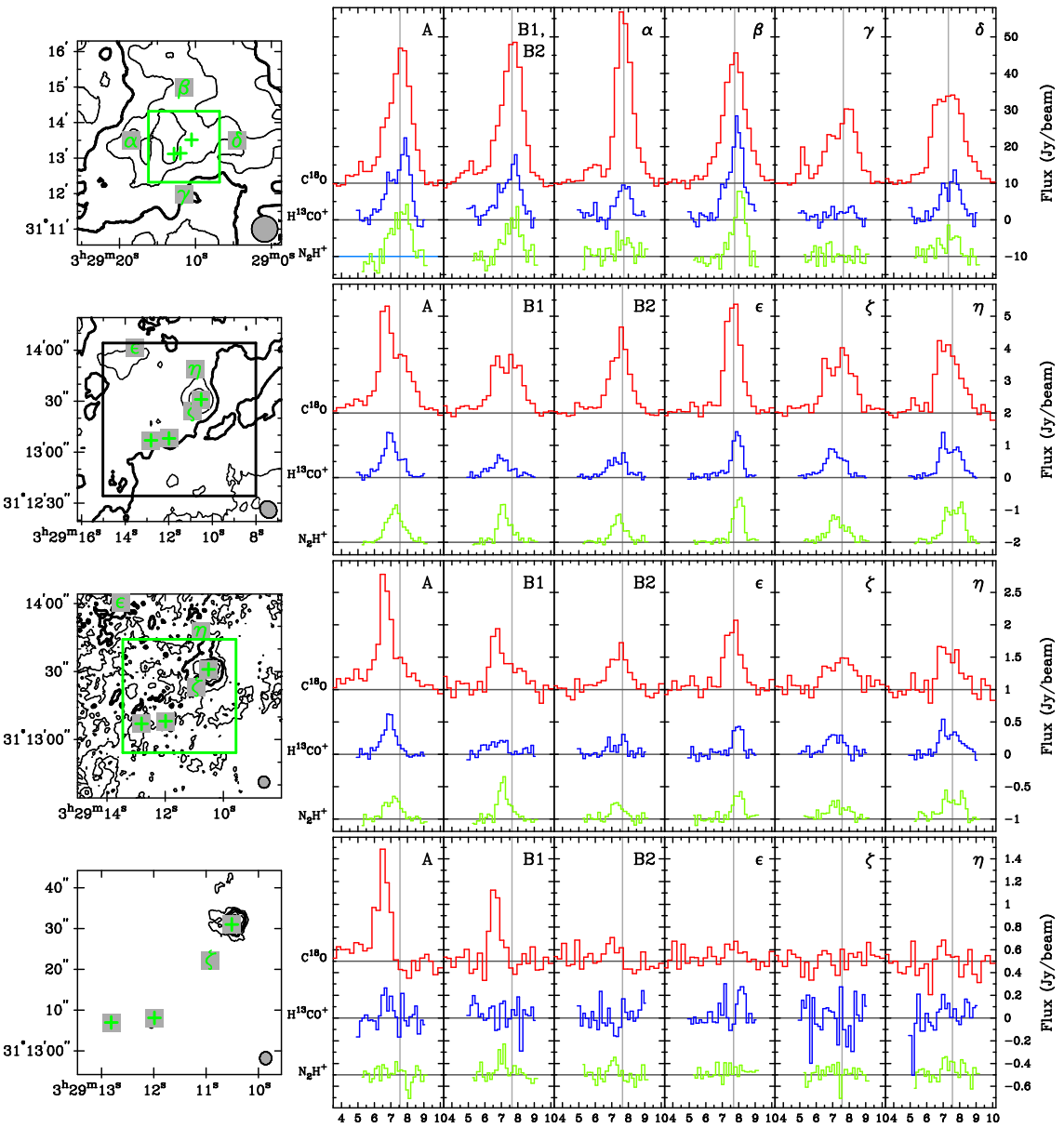

Figure 2.16: NGC1333 IRAS4 Spectra. The left-most panel in each row shows contours from the $C^{18}O$ integrated intensity map in Figure 2.13. The panels to the right of each plot show $C^{18}O$ (red), $H^{13}CO^+$ (blue), and N_2H^+ (green) spectra taken from the positions in the map indicated by the plus symbols (continuum sources) and the letters α through η. All spectra show flux in Jy beam^{-1} averaged over the beam area. The $C^{18}O$ and N_2H^+ spectra are offset by an equal amount above and below (respectively) the $H^{13}CO^+$ spectra. In the FCRAO map (top row), the offset is ± 10 Jy beam^{-1}; in the $10''$ map (second row), the offset is ± 2 Jy beam^{-1}; in the $5''$ map (third row), the offset is ± 1 Jy beam^{-1}; in the $3''$ map (bottom row), the offset is ± 0.5 Jy beam^{-1}. In all rows, gray vertical lines show the central velocity of a Gaussian function fitted to the $C^{18}O$ profile from the FCRAO map (top row). For positions ϵ, ζ, and η, the gray lines indicate the central velocities from FCRAO spectra *not* shown in the top row.

Table 2.7. NGC1333 IRAS4 $C^{18}O$ Spectra

ID	Beam (arcsec)	I_ν^{peak} (Jy beam^{-1})	V_C (km s^{-1})	ΔV (km s^{-1})
A	44/56.5/52	35.02 ± 1.07	7.6 ± 0.1	1.6 ± 0.1
	10	2.66 ± 0.07	7.0 ± 0.1	1.9 ± 0.1
	5	1.55 ± 0.09	6.7 ± 0.1	1.1 ± 0.2
	3	0.87 ± 0.10	6.5 ± 0.2	0.9 ± 0.3
B1	44/56.5/52[a]	38.02 ± 1.11	7.6 ± 0.1	1.5 ± 0.1
	10	1.71 ± 0.07	7.3 ± 0.2	2.0 ± 0.2
	5	0.75 ± 0.08	6.9 ± 0.3	1.4 ± 0.4
	3	0.69 ± 0.13	6.6 ± 0.2	0.6 ± 0.3
B2	44/56.5/52[a]	38.02 ± 1.11	7.6 ± 0.1	1.5 ± 0.1
	10	2.28 ± 0.09	7.5 ± 0.1	1.3 ± 0.1
	5	0.60 ± 0.08	7.4 ± 0.3	1.3 ± 0.5
	3	0.19 ± 0.11	7.0 ± 0.8	
α	44/56.5/52	46.53 ± 1.29	7.7 ± 0.1	1.1 ± 0.1
β	44/56.5/52	33.91 ± 1.07	7.7 ± 0.1	1.6 ± 0.1
γ	44/56.5/52	18.11 ± 0.95	7.6 ± 0.2	2.1 ± 0.3
δ	44/56.5/52	25.79 ± 0.95	7.3 ± 0.1	2.1 ± 0.2
ϵ	10	3.52 ± 0.10	7.7 ± 0.1	1.1 ± 0.1
	5	1.02 ± 0.09	7.6 ± 0.2	1.1 ± 0.3
	3	0.15 ± 0.09	7.6 ± 1.2	1.0 ± 1.7
ζ	10	1.77 ± 0.07	7.4 ± 0.1	2.0 ± 0.2
	5	0.46 ± 0.07	7.5 ± 0.5	2.1 ± 0.8
	3	0.08 ± 0.08	9.2 ± 3.0	
η	10	2.14 ± 0.08	7.3 ± 0.1	1.6 ± 0.2
	5	0.64 ± 0.08	7.3 ± 0.3	1.4 ± 0.5
	3	0.16 ± 0.12	7.0 ± 0.9	

[a]Spectra of IRAS2B1 and IRAS2B2 from FCRAO data are identical.

Asymmetries in the line profiles become clearer at higher resolutions because the contribution to the line from the interferometer data is emphasized. In the 10″ map, the $C^{18}O$ profile at IRAS4A is double-peaked and skewed toward the blue. The secondary peak is aligned with the central velocity from the FCRAO map. The change in the $H^{13}CO^+$ profile mimics the change in the $C^{18}O$ profile. At 10″ resolution, the blueward peak dominates, and a redward shoulder on the profile aligns with the central velocity from the FCRAO map. The weaker N_2H^+ spectrum shows only a single peak, but this peak has shifted blueward.

Table 2.8. NGC1333 IRAS4 $H^{13}CO^+$ Spectra

ID	Beam (arcsec)	I_ν^{peak} (Jy beam^{-1})	V_C (km s^{-1})	ΔV (km s^{-1})
A	44/56.5/52	17.26 ± 1.55	7.6 ± 0.4	1.4 ± 0.5
	10	1.24 ± 0.05	7.0 ± 0.2	1.2 ± 0.2
	5	0.57 ± 0.06	6.9 ± 0.3	0.9 ± 0.4
	3	0.22 ± 0.14	6.7 ± 1.1	
B1	44/56.5/52[a]	14.00 ± 1.59	7.6 ± 0.4	1.3 ± 0.6
	10	0.56 ± 0.05	7.0 ± 0.4	1.5 ± 0.5
	5	0.19 ± 0.05	6.8 ± 1.1	1.5 ± 1.5
	3	0.20 ± 0.17	5.3 ± 1.0	
B2	44/56.5/52[a]	14.00 ± 1.59	7.6 ± 0.4	1.3 ± 0.6
	10	0.58 ± 0.05	7.3 ± 0.3	1.3 ± 0.5
	5	0.16 ± 0.05	7.4 ± 1.2	1.3 ± 1.6
	3			
α	44/56.5/52	9.56 ± 1.86	7.7 ± 0.6	1.0 ± 0.8
β	44/56.5/52	23.41 ± 1.75	7.9 ± 0.2	1.1 ± 0.3
γ	44/56.5/52	2.63 ± 1.53	7.7 ± 2.5	
δ	44/56.5/52	10.69 ± 1.57	7.5 ± 0.6	1.4 ± 0.8
ϵ	10	1.47 ± 0.07	7.9 ± 0.1	0.6 ± 0.1
	5	0.49 ± 0.07	7.9 ± 0.3	0.6 ± 0.4
	3	0.25 ± 0.15	8.2 ± 0.9	
ζ	10	0.84 ± 0.05	7.1 ± 0.2	1.3 ± 0.3
	5	0.30 ± 0.05	7.1 ± 0.6	1.2 ± 0.8
	3		6.7 ± 1.7	
η	10	1.03 ± 0.05	7.4 ± 0.2	1.5 ± 0.3
	5	0.37 ± 0.05	7.4 ± 0.5	1.5 ± 0.8
	3	0.17 ± 0.15	7.1 ± 1.3	

[a]Spectra of IRAS2B1 and IRAS2B2 from FCRAO data are identical.

At a resolution of 5″, the $C^{18}O$ line shows a blueward asymmetry, peaking at 6.7 km s^{-1}. A weak shoulder of emission extends beyond 7.6 km s^{-1} on the redward side of the line. The $H^{13}CO^+$ profile sharpens to a single peak with a central velocity of 6.9 km s^{-1}, and the N_2H^+ spectrum, although not well fit by a Gaussian function, has a central velocity of 7.1 km s^{-1}.

In the spectra from the 3″ resolution maps, all that remains of the $C^{18}O$ line is the 6.7 km s^{-1} feature. Around 7.6 km s^{-1}, a slight depression below the zero flux level hints of absorption: several channels in a row all show negative flux values. Although

Table 2.9. NGC1333 IRAS4 N_2H^+ Spectra

ID	Beam (arcsec)	I_ν^{peak} (Jy beam^{-1})	V_C (km s^{-1})	ΔV (km s^{-1})
A	44/56.5/52	12.41 ± 1.55	7.7 ± 0.5	1.2 ± 0.7
	10	1.04 ± 0.05	7.2 ± 0.2	1.1 ± 0.2
	5	0.32 ± 0.04	7.1 ± 0.4	1.0 ± 0.5
	3		7.0 ± 1.6	
B1	44/56.5/52[a]	10.22 ± 1.65	7.7 ± 0.5	1.1 ± 0.8
	10	1.12 ± 0.06	7.1 ± 0.1	0.8 ± 0.2
	5	0.60 ± 0.05	7.1 ± 0.2	0.7 ± 0.2
	3	0.21 ± 0.07	7.0 ± 0.5	
B2	44/56.5/52[a]	10.22 ± 1.65	7.7 ± 0.5	1.1 ± 0.8
	10	0.81 ± 0.06	7.4 ± 0.2	0.8 ± 0.3
	5	0.26 ± 0.04	7.3 ± 0.4	0.8 ± 0.6
	3	0.16 ± 0.07	7.1 ± 0.6	
α	44/56.5/52		7.4 ± 3.8	
β	44/56.5/52	18.32 ± 2.01	8.1 ± 0.2	0.7 ± 0.4
γ	44/56.5/52		6.9 ± 1.5	
δ	44/56.5/52	5.71 ± 1.65	7.5 ± 1.0	
ϵ	10	1.45 ± 0.06	8.0 ± 0.1	0.7 ± 0.1
	5	0.42 ± 0.05	8.0 ± 0.2	0.7 ± 0.3
	3	0.13 ± 0.00	6.7 ± 0.0	
ζ	10	0.72 ± 0.05	7.3 ± 0.3	1.3 ± 0.4
	5	0.21 ± 0.03	7.3 ± 0.7	1.6 ± 1.0
	3		8.6 ± 7.8	
η	10	1.12 ± 0.04	7.7 ± 0.2	1.3 ± 0.2
	5	0.34 ± 0.03	7.6 ± 0.4	1.5 ± 0.6
	3	0.13 ± 0.05	7.3 ± 1.0	

[a]Spectra of IRAS2B1 and IRAS2B2 from FCRAO data are identical.

only one channel extends below the 1σ noise level, the occurance of several negative channels in a row is significant. There is no detectable feature in the $H^{13}CO^+$ spectrum at this resolution, but the strongest feature in the N_2H^+ spectrum also appears to be an absorption feature.

The spectra from IRAS4B1 follow a similar pattern to those from IRAS4A. In the spectra from the FCRAO maps, all three lines closely resemble their counterparts in the IRAS4A spectra in the adjacent panel. Both sets of lines are skewed toward the red, and even the small emission feature at 5.2 km s^{-1} is seen in the $C^{18}O$

spectra. Depite its redward slant, the $C^{18}O$ profile is well fit by a Gaussian function with a central velocity of 7.6 km s^{-1}. The $H^{13}CO^+$ line has a secondary peak at 6.8 km s^{-1}, several channels blueward of the primary peak; the Gaussian fit to the profile is poor. In the N_2H^+ spectrum, the ragged edge of the blue side of the line profile results in a red bias to the fitted velocity.

In the spectra from the 10″ resolution maps, two distinct components create the $C^{18}O$ spectrum of IRAS4B1. Although a Gaussian function makes an atrocious fit to this profile, the resulting central velocity (7.3 km s^{-1}) splits the two intensity peaks. (Calculating the first moment over this profile has the same effect: the resultant velocity is 7.3 km s^{-1}.) This value is noticeably bluer than the larger cloud's velocity, which is indicated with the gray vertical line. The $H^{13}CO^+$ and N_2H^+ line profiles are both single-peaked, with a bias toward the blueshifted peak in the $C^{18}O$ spectrum. Gaussian functions fitted to the data have central velocities at 7.0 and 7.1 km s^{-1}, respectively.

The blueshift of the $C^{18}O$ line in the spectrum from the 5″ resolution map is obvious. A Gaussian function fit to the profile shifts the central velocity (6.9 km s^{-1}) toward the peak channels. The $H^{13}CO^+$ flux at IRAS4B1 is too weak to calculate a first moment, but in the N_2H^+ spectrum, the velocities are the same as in the 10″ map.

The $C^{18}O$ emission at IRAS4B1 is still prominent ($> 12\sigma$) in the 3″ resolution map. The central velocity of a Gaussian fit to the line is 6.6 km s^{-1}. The slope on the red side of the peak is not as steep as the corresponding slope in the IRAS4A line. Consequently, the first moment velocity is slightly redder (6.7 km s^{-1}). There is no consistent evidence for a redshifted absorption feature in the $C^{18}O$ or N_2H^+ spectra.

Because of the proximity of IRAS4B2 to IRAS4B1, the FCRAO spectra from

both sources are in the same beam. In the spectra from the 10″ resolution map, the mean velocity of the $C^{18}O$ line, determined from the first moment map and by fitting a Gaussian function to the line profile, is 7.5 km s^{-1}. This velocity differs only slightly from the velocity from the FCRAO spectrum (7.6 km s^{-1}). Unlike the profile of IRAS4B1, the $C^{18}O$ line from IRAS4B2 is single-peaked and nearly symmetrical. The shapes of the $C^{18}O$ line are similar at both 10″ and 5″ resolution. The center of the (5″ resolution) line, when fit with a Gaussian function, is 7.4 km s^{-1}. In the 3″ map, the barely detectable line peaks at 7.0 km s^{-1}, even further blueward of the FCRAO spectrum velocity. In the $H^{13}CO^+$ lines at 10″ and 5″, a second peak appears in the spectra, although the peak near the FCRAO velocity dominates. At 10″ resolution, the two peaks produce a central velocity at 7.3 km s^{-1}. At 5″ resolution, fitting a Gaussian function to the spectrum yields a central velocity that is still blueward (7.4 km s^{-1}) of the FCRAO line. In the 3″ map, there is a hint of an absorption-like feature in the $H^{13}CO^+$ spectrum from 7.0-7.5 km s^{-1}. The N_2H^+ lines in the 10″ and 5″ spectra have peak intensities comparable to the $H^{13}CO^+$ lines; in the 3″ spectra, the peak intensity is comparable with the $C^{18}O$ line. Unlike the $H^{13}CO^+$ spectra, the N_2H^+ lines are all single-peaked. The mean velocities of these lines move blueward with increasing resolution. Fitting Gaussian functions to the profiles yield central velocities of 7.4, 7.3, and 7.1 km s^{-1} for the 10″, 5″, and 3″ maps, respectively.

The spectra in Figure 2.16 labeled α through η sample regions in and around the IRAS4 core. The spectra from α, β, γ, and δ are only taken from the FCRAO datacubes. The α, β, γ, and δ positions are offset in the cardinal directions (east, north, south, and west, respectively) by 90″ from the field center. The spectra from ϵ, ζ, and η were taken from each of the higher-resolution maps. The position ϵ (R.A.= $3^h29^m13\overset{s}{.}54$, Dec. = $31°13'58\overset{''}{.}33$) coincides with the position of IRAS4C

(Reipurth *et al.* 2002). The position ζ (R.A.= $3^h29^m10\overset{s}{.}96$, Dec. = $31°13'20\overset{''}{.}61$) samples a location along the southwest (blueshifted) edge of the ridge of emission and lies in between the IRAS4 continuum sources. The position of η (R.A.= $3^h29^m10\overset{s}{.}75$, Dec. = $31°13'45\overset{''}{.}81$) coincides with the $H^{13}CO^+$ and N_2H^+ emission peaks on the north side of IRAS4A.

At position α, $90''$ east of the center of the FCRAO map, the peak of the $C^{18}O$ line is obviously stronger than the peaks at either of the continuum positions. However, the integrated intensity at α is somewhat less, indicating that the $C^{18}O$ emission is confined to fewer channels. The narrowness of the line is evident on the blue side of the peak, where the steep slope contrasts with the profiles seen at the continuum sources. The central velocity of the line is 7.7 km s^{-1}. The $H^{13}CO^+$ and N_2H^+ lines at α are weaker than at the continuum positions. The $H^{13}CO^+$ line is well fit by a Gaussian function, and the central velocity aligns with the $C^{18}O$ line at 7.7 km s^{-1}. A Gaussian function makes a poor fit to the ragged N_2H^+ line.

All three lines are strong and nearly Gaussian in shape at position β, $90''$ north of the field center. This position is in the region of high $C^{18}O$ emission that emanates from SVS13. In the $H^{13}CO^+$ and N_2H^+ intensity maps, β appears at the border between the SVS13 and IRAS4 clouds. Consequently, the star-formation activity in SVS13 should contribute to the shapes of the line profiles. For each line, the Gaussian fit velocities match the velocities of the first moment maps. The mean velocities are 7.7, 7.8, and 8.1 km s^{-1} for the $C^{18}O$, $H^{13}CO^+$, and N_2H^+ lines, respectively.

The γ position, $90''$ south of the field, lies beyond the edge of the $H^{13}CO^+$ and N_2H^+ emitting regions, so no measurable lines are seen from either of these molecules. The $C^{18}O$ profile, on the other hand, is quite complex. Three peaks are visible in the spectrum. The strongest peak is also the reddest and has the greatest

effect upon the fit of a Gaussian function. The central velocity of a Gaussian fit to the line is 7.6 km s^{-1}. The secondary peak is at 7.5 km s^{-1}, and the third peak is the emission spike at 5.2 km s^{-1}, which was also seen in the spectra from IRAS4A and IRAS4B. An integrated intensity map of only the channels surrounding this line (4.9-5.4 km s^{-1}) shows a clump of $C^{18}O$ emission centered at approximately R.A.= $3^h29^m08^s$, Dec. = $31°11'30''$. The clump is irregular in shape, and some blobs of 3σ emission cross the locations of the continuum sources.

At position δ, (R.A.= $3^h29^m04^s.53$, Dec. = $31°13'19''.21$), $90''$ west of the field center, the $C^{18}O$ line profile is broader than at any other measured position. The FWHM of a Gaussian function fit to the profile is 2.1 ± 0.2 km s^{-1}, and the central velocity is 7.3 km s^{-1}. The width of the $C^{18}O$ line may be the result of the blending of several components. The $H^{13}CO^+$ spectrum at δ is double-peaked, and the N_2H^+ spectrum appears even more complex. Gaussian functions fit to both of these spectra yield identical central velocities (7.5 km s^{-1}).

The ϵ position was chosen to coincide with the location of IRAS4C given by Reipurth *et al.* (2002). All three molecules show a clump of emission at this location in the $10''$ and $5''$ maps. The $C^{18}O$ line is strong and narrow in the $10''$ map, with a mean velocity of 7.7 km s^{-1}. In the $5''$ map, the $C^{18}O$ line is weaker, but the shape is nearly the same. The central velocity of the line is 7.6 km s^{-1}. The $H^{13}CO^+$ and N_2H^+ lines from the $10''$ map are nearly identical in shape and strength. The lines are also nearly identical in the spectra from the $5''$ map. At both resolutions, the central velocity of the $H^{13}CO^+$ line is 7.9 km s^{-1}. For the N_2H^+ line, the central velocity is 8.0 km s^{-1}. At $3''$ resolution, the $C^{18}O$ and N_2H^+ lines are no longer visible. The $H^{13}CO^+$ spectrum seems to show emission at 8.2 km s^{-1}, but nothing is observed at ϵ in the integrated intensity map.

The position ζ is just $12''$ south and east of IRAS4A, along the blueshifted edge

of the emission ridge in the intensity maps. The $C^{18}O$ profiles from both the 10″ and 5″ maps are double-peaked, and the secondary peak pulls the mean velocity of the line significantly blueward. In the 10″ map, fitting a Gaussian function to the line yields a mean velocity of 7.4 km s^{-1}. In the 5″ map, the the central velocity shifts redward by 0.1 km s^{-1}. The $H^{13}CO^+$ and N_2H^+ lines have similar heights and widths at this location. The profiles are noticeably slanted towards the blue. The $H^{13}CO^+$ profiles from both the 10″ and 5″ maps have central velocities of 7.1 km s^{-1}. The N_2H^+ profiles are noisier and yield central velocities at 7.3 km s^{-1}. No molecule shows significant emission in the 3″ resolution maps.

The position η was chosen to probe the clump of emission 15″ north of IRAS4A, at the $H^{13}CO^+$ and N_2H^+ emission peaks. Although the peaks in the $H^{13}CO^+$ and N_2H^+ spectra aren't extraordinary, the widths of these lines are greater than at any other measured position in the maps. Gaussian functions fit to the lines in the 10″ spectra have FWHM of 1.5 and 1.3 km s^{-1}, respectively. The corresponding central velocities of these multi-peaked profiles are 7.4 and 7.7 km s^{-1}. In the spectra from the 5″ maps, the FWHM of the $H^{13}CO^+$ line is the same (1.5 km s^{-1}), and the FWHM of the N_2H^+ line matches it. Similarly, the central velocity of the $H^{13}CO^+$ line is still 7.4 km s^{-1}, but the center of the N_2H^+ line has shifted to 7.6 km s^{-1}. The $C^{18}O$ profiles from the 10″ and 5″ maps are noticeably slanted toward the blue and have correspondingly bluer central velocities. In both spectra, the central velocity is only 7.3 km s^{-1}.

Considering all of the spectra from the various maps, the presence of a single-peaked, symmetrical line profile is the exception, rather than the rule. The interplay of various velocity components, although most conspicuous in the spectra from the continuum sources, is apparent at multiple locations in the maps. In general, one component (at $\sim$7.6 km s^{-1}) is contributed by the FCRAO data, and another com-

ponent (at $\sim$6.7 km s^{-1} is contributed by the BIMA data (although the clump of emission in the FCRAO map at 5.2 km s^{-1} demonstrates that additional components are present in the datasets). As a result, the mean velocity of a line shifts toward the blue as it is examined at higher resolutions.

2.7 Velocity Field Analysis

2.7.1 Systematic Motions

Systematic motions, such as core-wide rotation, contraction, or expansion, are detected in quiescent core gas from variations in the central velocities (V_C) of the emission lines across the cores. A uniformly rotating core can be distinguished from the superposition of gas clumps moving at different line-of-sight velocities by the smoothness of the observed gradient.

The accuracy with which systematic motions can be measured strongly depends on the spatial resolution of the observations. Finding gradients in velocity data requires the determination of V_C over several beams, and lower resolution observations limit the number of independent beams across an emitting region. Furthermore, the velocity field in the vicinity of embedded protostars, which may be included within only a single beam, cannot be precisely represented by an interpolation of the large-scale gradient. That is, the motions of the material at the center of a core may differ from motions in the envelope, just as low-resolution core gradients are found to differ in magnitude and orientation from the velocity field of clouds surrounding the cores (Barranco & Goodman 1998).

Features of the velocity maps of L1448 IRS3, NGC1333 IRAS2, and NGC1333 IRAS4 were described in the previous sections, and not one of these cores shows an indisputable signature of a rotating, quiescent core. Although the velocity maps

Table 2.10. L1448 IRS3 Measured Gradients

$C^{18}O$			$H^{13}CO^+$			N_2H^+		
Beam	Axis[a]	Gradient	Beam	Axis[a]	Gradient	Beam	Axis[a]	Gradient
44	C	3.7	56.5	C	2.8	52	C	3.1
10	C	23.5	10	C	25.7	10	C	16.2
	I	24.5		I	31.4		I	10.0[b]
	V	23.2		V	23.3		V	21.9
5	C	23.2	5	C	37.7	5	C	19.9
	I	28.8		I	50.4		I	... [c]
	V	46.4		V	52.6		V	65.0
3	C	38.0	3	...	...	3	...	...
	I	30.0		...	...		...	...

Note. — Beam sizes are given in arcseconds. Gradients are given in km s^{-1} pc^{-1}.

[a] C = continuum positions; I = intensity peaks; V = velocity extrema. (*See text.*)

[b] Western intensity peak on extended emission arm, see Figure 3*d*.

[c] No western intensity peak.

from the FCRAO data all show broad velocity gradients across the cores, the higher resolution maps reveal velocity structure that is considerably more complex.

Of the three cores, L1448 IRS3 has the velocity field that most strongly suggests uniform rotation. The velocity difference between the blueshifted western half and the redshifted eastern half is obvious. All three tracers show roughly the same resolution-dependent velocity differences at the positions of the continuum sources (*c.f.* Figure 2.6). The magnitudes of gradients along representative axes through the center of L1448 are summarized in Table 2.10. In the maps created from the FCRAO data, the gradients are measured along the axis that passes through the L1448NW continuum position and the midpoint between L1448N(A) and L1448N(B). The magnitudes are 3.7, 2.8, and 3.1 km s^{-1} pc^{-1} for the $C^{18}O$, $H^{13}CO^+$, and N_2H^+ lines, respectively. In the higher resolution maps, the velocity gradients are measured along three different axes: through the positions of the continuum sources

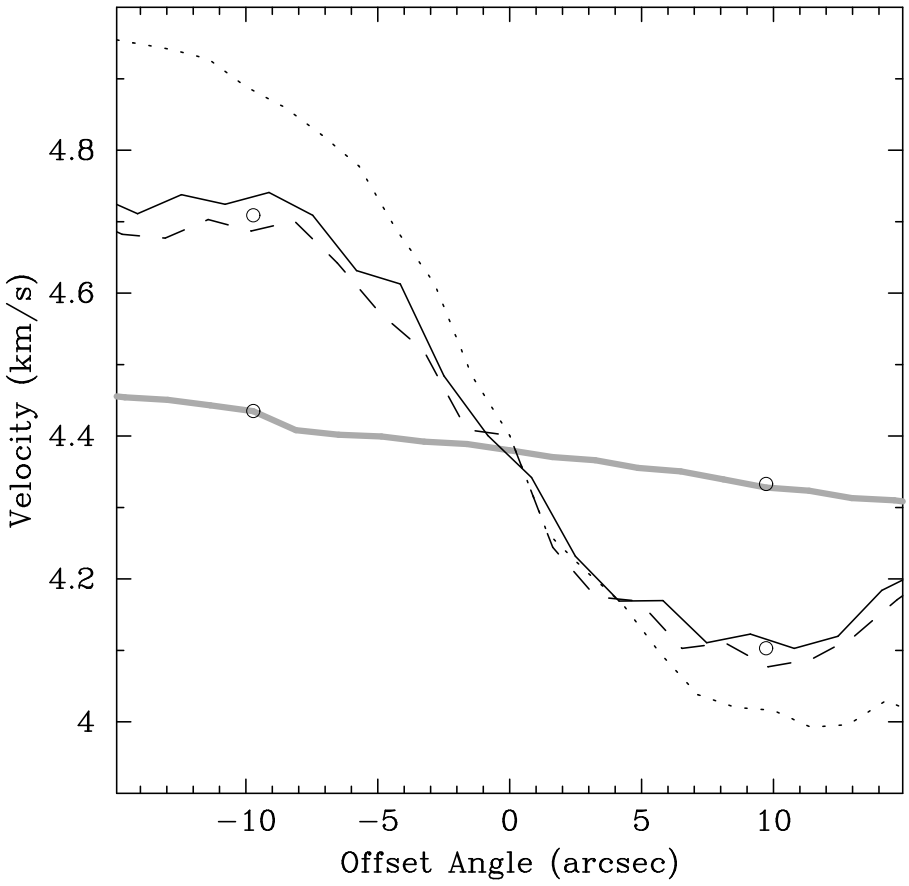

Figure 2.17: Gradients in the $C^{18}O$ velocity maps of L1448 IRS3. The wide gray line shows a gradient in the map made from the FCRAO data. The axis runs through the continuum positions (Axis C); the open circles indicate the positions of L1448N(AB) (negative offset) and L1448NW (positive offset). The solid line shows the gradient along Axis C in the 10″ map; the open circles indicate the positions of the continuum sources. The dashed line shows the gradient in the 10″ map along Axis I; the dotted line is the gradient along Axis V.

(Axis C), through the positions of the intensity maxima near L1448N(AB) and L1448NW (Axis I), and through the positions of the velocity extrema in the eastern and western halves of the map (Axis V). The average magnitude of the gradients measured from the 10″ maps is 22.2 km s^{-1} pc^{-1}. These three gradients are displayed, along with the gradient from the FCRAO map, in Figure 2.17. In the 5″ maps, the average gradient increases to 40.5 km s^{-1} pc^{-1}; excluding the highest value (along the V axis in the N_2H^+ map), the average of the remaining measurements

is 37.0 km s^{-1} pc^{-1}. The magnitudes of the gradients increase as the resolution of the velocity maps increases. Although the gradients have a range of values, they are all approximately an order of magnitude greater than the gradients measured from the FCRAO observations. Moreover, because the velocities level out in the regions of the map further away from the transition zone in between L1448N(AB) and L1448NW, the measured magnitudes are only lower limits. The large gradients reinforce the observation that the higher resolution maps contain information that is diluted in maps made with larger beams. The precision of the velocity information provides a ready explanation for the large gradient in the 5″ N_2H^+ map: the range of velocities in the map is greater than at lower resolutions, but the position of the velocity extrema does not change significantly.

To determine whether the L1448 IRS3 core rotates, the critical quality of the measured gradients is not their magnitudes but their continuity across the core. However, the variation in the gradient with map resolution *is* an indication of the continuity. If the core is unifromly rotating, then the same gradient will be observed at all resolutions. Our velocity maps clearly show that the magnitude of the gradient increases with map resolution. This trend suggests that the transition zone is an interface between independent emitting regions and not an axis of rotation. [Although *differential* rotation of a core would exhibit velocity gradients that vary with resolution, the central concentration of mass that would promote this rotation profile is not seen in the continuum data.]

Based upon the $\lambda = 2.7$ mm continuum observations, LMW00 estimated the mass of the emitting material around the three L1448 IRS3 protostars to be M(A) = 0.09 M$\odot$, M(B) = 0.52 M$\odot$, and M(NW) = 0.12 M$\odot$. These mass estimates are based upon a simplistic model which assumes an isothermal, optically thin emitting region with a uniform dust opacity. Because all three of the L1448 YSOs are Class

0 objects, the degree of optical/infrared extinction suggests that the mass of their embedded protostars is significantly less than the mass in the surrounding envelopes. If the L1448N(AB) and L1448NW condensations orbit each other, then the masses calculated by LMW00 set upper limits on the masses of the orbiting protostars, and the emission from the attendant gas envelopes produces a velocity gradient that can be compared with the observations. According to LMW00, the continuum sources are separated by 17″ or 5140 AU at the distance (300 pc) of the L1448 cloud. If the orbit is *assumed* to be circular and perpendicular to the plane of the sky, then an upper limit to the orbital velocities can be determined. Under these assumptions, the predicted velocity difference between L1448N(AB) and L1448NW is 0.34 km s^{-1}, which corresponds to a gradient of 13.5 km s^{-1} pc^{-1}. Although this value is an upper limit for the protostars to orbit, it is less than the measured gradients determined along the C Axis for all three emission lines in any of the higher resolution maps.

Conversely, the masses of L1448N(AB) and L1448NW can be approximated from the observed gradient. From the magnitude of the Axis C gradient in the $C^{18}O$ map with 10″ resolution, 23.5 km s^{-1} pc^{-1}, the velocity difference between the two continuum sources is 0.59 km s^{-1}. If the orbit is again *assumed* to be circular and oriented perpendicular to the plane of the sky, and if the mass ratio is assumed to be the same as the value determined by LMW00, M(AB)/M(NW)=5.08, then the velocity difference corresponds to the offset for masses of M(AB)=1.66 $M_\odot$ and M(NW)=0.33 $M_\odot$. These values are more than twice as large as the estimates based upon the continuum emission. The purpose of presenting this argument is *not* to estimate the masses in the L1448 IRS3 system, but to show that if the observed velocity gradient represented orbital motion, the required protostellar masses would be inconsistent with the continuum data.

In the NGC1333 cores, evidence for sustained velocity gradients around the po-

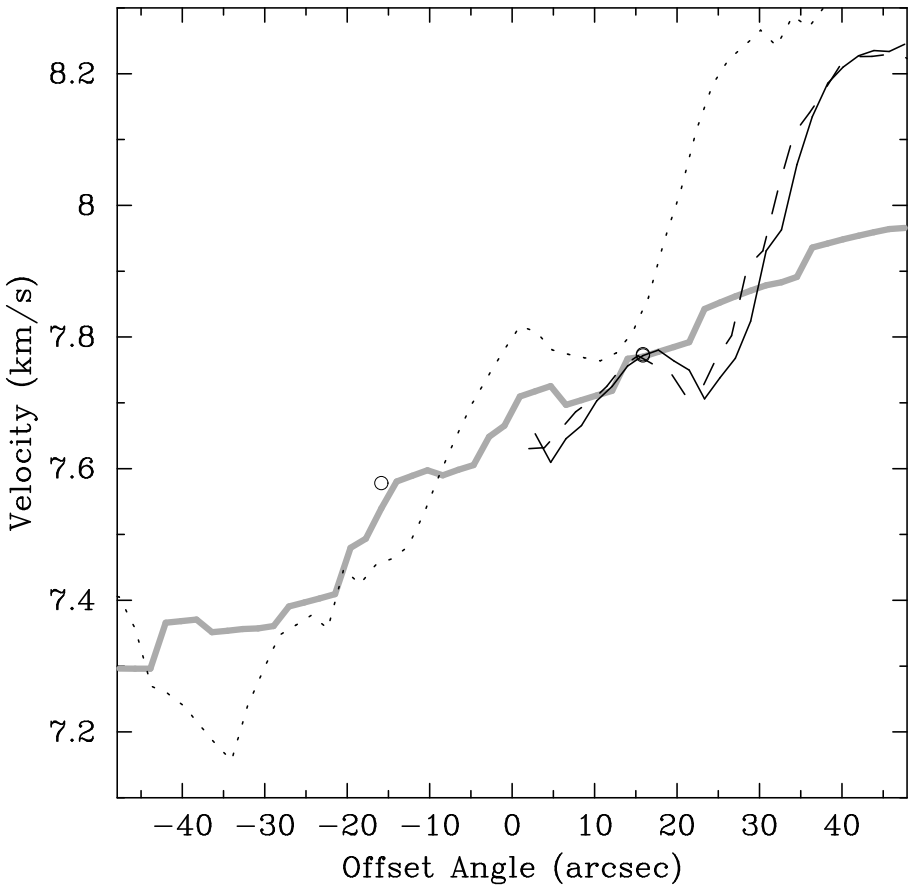

Figure 2.18: Gradients in the N_2H^+ velocity maps of NGC1333 IRAS2. The wide gray line shows a gradient in the map made from the FCRAO data. The axis runs through the continuum positions (Axis C); the open circles indicate the positions of IRAS2B (negative offset) and IRAS2A (positive offset). The solid line shows the gradient along Axis C in the 10″ map. There is insufficient N_2H^+ emission to follow the gradient to IRAS2B. The dashed line shows the gradient in the 10″ map along Axis I, the axis through the peaks in the N_2H^+ intensity on either side of IRAS2A. The dotted line is the gradient along Axis V, the velocity peaks. Note: Axis V does not have the same center as the other gradients, so the offset angles are shifted.

sitions of the continuum sources doesn't extend into the higher resolution velocity maps. All three lines from IRAS4 show a slight blueshift with respect to the background cloud, in addition to a velocity gradient that runs perpendicular to the long axis of the core. The dominant trend in the $C^{18}O$ and $H^{13}CO^+$ emission from IRAS2 is also a blueshift from the background cloud. The N_2H^+ velocity map of IRAS2 hints at the presence of a smooth gradient around the position of IRAS2A. From the FCRAO data, the gradient through the IRAS2A and IRAS2B continuum positions (Figure 2.18) appears fairly smooth; its magnitude, 3.6 km s^{-1} pc^{-1}, is similar to the gradients seen at this resolution in L1448 IRS3. In the higher resolution maps, the N_2H^+ emission in the vicinity of IRAS2B is absent, so the gradient axes cannot be extended. Instead, the velocity gradients through the N_2H^+ intensity peaks on either side of IRAS2A and through the positions of the velocity extrema are measured. In addition, Axis C is extended from the position of IRAS2B through IRAS2A toward the position of IRAS2C (which is not seen in the continuum data). The average magnitude of the gradient measured at 10″ resolution is 8.5 km s^{-1} pc^{-1} (see Figure 2.18); the average magnitude of the gradients measured in the 5″ maps is 9.7 km s^{-1} pc^{-1}. The smooth gradient suggested in the FCRAO maps looks more like two adjacent velocity plateaus in the higher resolution maps. At IRAS2A, the plateau levels at $V_C \sim 7.7$ km s^{-1}. Near IRAS2C, the plateau levels at $V_C \sim 8.2$ km s^{-1}.

2.7.2 Turbulent Motions

The overarching goal of this work is to assess the influence of turbulence upon the star formation process, insofar as turbulence leaves its imprint upon the molecular gas in dense cores. A satisfactory diagnostic of turbulence should be one that is easily applied to available velocity data and clearly indicates the presence and strength of turbulent motions in the gas. The method for analyzing velocity data

that is developed in this work is a natural extension of methods used in previous studies of dense cores. A summary of these studies is presented in the next section. Because this chapter offers L1448 IRS3, NGC1333 IRAS2, and NGC1333 IRAS4 as prototypical dense cores containing multiple protostars, the proposed analysis technique is first applied to the velocity maps of these cores.

Studies of Line Widths from Dense Cores.

As described in § 1.4, turbulent motions are detected from measurements of the widths (Δv) of molecular emission lines. In one of the first expansive surveys of its kind, Larson (1981) assembled data on the masses, densities, and emission line widths of molecular clouds in a wide range of sizes. In addition to confirming that line widths consistently exceeded the dispersions appropriate for purely thermal motions, Larson found a correlation between velocity dispersion and cloud size. This correlation, which applied to observations of various molecular lines tracing a range of densities, was roughly fit by the power law: $\Delta v_{obs} \propto R^{0.38}$.

Barranco & Goodman (1998) and Goodman *et al.* (1998) pointed out that, because different molecular transitions are sensitive to different physical conditions, the slope of the power law relation between line width and cloud size depends upon the number of emission lines and the number of clouds included in the same survey. They defined four types of line width–size correlations. Type 1 correlations are determined from measurements of multiple lines from multiple clouds; Larson's survey found a Type 1 correlation. In contrast, Type 4 correlations are determined from measurements of a single line from a single cloud; Type 4 correlations show the contributions of thermal and nonthermal motions to line widths at the specific densities probed by the observed tracer.

The physical basis for a correlation between line widths and cloud sizes is un-

certain. Several practicable theories have been advanced (*c.f.* Vázquez-Semadeni *et al.* (2000) and references therein); all agree that the correlation indicates a fundamental process in the ISM. However, the correlation between line width and cloud size must ultimately terminate because the thermal velocity dispersion of the tracer molecule sets a minimum observable line width: $(\Delta v_{obs})_{min} \geq \Delta v_T$. Larson (1981) estimated that condensations supported purely by thermal motions would have sizes $R \sim 0.04$pc and masses M~ 0.25M$\odot$, but a number of studies have sought observational evidence for the point at which the correlation breaks down. These studies have had two primary emphases: mapping cores with higher resolutions and separating thermal from nonthermal motions by observing multiple emission lines.

From surveying the $C^{18}O$, CS, and NH_3 emission from dense cores both with and without detectable protostars, (Fuller & Myers 1992) find an overall (Type 1) correlation between line width and cloud size similar to the one found by Larson (1981): $\Delta v_{obs} \propto R^{0.4\pm0.1}$. Moreover, they find that the nonthermal contributions to the observed line widths have a stronger dependence upon core size, $\Delta v_{NT} \propto R^{0.7\pm0.1}$, than the dependence observed in larger clouds. The fact that the nonthermal contributions decrease more rapidly in core interiors suggests that the turbulent motions responsible for the nonthermal contribution may be dissipated on small scales. Based on their sample of cores, Fuller & Myers (1992) estimate that the nonthermal and thermal components make equal contributions to the line widths for cores with size $R \approx 0.09$ pc (assuming T = 10 K).

The surveys by Barranco & Goodman (1998) and Goodman *et al.* (1998) emphasize the slopes from an ensemble of Type 4 correlations. The former study re-examines maps of the NH_3 emission from four dense cores observed by Benson & Myers (1989); the latter study folds in observations of $C^{18}O$ and OH^- emission. For the nonthermal components of the individual lower density tracers ($C^{18}O$,OH^-),

they find $\Delta v_{NT} \propto R^{0.2\pm0.06}$. Over the full NH_3 emission maps, the correlation is $\Delta v_{NT} \propto R^{0.1\pm0.08}$. And for the regions within the NH_3 half-power contours, the power law exponents are approximately zero, indicating that the line widths are nearly constant across the densest parts of the cores. The observed widths are never as narrow as purely thermal line widths (*i.e.* $\Delta v_{NT} > 0$), but the nonthermal components always make smaller contributions (*i.e.* $\Delta v_{NT} \lesssim \Delta v_{therm}$). Thus, if turbulence contributes to the nonthermal line width, it must be subsonic. The departure from a single power law in the line width–size correlations led Barranco & Goodman (1998) and Goodman *et al.* (1998) to define the break point as a threshold of "coherence," the size of the smallest eddies in the turbulent spectrum. Below this threshold, the dissipation of turbulence minimizes the nonthermal component of the line width.

Maps of the N_2H^+ emission from a set of both "starred" and "starless" cores by Caselli *et al.* (2002a) revealed that, although line widths are uniform (0.3–0.4 km s^{-1}) in the core centers (near the locations of peak emission), they do not consistently increase toward the edges of the cores. However, Caselli *et al.* (2002a) do find that the *deviation* in line widths tends to increase toward the core edges. They suggest that the line width deviations arise over approximately 10 "coherence lengths" along the line of sight; they estimate that a single coherence length, over which the line width is constant, has a size of $\sim$0.01 pc. They conclude that their data indicate that typical cores must be subject to incoherent motions that are responsible for the variations in velocity dispersions.

The Importance of High Resolution Data.

The studies of core velocity fields summarized above (Barranco & Goodman (1998); Goodman *et al.* (1998); Caselli *et al.* (2002a)) all conclude that the minimum line widths observed from core centers must include some nonthermal component. Furthermore, these studies find that although emission line widths vary significantly across cores, the variations diminish within some critical radius. The coherence of line widths may indicate a critical size scale below which turbulent motion cannot be maintained.

Perceived variations of line width with position are necessarily a function of the spatial resolution of the observations from which the lines are measured. The macroturbulent motions that contribute to the width of an emission line may originate from anywhere within the beam over which the spectrum is taken. Therefore, a measured line width represents an average over the area of the beam. If a large fraction of a core's volume is included in the beam, then details of the velocity field in the core are diluted in the beam. As described in §§ 2.4-2.6, the range of velocities appearing in the maps increases as the resolution increases.

The $C^{18}O$ observations of Goodman *et al.* (1998) have a resolution of 48″; at the distance of TMC-1C (140 pc), they resolve structures of ∼6700 AU (0.033 pc). The N_2H^+ observations of Caselli *et al.* (2002a) have a resolution of 54″, equivalent to ∼7600 AU (0.037 pc) at the distance of Taurus. In this study, the high resolution BIMA data sample the cores in even greater detail. For the cores in NGC1333, the maps with resolutions of 10″, 5″, and 3″ show structures down to 3500, 1750, and 1050 AU, respectively. For L1448N IRS3, which is slightly closer, the map resolutions correspond to physical scales of 3000, 1500, and 900 AU, respectively. Although these resolutions are much finer than the single-dish studies, emission structures on these scales are large enough that they are not directly associated

with individual protostars (*e.g.* individual circumstellar disks). The BIMA data bridge the gap between the kinematics revealed by the single-dish observations and the smaller, protostellar kinematics.

The method that is applied to the BIMA/FCRAO datacubes to examine the velocity dispersions was developed and applied to *model* clouds data by Ostriker, Stone, & Gammie (2001). One important aspect of this method is that *no correlation between line width and radial distance from the core center is implied.*

The OSG Model Clouds and Gridding Method.

The turbulent model clouds constructed by Ostriker, Stone, & Gammie (2001) (hereafter OSG) have an initially uniform density, an initially unidirectional magnetic field, and are constrained to obey an isothermal equation of state. Turbulence is introduced by a Gaussian random velocity field that obeys a power law of the form $|\delta v_k|^2 \propto k^{-4}$. Solutions to the magnetohydrodynamic equations are generated within a box with dimensions $256 \times 256 \times 256$ that is subject to periodic boundary conditions. OSG use their model clouds to examine the effect of projection on emission line widths; they compare the kinematic structure of the models in three dimensions with the properties observed in two dimensions. They subdivide their model into cells with length s (so each volume element has a volume s^3, and each face is gridded into squares with area s^2) and then define a "region of contrast" (ROC) for a particular spatial scale as a square where the projected surface density exceeds the mass-weighted mean surface density, $\Sigma[s]$. For each ROC, they calculate the mass-weighted dispersion in the line-of-sight velocity component (σ_v) and use it as a proxy for the emission line width that would be observed from the grid square. They also calculate the mean line-of-sight velocity dispersions for the 3D cells. For both 2D and 3D velocity dispersions, only contributions from cells with densities

$\rho > 3\bar{\rho}$ are included.

OSG discover several trends when they plot the correlations between σ_v and s (*c.f.* OSG Figures 10a & 11a). For the 3D cubes, σ_v increases steeply as a function of scale length. In contrast, σ_v in the projected (2D) ROCs shows significant scatter at smaller scale lengths. The lower envelope of the 2D σ_v values follows the steep trend seen in the σ_v of the 3D cubes. The upper envelope of the 2D σ_v values gradually decreases with increasing size scale. Least-square linear fits to the correlations reveal a range of slopes of $d\log(\sigma_v)/d\log(s) = 0.07$-$0.12$ for projections perpendicular to the mean magnetic field and $d\log(\sigma_v)/d\log(s) = 0.11$-$0.19$ for projections parallel to the mean field. The contrasting trends in the 2D and 3D data show that the spread in σ_v of the projected ROCs is the result of the superposition of 3D cells of emitting gas, with different mean velocities, along the line of sight. OSG conclude that there is an observable difference between coherent parcels of gas that are truly independent from their surroundings and regions of spatially-separated gas that are identified from position-velocity datacubes. Whereas a coherent parcel of gas yields a steep dispersion power spectrum, multiple spatially-separated components along the line of sight yield shallower power spectra with a large amount of scatter.

Application of the OSG Gridding Method.

When applying the OSG gridding method to the $C^{18}O$, $H^{13}CO^+$, and N_2H^+ datacubes of L1448 IRS3, NGC1333 IRAS2, and NGC1333 IRAS4, the largest dimension corresponds to the full area of the FCRAO maps ($6' \times 6'$). The maps are subdivided into 2^n intervals, where the maximum value of n is chosen so that the interval is not less than the diameter of the beam (*i.e.* $\theta_{map}/2^n \geq \theta_{beam}$). Thus, all spectra for a given beamsize are independent. The combined and BIMA-only datacubes are treated in a similar manner, except that the largest scale size is re-

stricted to the area of the BIMA primary beam, rather than the full area of the map. The maps are then subdivided to the limit set by the diameter of the appropriate beam. Spectra are taken through the 25-channel datacubes using the MIRIAD task `gridspec`, which also fits a single Gaussian function to the emission profile in each grid square. The velocity dispersions plotted in Figures 2.19, 2.20, and 2.21 are the FWHM of the fitted Gaussian functions.

Four criteria are imposed to assure the quality of the spectra used to determine the correlations. First, all pixels that are masked in the velocity maps are also masked in the datacubes; the cutoff is set at twice the rms noise of the intensity map. Second, at least 25% of the pixels in a grid square must be valid (unmasked) for a spectrum to be calculated. While testing `gridspec`, this percentage was set as low as 0% and as high as 50%. Percentages $< 20\%$ were disqualified because line widths measured from these grid squares might emphasize contibutions from only a few aberrant pixels. In general, percentages between 20% and 50% yielded similar results. The 25% cutoff was selected as a reasonable intermediate value. Third, the line peak from a grid square must be greater than $3\times$ the rms noise in the spectrum. Fourth, the normalized χ^2 of the Gaussian function fit must be one or less. Enforcing these four criteria assures that the fitted spectra included in the displayed correlations are single-lined and only from regions with sufficiently strong emission. In the higher resolution maps, the valid spectra are generally concentrated around the continuum positions.

The line width *vs.* grid size correlations of all three cores (Figures 2.19, 2.20, 2.21) have several common characteristics. The number of points naturally increases as the size of the individual grid squares decreases, but few points are included at $3''$ resolution primarily because of the reduced S/N ratio. In general, the lower envelopes of the correlations are relatively steep, and the upper envelopes are roughly

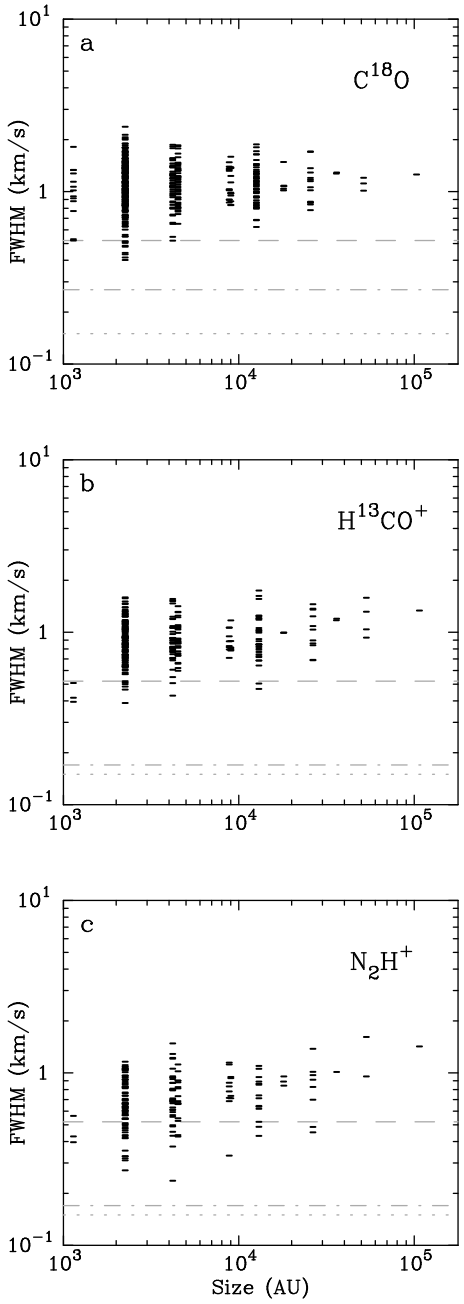

Figure 2.19: L1448 IRS3 line width (FWHM) *vs.* size (grid square) correlations. In each panel, the dashed line indicates the line width corresponding to the sound speed of the medium (FWHM_{c_s}), the dotted line indicates the thermal line width (FWHM_T), and the dash-dot line indicates the channel width of the spectra (δV). (a) $C^{18}O$ spectra: $\mathrm{FWHM}_{c_s}(14\ \mathrm{K}) = 0.52$ km s^{-1}; $\mathrm{FWHM}_T(14\ \mathrm{K}) = 0.15$ km s^{-1}; $\delta V = 0.27$ km s^{-1}. (b) $H^{13}CO^+$ spectra: $\mathrm{FWHM}_{c_s}(14\ \mathrm{K}) = 0.52$ km s^{-1}; $\mathrm{FWHM}_T(14\ \mathrm{K}) = 0.15$ km s^{-1}; $\delta V = 0.17$ km s^{-1}. (c) N_2H^+ spectra: $\mathrm{FWHM}_{c_s}(14\ \mathrm{K}) = 0.52$ km s^{-1}; $\mathrm{FWHM}_T(14\ \mathrm{K}) = 0.15$ km s^{-1}; $\delta V = 0.17$ km s^{-1}.

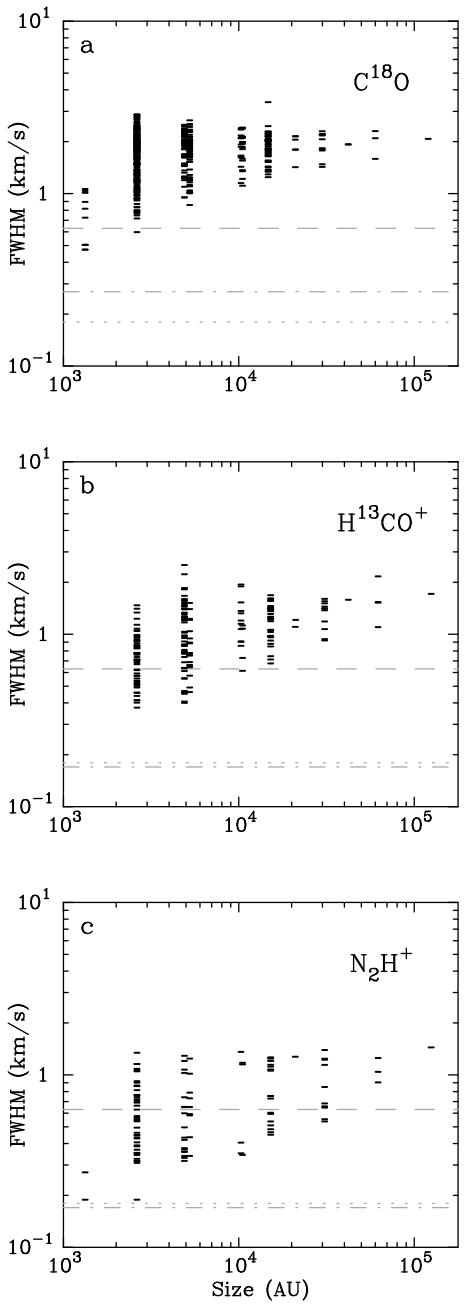

Figure 2.20: NGC1333 IRAS2 line width (FWHM) *vs.* size (grid square) correlations. In each panel, the dashed line indicates the line width corresponding to the sound speed of the medium (FWHM_{c_s}), the dotted line indicates the thermal line width (FWHM_T), and the dash-dot line indicates the channel width of the spectra (δV). (a) $C^{18}O$ spectra: $\mathrm{FWHM}_{c_s}(20\ \mathrm{K}) = 0.63$ km s^{-1}; $\mathrm{FWHM}_T(20\ \mathrm{K}) = 0.18$ km s^{-1}; $\delta V = 0.27$ km s^{-1}. (b) $H^{13}CO^+$ spectra: $\mathrm{FWHM}_{c_s}(20\ \mathrm{K}) = 0.63$ km s^{-1}; $\mathrm{FWHM}_T(20\ \mathrm{K}) = 0.18$ km s^{-1}; $\delta V = 0.17$ km s^{-1}. (c) N_2H^+ spectra: $\mathrm{FWHM}_{c_s}(20\ \mathrm{K}) = 0.63$ km s^{-1}; $\mathrm{FWHM}_T(20\ \mathrm{K}) = 0.18$ km s^{-1}; $\delta V = 0.17$ km s^{-1}.

flat or gradually declining. For each core, the slope of a least-squares linear fit to the data (not shown in the figures) increases from the $C^{18}O$ data set to the $H^{13}CO^+$ dataset to the N_2H^+ dataset. Additionally, there is a trend in the absolute line widths from the three molecules; although there is considerable overlap, the $C^{18}O$ lines are generally the widest, the N_2H^+ lines are the narrowest, and the $H^{13}CO^+$ lines fall somewhere in between. The dashed lines indicate the line broadening corresponding to the sound speed of the local medium. In calculating the sound speed, the temperature of the medium is assumed to be the average value at the outer radius from the envelope models derived by Looney (1998). This value approximates the kinetic temperature of the bulk of the core volume. The temperatures are 14, 20, and 21 K for L1448 IRS3, NGC1333 IRAS2, and NGC1333 IRAS4, respectively. The dotted lines show the contribution of thermal broadening to the line widths; the temperature is assumed to be the same as in the calculation of the sound speed. Because all three molecules have similar masses $[m(C^{18}O) = m(H^{13}CO^+) = 30m(H_2); m(N_2H^+) = 29m(H_2)]$, their thermal line widths are also similar. The dash-dot lines indicate the channel widths of the spectra.

In the line width *vs.* grid size correlations determined from the L1448 IRS3 spectra (Figure 2.19), the thermal line width is below the lower envelope of the measured FWHM, even at the smallest size scale, indicating that the thermal velocities are insufficient to produce the observed line widths. The lower envelopes of the distributions from all three molecules do, however, extend below the broadening contributed by the sound speed of the medium. If the nonthermal contribution to the observed line were entirely due to sonic broadening, then the line width would be:

$\mathrm{FWHM}_{obs} = [(\mathrm{FWHM}_T)^2 + (\mathrm{FWHM}_{c_s})^2]^{0.5} = [(0.15)^2 + (0.52)^2]^{0.5} = 0.54$ km s^{-1}.

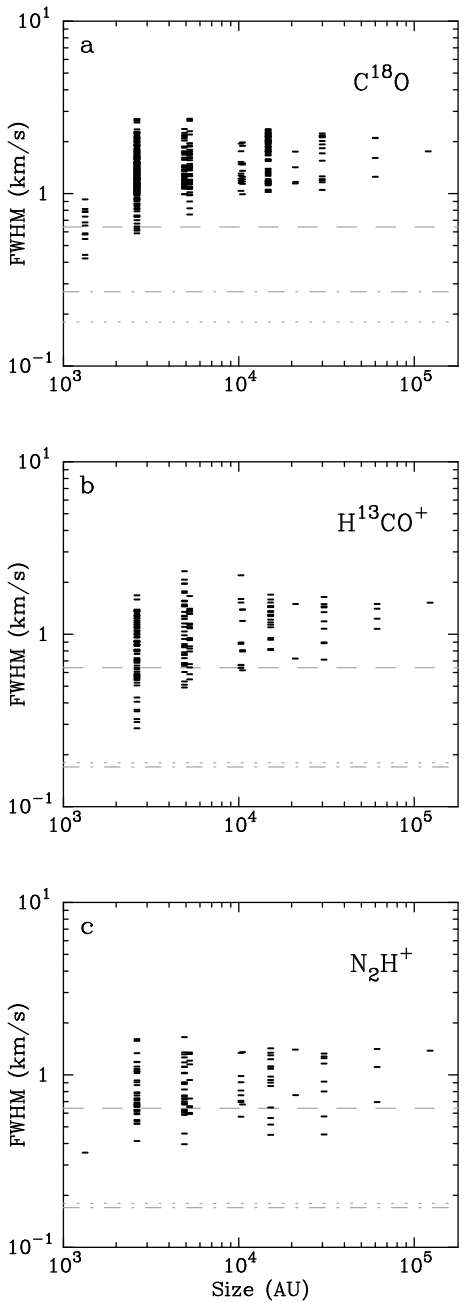

Figure 2.21: NGC1333 IRAS4 line width (FWHM) *vs.* size (grid square) correlations. In each panel, the dashed line indicates the line width corresponding to the sound speed of the medium (FWHM_{c_s}), the dotted line indicates the thermal line width (FWHM_T), and the dash-dot line indicates the channel width of the spectra (δV). (a) $C^{18}O$ spectra: $\mathrm{FWHM}_{c_s}(21\ \mathrm{K}) = 0.64$ km s^{-1}; $\mathrm{FWHM}_T(21\ \mathrm{K}) = 0.18$ km s^{-1}; $\delta V = 0.27$ km s^{-1}. (b) $H^{13}CO^+$ spectra: $\mathrm{FWHM}_{c_s}(21\ \mathrm{K}) = 0.64$ km s^{-1}; $\mathrm{FWHM}_T(21\ \mathrm{K}) = 0.18$ km s^{-1}; $\delta V = 0.17$ km s^{-1}. (c) N_2H^+ spectra: $\mathrm{FWHM}_{c_s}(21\ \mathrm{K}) = 0.64$ km s^{-1}; $\mathrm{FWHM}_T(21\ \mathrm{K}) = 0.18$ km s^{-1}; $\delta V = 0.17$ km s^{-1}.

However, the majority of the L1448 IRS3 spectra have FWHM *greater* than this. Only ~3% of the $C^{18}O$ spectra and ~5% of the $H^{13}CO^+$ spectra suggest subsonic motions; the percentage of N_2H^+ spectra with FWHM below the sonic threshold is ~20%. Thus, the observed line widths must be dominated by sonic or supersonic motions in the material.

The line width *vs.* grid size correlations from the NGC1333 IRAS2 spectra are displayed in Figure 2.20. As with the L1448 IRS3 spectra, no line widths are narrower than the thermal line width; more are narrower than the sonic line width. Because the sound speed is larger at the higher temperature of the IRAS2 envelope (T_k = 20 K), the number of lines with subsonic widths is expected to increase. For IRAS2, the sonic threshold is:

$\mathrm{FWHM}_{obs} = [(\mathrm{FWHM}_T)^2 + (\mathrm{FWHM}_{c_s})^2]^{0.5} = [(0.18)^2 + (0.63)^2]^{0.5} = 0.66$ km s^{-1}.

The percentage of $H^{13}CO^+$ and N_2H^+ spectra with widths below the sonic threshold are ~18% and ~52%, respectively. However, only ~1% of the $C^{18}O$ line widths are below this threshold.

In the line width *vs.* grid size correlations from the NGC1333 IRAS4 spectra (Figure 2.21), the thermal line width is again considerably narrower than any of the observed lines. The threshold below which the nonthermal contribution to the observed line width is subsonic is:

$\mathrm{FWHM}_{obs} = [(\mathrm{FWHM}_T)^2 + (\mathrm{FWHM}_{c_s})^2]^{0.5} = [(0.18)^2 + (0.64)^2]^{0.5} = 0.66$ km s^{-1}.

The percentage of observed line widths below the sonic threshold is ~2%, ~17%, and ~33% for the $C^{18}O$, $H^{13}CO^+$, and N_2H^+ lines, respectively.

The $C^{18}O$ line traces lower density gas than either the $H^{13}CO^+$ or the N_2H^+ line, and the intensity maps show that the $C^{18}O$ is widely distributed in the core. However, in each core, at least some fraction of the spectra from every tracer has narrower FWHM than the sonic broadening. These narrow spectra are evidence

that there are lines of sight through which the turbulent motions in the core are diminished. There are clearly many spectra with FWHM great enough that the nonthermal contributions to the line widths cannot be subsonic. The emission lines within the cores cannot originate entirely from a single clump of quiescent gas.

The figures displayed here show the correlations between line width and grid size for single cores probed by single molecular tracers, *i.e.* for each core, the FWHM measurements of the three lines are plotted on different diagrams. Such single-line, single-core correlations are classified as Type 4 correlations according to the nomenclature advanced by Barranco & Goodman (1998) and Goodman *et al.* (1998). They assert that because a Type 4 correlation relies upon only a single molecular line with a known critical density, it provides a targeted probe of a velocity field at that particular density. Goodman *et al.* (1998) map three cores (B1, TMC-1C, L1251A) in the $C^{18}O$ $J = 1 \rightarrow 0$ line and the 1667 MHz line of OH^-, two transitions that have similar critical densities, $n \gtrsim 10^3 cm^{-3}$. They determine individual Type 4 correlations that have a mean slope of $a_4 \sim 0.2 \pm 0.06$. The slopes of linear least-squares fits to the $C^{18}O$ data presented here (not shown) are all shallower (a_4 =0.042, 0.066, and 0.080, for L1448, IRAS2, and IRAS4, respectively), with a mean slope of $a_4 \sim 0.063 \pm 0.032$. Because of the dispersion in the measured FWHM, however, these values are of limited usefulness in drawing a firm comparison; between the lower and upper envelopes of the data points, there is a range of possible slopes. The value determined from the single-dish studies is a reasonable fit to the lower envelope of the $C^{18}O$ FWHM for all three cores, suggesting that an extrapolation of the lower envelope might be an appropriate slope for the correlation on larger scales.

The data presented here also underscore the importance of the high resolution observations. Very few $H^{13}CO^+$ and N_2H^+ spectra from the $3''$ maps meet all four

quality criteria and are included in the correlations. (The few that are included have a negligible effect upon the least-squares fitting.) Because the $C^{18}O$ observations include A-array data, there are more high quality $C^{18}O$ spectra at $3''$ resolution. In the line width *vs.* grid size diagram for L1448 IRS3 (Figure 2.19*a*), the measured FWHM from the highest resolution spectra are evenly distributed about the mean, and there are no FWHM near the upper or lower extremes. In contrast, the FWHM from the highest resolution spectra of IRAS2 and IRAS4 all appear below the center of the distribution and extend down to the lower extreme. It is uncertain whether any of these cores has been adequately sampled at $3''$ resolution. Additional high-resolution interferometric observations would improve the S/N ratio in the $3''$ maps and enable more high quality spectra to be measured. The inclusion of additional spectra would clarify whether the distribution of high-resolution FWHM from IRAS2 and IRAS4 extends up to the current fitted line, or whether the distribution of FWHM from L1448 IRS3 has been biased toward higher values.

Another factor that influences the correlations is the number of features in the spectra. In many cases (*c.f.* Figures 2.6, 2.11, 2.16), the spectra contain multiple emission lines, and some lines have non-Gaussian shapes. The `gridspec` task only fits one of the lines, but the presence of the other line contributes to a high value for χ^2, so many of the spectra are excluded from the line width *vs.* grid size diagrams. Although some velocity information may be discarded by only fitting single Gaussian functions, the fraction of spectra that are are poorly fit by Gaussians are in the minority. Because of the χ^2 criterion, the FWHM of a double-peaked spectrum was rarely represented by a single (poorly-fit) Gaussian function.

Chapter 3

Molecular Depletion in Dense Cores

3.1 Suppression of Molecular Line Emission by Depletion onto Dust Grains

Within the range of physical conditions probed by the $C^{18}O$, $H^{13}CO^+$, and N_2H^+ lines, several factors may contribute to the suppression of emission and therefore an inadequate representation of the core velocity field. The strength of a particular line may be suppressed if the absolute abundance of the emitting molecule is somehow reduced in the star-forming region where the core is located. The molecular abundances in different regions of the Galaxy depend upon the star formation histories of those regions, but the variation within any one large cloud should be comparatively smaller (*c.f.* Bergin *et al.* (1997); Greaves & Nyman (1996); Irvine, Goldsmith, & Hjalverson (1987).

A more likely cause of suppressed line emission is the reduction of the number of emitting molecules *in the gas phase* within the core. The observed rotational transitions are only stimulated in gas-phase molecules. In cold, shielded environments, however, many molecular species "freeze out" onto dust grains, depleting the gas-phase population. In addition to reducing the observed line strength, molecular

depletion may significantly influence a core's evolution by affecting the ionization fraction. In the standard star formation theory, the timescale for a subcritical core to reach the collapse threshold is regulated by the ambipolar diffusion of ionized and neutral species, and the degree of ionization is a critical quantity. A number of studies have found that CO and its isotopomers become significantly depleted in core environments (Hotzel *et al.* 2002; Bergin *et al.* 2001; Jessop & Ward-Thompson 2001; Caselli *et al.* 1999). In contrast, ionized species such as $H^{13}CO^+$ and N_2H^+ are likely to remain abundant even in cold, dense regions where the CO isotopomers have frozen out (Bergin & Langer 1997; Tafalla *et al.* 2002). Chemical models suggest that N_2H^+ may be the most robust tracer of high-depletion zones (Bergin & Langer 1997; Benson, Caselli, & Myers 1998), although observational evidence for depletion of N_2H^+ in the center of an isolated, pre-protostellar cloud has recently been found (Bergin *et al.* 2002).

3.2 A Study of $C^{18}O$ Depletion in L1448 IRS3, NGC1333 IRAS2, NGC1333 IRAS4

Synthetic spectral maps were developed based upon models of the envelopes of L1448N(B), IRAS2A, and IRAS4A derived by Looney (1998) from observations of the $\lambda = 2.7mm$ continuum. Realistic models of the envelopes must justify not only the observed continuum fluxes, but also the molecular line profiles. Thus, the $C^{18}O$ spectra from these sources help to constrain the range of appropriate parameters.

Looney's derived models are spherically symmetric. They describe the envelopes in terms of power law distributions of temperature and density. The radial distribution of the temperature is assumed to obey a power law with an index of -0.4

(Wilner, Welch, & Forster 1995):

$$T = T_0 \left(\frac{R}{1AU} \right)^{-0.4}, \tag{3.1}$$

and the distribution of the density in the envelope is determined by a power law:

$$\rho = \rho(R_{in}) \left(\frac{R}{R_{in}} \right)^{-p}. \tag{3.2}$$

with an index (p) that varies from model to model. The models are described by five parameters: the index of the density power law (p), the total mass of the envelope (M), the inner and outer radii of the envelope (R_{in}, R_{out}), and the flux of the central source (S). An additional sixth parameter, the temperature (T) at a fiducial inner radius of $1AU$, is estimated from the central source luminosity. These parameters alone permit the calculation of power law emission profiles, but the models also include variables that describe the velocity distributions and molecular fractional abundances (*e.g.*, X($C^{18}O$)) in the envelope. The additional velocity variables are the infall velocity ($V_{\rm infall}$), which is assumed to obey:

$$V_{\rm infall} = V_{\rm infall}(R_{in}) \left(\frac{R}{1AU} \right)^{-0.5}, \tag{3.3}$$

and the sum of the thermal and turbulent velocities (V_{t+T}).

To create synthetic spectra, a gridded model is generated from the set of initial parameters and their power law distributions. The grid is set up in logarithmic increments of the envelope radius, and a Λ-iteration scheme is used to derive a solution to non-LTE multi-level radiative transfer equations (Dickel & Auer 1994). Line strengths are then calculated from level populations and the calculated emission is converted into a MIRIAD image. The size of the emitting cloud and its distance are also specified.

Seven models of each of the three Class 0 objects L1448N(B), IRAS2A, and IRAS4A (21 models total) were selected from the full set that satisfactorily reproduced the continuum emission. The parameters identifying these models are listed

in Table 3.1. The selected models are not "better" than others generated by Looney (1998); instead, they were chosen to represent a range of the applicable model parameters. For the L1448N(B) models, $T_0 = 380K$. For IRAS2A, $T_0 = 555K$, and for IRAS4A, $T_0 = 457K$. The exponents of the density profiles specify the H_2 and $C^{18}O$ number densities. Fiducial values for the central densities are calculated using the envelope masses and density distributions:

$$M = \int_R \rho_0 \left(\frac{R}{1AU} \right)^{-p} 4\pi R^2 dR. \tag{3.4}$$

Initial values for the $C^{18}O$ abundances are set by assuming an interstellar abundance ratio of $X(C^{18}O) = 2 \times 10^{-7}$. The initial value of V_{t+T} is calculated by assuming thermal equilibrium of $C^{18}O$ at the temperature of R_{out}, a temperature appropriate for much of the volume of the envelope.

The observed spectra (*i.e.* the spectra which the models are intended to match) are centered on the positions of the continuum emission peaks, as given in Table 4.3 of Looney (1998). The spectra are taken over the area of a beam at the resolution of the map, *i.e.* a $10''$ area for the $10''$ resolution map, *etc.*. Moreover, the spectra are extracted from the datacubes created from *only* the BIMA observations, as only the BIMA observations were used to create the envelope models. The peak fluxes and widths of the $C^{18}O$ emission lines are quantified by fitting Gaussian functions to the lines. These properties are listed in Table 3.2.

The best model spectral lines are found in an iterative fashion. The radiative transfer code (Dickel & Auer 1994) is run with an initial set of model-specific parameters to produce a datacube of the same size as the BIMA datacube. A spectrum is taken through the datacube over the area of a single beam ($10''$, $5''$, or $3''$), and a single Gaussian function is fitted to the emission profile. The peak and FWHM of the fitted Gaussian function are compared with the Gaussian function fitted to the observed spectrum to assess the quality of the model, then the input parameters

Table 3.1. Selected Protostellar Envelope Models

Source	Model Number	exponent	R_{in} (AU)	R_{out} (AU)	M_{env} ($M_\odot$)
L1448N(B)	1	2.1	40	2000	1.01
	2	2.1	40	3000	1.01
	3	2.3	40	2000	1.17
	4	2.3	40	4000	1.17
	5	2.3	40	10000	1.17
	6	2.5	40	5000	1.77
	7	2.5	40	10000	1.77
IRAS2A	1	0.5	40	2000	0.40
	2	1.5	40	3000	0.47
	3	1.5	40	4000	0.47
	4	1.9	40	6000	0.63
	5	1.9	40	7000	0.63
	6	2.3	40	5000	0.65
	7	2.3	40	6000	0.65
IRAS4A	1	1.9	40	1000	2.07
	2	2.1	40	2000	3.02
	3	2.1	40	3000	3.02
	4	2.3	40	3000	3.34
	5	2.3	40	4000	3.34
	6	2.5	40	2000	3.69
	7	2.5	40	3000	3.69

are adjusted, and the code is run again. For each of the models, the following four cases are examined:

No Infall Case. Free parameters: V_{t+T}, X($C^{18}O$). This case assumes that the envelope is not undergoing infall; consequently, $V_{\rm infall}$= 0. The line width is strictly a function of V_{t+T}, which is assumed to be constant throughout the envelope. The H_2 density is set to the model-specified value, and X($C^{18}O$) is varied to match the flux of the observed lines.

Infall Case. Free parameters: $V_{\rm infall}$, X($C^{18}O$). This case assumes the envelope to be uniformly thermalized ($V_{t+T}(1D)=\sqrt{kT/m}$). V_{t+T} is set to the value corresponding to thermal equilibrium of $C^{18}O$ at a temperature of R_{out}. This value is the *minimum* contribution to the line width that can be made by

$C^{18}O$ at a reasonable envelope temperature with no turbulent velocity. Thus, variation in the width of the line is strictly a function of $V_{\rm infall}$. The H_2 density is set to the model-specified value, and $X(C^{18}O)$ is adjusted to match the flux of the observed lines.

Shell Case. Free parameters: V_{t+T}, R_{in}. This case simulates the depletion of $C^{18}O$ onto dust grains within the inner portion of the envelope. There is no infall motion ($V_{\rm infall}= 0$), and V_{t+T} is adjusted to match the FWHM of the observed line. The flux of the line is adjusted by moving the inner radius (R_{in}) of the envelope, but fixing $X(C^{18}O)$. The envelope retains the density distribution required by the model; the amount of emitting $C^{18}O$ is adjusted by setting $X(C^{18}O)= 0$ inside R_{in} and $X(C^{18}O)= 2.0 \times 10^{-7}$ outside R_{in}.

Core Case. Free parameters: V_{t+T}, R_{out}. This case simulates the depletion of $C^{18}O$ outside of a central "core" region, where the density is great enough for $C^{18}O$ molecules to be sputtered off of dust grains by collisions. As in the Shell case, $V_{\rm infall}= 0$, V_{t+T} determines the FWHM, and $X(C^{18}O)= 2.0 \times 10^{-7}$. In the Core Case, however, $R_{in}= 1AU$, and R_{out} is adjusted to match the flux of the line.

The complete results of fitting the observed BIMA spectra are given in the Appendix.

Accepting the limitations of the four cases, the No Infall cases reproduce the line shapes and the morphologies of the envelopes with greater fidelity than any of the other three. However, for no object (L1448N(B), IRAS2A, or IRAS4A) can one set of values for the free parameters V_{t+T} and $X(C^{18}O)$ provide the best solution at all three resolutions.

Of the three Class 0 YSOs modeled, L1448N(B) presents the widest line profiles. At the $10''$, $5''$, and $3''$ resolutions, the mean values for V_{t+T} of the No Infall models are 1.4, 1.6, and 2.0 km s^{-1}, respectively. If these values represent solely

Table 3.2. Spectra Used for Model Fitting

Source	Position (J2000)	Beam Size (arcsec)	Fitted Peak (Jy/beam)	Fitted FWHM (km/s)
L1448N(B)	$3^h25^m36^s.339$, $+30°45'14''.94$	10	1.87	1.45
		5	0.80	1.68
		3	0.45	2.10
IRAS2A	$3^h28^m55^s.571$, $+31°14'37''.22$	10	2.53	0.88
		5	1.26	0.92
		3	0.60	1.00
IRAS4A	$3^h29^m10^s.510$, $+31°13'31''.01$	10	2.85	0.67
		5	1.61	0.75
		3	0.87	0.92

thermal velocities within the L1448N(B) envelope, they correspond to temperatures of 1280, 1672, and 2612 K, respectively: impossibly high values, given the central temperature of the envelope ($T_0 = 380K$). At all three resolutions, the values for X($C^{18}O$) are significantly reduced from the typical interstellar value. In the $10''$ spectrum, the mean X($C^{18}O$) is 4.5×10^{-8}; in the $5''$ spectrum, the mean X($C^{18}O$) is 3.7×10^{-8}, and in the $3''$ spectrum, the mean X($C^{18}O$) is 5.7×10^{-8}. These mean values are particularly increased by the results from models 1 and 5; the median values for X($C^{18}O$) are: 4.2×10^{-8}, 3.6×10^{-8}, and 4.4×10^{-8}, respectively.

A graphical summary of the No Infall models of L1448N(B) is presented in Figure 3.1. The three panels display, from top to bottom, the flux profiles from the $10''$, $5''$, and $3''$ resolution maps of L1448N(B), respectively. These profiles are displayed as brightness temperatures (T_B) that have been azimuthally-averaged in half-beamwidth intervals from the continuum position ($R = 0$). The gray area in each panel shows the range of flux profiles from the seven envelope models. Because the model spectra were adjusted to match spectra taken from the area of a single beamwidth centered on the position of the continuum source, it is natural for the observed and model flux profiles to intersect near the half-beamwidth radius. The

point at $R = 0$ shows the flux from the central pixel. The models systematically overestimate the flux at this point because continuum position of L1448N(B) is offset from the position of peak $C^{18}O$ emission, which appears 3-4″ in the direction of L1448N(A). At larger radii from the continuum position, the profiles from the models systematically underestimate the flux in the 5″ and 3″ maps. The lack of sufficient flux at larger radii suggests that the power laws determining the density distribution of the L1448N(B) envelope are too steep.

In the IRAS2A No Infall models, the mean values for V_{t+T} are 0.84, 0.87, and 0.96 km s^{-1} for the 10″, 5″, and 3″ spectra, respectively. If these values represent solely thermal velocities, then the corresponding temperatures are 461, 494, and 602 K, respectively. For the IRAS2A envelope, $T_0 = 555K$, so a $V_{thermal}$ of 602 K is impossible, and the other values, appropriate for radii within 2AU, are ridiculous. As in the L1448N(B) models, the IRAS2A models also require X($C^{18}O$) abundances below the normal interstellar value, but the reductions are less than a factor of two. To match the spectra at all three resolutions, the mean and median values for X($C^{18}O$) are in the narrow range $1.3 - 1.4 \times 10^{-7}$.

The graphical summary of the No Infall models of IRAS2A is shown in Figure 3.2. As in the Figure for L1448N(B), the three panels show azimuthally-averaged brightness temperatures of IRAS2A at 10″, 5″, and 3″ resolutions. The range of flux profiles from the seven envelope models of IRAS2A is indicated by the gray shaded area in each panel. The observed profiles at each resolution are generally well-matched by the upper boundary of the gray area, but this boundary does not represent a single best-fitting model. In the 10″ profiles, model 1 matches within the central beam, model 5 gives the best match across three beamwidths, and both models 4 and 5 match the outer radii. In the 5″ profiles, there is no good match to the central beam. Nevertheless, models 3 and 5 match well across three beamwidths,

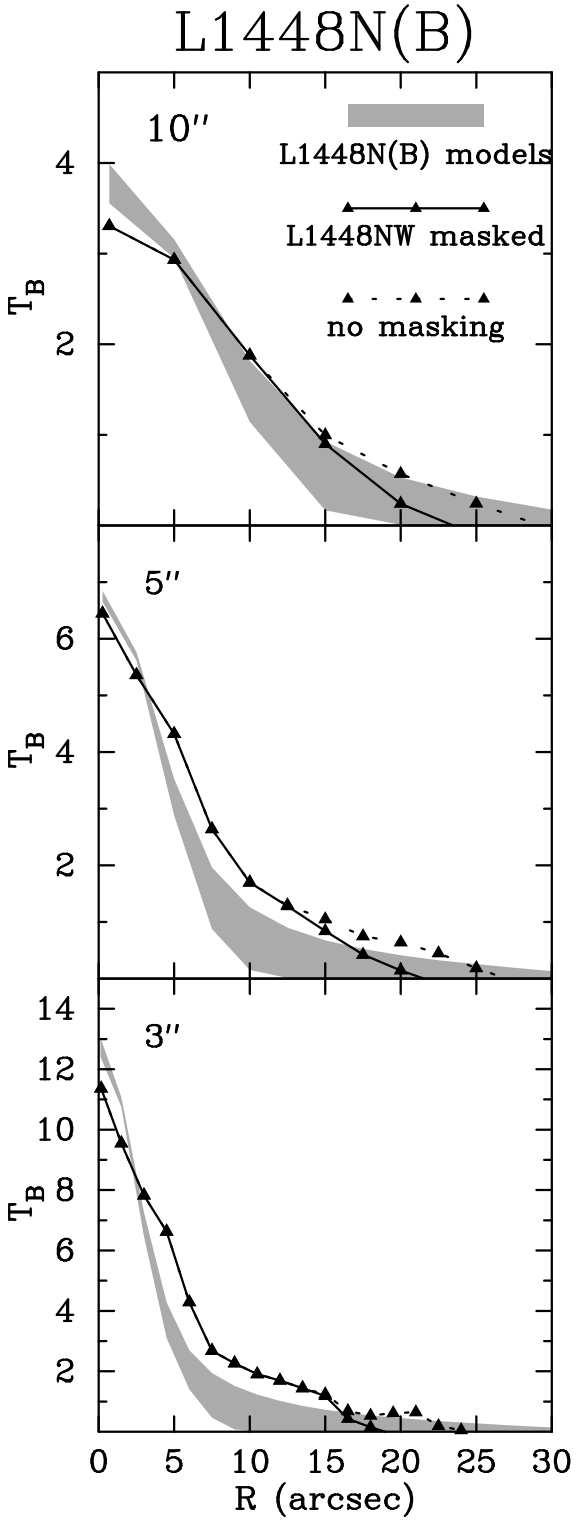

Figure 3.1: Azimuthally averaged flux profiles of L1448N(B) from the 10″ (top), 5″ (middle), and 3″ (bottom) resolution maps. The dotted line shows the flux taken directly from the BIMA map; the solid line shows the the flux after the contribution from L1448NW is masked out. The gray area shows the range of flux profiles from the seven envelope models.

and models 4 and 5 match at the outer radii. In the 3″ profiles, models 5, 6, and 7 all match fairly well in the central beam. Model 1 shows a near-perfect fit in the central three beams; models 3 and 4 also show adequate fits in this region. In the outer regions, models 4 and 5 fit the observed profile well. Examining the various models in aggregate leads to the conclusion that a best fitting model must be more centrally concentrated, a condition which might be either stipulated directly (as in models 5, 6, and 7, with $p = 1.9\,, 2.3$) or approximated with a shallow density dropoff within ~1000 AU (as in model 1, with $p = 0.5$). The model with the worst fit at all resolutions and all radii is model 2. The best fitting model across all resolutions and radii is model 5; this is also the model with the largest envelope (R_{out}= 7000 AU).

The IRAS4A spectra show the narrowest line profiles. For these lines, the No Infall models have mean V_{t+T} values of 0.59, 0.67, and 0.83 km s^{-1} for the 10″, 5″, and 3″ spectra, respectively. The temperatures corresponding to solely thermal velocities with these values are 227, 293, and 450 K, respectively; these values all occur within 6AU of the center in the IRAS4A models, which has $T_0 = 457K$. As with the results from the L1448N(B) and IRAS2A models, the derived values for V_{t+T} clearly cannot represent purely thermal velocities of $C^{18}O$. Regarding the $C^{18}O$ abundances: to reproduce the observed IRAS4A spectra from the models requires $X(C^{18}O)$ to be reduced by at least an order of magnitude. Including the spectra from all three resolutions, the range of mean values for $X(C^{18}O)$ is $1.4 - 2.0 \times 10^{-8}$. Looking at the median values instead reduces the influence of the 10″ spectrum from Model 1 and narrows the range of $X(C^{18}O)$ to $1.4 - 1.6 \times 10^{-8}$. Both the mean and median values are significantly smaller than the normal interstellar value.

A graphical summation of the various No Infall models of IRAS4A is shown in Figure 3.3. IRAS4A is the most compact YSO of the three that were modeled

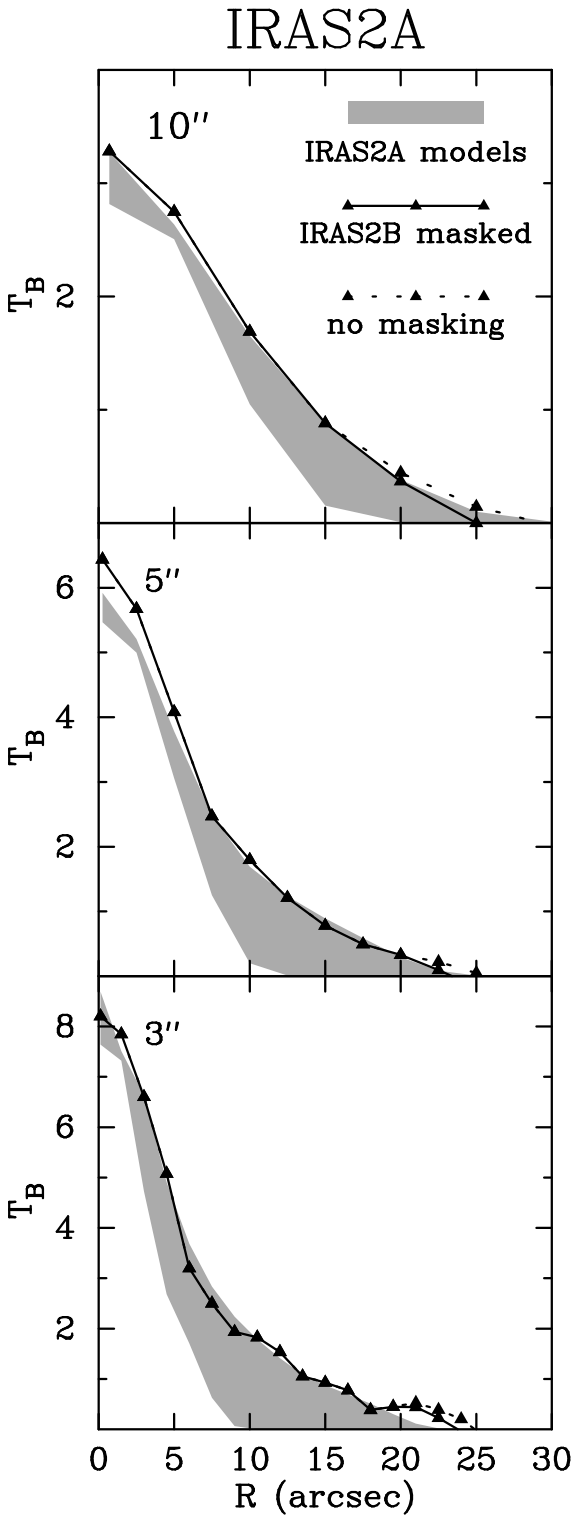

Figure 3.2: Azimuthally averaged flux profiles of IRAS2A from the 10″ (top), 5″ (middle), and 3″ (bottom) resolution maps. The difference between the flux profiles of IRAS2A with the contribution from IRAS2B included (dotted line) and with IRAS2B masked out (solid line) is negligible for evaluating the quality of the models.

for this study. All of the flux that is relevant for evaluating the models (the gray area indicates the range of model flux profiles) is contained within approximately $20''$. Within the central beam, the flux profile is best matched by model 3 at all three resolutions, although model 2 overlaps it in the $3''$ profiles. In the $10''$ maps specifically, even though all models fit the flux profile well, the match with model 3 is nearly exact at all radii. Model 3 is equally exact in matching the $5''$ profile at all radii. The match with model 4 is as good as model 3, except at the smallest radii, and models 5 and 7 also match well across three beamwidths. In the $3''$ maps, all models underestimate the flux at the outer radii; model 5 (which features the largest outer radius) comes closest. At small and intermediate radii, models 2, 3, and 5 fit the observed flux profiles equally well. The results of modeling the IRAS4A envelope clearly illustrate the degeneracy between the exponent and the outer radius of the power law descriptions of the density distribution. The observed profiles are matched best by either a shallower distribution and smaller outer radius ($p = 2.1$, R_{out}= 2000 – 3000 AU, models 2 & 3) or a slightly steeper distribution and a larger outer radius ($p = 2.3$, R_{out}= 4000 AU, model 5).

Trends that manifest in the models of all three YSOs preclude giving the Infall, Shell, and Core cases the same rigorous treatment as the No Infall cases.

In the Infall models, the free parameters are the infall velocity ($V_{\rm infall}$) at R_{in} and the fractional abundance of $C^{18}O$. The V_{t+T} is set at the thermal velocity of $C^{18}O$ at the temperature at R_{out}, a temperature that applies to much of the volume of the envelope. In all Infall models, the value for V_{t+T} is far narrower than the width of the observed line profiles, and so the difference must be accounted for by adjusting $V_{\rm infall}$. The problem is that increasing $V_{\rm infall}$ affects not only the width of the line but also its shape. For the line to be wide enough to match the observed line profile, the infall velocities of the material on the near and far sides of the protostar create

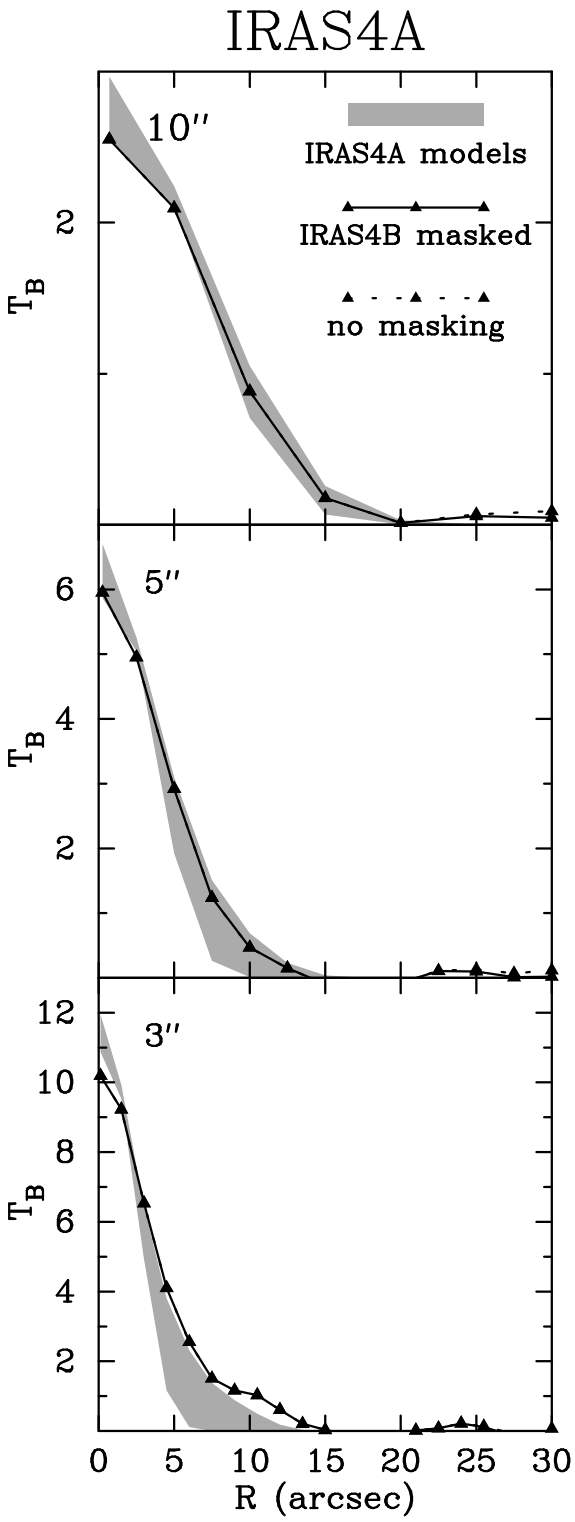

Figure 3.3: Azimuthally averaged flux profiles of IRAS4A from the 10″ (top), 5″ (middle), and 3″ (bottom) resolution maps. Differences between its azimuthally-averaged flux profile with IRAS4B included (dotted line) and excluded (solid line) are barely perceptable.

a line profile that is noticeably double-peaked. The observed spectra never show double-peaked profiles.

In the Shell models, the fractional abundance of $C^{18}O$ in the envelope is set at the normal interstellar value, and the peak of the line profile is set by adjusting the volume of the emitting region in the envelope. With these cases, it is the morphologies of the model envelopes that make them unsuitable. Many of the model sources appear like planetary nebulae in the channel maps, *i.e.* the emission appears stronger from a projected outer ring than along the line of sight toward the center of the source. This morphology is clearly not seen in the BIMA maps. Because the normal interstellar abundance of $C^{18}O$ provides too much flux to the line, the $C^{18}O$ must be absent in the center of the beam to account for the observed line flux. To place just enough flux in the line, the inner radius of the envelope must be brought in just enough to place the right amount of flux at the edges of the beam area.

The unsuitability of the Core models is, like the Shell models, betrayed by the incongruity of the model and observed morphologies. For most of these cases, the central regions of the models are substantially more compact than the beam areas, so the beam is only partially filled by emission from the source. The Core models cannot matched the extended stucture of the envelopes.

Based upon the characteristics of the synthetic spectra generated from the L1448N(B), IRAS2A, and IRAS4A envelope models, some general conclusions are apparent. For each of the three YSOs, if the $C^{18}O$ abundance in the envelopes specified by the models is set to the normal interstellar value ($X(C^{18}O) = 2.0 \times 10^{-7}$), then the resultant fluxes consistently exceed the peaks of the observed spectra. For L1448N(B), $X(C^{18}O)$ of both the No Infall and Infall models must be reduced to roughly 4.4×10^{-8}, almost a factor of 5 below the interstellar value. For IRAS2A,

the $C^{18}O$ abundance is reduced by only a small amount ($X(C^{18}O) = 1.3 \times 10^{-7}$), but IRAS4A, like L1448N(B), also requires a sharply reduced $C^{18}O$ abundance. For the IRAS4A models, the approximate value of $X(C^{18}O)$ is 1.6×10^{-8}, only 8% of the interstellar value.

In general, the No Infall models do the best job of matching both the line profiles and the morphologies of the emitting regions shown in the BIMA maps. If the true thermal velocity of the $C^{18}O$ molecules corresponds to the temperatures characteristic of the bulk of the volume of the envelopes (for these three YSOs, typically $T < 30K$), then the contribution of the turbulent velocity to the linewidths must be substantial. Assuming $T = 30K$ (as an upper limit), then $V_{therm} = 0.21$km s^{-1}. If one assumes an average value for V_{t+T} of 0.70 km s^{-1} for IRAS4A (the YSO that exhibits the narrowest lines), then:

$$V_{turb} = [(V_{t+T})^2 - (V_{therm})^2]^{0.5} = [(0.70)^2 - (0.21)^2]^{0.5} = 0.67 kms^{-1}.$$

This value for the turbulent velocity is sonic with respect to the ambient sound speed ($c(30K) = 0.77$km s^{-1}). However, if one assumes $V_{t+T} = 1.67$km s^{-1} for the envelope of L1448N(B), the YSO with the widest lines, then:

$$V_{turb} = [(V_{t+T})^2 - (V_{therm})^2]^{0.5} = [(1.67)^2 - (0.21)^2]^{0.5} = 1.66 kms^{-1}.$$

a value that clearly exceeds the ambient sound speed. Because the three YSOs are Class 0 objects that are known to harbor developing protostars at their centers, the observed line widths are likely the product of a combination of thermal, turbulent and infall velocities. The No Infall and Infall models demonstrate that the line widths cannot be created entirely from thermal velocity of the $C^{18}O$ or entirely from infalling gas. The current analysis lacks the subtlety to determine the proportions of V_{therm}, V_{turb}, and $V_{\rm infall}$.

For the Infall models, the mean value of $V_{\rm infall}$ required to match the L1448N(B)

line widths is 4.2 km s^{-1} at 40 AU. For IRAS2A, the mean value of $V_{\rm infall}$ is 2.5 km s^{-1}, and for IRAS4A, the mean value is 1.8 km s^{-1}. Although the pure Infall models are discredited based upon the line shapes, the values for $V_{\rm infall}$ can help constrain the protostellar masses embedded in these envelopes. For L1448N(B), the mean value for $V_{\rm infall}$ is representative of the free fall speed associated with a 0.40 M$\odot$ central source. For IRAS2A, if $V_{\rm infall}$ indicates a free fall speed at 40 AU, then the central source has 0.14 M$\odot$. For IRAS4A, the mass of a central source is constrained by the value of $V_{\rm infall}$ is 0.073 M$\odot$.

One severe limitation of this investigation of the envelope models is their spherical symmetry. Because the models are spherically symmetric, the radiative transfer code produces emission that is centered upon the source. However, the observed emission from the YSOs is clearly not symmetrical, although the $C^{18}O$ emission from IRAS4 appears approximately so. The asymmetry of the observed emission may originate from an inhomogeneous distribution of $C^{18}O$ within the envelope (*i.e.* "clumpy" $C^{18}O$), but a more likely explanation is that the $C^{18}O$ is affected by the energetics of (inherently asymmetrical) outflows.

Although the Shell and Core models are generally discredited in this investigation because the envelope morphologies that they produce are inconsistent with the observed morphologies of L1448N(B), IRAS2A, and IRAS4A, there are valid reasons for proposing them. The Shell and Core models were proposed to determine a range of radii in the envelope from which $C^{18}O$ may be depleted. Regions lacking $C^{18}O$ emission would indicate characteristic densities and temperatures where $C^{18}O$ molecules may freeze out onto dust grains. Both the Shell and Core models are extreme cases and reflect the limits of the gridded envelope model that can be used as input for the radiative transfer code. A model that combines aspects of the Shell and Core models is possible. In such a model, the $C^{18}O$ is depleted at

"intermediate" radii, where "intermediate" indicates a region *outside* of a central core, where temperatures are high enough to liberate $C^{18}O$ molecules from grain surfaces, and *inside* an outer shell, where the grain density is low enough to maintain a certain fraction of gas-phase $C^{18}O$. At present, the code used for this study cannot generate independent power law profiles fixed at different radii. However, models that bracket a molecular depletion zone with an inner thermal evaporation zone and an outer undepleted zone have been used successfully by other authors to explain core emission profiles for several molecular species (Schöier *et al.* 2004; Jørgensen, Schöier, & van Dishoeck 2002, 2004).

The most relevant point for the broad goal of this thesis is that the models best reproduce the $C^{18}O$ spectra when the emission arises throughout the core, with reduced abundances, from kinematics that are not dominated by infall.

Chapter 4

The BIMA Survey of Dense Cores in the Perseus Cloud

4.1 Overview

In the summer of 2000, a proposal to undertake a Key Project to observe a number of dense cores in the Perseus molecular cloud was submitted to the BIMA Board. The proposal was timed to meet two primary objectives. First, the new Key Project would augment the sample of dense cores that had already been mapped with the BIMA array for the survey of bright YSOs analyzed by Looney (1998) and LMW00. The new observations would allow the compilation of a database of dense core observations, with a uniform set of observing parameters, before the BIMA array would be dismantled and regenerated as part of the Combined Array for Research in Millimeter-wave Astronomy (CARMA[1]). Second, the Key Project was proposed to provide complementary data to the Cores to Disks (c2d) Legacy Science Project, which would undertake an expansive investigation of the star formation process with the Spitzer Space Telescope.

[1] `http://www.mmarray.org/`

The goal of the c2d Project, formally titled "From Molecular Cores to Planet-forming Disks" (Evans *et al.* 2003), is to examine the stages of early stellar evolution by surveying several nearby molecular clouds and compiling a census of the stellar and sub-stellar content. The c2d Project will assemble large-scale, high-resolution maps of five molecular clouds, including Perseus, at wavelengths of 3.6, 4.5, 5.8, 8.0, 24, and 70 μm. Although the remarkable sensitivity of the Spitzer instruments will enable infrared sources with masses as low as 10 M_{Jup} to be detected, much of the colder gas and dust in the vicinity of these sources will remain invisible. Understanding the influence of the cold, dense ISM on the Spitzer sources requires complementary observations at millimeter and submillimeter wavelengths.

4.2 The Survey Sample

Eighteen dense cores were selected for the new BIMA observations, bringing the total number of objects (including L1448 IRS3, NGC1333 IRAS2, and NGC1333 IRAS4) in the survey to twenty-one (see Table 4.1). All of the cores are located within the boundaries of the Perseus molecular cloud shown in the ^{13}CO $J = 1 \rightarrow 0$ emission map of Padoan *et al.* (1999). Many of the cores are associated with IRAS point sources. Some are well-known sites of star formation (*e.g.* L1448, L1455, Barnard 5); others are only known from the single-dish surveys by which they were discovered (*e.g.* Per6, Per7W, Per7E, Per9W). However, all of the cores are detected in emission from the NH_3 (1,1) transition at 1.3 cm and are identified in the database of NH_3 cores collected by Jijina, Myers, & Adams (1999). Unlike the previous BIMA survey of YSOs, the targets were not selected because of their brightness at millimeter wavelengths. Instead, the sample includes a range of core masses, luminosities, and apparent sizes.

Table 4.1. Perseus Cores Survey Source List

Source	Pointing Center α (J2000)	δ (J2000)	IRAS PSC	V_{LSR} (km s^{-1})	M (M$\odot$)	L$_{bol}$ (L$\odot$)	Ref.
L1448 IRS2	$3^h25^m22^s.42$	$+30°45'12''.2$	03222+3034	4.2	0.86	5.2	1
L1448 IRS3	$3^h25^m36^s.45$	$+30°45'20''.3$	03225+3034	5.0	(0.61,0.12)	(10,2.7)	2,3
L1448 C	$3^h25^m38^s.82$	$+30°44'05''.3$		4.7	1.5	6.0	4,5
L1455 A1	$3^h27^m42^s.19$	$+30°12'43''.2$	03245+3002	4.9	3.5	9.7	6,7
L1455 A2	$3^h27^m49^s.88$	$+30°11'42''.8$	03247+3001	4.9	2.0	4	6,8
L1455 B	$3^h28^m00^s.64$	$+30°08'02''.2$	03249+2957	4.8	0.7	0.4	6,8
L1455 C	$3^h28^m05^s.20$	$+30°05'41''.9$		4.9	2.0	...	6
NGC1333 IRAS2	$3^h28^m56^s.51$	$+31°14'24''.9$	03258+3104	7.7	(0.44,0.14)	6.3*	3,9
NGC1333 IRAS8	$3^h29^m09^s.01$	$+31°21'48''.2$	03260+3111	7.5	...	< 161	10
NGC1333 IRAS4	$3^h29^m11^s.51$	$+31°13'19''.2$	03259+3105	7.7	2.88,0.96,0.26	21	3,10
Per4 S	$3^h29^m17^s.93$	$+31°27'30''.8$		7.5	12	< 70	11,12
NGC1333 SK32	$3^h29^m18^s.66$	$+31°23'13''.2$		7.5	6.4	< 42	13,10
Per4 N	$3^h29^m22^s.76$	$+31°33'30''.5$	03262+3123	7.5	6	< 2	11,14
Per5	$3^h29^m51^s.63$	$+31°39'03''.9$	03267+3128	8.1	6	< 1.7	11,14
Per6	$3^h30^m14^s.88$	$+30°22'48''.5$	03271+3103†	5.8	5	2.7	11,12
IRAS 03282+3035	$3^h31^m21^s.00$	$+30°45'30''.7$	03282+3035	7.1	0.8	1.6	15
Per7 W	$3^h32^m28^s.90$	$+30°59'56''.8$	03295+3050‡	6.7	1	< 1.3	11,14
Per7 E	$3^h32^m45^s.24$	$+30°59'55''.8$	03295+3050‡	6.7	2	...	11
Per9 W	$3^h33^m17^s.14$	$+31°20'18''.0$	03303+3108‡	6.9	5	< 6.5	11,14
Barnard1 b	$3^h33^m21^s.34$	$+31°07'35''.2$	03301+3057	6.4	1.6-1.8¶	2.6-3.1¶	16
Barnard5 IRS1	$3^h47^m41^s.64$	$+32°51'42''.7$	03445+3242	10.1	2.5	9.4	17,18

References. — 1. O'Linger *et al.* (1999), 2. Barsony *et al.* (1998), 3. Looney, Mundy, & Welch (2000), 4. Curiel *et al.* (1999), 5. Shirley *et al.* (2000), 6. Juan *et al.* (1993), 7. Clark (1991), 8. Bachiller & Cernicharo (1986b), 9. Jørgensen, Schöier, & van Dishoeck (2002), 10. Jennings *et al.* (1987), 11. Ladd, Myers, & Goodman (1994), 12. Ladd, Lada, & Myers (1993), 13. Sun *et al.* (2000), 14. Jijina, Myers, & Adams (1999), 15. Barsony *et al.* (1998), 16. Hirano *et al.* (1999), 17. Pendleton *et al.* (1990), 18. Myers *et al.* (1987)

*Luminosity adjusted for distance used in this text.

†IRAS source at edge of BIMA primary beam.

‡IRAS source outside of BIMA map.

¶Mass and luminosity ranges apply to both sources.

4.3 Observations

All 18 cores selected for the Key Project were observed with the BIMA array between the Fall 2000 and the Fall 2002 observing seasons. The cores were observed in the continuum at $\lambda = 2.7$ mm and in the emission from the ^{13}CO and C^{18}O $J = 1 \rightarrow 0$ lines. Although both molecular lines were observed simultaneously, only the results from the continuum and C^{18}O lines ($\nu = 109.782$ GHz) are presented here.

4.3.1 BIMA Observations

The observations of the Perseus cores were made with the B, C, and D configurations of the ten element BIMA array. These configurations sample the brightness distribution on the sky with spatial resolutions of approximately $2''$, $6''$, and $14''$, respectively. The pointing centers for the observations (Table 4.1) were set to the positions of peak NH_3 intensity, as identified by the references listed in the Jijina, Myers, & Adams (1999) database. Thus, the pointing centers do not necessarily coincide with the positions of the associated IRAS sources or the map centers of earlier single-dish observations.

A small number of the first C-array observations made in Fall 2000 used 3C111 as the phase calibrator to remain consistent with the observations made for the earlier (1996-1997) survey. However, the flux from the secondary calibrator, 0336+323, was sufficient for it to be used as the sole calibrator and thus spare the slewing time. During the Fall 2000 and Spring 2001 seasons, the flux of 0336+323 (at $\nu \approx 110$ GHz) hovered around 0.9 Jy. During the summer of 2001, its flux increased, quickly but steadily, to approximately 1.5 Jy. From then until the last Key Project observations were made, the flux gradually increased to approximately 1.8 Jy. The coherent integration times on the target objects ranged from 11.5 s to 30 s, and observations of the calibrator were inserted either every 12 m (for the B-array) or every 24 m (for the C- and D-array). A variety of flux calibrators were used for the observations, including 3C84, W3OH, and the planets Mars, Uranus, and (rarely) Venus.

The correlator spectrometer was used in Mode 6, which creates two narrow frequency windows and four wide frequency windows in both the lower and upper side bands. The narrow windows subdivide a 25 MHz bandwidth over 256 channels, for a velocity resolution of 0.27 km s^{-1}. The ^{13}CO and $C^{18}O$ lines were set in the

narrow windows in the upper side band. The continuum emission was observed in the wide windows in both the lower and upper side bands; each window samples 100 MHz of bandwidth with 32 channels. Thus, the total continuum bandwidth was 450 MHz in each of the lower and upper sidebands.

4.3.2 FCRAO Observations

The shortest possible baseline that can be achieved with the BIMA array is slightly greater than the diameter of a single antenna (~6.1 m). Because the interferometer operates as a spatial filter of the incoming radiation, the minimum baseline places a limit on the large-scale structure that the array can detect. However, large-scale turbulence in the Perseus cloud may affect the velocity fields of the cores, so attaining single-dish observations was crucial. A proposal to observe the cores at FCRAO was submitted and accepted for the Spring 2001 observing season. The observations at FCRAO were made with the SEQUOIA 16-element receiver in its "footprint" mode, which was described in § 2.2.2. During the week that the observations were made, the weather conditions gradually improved: initial observations had system temperatures as high as T_{sys}=330 K, but later observations had system temperatures around T_{sys}=170 K. All of the cores were observed at least twice; most were observed three times. Pointing checks were made before and after each field was observed; the pointing targets were the IK Tau and Orion SiO masers for the first and second half (respectively) of each night's observing. Background subtraction was done by frequency switching with a throw of 5 MHz. The $C^{18}O$ line was observed within a 20 MHz bandwidth window with individual channels of 20 kHz. During the reduction process, the channels were smoothed to 100 kHz, equivalent to a velocity resolution of approximately 0.25 km s^{-1}.

4.4 Data Reduction and Mapping

Since the procedures for reducing and mapping the data are described in detail in Chapter 2, only some of the more important elements will be mentioned here.

The reduction and mapping of the BIMA datasets were performed with the MIRIAD software package. Following data flagging and calibration, the u,v-visibilities from all of the observations of a core were combined and Fourier transformed simultaneously. In the transform process, the visibilities were weighted (by adjusting the cell size, the "robust" parameter, and a 2D Gaussian tapering function) to create maps that emphasized structures at three specific resolutions: $10''$, $5''$, and $3''$.

The data from the FCRAO observations were reduced and mapped with the CLASS software package. The beam efficiency of the observations was estimated to be $\eta_B = 0.50$ (at 110 GHz), resulting in a temperature-to-flux conversion factor of 35.90 Jy/K.

The BIMA and FCRAO datacubes were combined with the `VTESS` maximum entropy algorithm within the AIPS software package. To find the best `VTESS` solution when combining the data:

- The number of iterations of the algorithm was fixed at 50.
- The FCRAO map was boxcar-smoothed at its edges to diminish gradually to zero flux.
- The initial value for the flux of the combined map was the flux in the FCRAO map.
- The initial estimates for the residuals of the combined map were the rms noise levels of the individual input maps. The best combined maps always yielded residuals below these levels.

Two quality checks were performed on the final solution. First, the VTESS map was convolved to the resolution of the FCRAO map, then was subtracted to examine a residual map. Second, the VTESS map was weighted by the BIMA primary beam, re-observed with the BIMA u,v-spacings, and inverted; the result was then subtracted from the original BIMA map to create a residual map. The VTESS solutions were adjusted on a plane-by-plane basis until the residual maps of each plane in the datacube were as low as possible and uniformly distributed throughout the map. The final maps presented in the rest of this chapter are the best VTESS-combined maps *with the residuals added.* Only the $10''$ and $5''$ maps were combined with the FCRAO data; the $3''$ maps show the BIMA data alone.

A list of the number of $\lambda = 2.7$ mm continuum sources detected in each core and the peak and integrated fluxes at each resolution is given in Table 4.2.

4.5 L1448 IRS2

4.5.1 Background[2]

L1448 IRS2 (IRAS 03222+3034) lies about $3'$ west of the NH_3 emission peak of the L1448 core (Anglada *et al.* 1989) and was only detected by IRAS in the 25 μm and 60 μm bands (Bachiller & Cernicharo 1986b). HIRES-processed IRAS images, combined with observations at submillimeter, millimeter (O'Linger *et al.* 1999), and centimeter wavelengths (Anglada & Rodríguez 2002) show that its SED peaks at far

[2]Because of the large number of cores in the BIMA survey, the background material on each object is restricted to only a few paragraphs. For the less-well-known cores, this restriction still allows an adequate introduction. For several of the cores, however, this restriction will not do justice to the wealth of observations that have been made at other wavelengths or with other millimeter observatories.

Table 4.2. Perseus Cores $\lambda = 2.7$ mm Fluxes

Core	Continuum Source	Beam (arcsec)	Peak Flux (mJy beam^{-1})	Integrated Flux (mJy)	Box Size (arcsec)
L1448 IRS2		10	35.1±1.0	54.4±8.1	30.8 × 30.8
		5	24.6±0.7	61.6±4.3	25.0 × 22.0
		3	17.5±0.8	50.9±3.2	15.0 × 13.0
L1448 C		10	46.2±0.8	71.3±10.1	30.8 × 36.4
		5	33.8±0.6	72.5±5.7	22.0 × 28.0
		3	28.3±0.9	77.6±3.7	17.0 × 20.5
L1455 A1	IRS1	10	9.1±0.7	14.6±2.2	22.4 × 22.4
	IRS1	5	6.6±0.6	14.9±1.3	15.0 × 18.0
	IRS1	3	5.7±0.7	8.8±1.3	7.0 × 8.0
	IRS1E	10	5.8±0.7	9.6±1.4	22.4 × 16.8
	IRS1E	5	4.3±0.6	14.2±0.8	20.0 × 16.0
	IRS1E	3	2.7±0.7	5.5±2.7	5.5 × 8.0
L1455 A2	IRS2	10	3.5±1.0	12.1±1.3	42.0 × 30.8
L1455 B	IRS3	10	2.4±0.7	2.8±0.5	14.0 × 11.2
	IRS3E	10	3.6±0.7	4.1±1.0	14.0 × 14.0
	IRS3E	5	2.7±0.6	5.4±0.8	10.0 × 11.0
L1455 C			...	...	...
NGC1333 IRAS8	SK 29	10	21.1±1.1	33.3±4.5	33.6 × 28.0
	SK 29	5	21.0±0.8	25.5±4.3	13.0 × 16.0
	SK 29	3	20.5±1.1	21.2±5.3	5.5 × 6.5
	SK 28	10	6.3±1.1	23.8±2.3	39.2 × 28.0
	SK 28	5	4.1±0.8	29.9±1.1	37.0 × 24.0
Per4 S		10	9.5±0.8	28.9±2.3	28.0 × 50.4
		5	4.7±0.6	27.6±1.2	22.0 × 31.0
NGC1333 SK 32		10	10.2±1.1	25.2±2.4	44.8 × 42.0
		5	6.3±0.8	11.6±1.5	10.0 × 15.0
		3	5.2±1.0	9.1±1.5	8.0 × 6.5
Per4 N		10	5.5±0.7	14.7±1.4	30.8 × 28.0
		5	3.8±0.6	6.4±1.0	9.0 × 13.0
		3	3.9±0.9	6.6±0.9	5.0 × 7.5
Per5		10	9.7±0.8	18.0±2.4	30.8 × 25.2
		5	5.3±0.7	19.0±1.3	21.0 × 20.0
		3	4.3±0.9	9.3±1.1	9.0 × 6.0
Per6		10	2.9±0.7	6.5±0.7	19.6 × 28.0
		5	2.2±0.6	7.0±0.6	11.0 × 23.0
IRAS 03282+3035		10	54.6±0.9	65.6±12.2	30.8 × 28.0
		5	48.3±1.0	63.4±8.9	20.0 × 18.0
		3	44.9±1.5	57.3±10.0	8.5 × 7.5
Per7 W		10	3.2±0.7	3.9±0.9	16.8 × 19.6
		5	2.7±0.7	6.8±0.8	14.0 × 23.0
Per7 E			...	...	...
Per9 W			...	...	...
Barnard1 b	N	10	44.9±1.1	61.5±9.3	28.0 × 42.0
	N	5	37.6±0.8	62.2±6.8	19.0 × 22.0
	N	3	32.6±1.0	50.0±6.7	11.0 × 10.5
	S	10	52.5±1.1	67.4±12.3	28.0 × 25.2
	S	5	46.2±0.8	70.3±7.9	18.0 × 26.0
	S	3	41.2±1.0	56.1±8.4	12.0 × 8.5
Barnard5 IRS1		10	7.9±0.8	10.2±2.1	19.6 × 22.4
		5	5.5±0.6	13.1±1.3	15.0 × 15.0
		3	4.0±0.8	11.1±1.0	10.5 × 8.5

infrared wavelengths, consistent with a Class 0 YSO. Assuming a source diameter of 20″, O'Linger *et al.* (1999) derived an envelope mass of 0.86 M⊙ with a bolometric luminosity of 5.2 L⊙. Observations of Hα and [S II] optical emission lines (Bally *et al.* 1997) and 2.12 μm H_2 emission (Eislöffel 2000) revealed a series of bow-shaped knots, including HH195A-D, extending $\sim$3′ on either side of IRS2 along a northwest-southeast axis, indicating the presence of a bipolar outflow. Extended outflow activity, centered on IRS2, is detected in a wide-field (47′ × 7′) map of CO $J = 1 \rightarrow 0$ emission (Wolf-Chase, Barsony, & O'Linger 2000). The CO suggests that IRS2 may be an unresolved binary powering two outflows along different position angles.

4.5.2 Continuum Data[3]

The continuum maps of L1448 IRS2 (Figure 4.1) verify the presence of two discrete protostars. At 10″ resolution, L1448 IRS2 appears as a single source with a peak intensity of 35.1 mJy beam^{-1}. The emitting region is roughly three beamwidths across, but it is not circularly symmetric. The low-level contours fan out slightly on the northwestern edge. In the 5″ resolution map, the reason for the extra emission to the northwest of the main source is clear: a second protostar emerges in the emission map like a bud from the stem of a plant. The peak intensity at the secondary source (IRS2B) is 4.9 mJy beam^{-1}, considerably less than the peak at the primary source (IRS2A), 24.6 mJy beam^{-1}. In the 3″ resolution map, the two protostars are discrete objects. IRS2B appears unresolved at this resolution and has a peak intensity of

[3]For all of the sources in the BIMA survey, the contour maps of the continuum emission have the same format as the maps presented in the survey by LMW00. The contours are set at multiples of the rms noise, and the noise level is adjusted in each panel. Dotted lines in each panel indicate the zoom in the subsequent panel.

3.5 mJy beam^{-1}. IRS2A, in contrast, appears extended by several beamwidths in a northeast-southwest direction. This orientation is roughly perpendicular to the axes of the CO outflows (PA$\sim$138° and PA$\sim$152°) that emanate from L1448 IRS2 (Wolf-Chase, Barsony, & O'Linger 2000). The peak intensity of IRS2A is 17.5 mJy beam^{-1}.

4.5.3 $C^{18}O$ Data[4]

The FCRAO map, Figure 4.2*a*, shows the $C^{18}O$ emission from the western end of the L1448 cloud. The central part of the cloud was shown previously in Figure 2.3. Clearly, the peak in $C^{18}O$ intensity is near the center of the cloud, far away from the center of this map. The $C^{18}O$ emission from the location of the L1448 IRS2 continuum sources, indicated by the plus symbols, is unremarkable at this resolution. In the velocity map (Figure 4.2*b*), the dominant feature is the large-scale contrast between the blueshifted northwestern end of the cloud and the redshifted southeastern end. Unlike the trend seen in the neighboring L1448 IRS3 core, no overall velocity gradient is evident in the area of the BIMA primary beam. Except for the redshifted zones (4.3-4.4 km s^{-1}) along the northern and eastern edges of the primary beam area, the velocities in the center of the map (4.0-4.1 km s^{-1}) appear fairly uniform.

At 10″ resolution (Figure 4.2*c*), the L1448 IRS2 core appears as a slightly-brighter clump of $C^{18}O$ emission (3.9 Jy beam^{-1}·km s^{-1}) in a series of clumps aligned east-west across the middle of the map. The $C^{18}O$ contours centered on L1448 IRS2 are slightly elongated in the east-west direction. In the velocity map (Figure 4.2*d*), the core appears at the boundary of a redshifted zone (4.3-4.4 km s^{-1}), along the northern edge of the cloud, and the bluer velocities (3.8-3.9 km s^{-1}) associated with

[4]For all of the sources in the BIMA survey, the $C^{18}O$ intensity maps, velocity maps, and plots of representative spectra are presented in the same format as the corresponding maps in Chapter 2.

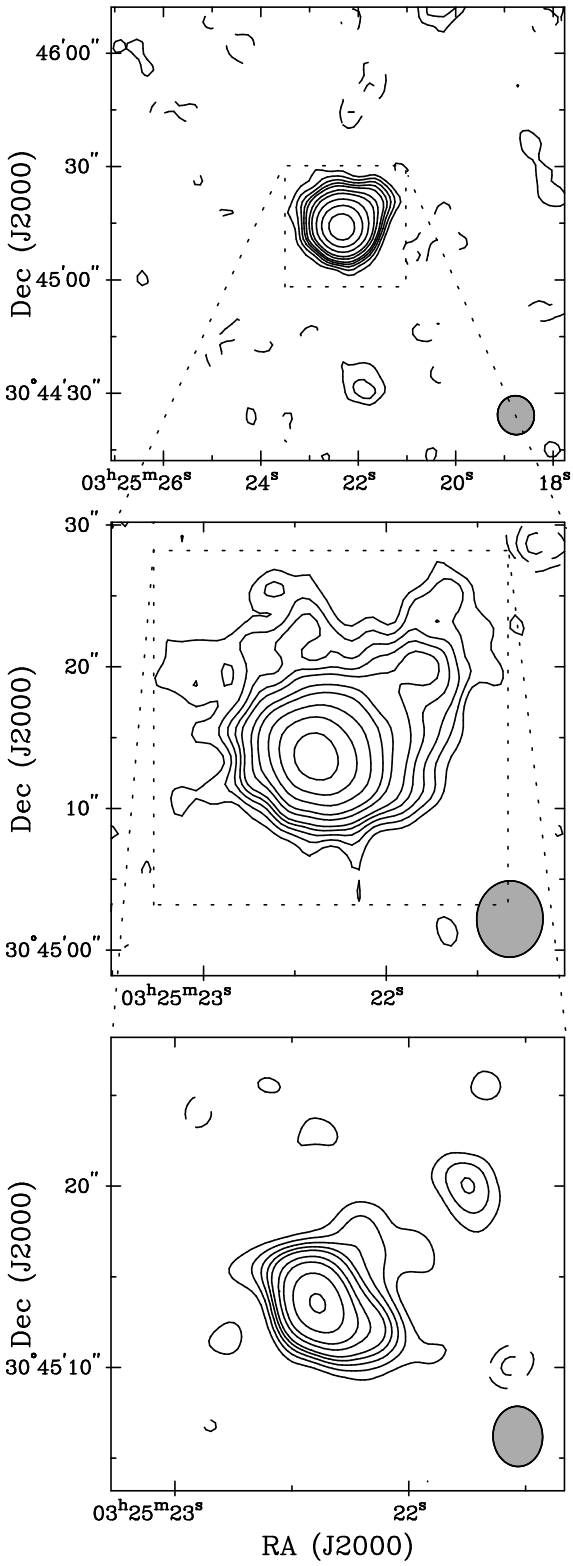

Figure 4.1: Maps of the $\lambda = 2.7$ mm continuum emission from L1448 IRS2. The contour intervals are $(-4, -3, -2, 2, 3, 4, 5, 6, 8, 10, 14.14, 20, 28.28) \times \sigma$ in mJy beam^{-1}. *Top:* $\sigma = 1.0$ mJy beam^{-1}; beam is $10.3'' \times 9.7''$, P.A.$= 11.1°$. *Middle:* $\sigma = 0.7$ mJy beam^{-1}; beam is $5.4'' \times 4.7''$, P.A.$= -2.3°$. *Bottom:* $\sigma = 0.8$ mJy beam^{-1}; beam is $3.3'' \times 2.7''$, P.A.$= 2.2°$.

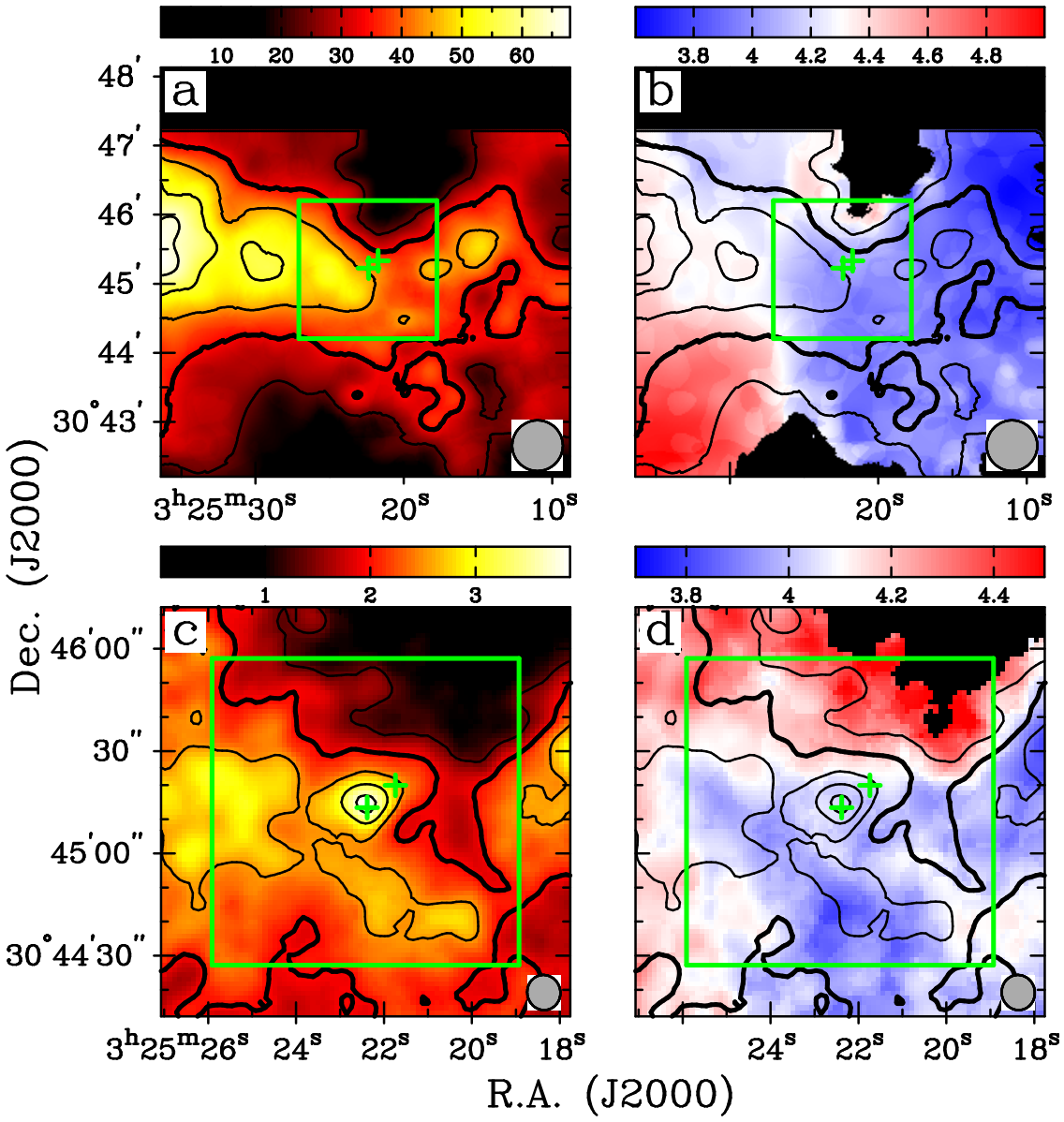

Figure 4.2: $C^{18}O$ $J = 1 \rightarrow 0$ integrated intensity and velocity of L1448 IRS2. Velocity range is 3.6-5.0 km s^{-1} in panel *b*, 3.7-4.5 km s^{-1} in panels *d,f,h*. Plus symbols indicate positions of continuum sources, see Figure 4.1. (a,b) I_ν^{peak} = 68.01 Jy $beam^{-1}$·km s^{-1}; σ = 5.7 Jy $beam^{-1}$·km s^{-1}; beam is $44'' \times 44''$. (c,d) I_ν^{peak} = 3.85 Jy $beam^{-1}$·km s^{-1}; σ = 0.33 Jy $beam^{-1}$·km s^{-1}; beam is $10.33'' \times 9.70''$, P.A.= 11.1°.

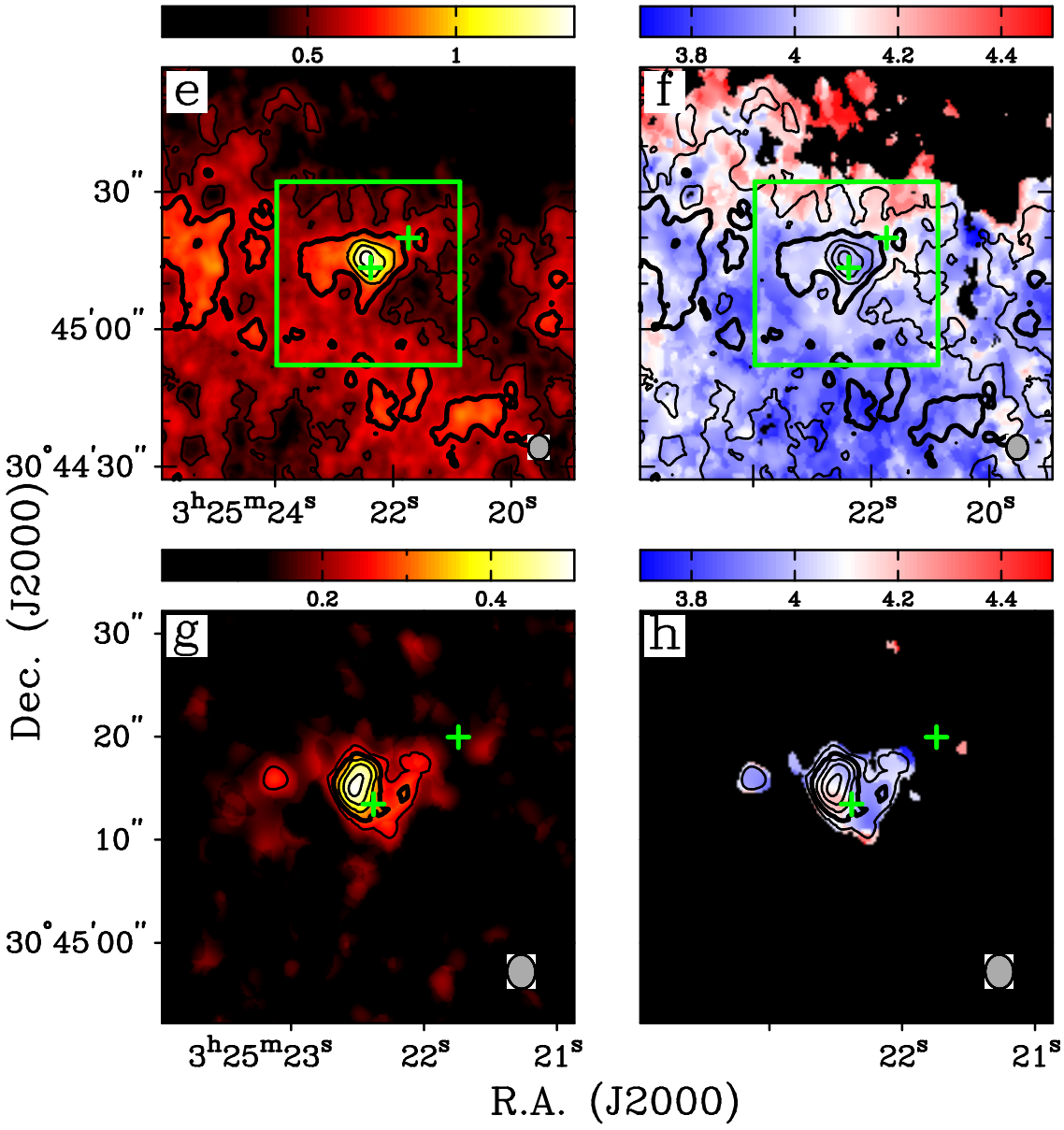

Figure 4.2: *Continued.* (e,f) I_ν^{peak} = 1.31 Jy beam^{-1}·km s^{-1}; σ = 0.10 Jy beam^{-1}·km s^{-1}; beam is 5.39″ × 4.68″, P.A.= −2.3°. (g,h) I_ν^{peak} = 0.49 Jy beam^{-1}·km s^{-1}; σ = 0.05 Jy beam^{-1}·km s^{-1}; beam is 3.32″ × 2.73″, P.A.= 2.2°.

the clumps of $C^{18}O$ emission. Despite the north-south velocity contrast, no smooth velocity gradient is apparent over the area of the core; the amplitude of the velocity variations at the continuum sources is small.

The $C^{18}O$ emission breaks up into a string of small clumps in the 5″ resolution map (Figure 4.2*e*). The clump around L1448 IRS2A is clearly the most prominent source (1.3 Jy beam^{-1}·km s^{-1}), and a tiny clump of emission is nearly coincident with the position of IRS2B (0.7 Jy beam^{-1}·km s^{-1}). The east-west elongation of the IRS2A region is evident at this resolution, with the eastern lobe extending over approximately three beamwidths. The velocities (Figure 4.2*f*) within these $C^{18}O$ contours is unremarkable. In general, the velocity field is flat (3.9-4.0 km s^{-1}), with the exception of the weak emission ($\sim$4.3 km s^{-1}) along the northern edge of the map.

In the highest resolution map (Figure 4.2*g*), the $C^{18}O$ emission around L1448 IRS2A shows the same orientation as the continuum emission in Figure 4.1: the emitting zone is extended along a northeast-southwest axis. The peak of the $C^{18}O$ emission (0.5 Jy beam^{-1}·km s^{-1}) is displaced, however, approximately one beamwidth to the northeast of the continuum emission peak. No significant emission is detected from L1448 IRS2B. The velocity map at this resolution (Figure 4.2*h*) largely maintains the trend that was observed in the lower resolution maps. Over most of the core, the velocity field is flat with values around 3.9-4.0 km s^{-1}. However, at the southern edge of the $C^{18}O$ emission peak, the velocities shift sharply redward to values of 4.2-4.3 km s^{-1}. This abrupt change is not detected in the lower-resolution velocity maps.

Representative spectra from the L1448 IRS2 datacube are shown in Figure 4.3. The spectra are taken through the positions of the continuum objects, IRS2A and IRS2B, and are averaged over the area of a beam. In the top row, the spectra

are taken from the FCRAO maps. Because of the size of the beam (44″), there is considerable overlap in the areas over which the two spectra are taken. The mean velocity of a Gaussian function fitted to the IRS2A spectrum is 4.02 km s^{-1}. A fit to the IRS2B spectrum yields a central velocity of 4.05 km s^{-1}. This difference is insignificant, considering the 0.27 km s^{-1} channel width. The gray vertical lines in each of the spectra mark the central velocities of the FCRAO spectra; the lines are extended to the higher resolution spectra (second, third, and fourth rows) to detect line shifts. For both IRS2A and IRS2B, no significant shifts are detected. The line profiles from both sources maintain their central velocities, and largely maintain their symmetry, at both 10″ and 5″ resolution, even when there is no overlap in the beam areas. In the 3″ resolution data, the IRS2A spectrum no longer has a Gaussian profile; most of the flux is in a single strong channel. The $C^{18}O$ line is not detected from IRS2B at this resolution.

The results from applying the OSG gridding method to the $C^{18}O$ datacubes of L1448 IRS2 are displayed in Figure 4.4. [The OSG gridding method is described in Chapter 2, along with the quality criteria that are imposed to insure that only the FWHM of spectral lines that can be accurately fitted with Gaussian function are included.] The plot shows the correlation between the FWHM of the measured spectral lines and the size of the grid square over which the spectra are taken. A total of 420 spectra met the quality criteria and are included in this figure. At 2250 AU resolution, the range of measured FWHM extends from 0.30 to 2.12 km s^{-1}, and the mean uncertainty is 0.17 km s^{-1}. Several trends that are observed in the line width *vs.* grid size correlations of the three cores presented in Chapter 2 are also evident here. There is sufficient signal in each of the datacubes with combined BIMA and FCRAO data that the number of measurable spectra consistently increases down to the 2250 AU grid squares. At 1140 AU resolution, only a few squares coincident

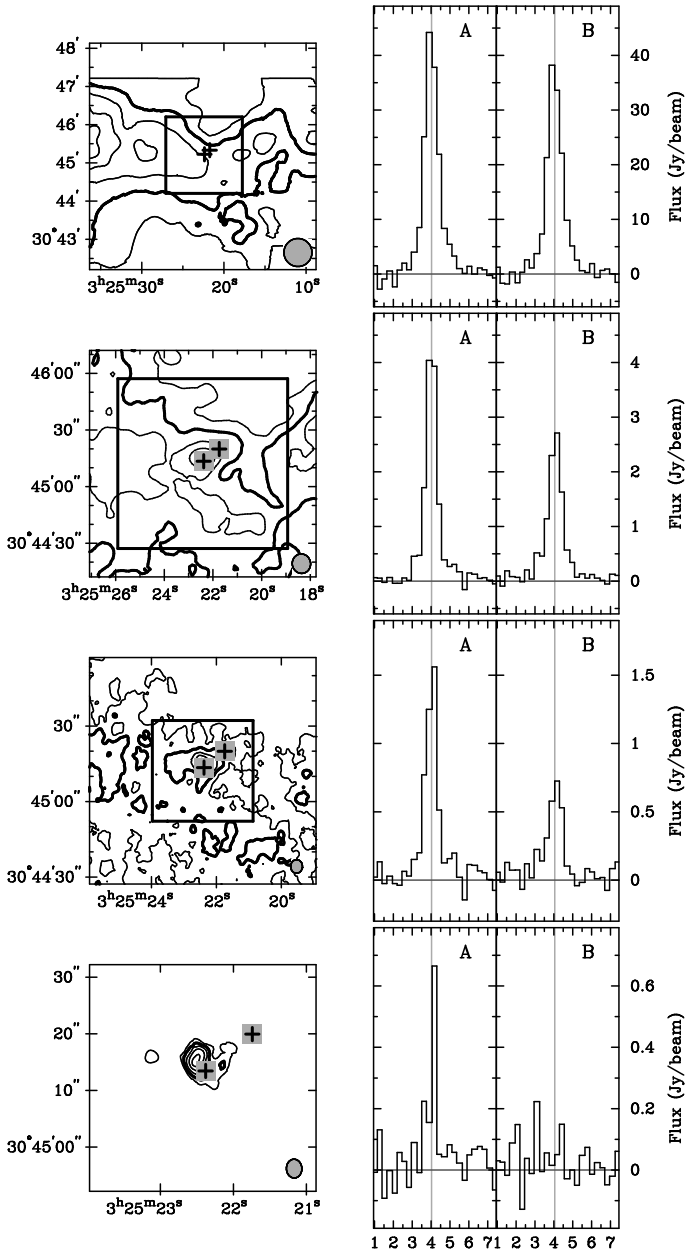

Figure 4.3: L1448 IRS2 spectra. The plots at left show integrated intensity contours from the $C^{18}O$ data, as in Figure 4.2. The plus symbols indicate the positions of the continuum sources identified in Figure 4.1. To the right of each contour plot are spectra from the $C^{18}O$ datacubes. All spectra display the mean flux in Jy beam^{-1} taken over a beam area. In all rows, the gray vertical lines show central velocities of Gaussian functions fit to the profile from the FCRAO map (top row).

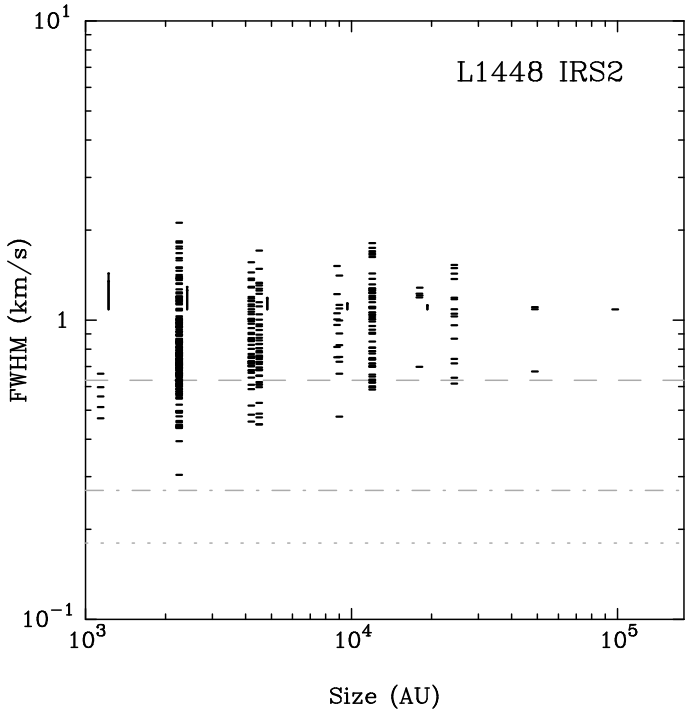

Figure 4.4: L1448 IRS2 line width (FWHM) *vs.* grid size correlations for $C^{18}O$ spectra. The solid lines to the right side of the vertical clusters of points indicate the mean uncertainty in the FWHM measurements at that grid size; all uncertainties are displayed at the FWHM of the spectrum from the full FCRAO map (rightmost point). The dashed line indicates the line width corresponding to the sound speed of the medium: $\mathrm{FWHM}_{c_s}(20\ \mathrm{K}) = 0.63$ km s^{-1}. The dotted line indicates the thermal line width: $\mathrm{FWHM}_T(20\ \mathrm{K}) = 0.18$ km s^{-1}. The dash-dot line indicates the channel width of the spectra: $\delta V = 0.27$ km s^{-1}.

with the continuum source produce measurable spectra. The lower envelope of the measured FWHM increases with increasing grid size, and the upper envelope gradually decreases. The largest spread in the FWHM occurs at the smallest grid sizes.

Except for the three cores presented in Chapter 2, the continuum emission from the BIMA survey targets have not been modeled to determine the density and temperature distributions of the core envelopes. In Chapter 2, the prevailing temperatures of the envelopes, as determined by the models of LMW00 and LMW03, were used to calculate the thermal line widths of the emitting molecules and the

sonic line widths of the circumstellar material. Here, with no models available, a characteristic temperature of 20 K is assumed. This value is a rough average of the temperatures used for the three cores in Chapter 2, and it is assumed to be a reasonable first estimate for the rest of the cores in the survey. The thermal line width of $C^{18}O$ at this temperature, $FWHM_T(20\ K) = 0.18$ km s^{-1}, is indicated by the dotted line in Figure 4.4. The sonic line width at this temperature, $FWHM_{c_s}(20\ K) = 0.63$ km s^{-1}, is indicated by the dashed line. With these lines in place as visual guides, one difference between the measured FWHM of the L1448 IRS2 core and the three cores from Chapter 2 becomes apparent. *On average*, the $C^{18}O$ lines from L1448 IRS2 are slightly narrower than the $C^{18}O$ lines from the other cores. Both the upper and lower envelopes of the measured FWHM are shifted to slightly lower values. And, although no L1448 IRS2 lines approach the thermal line width, a greater fraction of the lines have FWHM below the sonic line width. At 2250 AU resolution, the percentage of lines with FWHM below the sonic value is 20.9%; across all grid sizes, this percentage is 17.9%.

4.6 L1448 C

4.6.1 Background

Located approximately 75″ south of L1448 IRS3, L1448C is a Class 0 YSO that was not detected by IRAS. This deeply embedded object, dubbed L1448-mm by some authors, was first detected in observations of $NH_3(1,1)$ and $NH_3(2,2)$ emission and is noteworthy because of the bipolar outflows that it powers (Bachiller *et al.* 1990). Its well-collimated, high-velocity outflow has been studied in emission from multiple CO transitions: $J = 4 \rightarrow 3$, $3 \rightarrow 2$ (Nisini *et al.* 2000), $J = 2 \rightarrow 1$ (Bontemps *et al.* 1996), $J = 1 \rightarrow 0$ (Bachiller *et al.* 1995). The shocks produced by the interaction

of the outflow with the ambient cloud have also been investigated in SiO emission (Girart & Acord 2001; Dutrey, Guilloteau, & Bachiller 1997; Guilloteau *et al.* 1992; Bachiller, Martín-Pintado, & Fuente 1991) and shock-excited H_2 $1 \rightarrow 0$ $S(1)$ emission (Eislöffel 2000; Curiel *et al.* 1999; Davis & Smith 1996, 1995; Davis *et al.* 1994; Bally, Lada, & Lane 1993). L1448C and its accompanying outflows may complicate the environment of L1448 IRS3 because the blue-shifted northern outflow lobe overlaps the L1448 IRS3 core. The westward bend in this lobe is attributed to an interaction between the L1448C and L1448 IRS3 outflows, first suggested by Bachiller *et al.* (1995).

4.6.2 Continuum Data

The extended envelope surrounding the L1448C core is a powerful source of $\lambda =$ 2.7 mm continuum emission (Figure 4.5). In the map made with $10''$ resolution (top panel), the emitting region is elliptical, approximately three beamwidths by four beamwidths in area, and has a peak of 46.2 mJy beam^{-1}. The major axis of the ellipse is oriented in the same direction as the axis of the well-known CO outflow lobes. Following this axis to the north, the low-level contours of another strong emission source appear near the edge of the primary beam. This is L1448 IRS3, which was described in Chapter 2. At $5''$ resolution, the elongation of the core is even more pronounced. Roughly $10''$ northeast of the primary emission peak (33.8 mJy beam^{-1}) is a shallow (3σ) secondary peak. In the opposite direction, a prominent bulge of emission extends toward the southwest. The $3''$ resolution map reveals that this bulge arises from (at least) two different components. One component, $4''$ east of the central emission peak (28.3 mJy beam^{-1}), is distinguished by the 6σ contour; the other component, $7''$ further south, shows a separate emission peak at the 5σ level. The weak source to the northwest appears as an independent,

unresolved 3σ peak. Although the organization of this tight cluster of emission peaks (*i.e.* lined up in the same northwest-southeast direction as the outflow axis) *may* indicate some redistribution of the envelope material by the outflow jets, such an interaction is unlikely. Consequently, the four continuum peaks are labeled as though they are members of a quadruple protostellar system. The strongest source, at the center of the map, is C1. The other three sources are named in order of their apparent distance from the center: C2 is $4''$ east of C1; C3 is $8''$ southeast of C1, and the weakest source, $11''$ northwest of C1, is called C4.

4.6.3 $C^{18}O$ Data

In the FCRAO map centered on the position of the L1448C core (Figure 4.6*a*), most of the $C^{18}O$ emission from the large L1448 cloud appears to curl around the center of the map. The zone of peak emission (69.4 Jy beam^{-1}·km s^{-1}) is located just above the area of the BIMA primary beam, closer to the L1448 IRS3 core. No strong emission peak indicates the presence of L1448C; the local maximum just east of the continuum sources has a peak intensity of 46.8 Jy beam^{-1}·km s^{-1}. The velocity map of the same region, Figure 4.6*b*, looks different from the corresponding map centered on the position of L1448 IRS3 (Figure 2.3*b*), but this is only due to a shift in the stretch of the colorscale. The general behavior of the velocities is, as expected, very similar. The velocities near the southern edge of the cloud are redshifted to $\sim$5.0 km s^{-1}; the northern and western edges of the map are blueshifted to almost 4.0 km s^{-1}. A shallow velocity gradient passes from northwest ($\sim$4.5 km s^{-1}) to southeast ($\sim$4.9 km s^{-1}) across the area of the primary beam.

The L1448C core conspicuously pops out from the background emission in the $10''$ resolution map (Figure 4.6*c*). The emission peak centered on the core is 4.4 Jy beam^{-1}·km s^{-1}, and the surrounding contours are elongated in the northwest-

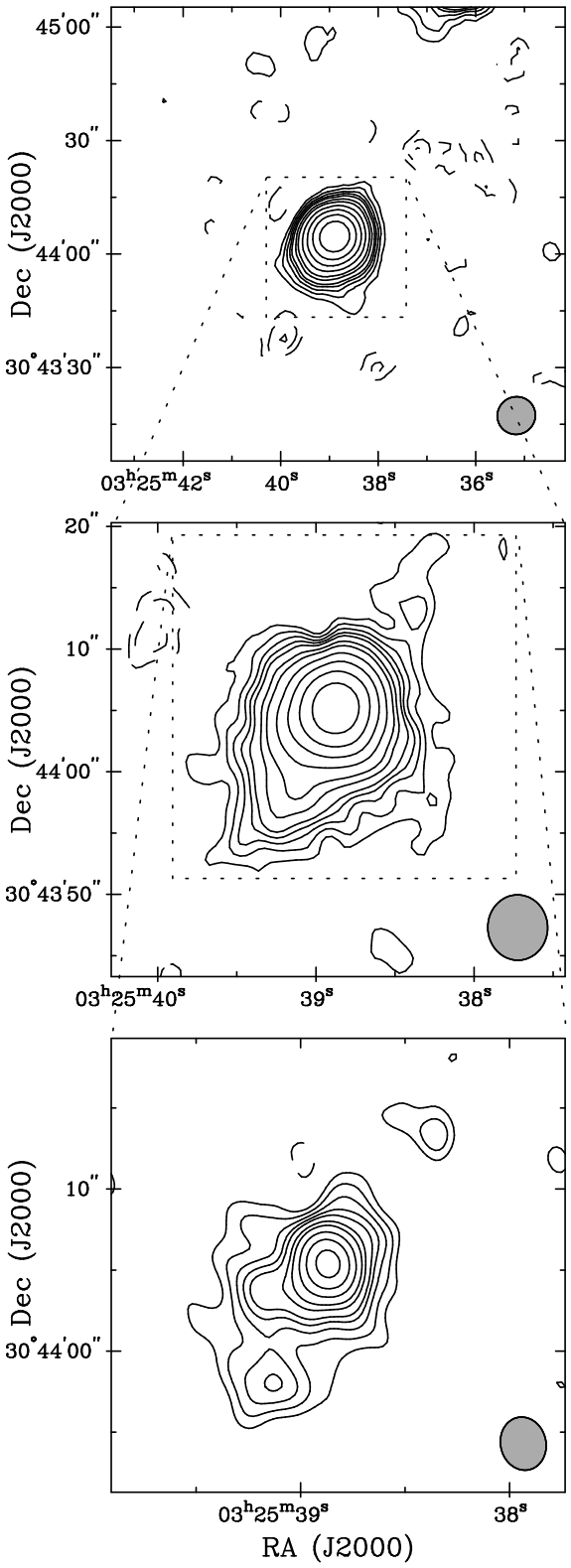

Figure 4.5: Maps of the $\lambda = 2.7$ mm continuum emission from L1448 C. The contour intervals are $(-4, -3, -2, 2, 3, 4, 5, 6, 8, 10, 14.14, 20, 28.28, 40) \times \sigma$ in mJy beam^{-1}. *Top:* $\sigma = 0.8$ mJy beam^{-1}; beam is $10.1'' \times 9.9''$, P.A.$= -59.2°$. *Middle:* $\sigma = 0.6$ mJy beam^{-1}; beam is $5.3'' \times 4.9''$, P.A.$= 1.5°$. *Bottom:* $\sigma = 0.9$ mJy beam^{-1}; beam is $3.3'' \times 2.8''$, P.A.$= 13.2°$.

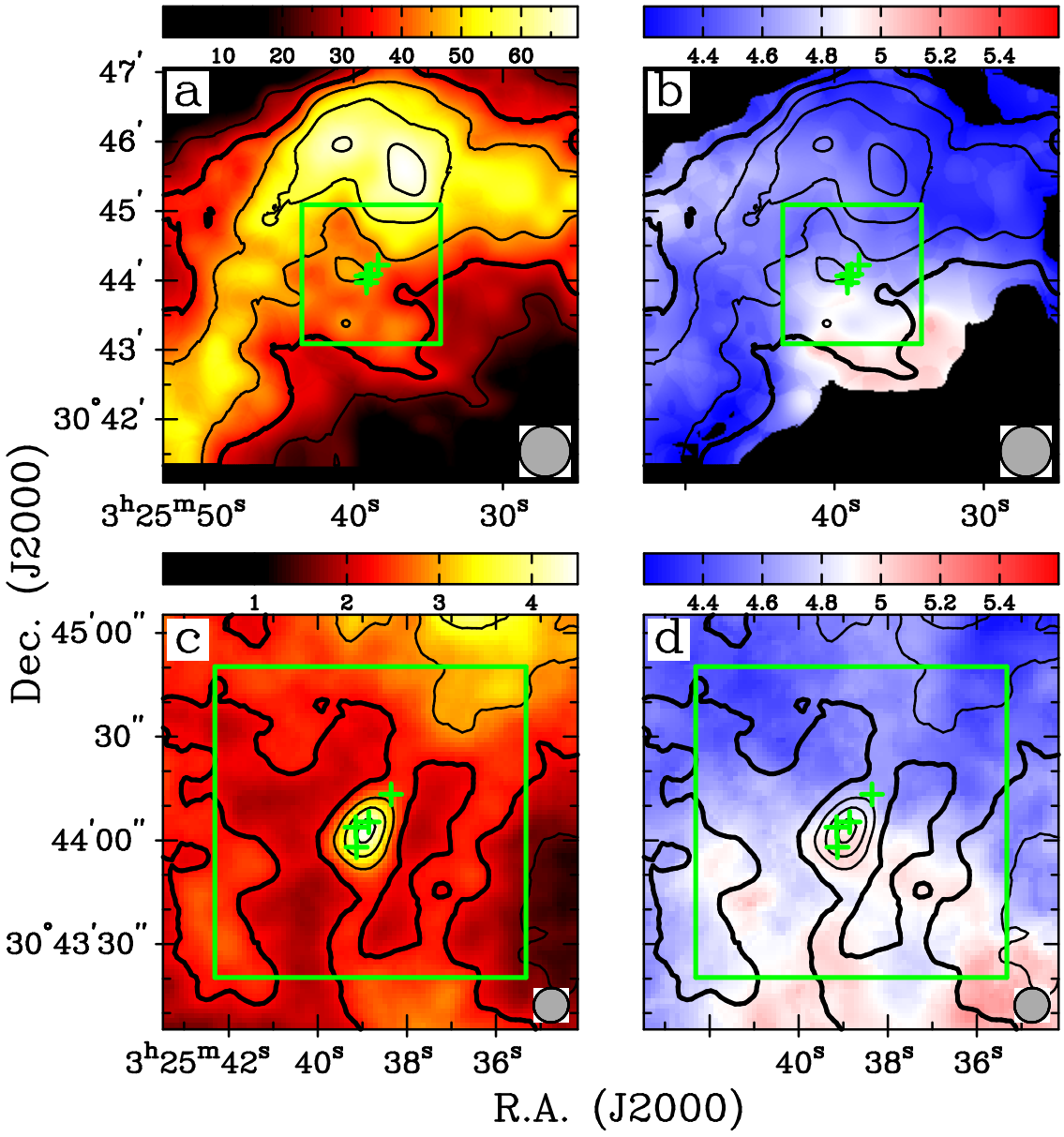

Figure 4.6: $C^{18}O$ $J = 1 \rightarrow 0$ integrated intensity and velocity of L1448 C. Velocity range is 4.2-5.6 km s^{-1} in all panels. Plus symbols indicate positions of continuum sources from Figure 4.5. (a,b) $I_\nu^{peak} = 69.43$ Jy beam^{-1}·km s^{-1}; $\sigma =$ 9.0 Jy beam^{-1}·km s^{-1}; beam is $44'' \times 44''$. (c,d) $I_\nu^{peak} = 4.43$ Jy beam^{-1}·km s^{-1}; $\sigma = 0.29$ Jy beam^{-1}·km s^{-1}; beam is $10.13'' \times 9.90''$, P.A.$= -59.2°$.

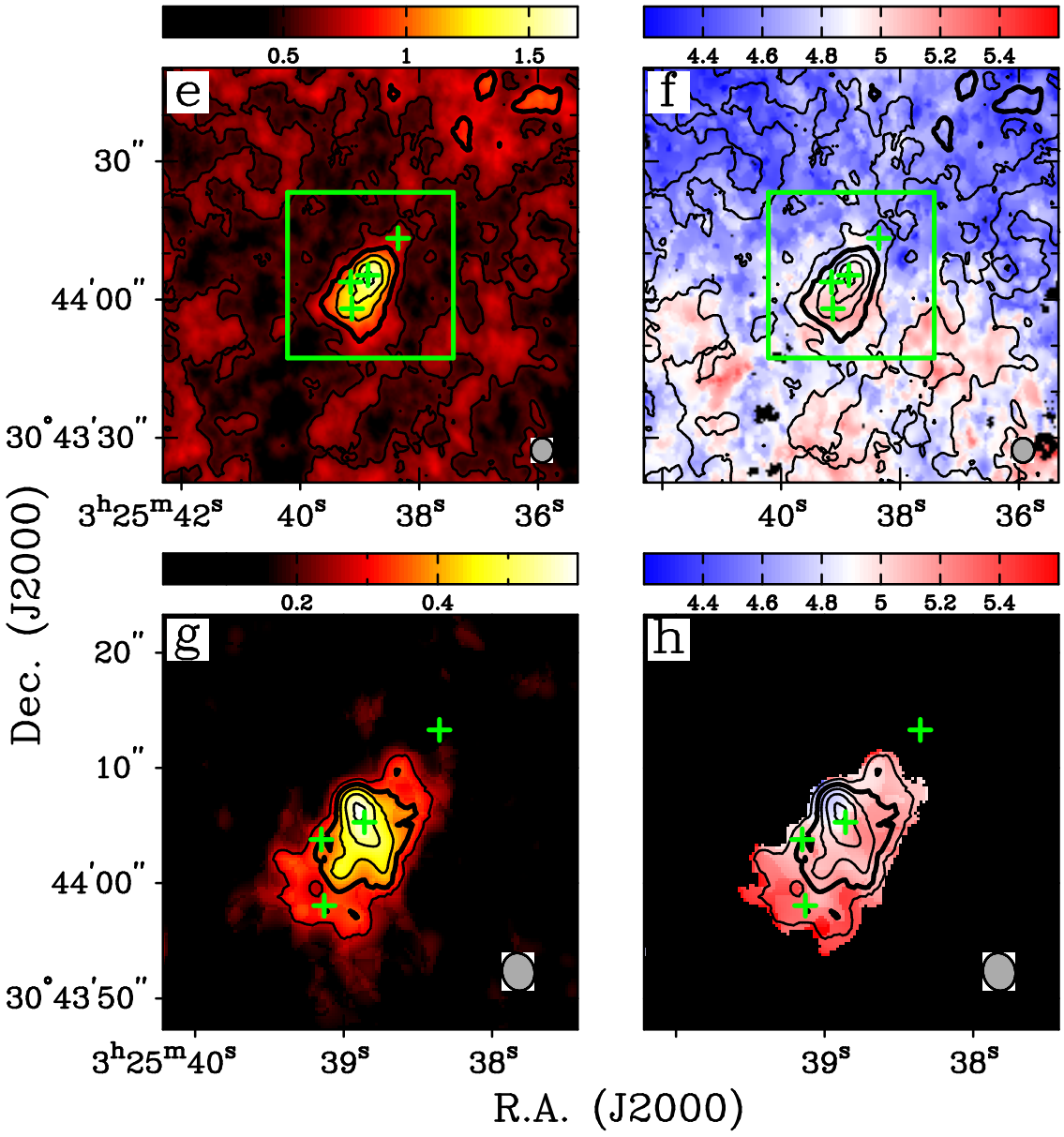

Figure 4.6: *Continued.* (e,f) I_ν^{peak} = 1.63 Jy beam^{-1}·km s^{-1}; σ = 0.11 Jy beam^{-1}·km s^{-1}; beam is 5.33″ × 4.88″, P.A.= 1.5°. (g,h) I_ν^{peak} = 0.55 Jy beam^{-1}·km s^{-1}; σ = 0.05 Jy beam^{-1}·km s^{-1}; beam is 3.30″ × 2.80″, P.A.= 13.2°.

southeast direction with roughly the same position angle that is seen in the continuum emission. Except for the strong $C^{18}O$ peak at L1448 IRS3, at the northern edge of the map, the background emission surrounding L1448C is fairly uniform. In the accompanying velocity map (Figure 4.6*d*), the gradient that is observed in the FCRAO velocity map is brought into sharper relief. The velocities in the northern half of the map are slightly bluer (4.4-4.5 km s^{-1}); the velocities in the southern half are redder (4.9-5.0 km s^{-1}), and L1448C is located at exactly one of the transition zones. The gradient in the direction of the core's elongation proceeds smoothly from 4.5 to 5.0 km s^{-1}.

The 5″ resolution map (Figure 4.6*e*) shows only dappled emission from the background cloud. The most prominent feature is the L1448C core, which is clearly elongated along the direction of the four continuum sources. The emission peak, at the position of L1448C1, is 1.6 Jy $beam^{-1}$·km s^{-1}. In the velocity map (Figure 4.6*f*), the core still appears at the interface between blue- and redshifted zones, but the case for a smooth gradient is less strong. Most of the area of the core delineated by the intensity contours appears at velocities in the range 4.8-5.1 km s^{-1}; only the northern edge shows bluer velocities (4.4-4.5 km s^{-1}). The transition between blue and red velocities is more patchy than at 10″ resolution.

At 3″ resolution (Figure 4.6*g*), the $C^{18}O$ emission is concentrated on the location of the continuum sources. The point of peak emission (0.5 Jy $beam^{-1}$·km s^{-1}) is nearly coincident with L1448C1. The high emission contours (65%, 80%) appear slightly elongated (2-3 beamwidths) in a northeast-southwest direction, and the lower contours (35%, 50%) are elongated almost perpendicularly, in the northwest-southeast direction. The four continuum sources are nearly aligned in this direction, but otherwise, they are not distinguished in the $C^{18}O$ emission. The velocity map (Figure 4.6*h*) of this tiny cluster also eschews an easy interpretation. In general,

the velocities at this resolution are redder than those seen over the same area in the lower resolution maps. There is no clear evidence for a gradient. The bluest velocities (4.6 km s^{-1}) appear at the northeast edge, leading to the suggestion of disk-like rotation around L1448C1 in the high emission contours (65%, 80%). There is no evidence for systematic motion around C2 and C3.

Figure 4.7 shows the shapes of the $C^{18}O$ emission lines from each of the proposed continuum positions. The top row shows the spectra from the FCRAO datacube, and of course, because the four continuum positions are all within a 44″ beamwidth of one another, the lines are nearly identical. A careful eye reveals that all four of the profiles are slightly skewed toward the blue. L1448C4, which is marginally closer to the center of the L1448 cloud, shows a slightly higher and broader line. When fitted by Gaussian functions, the central velocities of the four lines are all within 0.05 km s^{-1} of 4.7 km s^{-1}. The four line profiles begin to differentiate in the spectra made from the 10″ resolution datacubes, shown in the second row. L1448C1, at the center of the core, shows the strongest line; L1448C4, furthest from the center, has the weakest line. With the influence of the FCRAO data reduced at this resolution, all four lines are now slightly skewed toward the red; the central velocities of the fitted Gaussians are all on the red side of the vertical line showing the velocity from the FCRAO data. This redward slant to the line profiles persists in the spectra from the 5″ datacubes. The amount of skew corresponds to the trends seen in the velocity maps. For example: L1448C1, at the center of the main emission peak, shows only a slight redward slant. L1448C3, further south of the main emission peak, appears at a redder velocity in Figure 4.6*f* and also has a line profile with a more pronounced skew. The weaker line from L1448C4 shows a double peaked profile, with a single-channel spike of emission on the blue side of the main line. In the spectrum from the 3″ datacube, this blue, single-channel spike is the only

remnant of the emission line. The central velocities of C1 and C3 are skewed even further toward the red.

The correlation between the FWHM of the gridded spectral lines and the grid sizes are displayed in Figure 4.8. The dashed gray line shows the FWHM (0.63 km s^{-1}) of a line broadened by the sound speed at T=20 K. This is the same temperature that was used in the corresponding figure for L1448 IRS2, and it will be used as a characteristic core temperature for the rest of the BIMA survey targets. The dotted line shows the thermal line width of $C^{18}O$ at this same temperature.

The correlation shown is drawn from a total of 447 measured spectra. As with the correlation shown in the L1448 IRS2 spectra, the range of measured FWHM clearly widens in the spectra from the smaller grid squares. At 2250 AU resolution, the narrowest and widest lines are 0.43 and 2.16 km s^{-1}, respectively, and the mean uncertainty is 0.17 km s^{-1}. The FWHM of the spectra from the 1140 AU grid squares are, on average, narrower than the lines from the 2250 AU squares. Moreover, 68.4% of the highest resolution lines are narrower the sonic line width. Overall, only 3.8% of all measured line widths appear below the sonic threshold, and all of these are contributed by spectra measured in 2250 AU and 1140 AU grid squares.

4.7 L1455

4.7.1 Background

The L1455 dark cloud lies $\sim 40'$ southeast of L1448 and $\sim 1^\circ$ south of NGC1333 (Lynds 1962). In large-scale maps of ^{13}CO emission from the Perseus cloud (Bachiller & Cernicharo 1986a), L1455 occupies an approximately $10' \times 10'$ area. The cloud harbors three infrared sources that were detected by the IRAS satellite. L1455 IRS1 (IRAS 03245+3002) is the strongest source in the cloud at far-infrared wavelengths.

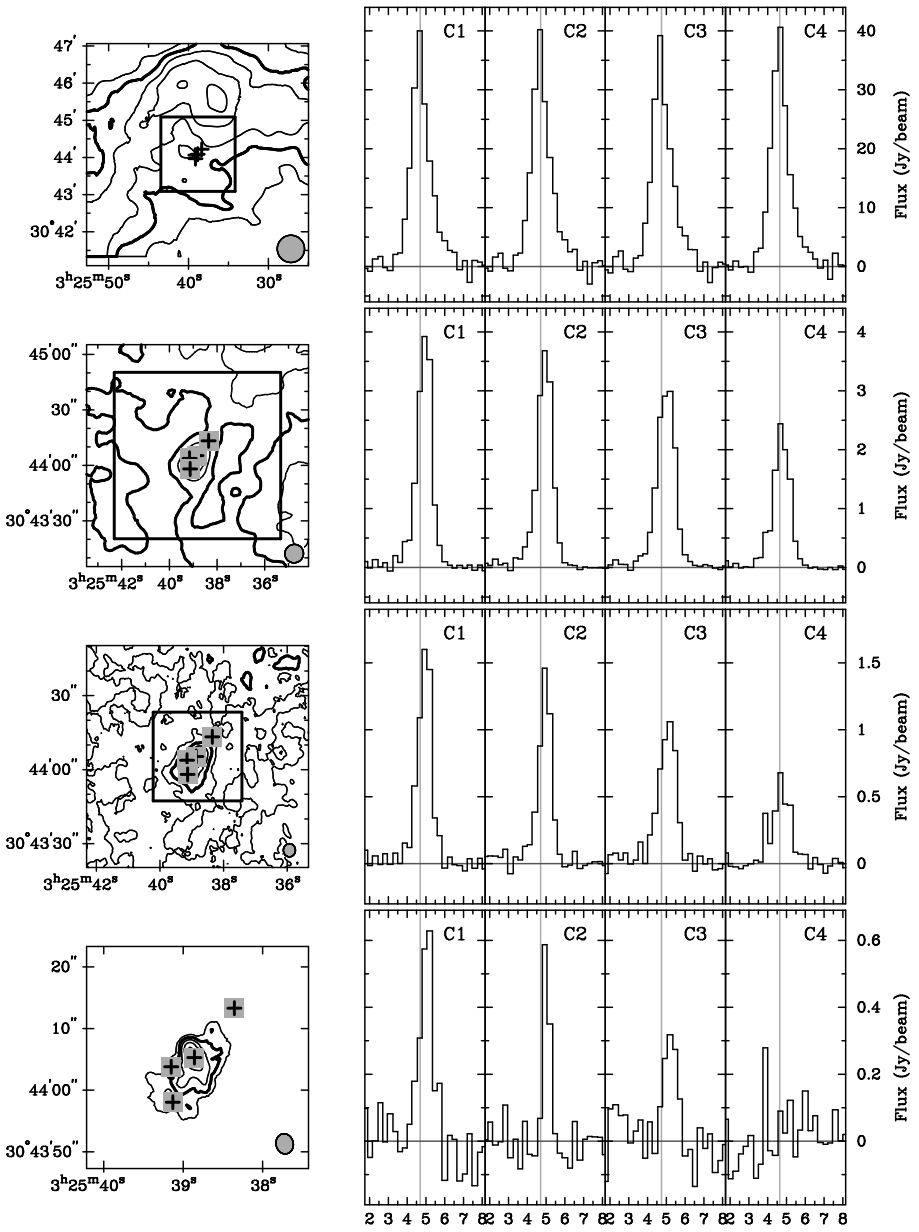

Figure 4.7: L1448 C spectra. The plots at left show integrated intensity contours from the $C^{18}O$ data, as in Figure 4.6. To the right of each contour plot are spectra from the $C^{18}O$ datacubes. The plus symbols indicate the positions of the continuum sources C1, C2, C3, and C4. All spectra display the flux in Jy beam^{-1} averaged over the area of a beam. In all rows, the gray vertical lines show central velocities of Gaussian functions fit to the profiles from the FCRAO map (top row).

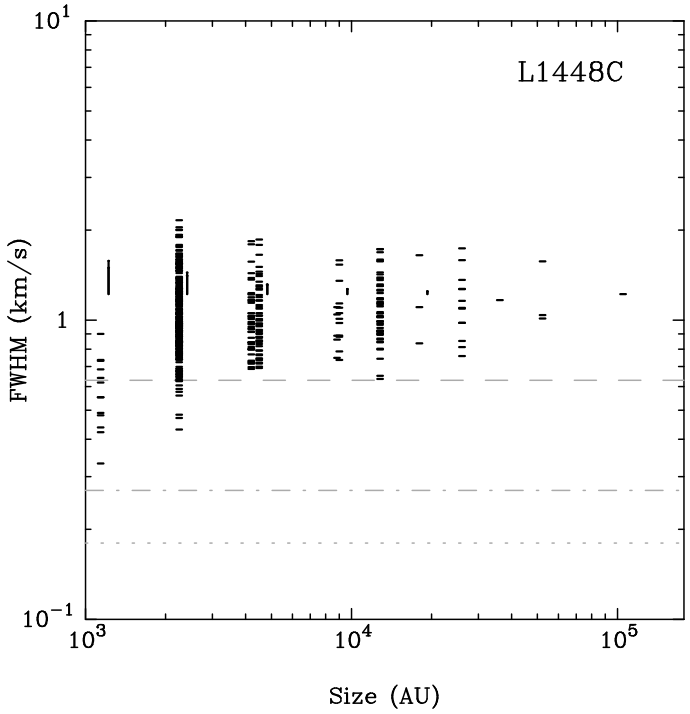

Figure 4.8: L1448 C line width (FWHM) *vs.* grid size correlations for $C^{18}O$ spectra. The solid lines to the right side of the vertical clusters of points indicate the mean uncertainty in the FWHM measurements at that grid size; all uncertainties are displayed at the FWHM of the spectrum from the full FCRAO map (rightmost point). The dashed line indicates the line width corresponding to the sound speed of the medium: $\mathrm{FWHM}_{c_s}(20\ \mathrm{K}) = 0.63$ km s^{-1}. The dotted line indicates the thermal line width: $\mathrm{FWHM}_T(20\ \mathrm{K}) = 0.18$ km s^{-1}. The dash-dot line indicates the channel width of the spectra: $\delta V = 0.27$ km s^{-1}.

Based upon KAO observations in six different wavebands, Davidson & Jaffe (1984) estimated the luminosity of IRS1 to be ∼7.2 L⊙ (adjusted for a distance of 350 pc). A more recent re-evaluation of the fluxes in the IRAS bands yielded a total luminosity of 9.7 L⊙ (Clark 1991). The likelihood of IRS1 being a site of star formation activity is reinforced by the presence of a nearby H_2O maser (Cesaroni *et al.* 1988; Persi, Palagi, & Felli 1994). L1455 IRS2 (IRAS 03247+3001) lies ∼2′ southeast of IRS1 and coincides with the position of "NGC1333 star 2," a faint Hα emission star (Cohen & Kuhi 1979). It also lies at the edge of a patch of nebulosity (RNO15, Cohen (1980)) that extends roughly 1′ southward. IRS2 is brighter than

IRS1 in the 12 μm IRAS band, but fainter in the other three bands, and has a total luminosity of less than 4 L$\odot$ (Bachiller & Cernicharo 1986b). L1455 IRS3 (IRAS 03249+2957), another 5$'$ to the southeast, is the weakest of the three sources, with a total luminosity less than 0.4 L$\odot$ (Bachiller & Cernicharo 1986b).

The cloud surrounding the three infrared sources has been probed with a number of molecular line studies (*e.g.* Torrelles *et al.* (1986); Heyer *et al.* (1986)), which reveal an intricate network of clumps. The ^{13}CO and C^{18}O observations by Walmsley & Menten (1987) showed two overlapping velocity components at 4.97 and 5.95 km s^{-1}. The outflows emerging from L1455 are correspondingly complex. The regions of high-velocity CO emission are generally grouped into a "Main" outflow region, roughly centered on RNO15, and a "Northwest" outflow region about 6$'$ away (after Goldsmith *et al.* (1984)), but a satisfactory determination of which condensations are responsible for which outflows is elusive. Based upon an optical survey of Hα and [S II] emission, Bally *et al.* (1997) linked a number of new HH objects to the distribution of outflow material. They speculated that IRS2 drives a north-south outflow (PA=170°) that energizes the RNO15 nebulosity. IRS1 drives either an east-west outflow with a blue lobe that stimulates HH317 ($\sim$8$'$ to the west) *or* a northwest-southeast outflow, with a blue lobe that stiumulates the HH279 nebulosities ($\sim$7$'$ to the northwest).

The cores within the L1455 cloud targeted in the BIMA survey are identified in the maps of NH_3 (1,1) emission by Juan *et al.* (1993), see Figure 4.9. In their comprehensive study, Juan *et al.* (1993) observed L1455 in the low level transitions of several molecular species, including CS, C^{34}S, and NH_3. The CS observations confirmed the presence of the multiple velocity components detected by Walmsley & Menten (1987). The CS $J = 2 \rightarrow 1$ lines are double-peaked; a component at 4.8 km s^{-1} is concentrated in the area between IRS1 and IRS2, and another com-

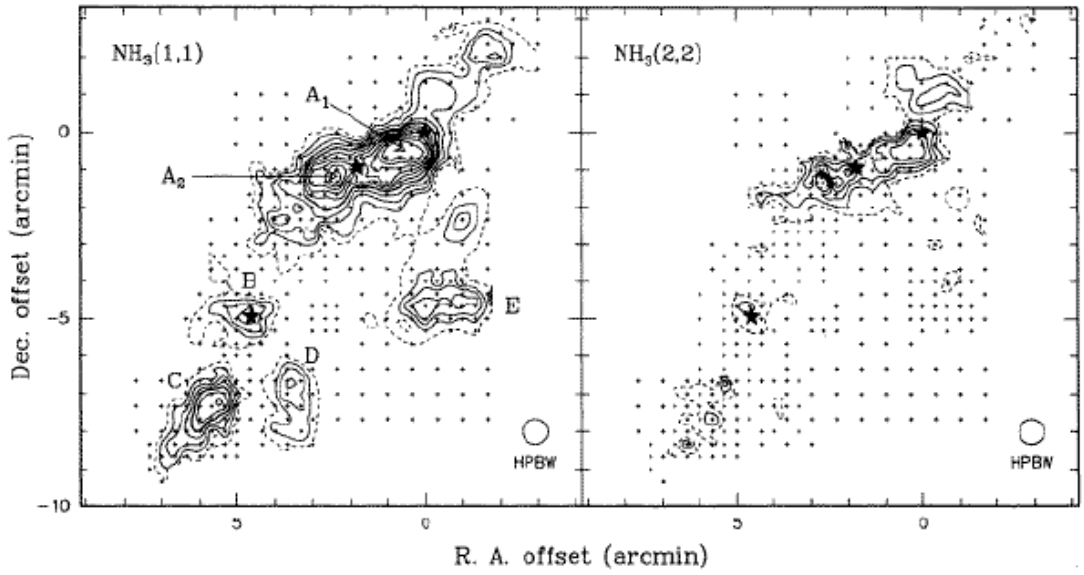

Figure 4.9: Maps of the integrated intensity from the NH_3 (1,1) (*left*) and (2,2) (*right*) transitions in L1455, as shown in Figure 6 of Juan *et al.* (1993). The positions of the three IRAS sources are indicated by stars. The cores observed for the BIMA survey are the NH_3 emission peaks denoted A1, A2, B, and C.

ponent at 5.5 km s^{-1} has a lumpy distribution throughout the cloud. NH_3 maps reveal a long filamentary structure subdivided into a series of clumps, labeled A1, A2, B, and C. Two additional clumps, D and E (with V_{LSR}=5.5 km s^{-1}) are located a few arc-minutes southwest of the filament.

4.7.2 Continuum Data

The four NH_3 cores in the L1455 cloud observed for the BIMA survey are A1, A2, B, and C. Maps of the $\lambda = 2.7$ mm continuum emission from L1455A1 is displayed in Figures 4.10 & 4.11. The top panels in both of these figures show two sources of continuum emission. The object in the northeast quadrant of the map is L1455 IRS1 (IRAS 03245+3002). At $10''$ resolution, IRS1 has a peak intensity of 9.1 mJy $beam^{-1}$ and the extended envelope ($\sim 2 \times 2.5$ beamwidths) appears slightly elongated in the northwest-southeast direction. The middle and bottom

panels of Figure 4.10 zoom in on this object. With finer resolution, the elongation of IRS1 becomes even more pronounced. At both 5″ (S_{peak} = 6.6 mJy beam^{-1}) and 3″ resolution (S_{peak} = 5.7 mJy beam^{-1}), a finger of extended emission points southeast from the central peak. Figure 4.11 zooms in on the other prominent source of continuum emission in L1455A1. This object is *not* one of the three IRAS sources detected in the L1455 cloud; it appears roughly halfway between IRS1 and IRS2 (see below). At 10″ resolution, this object (IRS1 East) is elongated by roughly three beamwidths in the east-west direction. The peak intensity of the IRS1 East at this resolution is 5.8 mJy beam^{-1}. Unlike its westerly companion, the emission from IRS1 East is not as centrally condensed; the continuum emission appears to dissolve in the higher resolution observations. At 5″ resolution (middle panel), most of the contibuting emission appears spread out over a broad area. The peak intensity is only 4.3 mJy beam^{-1}, but the higher contours ($5\sigma, 6\sigma$) maintain the east-west elongation. At 3″ resolution, this suggestion of an elongated source is maintained only at the 3σ level; the peak intensity here is 2.7 mJy beam^{-1}.

The continuum emission from the L1455A2 core is displayed in Figure 4.12. The center of the NH_3 core itself is not a source of millimeter continuum radiation, but the map does reveal the presence of L1455 IRS2 (IRAS 03247+3001) in the northwest quadrant. Unlike the two objects in the vicinity of the A1 cloud, IRS2 is relatively diffuse and relatively weak. The peak flux at 10″ resolution (upper panel) is 3.5 mJy beam^{-1}, and at 5″ the emitting region breaks up into a string of unremarkable 2σ and 3σ peaks.

The map of continuum emission from the L1455B core (Figure 4.13) is similar, in sofar as there is little evidence for a compact emission source. L1455 IRS3 (IRAS 03249+2957) is located at the center of the map, but only a small clump of 3σ emission hints at its presence. The strongest source in the field (S_{peak} = 3.6 mJy

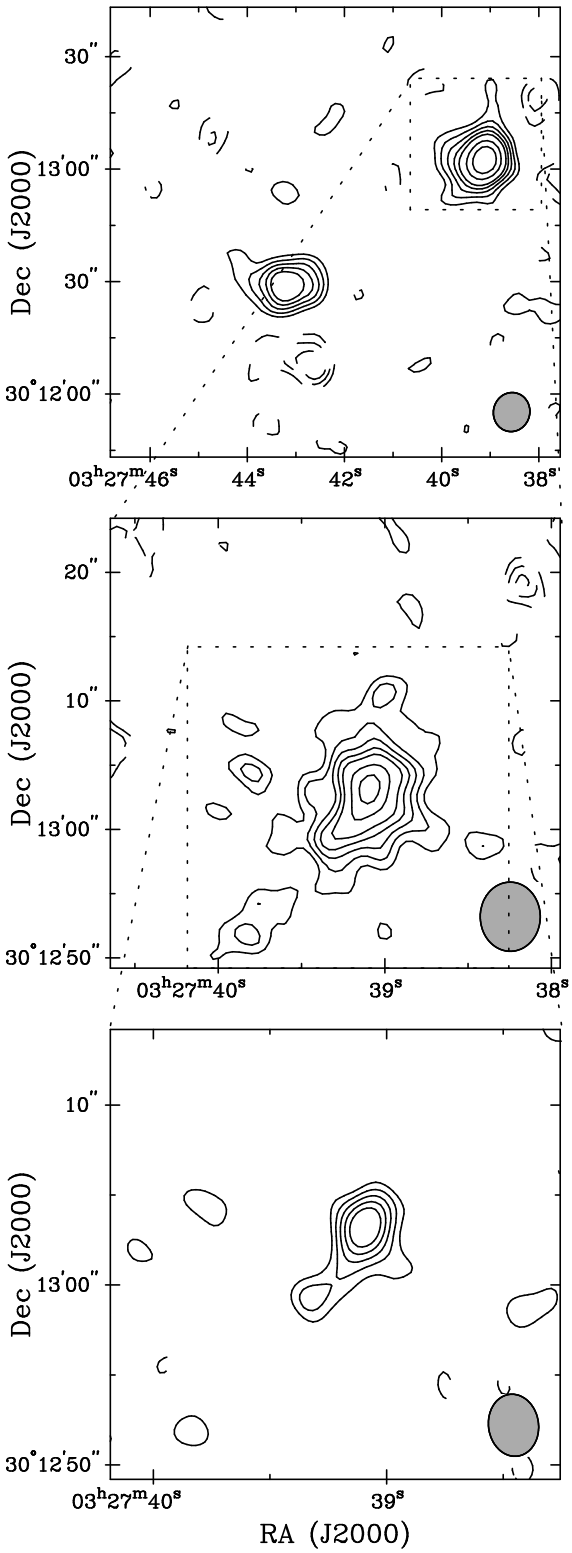

Figure 4.10: Maps of the $\lambda = 2.7$ mm continuum emission from L1455A1 IRS1. The contour intervals are $(-4, -3, -2, 2, 3, 4, 5, 6, 8, 10) \times \sigma$ in mJy beam^{-1}. *Top:* $\sigma = 0.7$ mJy beam^{-1}; beam is $10.5'' \times 9.7''$, P.A.$= -12.9°$. *Middle:* $\sigma = 0.6$ mJy beam^{-1}; beam is $5.4'' \times 4.7''$, P.A.$= 0.5°$. *Bottom:* $\sigma = 0.7$ mJy beam^{-1}; beam is $3.5'' \times 2.8''$, P.A.$= 7.7°$.

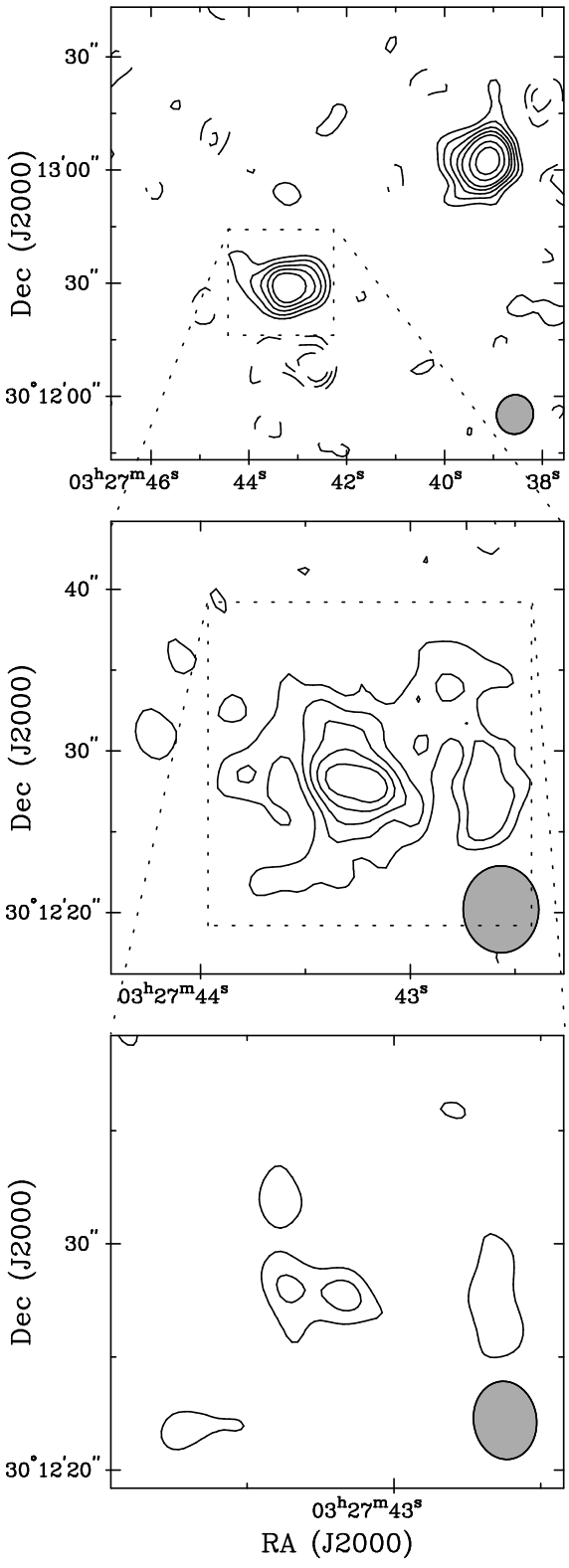

Figure 4.11: Maps of the $\lambda = 2.7$ mm continuum emission from L1455A1 IRS1 East. The contour intervals are $(-4, -3, -2, 2, 3, 4, 5, 6, 8) \times \sigma$ in mJy beam^{-1}. *Top:* $\sigma = 0.8$ mJy beam^{-1}; beam is $10.5'' \times 9.7''$, P.A.$= -12.9°$. *Middle:* $\sigma = 0.6$ mJy beam^{-1}; beam is $5.4'' \times 4.9''$, P.A.$= 1.5°$. *Bottom:* $\sigma = 0.7$ mJy beam^{-1}; beam is $3.5'' \times 2.8''$, P.A.$= 7.7°$.

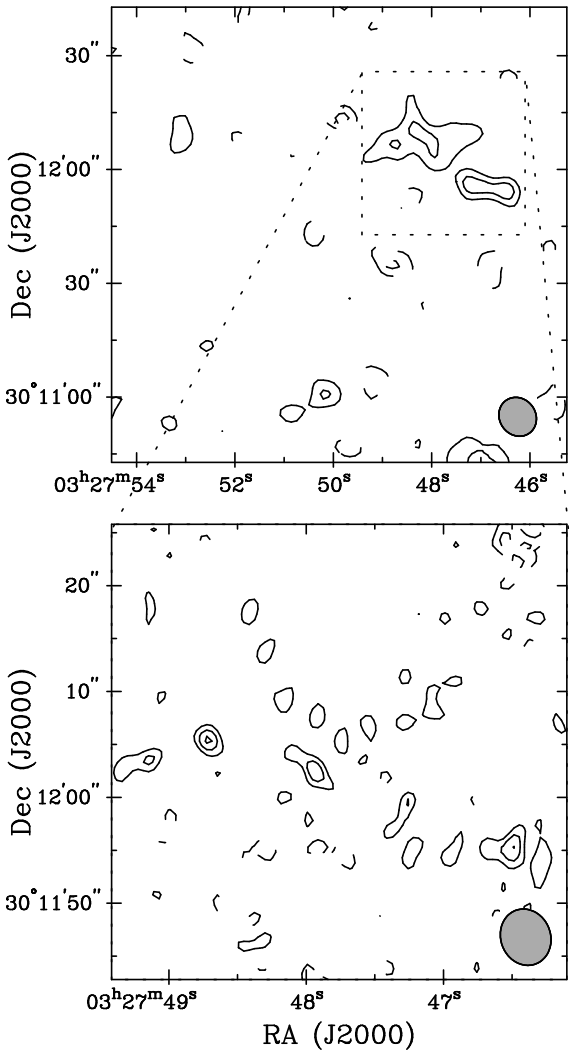

Figure 4.12: Maps of the $\lambda = 2.7$ mm continuum emission from L1455 A2. The contour intervals are $(-4, -3, -2, 2, 3, 4) \times \sigma$ in mJy beam^{-1}. *Top:* $\sigma = 1.0$ mJy beam^{-1}; beam is $10.6'' \times 9.5''$, P.A.$= 35.8°$. *Bottom:* $\sigma = 1.0$ mJy beam^{-1}; beam is $5.4'' \times 4.7''$, P.A.$= 20.3°$.

beam^{-1}) is located in the northeast quadrant near the edge of the map. When magnified in the $5''$ resolution map (lower panel), this object neither dissolves like L1455 IRS2, nor concentrates like a compact source. It appears as a patch of low level emission ($S_{peak} = 2.7$ mJy beam^{-1}) barely two beamwidths across. At higher resolution, this object is no longer detectable above the noise.

No significant source of continuum emission was detected from the L1455C core

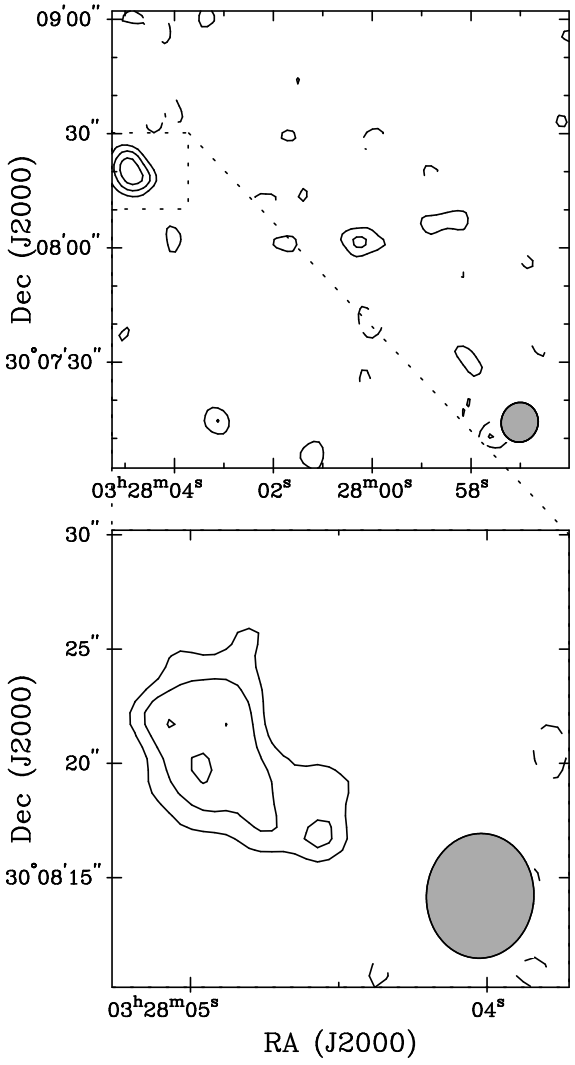

Figure 4.13: Maps of the $\lambda = 2.7$ mm continuum emission from L1455 B. The contour intervals are $(-4, -3, -2, 2, 3, 4) \times \sigma$ in mJy beam^{-1}. *Top:* $\sigma = 0.7$ mJy beam^{-1}; beam is $10.5'' \times 9.7''$, P.A.$= -13.0°$. *Bottom:* $\sigma = 0.6$ mJy beam^{-1}; beam is $5.5'' \times 4.7''$, P.A.$= -3.5°$.

at any resolution. The continuum maps of this core have been omitted.

4.7.3 $C^{18}O$ Data

Maps of the $C^{18}O$ emission from L1455A1 are shown in Figure 4.14. As in the maps of the continuum, no strong emission peak distinguishes the NH_3 core, but the continuum objects IRS1 and IRS1E are sources of $C^{18}O$ emission. In the map constructed from the FCRAO data alone (Figure 4.14*a*), the $C^{18}O$ seems to conspicuously avoid the A1 core. The peak emission zones in the L1455 cloud are just west and south of the primary beam area, and the center of the A1 core, between the two continuum sources, is marked by an emission trough. In the velocity map (Figure 4.14*b*), the patches of redshifted and blueshifted material resist interpretation. The northwest quadrant of the map favors velocities around 4.7-4.8 km s^{-1}, but otherwise, there is little evidence for systematic motion on the size scale of the L1455 cloud. The positions of the two continuum sources are undistinguished in velocity space.

At 10″ resolution (Figure 4.14*c*), the positions of IRS1 and IRS1E *are* distinguished as centers of $C^{18}O$ emission. The peak flux from IRS1 is 2.1 Jy $beam^{-1}$·km s^{-1}, and the peak flux from IRS1E is 2.0 Jy $beam^{-1}$·km s^{-1}. Both objects appear at the "edges" of the strong emitting regions seen in the FCRAO, and both objects are elongated by a few beamwidths in a north-south direction. The velocity field of the region (Figure 4.14*d*) has a mottled appearance throughout the full area of the map. The positions of the continuum sources are marked by patches of ∼5.1 km s^{-1}, but on the whole, the velocity field is flat, with no detectable gradients.

In the 5″ resolution map (Figure 4.14*e*), the $C^{18}O$ emission from IRS1 and IRS1E is still strong enough (S_{peak} = 0.64 and 0.70 Jy $beam^{-1}$·km s^{-1}, respectively) to be detected above the background emission. Both objects are extended in a north-south direction over approximately three beamwidths. The velocity field surrounding these

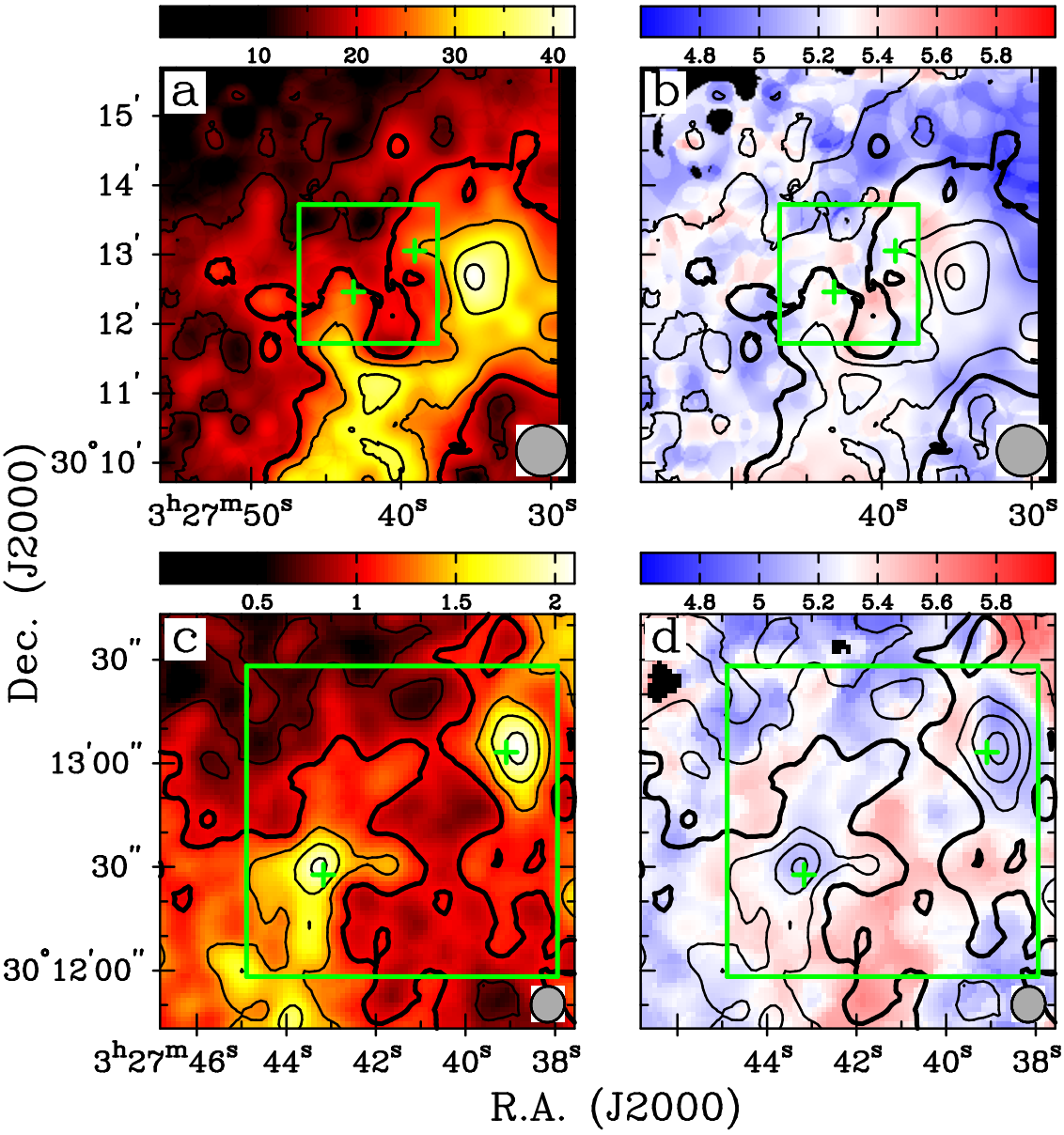

Figure 4.14: $C^{18}O$ $J = 1 \rightarrow 0$ integrated intensity and velocity of L1455 A1. Velocity range is 4.6-6.0 km s^{-1} in all panels. Plus symbols indicate positions of continuum sources, see Figures 4.10 & 4.11. (a,b) $I_\nu^{peak} = 42.17$ Jy beam^{-1}·km s^{-1}; $\sigma =$ 3.10 Jy beam^{-1}·km s^{-1}; beam is $44'' \times 44''$. (c,d) $I_\nu^{peak} = 2.06$ Jy beam^{-1}·km s^{-1}; $\sigma = 0.17$ Jy beam^{-1}·km s^{-1}; beam is $10.45'' \times 9.70''$, P.A.$= -12.9°$.

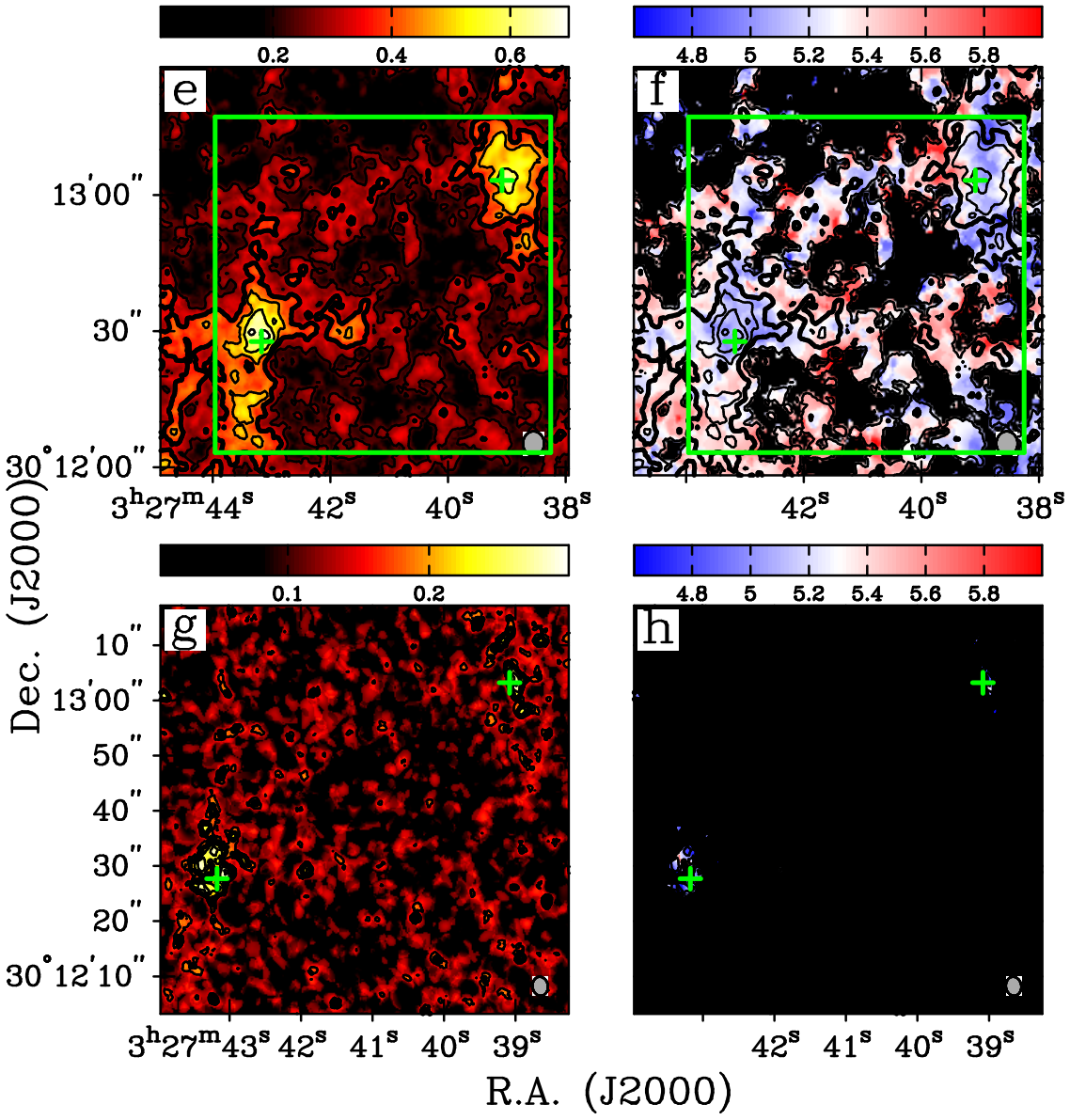

Figure 4.14: *Continued.* (e,f) I_ν^{peak} = 0.70 Jy beam^{-1}·km s^{-1}; σ = 0.08 Jy beam^{-1}·km s^{-1}; beam is 5.38″ × 4.67″, P.A.= 0.5°. (g,h) I_ν^{peak} = 0.23 Jy beam^{-1}·km s^{-1}; σ = 0.05 Jy beam^{-1}·km s^{-1}; beam is 3.46″ × 2.78″, P.A.= 7.7°.

objects (Figure 4.14*d*) continues to show no evidence for systematic motions. Both IRS1 and IRS1E are slightly blueshifted (4.9-5.0 km s^{-1}) with respect to the clumps of emission that surround them.

The continuum objects are still detectable in the 3″ resolution map (Figure 4.14*g*), but their intensities have waned. IRS1 is the weaker emitter; the position of peak emission (0.22 Jy $beam^{-1}$·km s^{-1}) is displaced roughly one beamwidth to the northwest of the continuum position. IRS1E appears near the center of a tight ring of emission. The peak intensity, on the western edge of this ring, is 0.22 Jy $beam^{-1}$·km s^{-1}. Although difficult to discern in Figure 4.14*h*, the velocity fields around both sources are exceptionally complex. The average velocity is bluer than the values found in the larger scale maps, but there is no preferred value. The velocities vary from pixel to pixel within a range of 4.5-5.6 km s^{-1}.

Figure 4.15 shows maps of the $C^{18}O$ emission from the L1455A2 core. Because there is no compact source of $C^{18}O$ emission in the core, maps made with the BIMA data at 3″ resolution showed only noise. These have been omitted. Even on 5″ scales (Figure 4.15*e*), no discrete source of $C^{18}O$ emission is detected.

The FCRAO map of the region shows the proximity of the L1455A2 and L1455A1 cores. In Figure 4.15*a*, L1455A1 appears in the pocket of reduced emission just west of the square denoting the primary beam area. Like L1455A1, L1455A2 is also not a strong $C^{18}O$ emitter. The bulk of the $C^{18}O$ emission from the L1455 cloud arises from the region in the southwest corner of the map. In the velocity map of the region (Figure 4.15*b*), the high emission zones along the western edge of the map are redshifted ($\sim$5.4 km s^{-1}) with respect to the weaker portions of the cloud. L1455A2 appears to be in a transition zone, although there is no smooth red-to-blue gradient across the primary beam area.

In the higher resolution maps of the core, the entire primary beam area is shown.

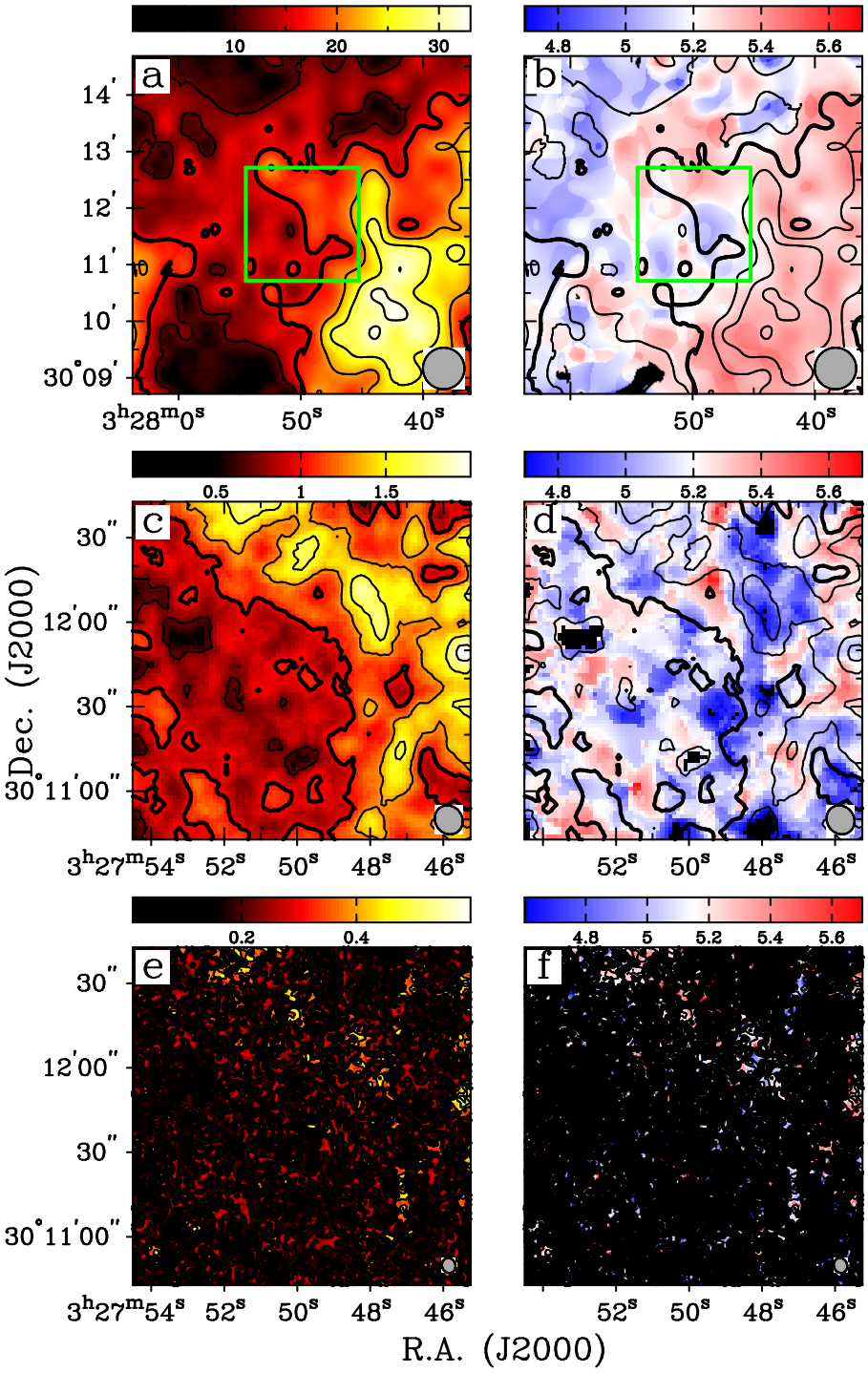

Figure 4.15: $C^{18}O$ $J = 1 \rightarrow 0$ integrated intensity and velocity of L1455 A2. Velocity range is 4.7-5.7 km s^{-1} in all panels. (a,b) I_ν^{peak} = 33.08 Jy $beam^{-1}$·km s^{-1}; σ = 2.7 Jy $beam^{-1}$·km s^{-1}; beam is $44'' \times 44''$. (c,d) I_ν^{peak} = 1.96 Jy $beam^{-1}$·km s^{-1}; σ = 0.20 Jy $beam^{-1}$·km s^{-1}; beam is $10.61'' \times 9.52''$, P.A.= 35.8°. (e,f) I_ν^{peak} = 0.59 Jy $beam^{-1}$·km s^{-1}; σ = 0.09 Jy $beam^{-1}$·km s^{-1}; beam is $5.40'' \times 4.70''$, P.A.= 20.3°.

L1455 IRS2, shown previously (Figure 4.12) to be a weak continuum source, is also not a substantial source of $C^{18}O$ emission. Although there is detectable $C^{18}O$ emission at the position of the continuum source (1.8 Jy beam^{-1}·km s^{-1} at 10″ resolution and 0.5 Jy beam^{-1}·km s^{-1} at 5″ resolution), this may be simply the diminishing contribution from the background cloud. The velocity field of this region is chaotic at both resolutions. There is no evidence for systematic motions associated with the emitting regions.

The integrated intensity and velocity maps from both the L1455B and L1455C cores, Figures 4.16 & 4.17 respectively, are similar to the maps of L1455A2: there is no compact source of $C^{18}O$ emission in either core. Consequently, the maps with 3″ resolution show only noise and have been omitted.

L1455B is only ∼4′ south of L1455A2, but it still does not appear in a region of strong $C^{18}O$ emission within the L1455 cloud. In the FCRAO data (Figure 4.16*a*), L1455B appears at the "edge" of a bright emission zone. The eastern half of the primary beam area shows an abundance of $C^{18}O$ emission, but the emission is much weaker in the western half. The region of strongest emission in the cloud (∼29 Jy beam^{-1}·km s^{-1}) appears in the northeast corner of the map. In the large-scale velocity map (Figure 4.16*b*), the peninsula of emission that extends southward from the northeastern corner, and which includes L1455B, is blueshifted with respect to the rest of the L1455 cloud.

In the higher resolution maps of the core, the entire area of the primary beam is shown, but no compact source of emission corresponding to IRS3 is detected. At both 10″ and 5″ resolutions, the emission peaks appear along the eastern edge of the maps and are contributed by the large-scale cloud seen in the FCRAO data. The behavior of the velocity field at higher resolutions upholds the trend identified in the FCRAO map: the emission zone in the eastern half of the map is generally

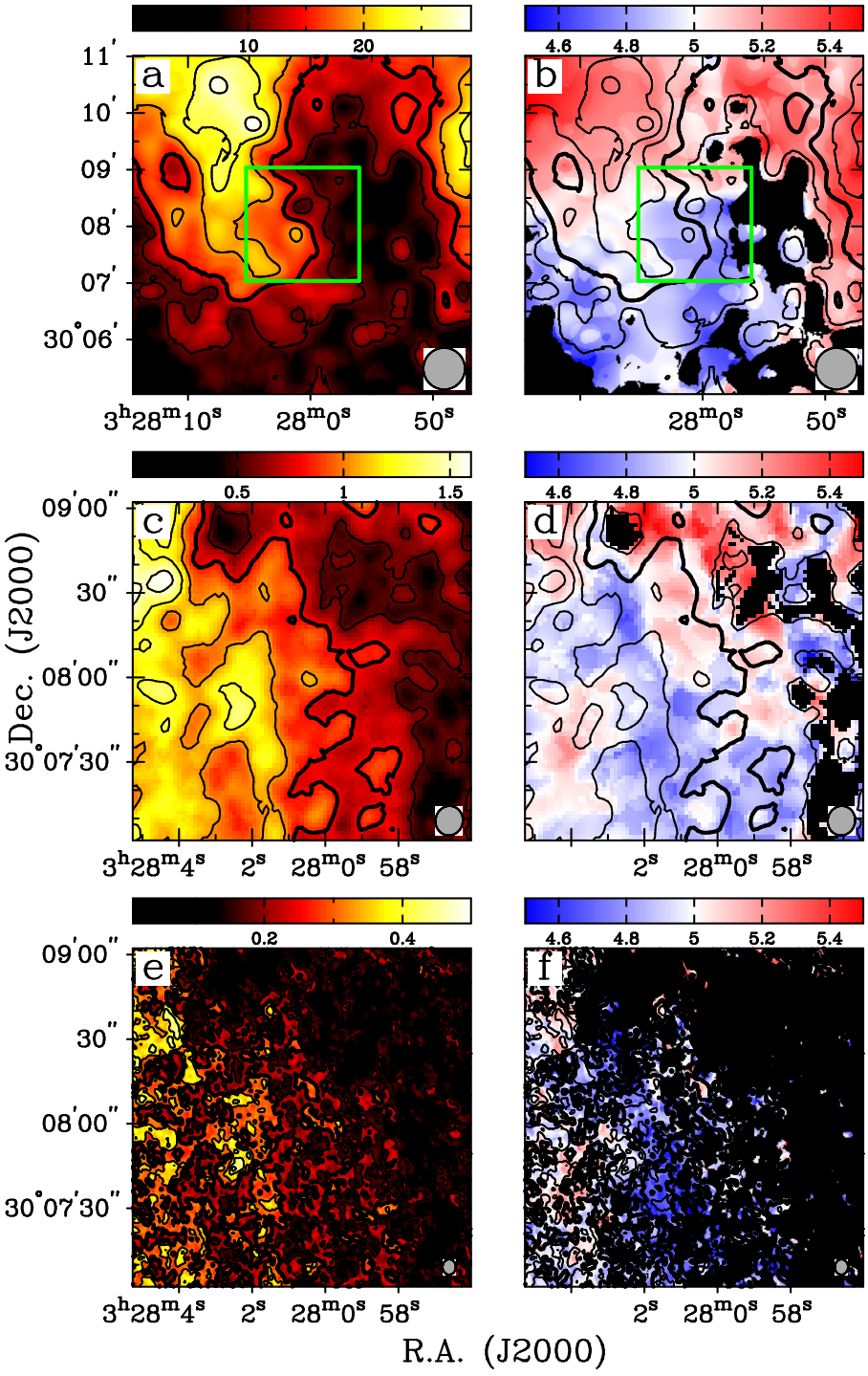

Figure 4.16: $C^{18}O$ $J = 1 \rightarrow 0$ integrated intensity and velocity of L1455 B. Velocity range is 4.5-5.5 km s^{-1} in all panels. (a,b) $I_\nu^{peak} = 29.24$ Jy beam^{-1}·km s^{-1}; $\sigma =$ 2.8 Jy beam^{-1}·km s^{-1}; beam is $44'' \times 44''$. (c,d) $I_\nu^{peak} = 1.52$ Jy beam^{-1}·km s^{-1}; $\sigma = 0.16$ Jy beam^{-1}·km s^{-1}; beam is $10.48'' \times 9.68''$, P.A.$= -13.0°$. (e,f) $I_\nu^{peak} =$ 0.46 Jy beam^{-1}·km s^{-1}; $\sigma = 0.06$ Jy beam^{-1}·km s^{-1}; beam is $5.46'' \times 4.70''$, P.A.$= -3.5°$.

blueshifted with respect to the rest of the L1455 cloud to the north. Although there are variations of a few km s^{-1}, the mean velocity of the emission zone in the 10″ and 5″ velocity maps is ∼4.8 km s^{-1}.

The $C^{18}O$ emission from L1455C in the FCRAO data (Figure 4.17*a*) appears on an "edge" of a portion of the L1455 cloud. Thus, all four of the L1455 cores mapped for the BIMA survey are *near* the clumps of peak $C^{18}O$ emission in the L1455 cloud, but (unlike the three cores presented in Chapter 2) no core is located *on* a bright emission clump. L1455C is the weakest $C^{18}O$ emitter of the four L1455 cores. No compact source was seen in the continuum emission maps, and no compact source is seen in the $C^{18}O$ emission maps (Figure 4.17) either. The scattered clumps of $C^{18}O$ emission that appear near the northern edge of the primary beam area in the 10″ and 5″ resolution maps are simply residual emission contributed by the FCRAO data. The velocity field of this area is remarkably flat, with no obvious systematic motions.

Figure 4.18 shows two representative spectra from the L1455 cloud. The spectra are taken through the two consistent continuum sources, L1455 IRS1 and L1455 IRS1E, seen in the L1455A1 maps. As in previous figures of this type, the spectra in the top row show the emission from the FCRAO data alone. The peak intensities immediately show how much weaker these sources are than the sources from the L1448 cloud. The lines from IRS1 and IRS1E are also do not have "clean" Gaussian shapes; the profiles from both sources are double peaked. When Gaussian functions are fitted to the profiles, the central velocities of the functions split the two peaks at 5.38 and 5.37 km s^{-1} for IRS1 and IRS1E, respectively. In the higher resolution spectra shown in the second, third, and fourth rows, the profiles tend to remain double-peaked, but for both sources, the blue peaks are stronger. The degree of the blue shift increases as the resolution of the map increases.

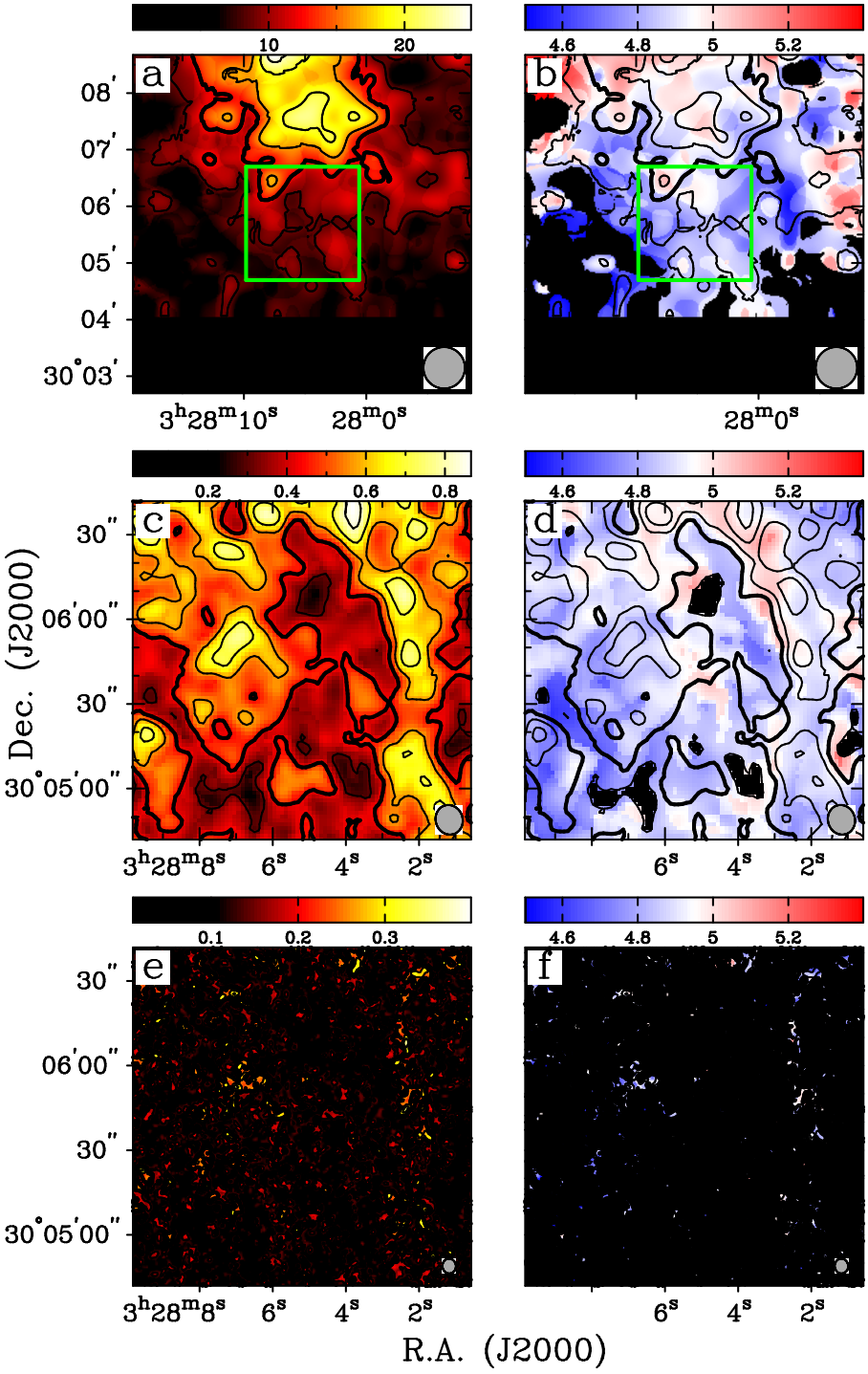

Figure 4.17: $C^{18}O$ $J = 1 \rightarrow 0$ integrated intensity and velocity of L1455C. Velocity range is 4.5-5.4 km s^{-1} in all panels. (a,b) $I_\nu^{peak} = 24.82$ Jy beam^{-1}·km s^{-1}; $\sigma =$ 2.3 Jy beam^{-1}·km s^{-1}; beam is $44'' \times 44''$. (c,d) $I_\nu^{peak} = 0.87$ Jy beam^{-1}·km s^{-1}; $\sigma = 0.10$ Jy beam^{-1}·km s^{-1}; beam is $10.62'' \times 9.55''$, P.A.$= 18.5°$. (e,f) $I_\nu^{peak} =$ 0.36 Jy beam^{-1}·km s^{-1}; $\sigma = 0.06$ Jy beam^{-1}·km s^{-1}; beam is $5.28'' \times 4.78''$, P.A.$= 5.6°$.

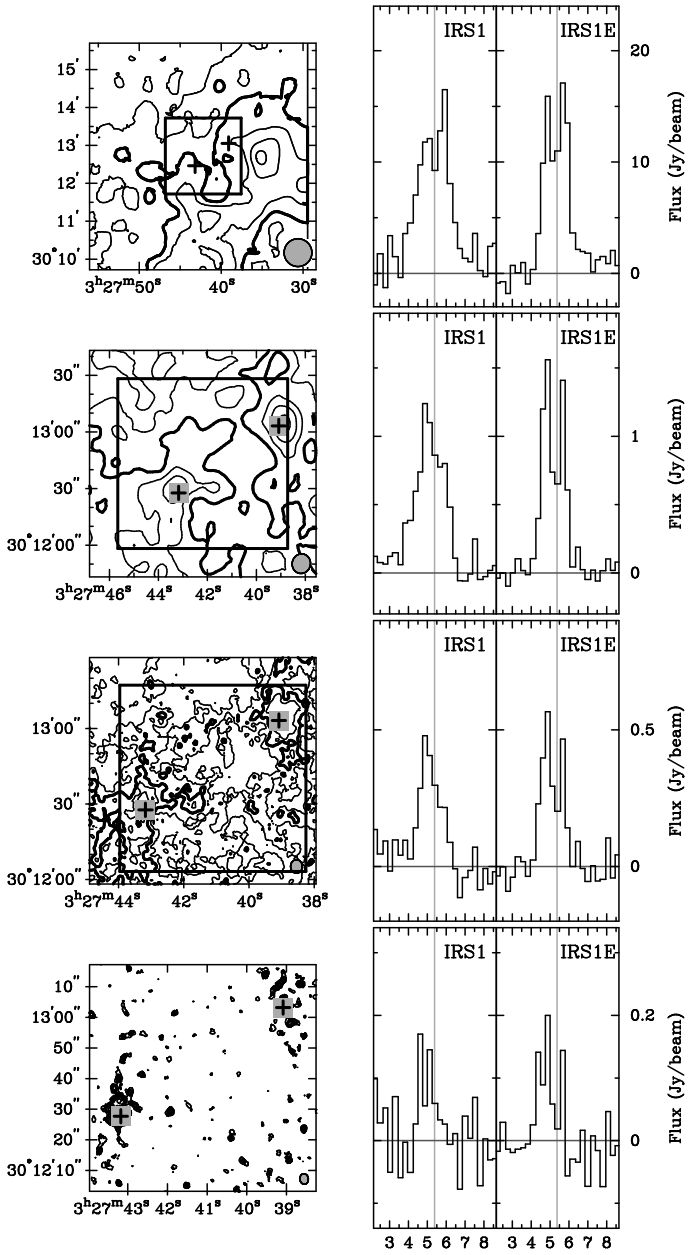

Figure 4.18: L1455A1 spectra. The plots at left show integrated intensity contours from the $C^{18}O$ data, as in Figure 4.14. To the right of each contour plot are spectra from the $C^{18}O$ datacubes. The plus symbols indicate the positions of the continuum sources IRS1 and IRS1 East. All spectra display the mean flux in Jy beam^{-1} taken over a beam area. In all rows, the gray vertical lines show central velocities of Gaussian functions fit to the profile from the FCRAO map (top row).

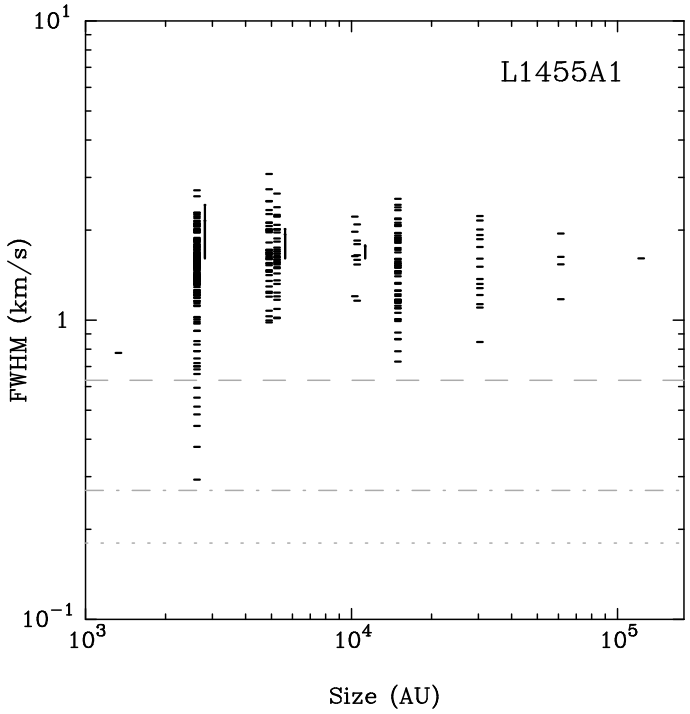

Figure 4.19: L1455A1 line width (FWHM) *vs.* grid size correlations for $C^{18}O$ spectra. The solid lines to the right side of the vertical clusters of points indicate the mean uncertainty in the FWHM measurements at that grid size; all uncertainties are displayed at the FWHM of the spectrum from the full FCRAO map (rightmost point). The dashed line indicates the line width corresponding to the sound speed of the medium: $\mathrm{FWHM}_{c_s}(20\ \mathrm{K}) = 0.63$ km s^{-1}. The dotted line indicates the thermal line width: $\mathrm{FWHM}_T(20\ \mathrm{K}) = 0.18$ km s^{-1}. The dash-dot line indicates the channel width of the spectra: $\delta V = 0.27$ km s^{-1}.

The generally noisy appearance of the spectra from L1455 IRS1 and IRS1E are indicative of the spectra from all of the cores in the L1455 cloud. Consequently, when the gridding method is applied to the datacubes from the L1455 A1, A2, B, and C cores to assess the correlation between line width and grid size, a significant number of spectra are excluded by the quality criteria. This is particularly true for L1455C, which has the smallest total of acceptable spectra. The correlations for the four cores are shown in Figures 4.19-4.22.

In addition to reducing the number of spectra included in the correlations, the noise in the spectra also increases the uncertainties in the measured FWHM of the

accepted lines. The thin vertical lines shown alongside the clusters of points representing the smaller grid squares in Figures 4.19-4.22 indicate the mean uncertainties in the FWHM measurements at that grid size. Because the correlations are plotted in logarithmic increments along the vertical axis, the line representing the uncertainty would vary in length depending upon where it is plotted. For the sake of uniformity, the line has been placed at the FWHM of the spectrum from the full FCRAO map, *i.e.* the rightmost point. Further down in the plot, the line would be longer; higher up in the plot, the line would be shorter. Because the line indicates a *mean* rather than a *median* uncertainty, its length may be somewhat biased toward larger values. Line widths with extremely high uncertainties, however, would have been excluded *a priori* from the diagram.

The uncertainties in the FWHM measurements from the L1455 spectra are categorically higher than the uncertainties seen in the measurements from the L1448 spectra. The mean uncertainties in the four L1455 cores are greater by factors ranging from $\sim$1.5 (L1455B) to $\sim$3 (L1455A1). As a result, the range of FWHM measured in the smaller grid squares gains less significance and is clearly a less reliable indicator of core turbulence. As an example, the line widths measured in the spectra from the L1455C core (Figure 4.22) are approximately within the same range at grid sizes of 10500, 5250, and 2625 AU. These lines are all quite narrow, with no FWHM exceeding 1 km s^{-1}. The uncertainty in the measurements increases at smaller grid sizes; at 2625 AU, the mean uncertainty is 0.37 km s^{-1}, a value nearly as great as the width of the narrowest line. Thus, even though the uncertainty does not overlap the wide and narrow extremes, it may make a significant contribution to the observed range of FWHM. This is *in contrast* to the spread in FWHM seen in cores like L1448 IRS2 and L1448C. In those cores (Figures 4.4 & 4.8), the range of observed line widths *cannot* be attributed to the uncertainty in the fit of the

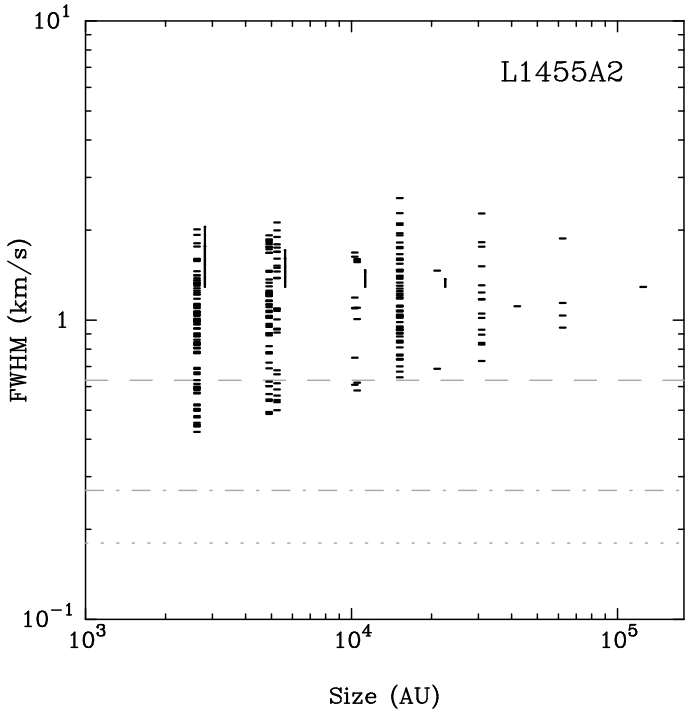

Figure 4.20: L1455A2 line width (FWHM) *vs.* grid size correlations for $C^{18}O$ spectra. The solid lines to the right side of the vertical clusters of points indicate the mean uncertainty in the FWHM measurements at that grid size; all uncertainties are displayed at the FWHM of the spectrum from the full FCRAO map (rightmost point). The dashed, dotted, and dash-dot lines are the same as in Figure 4.19.

Gaussian functions.

Keeping the measuring uncertainties in mind, the behavior of the line width *vs.* grid size correlation varies between the cores in the L1455 cloud. The FWHM measured from the L1455A1 spectra are, on average, greater than the FWHM from the other cores. L1455C has, on average, the narrowest lines. Only a few (2.0%) of the lines from L1455A1 fall below the sonic threshold: $\mathrm{FWHM}_{c_s}(20\ \mathrm{K}) = 0.63\ \mathrm{km\ s^{-1}}$. In l1455A2, L1455B, and L1455C, the percentages of FWHM below the sonic line are 14.1%, 29.4%, and 51.6%, respectively.

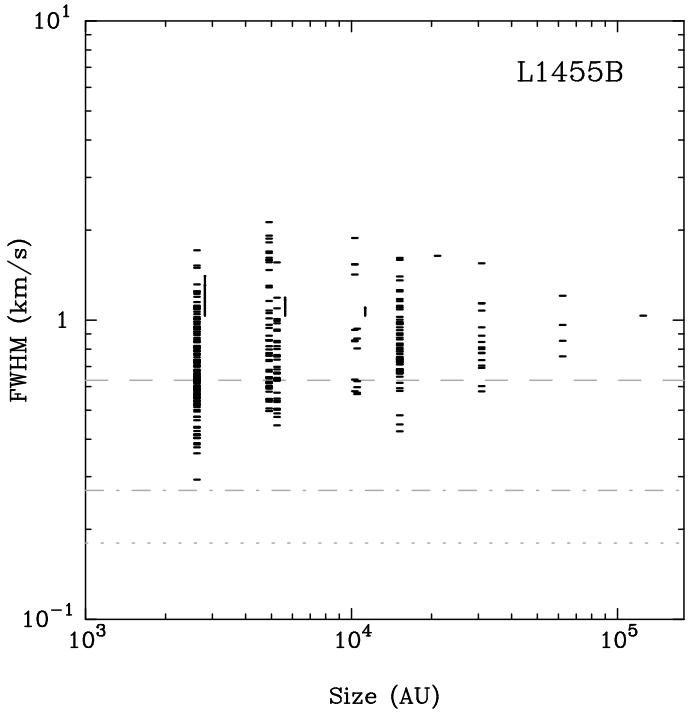

Figure 4.21: L1455B line width (FWHM) *vs.* size correlations for gridded $C^{18}O$ spectra. The solid lines to the right side of the vertical clusters of points indicate the mean uncertainty in the FWHM measurements at that grid size; all uncertainties are displayed at the FWHM of the spectrum from the full FCRAO map (rightmost point). The dashed, dotted, and dash-dot lines are the same as in Figure 4.19.

4.8 NGC1333 IRAS8

4.8.1 Background

IRAS8 lies near the center of the NGC1333 reflection nebula. It is the most powerful source in NGC1333 detected with the IRAS CPC at 50 and 100 μm (Jennings *et al.* 1987). IRAS8 is assumed to be associated with the optically visible source SVS3, which is likely an obscured Herbig Ae-Be star, roughly 30″ away Harvey, Wilking, & Joy (1984). The target for the BIMA survey was *not* specifically IRAS8 or SVS3. Instead, the pointing center for the BIMA observations was selected based upon the SCUBA maps of 450 and 850 μm emission of Sandell & Knee (2001). The maps (see

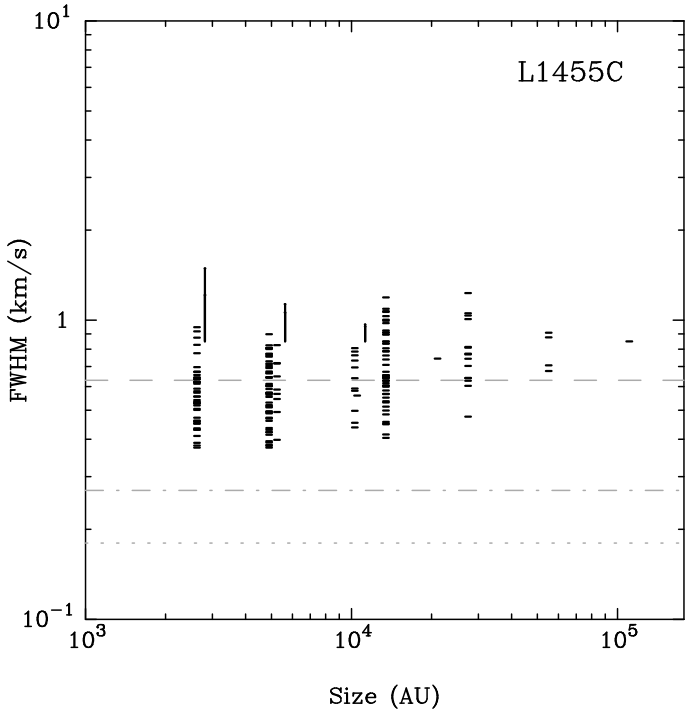

Figure 4.22: L1455C line width (FWHM) *vs.* size correlations for gridded $C^{18}O$ spectra. The solid lines to the right side of the vertical clusters of points indicate the mean uncertainty in the FWHM measurements at that grid size; all uncertainties are displayed at the FWHM of the spectrum from the full FCRAO map (rightmost point). The dashed, dotted, and dash-dot lines are the same as in Figure 4.19.

their Figure 1) show clumps of emission slightly south and west of SVS3; on their list of "compact sources," these clumps are assigned numbers 28 and 29. [These clumps are also detected in the BIMA maps of 2.7 mm continuum emission (see below) and will be referred to as SK28 and SK29.] The BIMA pointing center was placed in between the two "compact sources." Within the primary beam area are included SVS3, $\sim 10''$ north of SK28, and an IRAS point source, 03260+3111, which is another $8''$ further north. IRAS8 is offset to the northeast quadrant.

A number of optical (Bally, Devine, & Reipurth 1996), submillimeter (Sandell & Knee 2001), and millimeter (Sun *et al.* 2000) observations collectively suggest that the northern end of the NGC1333 star formation region is quite complex. Large-

scale single-dish observations of the ^{13}CO and C^{18}O lines, made with a resolution of 55″ indicate that the region identified as IRAS8 may harbor several embedded YSOs (Sun *et al.* 2000).

4.8.2 Continuum Data

The continuum maps of the NGC1333 IRAS8 region with 10″ resolution (Figures 4.23 and 4.24) look strikingly similar to the 850 μm map of the same region presented by Sandell & Knee (2001). The extended emission zone just east of map center (S_{peak} = 6.3 mJy beam^{-1}) and the stronger emission peak (S_{peak} = 21.1 mJy beam^{-1}) just west of center each have their counterparts, SK28 and SK29 respectively, in the 850 μm map. In the upper panel of Figure 4.23, the northernmost of the three 5σ contours marks the precise location of SVS3, while the 5σ contour 8″ below it marks the location of the 850 μm peak of SK28. When the resolution of the map is increased to 5″, however (lower panel), SK28 dissolves into a cluster of emission clumps. Neither the location of SVS3 (2.2 mJy beam^{-1}) nor that of the SK28 850 μm peak (0.8 mJy beam^{-1}) distinguishes itself as a source of compact emission. The point of peak 2.7 mm flux in SK28 (S_{peak} = 4.1 mJy beam^{-1}) appears $\sim$15″ further west.

The three panels of Figure 4.24 zoom in on SK29. At 10″ resolution, the source is strong and compact but not circularly symmetric: the lower-level contours show a bulge of emission on the southwest side. At 5″ resolution, the bulge has broken off from the main source and is seen as a separate, relatively weak (S_{peak} = 3.4 mJy beam^{-1}), kidney-shaped emission zone. At higher resolution, this zone is not seen above the noise. The SK29 object, on the other hand, remains compact and unresolved at all resolutions. At 5″, its flux is 21.0 mJy beam^{-1}, and at 3″, the flux is 20.5 mJy beam^{-1}. No continuum emission is detected from IRAS 03260+3111; the

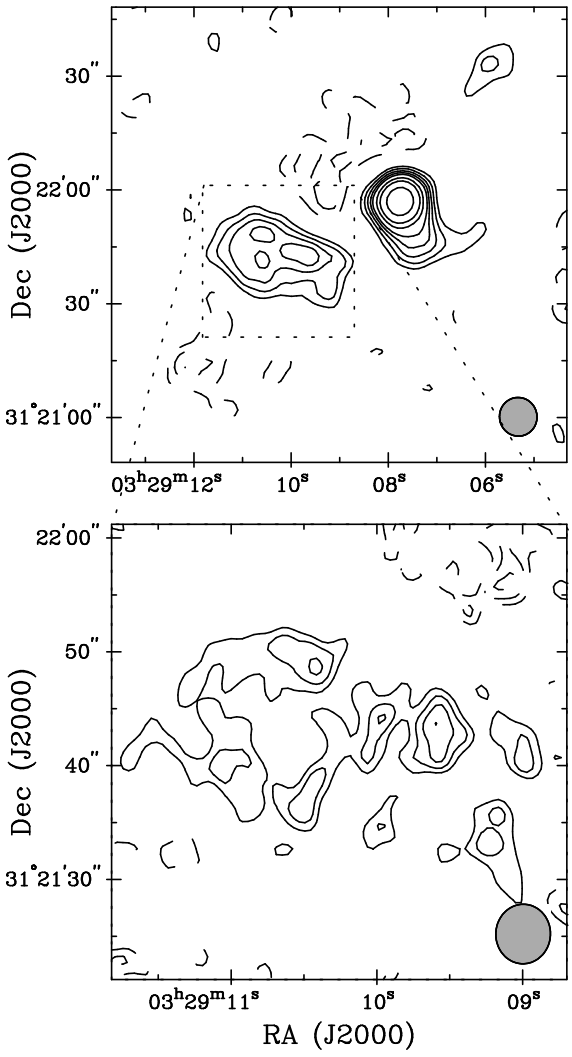

Figure 4.23: Maps of the $\lambda = 2.7$ mm continuum emission from NGC1333 IRAS8 SK28. The contour intervals are $(-4, -3, -2, 2, 3, 4, 5) \times \sigma$ in mJy beam^{-1}. *Top:* $\sigma = 1.1$ mJy beam^{-1}; beam is $10.2'' \times 9.9''$, P.A.$= 10.6°$. *Bottom:* $\sigma = 0.8$ mJy beam^{-1}; beam is $5.2'' \times 4.8''$, P.A.$= -2.9°$.

coordinates from the Point Source Catalog place it $\sim 30''$ east of SK29 (and north of SK28). Because of the uncertainty in PSC coordinates, it is plausible that IRAS 03260+3111 and SK29 are the same object.

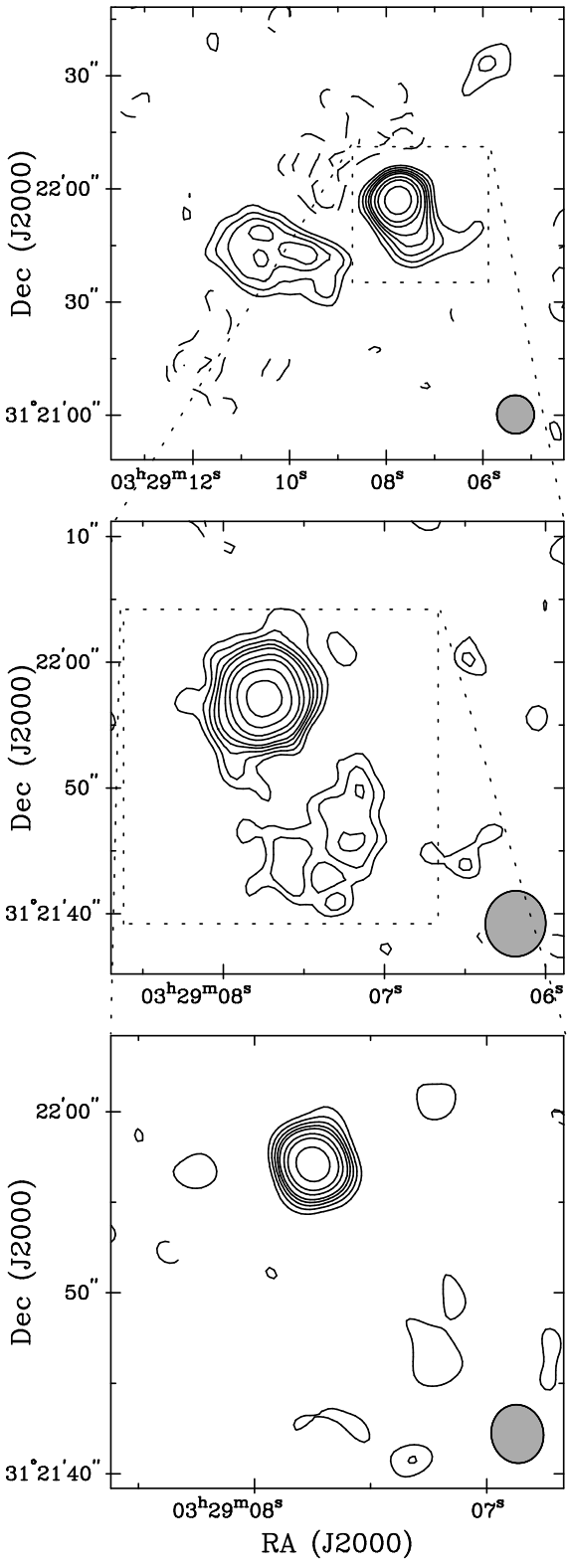

Figure 4.24: Maps of the $\lambda = 2.7$ mm continuum emission from NGC1333 IRAS8 SK29. The contour intervals are $(-4, -3, -2, 2, 3, 4, 5, 6, 8, 10, 14.14, 20) \times \sigma$ in mJy beam^{-1}. *Top:* $\sigma = 1.1$ mJy beam^{-1}; beam is $10.2'' \times 9.9''$, P.A.$= 10.6°$. *Middle:* $\sigma = 0.8$ mJy beam^{-1}; beam is $5.2'' \times 4.8''$, P.A.$= -2.9°$. *Bottom:* $\sigma = 1.1$ mJy beam^{-1}; beam is $3.2'' \times 2.9''$, P.A.$= 9.8°$.

4.8.3 $C^{18}O$ Data

The positions of SK28 and SK29 are indicated by the plus symbols in the panels of Figure 4.25, which show maps of the $C^{18}O$ emission from the NGC1333 IRAS8 region. Unlike the continuum maps, neither SK object distinguishes itself as a site of strong $C^{18}O$ emission. In the maps made from the FCRAO data (Figure 4.25*a*), the continuum positions are located along the upper edge of a strong filament of emission that extends diagonally through the map between the northwest and southeast corners. This filament is the northern arc of a prominent "shell-like" feature that is seen in lower resolution observations of $C^{18}O$ (Warin *et al.* 1996) and ^{13}CO (Sun *et al.* 2000). The point of peak emission in the filament (S_{peak} = 140.5 Jy beam^{-1}·km s^{-1}) appears just off the western edge of the BIMA primary beam. The intensities at SK28 and SK29 are 82 and 95 Jy beam^{-1}·km s^{-1}, respectively. In the velocity map of the FCRAO data (Figure 4.25*b*), the behavior of the velocities does not seem to be dictated by any systematic large-scale either along or across the long axis of the filament. The reddest velocities in the map (8.1-8.2 km s^{-1}) are found at the northwest and southeast extremes of the filament. Near the point of peak emission, the velocity is bluer (7.5-7.6 km s^{-1}). Thus, along the length of the filament and across the area of the BIMA primary beam there is a velocity gradient of $\sim$0.5 km s^{-1}.

In the 10″ resolution maps (Figure 4.25*c,d*), SK28 and SK29 appear, again, on the fringes of the $C^{18}O$ emitting region. The broad filament of $C^{18}O$ emission dominates three-quarters of the map area. Both SK28 and SK29 are located on the 50% contour that snakes through the middle of the map, but no clump of enhanced emission signals their presence. The strongest emission, in the northwest corner, peaks at 9.0 Jy beam^{-1}·km s^{-1}. The velocity map highlights the contrast between the blueshifted zone near the emission peak (7.5 km s^{-1}) and the redshifted zone

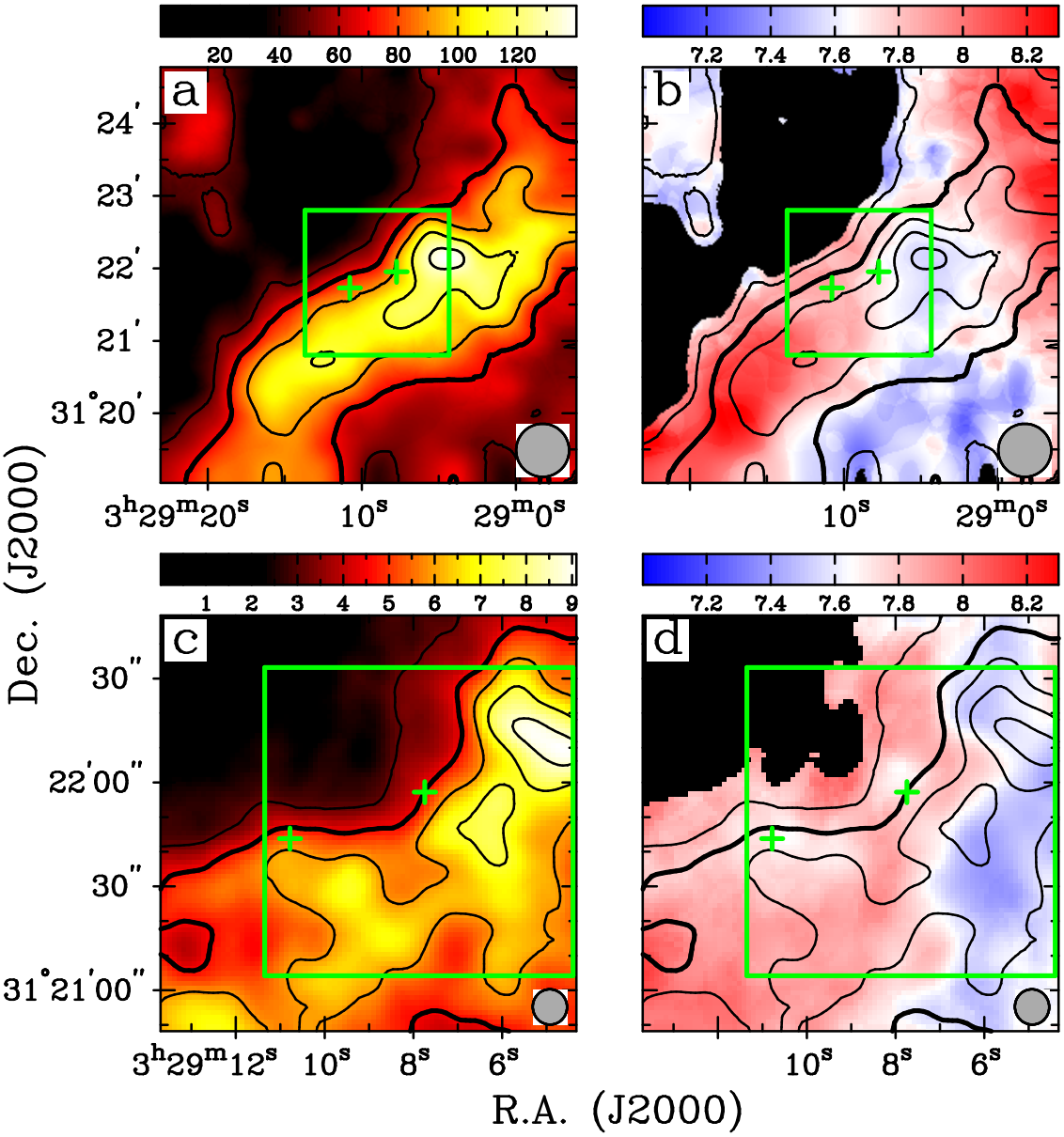

Figure 4.25: $C^{18}O$ $J = 1 \rightarrow 0$ integrated intensity and velocity of NGC1333 IRAS8. Velocity range is 7.0-8.3 km s^{-1} in all panels. Plus symbols indicate positions of continuum sources from Figures 4.24. (a,b) I_ν^{peak} = 140.49 Jy $beam^{-1}$·km s^{-1}; σ = 14.2 Jy $beam^{-1}$·km s^{-1}; beam is $44'' \times 44''$. (c,d) I_ν^{peak} = 9.03 Jy $beam^{-1}$·km s^{-1}; σ = 0.85 Jy $beam^{-1}$·km s^{-1}; beam is $10.20'' \times 9.88''$, P.A.= 10.6°.

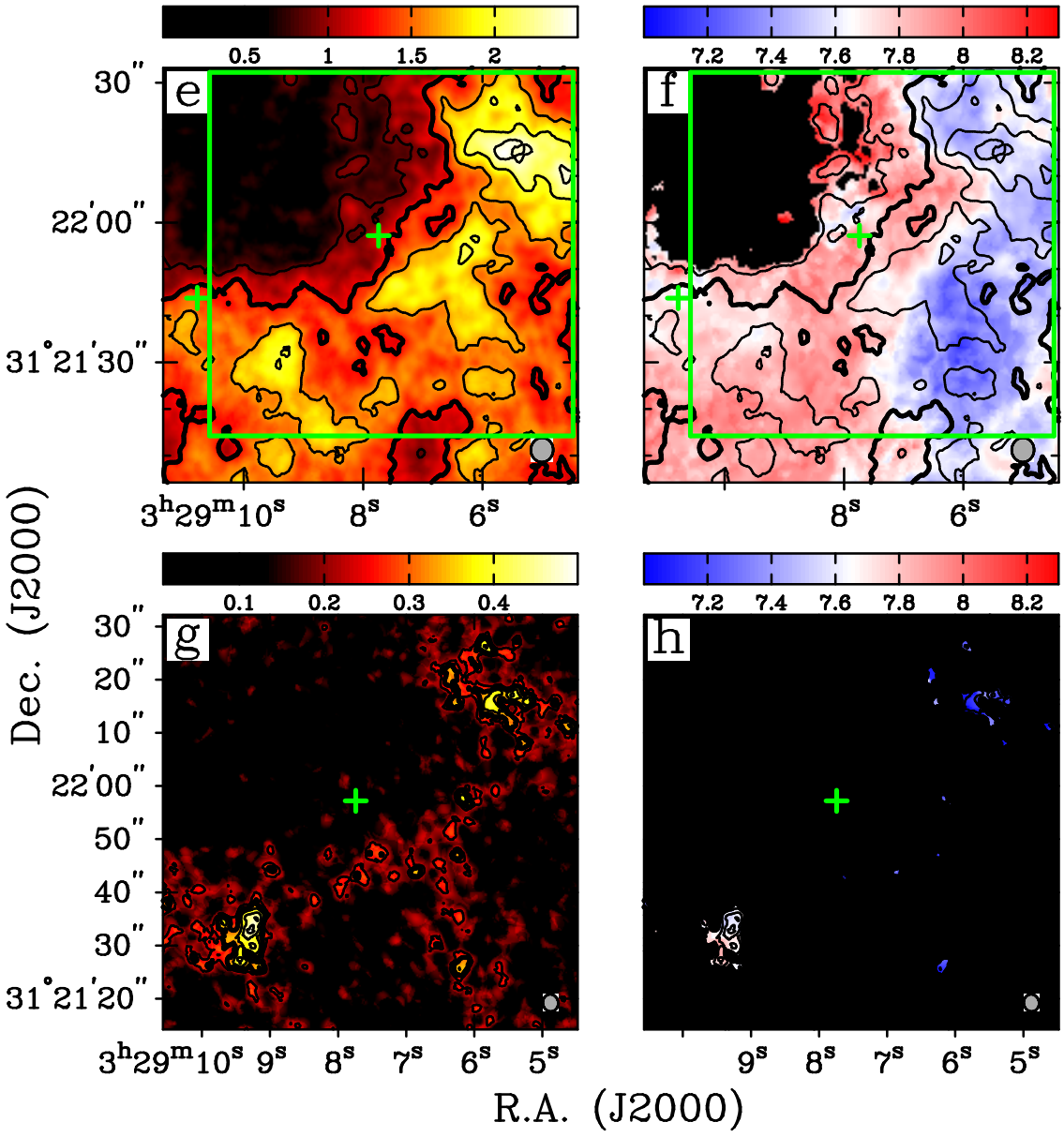

Figure 4.25: *Continued.* (e,f) I_ν^{peak} = 2.43 Jy beam^{-1}·km s^{-1}; σ = 0.25 Jy beam^{-1}·km s^{-1}; beam is 5.23″ × 4.80″, P.A.= −2.9°. (g,h) I_ν^{peak} = 0.44 Jy beam^{-1}·km s^{-1}; σ = 0.07 Jy beam^{-1}·km s^{-1}; beam is 3.24″ × 2.88″, P.A.= 9.8°.

in the eastern half of the map. The higher resolution reveals that the changes in velocity along the length of the $C^{18}O$ filament are not as smooth as they appear in the FCRAO map. Over the width of a beam, the velocities vary between 7.7 and 8.1 km s^{-1}.

At 5″ resolution (Figure 4.25*e,f*), the sites of continuum emission remain undistinguished in the $C^{18}O$ intensity map. Within the filament, however, the $C^{18}O$ emission traces at least three compact clumps of emission; the peak intensities from these clumps are 2.4, 2.0, and 2.0 Jy $beam^{-1}$·km s^{-1}. The velocity map at this resolution accents the lumpiness of the velocity structure within the filament. The overall velocity field still features a blueshifted western half and a redshifted eastern half, but there is no evidence for a smooth, large-scale trend. The presence of small-scale gradients within the three compact $C^{18}O$ emission clumps is uncertain. Another notable feature is that the full range of velocities identified in the colorscale are only seen (in the BIMA beam area) in the high resolution velocity maps.

The three compact $C^{18}O$ features are still detectable in the 3″ resolution emission map (Figure 4.25*g*); they appear above the noise at the 6σ, 5σ, and 4σ level. SK28 and SK29 are still not. In the corresponding velocity map, the remaining emission clumps still show the range of velocities along the filament. The northwestern clump is centered at 7.0 km s^{-1}, and the southeastern clump is centered at 7.8 km s^{-1}.

In keeping with the trend established from previous cores in the survey, Figure 4.26 shows examples of spectra from the core taken at the positions of the continuum sources. Because of the paucity of $C^{18}O$ emission at these locations, this choice has its drawbacks. The lines from SK28 and SK29 shown in the four rows of Figure 4.26 are not as strong as the lines from other positions along the $C^{18}O$ filament, but nevertheless, they share a crucial feature with most other spectra: their profiles show multiple emission peaks. At all resolutions, the $C^{18}O$ spectra

from SK28 and SK29 are double-peaked. A strong emission peak appears on the blueward side of the mean velocity, and a secondary peak appears on the redward side. Spectra taken from other positions in the map also show complicated profiles, in some cases with more than two line peaks.

Multi-component line profiles complicate the application of the gridding method of analyzing the line widths. Because the `gridspec` routine fits each spectrum with a single Gaussian function, information about multiple lines is lost. Furthermore, fitting single Gaussian functions to obviously double-peaked spectra such as those in Figure 4.26 systematically increases the measured line widths, as well as the χ^2 values of the fits. The value of χ^2 is employed as a quality criterion, and consequently, a larger number of spectra with strong lines are excluded from the line width *vs.* grid size diagram.

The total number of measured FWHM displayed in Figure 4.27 is 251. As with the line width *vs.* grid size correlations displayed for other cores, the measured FWHM for a particular grid size have a range of values. In most cores, the FWHM are either evenly distributed around a central value or favor a value toward the low end of the full range. However, the FWHM measured in the NGC1333 IRAS8 region tend to cluster around values at the large end of the distribution. On 5000 and 2500 AU scales, most FWHM have values around 2 km s^{-1}. Only 2% of the 2500 AU grid squares have FWHM below the sonic value (0.63 km s^{-1}). The sudden drop in the FWHM of the lines from the 1250 AU grid squares is unexepected. At that resolution, 60% of the lines are below the sonic threshold and all of the lines are well below the trend in mean values established by the larger grid squares.

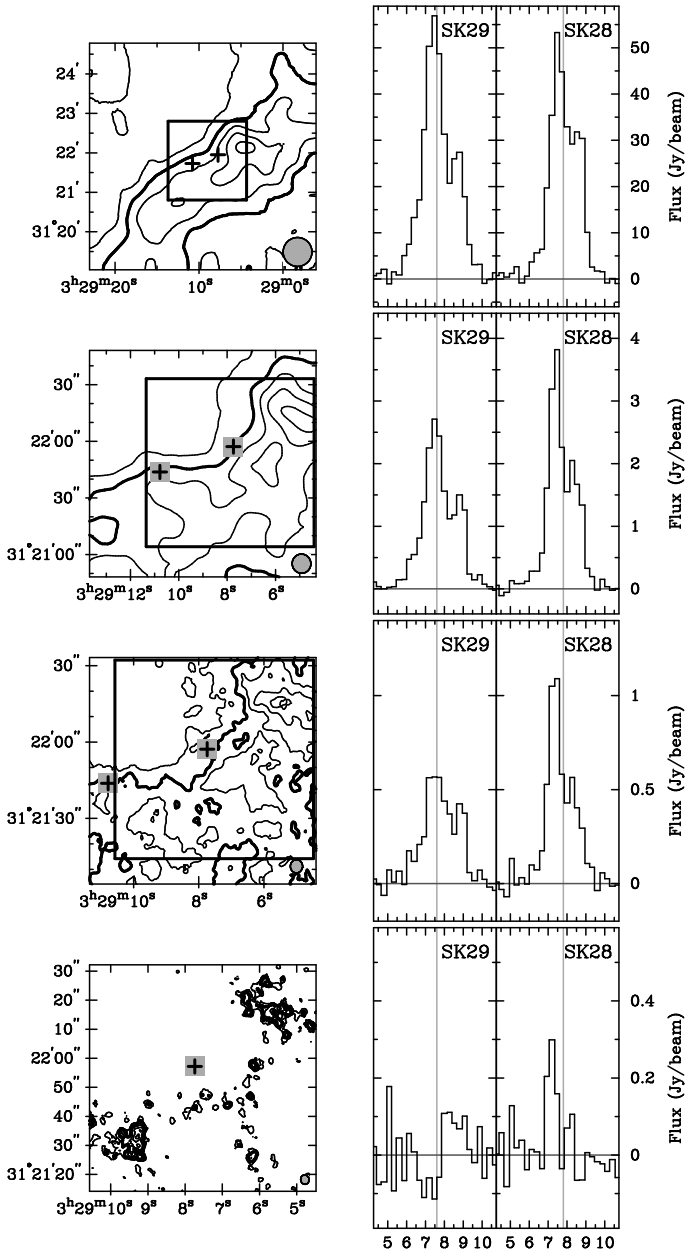

Figure 4.26: NGC1333 IRAS8 spectra. The plots at left show integrated intensity contours from the $C^{18}O$ data, as in Figure 4.25. To the right of each contour plot are spectra from the $C^{18}O$ datacubes. The plus symbols indicate the positions of the SK28 and SK29 continuum sources, shown in Figures 4.23 & 4.24. All spectra display the flux in Jy beam^{-1} averaged over the area of a beam. In all rows, the gray vertical lines show central velocity of a Gaussian function fit to the profile from the FCRAO map (top row).

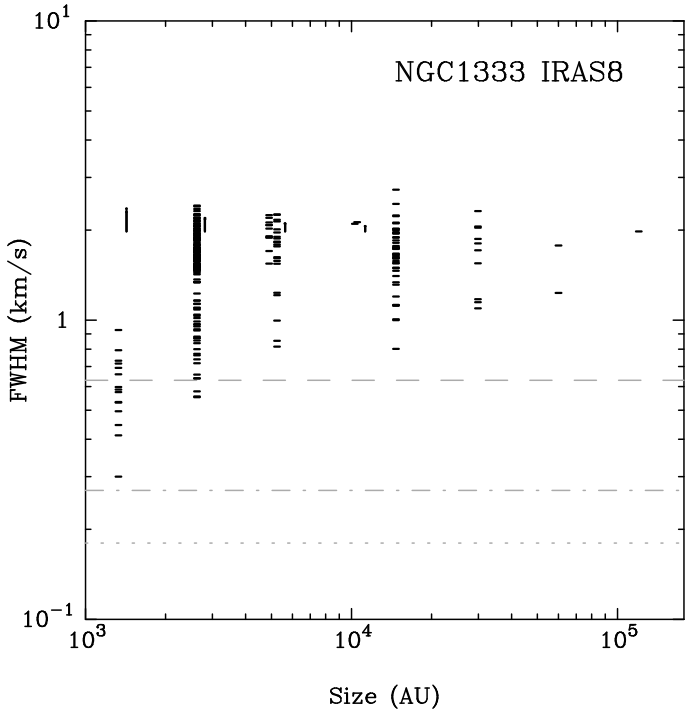

Figure 4.27: NGC1333 IRAS8 line width (FWHM) *vs.* size correlations for gridded $C^{18}O$ spectra. The dashed line indicates the line width corresponding to the sound speed of the medium: $\mathrm{FWHM}_{c_s}(20\ \mathrm{K}) = 0.63$ km s^{-1}. The dotted line indicates the thermal line width: $\mathrm{FWHM}_T(20\ \mathrm{K}) = 0.18$ km s^{-1}. The dash-dot line indicates the channel width of the spectra: $\delta V = 0.27$ km s^{-1}.

4.9 Per4 South

4.9.1 Background

The Per4 South core is located in a high density region that curls northeastward of the NGC1333 nebula (Cernicharo, Bachiller, & Duvert 1985), approximately 5′ north of NGC1333 SK32 (see below). Per4S was first identified as a site of compact NH_3 emission in a survey of IRAS point source by Ladd, Myers, & Goodman (1994), where it is identified as Per4[-1,-6] for its offset (in arc-minutes) from IRAS 03262+3123. Using a constant density sphere as a model, they estimated a core mass of 12 M⊙. In a more recent study, Per4S was examined by Caselli *et al.*

(2002a) as part of a large survey of N_2H^+ emission from cores. They divide the Per4 region into three clumps; the Per4S core in the BIMA survey corresponds to their Per4B. From the N_2H^+ lines, they detect a shallow velocity gradient with a magnitude of 0.64 ± 0.05 km s^{-1} pc^{-1} and a position angle of $-17° \pm 6°$. Moreover, Per4S is one of only four cores in their survey in which the observed line widths are inversely correlated with impact parameter. The line widths narrow at greater distances from the core center. Per4S also showed an inverse correlation between line width *dispersion* and impact parameter. So, not only do line widths decrease at further from the core center, but the variation in line widths also decreases.

4.9.2 Continuum Data

Although not associated with a known infrared source, Per4S shows up clearly in $\lambda = 2.7$ mm continuum emission (Figure 4.28). In the top panel, the envelope around Per4S is resolved by the $10''$ beam. The emitting region is extended by roughly 5 beam widths in the north-south direction; in the east-west direction, the emission is roughly 2.5 beam widths. The peak intensity at this resolution is 9.5 mJy beam^{-1}. At $5''$ resolution (middle panel), the morphology of the emitting region becomes more difficult to interpret. The structure suggests neither a smooth envelope distribution nor a flattened disk. Although primarily elongated in the north-south direction, the high emission contours near the peak (4.7 mJy beam^{-1}) are extended by $\sim$4 beam widths along a northwest-southeast axis. Conclusive evidence that this complicated structure obscures the presence of multiple protostars is not forthcoming in the $3''$ map (bottom panel). At this resolution, the emission structure evaporates into a collection of 3σ clumps.

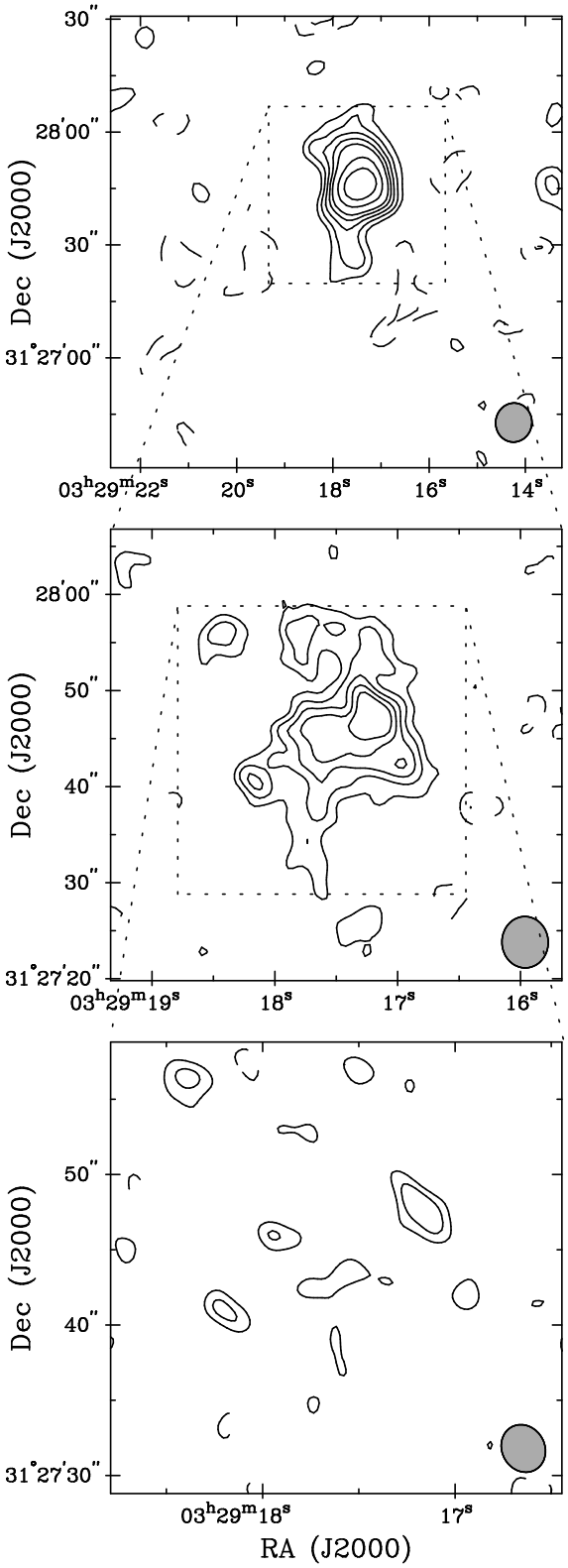

Figure 4.28: Maps of the $\lambda = 2.7$ mm continuum emission from Per4 South. The contour intervals are $(-4, -3, -2, 2, 3, 4, 5, 6, 8, 10) \times \sigma$ in mJy beam^{-1}. *Top:* $\sigma = 0.8$ mJy beam^{-1}; beam is $10.4'' \times 9.6''$, P.A.$= -7.2°$. *Middle:* $\sigma = 0.6$ mJy beam^{-1}; beam is $5.4'' \times 4.8''$, P.A.$= 2.2°$. *Bottom:* $\sigma = 0.9$ mJy beam^{-1}; beam is $3.3'' \times 2.8''$, P.A.$= 29.1°$.

4.9.3 $C^{18}O$ Data

The Y-shaped morphology of the large-scale $C^{18}O$ emission in the vicinity of the Per4S core (Figure 4.29*a*) is very similar to the shape of the N_2H^+ emission in the map of the region created by Caselli *et al.* (2002a). In the N_2H^+ map, the emission peaks in the "arms" of the Y; in the $C^{18}O$ map presented here, the emission clearly peaks in the base of the Y. The emission peak, 54.3 Jy beam^{-1}·km s^{-1}, is located just below the southern edge of the BIMA primary beam area. The secondary peak, within the primary beam area, is only slightly lower at 54.1 Jy beam^{-1}·km s^{-1}. Although the position of Per4S itself is not marked by an emission peak, it appears near the vertex of the Y. In the velocity fields shown in Figure 4.29*b*, the center of the map is a hodge-podge. Within the primary beam area, no trends are apparent, but the range of velocities in this area is fairly narrow ($\sim$0.4 km s^{-1}). Although the eastern edge of the larger map generally exhibits bluer ($\sim$7.2 km s^{-1}) velocities, and the western edge of the map generally exhibits redder ($\sim$7.9 km s^{-1}) velocities, no correlation with intensity is apparent.

In the intensity map with 10″ resolution (Figure 4.29*a*), the location of the Per4S continuum source is revealed to also be a center of $C^{18}O$ emission. The peak flux here, 3.9 Jy beam^{-1}·km s^{-1}, is displaced by less than a beam width from the continuum position. The envelope of $C^{18}O$ emission around Per4S is clearly elongated in a north-south direction; the long tendrils of emission traced by the 35% and 50% contours extend for 3-4 beam widths in either direction from the peak. The emission peak in the southwestern corner of the map, 3.8 Jy beam^{-1}·km s^{-1}, shows the proximity of the denser region seen in the FCRAO map. In the velocity map of the region (Figure 4.29*b*), the velocity at the center of Per4S is 7.5 km s^{-1}. West of this position, the velocity remains about the same. To the north and south,

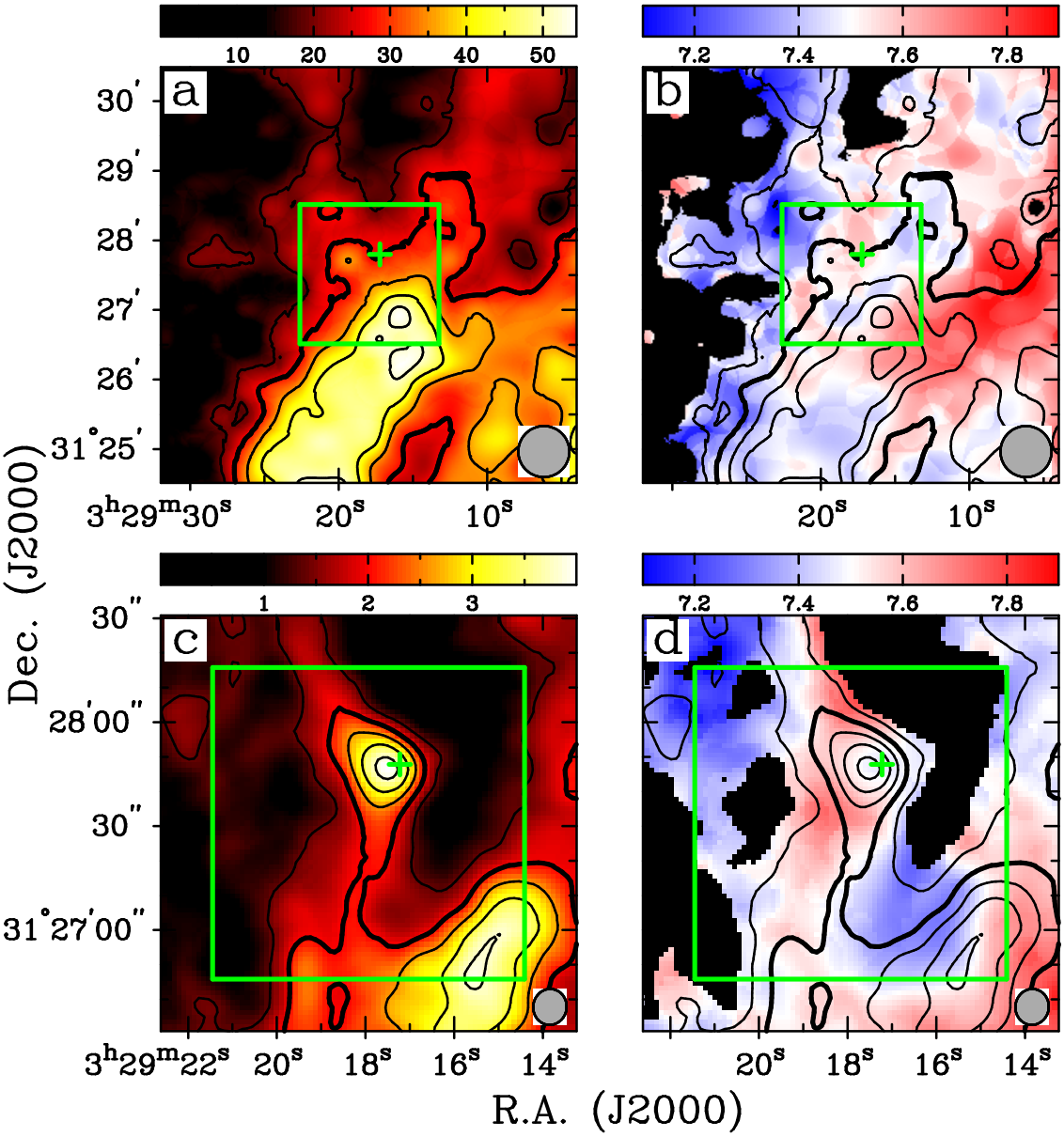

Figure 4.29: $C^{18}O$ $J = 1 \rightarrow 0$ integrated intensity and velocity of Per4 South. Velocity range is 7.1-7.9 km s^{-1} in all panels. Plus symbol indicates the position of the continuum source from Figure 4.28. (a,b) I_ν^{peak} = 54.32 Jy $beam^{-1}$·km s^{-1}; σ = 5.0 Jy $beam^{-1}$·km s^{-1}; beam is $44'' \times 44''$. (c,d) I_ν^{peak} = 3.94 Jy $beam^{-1}$·km s^{-1}; σ = 0.37 Jy $beam^{-1}$·km s^{-1}; beam is $10.39'' \times 9.63''$, P.A.= $-7.2°$.

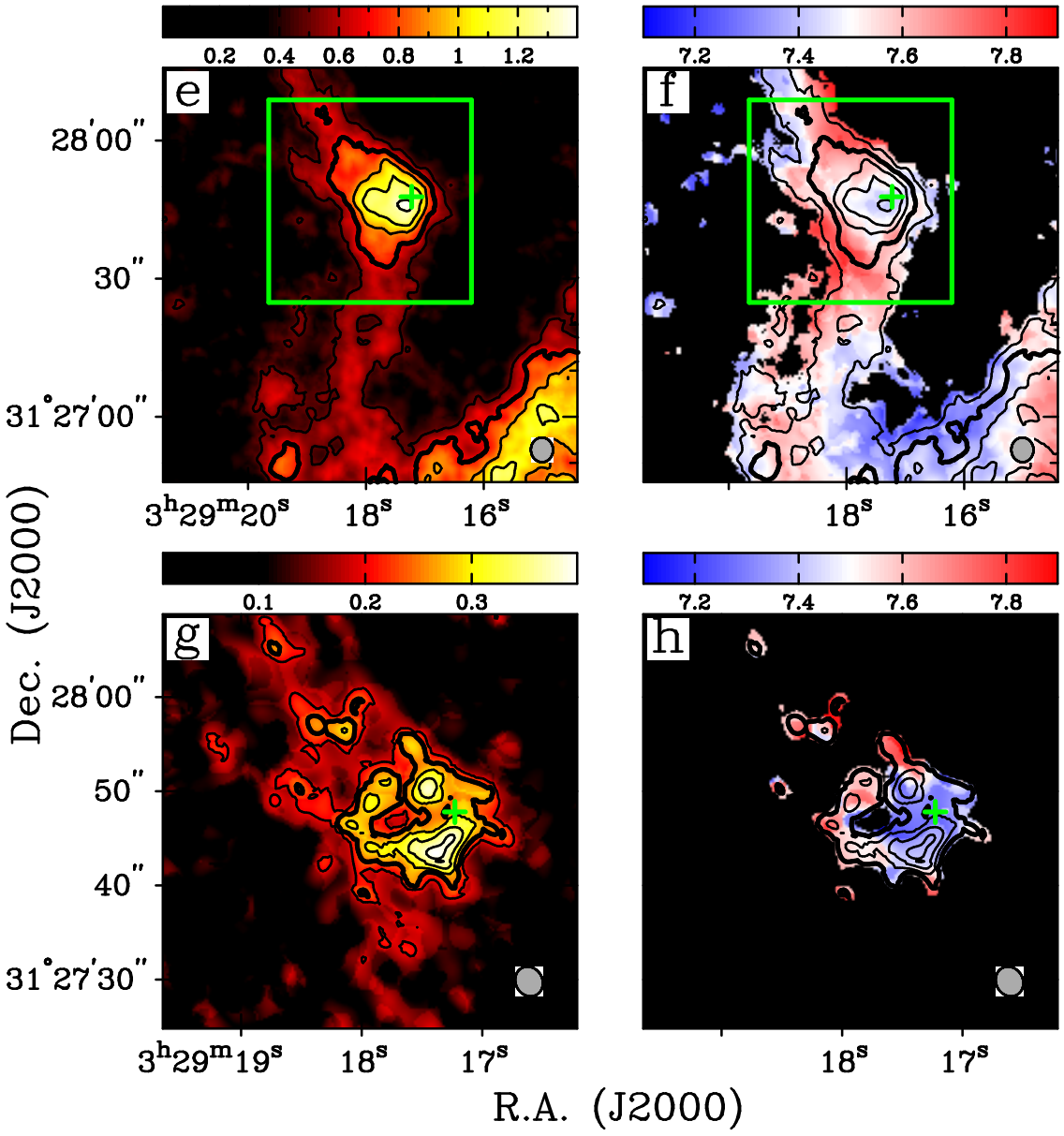

Figure 4.29: *Continued.* (e,f) I_ν^{peak} = 1.31 Jy beam^{-1}·km s^{-1}; σ = 0.13 Jy beam^{-1}·km s^{-1}; beam is 5.35″ × 4.82″, P.A.= 2.2°. (g,h) I_ν^{peak} = 0.39 Jy beam^{-1}·km s^{-1}; σ = 0.05 Jy beam^{-1}·km s^{-1}; beam is 3.25″ × 2.84″, P.A.= 29.1°.

however, the velocity field reddens to 7.8 km s^{-1}. Approximately 5 beam widths to the northeast and southwest of the center, the velocity field shifts blueward again to 7.2 (NE) and 7.3 (SW) km s^{-1}. The changes in velocity do not strictly follow the decline in emission, and the velocity field defies a simple interpretation.

The trends in both the intensity and velocity fields are largely preserved in the 5″ resolution maps (Figures 4.29*e,f*). The Per4S emission peak, 1.3 Jy $beam^{-1}$·km s^{-1}, is slightly displaced from the continuum peak, and the envelope of extended $C^{18}O$ emission surrounding the peak retains its long, filamentary structure. The central velocity is 7.5 km s^{-1}, and the redshift-blueshift pattern is maintained (with the same magnitude) along the extended envelope.

The maps with 3″ resolution (Figures 4.29*g,h*) zoom in on a 20″×20″ box around Per4S. The intensity map's high resolution reveals a ring-like structure of emission. The continuum peak is located on the western side of the ring; the point of peak $C^{18}O$ emission (0.4 Jy $beam^{-1}$·km s^{-1}) is on the southern side. Remnants of the long, filamentary envelope are seen in several clumps of emission to the north and south. In the corresponding velocity map, the velocity at the continuum position is 7.3 km s^{-1}, and except for a few points on the western and northern edges of the ring, the velocity field is fairly flat.

Spectra from the continuum position of Per4S are displayed in Figure 4.30. In the top row, the spectrum is taken through the FCRAO datacube alone. The line is strong, symmetrical, narrow, and well fit by a Gaussian function with a central velocity of 7.56 km s^{-1}. In the second, third, and fourth rows, the spectra are made from the 10″, 5″, and 3″ datacubes, respectively, and the line profiles are remarkably similar in shape if not in strength. At all resolutions, the lines remain narrow and nearly symmetrical, and the central velocities and widths are well determined by fitting Gaussian functions.

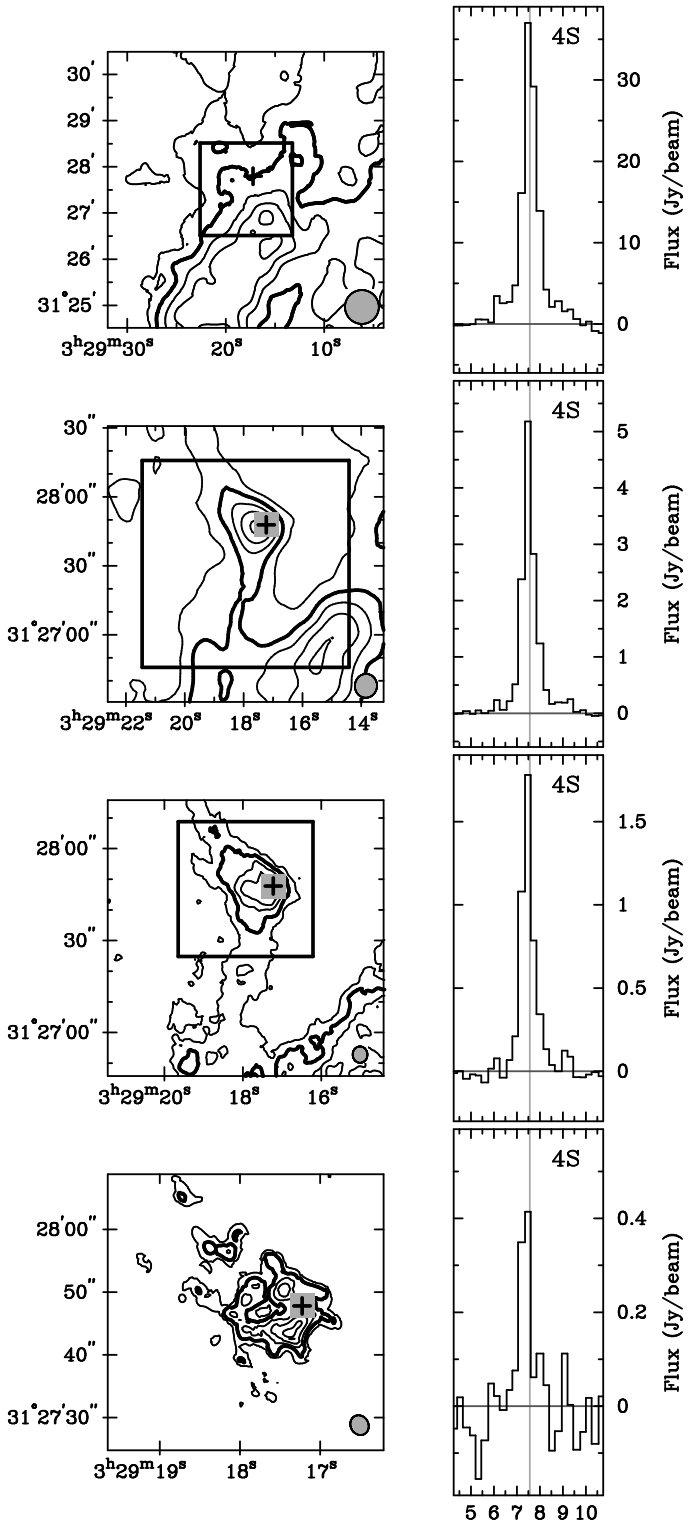

Figure 4.30: Per4 South spectra. The plots at left show integrated intensity contours from the $C^{18}O$ data, as in Figure 4.29. To the right of each contour plot are spectra from the $C^{18}O$ datacubes. The plus symbol indicates the position of the continuum source. All spectra display the flux in Jy beam^{-1} averaged over the area of a beam. In all rows, the gray vertical lines show the central velocity of a Gaussian function fit to the profile from the FCRAO map (top row).

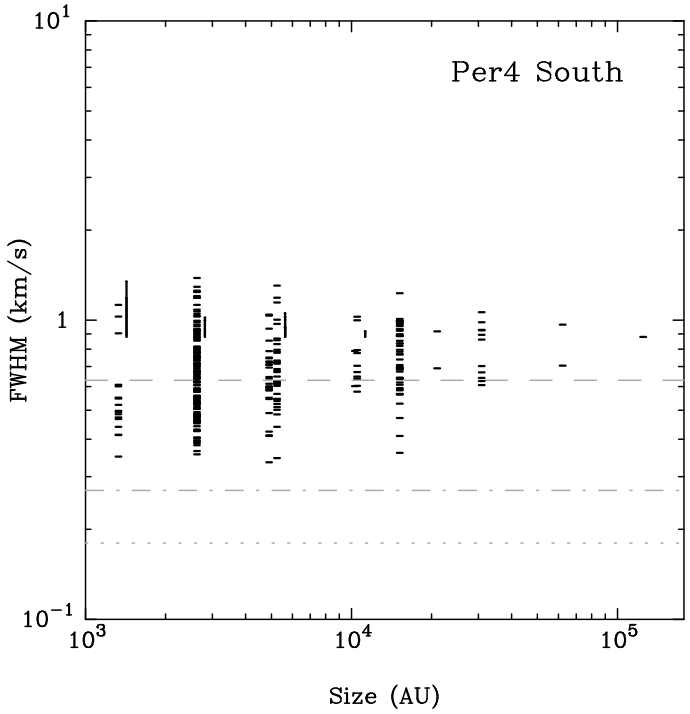

Figure 4.31: Per4 South line width (FWHM) *vs.* size correlations for gridded $C^{18}O$ spectra. The dashed line indicates the line width corresponding to the sound speed of the medium: $\mathrm{FWHM}_{c_s}(20\ \mathrm{K}) = 0.63$ km s^{-1}. The dotted line indicates the thermal line width: $\mathrm{FWHM}_T(20\ \mathrm{K}) = 0.18$ km s^{-1}. The dash-dot line indicates the channel width of the spectra: $\delta V = 0.27$ km s^{-1}.

The overall narrowness of the Per4S spectral lines is reflected in the distribution of points on the line width *vs.* grid correlation shown in Figure 4.31. The full range of measured FWHM is roughly the same for the 5250, 2625, and 1330 AU grid squares, but the limits have shifted downward compared with the values found from most other cores. The widest FWHM is only 1.38 km s^{-1}. Consequently, a large percentage (42.3%) of the total number of lines are narrower than the sonic line width (0.63 km s^{-1}) at 20 K. The total number of spectra included in the diagram is 307, and perhaps because of the general shift toward narrower line widths, the steep increase in the lower envelope of points is not evident.

4.10 NGC1333 SK32

4.10.1 Background

NGC1333 SK32 is listed among the "compact sources" in the 450 and 850 μm maps of Sandell & Knee (2001). It appears as a clump of emission near the center of a narrow arc of material that extends between the visible stars SVS3 (in IRAS8) and BD+30°549 (in IRAS9). Two (visible) stars appear within the area of the BIMA maps: LkHα 270, an infrared excess star, is in the southwest quadrant, and GSC2342441, an x-ray emitting star (Preibisch 1997), is just north of map center. SK32 appears near a peak in ^{13}CO emission detected at 55″ resolution by Sun *et al.* (2000); they identify this peak as Core B and estimate its mass as 6.4 M$\odot$.

Although SK32 is not known as an outflow source, it is located near the point of origin of the HH335 jet (Bally & Reipurth 2001). This 1′ long arc of emission, detected in Hα and S II emission, is oriented approximately north-south at its southern end and bends to a position angle of $\sim$25° at its northern end.

4.10.2 Continuum Data

The $\lambda = 2.7$ mm emission from the SK32 region (Figure 4.32) peaks near the center of the map ($S_{peak} = 10.2$ mJy beam^{-1}) and appears extended in the same northeast-southwest direction as the arc of material seen in the 850 μm maps of Sandell & Knee (2001). The extended emission zone resembles two satellite clumps of emission with peak fluxes of 4.6 and 4.1 mJy beam^{-1} (for the northeast and southwest clumps, respectively). In the 5″ resolution map (middle panel), the satellite clumps have disappeared, but the central source still appears lengthened along the same axis. The peak flux at center is 6.3 mJy beam^{-1}, and the bulge in the emission contours toward

the southwest suggests that the core may contain a second source. At 3″ resolution (bottom panel), the possibility of a second source remains: the low emission contours are substantially extended in the southwest direction. The peak flux of the central source is 5.2 mJy beam^{-1}.

4.10.3 $C^{18}O$ Data

The SK32 core is located within the NGC1333 reflection nebula, about halfway in between the IRAS8 and IRAS9 cores. The SK28 and SK29 objects are within the area of the FCRAO map in Figure 4.33*a*, and the broad filament of $C^{18}O$ emission that was described in the section on IRAS8 is visible in the southwest corner. SK32 is not marked by an emission peak at this low resolution, but the core is located near the tip of a peninsula of $C^{18}O$ emission that slices down into the primary beam area from the northern edge of the map. The peak within this peninsular region, 68.7 mJy beam^{-1}, appears just inside the primary beam area. The velocity field traced by the FCRAO data (Figure 4.33*b*) cover a full range of 7.0-8.2 km s^{-1}. The velocities along the strong $C^{18}O$ ribbon in the southwest corner are, reassuringly, identical to those seen in the IRAS8 map (Figure 4.25*b*). The velocities along the narrow filament that includes SK32 (and continues up into the IRAS9 region) show a slight oscillation, from ∼7.4 km s^{-1} at the southern tip, to ∼7.8 km s^{-1} near the emission peak, then back to ∼7.3 km s^{-1} at the northern edge. The velocity at the position of SK32 is 7.5 km s^{-1}.

In the $C^{18}O$ map with 10″ resolution (Figure 4.33*c*), SK32 appears at the head of a cometary emission structure that tapers toward the high emission peaks (4.9 mJy beam^{-1}) near the northern edge of the map. The position angle of the $C^{18}O$ emission "tail" is almost due north, unlike the clear northeast extension seen in the continuum maps. The velocity map of the material around SK32 (Figure 4.33*d*)

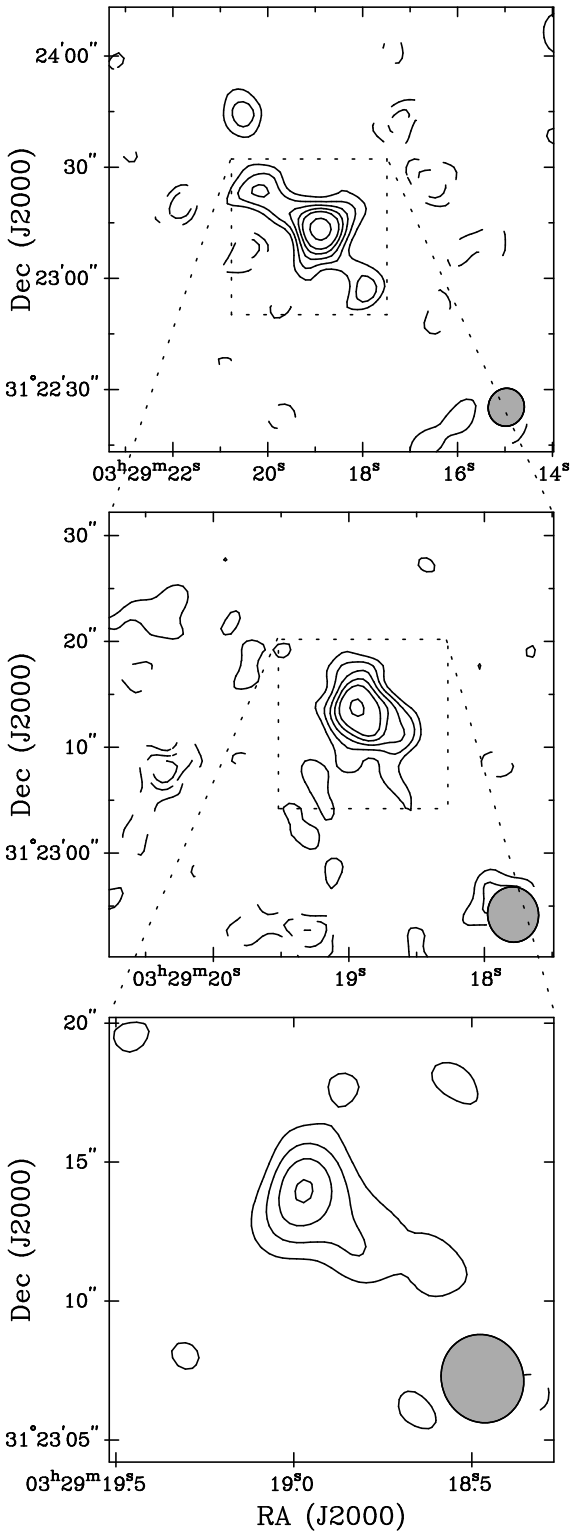

Figure 4.32: Maps of the $\lambda = 2.7$ mm continuum emission from NGC1333 SK32. The contour intervals are $(-4, -3, -2, 2, 3, 4, 5, 6, 8) \times \sigma$ in mJy beam^{-1}. *Top:* $\sigma = 1.1$ mJy beam^{-1}; beam is $10.3'' \times 9.7''$, P.A.$= -13.8°$. *Middle:* $\sigma = 0.8$ mJy beam^{-1}; beam is $5.2'' \times 4.8''$, P.A.$= 9.1°$. *Bottom:* $\sigma = 1.0$ mJy beam^{-1}; beam is $3.2'' \times 2.9''$, P.A.$= 20.6°$.

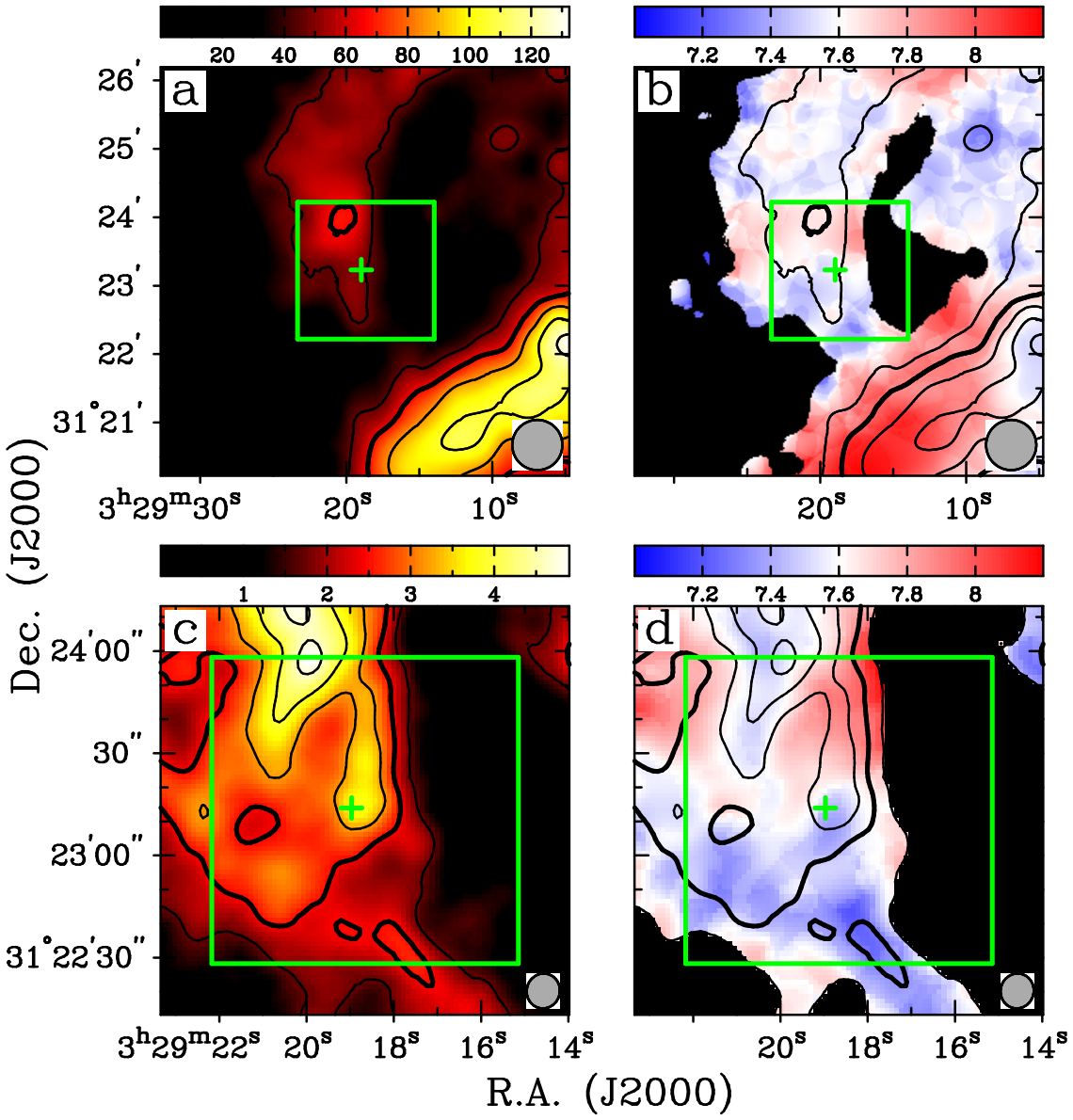

Figure 4.33: $C^{18}O$ $J = 1 \rightarrow 0$ integrated intensity and velocity of NGC1333 SK32. Velocity range is 7.0-8.2 km s^{-1} in all panels. Plus symbols indicate the position of the continuum source from Figure 4.32. (a,b) I_ν^{peak} = 132.39 Jy $beam^{-1}$·km s^{-1}; σ = 9.8 Jy $beam^{-1}$·km s^{-1}; beam is $44'' \times 44''$. (c,d) I_ν^{peak} = 4.85 Jy $beam^{-1}$·km s^{-1}; σ = 0.57 Jy $beam^{-1}$·km s^{-1}; beam is $10.27'' \times 9.71''$, P.A.= $-13.8°$.

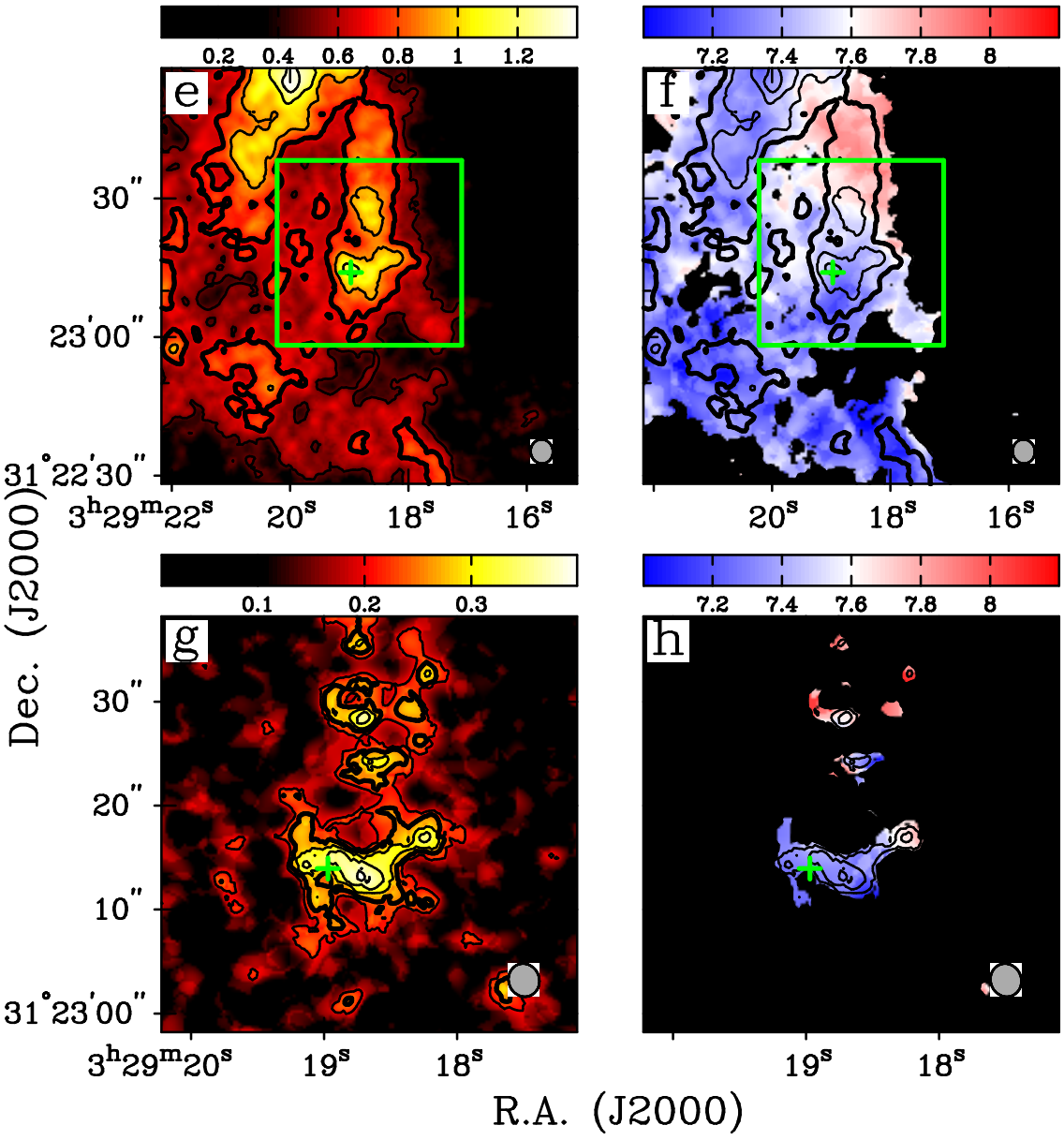

Figure 4.33: *Continued.* (e,f) I_ν^{peak} = 1.34 Jy beam^{-1}·km s^{-1}; σ = 0.17 Jy beam^{-1}·km s^{-1}; beam is 5.24″ × 4.81″, P.A.= 9.1°. (g,h) I_ν^{peak} = 0.33 Jy beam^{-1}·km s^{-1}; σ = 0.06 Jy beam^{-1}·km s^{-1}; beam is 3.21″ × 2.94″, P.A.= 20.6°.

reveals the trends seen in the FCRAO data. The SK32 position shows a velocity of 7.5 km s^{-1}. To the immediate north, the velocities are redshifted, and at the tip of the emission peninsula to the south, the velocities are blueshifted. In contrast to the low resolution velocity map, however, the $C^{18}O$ emission peak now appears slightly bluer at 7.4 km s^{-1}.

At 5″ resolution (Figure 4.33*e*), the cometary structure of the extended SK32 envelope is still prominent, but the high emission contours delineate two separate clumps. The SK32 source appears at the peak (1.3 mJy $beam^{-1}$) of the southern clump. In the 5″ velocity map (Figure 4.33*f*), most of the emitting region around SK32 appears blue. The velocities vary from 7.2-7.5 km s^{-1}, except for the cometary "tail" to the north. From the secondary emission clump to the northern extreme, the velocity shifts from 7.7 to 7.9 km s^{-1}.

At the highest available resolution (Figure 4.33*g*), the SK32 continuum location appears within a butterfly-wing clump of extended emission. The peak, 0.3 mJy $beam^{-1}$, is roughly one 3″ beam width west of the continuum location. Lesser clumps, the peaks in the "tail" seen at lower resolution, trail off to the north. In the velocity map (Figure 4.33*h*), the most obvious feature is the dichotomy between the velocities in the central clump (7.2-7.4 km s^{-1}) and those in the northern clumps (7.7-8.0 km s^{-1}).

The spectra from NGC1333 SK32, displayed in Figure 4.34, seem to represent a "compromise" between the complex, multi-peaked spectra from the IRAS8 sources, 2′ to the southwest, and the symmetrical, single-peaked spectra from Per4S, several arc-minutes to the north. In the spectrum from the FCRAO data, the line profile appears roughly Gaussian in shape. But, the line is double-peaked, and a red wing skews the profile toward the blue. The central velocity of a fitted Gaussian function splits the double peak at 7.48 km s^{-1}. In the spectra from the higher resolution

datacubes, as the contribution from the FCRAO data diminishes, the red line wing also diminishes, and the line center shifts subtlely toward the blue. The spectrum from the 3″ data is still prominent above the noise, and the line center is distinctly blueward of the FCRAO velocity.

Although the spectra from SK32 and its vicinity are less complicated than the spectra from IRAS8, fewer are included in the diagram of line width *vs.* grid size shown in Figure 4.35. The 193 spectra from SK32 are taken from the ribbon of $C^{18}O$ emisson that extends from the northern edge of the map; outside of that ribbon, many pixels are masked. The upper envelope of the plotted FWHM remains fairly constant with grid size. The lower envelope, however, shows a steep rise, except for a few low values at ∼15000 AU. For the 2625 AU grid squares, the range of FWHM is quite broad, but for the 1330 AU grid squares, all of the lines are narrow. The percentage of the total number of lines that appears below the sonic line width is 29.5%.

4.11 Per4 North

4.11.1 Background

Per4 North lies approximately 6′ north of Per4 South, near the tip of the curl of high density material extending northeast of the NGC1333 nebula. Per4N hosts IRAS 03262+3123, which was the reference position for the Per4 region in the NH_3 observations made by Ladd, Myers, & Goodman (1994). Based upon the intensity of the NH_3 peak, they estimated the mass of the core to be ∼6 M⊙.

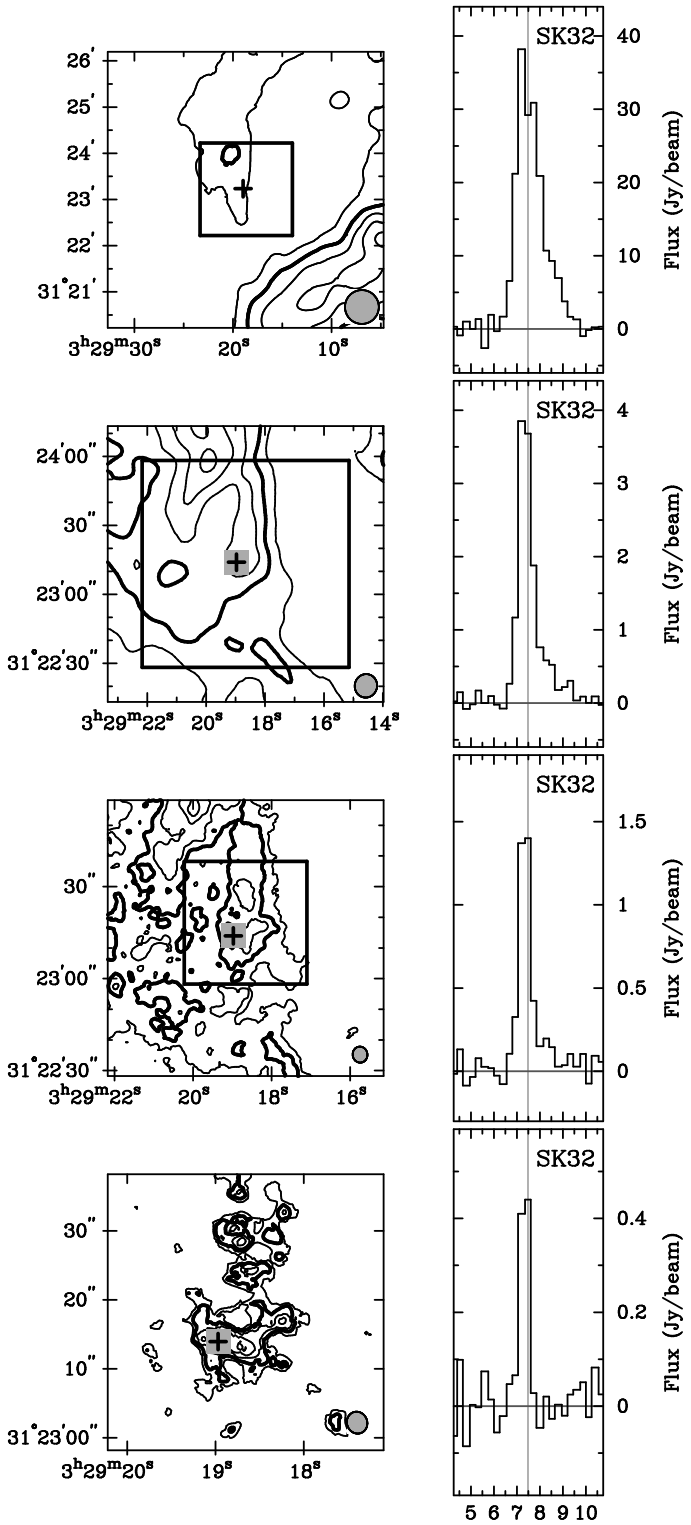

Figure 4.34: NGC1333 SK32 spectra. The plots at left show integrated intensity contours from the $C^{18}O$ data, as in Figure 4.33. To the right of each contour plot are spectra from the $C^{18}O$ datacubes. The plus symbols indicate the positions of the continuum source. All spectra display the flux in Jy beam^{-1} averaged over the area of a beam. In all rows, the gray vertical lines show the central velocity of a Gaussian function fit to the profiles from the FCRAO map (top row).

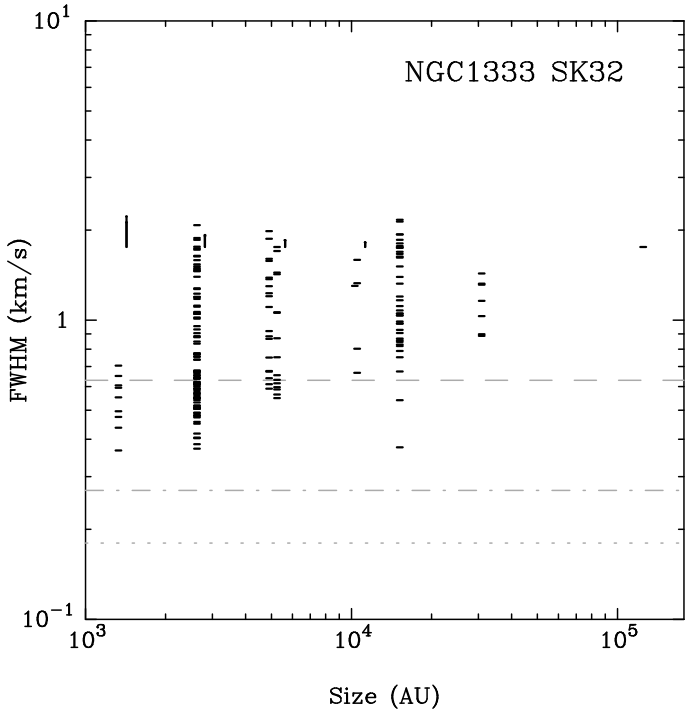

Figure 4.35: NGC1333 SK32 line width (FWHM) *vs.* size correlations for gridded $C^{18}O$ spectra. The dashed line indicates the line width corresponding to the sound speed of the medium: $\mathrm{FWHM}_{c_s}(20\ \mathrm{K}) = 0.63$ km s^{-1}. The dotted line indicates the thermal line width: $\mathrm{FWHM}_T(20\ \mathrm{K}) = 0.18$ km s^{-1}. The dash-dot line indicates the channel width of the spectra: $\delta V = 0.27$ km s^{-1}.

4.11.2 Continuum Maps

The $\lambda = 2.7$ mm continuum emission from the Per4N core has a peak flux of 5.5 mJy beam^{-1} located near the center of the BIMA map (Figure 4.36). In the $10''$ resolution map (top panel), the emission contours fan out on the southern and eastern sides of the peak, such that the 2σ contour encloses an area of approximately 3×3 beam widths. With the $5''$ beam (middle panel), the extended envelope suggested by the lower resolution map is resolved out except for a small 3σ peak. The emission centered on Per4N is extended by nearly three beam widths in a north-south direction and has a peak flux of 3.8 mJy beam^{-1}. Some evidence for this elongated emission structure remains in the map with $3''$ resolution, although

here, the peak is 3.5 mJy beam^{-1}, only 3σ above the noise.

4.11.3 C^{18}O Data

The long ribbon of cloud material that extends northwest from the NGC1333 nebula and beyond Per4N clearly passes through the FCRAO map in Figure 4.37*a*. The ribbon of C^{18}O emission knots extends from the southern to the northern edge of the full $6' \times 6'$ map. The Per4N core appears along the ribbon, although in a knot where the emission is not quite as strong as elsewhere. The position of peak emission in the map, 31.1 Jy beam^{-1}·km s^{-1}, is south of the BIMA primary beam area. The velocity map of the region (Figure 4.37*b*) features one prominent characteristic: unlike Per4S to the south, the high intensity zones systematically exhibit bluer velocities (7.1-7.2 km s^{-1}) than the lower intensity zones (7.6-7.7 km s^{-1}). In the vicinity of Per4N, where the intensity is weaker, the velocity contrast is not so clear. Overall, the full velocity range is rather small compared with other cores in the survey.

That Per4N is unquestionably a source of C^{18}O emission is demonstrated in Figure 4.37*c*, which shows the combined BIMA and FCRAO data at 10″ resolution. The peak is 2.0 Jy beam^{-1}·km s^{-1}, and the emission fans out to the southeast, similar to the behavior of the continuum emission at this resolution. Roughly 22″ from the core center, the envelope appears to join with the narrow strip of C^{18}O emission that peaks (2.1 Jy beam^{-1}·km s^{-1}) just at the eastern edge of map. In the corresponding velocity map (Figure 4.37*d*), the contrast seen in the FCRAO data is no longer apparent. The velocity field in the vicinity of the Per4N emission peak is messy. The velocity at the continuum position is 7.5 km s^{-1}, and there is no evidence for a gradient along the direction of the extended envelope.

In the 5″ maps (Figures 4.37*e,f*), there are no surprises. The ribbon of emission that extends from the eastern edge of the map begins to dissolve into clumps. The

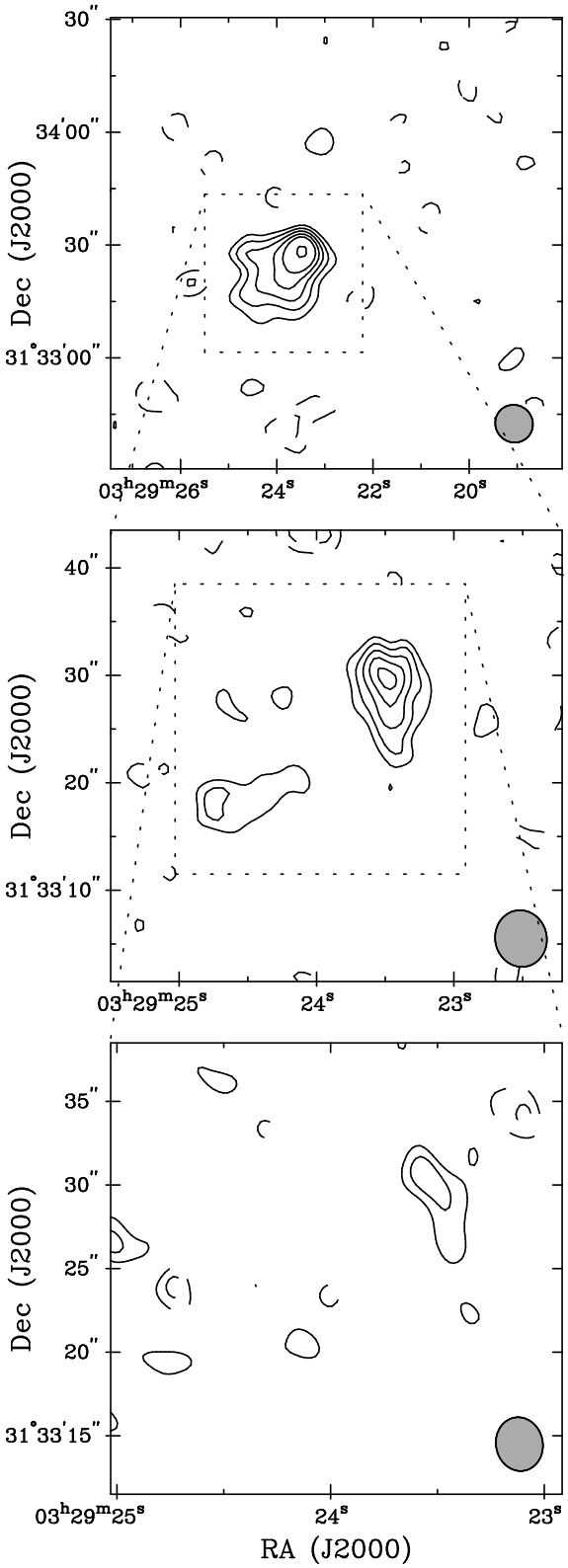

Figure 4.36: Maps of the $\lambda = 2.7$ mm continuum emission from Per4 North. The contour intervals are $(-4, -3, -2, 2, 3, 4, 5, 6, 8) \times \sigma$ in mJy beam^{-1}. *Top:* $\sigma = 0.7$ mJy beam^{-1}; beam is $10.2'' \times 9.9''$, P.A.$= 43.4°$. *Middle:* $\sigma = 0.6$ mJy beam^{-1}; beam is $5.3'' \times 4.8''$, P.A.$= 11.6°$. *Bottom:* $\sigma = 0.9$ mJy beam^{-1}; beam is $3.2'' \times 2.8''$, P.A.$= 11.1°$.

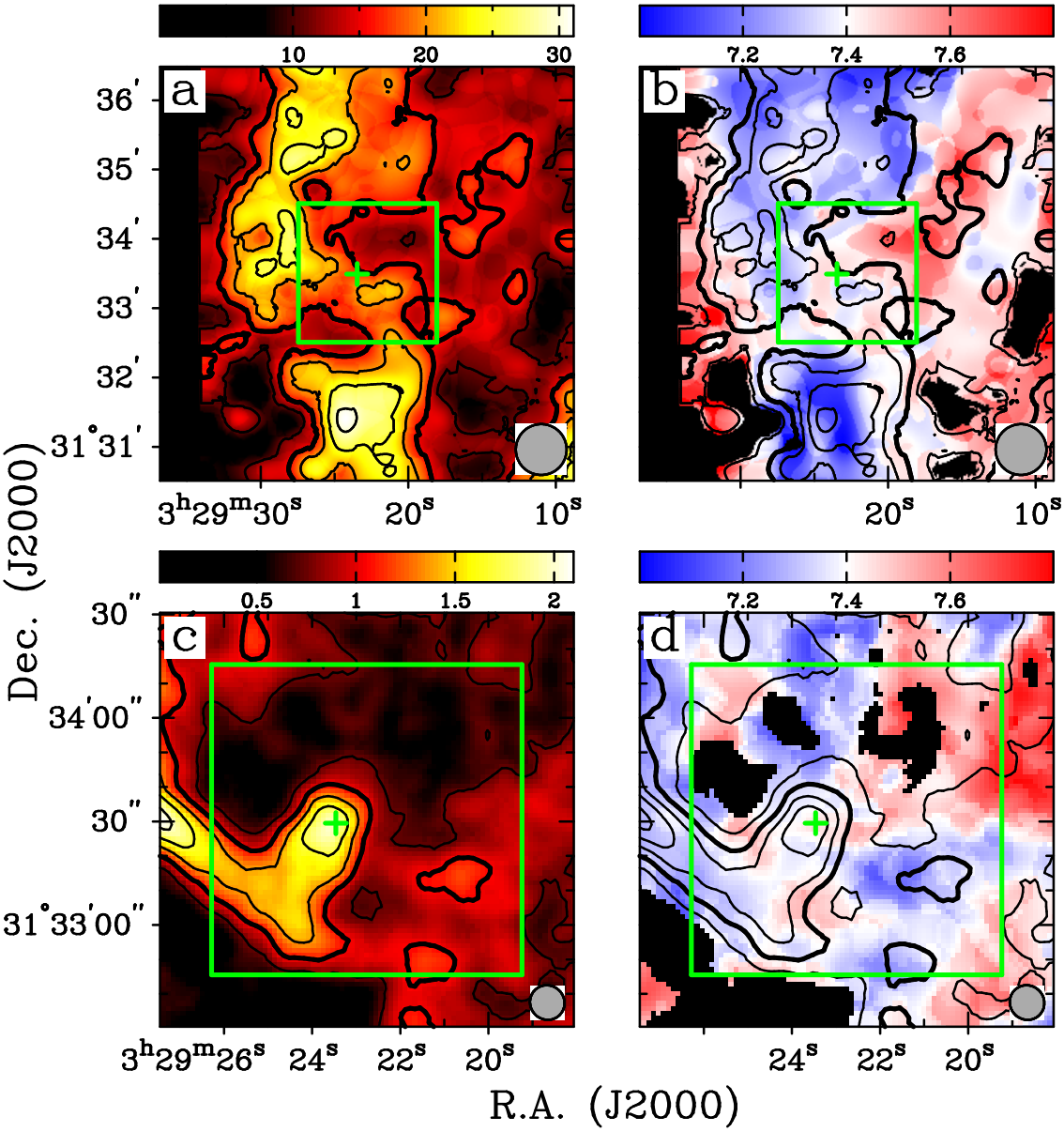

Figure 4.37: $C^{18}O$ $J = 1 \rightarrow 0$ integrated intensity and velocity of Per4 North. Velocity range is 7.0-7.8 km s^{-1} in all panels. Plus symbols indicate the position of the continuum source from Figure 4.36. (a,b) I_ν^{peak} = 31.09 Jy beam^{-1}·km s^{-1}; σ = 3.3 Jy beam^{-1}·km s^{-1}; beam is $44'' \times 44''$. (c,d) I_ν^{peak} = 2.07 Jy beam^{-1}·km s^{-1}; σ = 0.18 Jy beam^{-1}·km s^{-1}; beam is $10.19'' \times 9.86''$, P.A.= 43.4°.

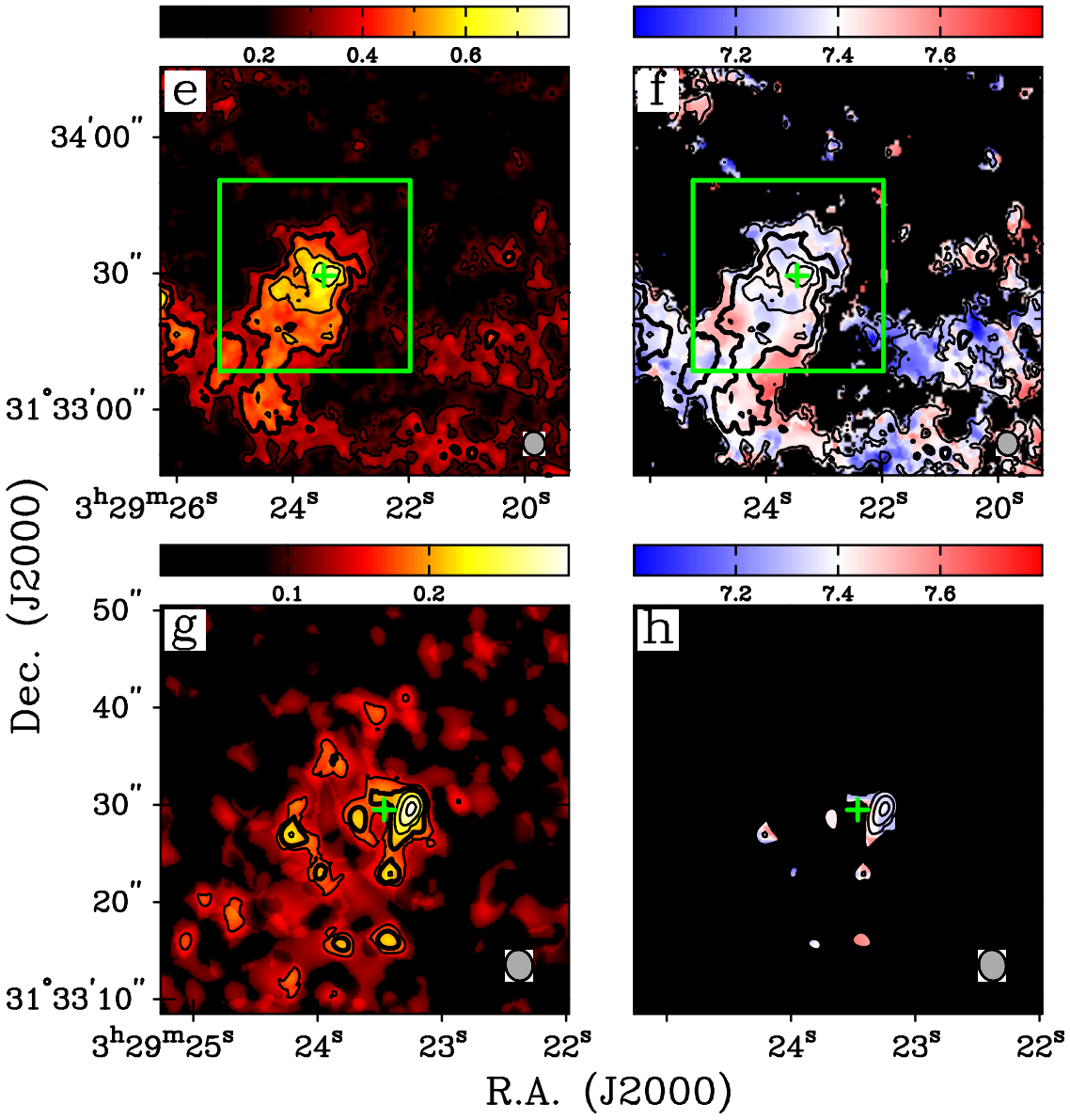

Figure 4.37: *Continued.* (e,f) I_ν^{peak} = 0.73 Jy beam^{-1}·km s^{-1}; σ = 0.08 Jy beam^{-1}·km s^{-1}; beam is 5.29″ × 4.80″, P.A.= 11.6°. (g,h) I_ν^{peak} = 0.27 Jy beam^{-1}·km s^{-1}; σ = 0.05 Jy beam^{-1}·km s^{-1}; beam is 3.23″ × 2.80″, P.A.= 11.1°.

$C^{18}O$ emission peak, 0.7 Jy beam^{-1}·km s^{-1}, is centered upon the continuum peak position. In the velocity map, there is still no evidence for systematic rotation in the core. In fact, the velocity field throughout the envelope is incredibly flat, with values that, except for a few isolated pixels, remain within a single channel width (0.27 km s^{-1}).

For the 3″ resolution maps (Figures 4.37*g,h*), the full area of the map is approximately 20″ × 20″, centered upon the continuum position. At this resolution, the Per4N envelope breaks up into a cluster of beam-sized clumps. The highest emission peak, 0.3 Jy beam^{-1}·km s^{-1}, is 5σ above the noise. The velocity at the continuum position is 7.4 km s^{-1}.

Figure 4.38 shows a series of spectra taken through the Per4N continuum position. Much like the spectra from Per4S, its "neighbor" to the south, the spectra from Per4N are consistently narrow and symmetrical. They are also well fit by Gaussian functions; the central velocity found for the spectrum from the FCRAO datacube, 7.48 km s^{-1}, is applicable for the higher resolution spectra as well.

The narrowness of the spectral line from the center of Per4N is indicative of the general narrowness of the lines throughout the core. The prevalence of narrow lines is manifest in the range of FWHM in the line width *vs.* grid size correlation shown in Figure 4.39. The correlation revealed for Per4N is very similar to the behavior seen in Per4S: for grid squares of different sizes, there is a large range of measured line widths, but the range is shifted to smaller values. For the FWHM from the 5250 AU squares, the maximum line width is only 1.09 km s^{-1}. The total number of spectra included in the diagram is 313, and more than half (71.2%) have measured FWHM below the 20 K sonic line width.

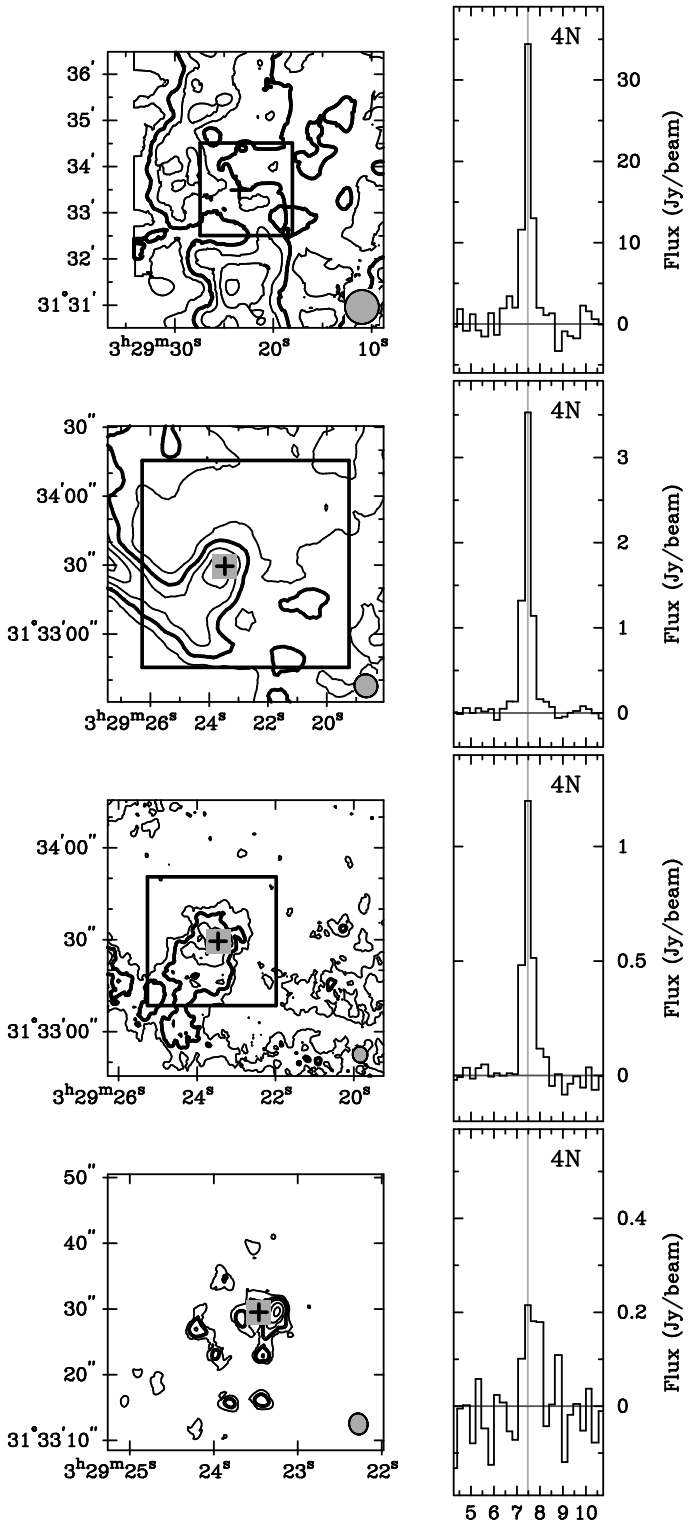

Figure 4.38: Per4 North spectra. The plots at left show integrated intensity contours from the $C^{18}O$ data, as in Figure 4.37. To the right of each contour plot are spectra from the $C^{18}O$ datacubes. The plus symbols indicate the positions of the continuum source. All spectra display the flux in Jy beam^{-1} averaged over the area of a beam. In all rows, the gray vertical lines show the central velocity of a Gaussian function fit to the profile from the FCRAO map (top row).

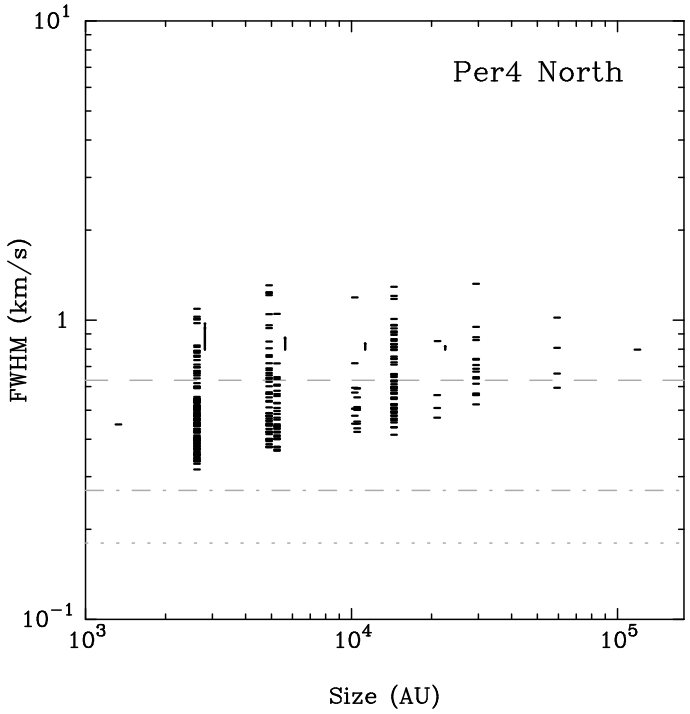

Figure 4.39: Per4 North line width (FWHM) *vs.* size correlations for gridded $C^{18}O$ spectra. The dashed line indicates the line width corresponding to the sound speed of the medium: $\mathrm{FWHM}_{c_s}(20\ \mathrm{K}) = 0.63$ km s^{-1}. The dotted line indicates the thermal line width: $\mathrm{FWHM}_T(20\ \mathrm{K}) = 0.18$ km s^{-1}. The dash-dot line indicates the channel width of the spectra: $\delta V = 0.27$ km s^{-1}.

4.12 Per5

4.12.1 Background

Per5 lies approximately 8′ northeast of Per4N. The core is centered on IRAS 03267 +3128 and has a mass of approximately 6 M$\odot$. Single-dish maps of the NH_3 (Ladd, Myers, & Goodman 1994) and N_2H^+ (Caselli *et al.* 2002a) emission show that Per5 is slightly elongated, with an aspect ratio of roughly 1.5. In the NH_3 maps, the elongation is in the north-south direction; in the N_2H^+ maps, the elongation is more northeast-southwest.

4.12.2 Continuum Data

The continuum emission from Per5 (Figure 4.40) is strong ($S_{peak} = 9.7$ mJy beam^{-1}) and obviously extended along an east-west axis. Even at 10″ resolution, the extension of the western lobe by several beam widths from the central peak suggests the presence of multiple sources. In the 5″ map (middle panel), however, the morphology of the emitting region is considerably more complex than a side-by-side pair of protostars. The highest emission peak (5.3 mJy beam^{-1}) still appears near the center of the map. The western extension appears as a shallow peak of 3σ emission (2.4 mJy beam^{-1}). To the east, an extended zone of emission, approximately three beam widths long, cascades southward from a secondary emission peak (5.3 mJy beam^{-1}) that's one beam width east of the central source. At 3″ resolution, no evidence remains of the southward cascade, and the three continuum peaks are weak, rather than centrally condensed. The eastern peak is the strongest at 4.3 mJy beam^{-1}; the central and western peaks are 3.5 and 2.6 mJy beam^{-1}, respectively.

4.12.3 $C^{18}O$ Data

In the maps of the $C^{18}O$ emission from Per5, the three plus symbols indicate the positions of the three clumps identified in the high resolution continuum maps. In general, these three positions are undifferentiated in the $C^{18}O$ maps. In the FCRAO data (Figure 4.41*a*), they appear at the tip of an elongated emission region. This filamentary structure fills most of the northeastern quadrant of the BIMA primary beam area and extends all the way to the northeast corner of the full FCRAO map. The peak emission in the map (32.6 mJy beam^{-1}), however, arises from another large cloud in the northwestern quadrant of the map. Although a low level of $C^{18}O$ emission permeates the primary beam area, the environment of Per5 appears to

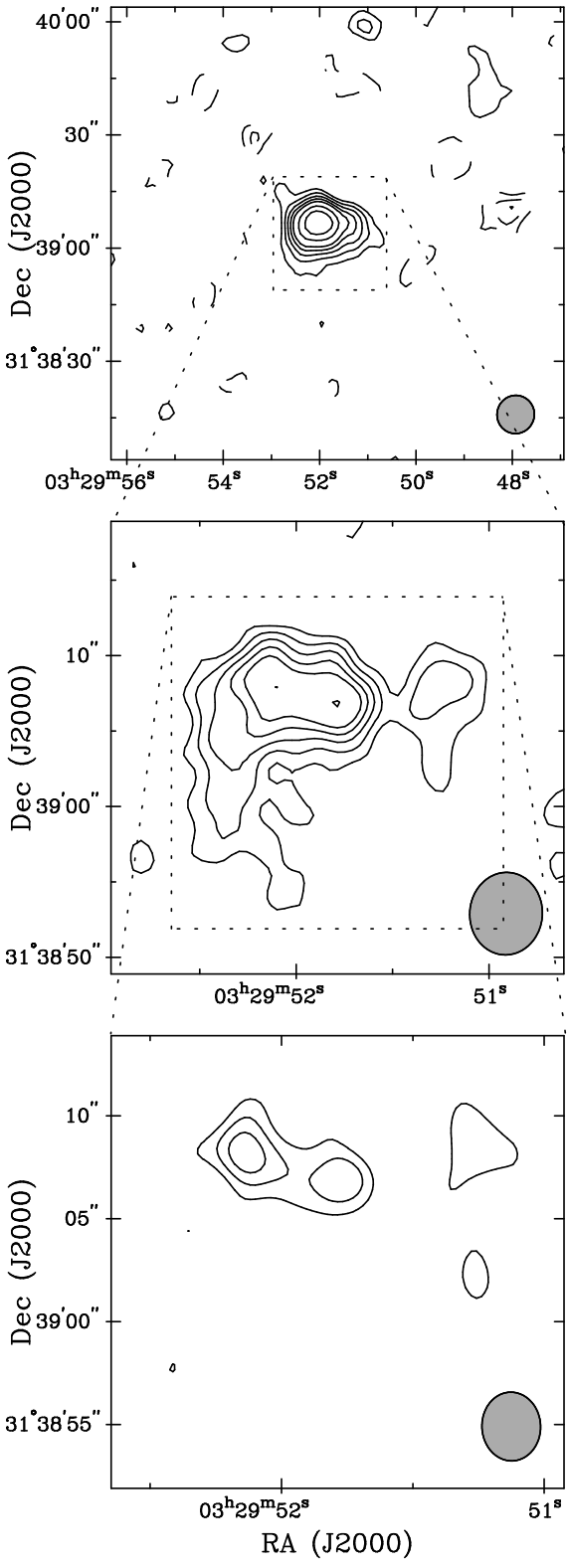

Figure 4.40: Maps of the $\lambda = 2.7$ mm continuum emission from Per5. The contour intervals are $(-4, -3, -2, 2, 3, 4, 5, 6, 8, 10) \times \sigma$ in mJy beam^{-1}. *Top:* $\sigma = 0.8$ mJy beam^{-1}; beam is $10.2'' \times 9.9''$, P.A.$= -13.1°$. *Middle:* $\sigma = 0.7$ mJy beam^{-1}; beam is $5.5'' \times 4.8''$, P.A.$= -3.8°$. *Bottom:* $\sigma = 0.9$ mJy beam^{-1}; beam is $3.3'' \times 2.9''$, P.A.$= 2.4°$.

be a gap in between the northeast filament and the northwest cloud. The velocity map of the cloud interface (Figure 4.41*b*) indicates that the two large structures are centered at different V_{LSR}. The northeastern filament is redshifted ($\sim$8.3 km s^{-1}) with respect to the northwestern cloud ($\sim$7.4 km s^{-1}).

The 10″ map (Figure 4.41*c*) of the region highlights the relative isolation of the Per5 core. A low level of $C^{18}O$ emission is detected throughout the primary beam area, but the only indication of the larger filament outside of the primary beam area is the relatively thin (2-3 beam widths) umbilical cord of $C^{18}O$ emission that extends away from Per5 to the northeast. The velocities of the low level $C^{18}O$, shown in Figure 4.41*d*, suggest that the gas is associated with the large northeastern filament. However, the northern edge of the Per5 envelope is shifted slightly blueward (7.8-7.9 km s^{-1}) from the rest of the field (8.1-8.4 km s^{-1}).

In the 5″ resolution map (Figure 4.41*e*), the Per5 core is an island of emission. The peak intensity at its center is 1.1 Jy beam^{-1}·km s^{-1}. The Per5E and Per5W continuum clumps fall within the $C^{18}O$ envelope contours, but they are not distinguished by their own emission peaks. Only a few small emission clumps mark the connection to the larger filament. The redshift of the low level emission makes this connection more apparent in the velocity map (Figure 4.41*d*). As with the 10″ velocity map, the Per5 envelope is slighly bluer (7.8-7.9 km s^{-1}) than the surrounding cloud.

The 3″ resolution maps (Figure 4.41*g,h*) make the blueshift of the Per5 core obvious. The envelope on the central continuum source even reveals a slight velocity gradient along a northwest-southeast axis. The velocities range from 8.0 km s^{-1} south of the emission peak (0.5 Jy beam^{-1}·km s^{-1}) to 7.6 km s^{-1} on the northern edge.

Spectra taken from the three positions identified from the continuum emission

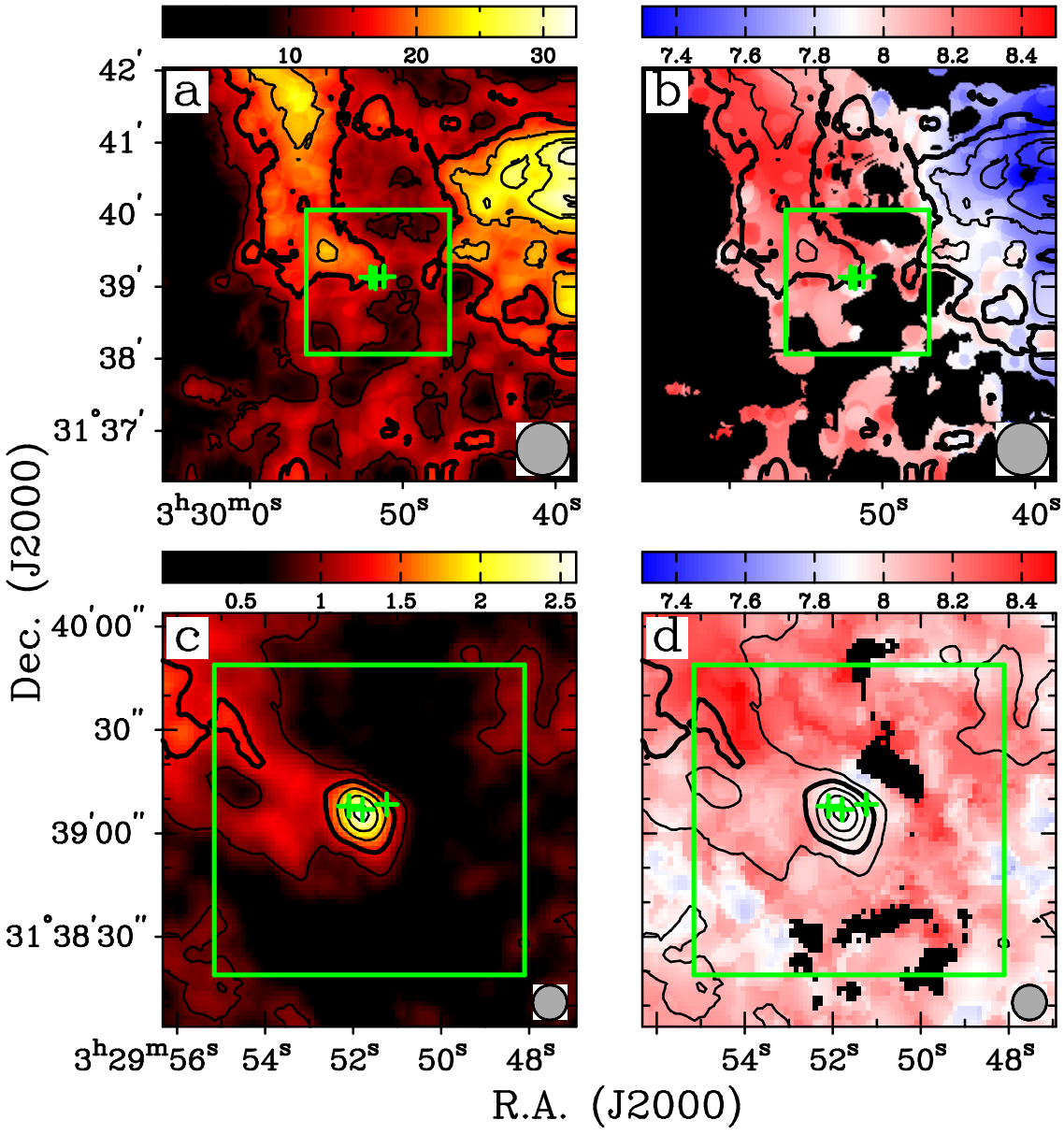

Figure 4.41: $C^{18}O$ $J = 1 \rightarrow 0$ integrated intensity and velocity of Per5. Velocity range is 7.3-8.5 km s^{-1} in all panels. Plus symbols indicate positions of continuum sources from Figure 4.40. (a,b) $I_\nu^{peak} = 32.58$ Jy beam^{-1}·km s^{-1}; $\sigma =$ 4.3 Jy beam^{-1}·km s^{-1}; beam is $44'' \times 44''$. (c,d) $I_\nu^{peak} = 2.52$ Jy beam^{-1}·km s^{-1}; $\sigma = 0.15$ Jy beam^{-1}·km s^{-1}; beam is $10.15'' \times 9.88''$, P.A.$= -13.1°$.

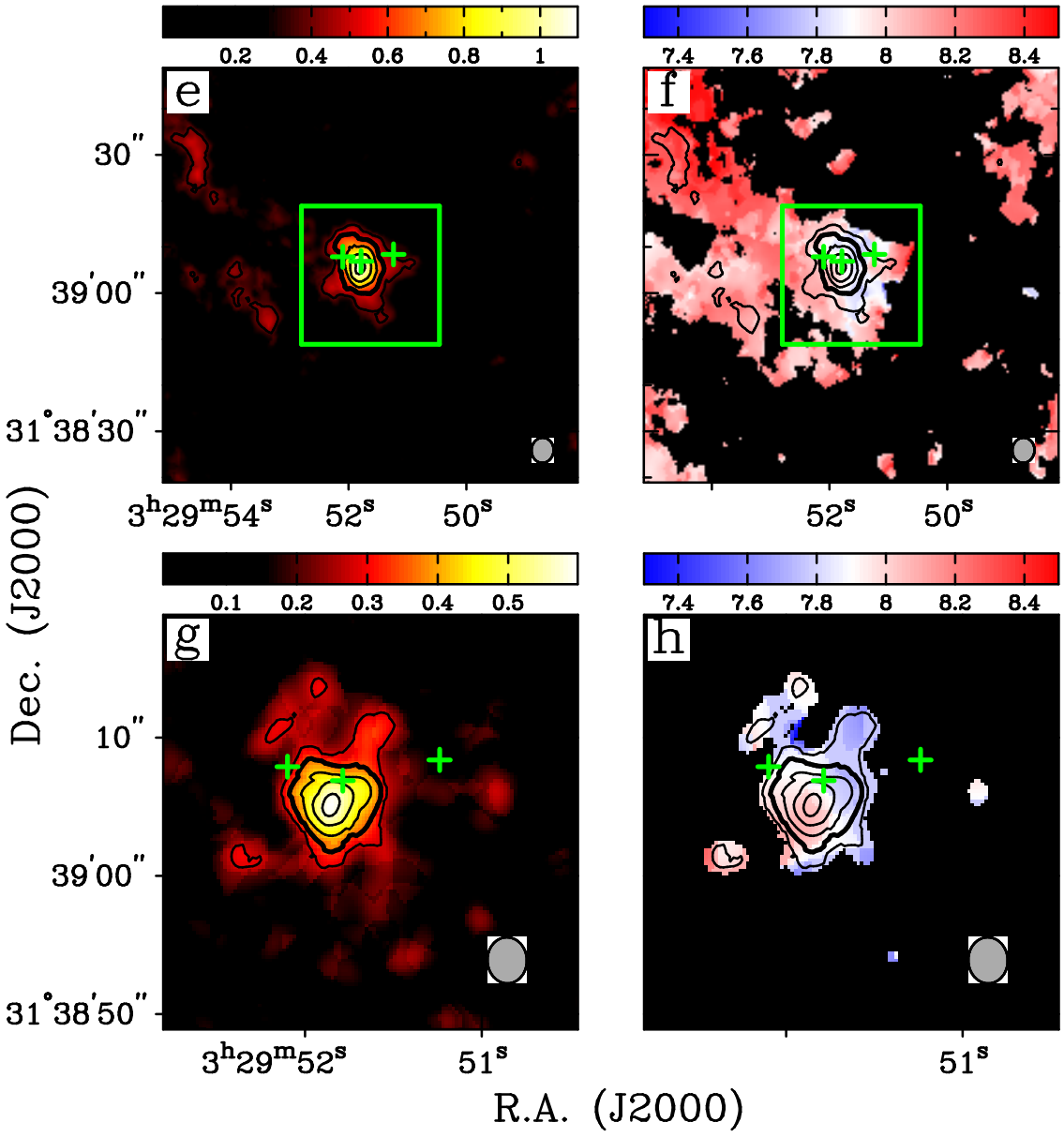

Figure 4.41: *Continued.* (e,f) I_ν^{peak} = 1.07 Jy beam^{-1}·km s^{-1}; σ = 0.07 Jy beam^{-1}·km s^{-1}; beam is 5.47″ × 4.81″, P.A.= −3.8°. (g,h) I_ν^{peak} = 0.51 Jy beam^{-1}·km s^{-1}; σ = 0.05 Jy beam^{-1}·km s^{-1}; beam is 3.34″ × 2.85″, P.A.= 2.4°.

maps are shown in Figure 4.42. Because of the close proximity of the sources, the spectra from the FCRAO data are nearly identical. They each have a fitted central velocity of 8.1 km s^{-1}, and they each show a small peak in their red line wings. As the resolution of the datacubes increases, the intensities in the three lines wane at different rates, but the shapes of the profiles remain almost the same. The spectrum from Per5C maintains the highest intensity because it is the only source located in the high emission envelope on the $C^{18}O$ maps (left panels). All three lines are narrow, nearly symmetrical, and slightly blueshifted from the velocity of the FCRAO lines. The magnitude of the blueshift increases as the resolution increases.

The narrowness of all of the measured lines in the Per5 core, not only those at the continuum positions, is brought into sharp relief by the line width *vs.* grid size diagram in Figure 4.43. FWHM for a total of 291 spectra are included in the diagram. Many of the spectra arise from the low level emission regions that surround the central Per5 envelope. The range of line widths is fairly uniform at all grid sizes. The lower envelope appears just at the channel width (0.27 km s^{-1}), and the upper envelope is only slightly above 1 km s^{-1}. Because of the generally narrower FWHM of the measured lines, Per5 has the highest percentage (91.1%) of lines that fall below the sonic line width for all of the cores in the survey.

4.13 Per6

4.13.1 Background

The Per6 core anchors the southwestern end of the Perseus cloud's "central ridge," a broad filament of material that extend from south of NGC1333 to the IC348 star forming region. Seen in NH_3 emission (Ladd, Myers, & Goodman 1994), the core peaks 1′ south of IRAS 03271+3013 and has a total mass of approximately 5 $M_\odot$.

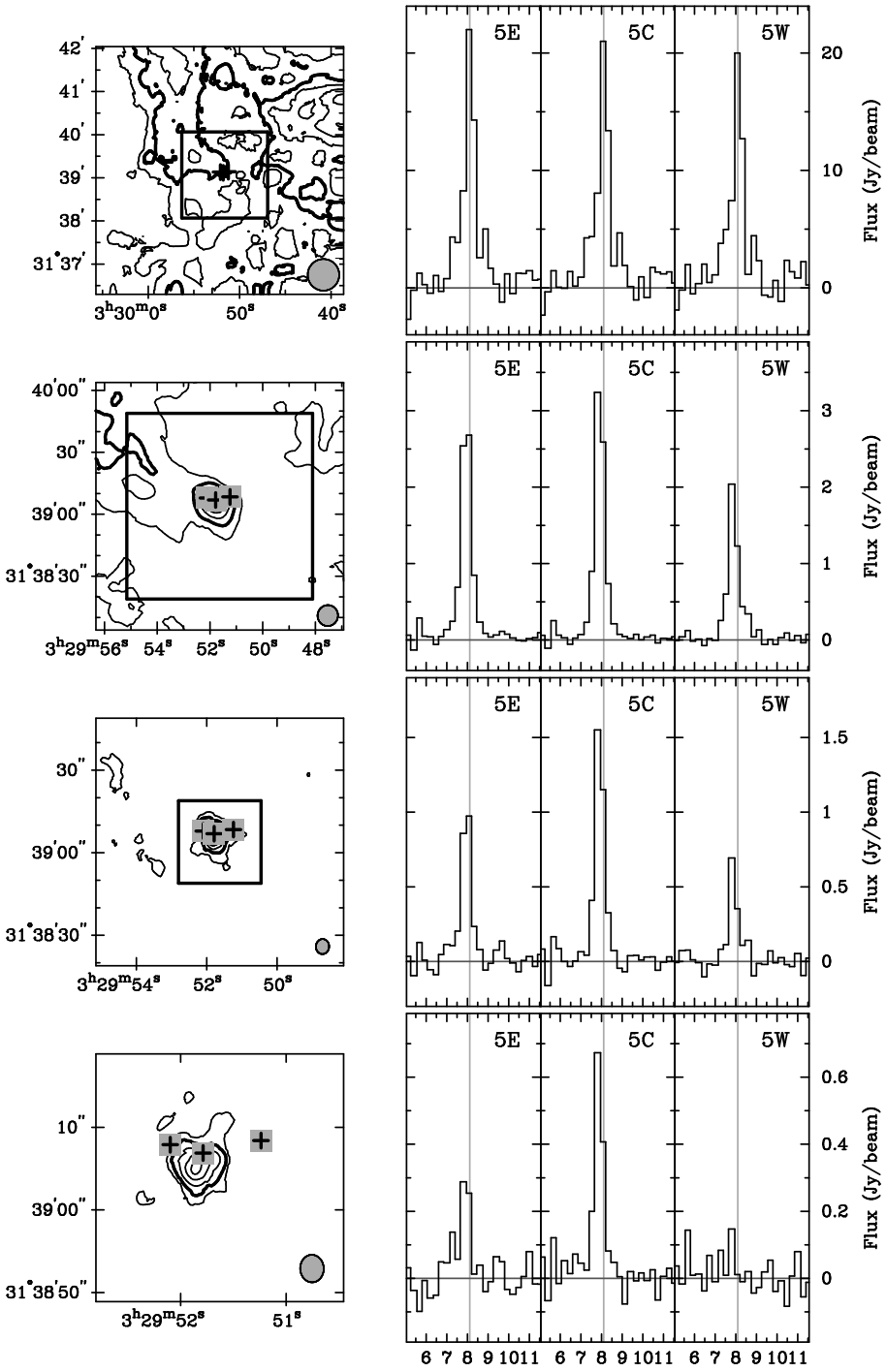

Figure 4.42: Per5 spectra. The plots at left show integrated intensity contours from the $C^{18}O$ data, as in Figure 4.41. To the right of each contour plot are spectra from the $C^{18}O$ datacubes. The plus symbols indicate the positions of the continuum sources. All spectra display the flux in Jy beam^{-1} averaged over the area of a beam. In all rows, the gray vertical lines show central velocities of Gaussian functions fit to the profiles from the FCRAO map (top row).

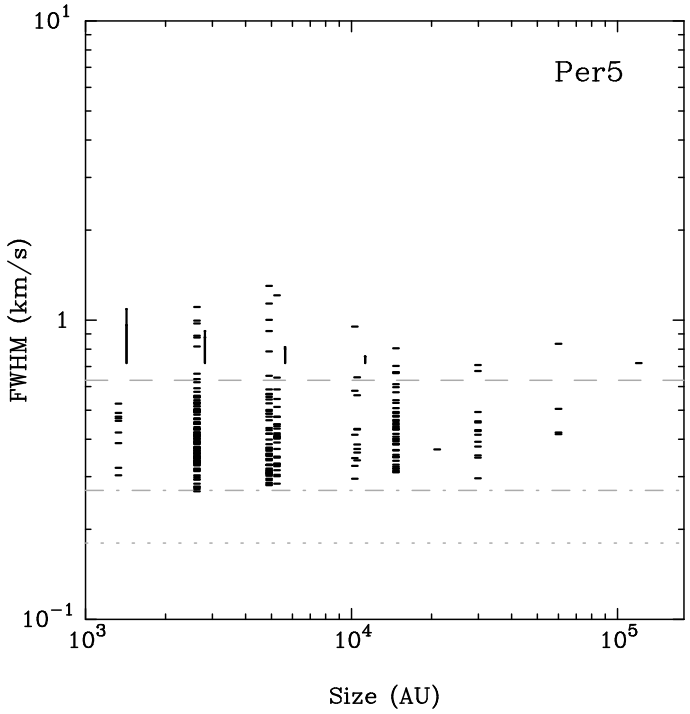

Figure 4.43: Per5 line width (FWHM) *vs.* size correlations for gridded $C^{18}O$ spectra. The dashed line indicates the line width corresponding to the sound speed of the medium: $\mathrm{FWHM}_{c_s}(20\ \mathrm{K}) = 0.63$ km s^{-1}. The dotted line indicates the thermal line width: $\mathrm{FWHM}_T(20\ \mathrm{K}) = 0.18$ km s^{-1}. The dash-dot line indicates the channel width of the spectra: $\delta V = 0.27$ km s^{-1}.

The pointing center of the BIMA observations (see Table 4.1) is the position of the NH_3 peak. In maps of the N_2H^+ emission (published after the BIMA observations were made), the displacement is less than $1'$. Caselli *et al.* (2002a) modeled the N_2H^+ emission from Per6 with two different spherically symmetric cloud models: one with a single power law description of the density, the other with a "broken" power law. In the first case, the best fit to the integrated N_2H^+ intensity profile was produced with a power law exponent of 1.9. In the second case, the best breakpoint between the inner and outer power laws was 0.05 pc ($30''$ at the distance of Perseus). Based upon these results, Per6 has the most flattened inner density profile among the set of embedded cores modeled by Caselli *et al.* (2002a).

4.13.2 Continuum Data

In Figure 4.44, the $\lambda = 2.7$ mm continuum emission peaks ($S_{peak} = 2.9$ mJy beam^{-1}) right at the northern edge of the BIMA primary beam area. This is close to the position of IRAS 03271+3013, the IRAS source associated with the Per6 core. From the center of the map (the position of the NH_3 peak observed by Ladd, Myers, & Goodman (1994)), no continuum emission emerges from the noise. In the continuum map with $5''$ resolution, the emission from near IRAS 03271+3013 appears weak (2.2 mJy beam^{-1}) and is extended by roughly three beam widths along a northwest-southeast axis.

4.13.3 $C^{18}O$ Data

The dominant feature in the FCRAO data from the vicinity of Per6 (Figure 4.45*a*) is the large cloud that fills the eastern half of the map. This cloud is one of the series of clouds that comprise the "central ridge" through Perseus. The emission peak, 23.9 Jy beam^{-1}·km s^{-1}, is located just outside of the BIMA primary beam area. The location of Per6 itself is largely void of emission. A small extension of the eastern cloud protrudes into the northeastern quadrant of the primary beam area and seems to indicate the position of the IRAS source. The velocity map of the region (Figure 4.45*b*) appears to show a collision of redshifted and blueshifted clumps within the BIMA primary beam area. However, the full range of velocities in the maps of Per6 is narrower than for any other survey target, so the colors exaggerate the differences.

In the intensity maps at both $10''$ and $5''$ resolution (Figures 4.45*c,e*), the central position of Per6 truly appears as a void of $C^{18}O$ emission. However, IRAS 03271+3013 is just within the edge of the primary beam, and it is also the point of

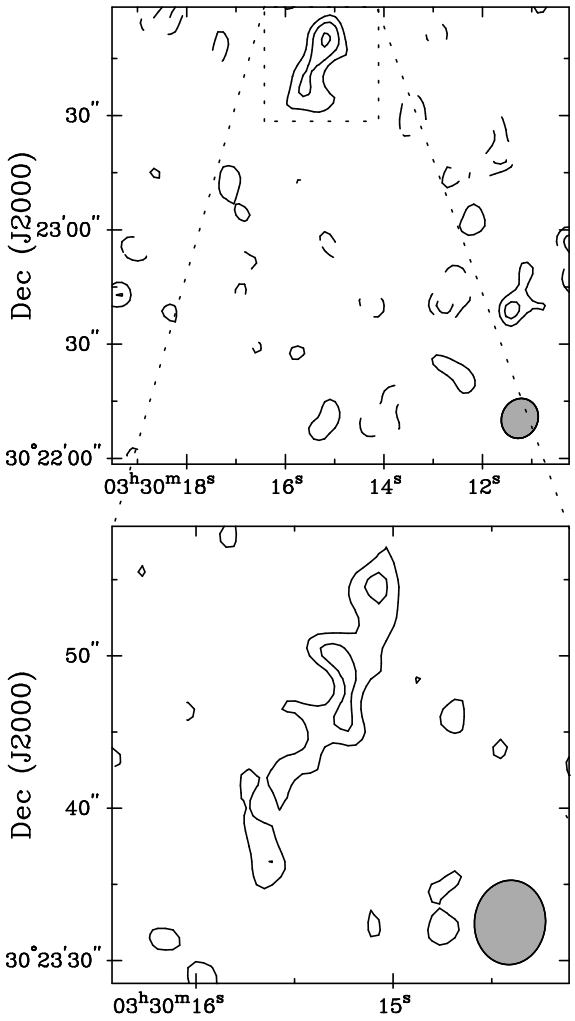

Figure 4.44: Maps of the $\lambda = 2.7$ mm continuum emission from Per6. The contour intervals are $(-4, -3, -2, 2, 3, 4) \times \sigma$ in mJy beam^{-1}. *Top:* $\sigma = 0.7$ mJy beam^{-1}; beam is $10.7'' \times 9.5''$, P.A.$= -24.6°$. *Bottom:* $\sigma = 0.6$ mJy beam^{-1}; beam is $5.5'' \times 4.7''$, P.A.$= -5.1°$.

peak C^{18}O emission. In the $10''$ map, the peak is 1.3 Jy beam^{-1}·km s^{-1}, and in the $5''$ map, the peak is 0.4 Jy beam^{-1}·km s^{-1}. The velocity maps of the same regions (Figures 4.45*d,f*) also highlight the lack of emission from the center of Per6. The low level emission that is barely evident in the intensity maps doesn't pass the 3σ cutoff for inclusion in the velocity map. The trends in the velocity field around the IRAS source (5.8 km s^{-1}) remain consistent at the higher resolutions.

Although IRAS 03271+3013 is the strongest source in the combined maps of

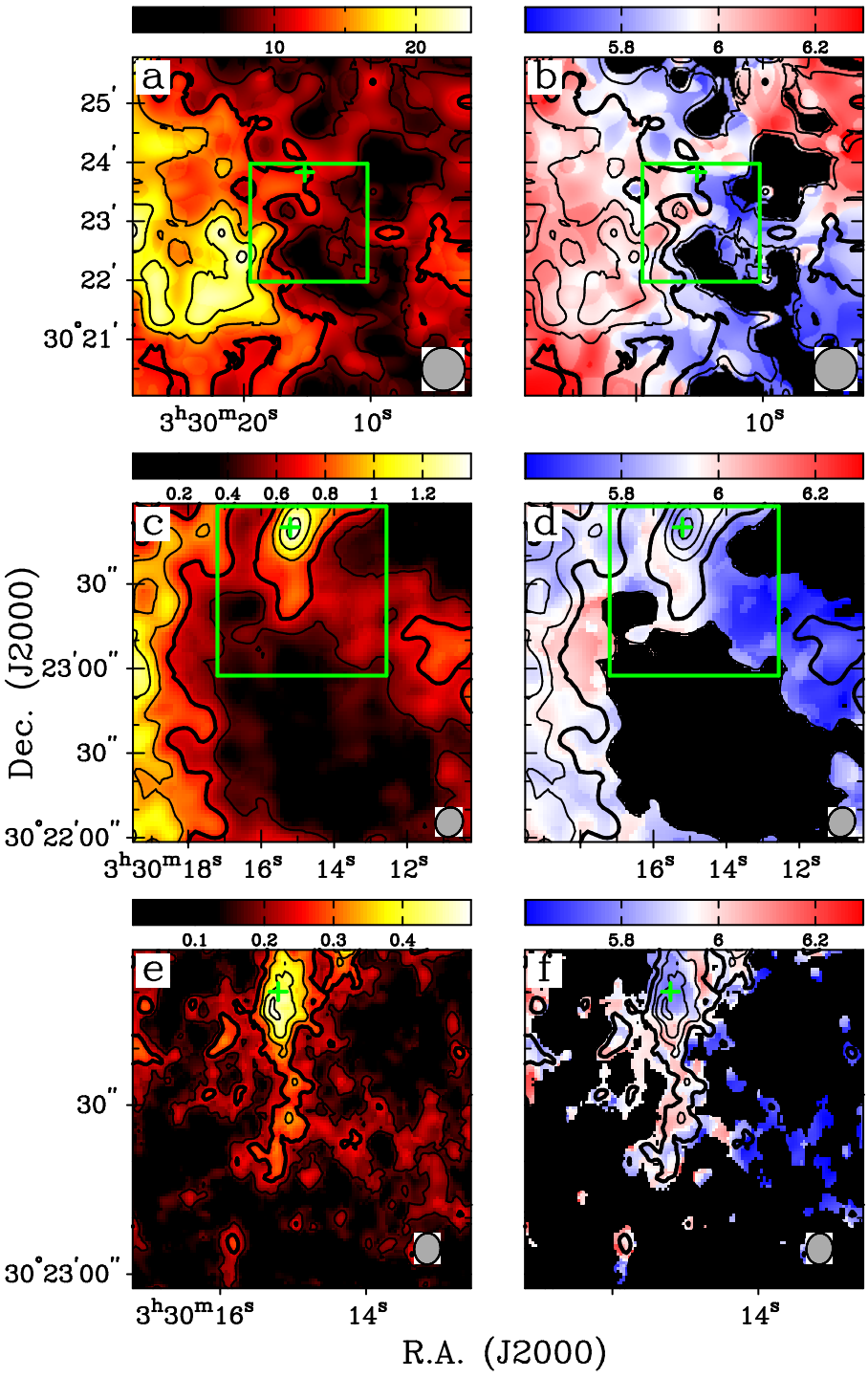

Figure 4.45: $C^{18}O$ $J = 1 \rightarrow 0$ integrated intensity and velocity of Per6. Velocity range is 5.6-6.3 km s^{-1} in all panels. The plus symbol indicates the position of the continuum source shown in Figure 4.44. (a,b) I_ν^{peak} = 23.88 Jy beam^{-1}·km s^{-1}; σ = 2.5 Jy beam^{-1}·km s^{-1}; beam is 44″ × 44″. (c,d) I_ν^{peak} = 1.31 Jy beam^{-1}·km s^{-1}; σ = 0.15 Jy beam^{-1}·km s^{-1}; beam is 10.66″ × 9.48″, P.A.= −24.6°. (e,f) I_ν^{peak} = 0.44 Jy beam^{-1}·km s^{-1}; σ = 0.06 Jy beam^{-1}·km s^{-1}; beam is 5.54″ × 4.66″, P.A.= −5.1°.

Per6, its position at the edge of the primary beam makes both its appearance and flux suspect, as the edge of the primary beam is one of the less sensitive positions on the map. The spectra taken from the position of IRAS 03271+3013, however (Figure 4.46), appear symmetrical and strong at all resolutions. The central velocity from the FCRAO map is 5.88 km s^{-1}.

The trends in the line width *vs.* grid size correlation, displayed in Figure 4.47, also reflect the absence of flux from the central core. The main contribution to the flux within the primary beam area come from the FCRAO maps. There are still a significant number of measured FWHM to contribute to the correlation, but none from the smallest grid squares, where there is no flux in the BIMA maps. The distribution in the line widths is flat across all grid sizes, and fairly narrow at each individual grid size. The means of the distributions are narrow, too. Consequently, a large fraction of the FWHM (74.0%) are below the sonic threshold.

4.14 IRAS 03282+3035

4.14.1 Background

IRAS 03282+3035 and its eponymous embedding core (which will, for brevity's sake, be identified simply as I03282) is located $\sim 45'$ southeast of the NGC1333 region. Extensive interferometer and single-dish observations of the NH_3 (1,1) and (2,2) inversion lines (Bachiller, Martín-Pintado, & Planesas 1991; Tafalla *et al.* 1993) reveal that I03282 is a very cold ($\sim$10 K) low-mass dense core that is relatively isolated from other Perseus cores. The core is slightly elongated in the north-south direction, and a single-temperature blackbody fit to the SED from 12 to 1300 μm yields an estimated luminosity of 1.55 $L_\odot$ (Barsony *et al.* 1998).

The star-forming activity of I03282 is highlighted by the core's strong bipolar

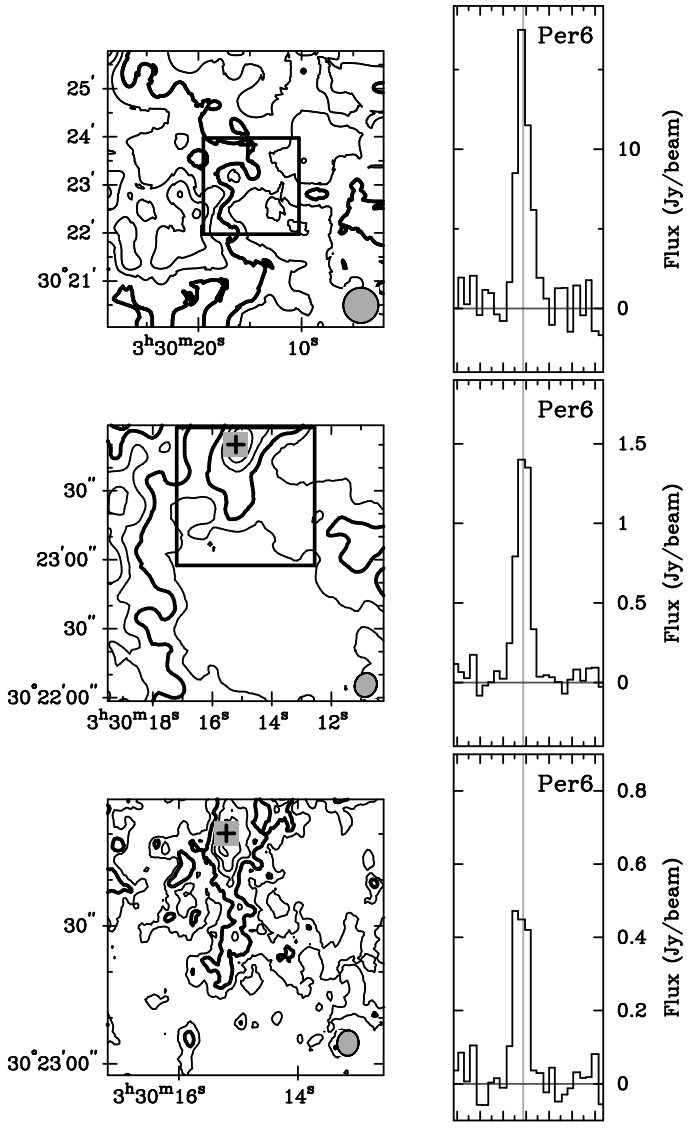

Figure 4.46: Per6 spectra. The plots at left show integrated intensity contours from the $C^{18}O$ data, as in Figure 4.45. To the right of each contour plot are spectra from the $C^{18}O$ datacubes. The plus symbol indicates the position of the continuum source. All spectra display the flux in Jy beam^{-1} averaged over the area of a beam. In all rows, the gray vertical lines show central velocity of a Gaussian function fit to the profile from the FCRAO map (top row).

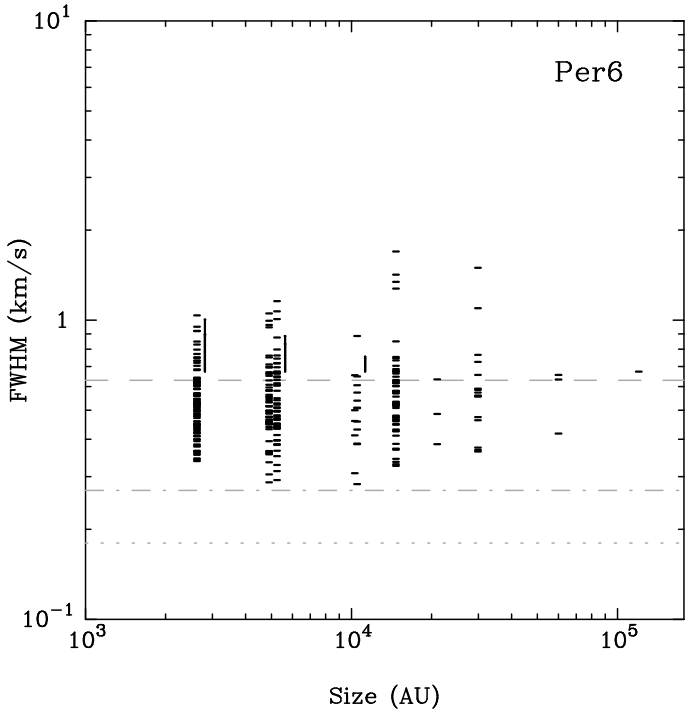

Figure 4.47: Per6 line width (FWHM) *vs.* size correlations for gridded $C^{18}O$ spectra. The dashed line indicates the line width corresponding to the sound speed of the medium: $\mathrm{FWHM}_{c_s}(20\ \mathrm{K}) = 0.63$ km s^{-1}. The dotted line indicates the thermal line width: $\mathrm{FWHM}_T(20\ \mathrm{K}) = 0.18$ km s^{-1}. The dash-dot line indicates the channel width of the spectra: $\delta V = 0.27$ km s^{-1}.

outflow. Jets of material emerge from the center of the core at extremely high velocities ($\sim$60 km s^{-1}), then appear to slow down when they interact with the surrounding medium. A string of shock features (*e.g.* knots of SiO and H_2 λ = 2.122 μm emission) indicates that the I03282 outflows have a complicated history; the displacement of the shock features from the jets suggests a punctuated, rather than continuous, outflow (Bally *et al.* 1993; Bachiller *et al.* 1994). The two jets have different strengths: the blueshifted lobe, directed southeast, is stronger than the redshifted lobe, which extends to the northwest. The asymmetry of the outflow may be a consequence of the displacement of the protostar from the center of the core. Because IRAS 03282+3035 is closer to the near edge of the core, the redshifted jet weakens as it pushes through the dense gas at the core center (Tafalla *et al.* 1993).

4.14.2 Continuum Data

I03282 appears as a strong 2.7 mm continuum emitter at all three resolutions probed by the BIMA data (Figure 4.48). At both 10″ resolution (S_{peak} = 54.6 mJy beam^{-1}) and 5″ resolution (S_{peak} = 48.3 mJy beam^{-1}), the source appears compact and unresolved. In the map with 3″ resolution, the emission peak is 44.9 mJy beam^{-1}, and the low level emission contours begin to spread out toward the north and west. There is no indication of a secondary source.

4.14.3 $C^{18}O$ Data

The I03282 core appears near the northern edge of a larger cloud in the FCRAO map of the $C^{18}O$ emission (Figure 4.49*a*). The high emission contours of the cloud appear to avoid the area of the BIMA primary beam. The emission peak (46.8 Jy beam^{-1}·km s^{-1}) is located just outside the primary beam area to the southwest. The position of I03282 itself is marked by a hole in the large scale emission. In the velocity map of the cloud (Figure 4.49*b*), I03282 is located in one of the few red velocity positions (7.3—km s^{-1}) on the map. The majority of the cloud appears at bluer velocities, with the southern edge, on the far side of the emission peak, blueshifted to 6.5-6.6 km s^{-1}.

At 10″ resolution (Figure 4.49*c*), I03282 is clearly a source of $C^{18}O$ emission. The peak intensity at the continuum position, 2.1 Jy beam^{-1}·km s^{-1}, is equal to the peak along the southern edge of the map that arises from the larger cloud. The contours suggest that the emission is spherical. In the velocity map (Figure 4.49*d*), no pattern is apparent in the velocities. Red velocities appear as often as blue velocities, with no large scale trends.

When the core is examined with 5″ resolution (Figure 4.49*e*), much of the low

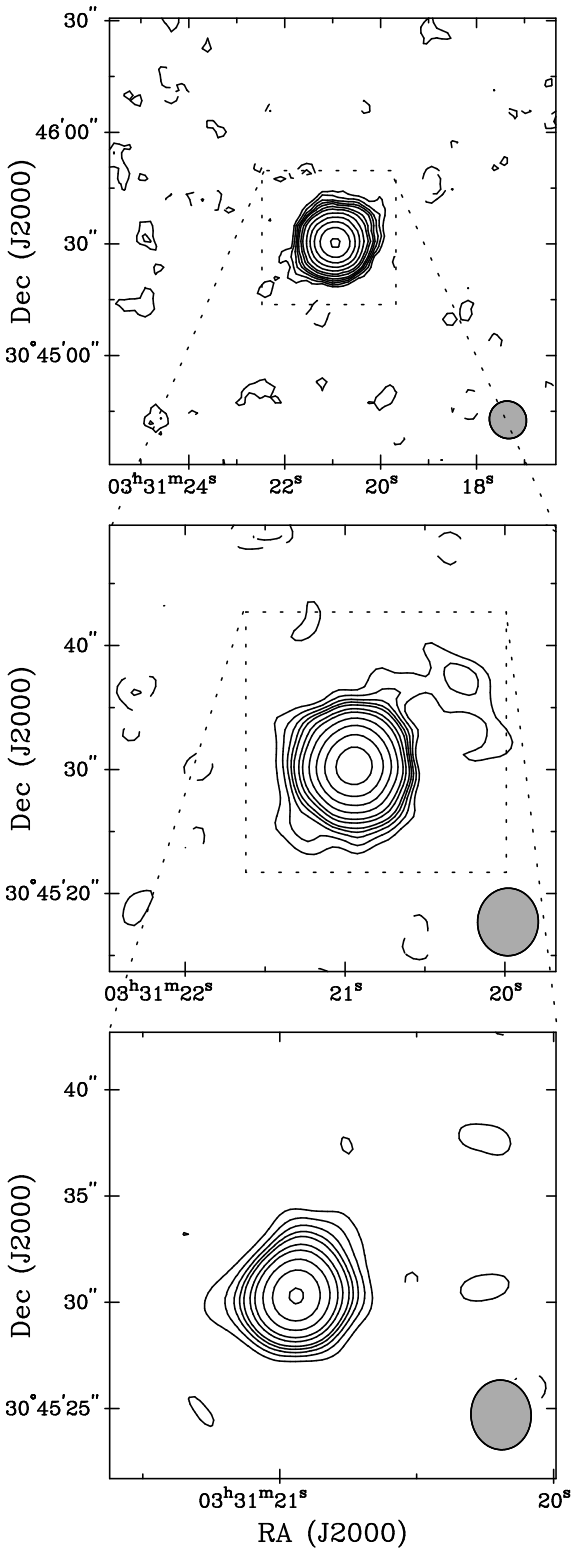

Figure 4.48: Maps of the $\lambda = 2.7$ mm continuum emission from IRAS 03282+3034. The contour intervals are $(-4, -3, -2, 2, 3, 4, 5, 6, 8, 10, 14.14, 20, 28.28, 40, 56.56) \times \sigma$ in mJy beam^{-1}. *Top:* $\sigma = 0.9$ mJy beam^{-1}; beam is $10.3'' \times 9.8''$, P.A.$= 38.1°$. *Middle:* $\sigma = 1.0$ mJy beam^{-1}; beam is $5.5'' \times 4.9''$, P.A.$= -2.4°$. *Bottom:* $\sigma = 1.5$ mJy beam^{-1}; beam is $3.3'' \times 2.8''$, P.A.$= 4.4°$.

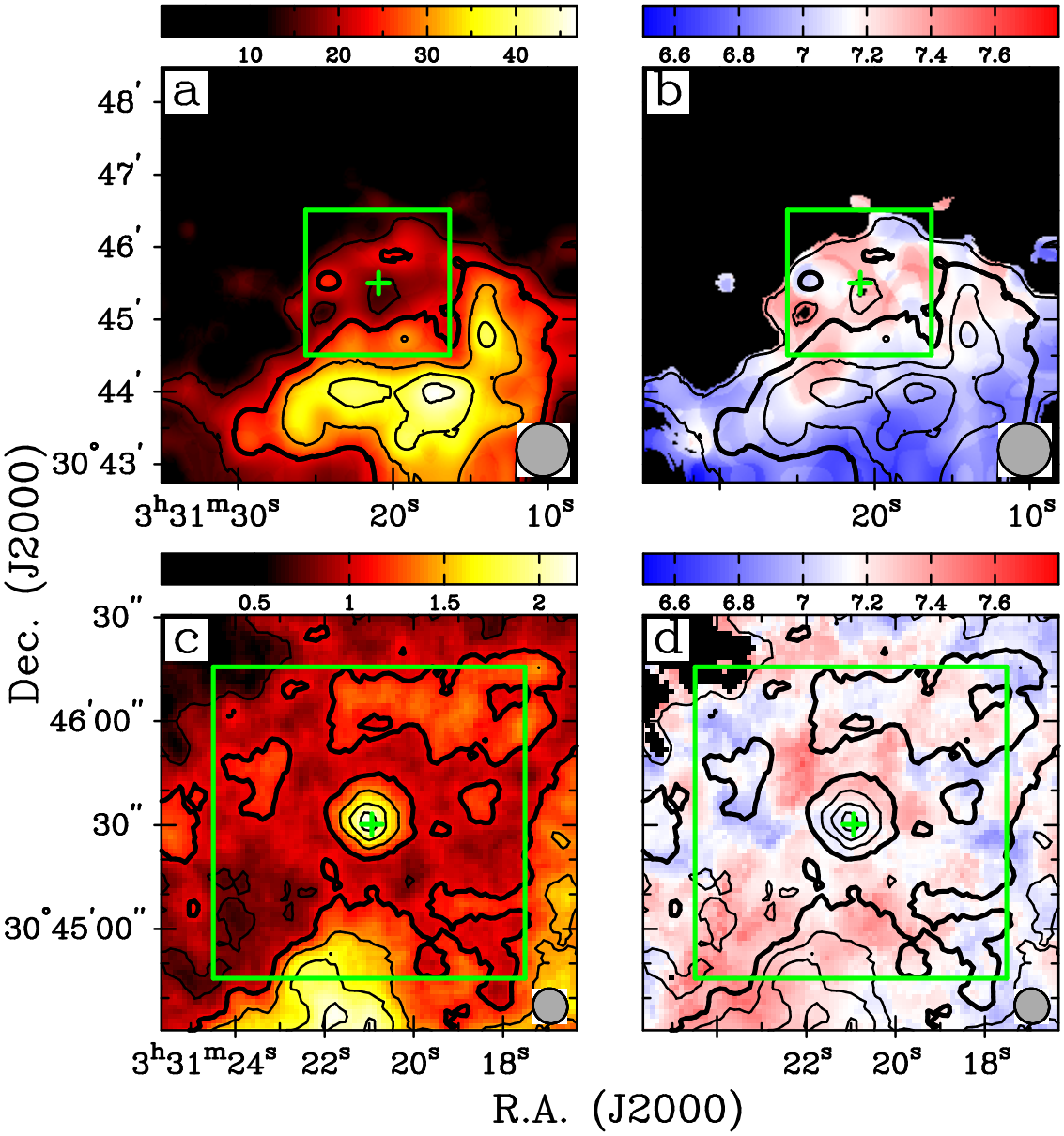

Figure 4.49: $C^{18}O$ $J = 1 \rightarrow 0$ integrated intensity and velocity of IRAS 03282+3034. Velocity range is 6.5-7.8 km s^{-1} in all panels. The plus symbols indicate the position of the continuum source from Figure 4.48. (a,b) $I_\nu^{peak} = 46.85$ Jy beam^{-1}·km s^{-1}; $\sigma = 4.9$ Jy beam^{-1}·km s^{-1}; beam is $44'' \times 44''$. (c,d) $I_\nu^{peak} = 2.14$ Jy beam^{-1}·km s^{-1}; $\sigma = 0.21$ Jy beam^{-1}·km s^{-1}; beam is $10.27'' \times 9.79''$, P.A.$= 38.1°$.

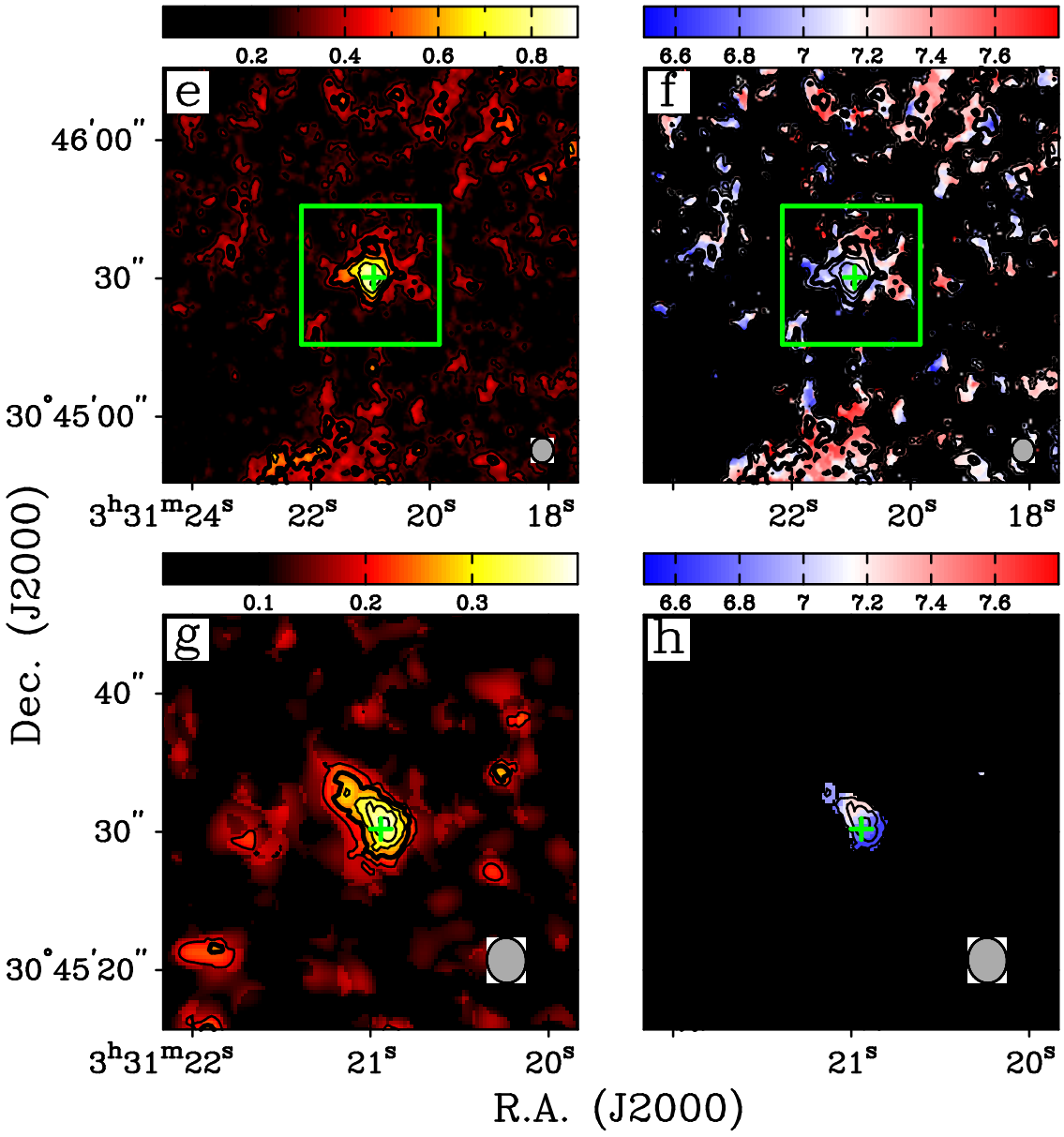

Figure 4.49: *Continued.* (e,f) I_ν^{peak} = 0.89 Jy beam^{-1}·km s^{-1}; σ = 0.10 Jy beam^{-1}·km s^{-1}; beam is 5.45″ × 4.90″, P.A.= −2.4°. (g,h) I_ν^{peak} = 0.39 Jy beam^{-1}·km s^{-1}; σ = 0.08 Jy beam^{-1}·km s^{-1}; beam is 3.28″ × 2.83″, P.A.= 4.4°.

level emission from the background cloud breaks up into scattered clumps. The only notable emission peak (0.9 Jy beam^{-1}·km s^{-1}) is centered exactly on the continuum position of I03282. The velocity map at this resolution (Figure 4.49*f*) reveals some apparent trends in the motions of the I03282 envelope. In general, the southern and eastern edges of the envelope are blueshifted (6.7-6.9 km s^{-1}) with respect to the northern and western edges (7.5-7.7 km s^{-1}).

Zooming in on the center of the I03282 core with 3″ resolution (Figure 4.49*g*), the envelope surrounding the continuum source now appears elongated over ∼3 beam widths in a northeast-southwest direction. The peak of the $C^{18}O$ emission (0.4 Jy beam^{-1}·km s^{-1}) is still centered on the continuum source. The velocity field of the elongated emission zone (Figure 4.49*h*) does not suggest a rotating disk. The emitting region is blueshifted (6.8 km s^{-1}) at its extremes and redshifted (7.3 km s^{-1}) in the middle.

The spectrum from I03282 (Figure 4.50) taken from the FCRAO data reveal a broad, symmetrical line with a central velocity of 7.30 km s^{-1}. At this resolution, the line shape is well fit by a Gaussian. As the resolution of the map improves, however, the line profiles become increasingly complicated. At 10″ resolution, the line center is shifted blueward, and a secondary peak emerges on the red line wing. The line profile from the 5″ map is similar, and in the 3″ map, the central velocity has shifted to 6.7 km s^{-1}.

A total of 239 lines are measured and included in the line width *vs.* grid size diagram shown in Figure 4.51. The trends in the measured FWHM are apparent. The lower envelope of the FWHM points gradually increases with grid size, and the upper envelope gradually decreases. Only 8.8% of the lines are narrower than the sonic line width.

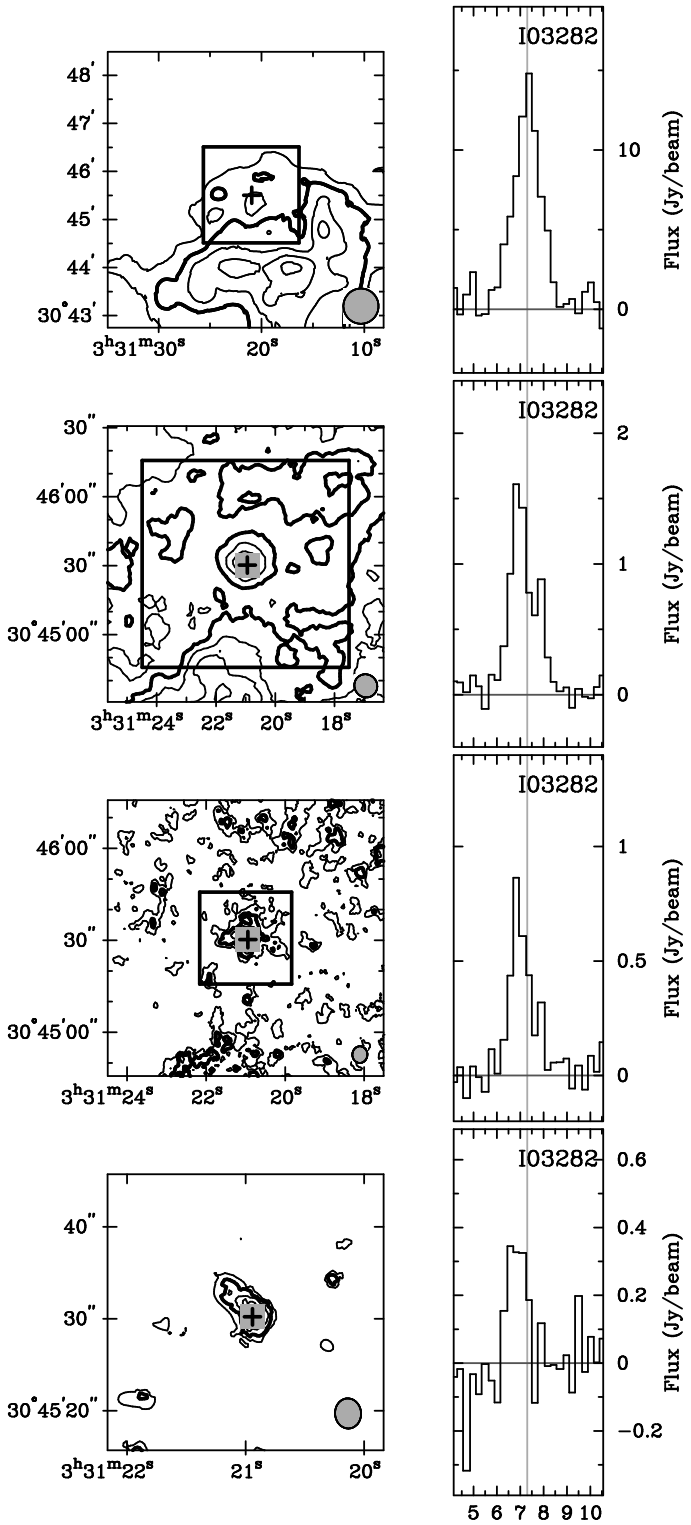

Figure 4.50: IRAS 03282+3034 spectra. The plots at left show integrated intensity contours from the $C^{18}O$ data, as in Figure 4.49. To the right of each contour plot are spectra from the $C^{18}O$ datacubes. The plus symbols indicate the position of the continuum source. All spectra display the flux in Jy beam^{-1} averaged over the area of a beam. In all rows, the gray vertical lines show the central velocity of a Gaussian functions fit to the profile from the FCRAO map (top row).

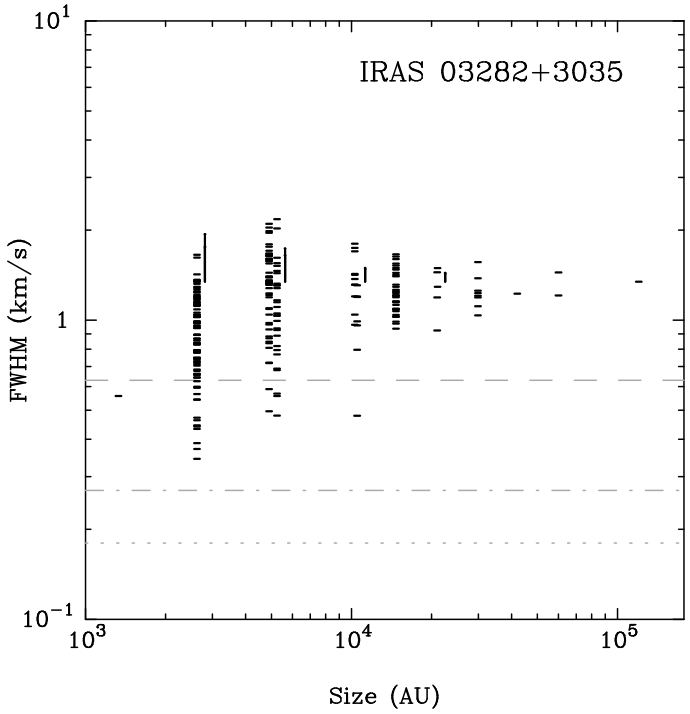

Figure 4.51: IRAS 03282+3034 line width (FWHM) *vs.* size correlations for gridded $C^{18}O$ spectra. The dashed line indicates the line width corresponding to the sound speed of the medium: $\mathrm{FWHM}_{c_s}(20\ \mathrm{K}) = 0.63$ km s^{-1}. The dotted line indicates the thermal line width: $\mathrm{FWHM}_T(20\ \mathrm{K}) = 0.18$ km s^{-1}. The dash-dot line indicates the channel width of the spectra: $\delta V = 0.27$ km s^{-1}.

4.15 Per7

4.15.1 Background

The Per7 cloud is centered on IRAS 03295+3050. The single-dish (Haystack 37 m antenna) observations of Ladd, Myers, & Goodman (1994) identified two centers of NH_3 concentration: one $\sim 2'$ west and the other $\sim 2'$ east. In the BIMA survey, IRAS 03295+3050 was outside the primary beam area of both the Per7W and Per7E observations. The N_2H^+ observations by Caselli *et al.* (2002a) focused on the position of Per7E, revealing it to be elongated in a northeast-southwest direction with an aspect ratio of ~ 1.5.

4.15.2 Continuum Data

The map of 2.7 mm continuum emission in Figure 4.52 shows only the result from the map centered on the Per7W core. A 4σ emission peak (3.2 mJy beam^{-1}) appears just east of the map center. In the higher resolution map (lower panel), however, the clump dissolves into a cluster of unimpressive 3σ clumps. There is no better evidence for a source of 2.7 mm continuum emission in either the Per7W or Per7E core.

4.15.3 $C^{18}O$ Data

Maps of the $C^{18}O$ emission from the Per7W and Per7E cores are displayed in Figures 4.53 & 4.54, respectively. The appearance of the FCRAO maps shows that the BIMA observations zoom in on nearly adjacent regions within the same cloud. The Per7W cloud appears along the western edge of the Per7 cloud, where the $C^{18}O$ emission is quickly declining, and Per7E is in the center of the cloud, where the emission peaks. Neither core harbors a strong, centralized $C^{18}O$ emission source, and neither core shows strong, systematic trends in the velocity maps. In the velocity maps of Per7W, the regions delineated by the higher emission contours have bluer velocities. In the maps of Per7E, the western half of the Per7 cloud is blueshifted with respect to the eastern half of the cloud in the FCRAO map, but this overall trend does not persist down to the scales of the $10''$ and $5''$ resolution maps.

The line width *vs.* grid size correlations (Figures 4.55 & 4.56) for both cores are quite similar. The number of included spectra is 415 for Per7W and 455 for Per7E. Both correlations show relatively narrow distributions of the FWHM. The percentage of line widths less than the sonic line width is 4.3% and 0.9% for Per7W and Per7E, respectively.

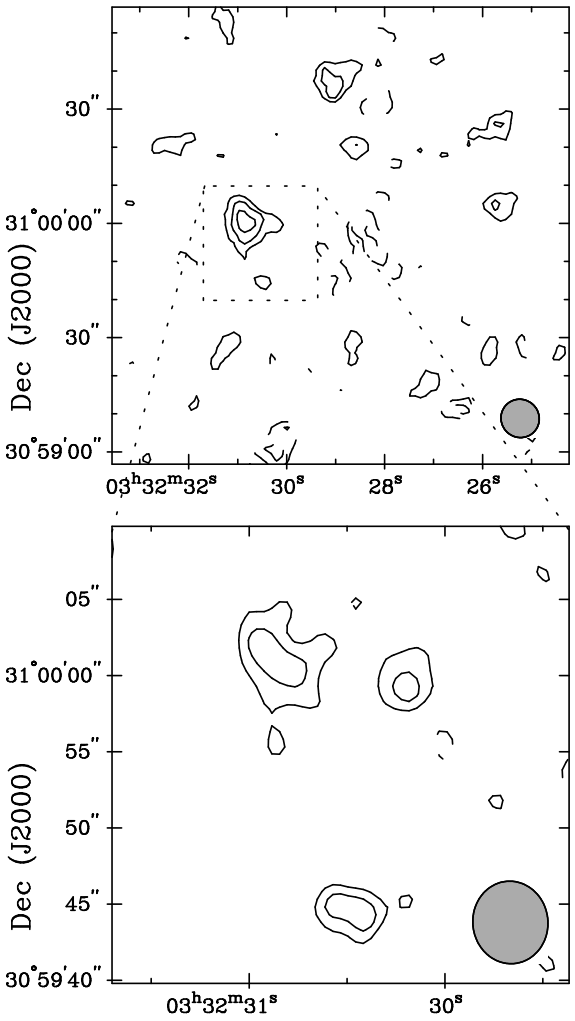

Figure 4.52: Maps of the $\lambda = 2.7$ mm continuum emission from Per7 West. The contour intervals are $(-4, -3, -2, 2, 3, 4) \times \sigma$ in mJy beam^{-1}. *Top:* $\sigma = 0.9$ mJy beam^{-1}; beam is $10.2'' \times 9.9''$, P.A.$= 43.8°$. *Bottom:* $\sigma = 0.7$ mJy beam^{-1}; beam is $5.4'' \times 4.9''$, P.A.$= 5.8°$.

4.16 Per9 W

4.16.1 Background

Like the Per7 cloud $20'$ to the south, the Per9 cloud was also revealed to have a bilateral morphology in the NH_3 observations of Ladd, Myers, & Goodman (1994). The two clumps are separated by $\sim 2'$ in R.A., but the western clump, identified

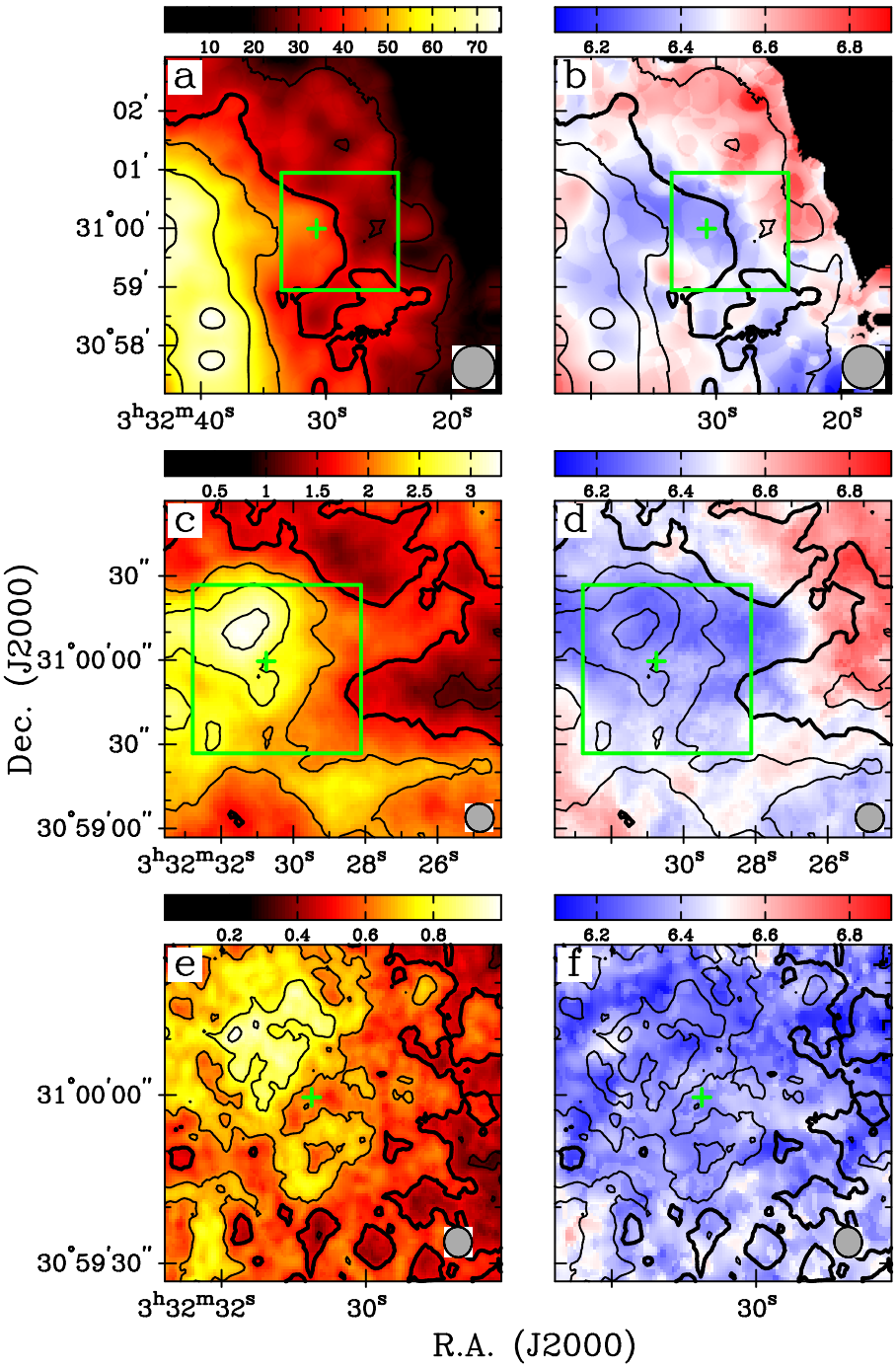

Figure 4.53: $C^{18}O$ $J = 1 \rightarrow 0$ integrated intensity and velocity of Per7 West. Velocity range is 6.1-6.9 km s^{-1} in all panels. The plus symbol indicates the position of the continuum source in Figure 4.52. (a,b) $I_\nu^{peak} = 75.39$ Jy beam^{-1}·km s^{-1}; $\sigma =$ 6.6 Jy beam^{-1}·km s^{-1}; beam is $44'' \times 44''$. (c,d) $I_\nu^{peak} = 3.22$ Jy beam^{-1}·km s^{-1}; $\sigma = 0.26$ Jy beam^{-1}·km s^{-1}; beam is $10.18'' \times 9.94''$, P.A.$= 43.8°$. (e,f) $I_\nu^{peak} =$ 0.98 Jy beam^{-1}·km s^{-1}; $\sigma = 0.10$ Jy beam^{-1}·km s^{-1}; beam is $5.42'' \times 4.93''$, P.A.$= 5.8°$.

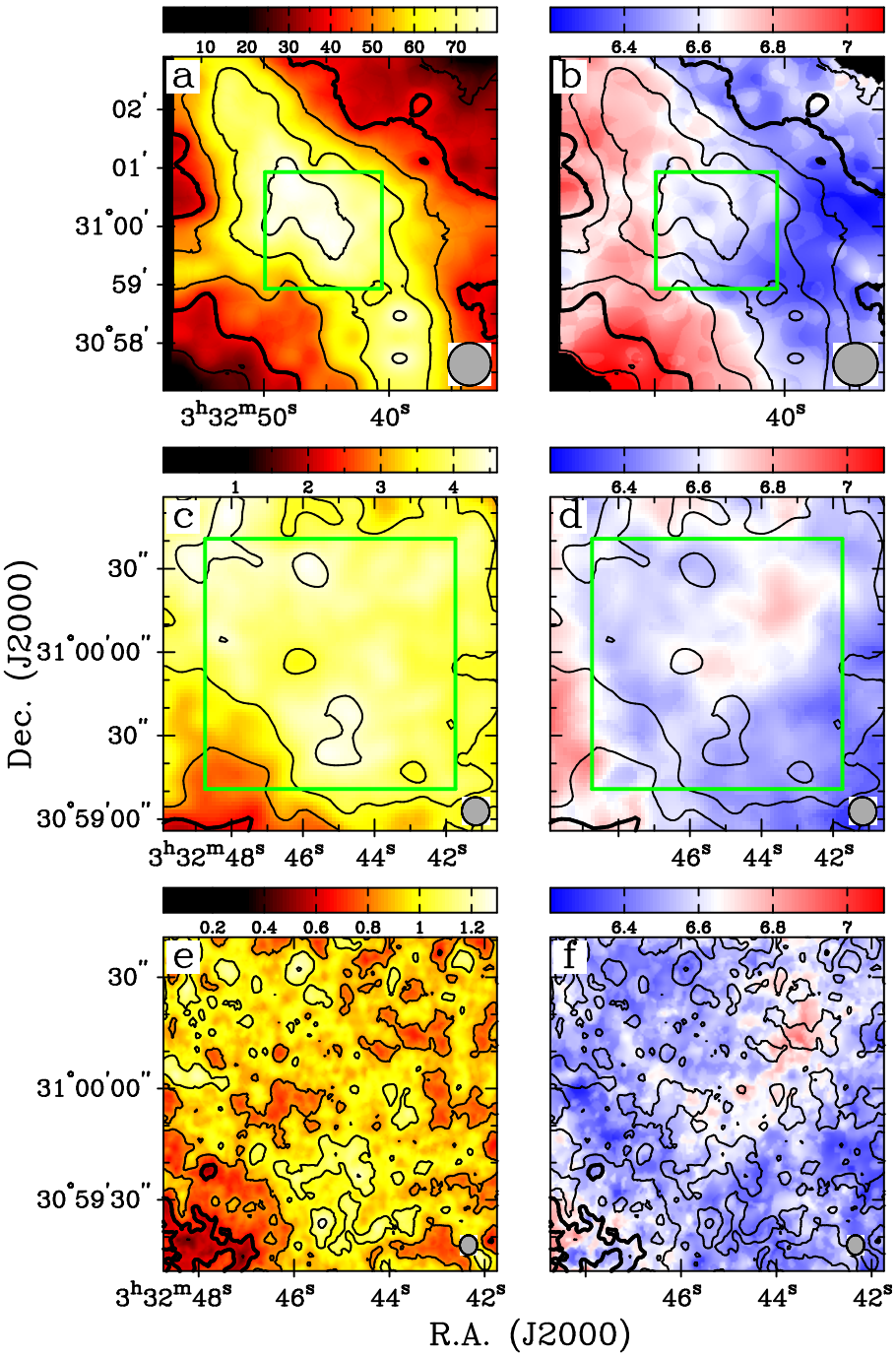

Figure 4.54: $C^{18}O$ $J = 1 \rightarrow 0$ integrated intensity and velocity of Per7 East. Velocity range is 6.2-7.1 km s^{-1} in all panels. (a,b) I_ν^{peak} = 79.79 Jy $beam^{-1}$·km s^{-1}; σ = 8.7 Jy $beam^{-1}$·km s^{-1}; beam is $44'' \times 44''$. (c,d) I_ν^{peak} = 4.53 Jy $beam^{-1}$·km s^{-1}; σ = 0.25 Jy $beam^{-1}$·km s^{-1}; beam is $10.19'' \times 9.89''$, P.A.= 22.8°. (e,f) I_ν^{peak} = 1.29 Jy $beam^{-1}$·km s^{-1}; σ = 0.12 Jy $beam^{-1}$·km s^{-1}; beam is $5.30'' \times 4.68''$, P.A.= −1.6°.

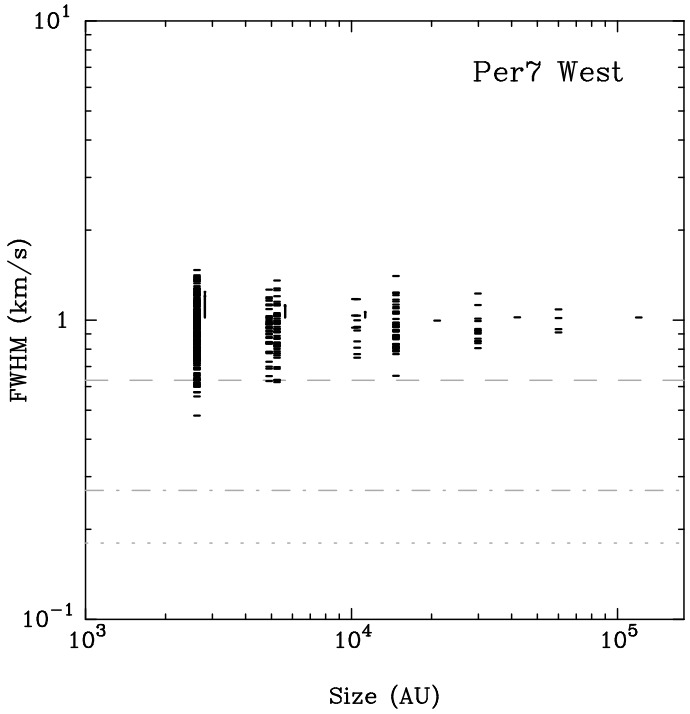

Figure 4.55: Per7 West line width (FWHM) *vs.* size correlations for gridded $C^{18}O$ spectra. The dashed line indicates the line width corresponding to the sound speed of the medium: $\mathrm{FWHM}_{c_s}(20\ \mathrm{K}) = 0.63$ km s^{-1}. The dotted line indicates the thermal line width: $\mathrm{FWHM}_T(20\ \mathrm{K}) = 0.18$ km s^{-1}. The dash-dot line indicates the channel width of the spectra: $\delta V = 0.27$ km s^{-1}.

as Per9[-3,2] in their survey, is clearly the stronger of the two. Per9 appears in between two IRAS sources: IRAS 03303+3108 is $\sim 3'$ to the southeast, and IRAS 03301+3111 is $\sim 1.5'$ to the northwest. Neither IRAS source falls within the primary beam area of the BIMA observations. In the N_2H^+ maps of Per9 by Caselli *et al.* (2002a), the emission peak of Per9W is displaced another arc-minute further west of the NH_3 peak.

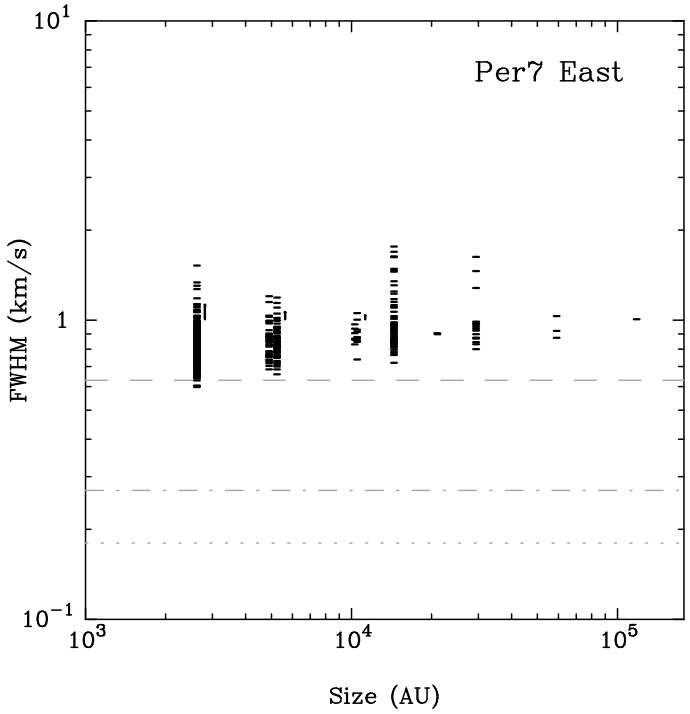

Figure 4.56: Per7 East line width (FWHM) *vs.* size correlations for gridded $C^{18}O$ spectra. The dashed line indicates the line width corresponding to the sound speed of the medium: $FWHM_{c_s}(20\ K) = 0.63$ km s^{-1}. The dotted line indicates the thermal line width: $FWHM_T(20\ K) = 0.18$ km s^{-1}. The dash-dot line indicates the channel width of the spectra: $\delta V = 0.27$ km s^{-1}.

4.16.2 Continuum Data

No continuum emission is detected from the Per9W core.

4.16.3 $C^{18}O$ Data

The map of $C^{18}O$ emission from Per9W is displayed in Figure 4.57. The top panels (*a,b*) show the regions mapped by the FCRAO data alone. In the integrated intensity map, the Per9W core appears within a trough of $C^{18}O$ intensity, in between two brighter clumps. The peak of the brighter clump, near the eastern edge of the map, is 72.6 Jy beam^{-1}·km s^{-1}. In the velocity map of the Per9 region, the Per9W core appears within a transition region between the bluer velocities (6.5-6.7 km s^{-1}) that

occupy the material in the eastern and northern edges of the map, and the redder velocities (6.9-7.1 km s^{-1}) in the southwestern quadrant of the map.

As the maps zoom in on the position of the Per9W core with $10''$ and $5''$ resolution, there is no sign of a compact $C^{18}O$ emission source within the cloud. The dominant contribution to the intensities in the maps comes from the FCRAO data. The velocity field of the Per9W region is disorganized. There are no discernable trends that might signal systematic motions in the Per9W core.

The line width *vs.* grid size correlation shown in Figure 4.58 is the "average" correlation for the set of BIMA survey cores. The number of spectra contributing to the correlation (424) is about average; the spread in the line widths is about average; and the mean line width is also about average. The trends in the upper and lower envelopes of the points are not as pronounced as for some of the other sources, indicating that the variations in FWHM are more uniform across the grid sizes. The percentage of FWHM below the sonic line width is 8.3%.

4.17 Barnard1 b

4.17.1 Background

Barnard 1 lies along the central ridge of the Perseus cloud, in between the NGC1333 and IC348 star forming regions. Three young (visible) stars, LZK21, LkHα327, and LkHα328, lie within the $\sim 30' \times 40'$ area surveyed by Bachiller, Menten, & del Rio-Alvarez (1990). These stars all produce Hα emission consistent with ages < 6 Myr (Cohen & Kuhi 1979), and they all suffer from several magnitudes of extinction, suggesting that they lie at the front edge of the massive ($M=1200M\odot$) Barnard 1 cloud. Based upon an extensive molecular line survey, Bachiller & Cernicharo (1984) proposed a multi-layered structure for the cloud. The densest part, the main core,

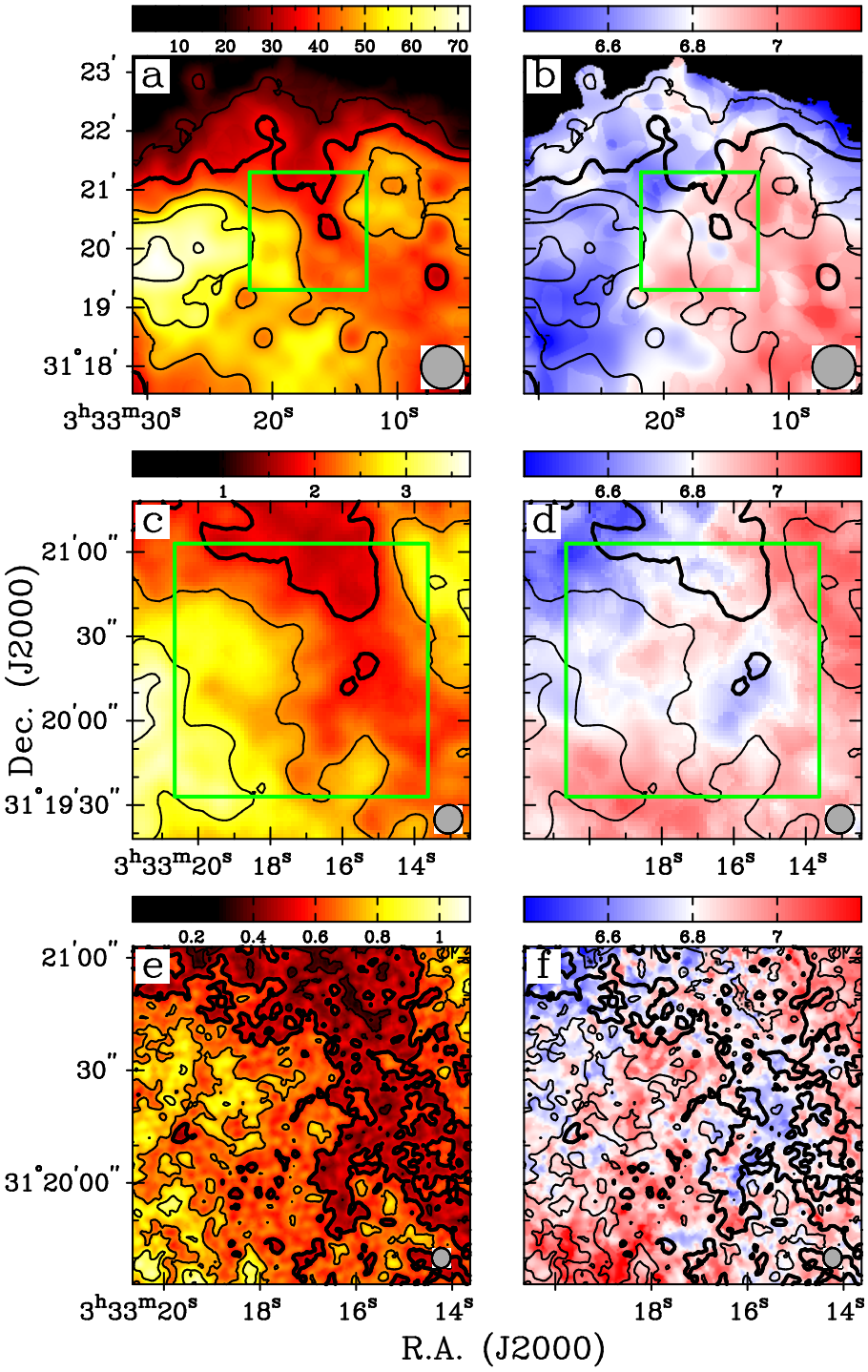

Figure 4.57: $C^{18}O$ $J = 1 \rightarrow 0$ integrated intensity and velocity of Per9 West. Velocity range is 6.4-7.2 km s^{-1} in all panels. (a,b) I_ν^{peak} = 72.57 Jy $beam^{-1}$·km s^{-1}; σ = 7.1 Jy $beam^{-1}$·km s^{-1}; beam is $44'' \times 44''$. (c,d) I_ν^{peak} = 3.69 Jy $beam^{-1}$·km s^{-1}; σ = 0.27 Jy $beam^{-1}$·km s^{-1}; beam is $10.28'' \times 9.86''$, P.A.= $-36.9°$. (e,f) I_ν^{peak} = 1.04 Jy $beam^{-1}$·km s^{-1}; σ = 0.10 Jy $beam^{-1}$·km s^{-1}; beam is $5.35'' \times 4.92''$, P.A.= $-0.8°$.

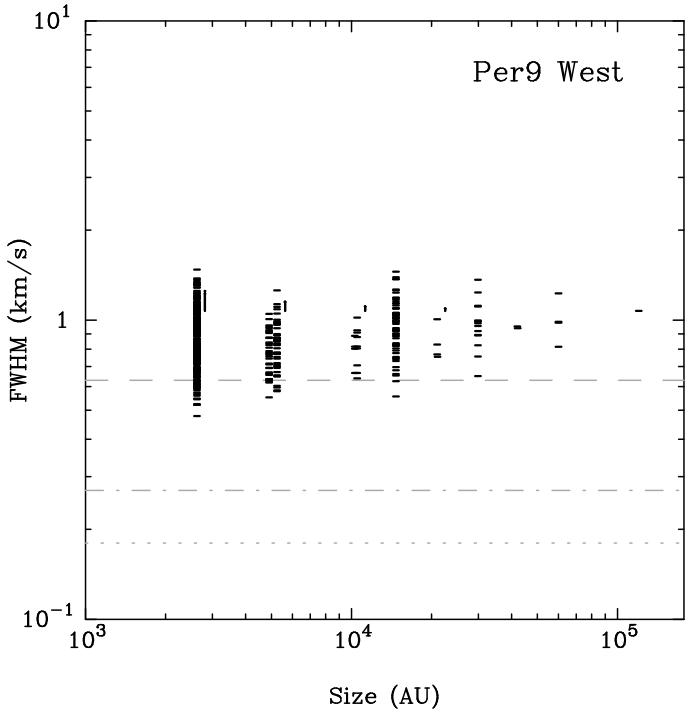

Figure 4.58: Per9 West line width (FWHM) *vs.* size correlations for gridded $C^{18}O$ spectra. The dashed line indicates the line width corresponding to the sound speed of the medium: $\mathrm{FWHM}_{c_s}(20\ \mathrm{K}) = 0.63$ km s^{-1}. The dotted line indicates the thermal line width: $\mathrm{FWHM}_T(20\ \mathrm{K}) = 0.18$ km s^{-1}. The dash-dot line indicates the channel width of the spectra: $\delta V = 0.27$ km s^{-1}.

corresponds to the region of peak extinction and also peak NH_3 emission. Only one IRAS source, 03301+3057, is located within the main core. This object is the source of a high-velocity outflow that lies nearly perpendicular to the line of sight (Hirano *et al.* 1997). The kinematic age of the outflow, based upon observations of the CO $J = 2 \rightarrow 1$ line and shock-stimulated SiO emission, is estimated to range from 10^3 (Bachiller, Menten, & del Rio-Alvarez 1990) to 10^4 (Yamamoto *et al.* 1992) years. Recent SCUBA maps of the 850μm continuum have identified *four* emission peaks within the core, dubbed B1 a, b, c, and d (Matthews & Wilson 2002). B1 a corresponds to the location of the IRAS source, but B1 b, roughly $1'$ to the east, is the site of strongest submillimeter emission. High resolution interferometric observations of B1 b resolved two continuum sources, B1 b North and South, approximately $20''$

apart (Hirano *et al.* 1999).

4.17.2 Continuum Data

The two Barnard 1 protostars are unmistakable in the $\lambda = 2.7$ mm continuum emission maps (Figure 4.59). At $10''$ resolution, they appear to be embedded in a common envelope of emission, extended in the north-south direction, that spans the center of the map. The peak fluxes at B1-bN and B1-bS are 44.9 and 52.5 mJy beam^{-1}, respectively. At $5''$ resolution, the bN and bS sources split apart. There is still evidense for residual continuum emission between them, but this dissolves in the highest resolution map (bottom panel). At $3''$ resolution, the protostars appear to be independent sources, separated by $20''$. The peak fluxes are 32.6 and 41.2 mJy beam^{-1} at bN and bS, respectively.

4.17.3 $C^{18}O$ Data

The morphology of the larger Barnard 1 cloud is evident in the $C^{18}O$ map created from the FCRAO data (Figure 4.60*a*). The cloud fills the entire area of the map. The B1-b continuum sources, indicated with the plus symbols, are located near the center, although not at one of the two emission peaks. The strongest peak, 116.3 Jy beam^{-1}·km s^{-1}, is located just north of the primary beam area; the second strongest peak, 113.8 Jy beam^{-1}·km s^{-1}, lies less than a beam width eastward of the B1 sources. The velocity map of the cloud (Figure 4.60*b*), rather than showing a combination of red and blue velocities, is dominated by the blue end of the velocity spectrum. (The velocities at the red end of the spectrum are only detected in the highest resolution observations, see below.) Nevertheless, some contrast is discernable in the map. The northern and eastern edges of the cloud have velocities in the range 6.2-6.4 km s^{-1}. In the western and southern regions, the velocities are

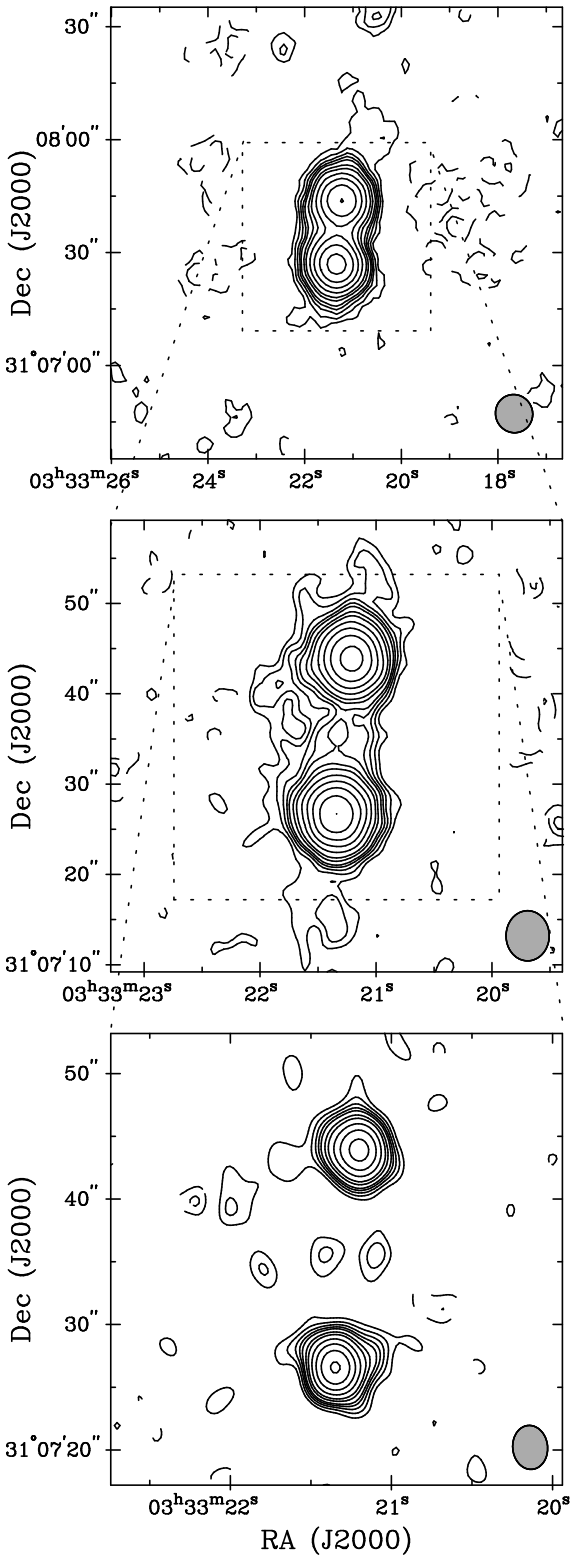

Figure 4.59: Maps of the $\lambda = 2.7$ mm continuum emission from Barnard1 b. The contour intervals are $(-4, -3, -2, 2, 3, 4, 5, 6, 8, 10, 14.14, 20, 28.28, 40) \times \sigma$ in mJy beam^{-1}. *Top:* $\sigma = 1.1$ mJy beam^{-1}; beam is $10.2'' \times 9.8''$, P.A.$= 23.2°$. *Middle:* $\sigma = 0.8$ mJy beam^{-1}; beam is $5.6'' \times 4.8''$, P.A.$= -0.4°$. *Bottom:* $\sigma = 1.0$ mJy beam^{-1}; beam is $3.5'' \times 2.8''$, P.A.$= 5.7°$.

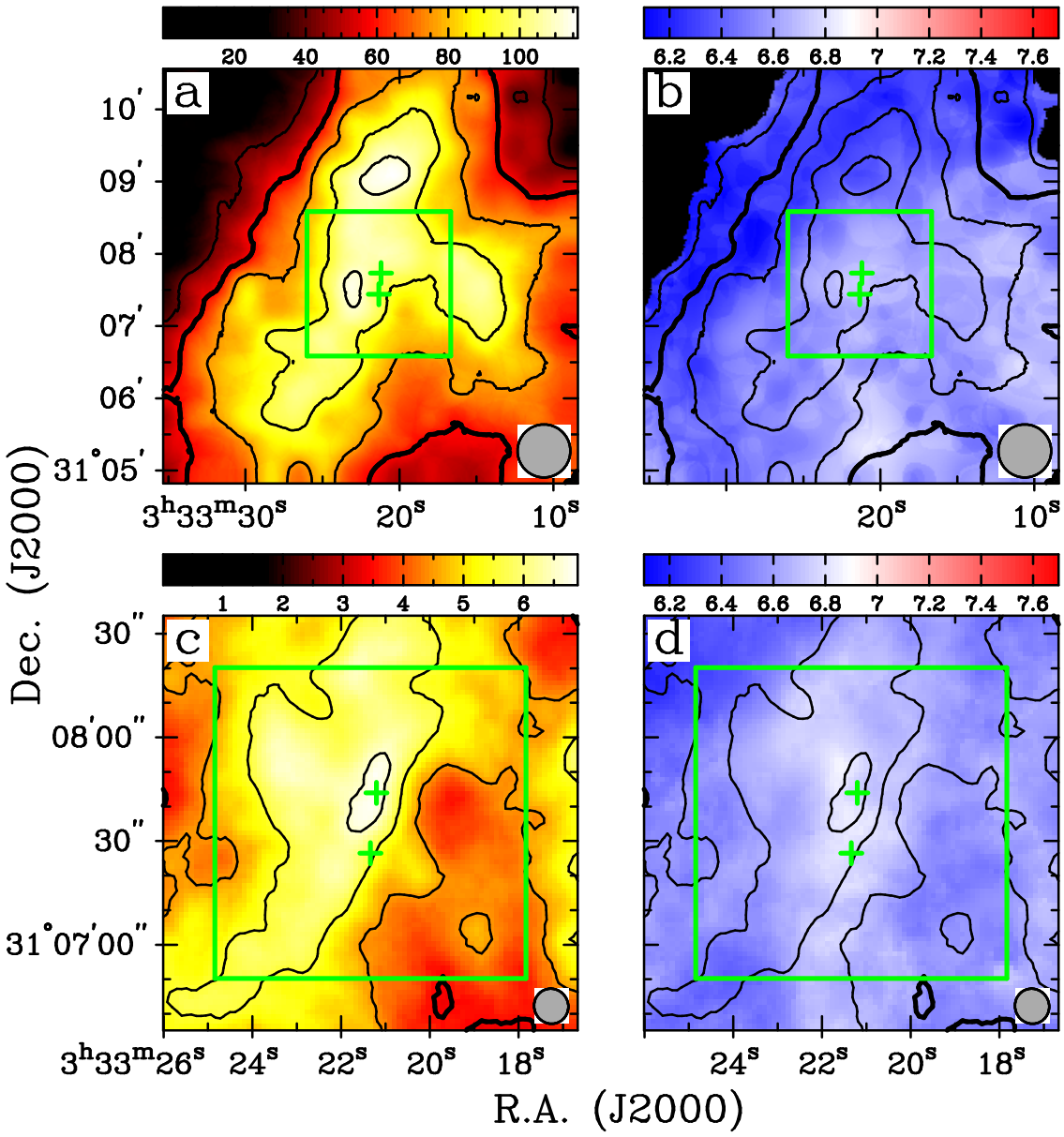

Figure 4.60: $C^{18}O$ $J = 1 \rightarrow 0$ integrated intensity and velocity of Barnard1 b. Velocity range is 6.1-7.7 km s^{-1} in all panels. Plus symbols indicate positions of continuum sources from Figure 4.59. (a,b) $I_\nu^{peak} = 116.3$ Jy beam^{-1}·km s^{-1}; $\sigma =$ 11.7 Jy beam^{-1}·km s^{-1}; beam is $44'' \times 44''$. (c,d) $I_\nu^{peak} = 6.84$ Jy beam^{-1}·km s^{-1}; $\sigma = 0.51$ Jy beam^{-1}·km s^{-1}; beam is $10.21'' \times 9.83''$, P.A.= 23.2°.

6.6-6.8 km s^{-1}.

In the map of the combined BIMA and FCRAO data with $10''$ resolution (Figure 4.60*c*), both of the continuum objects still appear near the center of the larger

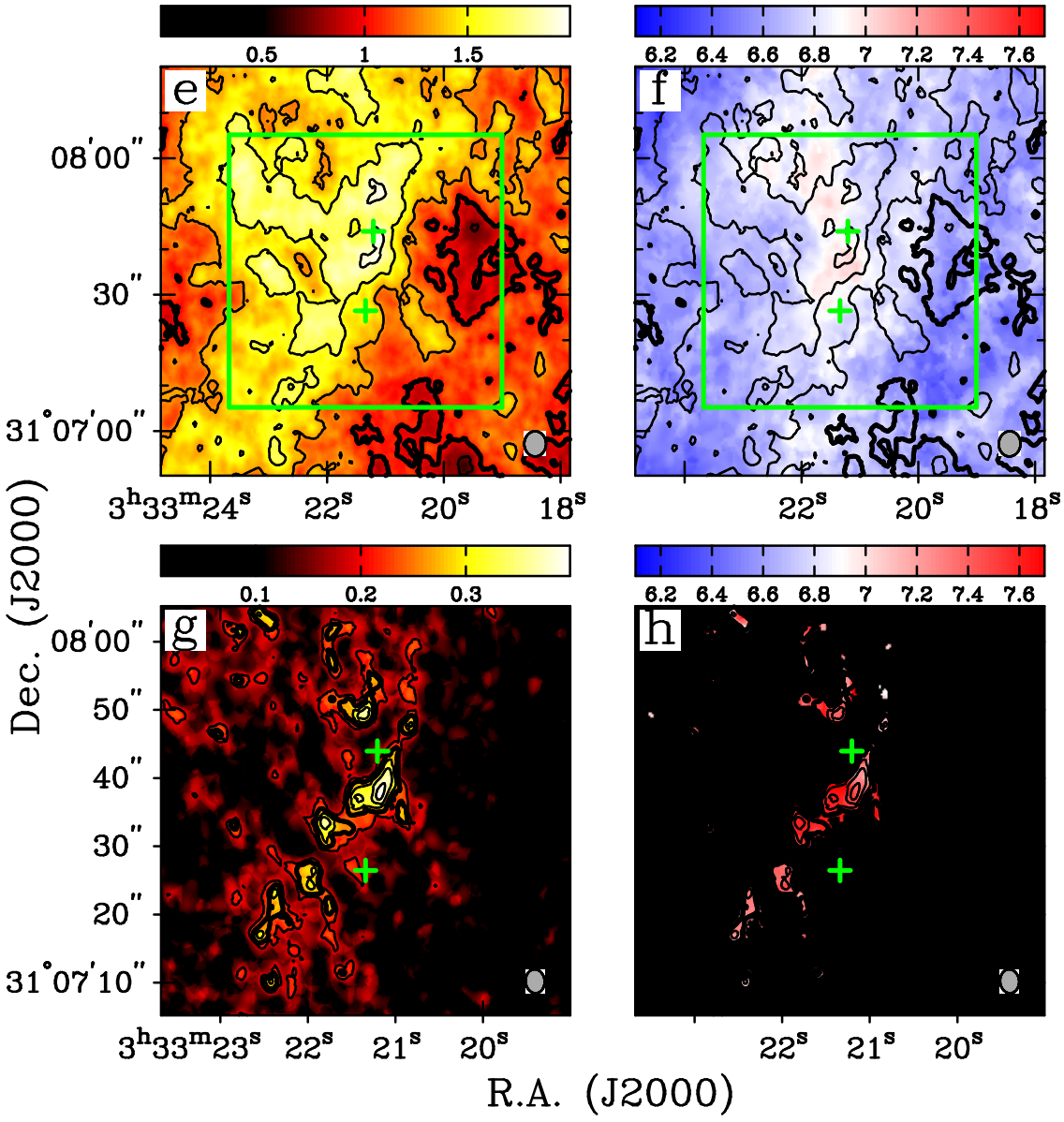

Figure 4.60: *Continued.* (e,f) I_ν^{peak} = 1.95 Jy beam^{-1}·km s^{-1}; σ = 0.16 Jy beam^{-1}·km s^{-1}; beam is 5.55″ × 4.78″, P.A.= −0.4°. (g,h) I_ν^{peak} = 0.36 Jy beam^{-1}·km s^{-1}; σ = 0.05 Jy beam^{-1}·km s^{-1}; beam is 3.51″ × 2.78″, P.A.= 5.7°.

cloud. The northern source, B1-bN, coincides with the point of peak emission in the map (6.8 Jy beam^{-1}·km s^{-1}), while B1-bS is located just off of the peak. The B1-b sources, themselves, are not distinguished in the map at this resolution. The dominant feature is still the larger cloud, extended along a north-south axis. In the velocity map of the region (Figure 4.60*d*), the first glimmer of a red velocity (6.9 km s^{-1}) emerges from the center of the otherwise blue cloud.

The B1 continuum objects still do not appear bright in C^{18}O emission in the 5″ resolution map (Figure 4.60*e*). The cloud itself is still bright, with emission clumps of 1.9 and 2.0 Jy beam^{-1}·km s^{-1} on the northern and southern side (respectively) of B1-bN. In the velocity map (Figure 4.60*f*), a splash of still more reddened velocity (7.0 km s^{-1}) cuts through the middle of the map, but the velocities don't coincide with either the C^{18}O of the continuum emission peaks.

In the 3″ resolution map (Figure 4.60*g*), only the BIMA data remain. The distribution of C^{18}O at this resolution reveals that the B1 objects are not strong C^{18}O emitters. The emission peaks (∼0.4 Jy beam^{-1}·km s^{-1}) are confined to a narrow filament that runs northwest-southeast in between the two source. In the velocity map (Figure 4.60*h*), the material in this filament is revealed as the anchor of the red end of the velocity spectrum. The gas in this narrow filament appears to be moving in a different velocity range (7.1-7.7 km s^{-1}) from the gas that surrounds it.

The spectra taken at the positions of the B1 continuum sources (Figure 4.61) evolve as the resolution of the maps increases. The behavior can be explained by the fact that the continuum objects themselves are not strong C^{18}O emitters. In the spectra made from the FCRAO data alone, the lines are strong and slightly skewed toward the blue. The central velocities are 6.71 km s^{-1}. As the resolution of the maps increases, the lines from both B1-bN and B1-bS become double-peaked. It

appears that the blue component is contributed by the FCRAO data, and the red component is contributed by the filamentary structure in the BIMA data. In the highest resolution maps, the FCRAO data are no longer included, but the beam size around the continuum objects is also too small to include any of the filamentary emission. The emission lines disappear.

The strong contribution from the large cloud to the combined maps distributes abundant $C^{18}O$ flux throughout the primary beam area, and many strong spectra contribute to the points on the line width *vs.* grid size correlation (Figure 4.62). The total number of measured spectral lines included is 432. Most of the FWHM are distributed evenly around a mean slightly greater than 1 km s^{-1}. There are a minority of the FWHM (2.5%) that fall below the sonic line width.

4.18 Barnard5 IRS1

4.18.1 Background

The Barnard5 cloud marks the eastern extreme of the Perseus cloud complex. Barnard5 encloses a total mass of approximately 1000 M$\odot$ (Langer *et al.* 1989) that includes a number of embedded YSOs. Four sources were detected in the far-infrared wavebands of the IRAS satellite (Beichman *et al.* 1984). The brightest of these four sources, IRAS 03445+3242, is located near the center of the cloud (the point of peak NH_3 emission) and is commonly referred to as B5 IRS1. Based upon the IRAS fluxes, the total luminosity of IRS1 is estimated to be 9.6 L$\odot$.

The Barnard5 IRAS sources generate a network of CO outflows (Goldsmith, Langer, & Wilson 1986). The outflows from IRS1 are the most spectacular of these: they are both powerful and highly collimated. CO observations trace the outflows to a full extent of $\sim 5'$ along a position angle of $\sim 65°$. The blueshifted lobe extends

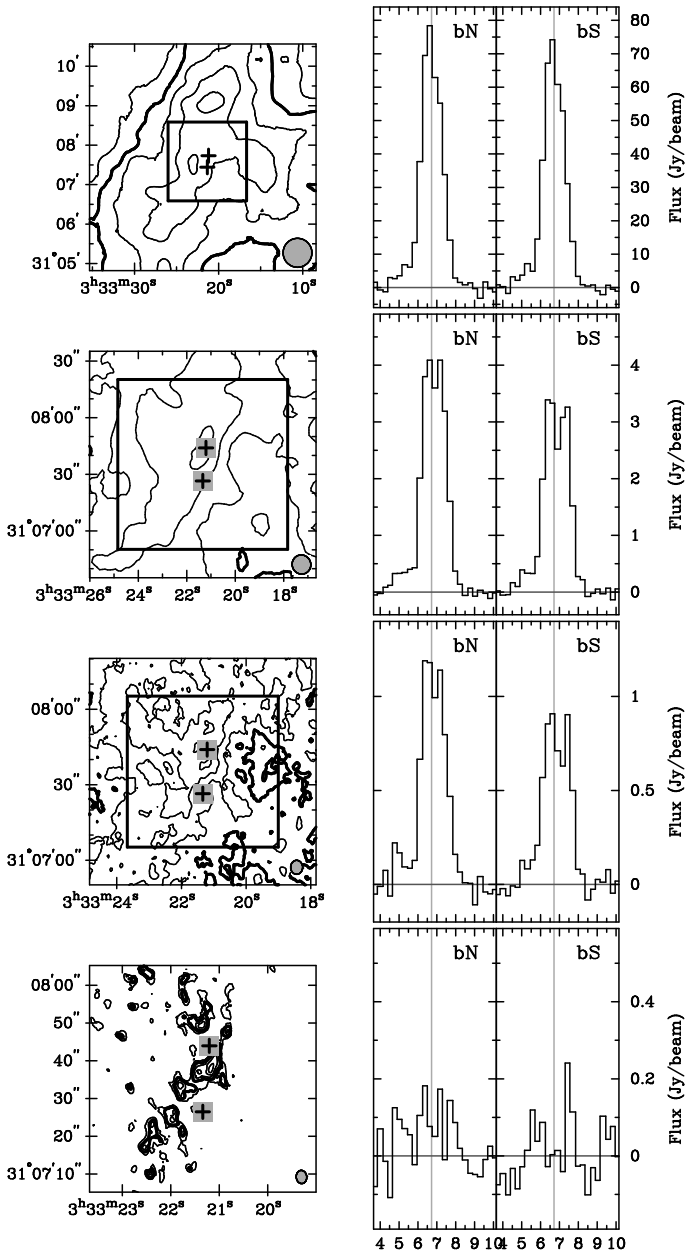

Figure 4.61: Barnard1 b spectra. The plots at left show integrated intensity contours from the $C^{18}O$ data, as in Figure 4.60. To the right of each contour plot are spectra from the $C^{18}O$ datacubes. The plus symbols indicate the positions of the continuum sources. All spectra display the flux in Jy beam^{-1} averaged over the area of a beam. In all rows, the gray vertical lines show central velocities of Gaussian functions fit to the profiles from the FCRAO map (top row).

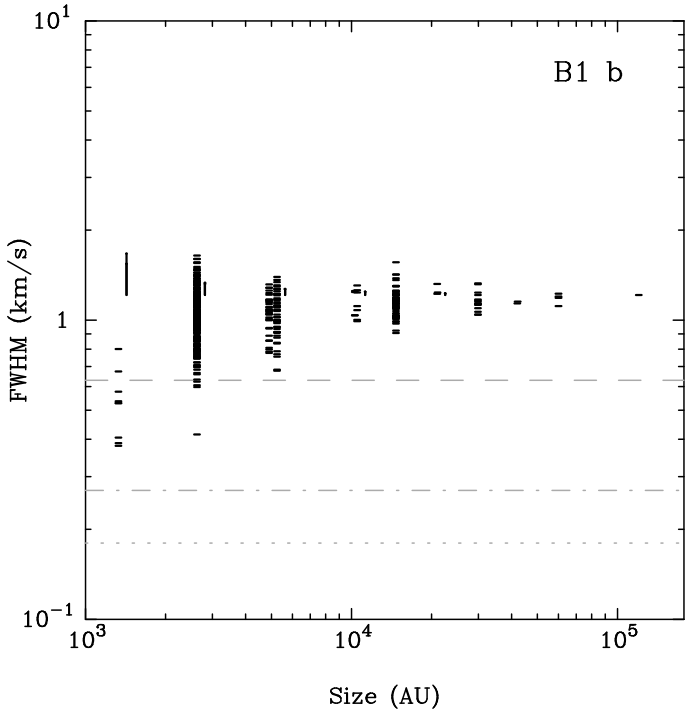

Figure 4.62: Barnard1 b line width (FWHM) *vs.* size correlations for gridded $C^{18}O$ spectra. The dashed line indicates the line width corresponding to the sound speed of the medium: $\mathrm{FWHM}_{c_s}(20\ \mathrm{K}) = 0.63$ km s^{-1}. The dotted line indicates the thermal line width: $\mathrm{FWHM}_T(20\ \mathrm{K}) = 0.18$ km s^{-1}. The dash-dot line indicates the channel width of the spectra: $\delta V = 0.27$ km s^{-1}.

toward the northeast; the redshifted lobe is slightly longer and extends toward the southwest. Observations of optical emission lines of H_2 and S II hint at the evolutionary history of the outflows (Bally, Devine, & Alten 1996). The emission lines reveal a chain of Herbig-Haro objects (HH366) with a position angle $\sim 75°$ and five-fold greater extent than the CO emission. Interferometric observations have revealed an "inner edge" to the outflows, where the CO emission appears to abut a flared disk (Langer, Velusamy, & Xie 1996). This "inner edge" has a dramatic conical shape in CO $J = 2 \rightarrow 1$ line emission (Velusamy & Langer 1998) and appears as an arc of nebulosity at near-infrared (0.8 μm) observations (Heyer *et al.* 1990). High resolution observations at millimeter wavelengths have also revealed a disk component embedded within the envelope. Velusamy & Langer (1998) propose that

their $C^{18}O$ $J = 2 \rightarrow 1$ observations trace a gaseous disk with approximate dimensions of 3500×1800 AU. The velocity gradient detected in the $C^{18}O$ emission is consistent with infall in a rotating, flared disk at an angle of inclination of 45°. The presence of this disk within a deeply embedded source suggests that B5 IRS1 may represent a YSO transitioning from a Class 0 to a Class I object (Yu, Billawala, & Bally 1999).

4.18.2 Continuum Data

The $\lambda = 2.7$ mm continuum emission is not particularly strong; the peak is only 7.9 mJy beam^{-1}. However, the continuum source does appear centrally condensed. In the continuum emission map with 10″ resolution (Figure 4.63), the full dimensions of the emitting envelope are less than 2×2 beam widths. At 5″ resolution (middle panel), the envelope begins to reveal some asymmetries. The emitting region has a peak intensity of 5.5 mJy beam^{-1} and appears extended in a northeast-southwest direction. The position angle of the elongation is approximately the same as the position angle of the CO outflows (PA = 65°). A sudden narrowing of the contours along the minor axis of the envelope hints that the northeastern extension may originate from the presence of a second source. At 3″ resolution (bottom panel), the shape of the contours perpetuates the hint. Although neither source is strong, the contours clearly outline two separate emission peaks. The stronger central peak has a flux of 4.0 mJy beam^{-1}; the flux of the secondary peak is 3.2 mJy beam^{-1}.

4.18.3 $C^{18}O$ Data

The map of the Barnard 5 region from the FCRAO data (Figure 4.64*a*) shows a morphology that is very similar to the map published by Fuller *et al.* (1991). The B5 IRS1 continuum positions appear along a ridge of strong $C^{18}O$ emission that dominates the northwest quadrant of the map as well as most of the primary beam

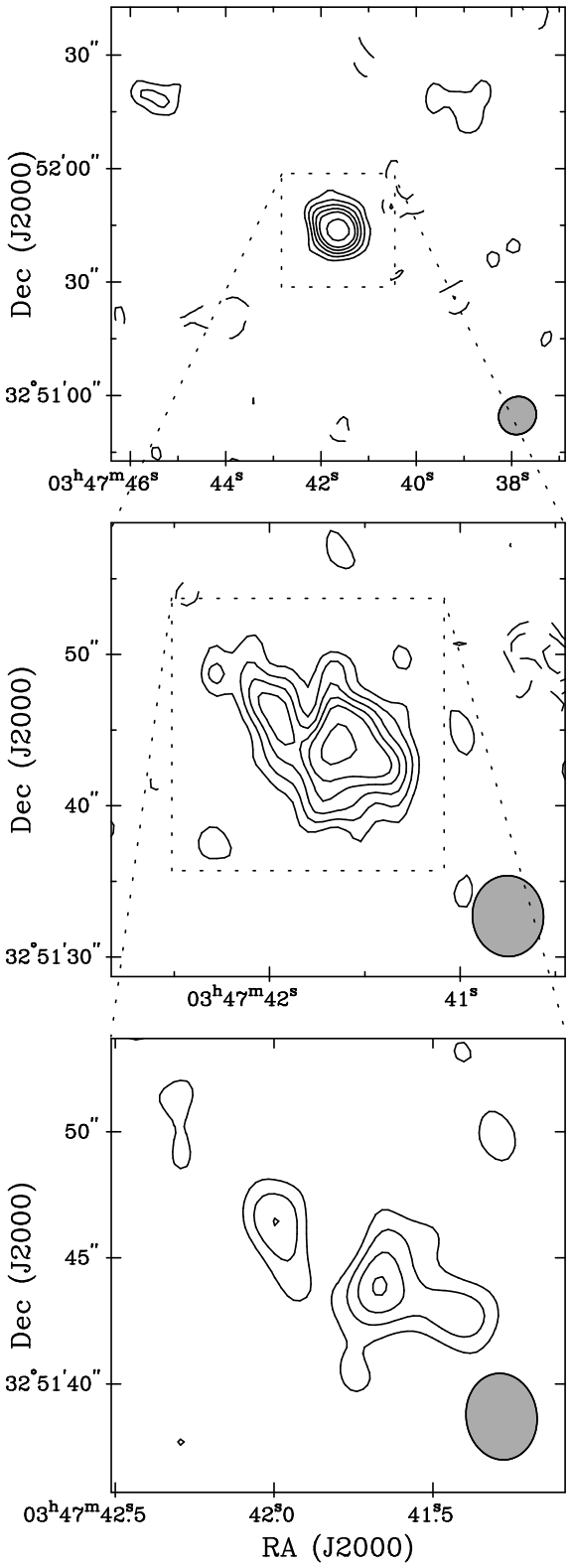

Figure 4.63: Maps of the $\lambda = 2.7$ mm continuum emission from Barnard5 IRS1. The contour intervals are $(-4, -3, -2, 2, 3, 4, 5, 6, 8) \times \sigma$ in mJy beam^{-1}. *Top:* $\sigma = 0.8$ mJy beam^{-1}; beam is $10.3'' \times 9.7''$, P.A.$= -40.7°$. *Middle:* $\sigma = 0.6$ mJy beam^{-1}; beam is $5.4'' \times 4.7''$, P.A.$= 3.7°$. *Bottom:* $\sigma = 0.8$ mJy beam^{-1}; beam is $3.4'' \times 2.8''$, P.A.$= 7.6°$.

area. The peak intensity along the emission ridge (63.3 Jy beam^{-1}·km s^{-1}) appears at the northern edge of the full map. The velocity map of the region (Figure 4.64*b*) shows a map-wide change in velocity between the northwest and southeast corners. The low emission regions on the far side (northwest side) of the emission ridge are blueshifted ($\sim$9.7 km s^{-1}) with respect to the low emission regions on the B5 side (southeast side) of the ridge ($\sim$10.5 km s^{-1}). The transition across the ridge is pocked by variations of $\Delta_{V_C} \approx 0.1$.

In the C^{18}O map with 10″ resolution (Figure 4.64*c*), the envelope of B5 IRS1 pops up out of the background emission, centered on the stronger continuum object, with a peak intensity of 4.0 Jy beam^{-1}·km s^{-1}. The envelope is extended in the northwest-southeast direction by approximately two beam widths. The "ridge" of emission seen in the FCRAO map still dominates the northwest quadrant of the map. B5 IRS1 clearly appears to be an extension of the ridge. The velocity field surrounding B5 IRS1 (Figure 4.64*d*) reinforces the trend seen at lower resolution. B5 IRS1 (10.0 km s^{-1}) appears to be in a transition region between the bluer velocities along the C^{18}O ridge (9.8 km s^{-1}) and the redder velocities to the southeast (10.3 km s^{-1}).

At 5″ resolution (Figure 4.64*e*), the extended emission from the ridge breaks up into clumps. The morphology of the C^{18}O emission surrounding the B5 IRS1 continuum sources strongly resembles the disk structure detected by Velusamy & Langer (1998). The C^{18}O emission is compact (S_{peak} = 1.4 Jy beam^{-1}·km s^{-1}) and elongated my several beam widths in the northwest-southeast direction. The velocity field surrounding B5 IRS1 (Figure 4.64*f*) is complex, with values in and around the 50% contour varying between 9.8-10.2 km s^{-1}. The velocities in the directions of the continuum emission axis (and of the outflows) are blueshifted with respect to the disk region.

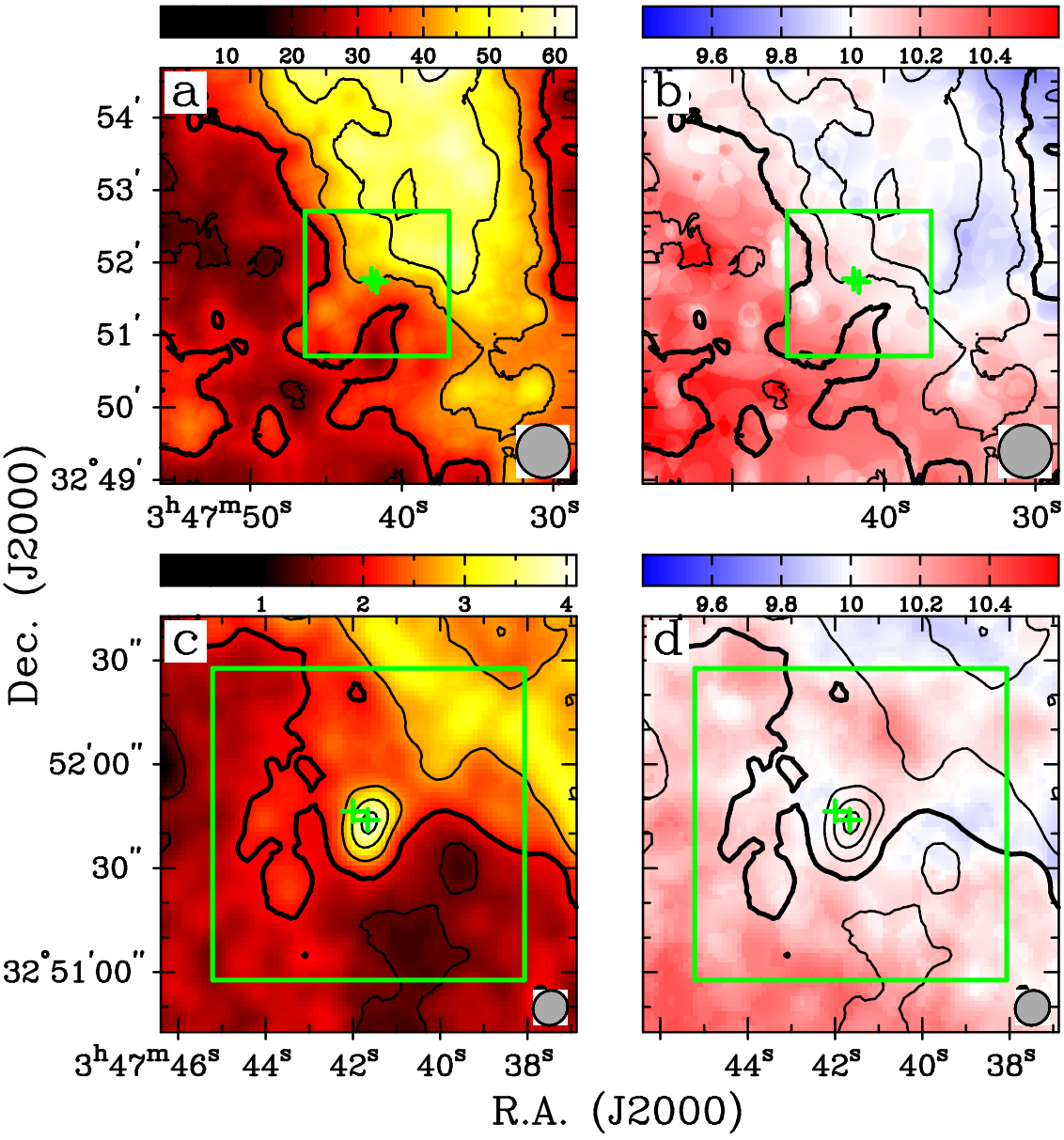

Figure 4.64: $C^{18}O$ $J = 1 \rightarrow 0$ integrated intensity and velocity of Barnard5 IRS1. Velocity range is 9.4-10.6 km s^{-1} in all panels. Plus symbols indicate positions of continuum sources from Figure 4.63. (a,b) $I_\nu^{peak} = 63.29$ Jy beam^{-1}·km s^{-1}; $\sigma =$ 6.4 Jy beam^{-1}·km s^{-1}; beam is $44'' \times 44''$. (c,d) $I_\nu^{peak} = 4.03$ Jy beam^{-1}·km s^{-1}; $\sigma = 0.19$ Jy beam^{-1}·km s^{-1}; beam is $10.33'' \times 9.69''$, P.A.$= -40.7°$.

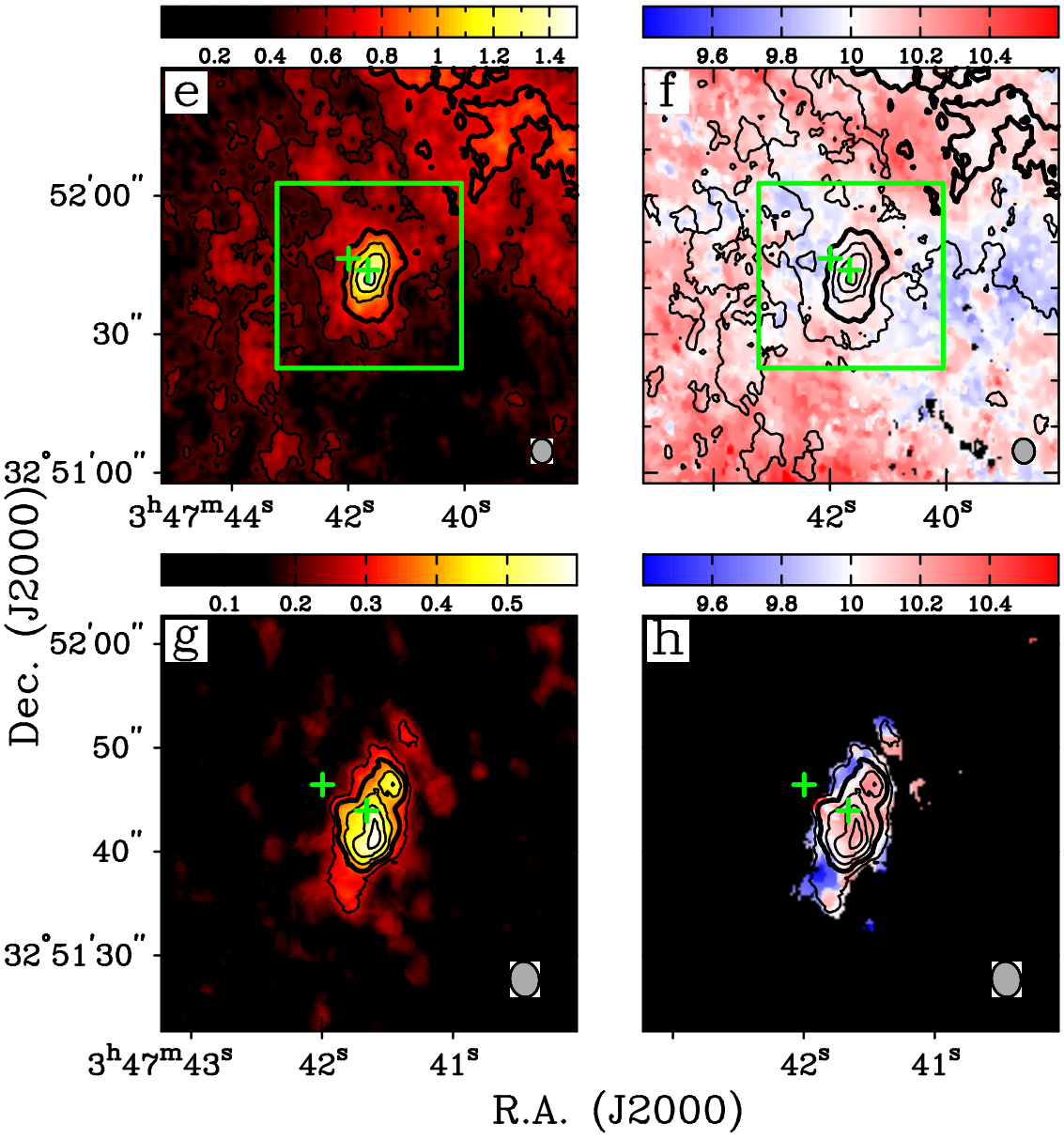

Figure 4.64: *Continued.* (e,f) I_ν^{peak} = 1.45 Jy beam^{-1}·km s^{-1}; σ = 0.08 Jy beam^{-1}·km s^{-1}; beam is 5.35″ × 4.70″, P.A.= 3.7°. (g,h) I_ν^{peak} = 0.50 Jy beam^{-1}·km s^{-1}; σ = 0.05 Jy beam^{-1}·km s^{-1}; beam is 3.44″ × 2.81″, P.A.= 7.6°.

In the 3″ resolution map (Figure 4.64*g*), the large aspect ratio of the $C^{18}O$ emission region is obvious. The central B5 IRS1 continuum source appears near the center of the disk-like distribution, although the $C^{18}O$ peak (0.5 Jy beam^{-1}·km s^{-1}) is located ∼1 beam width south. The velocities in the emitting region (Figure 4.64*h*) are difficult to interpret; they do not seem to represent a disk rotating around its minor axis. Bluer velocities (9.3-9.5 km s^{-1}) are located along the eastern edge, and redder velocities (10.1-10.3 km s^{-1}) appear near the center.

Spectra taken through the continuum positions B5 Center and B5 East are strong and symmetrical in both the FCRAO data and the combined data with the 10″ beam (Figure 4.65). Because the sources are less than 10″ apart, of course, the spectra are sampling almost identical regions of the core. In the 5″ map, B5 East appears at the edge of the 50% contours, and the intensity of the spectrum diminishes as expected. The peak of the line shifts blueward of the V_C from the FCRAO data (10.1 km s^{-1}). At this resolution, the B5 Center spectrum develops a slight asymmetry, but the central velocity doesn't change. In the high resolution map, however, the emission line is no longer symmetrical or Gaussian in shape. The profile suggests a single strong redward channel and a blue line wing.

The distribution of the measured FWHM of the B5 IRS1 core are displayed in Figure 4.66. A total of 497 spectra are included; this is a larger number of spectra than for any other core in the survey. However, even with this many lines, the distribution of the FWHM is tighter than the distribution for several other cores. There are no lines as wide as 1.5 km s^{-1} and also no lines as narrow as the channel width. Several different grid sizes yield spectra with FWHM as narrow as the sonic line width. The total percentage of lines below this threshold is 24.1%.

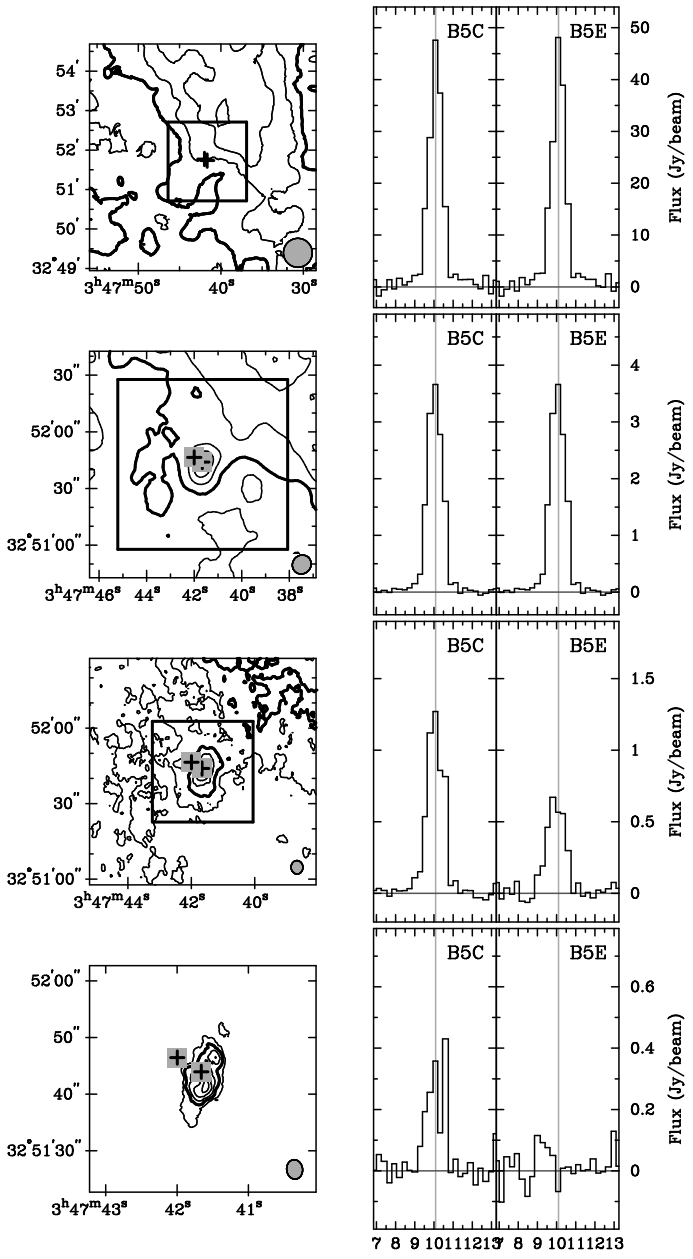

Figure 4.65: Barnard5 IRS1 spectra. The plots at left show integrated intensity contours from the $C^{18}O$ data, as in Figure 4.64. To the right of each contour plot are spectra from the $C^{18}O$ datacubes. The plus symbols indicate the positions of the continuum sources. All spectra display the flux in Jy beam^{-1} averaged over the area of a beam. In all rows, the gray vertical lines show central velocities of Gaussian functions fit to the profiles from the FCRAO map (top row).

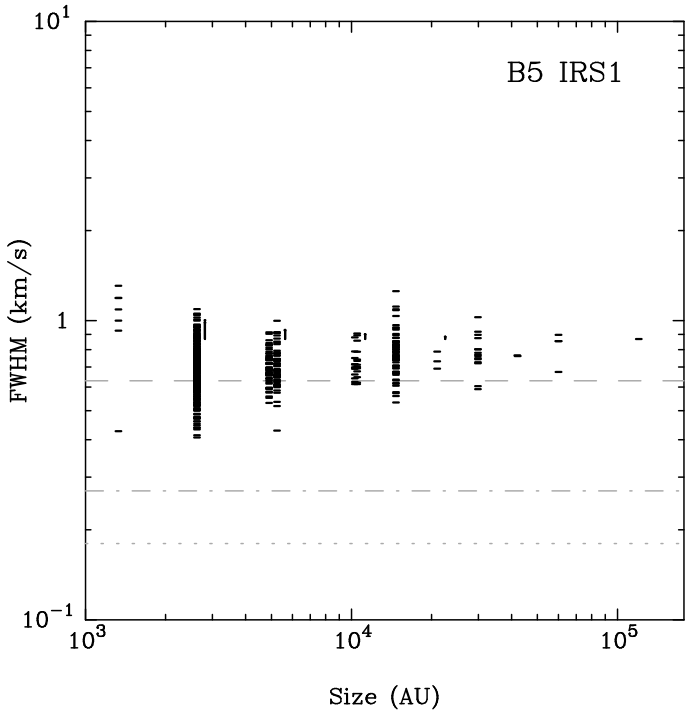

Figure 4.66: Barnard5 IRS1 line width (FWHM) *vs.* size correlations for gridded $C^{18}O$ spectra. The dashed line indicates the line width corresponding to the sound speed of the medium: $\mathrm{FWHM}_{c_s}(20\ \mathrm{K}) = 0.63$ km s^{-1}. The dotted line indicates the thermal line width: $\mathrm{FWHM}_T(20\ \mathrm{K}) = 0.18$ km s^{-1}. The dash-dot line indicates the channel width of the spectra: $\delta V = 0.27$ km s^{-1}.

Chapter 5

An Analysis of the Velocity Fields of the BIMA Cores

5.1 Velocity Maps

The observations made with the BIMA array are of critical importance to understanding the velocities of the Perseus cores. Because of the high resolution of the BIMA data, the maps presented in Chapter 4 reveal structures that have not been previously observed in most of the survey cores. At the distance of the Perseus cloud (350 pc), the angular resolutions correspond to physical scales that are well within the characteristic core radius ($\sim$0.1 pc) identified as important in single-dish studies.

The integrated intensity maps in Chapter 4 show that there are few cases (*e.g.* Per7E, B1-b) where a dense core is detectable from the $C^{18}O$ emission *in the FCRAO data alone*. The FCRAO maps *do* show that there are *no* examples of cores that are truly isolated (on arc-minute scales) from larger structures in the Perseus cloud. Of the 21 cores in the survey, eleven are located well within the half-peak contours of large clouds or strong filaments; the other ten cores are located at or outside the

half-peak contours, where emission is declining.

In the velocity maps constructed from the FCRAO data, ten of the 21 cores show fairly smooth changes in velocity across the area of the BIMA maps. Such systematic variations might, in the absence of additional information, imply core rotation. However, additional information *is* available, and on the size scales probed by the BIMA data, *no* core shows a velocity field that resembles a quiescent condensation undergoing simple systematic rotation. Throughout the survey sample, the maps made with 10″, 5″, and 3″ resolution reveal velocity fields that appear chaotic, with a range of variations typically on the order of 4 channel widths ($\sim$1 km s^{-1}). A few of the survey targets exhibit velocity fields that suggest some rotational component, but none of these objects shows an unequivocal signature of systematic rotation. Arguable exceptions are L1448 IRS3 (Chapter 2), where the AB pair and the NW continuum source may be undergoing "dumbbell" rotation around the minor axis of the extended envelope that surrounds them, and the highest resolution (3″) velocity maps of two cores (L1448C and Per5) which hint at the presence of a rotating disk.

Another critical result made clear by the high resolution velocity maps is that the full range of velocities traced by the C^{18}O is not apparent in lower resolution data. In the observed fields, velocity information present in the high resolution maps is obscured when the same field is observed at lower resolution. The most extreme velocity contrasts typically appear in the highest resolution maps. Two particularly striking illustrations of velocity contrasts that are only revealed at high resolution are shown in the velocity maps of NGC1333 IRAS4 (Figure 2.13) and B1-b (Figure 4.60). In the former case, the material in the circumstellar envelopes is blueshifted with respect to the velocity of the embedding cloud; in the latter case, the C^{18}O filament that splits the protostars is strongly redshifted with respect to the surrounding material. In general, these results show that essential details may

be overlooked in analyses of core velocity fields that are based solely upon lower resolution observations.

The fidelity of the velocity maps was examined for the three cores presented in Chapter 2 and then revisited for some of the cores presented in Chapter 4. At specific locations within the maps, usually the positions of the continuum sources, the velocities indicated in the maps were compared with the actual line profiles through the datacube. In general, the dominant velocities of spectra translated well to the central velocity (V_C) displayed in the velocity maps. Consequently, the first moment appears to be a reliable indicator of the velocity integrated along the line-of-sight through the cloud. One noteworthy exception is the region around NGC1333 IRAS8. Spectra from IRAS8 (Figure 4.26) are complicated by multiple emission components, which confound the determination of a line center by a single Gaussian function and undermine the reliability of the first moment.

5.2 Line Width *vs.* Grid Size Correlations

The gridding method described in § 2.7.2 was used to construct the line width *vs.* size correlations for each of the Perseus cores. There are four primary justifications for this approach. First, the gridding method provides a quantifiable metric for comparing different cores. Second, the method determines a correlation between line widths and size scales *without* fixing the size scales to absolute positions within a core (*e.g.* the distance from a continuum source). Third, the results from applying the method to sophisticated models of turbulent clouds (OSG) are already known. And fourth, the gridding method is efficient and practical, in that it is easily applied to large datacubes with incomplete sampling.

Despite the implementation of four different criteria to prevent the inclusion of

poor quality spectra, the ensemble of line width *vs.* grid size diagrams revealed that the correlations for some cores are better than for others. There are two cases in particular where spectra that pass the quality tests produce less reliable correlations. In one case, the spectra show multiple lines of comparable strength. Typically, such spectra are rejected because they yield large values for χ^2 when fit with a single Gaussian function. Multiple-line spectra that are not excluded by the χ^2 criterion produce measured FWHM with high uncertainties. (The NGC1333 IRAS8 core, described above, is a good example of this multiple-line case.) In the other case, the flux in the combined maps is weak. Many of the spectra are excluded by the two criteria that require a minimum number of unmasked pixels in a grid square and a minimum line amplitude of 3σ above the noise. Because relatively few valid spectra remain to contribute to the line width *vs.* grid size diagram, the resulting correlation is less reliable. (A good example of this weak-line case is the L1455C core.)

Bearing these less reliable cases in mind, the line width *vs.* grid size correlations derived from gridding the datacubes from the Perseus cores have several common characteristics. One significant result is that *none of the measured lines is as narrow as the thermal line width* of $C^{18}O$ (0.18 km s^{-1}). Although the velocity resolution of the observations (0.27 km s^{-1}) is also greater than the thermal line width, exceptionally few of the measured spectra are as narrow as only one or two channels. Thus, the thermal line width is not an appropriate description for the overwhelming majority of lines observed from the cores.

The measured FWHM must include the effects of both thermal and turbulent motions. Assuming that 20 K is an appropriate temperature for the core gas, then the narrowest observed lines have thermal and turbulent components that are approximately equal. However, across the entire survey there are only a handful of

measurable spectral lines in the smallest grid squares (dimensions of ∼2500 and ∼1200 AU) with widths this narrow. For most lines, the turbulent component exceeds the thermal component.

For the line width *vs.* grid size correlations displayed in Chapters 2 and 4, the points representing the measured FWHM have similar distributions. The upper envelope of the points is approximately flat, *i.e.* the maximum FWHM is roughly the same on all size scales, and the lower envelope shows an increase from small to large grid sizes. For many of the cores, the rate of increase is quite steep, and the lower envelope of points is roughly fit by the slope of "Larson's Law": $\Delta v_{obs} \propto R^{0.38}$. In general, least squares fits to the lower envelopes of the points (not shown in the diagrams) yield slopes ranging from 0.2 to 0.4.

The trends in the upper and lower envelopes imply one of the fundamental results of the survey: *even on the small scale sizes probed by the BIMA data, the cores display a wide range of line widths.* The range of measured FWHM broadens at the smaller grid square sizes, and because the mean uncertainties are consistently less than the FWHM, the spread in the line widths is real, rather than merely statistical. The detection of wide lines at high resolution, coupled with the unsystematic variations in the velocity maps, is evidence that the cores are not quiescent, homogeneous structures.

For many cores, the flux observed in the 3″ resolution BIMA maps is weak; these cores are incompletely sampled by the smallest grid squares (∼1200 AU), and not enough spectra can be measured to determine if the spread in the line widths continues. Seven cores have no measurable lines from the smallest grid squares. Three cores have only a single measurable line, so no trend can be inferred. The remaining cores have at least a handful of measurable lines. If the FWHM of these lines are compared with the positions of least-squares fits to the data, anchored at

the FWHM of the spectrum from the full FCRAO field (the rightmost point), then in four cores the FWHM are distributed both above and below the least-squares line. However, in the seven remaining cores, *all* of the FWHM fall below the least-squares line. If emission lines are turbulently broadened on scales of $\sim$1200 AU, the expectation is that all cores will show a substantial fraction of wide lines. Presently, there are an insufficient number of measured spectra to determine whether the apparent drop in the number of wide lines is real. The verification or refutation of this trend will depend upon the acquisition of even higher resolution observations. A number of the cores were observed with the A configuration of the BIMA array, although these data are not included here. In the three cores that have A-array data already included, L1448 IRS3 shows an even distribution of FWHM at high resolution, but NGC1333 IRAS2 and IRAS4 show primarily narrow lines.

One possible interpretation of the observed correlation between line width and grid size is that the line widths indicate the contrast between the velocity of the embedding large-scale cloud (seen in the FCRAO maps) and the velocity of the embedded protostar (seen in the BIMA maps). A velocity difference between the two structures yields a wider emission line from the combined map. Turbulence is inferred from the line width, even though its origin is a displacement in velocity space. By this reasoning, the cores that show the greatest velocity differences between structures seen in the low resolution and high resolution maps should also have the widest lines. In the survey, the cores that exhibit the greatest velocity contrasts between the FCRAO and BIMA maps are NGC1333 IRAS4 and Barnard1-b. Although the lines from IRAS4 are generally very wide, B1-b provides a counter-example to the "velocity contrast" interpretation. On average, the lines from B1-b are narrower than other cores, such as *e.g.* L1448 IRS3 and L1448C, where the central velocities of the protostellar envelopes are similar to the velocity of the em-

bedding cloud.

A list of the survey targets, the number of continuum objects identified, and some properties derived from the gridding analysis is shown in Table 5.1. The third column ("16 × 16 Spectra") lists the number of spectra from the 16 × 16 grid of the 5″ map that are included in the line width *vs.* grid size correlation. For a distance of 350 pc, the grid squares have dimensions of 2625 AU. The fourth column ("% below FWHM_{c_s}") lists the percentage of 16 × 16 spectra with FWHM less than the sonic width of the $C^{18}O$ line. For all of the cores except L1448 IRS3, NGC1333 IRAS2, and NGC1333 IRAS4, the sonic line width was assumed to be $\mathrm{FWHM}_{c_s}(20\ \mathrm{K}) = 0.63\ \mathrm{km\ s^{-1}}$. The fifth, sixth, and last columns in the table list the full range of FWHM, the mean value, and the standard deviation of the distribution, respectively, for the 16 × 16 grid spectra.

Using the FWHM from the 2625 AU grid squares to quantify the range of line widths in the cores is a compromise between resolution and accuracy. The 32 × 32 grid of the 3″ map probes the cores with greater resolution, but relatively few spectra with this resolution pass the quality criteria. The 16 × 16 grid squares provide the largest number of spectra that can be reliably measured.

The mean value of the distribution of FWHM provides a crude estimate of the relative width of the lines from a particular core. Figure 5.1 illustrates the relation between ⟨FWHM⟩ and the percentage of lines with $\mathrm{FWHM}<\mathrm{FWHM}_{c_s}$ for all of the cores in the survey. Even for cores with high mean line widths, a small percentage of the lines are still narrower than the sonic line width. For cores with mean line widths less than about 1 km $\mathrm{s^{-1}}$, the relation between ⟨FWHM⟩ and the percentage of lines narrower than FWHM_{c_s} is approximately linear. This overall correlation is not surprising; it merely shows that cores with narrower ⟨FWHM⟩ have more narrow lines comprising the full distribution.

Table 5.1. Results from Gridding Analysis

Source	2.7 mm objects	16×16 spectra	% below FWHM_{c_s}	Δ_{FWHM} (km s^{-1})	$\langle\mathrm{FWHM}\rangle$ (km s^{-1})	σ_{FWHM} (km s^{-1})
L1448 IRS2	2	214	23.4	0.30 - 2.12	0.83	0.30
L1448 IRS3	3	225	6.7	0.40 - 2.14	1.14	0.36
L1448 C	4*	244	3.7	0.43 - 2.16	1.08	0.34
L1455 A1	2	173	4.0	0.29 - 2.72	1.49	0.42
L1455 A2	1*	88	23.9	0.42 - 2.01	0.98	0.37
L1455 B	1*	140	40.7	0.29 - 1.71	0.74	0.26
L1455 C	0	43	69.8	0.38 - 0.95	0.58	0.14
NGC1333 IRAS2	2	245	0.4	0.60 - 2.88	1.73	0.52
NGC1333 IRAS8	2*	142	2.1	0.55 - 2.42	1.57	0.42
NGC1333 IRAS4	4	232	1.7	0.59 - 2.71	1.37	0.44
Per4 S	1	145	46.9	0.36 - 1.38	0.69	0.23
NGC1333 SK32	1	98	41.8	0.37 - 2.08	0.85	0.42
Per4 N	1	120	81.7	0.32 - 1.09	0.51	0.16
Per5	3*	118	93.2	0.27 - 1.11	0.44	0.15
Per6	1	95	78.9	0.34 - 1.04	0.55	0.15
IRAS 03282+3035	1	89	15.7	0.34 - 1.65	0.91	0.29
Per7 W	1*	236	6.4	0.48 - 1.47	0.94	0.20
Per7 E	0	256	1.6	0.60 - 1.52	0.84	0.13
Per9 W	0	242	8.3	0.48 - 1.48	0.89	0.21
Barnard1 b	2	244	1.6	0.42 - 1.64	1.06	0.22
Barnard5 IRS1	2*	258	31.8	0.41 - 1.09	0.70	0.14

*Number of $\lambda = 2.7$ mm continuum peaks identified.

The $\langle\mathrm{FWHM}\rangle$ for all of the BIMA cores are plotted again in Figure 5.2, this time to show the correlation with σ_{FWHM}, the standard deviation of the distribution of FWHM. The σ_{FWHM} values measure the widths *of the distributions* of FWHM. The points show that, in general, cores with greater $\langle\mathrm{FWHM}\rangle$ tend to have wider distributions among the constituent FWHM. The implication is that the distribution of FWHM is spread out by the inclusion of more wide lines, which increase the mean value. No core shows a tight distribution of FWHM around a large $\langle\mathrm{FWHM}\rangle$ value.

To assess the possibility of a connection between the spread in the distribution of measured FWHM and a physical property of the cores, the correlation between

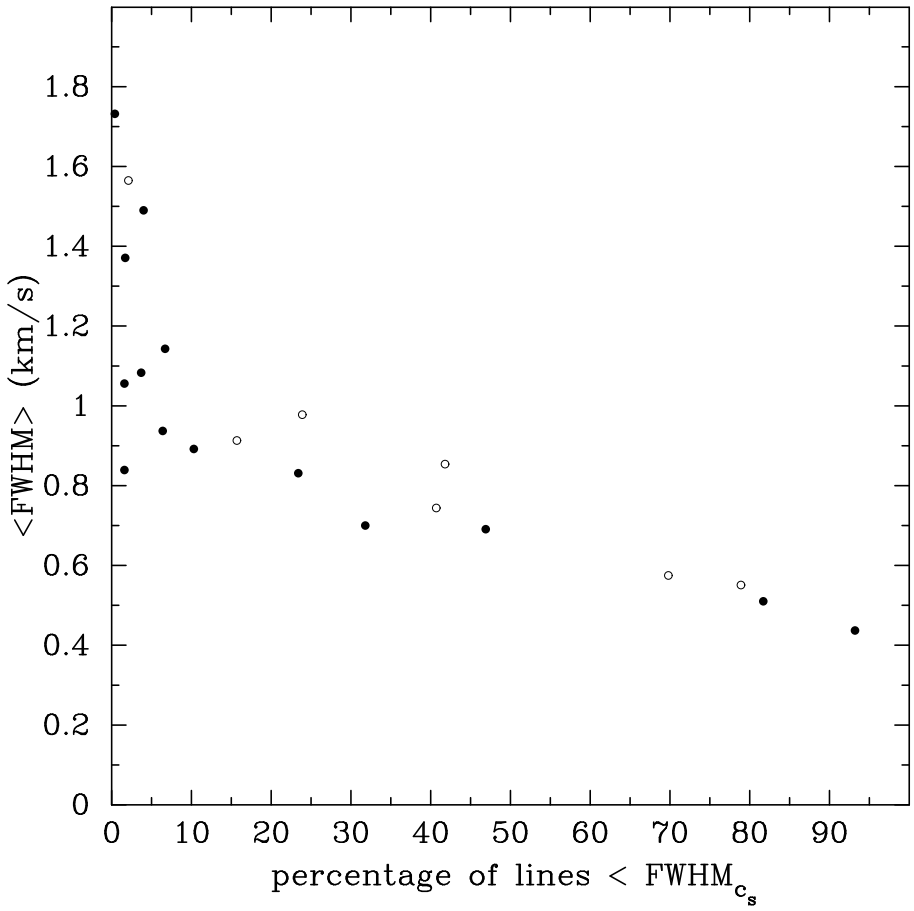

Figure 5.1: The correlation between mean FWHM and the percentage of spectra with FWHM less than the sonic width of the $C^{18}O$ line. Open circles indicate cores that have a higher degree of uncertainty in the measured FWHM (see Chapter 4).

$\sigma_{\rm FWHM}$ and the estimated core luminosities (from other published works) are displayed in Figure 5.3. Only 16 of the survey targets are included in the diagram; the luminosities of L1455C and Per7E are unknown, and only upper limits are known for NGC1333 IRAS8, Per4S, and NGC1333 SK32. Evidence for a trend in the $\sigma_{\rm FWHM}$ *vs.* luminosity diagram is weak. The suggestion that $\sigma_{\rm FWHM}$ increases with core luminosity is driven mainly by the point representing NGC1333 IRAS4; it is the core with the highest luminosity, and it also exhibits a wide distribution of FWHM. However, the points representing NGC1333 IRAS2 ($\sigma_{\rm FWHM}$=0.52 km s^{-1}, L=6.3 L$\odot$) and B5 IRS1 ($\sigma_{\rm FWHM}$=0.14 km s^{-1}, L=9.4 L$\odot$) provide counter exam-

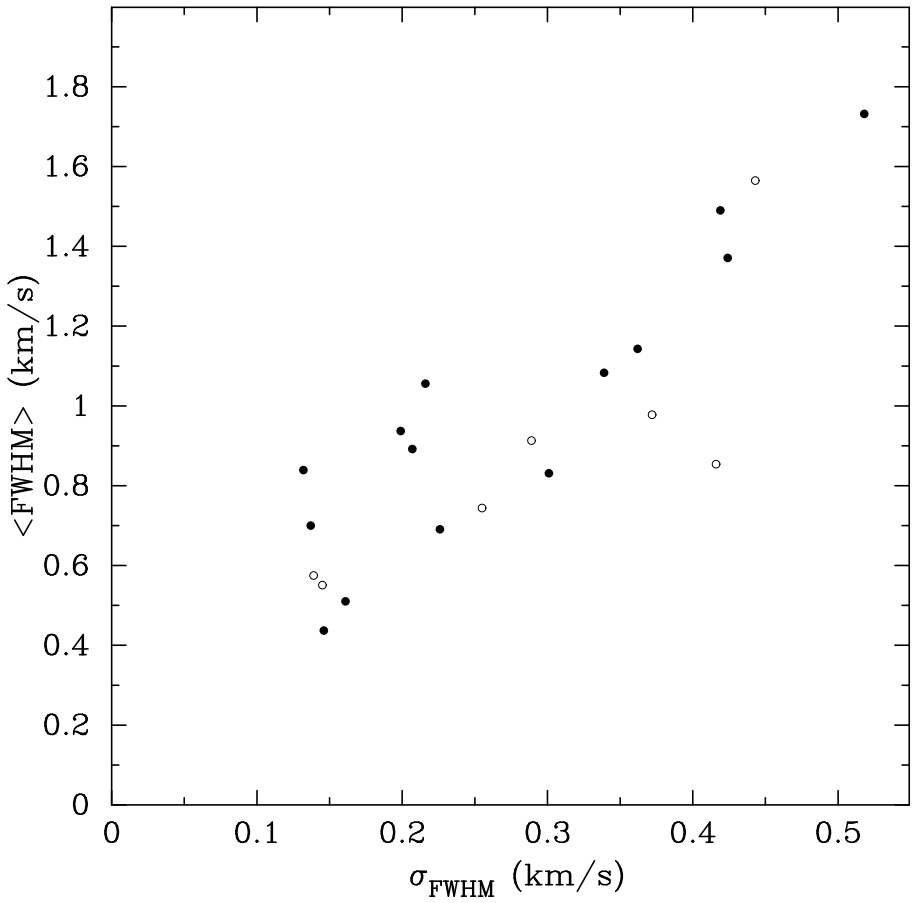

Figure 5.2: The correlation between the mean value and the standard deviation of the distribution of measured FWHM of the $C^{18}O$ lines. Open circles indicate cores that have a higher degree of uncertainty in the measured FWHM (see Chapter 4).

ples[1]. If an intrinsic correlation between $\sigma_{\rm FWHM}$ and core luminosity exists, it may be obscured in Figure 5.3 because, even after rejecting five cores from the sample, the luminosities of many of the survey cores (*c.f.* Ladd, Lada, & Myers (1993)) are not well determined.

Because IRAS2 is a binary and IRAS4 is a quadruple source, a better correlation might be found by normalizing core luminosity by the degree of multiplicity. How-

[1]The luminosity of B5 IRS1 may be lower. The value plotted in Figure 5.3 is from Myers *et al.* (1987), but Moore & Emerson (1994) reported that B5 IRS1 underwent a nearly color-independent decline in luminosity at infrared wavelengths from 1988 to 1993.

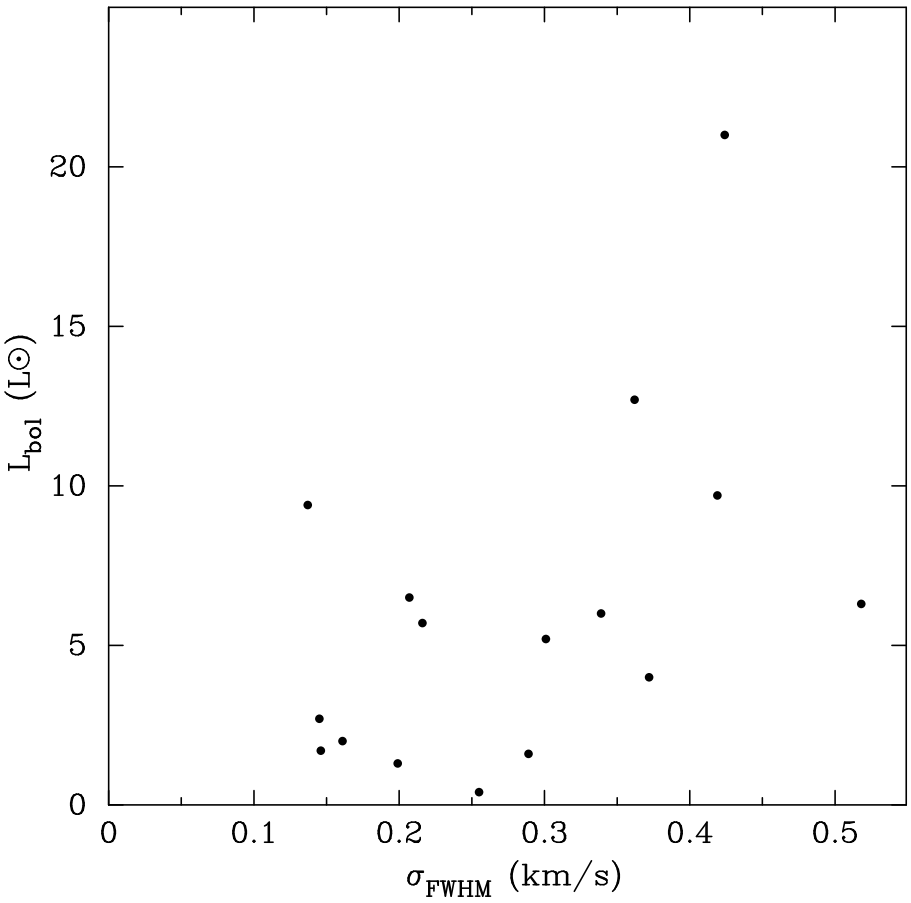

Figure 5.3: The correlation between the luminosity of the core and the standard deviation of the distribution of measured FWHM. Five cores (L1455C, NGC1333 IRAS8, Per4S, NGC1333 SK32, Per7E) are excluded because of the high degree of uncertainty in the luminosity.

ever, this compounds the uncertainty in luminosity with the uncertainty in the true number of protostars. Using the numbers of $\lambda = 2.7$ mm continuum peaks listed in Table 5.1 as normalization factors, the alignment of the $\sigma_{\rm FWHM}$ and luminosity points showed no significant improvement.

5.3 Spatial Variations in V_C and FWHM

A method for further quantifying the velocity fields in the cores is to examine the variations in the spectral lines as a function of separation in the map. Here, "separation" refers not to the distance of a particular grid square from a specific point (*e.g.* the position of a continuum source), but the distance of a particular grid square from all other grid squares. The expectation is that, because different velocity fields show different line profiles across a core, the degree to which a velocity field is organized may be revealed by the correlations between the line properties (V_C, FWHM) and separation. The correlations for a truly quiescent core with a smooth velocity gradient should differ from those of a turbulent core with a stochastic velocity field.

The differences in the central velocities (Δ_{V_C}) and FWHM ($\Delta_{\rm FWHM}$) were calculated as a function of the separation between grid squares using the spectra from the 16×16 grid squares (size$\sim$2625 AU). In the analyses that follow, one-third of the survey cores were excluded, either because the spectra were known to be complex (*e.g.* NGC1333 IRAS8) or, more often, because the number of measured lines was insufficient to determine statistically valid correlations.

5.3.1 Δ_{V_C} Data

The value for Δ_{V_C} indicates the uniformity of the velocity field. If the full range of velocities within a core is small (*i.e.* a "flat" velocity field), then the point-to-point velocity variations in the map should also be small. However, even a relatively quiescent core should show a gradual increase in Δ_{V_C} with separation, because at separations larger than the size of a coherent cell, the V_C will arise from independent cells. The critical characteristics of the correlation between Δ_{V_C} and separation are the *rate* of the increase and the value of Δ_{V_C} at the smallest separations.

Because the scales probed by the ∼2625 AU grid squares are significantly smaller than the characteristic size of a dense core (∼20000 AU), changes in Δ_{V_C} as a function of separation should be particularly effective in determining the presence of systematic motions. If a core is undergoing uniform rotation, then in the direction perpendicular to the rotation axis, Δ_{V_C} should increase linearly with separation. Orthogonal to this direction, Δ_{V_C} should remain nearly zero, regardless of separation. Consequently, a plot of Δ_{V_C} *vs.* separation from samples across the face of the core should show a uniform distribution between these two extremes. Both the mean and the variance of this distribution should increase linearly with separation to the extent that they can be reliably measured (*i.e.* at the largest separations, fewer measurable grid squares are available).

Figure 5.4 shows the relation between Δ_{V_C} and separation for eight of the survey cores. These eight cores were specifically chosen to highlight the contrast between cores with relatively flat velocity fields (Per4N, Per7E, Per5, Per9W) and cores that show a wider range of velocities (NGC1333 IRAS4, L1448 IRS3, L1455 A1, NGC1333 IRAS2). The four cores in the upper half of Figure 5.4 show smaller values for Δ_{V_C}. In Per4N and Per7E, the upper envelope of Δ_{V_C} remains relatively constant beyond ∼15000 AU, and the maximum differences are nearly all less than two channel widths (0.54 km s^{-1}). In Per5, Δ_{V_C} increases until roughly 20000 AU, and in Per9W, Δ_{V_C} increases gradually until roughly 35000 AU, but in both of these cores, values for Δ_{V_C} greater than two channel widths are rare. The four cores in the lower half of Figure 5.4 show contrasting behavior. In these four cores, a substantial fraction of the Δ_{V_C}, at nearly all separations, are greater than three channel widths (0.81 km s^{-1}). A few of the Δ_{V_C} values even exceed four channel widths (1.08 km s^{-1}). For NGC1333 IRAS4, L1448 IRS3, and L1455 A1, the upper envelope of Δ_{V_C} increases steeply, such that values near the maximum are reached

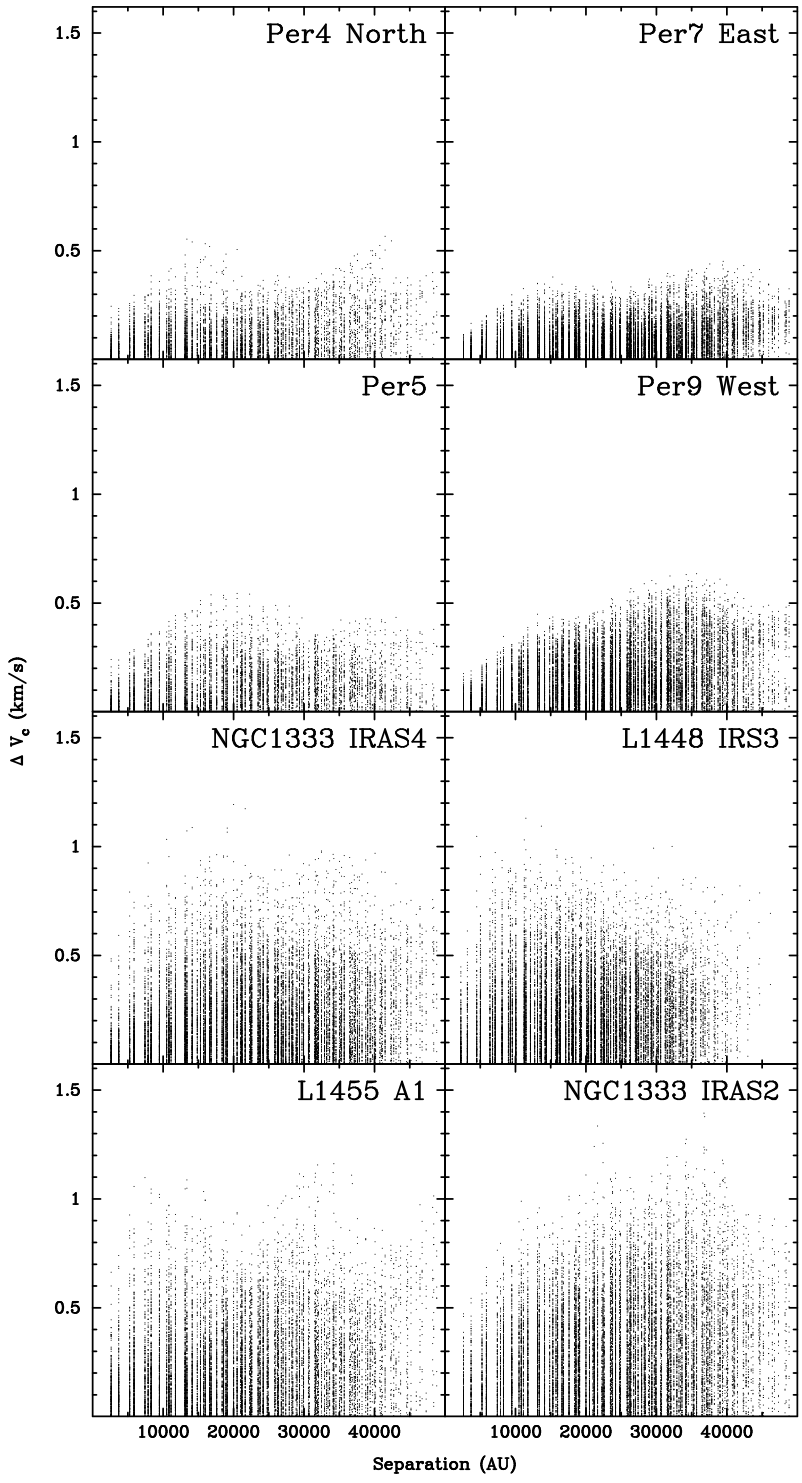

Figure 5.4: The correlation between differences in V_C and the spatial separation over which the differences are evaluated for a subset of eight of the survey cores.

within ~10000 AU. In NGC1333 IRAS2, the slope of the upper envelope of Δ_{V_C} is somewhat more gradual, but the peak values are also greater than in the other three cores. For all eight of the cores, the decline in the spread of Δ_{V_C} points beyond 40000 AU is due to the reduction in the number of available spectra at these separations, rather than a smoothing out of the velocity field. At separations >40000 AU (~16 grid squares), the spectra being compared are at opposite corners of the map.

A shortcoming of illustrating the relation between Δ_{V_C} and separation with scatter diagrams like those in Figure 5.4 is that redundant values of Δ_{V_C} at the same separation are plotted on top of each other, so the *density* of points at a particular location in the diagram is hidden. Although the upper envelope of the Δ_{V_C} points hints at the rate of increase of Δ_{V_C} with separation, the extreme points do not represent typical values at each separation. It is *possible* that the majority of Δ_{V_C} points for Per4N, Per7E, Per5, and Per9W cluster near the upper envelope of the distributions. Furthermore, it is *possible* that the majority of Δ_{V_C} points for IRAS4, L1448, L1455 A1, and IRAS2 cluster near values of zero, and the higher velocity differences represent only the minority of points in the tails of the distributions. Both of these possibilities are *unlikely*, but they cannot be eliminated based upon the information in the scatter diagrams alone. An accurate assessment of the trends in Δ_{V_C} requires a description of the shape of the distribution of Δ_{V_C} points at each separation.

The Δ_{V_C} points were divided into bins at 2625 AU (one grid square) intervals, and the mean of the distribution in each bin was calculated:

$$\overline{\Delta}_{V_C} = \frac{\sum_{i}^{n} (\Delta_{V_C})_i}{n}, \tag{5.1}$$

where n is the total number of points in the bin. The trends in the means for the

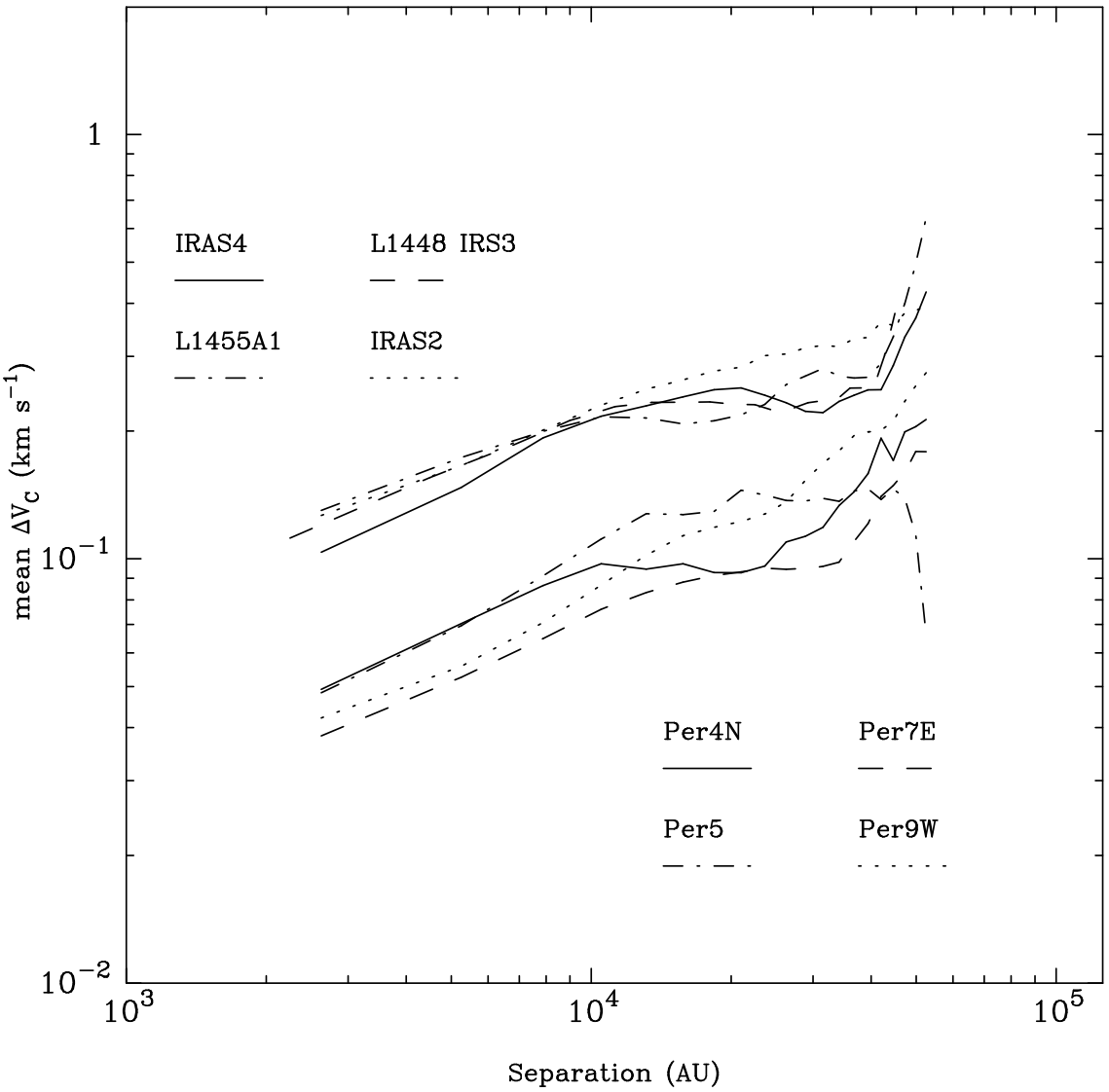

Figure 5.5: Logarithmic plot of the means of the distributions of Δ_{V_C} as a function of the separation interval for the eight cores shown in Figure 5.4. The solid, dashed, dotted, and dot-dash lines in the upper grouping show the means for the NGC1333 IRAS4, L1448 IRS3, NGC1333 IRAS2, and L1455 A1 cores, respectively; the solid, dashed, dotted, and dot-dash lines in the lower grouping correspond to the Per4N, Per7E, Per9W, and Per5 cores, respectively.

eight cores included in Figure 5.4 are shown on a log-log scale in Figure 5.5. All of the cores show the expected increase in Δ_{V_C} with separation. In general, the smallest values for $\overline{\Delta}_{V_C}$ occur at the smallest separation intervals, and larger values occur at larger separation intervals. The values for $\overline{\Delta}_{V_C}$ at the largest separations

are dubious, and the behavior of the lines at separations greater than ~40000 AU can be ignored. The divergence of the curves in $\overline{\Delta}_{V_C}$ at these large separations is a result of the decline in the number of included spectra. Two other features of the $\overline{\Delta}_{V_C}$ curves are common to all eight cores. First, the increase in $\overline{\Delta}_{V_C}$ flattens out at larger separations, indicating that the velocity differences approach a limit. In a region where the V_C values deviate from the same V_{LSR} of the larger-scale cloud, this flattening out is expected. Second, the slopes of the $\overline{\Delta}_{V_C}$ curves at small separations are all approximately linear and are all approximately the same. Because the means are plotted logarithmically, the linear slopes indicate a power law dependence:

$$\overline{\Delta}_{V_C} \propto (\text{separation})^{\alpha_1}. \tag{5.2}$$

Least-squares fits to the $\overline{\Delta}_{V_C}$ curves over the first four separation intervals (*i.e.* to a separation of 10500 AU) yields a range of slopes from 0.37 (L1455 A1) to 0.60 (Per5), with a weighted mean of 0.47 ± 0.02. If the curves are fit to the fifth separation interval (13125 AU), which encroaches on the flattened part of the curves for some of the cores, the range of slopes is 0.33 (L1455 A1) to 0.61 (Per5), but the weighted mean is the same (0.47 ± 0.03).

Beyond the similarities of the curves in Figure 5.5, the most obvious feature is the stark *difference* between the placement of the lower and upper groupings. For the lower set (Per4N, Per7E, Per5, Per9W), the mean value for $\overline{\Delta}_{V_C}$ at a separation of 2625 AU is 0.04 km s^{-1}. For the upper set (IRAS4, L1448 IRS3, L1455 A1, IRAS2), the mean value at this separation is 0.12 km s^{-1}. Clearly, the spread in the Δ_{V_C} values seen in the scatter diagrams is reflected in these mean values, and the unlikely possibilities that the distributions are strongly shifted toward zero or the maxima are invalidated. The four cores with the more compact scatter diagrams in Figure 5.4 also show lower values for $\overline{\Delta}_{V_C}$ at all separations in Figure 5.5. The four cores with more diffuse scatter diagrams in Figure 5.4 show systematically higher

values for $\overline{\Delta}_{V_C}$ at all separations in Figure 5.5.

The distributions of Δ_{V_C} at various separations can be further quantified by examining their variances:

$$\sigma^2_{\Delta_{V_C}} = \frac{\sum_i^n \left[(\Delta_{V_C})_i - \overline{\Delta}_{V_C}\right]^2}{n}, \tag{5.3}$$

where n again represents the total number of Δ_{V_C} points in a 2625 AU bin. The variances of the Δ_{V_C} for the same eight cores are displayed in Figure 5.6. The scale of the $\sigma^2_{\Delta V_C}$ values differs from the $\overline{\Delta}_{V_C}$ values (the y-axis is shifted by approximately an order of magnitude), but the trends in the correlations are the same. At the large separation end, the behavior of the curves is erratic because of the small number of spectra included; for separations greater than approximately 40000 AU, the curves should be ignored. At intermediate separations, the curves tend to flatten out, although this behavior is more evident for the cores in the upper grouping than the cores in the lower. The Δ_{V_C} variances for Per9W appear to increase throughout the range of separations, and for both Per4N and Per5, the $\sigma^2_{\Delta V_C}$ peak at $\sim$16000 AU and then decline before rising again. The variances are expected to approach a limit for separations much greater than the size scale of a coherent cell. At the small separation end, the slopes of the curves are approximately linear, indicating that, like the means, the variances increase with separation according to a power law:

$$\sigma^2_{\Delta_{V_C}} \propto (\text{separation})^{\alpha_2}. \tag{5.4}$$

Values for α_2 based upon least-squares fits to the $\sigma^2_{\Delta V_C}$ curves over the first four separation intervals range from 0.74 (IRAS2) to 1.13 (Per7E). The weighted mean for all eight cores is 0.83 ± 0.07. If least-squares fits are applied to the curves over the first five separation intervals, then the α_2 slopes range from 0.69 (L1455 A1) to 1.13 (Per5), but the weighted mean is nearly the same: 0.86 ± 0.07.

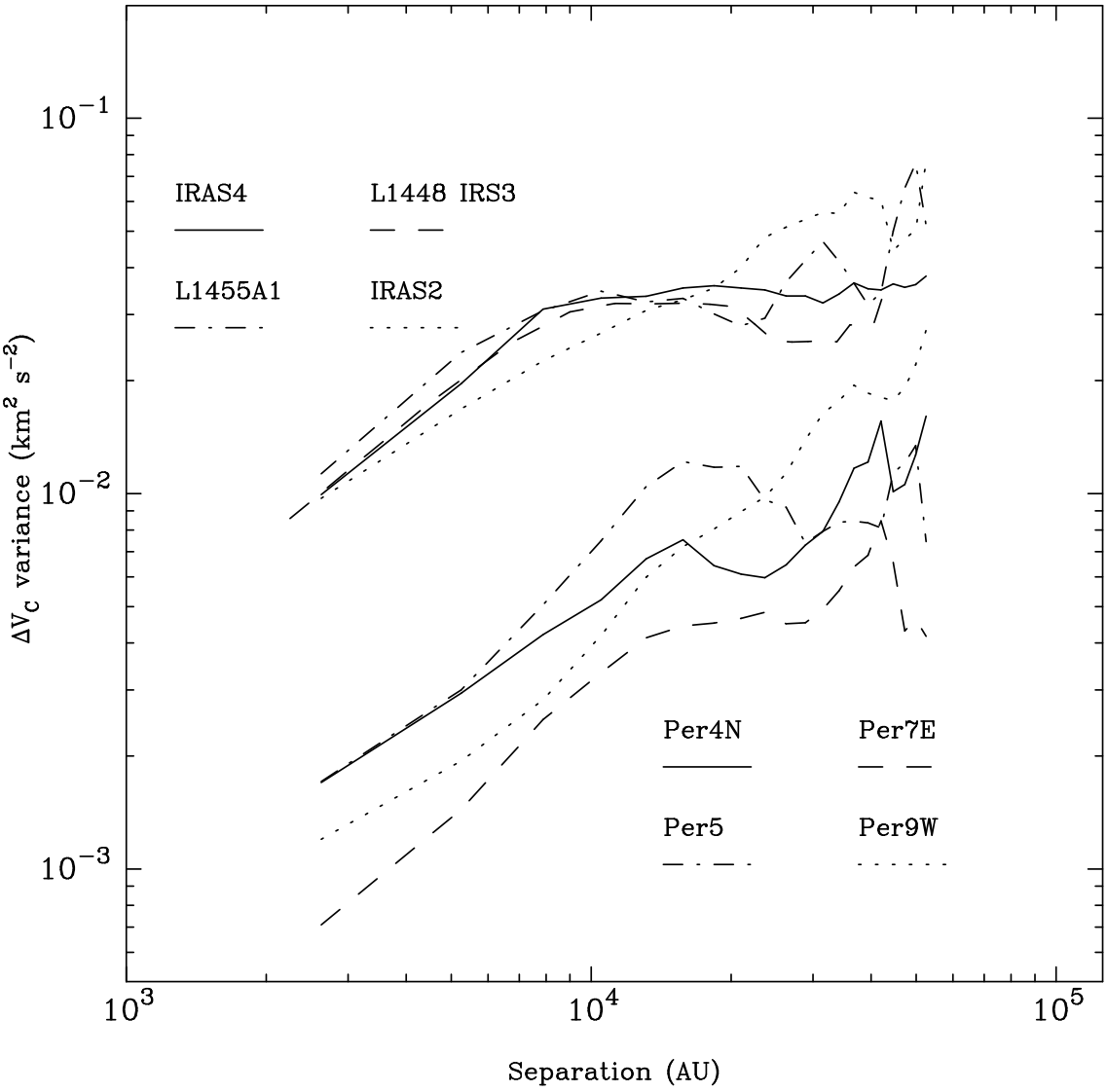

Figure 5.6: The variances of the distributions of Δ_{V_C} plotted as a function of the separation interval for the eight cores shown in Figure 5.4. The solid, dashed, dotted, and dot-dash lines in the upper grouping show the variances for the NGC1333 IRAS4, L1448 IRS3, NGC1333 IRAS2, and L1455 A1 cores, respectively; the solid, dashed, dotted, and dot-dash lines in the lower grouping correspond to the Per4N, Per7E, Per9W, and Per5 cores, respectively. The axes are on a logarithmic scale to highlight the similarity of the behavior of the variances with Figure 14 of Miesch, Scalo, & Bally (1999) (see Figure 5.7).

Among the eight cores, the variances cover a range of roughly an order of magnitude at most separations, and the curves clearly fall into two groups (similar to the behavior of the means). The cores with the more compact scatter diagrams in Figure 5.4 appear in the lower group and have a mean value for $\sigma^2_{\Delta V_C}$ (at a separation of 2625 AU) of 0.001 km^2 s^{-2}. The mean value (at the same separation) for the cores with the diffuse scatter diagrams is 0.010 km^2 s^{-2}.

The analysis of the velocity fields according to the variances of the V_C differences across the cores echoes one of the techniques employed by Miesch, Scalo, & Bally (1999) (hereafter MSB) in their study of the velocity fields of star-forming clouds. The choice of logarithmic axes for Figure 5.6 was made explicitly to facilitate a comparison with their Figure 14 (see Figure 5.7). The MSB study differs from the one presented here in several elementary ways. Their observations (Miesch & Bally 1994) included regions of both massive (Orion B, Mon R2) and low-mass (L1228, L1551, HH83) star formation. The velocity fields were traced with the ^{13}CO $J = 1 \rightarrow 0$ and (for HH83 only) $J = 2 \rightarrow 1$ lines, which are likely to be optically thick in the high density regions around the protostars. Furthermore, the observations were conducted exclusively with single-dish telescopes; the resolution of the observations is 100″, except for the observations of HH38, which have a resolution of 13″. The velocity field analysis is based upon a comparison of the central velocities and the central velocity differences between points on grids that *oversample* the maps. The grid spacing is 30″ (3″ for HH38), and the spectra are interpolated from an area with a radius of 66″ (15″ for HH38).

Because of the fundamental differences between the MSB study and the BIMA survey, the analysis of the Perseus cores is less a basis for critically evaluating the results of the MSB study as a means to extend it. The data shown in Figure 5.6 push the method of examining the variances of velocity differences down to the

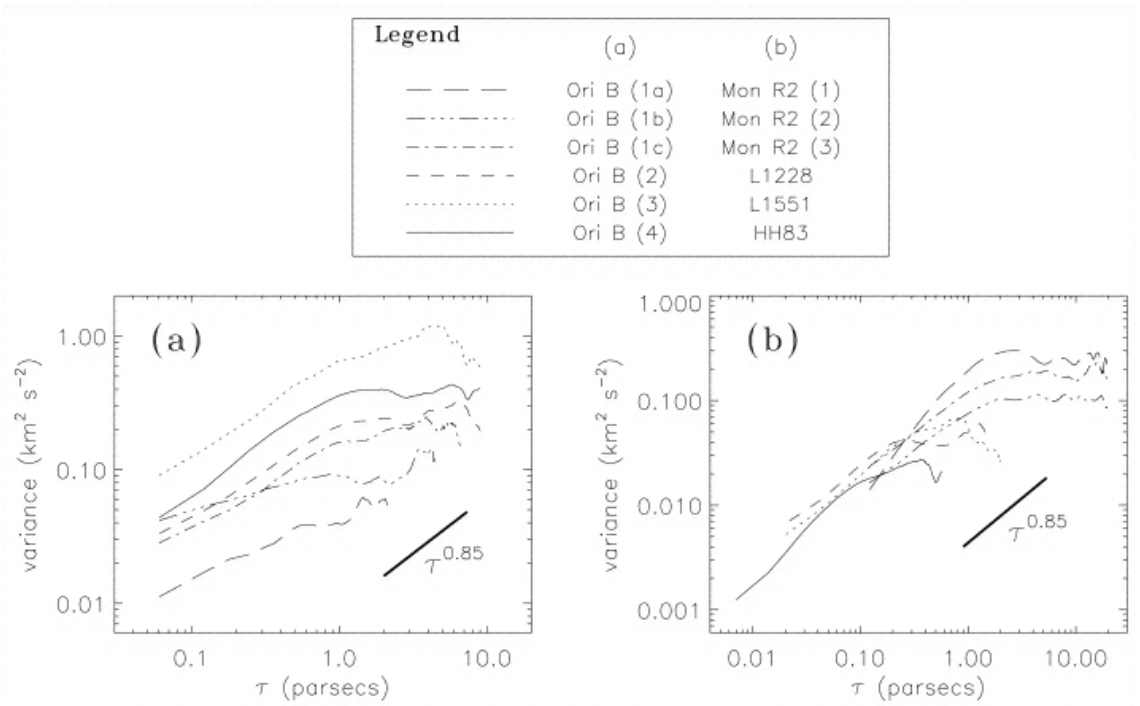

Figure 5.7: Figure 14 from Miesch, Scalo, & Bally (1999), showing the correlation between the variance of difference "pdfs" (probability density functions) and the "scalar lag" (spatial separation). The placement of the lines in the horizontal direction reflects the different distances to the observed regions. The bold line indicates the slope of a power law with an exponent of 0.85.

size scales of individual star-forming cores. The spatial resolutions probed by the BIMA data are finer than the resolution of the MSB observations of HH38, and moreover, the velocity differences are calculated for spectra that critically sample the maps at $\sim 5''$ resolution, rather than relying on oversampling of lower-resolution observations. Despite these differences, however, the trends in Figure 5.6 are quite similar to the results shown in Figure 14 of MSB (see Figure 5.7). All of the variances increase as the separation ("lag" in the parlance of MSB) increases and flatten out at intermediate separations. At any particular separation, the variances in the MSB regions range over roughly an order of magnitude, and for the only region (HH38) sampled over the range of separations probed by the BIMA observations, the calculated variances cover the same range (see MSB Figure 14b) as the BIMA

cores in the lower group (Per4N, Per7E, Per5, Per9W) of Figure 5.6. Perhaps the most remarkable similarity between the two studies is the exponent of the power law dependence fitted to the variances at small separations. For the variances of the BIMA cores, least-squares fits yield weighted mean slopes of $\alpha_2 = 0.83 \pm 0.07$ (fitting four points) and $\alpha_2 = 0.86 \pm 0.07$ (fitting five points). MSB made least-squares fits to "lags between 6 and 12 pixels" (*i.e.* excluding the smallest separations and the flattened-out parts of the curves) and found a "typical" slope of $\alpha_2 = 0.85$ for the regions they surveyed. The full range of slopes among the BIMA cores is $0.69 \leq \alpha_2 \leq 1.13$; the range among the MSB regions is $0.64 \leq \alpha_2 \leq 1.05$, and for L1228, L1551, and HH38 (the three low-mass star-forming regions), the slopes are $\alpha_2 = 0.66$, 1.01 and 1.05, respectively.

The tendency of the variances to conform to a power law is evidence that the gas motions are governed by turbulence (*c.f.* Miesch & Bally (1994) and MSB). Furthermore, the endurance of the power law exponent across the diverse star forming environments probed by this and the MSB study is an indication of the universality of the turbulent mechanism. The BIMA observations reveal that the hierarchy of turbulent motions extends down to the size scales of individual cores.

The other significant result revealed by the correlation between variance and separation is the order-of-magnitude range in $\sigma^2_{\Delta V_C}$ among the Perseus cores. The variances are all normalized by the total number of Δ_{V_C} points, so the offset between the upper and lower groupings is not a function of the number of included spectra. Because the curves at the shortest separations run approximately parallel, the differences in the $\sigma^2_{\Delta V_C}$ values between the cores with flat velocity fields (more compact scatter diagrams in Figure 5.4) and the cores with more active velocity fields (more diffuse scatter diagrams) imply real differences in the degree of turbulence in the core environments. Consequently, the positions of the $\sigma^2_{\Delta V_C}$ curves in the vertical

direction are markers for the relative degrees of turbulence in the cores.

5.3.2 $\Delta_{\rm FWHM}$ Data

In addition to differences in the central velocities, differences in the FWHM of spectral lines ($\Delta_{\rm FWHM}$) provide another method for evaluating the degree of turbulence in the cores. In particular, the changes in $\Delta_{\rm FWHM}$ as a function of separation should readily identify quiescent cores. For a core that behaves like a thermalized ball of gas and is unaffected by macroscopic turbulence throughout its volume, the expectation is that $\Delta_{\rm FWHM}$ will remain small at all separations. In scatter diagrams of $\Delta_{\rm FWHM}$ *vs.* separation, the distribution of points should remain below the thermal line width. Consequently, both the mean and variance of the distribution should be nearly zero at all separations.

On the other hand, turbulent cores exhibit poorly correlated velocity fields, so the probability for large point-to-point variations in $\Delta_{\rm FWHM}$ is greater, even for spectra from proximate grid squares. If the differences are assessed between grid squares that lie within the same turbulent cell, then the FWHM will be uniform and $\Delta_{\rm FWHM}$ approximately zero. For grid squares at separations larger than a turbulent cell, the variations in FWHM are likely to create larger $\Delta_{\rm FWHM}$ values. As with differences in V_C, the differences in FWHM are expected to naturally increase with separation. The influence of turbulence is detected by the *rate* of the increase, as well as the differences between adjacent grid squares.

Figure 5.8 shows $\Delta_{\rm FWHM}$ points plotted as a function of separation for the same eight cores presented in Figure 5.4. As the scaling of the vertical axis indicates, the spread of the $\Delta_{\rm FWHM}$ points is uniformly greater than the spread in the Δ_{V_C} points. The general trends, however, and the differences between the cores plotted in the upper and lower halves of the figure, are the same. The scatter diagrams

of Per4N, Per7E, Per5, and Per9W show smaller values for $\Delta_{\rm FWHM}$. In Per4N, the upper envelope of points remains constant across all separations at a difference of approximately three channel widths (0.81 km s^{-1}). The upper envelope of the Per7E points is also fairly constant at this difference, although it shows a steep increase over separations $<$ 10000 AU. In the scatter diagram for Per5, the upper envelope of the $\Delta_{\rm FWHM}$ points remains near three channel widths over the first $\sim$30000 AU and then quickly declines to roughly a single channel width. The sudden disappearance of the larger $\Delta_{\rm FWHM}$ values suggests that the spectra responsible for these $\Delta_{\rm FWHM}$ arise from a region that does not extend into a corner of the map. In Per9W, the upper envelope of the $\Delta_{\rm FWHM}$ points increases steadily to $\sim$20000 AU, where it reaches a peak of approximately three channel widths, and then declines slightly at larger separations. In the lower half of Figure 5.8, the scatter diagrams of NGC1333 IRAS4, L1448 IRS3, L1455 A1, and NGC1333 IRAS2 show $\Delta_{\rm FWHM}$ points whose upper envelopes never decline to three channel widths. For these four cores, the increase in $\Delta_{\rm FWHM}$ at small separations is steep. At separations greater than $\sim$10000 AU, the upper envelope of the points remains large until a decline at $\sim$40000 AU. This decline appears in the scatter diagrams of all eight cores and has the same origin as the decline seen in the Δ_{V_C} points in Figure 5.4: beyond $\sim$40000 AU, fewer grid squares are available from which the differences can be calculated.

To sidestep the problem of overplotted points (introduced in the description of the Δ_{V_C} scatter plots), the $\Delta_{\rm FWHM}$ points were divided into bins at 2625 AU intervals, and the means ($\overline{\Delta}_{\rm FWHM}$) and variances ($\sigma^2_{\Delta_{\rm FWHM}}$) of the distributions within each of the bins were calculated. Figure 5.9 shows the behavior of $\overline{\Delta}_{\rm FWHM}$ as a function of separation for the eight cores in the scatter diagrams. In general, the trends in the $\overline{\Delta}_{\rm FWHM}$ curves are similar to the trends seen in the means of the Δ_{V_C}

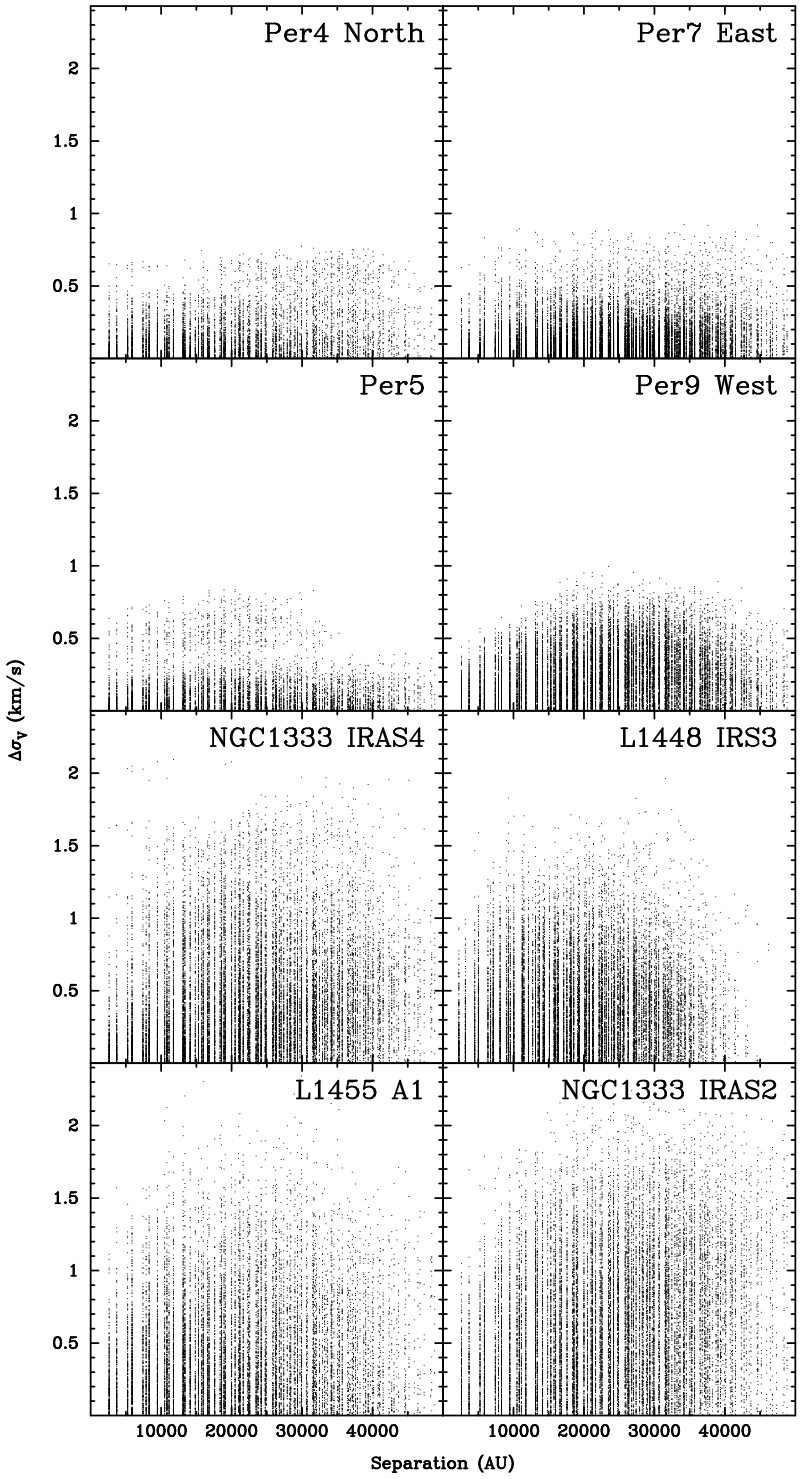

Figure 5.8: The correlation between differences in FWHM and the spatial separation over which the differences are evaluated for the eight cores displayed in Figure 5.4.

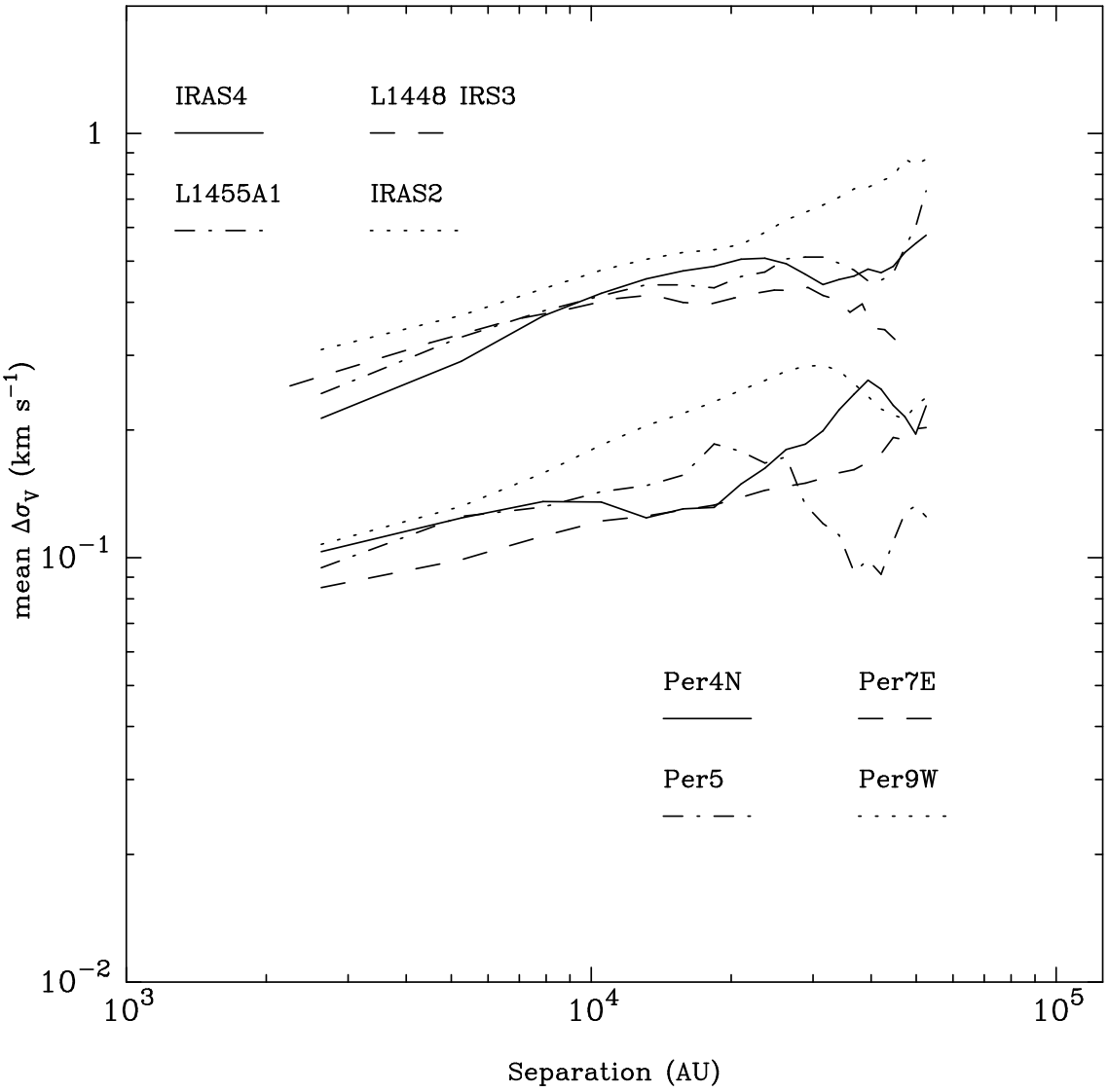

Figure 5.9: Logarithmic plot of the means of the distributions of $\Delta_{\rm FWHM}$ as a function of the separation interval. The solid, dashed, dotted, and dot-dash lines in the upper grouping show the means for the NGC1333 IRAS4, L1448 IRS3, NGC1333 IRAS2, and L1455 A1 cores, respectively; the solid, dashed, dotted, and dot-dash lines in the lower grouping correspond to the Per4N, Per7E, Per9W, and Per5 cores, respectively.

points. At the largest separations ($\gtrsim$ 40000 AU), the values for $\overline{\Delta}_{\rm FWHM}$ are unreliable because of the smaller number of spectra, and at the smallest separations, the curves systematically increase as expected. However, the flattening-out that was apparent in the $\overline{\Delta}_{V_C}$ curves in Figure 5.5 is not quite as pronounced here, because the $\overline{\Delta}_{\rm FWHM}$ curves are shallower to begin with. Over the smallest separation intervals, all eight curves are roughly linear with roughly the same slope; on the log-log grid of Figure 5.9, a linear trend indicates a power law relation between $\overline{\Delta}_{\rm FWHM}$ and separation:

$$\overline{\Delta}_{\rm FWHM} \propto (\text{separation})^{\alpha_3}. \tag{5.5}$$

The slopes of the $\overline{\Delta}_{V_C}$ curves over the first four separation intervals, determined from least-squares fitting, range from 0.21 (Per4N) to 0.50 (IRAS4). The weighted mean of the eight slopes is 0.33 ± 0.03. When least-squares fits are made over the first five separation intervals, the fifth bin is on the shallower part of the curves, and the range of slopes shifts to slightly lower values: from 0.14 (Per4N) to 0.48 (IRAS4), with a weighted mean of 0.32 ± 0.03.

The amount of spread in the $\Delta_{\rm FWHM}$ *vs.* separation scatter diagrams (Figure 5.8) is reflected in the vertical placement of the $\overline{\Delta}_{\rm FWHM}$ curves. The four cores with relatively compact scatter diagrams (Per4N, Per7E, Per5, Per9W) produce $\overline{\Delta}_{\rm FWHM}$ curves that are consistently below the curves for the cores with the more diffuse scatter diagrams (IRAS4, L1448 IRS3, L1455 A1, IRAS2). In the smallest separation bin (differences from adjacent grid squares), the mean $\overline{\Delta}_{\rm FWHM}$ value of the lower group is 0.10 km s^{-1}, and the mean value of the upper group is 0.26 km s^{-1}. Thus, the offset here (0.16 km s^{-1}) is twice as great as the offset of $\overline{\Delta}_{V_C}$ at this separation (0.08 km s^{-1}).

The variances of the $\Delta_{\rm FWHM}$ distributions are plotted as a function of separation in Figure 5.10. The trends that are observed in the Δ_{V_C} data are also observed in

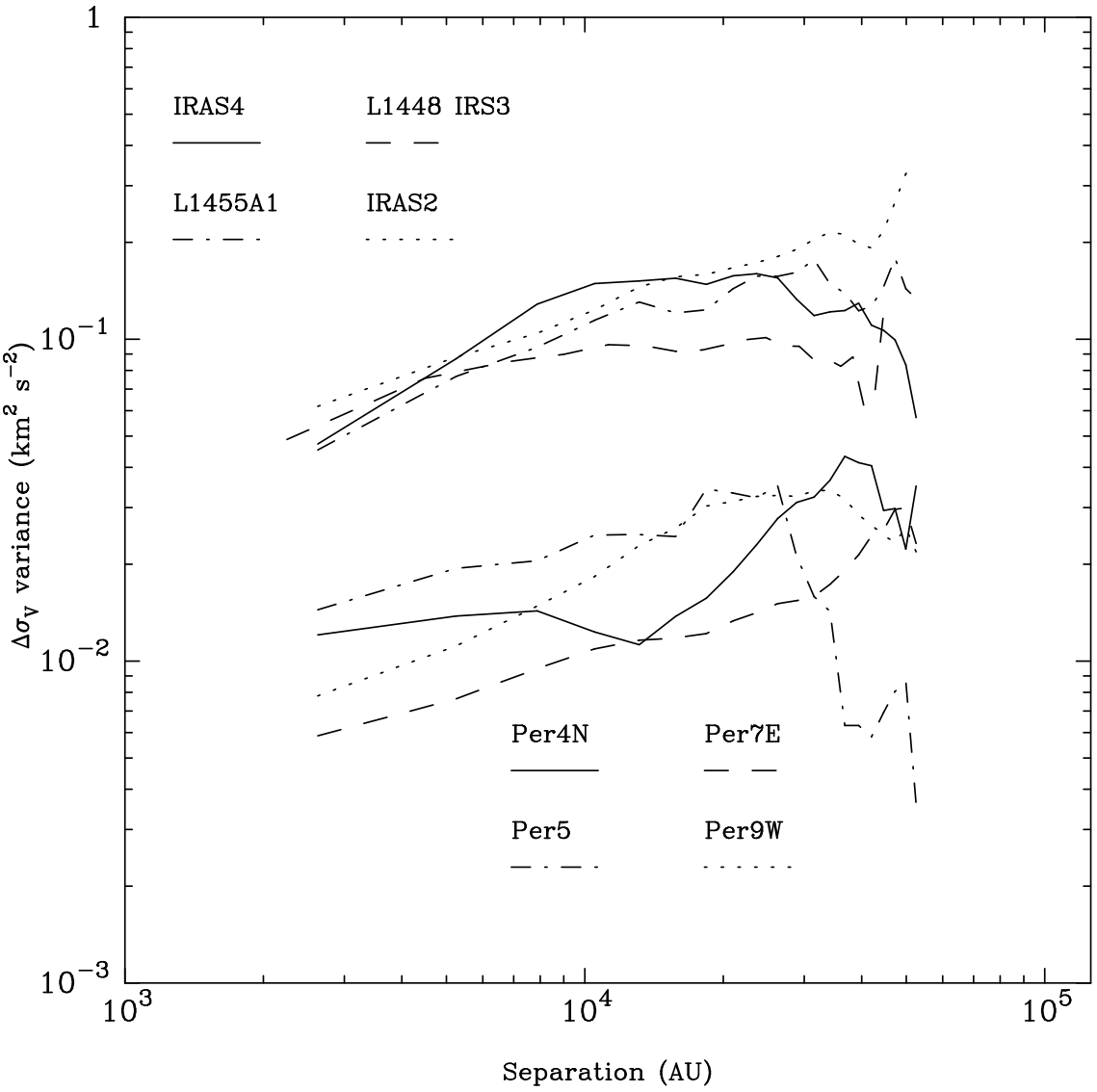

Figure 5.10: The variances of the distributions of $\Delta_{\rm FWHM}$ plotted as a function of the separation interval for the eight cores shown in Figure 5.8. The solid, dashed, dotted, and dot-dash lines in the upper group show the variances for the NGC1333 IRAS4, L1448 IRS3, NGC1333 IRAS2, and L1455 A1 cores, respectively; the solid, dashed, dotted, and dot-dash lines in the lower group represent the variances of Per4N, Per7E, Per9W, and Per5, respectively.

the $\Delta_{\rm FWHM}$ data: the scale of the variances is smaller than the scale of the means by approximately an order of magnitude (the y-axis in Figure 5.10 is extended to include three decades), but the shapes of the curves are approximately the same. Like the $\sigma^2_{\Delta V_C}$ curves, the $\sigma^2_{\Delta_{\rm FWHM}}$ curves are, on the whole, steeper than those of the corresponding means, although the steepening is not as great. One notable exception is the curve for Per4N, which flattens and even decreases slightly over two separation intervals. Acknowledging the deviation of the Per4N curve, the slopes are all approximately linear, signaling a power law relation between $\sigma^2_{\Delta_{\rm FWHM}}$ and separation:

$$\sigma^2_{\Delta_{\rm FWHM}} \propto (\text{separation})^{\alpha_4}. \tag{5.6}$$

Least-squares fits to the $\sigma^2_{\Delta_{\rm FWHM}}$ curves over the first four separation intervals yield values for α_4 from 0.05 (Per4N) to 0.85 (IRAS4), with a weighted mean of 0.51 ± 0.05. Over the first five intervals, the slopes of the curves are shallower, as expected, and range from -0.03 (Per4N) to 0.76 (IRAS4). The weighted mean, however, is nearly the same: 0.50 ± 0.05.

As with the $\overline{\Delta}_{\rm FWHM}$ values, the $\sigma^2_{\Delta_{\rm FWHM}}$ curves clearly separate the eight cores into a lower and an upper group. In the lower group, the mean value for $\sigma^2_{\Delta_{\rm FWHM}}$ for adjacent grid squares is 0.010 km^2 s^{-2}. The mean value of $\sigma^2_{\Delta_{\rm FWHM}}$ for the upper group at this separation is 0.051 km^2 s^{-2}. As expected, the offset between the upper and lower groups (0.041 km^2 s^{-2}) is several times greater than the corresponding offset of the $\sigma^2_{\Delta V_C}$ curves (0.009 km^2 s^{-2}).

The MSB study of central velocities and central velocity differences refers to a follow-up study of spectral line widths (and line width differences) drawn from the same set of observations. This study has not been published. Therefore, the results from the $\Delta_{\rm FWHM}$ analysis of the Perseus cores presented here cannot be compared with complementary results from the star-forming regions analyzed by

MSB. However, because the Δ_{V_C} and $\Delta_{\rm FWHM}$ variations both probe the stochastic nature of the velocity fields in the cores, the similarity between the $\sigma^2_{\Delta V_C}$ curves and the $\sigma^2_{\Delta_{\rm FWHM}}$ curves invites the likelihood that the conclusions drawn from the former are also germane to the latter (*c.f.* Miesch & Bally (1994)). Although the trend in the $\sigma^2_{\Delta_{\rm FWHM}}$ curves is less uniform than the trend in the $\sigma^2_{\Delta V_C}$ curves, if the behavior of the $\Delta_{\rm FWHM}$ variances truly corresponds to a single power law relation at the relevant separations, then the implication is that the gas motions on the scale of these separations are turbulent. The $\Delta_{\rm FWHM}$ variances are calculated from grid squares with dimensions of $\sim$2625 AU, a length that is significantly smaller than the characteristic size of dense cores.

Independent of the accuracy or universal applicability of the power law exponent, the spread in the $\Delta_{\rm FWHM}$ variances (at any particular separation) among the BIMA cores is unequivocal. At the smallest separations, the offset between the $\sigma^2_{\Delta_{\rm FWHM}}$ values of the cores with the more active and less active velocity fields (0.04 km^2 s^{-2}) is several times greater than the corresponding offset (0.01 km^2 s^{-2}) between the same two groups of cores. The obvious differences in the vertical positions of the $\sigma^2_{\Delta_{\rm FWHM}}$ lines reinforces the assertion from the $\sigma^2_{\Delta V_C}$ curves that the offset reflects real differences in the environments of the cores. Less turbulent cores produce more compact $\Delta_{\rm FWHM}$ *vs.* separation scatter diagrams that have lower $\sigma^2_{\Delta_{\rm FWHM}}$ values. In contrast, cores more affected by turbulence produce more diffuse scatter diagrams with consequently higher $\sigma^2_{\Delta_{\rm FWHM}}$ values.

5.4 Velocity Field Diagnostics

The goals of this work were stated in Chapter 1. The first goal was to present the velocity fields of the dense cores from the BIMA survey. That was accomplished in Chapters 2 and 4. The second goal was to use the BIMA data to define diagnostics for turbulence in cores. The pursuit of that goal has threaded through Chapters 2, 4, and 5. A summary describing the trail of that thread follows.

The gridding method, introduced by OSG and applied to their models of turbulent clouds, was applied to the combined BIMA and FCRAO datacubes using MIRIAD's `gridspec` task. The spectra were taken through the datacubes on a range of spatial scales determined by the resolution of the grid. The grid spacing ranged from the full area of the FCRAO maps ($6' \times 6'$) down to approximately $3''$ squares, the limit set by the BIMA maps. The `gridspec` task fitted the spectra with Gaussian functions to determine the line widths (FWHM), which were then plotted as a function of grid square size to determine the spread in the data on various size scales.

Using the line widths from *only* the 16×16 grid squares (the smallest squares that yield a sufficient number of spectra that can be reliably measured), the distributions of the FWHM were quantified by determining the mean ($\langle \mathrm{FWHM} \rangle$) and standard deviation (σ_{FWHM}) for each core. Additionally, the spatial variations of line properties were assessed by calculating the differences in central velocities (Δ_{V_C}) and line widths (Δ_{FWHM}) between the grid squares across the cores. These differences were then plotted as a function of separation, and the means ($\overline{\Delta}_{V_C}$, $\overline{\Delta}_{\mathrm{FWHM}}$) and variances ($\sigma^2_{\Delta V_C}$, $\sigma^2_{\Delta_{\mathrm{FWHM}}}$) of the difference distributions

were calculated in bins at single-grid-square intervals.

The various statistical quantities ($\sigma_{\rm FWHM}$, $\overline{\Delta}_{V_C}$, $\sigma^2_{\Delta V_C}$, $\overline{\Delta}_{\rm FWHM}$, $\sigma^2_{\Delta_{\rm FWHM}}$) are the crucial elements of the velocity field diagnostics. They not only verify the presence of turbulence in the cores but also quantify the amplitude of turbulence suggested by the appearance of the velocity maps. Specifically, three indicators of core turbulence are:

1. **The standard deviation of the distribution of line widths ($\sigma_{\rm FWHM}$).** The values for ($\sigma_{\rm FWHM}$) for all of the survey cores are listed in Table 5.1. Cores with less variable velocity fields have narrower FWHM distributions and therefore smaller $\sigma_{\rm FWHM}$ values. Conversely, cores with more variable velocity fields show a wider distribution of FWHM and therefore smaller $\sigma_{\rm FWHM}$ values.

2. **The power law relation between the Δ_{V_C} and $\Delta_{\rm FWHM}$ variances and separation.** The study by Miesch & Bally (1994) found that the apparent sizes of coherent cells in turbulent clouds are affected by the resolution of the observations from which they are determined. Despite this complication, they point out that in a medium permeated by hierarchical turbulence, various statistical measures will exhibit a power law dependence upon size scale, over the range of scales to which the observations are sensitive. Both MSB and this work find evidence for such a turbulent hierarchy in the power law dependence of $\sigma^2_{\Delta V_C}$ on the separation interval over which the differences are evaluated. The mean exponents of the power laws from the two studies are remarkably similar, despite the variety of the star-forming environments. Additionally, this work also detects a power law dependence, albeit with a smaller

exponent, between $\sigma^2_{\Delta_{\rm FWHM}}$ and separation on the scales probed by the BIMA data.

3. **The relative positions of $\sigma^2_{\Delta V_C}$ and $\sigma^2_{\Delta_{\rm FWHM}}$ at a particular separation.** Although the slopes of the $\sigma^2_{\Delta V_C}$ and $\sigma^2_{\Delta_{\rm FWHM}}$ curves show that the cores are generally affected by turbulence, the importance of the relative positions of the curves cannot be determined from the MSB sample. In the plots of the variances presented here, there is a direct correlation between the appearance of the velocity maps and the shift of a variance curve along the y-axis (*c.f.* Figures 5.6 and 5.10). Cores with relatively quiescent velocity fields have, overall, lower values for the variances at all separations; cores with more active velocity fields tend to have higher values.

In addition to determining diagnostics of core velocity fields, the analysis of the observations presented in this and previous chapters suggests several lines of evidence that turbulence is active in star-forming cores. First, from the entire sample of 21 cores, *not one* exhibits a velocity field that clearly signals the presence of systematic motions that are expected for a quiescent core in the standard star formation theory. Second, from the line widths measured from the cores, *no lines* are as narrow as the thermal line width of $C^{18}O$. If the thermal and turbulent contributions to an observed line width were equal, then the line would be approximately two channels wide. Only a handful of spectra (from the Per5 core) may be this narrow. *All* of the other lines from all of the other cores must have a turbulent component that is comparable to, or larger than, the gas sonic velocity. Furthermore, the line width *vs.* grid size diagrams are very similar in appearance to those in the analysis of the OSG turbulent cloud simulations. The similarity suggests that turbulence with speeds approaching the sonic speed are still present down to the ~2500 AU scale.

The broader lines and the variations in the line width are caused by the interception of multiple emitting clumps across the beam and along the line of sight. Third, the power law relations between the Δ_{V_C} and $\Delta_{\rm FWHM}$ variances and separation measured across the cores (described above) are a signature of hierarchical turbulence on the sub-core scales probed by the BIMA data. Fourth, the Δ_{V_C} and $\Delta_{\rm FWHM}$ variances at all separations (described above) are directly correlated with the degree of activity in the velocity maps. The most probable explanation for the range of variances is that they reflect real differences in the degree of turbulence across the cores.

This work is the first attempt to apply the OSG gridding method to real data and also the first time that the statistical quantities derived from the method have been used to examine turbulence on sub-core scales. The key element for the successful application of this method is the high resolution of the BIMA data. The observations allow the cores to be mapped down to $3''$ ($\sim$1250 AU) resolution and allow the statistical quantities to be calculated in squares of $5''$ ($\sim$2500 AU) resolution. The studies of velocity fields by MSB and Miesch & Bally (1994) determined that the size scales over which statistical measurements exhibit a power law dependence are sensitive to the resolution of the observations from which the statistics are calculated. In this study, the persistence of the power law behavior down to the smallest size scales that can be reliably measured is a strong indication that turbulent motions still influence gas motions in the cores. Determining the scale at which the turbulence dissipates will require observations with even finer resolution.

Chapter 6

Conclusions

6.1 Summary

This work presents the first results from the BIMA Survey of dense cores in the Perseus molecular cloud complex. The survey combines observations made with four configurations of the BIMA array and single-dish observations from the FCRAO 14 m antenna. The extensive coverage of u,v-space enables the cores to be examined with a range of resolutions. The FCRAO data are used to map the $C^{18}O$ $J = 1 \rightarrow 0$ emission from the cores and surrounding cloud material on scales of $44''$. With the BIMA data, the cores are mapped in both the $\lambda = 2.7$ mm continuum and the $C^{18}O$ $J = 1 \rightarrow 0$ emission on scales of $10''$, $5''$, and $3''$.

The main focus of this work is an examination of the $C^{18}O$ $J = 1 \rightarrow 0$ emission from the BIMA cores. Integrated intensity (0^{th} moment) maps of the $C^{18}O$ emission trace the distribution of intermediate density ($> 10^3$ cm^{-3}) gas in the cores. Furthermore, because the $C^{18}O$ line is optically thin at the prevailing densities and temperatures of the cores, intensity-weighted velocity (1^{st} moment) maps are used to probe the kinematics of the core material. The $C^{18}O$ $J = 1 \rightarrow 0$ line emission is not strongly enhanced in shocks or outflows, so the $C^{18}O$ emission traces the bulk

of the gas in the envelope.

A grid-based analysis technique, developed by Ostriker, Stone, & Gammie (2001), is used to extract velocity information from the datacubes. The technique breaks down the datacubes into grid squares with successively finer resolution, then compares the properties of spectra taken through those grid squares. The technique was applied to models of turbulent clouds by OSG; this is its first application to real datacubes. The primary advantage to this method is that the size scales probed by the grid squares are not tied to a reference position (such as an emission peak) within the core.

In Chapter 2, the intensity and velocity maps for three cores, L1448 IRS3, NGC1333 IRAS2, and NGC1333 IRAS4, were presented. These three cores were singled-out from the rest of the BIMA survey targets because of the substantial amount of additional data that was available. The cores had been observed with the A-configuration of the BIMA array, and they had been observed in the emission from the $J = 1 \rightarrow 0$ transition of $H^{13}CO^+$ and N_2H^+. Moreover, models of the protostellar envelopes in these cores had been developed by Looney, Mundy, & Welch (2003). The inclusion of the $H^{13}CO^+$ and N_2H^+ datasets enabled a comparison of the intensity and velocity fields probed by the three lines. The $C^{18}O$ emission was found to be stronger and more widely distributed than the emission from the $H^{13}CO^+$ and N_2H^+ lines, but despite these differences, the velocity maps constructed from the three lines were, on the whole, consistent.

Chapter 3 presented a study of the depletion of $C^{18}O$ in the protostellar envelopes within these cores. For all three protostars that were examined, the abundance of $C^{18}O$ in the envelope models developed by Looney, Mundy, & Welch (2003) had to be reduced by some factor to match the observed fluxes. This result implies that some gas-phase $C^{18}O$ is being frozen-out onto dust grains, resulting in depletions of

a factor of 2-5 compared to standard dark cloud abundances. In addition, models in which the effect of extreme depletion was simulated by removing material from the innermost or outermost AU of the envelope failed to produce the observed core morphologies. The modeling supports the underlying assumption that the $C^{18}O$ emission can be used to trace the core velocity field.

In Chapter 4, the $C^{18}O$ intensity and velocity maps from the BIMA survey of dense cores were presented. These observations (and the observations from the three cores in Chapter 2) revealed core substructures that were unknown from previous single-dish studies. Many of the cores clearly have structures on scales of $\sim$1000 AU, the spatial scales probed at $3''$ resolution. Furthermore, none of the cores exhibited the simple velocity field that might be expected from a quasi-stable clump of dense gas, a clump in systematic rotation, or an overdense clump undergoing spherically symmetrical collapse. The velocity data also revealed that the velocity ranges probed in the cores are a function of resolution: the largest range of velocities were typically found in the highest resolution maps.

By gridding the combined datacubes with a range of resolutions, then extracting spectra from the lines of sight through the grid squares and measuring the FWHM of the spectra, the cores were found to produce a wide range of line widths even on small size scales. [The grid size that was the foundation for the analysis in Chapter 5 corresponds to $\sim$2600 AU at the distance of 350 pc.] The range of FWHM was generally greater than the uncertainties in the individual measurements. The standard deviation of the line widths ($\sigma_{\rm FWHM}$) was directly correlated with the mean line width ($\langle$FWHM$\rangle$), indicating that cores with narrower lines also exhibit narrower distributions in the line widths across the maps.

The grid squares were also used to calculate the differences in central velocities (Δ_{V_C}) and line widths ($\Delta_{\rm FWHM}$) between spectra at different separations. Scatter

plots of Δ_{V_C} and $\Delta_{\rm FWHM}$ as a function of separation showed a correlation between the spread in the differences and the apparent degree of turbulence in the velocity maps. These scatter plots were quantified by examining the means ($\overline{\Delta}_{V_C}$, $\overline{\Delta}_{\rm FWHM}$) and variances ($\sigma^2_{\Delta V_C}$, $\sigma^2_{\Delta_{\rm FWHM}}$) of the distributions in single-grid-square intervals. For smaller separations (out to 4-5 grid squares), the curves of both the means and variances were correlated with separation according to a power law. According to the analysis of central velocity differences by Miesch & Bally (1994), this type of behavior is indicative of turbulent motions on the size scales probed by the data. The analyses presented here extended the results of Miesch, Scalo, & Bally (1999) and showed that turbulence persists down to scales smaller than the characteristic core radius. In addition, the relative positions of the mean and variance curves were correlated with the appearances of the velocity maps. Cores that appear more quiescent have correspondingly lower values for the means and variances at all separations, whereas cores that show a higher degree of activity in their velocity maps have correspondingly higher values for the means and variances at all separations.

6.2 Conclusions

The main conclusions that can be drawn from the observations and analyses presented in this work are the following:

1. High resolution observations are of critical importance in probing the distribution of dust and gas within dense cores. All of the cores in the survey show structure on scales less than the characteristic core radius (0.1 pc).

2. The velocity fields of the cores are complex. Not one of the cores in the BIMA survey exhibits a velocity field indicative of a quiescent clump of gas, or a broad systematic velocity gradient.

3. In all three of the protostellar envelope models, the abundance of $C^{18}O$ must be reduced by some factor (of order a few) to match the observed fluxes.

4. The $C^{18}O$ emission from cores exhibits a range of line widths, even on scales of ~2500 AU. The range of line widths is indicative of turbulence within the cores. No lines are as narrow as the thermal line width of $C^{18}O$; almost no lines are as narrow as the minimum line width for thermal and turbulent broadening to be equal. Thus, for most lines, turbulence is the dominant broadening mechanism.

5. Both the means and the variances of the central velocity and the FWHM difference distributions obey a power law relation with the spatial separation over which the differences are calculated, indicating that the motions altering the spectral lines likely arise from turbulence. The values for the means and variances are directly correlated with the degree of activity observed in the velocity maps.

6. Turbulence clearly persists on sub-core spatial scales. And turbulence is sufficiently strong to affect star formation on the scale of individual cores. The effects of turbulence must be included in a general theory of star formation.

6.3 Future Studies

BIMA observations of the N_2H^+ emission from sixteen of the cores in the $C^{18}O$ survey were made prior to the interferometer shutting down in June 2004. As articulated in Chapter 4, the N_2H^+ observations complement the $C^{18}O$ studies of the velocity fields. In addition to probing denser environments than the $C^{18}O$ line, the N_2H^+ molecule should be less susceptible to depletion than $C^{18}O$. In addition,

some of the cores observed for the BIMA survey (*e.g.* L1455C, Per6) are known centers of NH_3 emission but were found to be weak sources of $C^{18}O$. Although N_2H^+ was found to trace the $C^{18}O$ with reasonable fidelity in the cores shown in Chapter 2, the N_2H^+ line may reveal more about the dense core seen in the NH_3 emission.

During the last season of BIMA's A-array configuration, additional observations of the $C^{18}O$ emission were made of five objects from the BIMA survey (Per5, B5, B1, L1448I2, L1448C). All of these sources, based upon the $\lambda = 2.7$ continuum observations are sites of known or suspected binary stars. The high resolution A-array observations will be used to further probe the multiplicity of these sources and to determine if there is a correlation between turbulence and multiplicity.

All of the BIMA survey targets have been observed in the J, H, and K_s near-infrared wavebands with the KPNO 4 m telescope. Soon, the entire Perseus cloud will be observed at mid- and far-infrared wavelengths with the Spitzer Space Telescope. The Spitzer observations in particular will be a treasure trove of data for star formation astronomers. However, within the scope of the work presented here, both the KPNO and the Spitzer observations will help reveal the true stellar and protostellar content of the Perseus cores. These data will be used to search for correlations between the envelope structures and kinematics revealed in the BIMA data and number and mass distributions of protostars in the cores.

In the present study, a deliberate effort has been made to divorce the line width *vs.* size correlation from absolute positions within a core. This was one of the justifications for applying the gridding method to the datacubes. The grids pick out characteristic size scales in the cores *without* tethering the scales to some reference point. In previous studies of core velocity fields, the sizes adopted in constructing line width *vs.* size correlations relied upon *e.g.* the distance from an embedded

IRAS source or the size of a particular intensity contour. There are drawbacks to referencing size scales to absolute positions within a core. (If the position of a protostar is used as a reference point, the relation of the protostar to the embedding material may be uncertain, particularly along the line-of-sight. Turbulent motions may have redistributed the core material in the time since the protostar initially formed. Among the survey core, Per6 may be an example of this: the $\lambda = 2.7$ mm continuum source is displaced by $\sim 1'$ from the location of the NH_3 intensity peak.) However, because several studies have looked at some of the same Perseus cores in this way (*e.g.* Caselli *et al.* (2002a)), one clear avenue for further investigation would be to perform this type of analysis on the datasets presented here. The interferometric observations should either confirm or refute the conclusions drawn from lower resolution studies for the cores that are common to the surveys.

Appendix A

Results of Spectral Line Fitting

Table A.1. L1448 IRS3: Model Fits to $C^{18}O$ Spectral Lines

Model Number	Beam Size (arcsec)	Case	$V_{\rm infall}$ (km/s)	V_{t+T} (km/s)	X($C^{18}O$) ($\times 10^{-7}$)	R_{in} (AU)	T(R_{in}) (K)	R_{out} (AU)	T(R_{out}) (K)
1	10	No Infall	0	1.4	0.42	40	87	2000	18
		Infall	4.6	0.17	0.63	40	87	2000	18
		Shell	0	1.3	2.0	1604	20	2000	18
		Core	0	1.2	2.0	1	380	735	27
	5	No Infall	0	1.6	0.29	40	87	2000	18
		Infall	4.2	0.17	0.38	40	87	2000	18
		Shell	0	1.6	2.0	1471	21	2000	18
		Core	0	1.3	2.0	1	380	401	35
	3	No Infall	0	2.1	1.4	40	87	2000	18
		Infall	4.2	0.17	0.42	40	87	2000	18
		Shell	0	2.0	2.0	1070	23	2000	18
		Core	0	1.7	2.0	1	380	287	40
2	10	No Infall	0	1.4	0.42	40	87	3000	16
		Infall	4.6	0.15	0.44	40	87	3000	16
		Shell	0	1.4	2.0	1270	22	3000	16
		Core	0	1.3	2.0	1	380	936	25
	5	No Infall	0	1.6	0.36	40	87	3000	16
		Infall	3.9	0.15	0.36	40	87	3000	16
		Shell	0	1.6	2.0	1671	20	3000	16
		Core	0	1.4	2.0	1	380	468	32
	3	No Infall	0	2.0	0.44	40	87	3000	16
		Infall	3.9	0.15	0.47	40	87	3000	16
		Shell	0	2.0	2.0	1070	23	3000	16
		Core	0	1.8	2.0	1	380	361	36
3	10	No Infall	0	1.4	0.38	40	87	2000	18
		Infall	4.3	0.17	0.40	40	87	2000	18
		Shell	0	1.4	2.0	1537	20	2000	18
		Core	0	1.2	2.0	1	380	668	28
	5	No Infall	0	1.6	0.24	40	87	2000	18
		Infall	3.8	0.17	0.25	40	87	2000	18
		Shell	0	1.6	2.0	1471	21	2000	18
		Core	0	1.3	2.0	1	380	361	36
	3	No Infall	0	2.0	0.26	40	87	2000	18
		Infall	3.9	0.17	0.28	40	87	2000	18
		Shell	0	2.0	2.0	1070	23	2000	18
		Core	0	1.6	2.0	1	380	247	42
4	10	No Infall	0	1.4	0.45	40	87	4000	14
		Infall	4.7	0.14	0.45	40	87	4000	14
		Shell	0	1.4	2.0	2406	17	4000	14
		Core	0	1.2	2.0	1	380	869	25
	5	No Infall	0	1.6	0.38	40	87	4000	14
		Infall	4.0	0.14	0.39	40	87	4000	14
		Shell	0	1.6	2.0	1671	20	4000	14
		Core	0	1.4	2.0	1	380	428	34
	3	No Infall	0	2.0	0.44	40	87	4000	14
		Infall	4.0	0.14	0.47	40	87	4000	14
		Shell	0	2.0	2.0	1003	24	4000	14
		Core	0	1.7	2.0	1	380	307	38
5	10	No Infall	0	1.4	0.73	40	87	10000	10
		Infall	5.0	0.12	0.76	40	87	10000	10
		Shell	0	1.4	2.0	2273	17	10000	10
		Core	0	1.3	2.0	1	380	1270	22
	5	No Infall	0	1.6	0.67	40	87	10000	10
		Infall	4.1	0.12	0.70	40	87	10000	10
		Shell	0	1.6	2.0	1270	22	10000	10
		Core	0	1.5	2.0	1	380	615	29

Table A.1 (cont'd)

Model Number	Beam Size (arcsec)	Case	$V_{\rm infall}$ (km/s)	V_{t+T} (km/s)	X($C^{18}O$) ($\times 10^{-7}$)	R_{in} (AU)	T(R_{in}) (K)	R_{out} (AU)	T(R_{out}) (K)
	3	No Infall	0	2.0	0.79	40	87	10000	10
		Infall	4.1	0.12	0.88	40	87	10000	10
		Shell	0	2.0	2.0	668	28	10000	10
		Core	0	1.9	2.0	1	380	481	32
6	10	No Infall	0	1.4	0.33	40	87	5000	13
		Infall	4.6	0.14	0.34	40	87	5000	13
		Shell	0	1.4	2.0	2807	16	5000	13
		Core	0	1.1	2.0	1	380	668	28
	5	No Infall	0	1.6	0.26	40	87	5000	13
		Infall	3.9	0.14	0.27	40	87	5000	13
		Shell	0	1.6	2.0	1872	19	5000	13
		Core	0	1.2	2.0	1	380	341	37
	3	No Infall	0	2.0	0.28	40	87	5000	13
		Infall	3.9	0.14	0.31	40	87	5000	13
		Shell	0	2.0	2.0	1203	22	5000	13
		Core	0	1.5	2.0	1	380	254	41
7	10	No Infall	0	1.4	0.45	40	87	10000	10
		Infall	4.8	0.12	0.46	40	87	10000	10
		Shell	0	1.4	2.0	2807	16	10000	10
		Core	0	1.2	2.0	1	380	869	25
	5	No Infall	0	1.6	0.36	40	87	10000	10
		Infall	4.0	0.12	0.39	40	87	10000	10
		Shell	0	1.6	2.0	1671	20	10000	10
		Core	0	1.2	2.0	1	380	394	35
	3	No Infall	0	2.0	0.40	40	87	10000	10
		Infall	4.0	0.12	0.44	40	87	10000	10
		Shell	0	2.0	2.0	1003	24	10000	10
		Core	0	1.6	2.0	1	380	274	40

Table A.2. NGC1333 IRAS2: Model Fits to $C^{18}O$ Spectral Lines

Model Number	Beam Size (arcsec)	Case	$V_{\rm infall}$ (km/s)	V_{t+T} (km/s)	X($C^{18}O$) ($\times 10^{-7}$)	R_{in} (AU)	T(R_{in}) (K)	R_{out} (AU)	T(R_{out}) (K)
1	10	No Infall	0	0.83	1.4	40	127	2000	27
		Infall	2.8	0.20	1.4	40	127	2000	27
		Shell	0	0.83	2.0	1270	32	2000	27
		Core	0	0.82	2.0	1	555	1738	28
	5	No Infall	0	0.87	1.2	40	127	2000	27
		Infall	2.5	0.20	1.2	40	127	2000	27
		Shell	0	0.87	2.0	1270	32	2000	27
		Core	0	0.87	2.0	1	555	1537	29
	3	No Infall	0	0.96	1.4	40	127	2000	27
		Infall	2.3	0.20	1.4	40	127	2000	27
		Shell	0	0.95	2.0	936	36	2000	27
		Core	0	0.96	2.0	1	555	1471	30
2	10	No Infall	0	0.84	1.3	40	127	3000	23
		Infall	3.0	0.19	1.2	40	127	3000	23
		Shell	0	0.84	2.0	1604	29	3000	23
		Core	0	0.83	2.0	1	555	2340	25
	5	No Infall	0	0.87	1.3	40	127	3000	23
		Infall	2.4	0.19	1.3	40	127	3000	23
		Shell	0	0.87	2.0	1070	34	3000	23
		Core	0	0.87	2.0	1	555	1738	28
	3	No Infall	0	0.96	1.4	40	127	3000	23
		Infall	2.2	0.19	1.5	40	127	3000	23
		Shell	0	0.95	2.0	668	41	3000	23
		Core	0	0.96	2.0	1	555	1471	30
3	10	No Infall	0	0.84	1.5	40	127	4000	20
		Infall	3.2	0.17	1.5	40	127	4000	20
		Shell	0	0.84	2.0	1537	29	4000	20
		Core	0	0.84	2.0	1	555	2807	23
	5	No Infall	0	0.87	1.8	40	127	4000	20
		Infall	2.5	0.17	1.8	40	127	4000	20
		Shell	0	0.87	2.0	668	41	4000	20
		Core	0	0.87	2.0	1	555	2941	23
	3	No Infall	0	0.96	2.0	40	127	4000	20
		Infall	2.3	0.17	2.1	40	127	4000	20
		Shell	0	0.95	2.0	187	68	4000	20
		Core	0	0.96	2.0	1	555	3209	22
4	10	No Infall	0	0.84	1.3	40	127	6000	17
		Infall	3.2	0.16	1.3	40	127	6000	17
		Shell	0	0.84	2.0	1671	29	6000	17
		Core	0	0.83	2.0	1	555	2807	23
	5	No Infall	0	0.87	1.5	40	127	6000	17
		Infall	2.4	0.16	1.5	40	127	6000	17
		Shell	0	0.87	2.0	668	41	6000	17
		Core	0	0.87	2.0	1	555	2206	26
	3	No Infall	0	0.97	0.72	40	127	6000	17
		Infall	2.6	0.16	0.72	40	127	6000	17
		Shell	0	0.97	2.0	1671	29	6000	17
		Core	0	0.96	2.0	1	555	936	36
5	10	No Infall	0	0.84	1.5	40	127	7000	16
		Infall	3.1	0.16	1.4	40	127	7000	16
		Shell	0	0.84	2.0	1471	30	7000	16
		Core	0	0.83	2.0	1	555	3743	21
	5	No Infall	0	0.87	1.8	40	127	7000	16
		Infall	2.4	0.16	1.8	40	127	7000	16
		Shell	0	0.87	2.0	501	46	7000	16
		Core	0	0.87	2.0	1	555	3944	20

Table A.2 (cont'd)

Model Number	Beam Size (arcsec)	Case	$V_{\rm infall}$ (km/s)	V_{t+T} (km/s)	X($C^{18}O$) ($\times 10^{-7}$)	R_{in} (AU)	T(R_{in}) (K)	R_{out} (AU)	T(R_{out}) (K)
	3	No Infall	0	0.96	1.8	40	127	7000	16
		Infall	2.2	0.16	1.9	40	127	7000	16
		Shell	0	0.95	2.0	274	59	7000	16
		Core	0	0.96	2.0	1	555	3209	22
6	10	No Infall	0	0.83	1.1	40	127	5000	18
		Infall	3.0	0.17	1.2	40	127	5000	18
		Shell	0	0.84	2.0	1471	30	5000	18
		Core	0	0.81	2.0	1	555	2072	26
	5	No Infall	0	0.86	1.1	40	127	5000	18
		Infall	2.3	0.17	1.1	40	127	5000	18
		Shell	0	0.87	2.0	936	36	5000	18
		Core	0	0.84	2.0	1	555	2874	23
	3	No Infall	0	0.95	0.93	40	127	5000	18
		Infall	2.0	0.17	0.93	40	127	5000	18
		Shell	0	0.95	2.0	668	41	5000	18
		Core	0	0.91	2.0	1	555	602	43
7	10	No Infall	0	0.83	1.2	40	127	6000	17
		Infall	3.0	0.16	1.2	40	127	6000	17
		Shell	0	0.84	2.0	1471	30	6000	17
		Core	0	0.82	2.0	1	555	2540	24
	5	No Infall	0	0.86	1.2	40	127	6000	17
		Infall	2.3	0.16	1.2	40	127	6000	17
		Shell	0	0.87	2.0	802	38	6000	17
		Core	0	0.84	2.0	1	555	1270	32
	3	No Infall	0	0.95	1.0	40	127	6000	17
		Infall	2.1	0.16	1.1	40	127	6000	17
		Shell	0	0.95	2.0	628	42	6000	17
		Core	0	0.92	2.0	1	555	735	40

Table A.3. NGC1333 IRAS4: Models Fits to $C^{18}O$ Spectral Lines

Model Number	Beam Size (arcsec)	Case	$V_{\rm infall}$ (km/s)	V_{t+T} (km/s)	X($C^{18}O$) ($\times 10^{-7}$)	R_{in} (AU)	T(R_{in}) (K)	R_{out} (AU)	T(R_{out}) (K)
1	10	No Infall	0	0.50	0.48	40	105	1000	29
		Infall	1.5	0.21	0.45	40	105	1000	29
		Shell	0	0.55	2.0	802	31	1000	29
		Core	0	0.35	2.0	1	457	735	33
	5	No Infall	0	0.64	0.18	40	105	1000	29
		Infall	1.6	0.21	0.19	40	105	1000	29
		Shell	0	0.66	2.0	936	30	1000	29
		Core	0	0.43	2.0	1	457	528	37
	3	No Infall	0	0.83	0.15	40	105	1000	29
		Infall	1.8	0.21	0.15	40	105	1000	29
		Shell	0	0.83	2.0	936	30	1000	29
		Core	0	0.54	2.0	1	457	374	43
2	10	No Infall	0	0.60	0.16	40	105	2000	22
		Infall	1.9	0.18	0.16	40	105	2000	22
		Shell	0	0.64	2.0	1805	23	2000	22
		Core	0	0.42	2.0	1	457	735	33
	5	No Infall	0	0.68	0.13	40	105	2000	22
		Infall	1.8	0.18	0.13	40	105	2000	22
		Shell	0	0.68	2.0	1805	23	2000	22
		Core	0	0.45	2.0	1	457	528	37
	3	No Infall	0	0.83	0.13	40	105	2000	22
		Infall	1.9	0.18	0.14	40	105	2000	22
		Shell	0	0.85	2.0	1537	24	2000	22
		Core	0	0.55	2.0	1	457	381	42
3	10	No Infall	0	0.60	0.14	40	105	3000	19
		Infall	2.1	0.17	0.15	40	105	3000	19
		Shell	0	0.62	2.0	2741	19	3000	19
		Core	0	0.45	2.0	1	457	1003	29
	5	No Infall	0	0.67	0.15	40	105	3000	19
		Infall	1.8	0.17	0.15	40	105	3000	19
		Shell	0	0.67	2.0	2340	21	3000	19
		Core	0	0.53	2.0	1	457	561	36
	3	No Infall	0	0.84	0.17	40	105	3000	19
		Infall	1.8	0.17	0.18	40	105	3000	19
		Shell	0	0.81	2.0	1805	23	3000	19
		Core	0	0.60	2.0	1	457	388	42
4	10	No Infall	0	0.61	0.14	40	105	3000	19
		Infall	2.0	0.17	0.14	40	105	3000	19
		Shell	0	0.62	2.0	2741	19	3000	19
		Core	0	0.44	2.0	1	457	1003	29
	5	No Infall	0	0.68	0.14	40	105	3000	19
		Infall	1.7	0.17	0.14	40	105	3000	19
		Shell	0	0.68	2.0	2273	21	3000	19
		Core	0	0.44	2.0	1	457	561	36
	3	No Infall	0	0.83	0.15	40	105	3000	19
		Infall	1.8	0.17	0.16	40	105	3000	19
		Shell	0	0.81	2.0	1738	23	3000	19
		Core	0	0.55	2.0	1	457	401	42
5	10	No Infall	0	0.62	0.16	40	105	4000	17
		Infall	2.1	0.16	0.16	40	105	4000	17
		Shell	0	0.62	2.0	3409	18	4000	17
		Core	0	0.45	2.0	1	457	1003	29
	5	No Infall	0	0.68	0.17	40	105	4000	17
		Infall	1.8	0.16	0.18	40	105	4000	17
		Shell	0	0.68	2.0	2540	20	4000	17
		Core	0	0.47	2.0	1	457	561	36

Table A.3 (cont'd)

Model Number	Beam Size (arcsec)	Case	$V_{\rm infall}$ (km/s)	V_{t+T} (km/s)	X($C^{18}O$) ($\times 10^{-7}$)	R_{in} (AU)	T(R_{in}) (K)	R_{out} (AU)	T(R_{out}) (K)
	3	No Infall	0	0.83	0.19	40	105	4000	17
		Infall	1.8	0.16	0.19	40	105	4000	17
		Shell	0	0.81	2.0	1805	23	4000	17
		Core	0	0.58	2.0	1	457	401	42
6	10	No Infall	0	0.59	0.16	40	105	2000	22
		Infall	1.8	0.18	0.16	40	105	2000	22
		Shell	0	0.61	2.0	1804	23	2000	22
		Core	0	0.38	2.0	1	457	735	33
	5	No Infall	0	0.66	0.11	40	105	2000	22
		Infall	1.7	0.18	0.12	40	105	2000	22
		Shell	0	0.67	2.0	1738	23	2000	22
		Core	0	0.42	2.0	1	457	541	37
	3	No Infall	0	0.82	0.11	40	105	2000	22
		Infall	1.8	0.18	0.11	40	105	2000	22
		Shell	0	0.82	2.0	1471	25	2000	22
		Core	0	0.49	2.0	1	457	381	42
7	10	No Infall	0	0.61	0.14	40	105	3000	19
		Infall	2.0	0.17	0.14	40	105	3000	19
		Shell	0	0.61	2.0	2674	19	3000	19
		Core	0	0.41	2.0	1	457	735	33
	5	No Infall	0	0.67	0.12	40	105	3000	19
		Infall	1.7	0.17	0.13	40	105	3000	19
		Shell	0	0.68	2.0	2206	21	3000	19
		Core	0	0.42	2.0	1	457	528	37
	3	No Infall	0	0.82	0.12	40	105	3000	19
		Infall	1.8	0.17	0.13	40	105	3000	19
		Shell	0	0.82	2.0	1671	23	3000	19
		Core	0	0.52	2.0	1	457	374	43

Bibliography

Alves, J., Lada, C. J., & Lada, E. A. 1999, ApJ, 515, 265

André, P., Ward-Thompson, D., & Barsony, M. 1993, ApJ, 406, 122

André, P., Ward-Thompson, D., & Motte, F. 1996, A&A, 314, 625

Anglada, G., & Rodríguez, L. F. 2002, RMxAA, 38, 13

Anglada, G., Rodríguez, L. F., Torrelles, J. M., Estalella, R., Ho, P. T. P., Canto, J., Lopez, R., & Verdes-Montenegro, L. 1989, ApJ, 341, 208

Arquilla, R., & Goldsmith, P. F. 1985, ApJ, 297, 436

Arquilla, R., & Goldsmith, P. F. 1986, ApJ, 303, 356

Aspin, C., Sandell, G., & Russell, A. P. G. 1994, A&AS, 106, 165

Bachiller, R. 1996, ARA&A, 34, 111

Bachiller, R. 1997, IAU Symposium 178, Molecules in Astrophysics: Probes and Processes, ed. E. F. van Dishoeck, (Dordrecht: Kluwer), 31

Bachiller, R., Codella, C., Colomer, F., Liechti, S., & Walmsley, C. M. 1998, A&A, 335, 266

Bachiller, R., Guilloteau, S., Dutrey, A., Planesas, P., & Martín-Pintado, J. 1995, A&A, 299, 857

Bachiller, R., & Cernicharo, J. 1986, A&A, 166, 283

Bachiller, R., & Cernicharo, J. 1986, A&A, 168, 262

Bachiller, R., & Cernicharo, J. 1984, A&A, 140, 414

Bachiller, R., Cernicharo, J., Martín-Pintado, J., Tafalla, M., & Lazareff, B. 1990,

A&A, 231, 174

Bachiller, R., Martín-Pintado, J., & Fuente, A. 1991, A&A, 243, L21

Bachiller, R., Martín-Pintado, J., & Planesas, P. 1991, A&A, 251, 639

Bachiller, R., Menten, K. M., & del Rio-Alvarez, S. 1990, A&A, 236, 461

Bachiller, R., Terebey, S., Jarrett, T., Martín-Pintado, J., Beichman, C. A., & Van Buren, D. 1994, ApJ, 437, 296

Ballesteros-Paredes, J., Klessen, R. S., & Vázquez-Semadeni, E. 2003, ApJ, 592, 188

Bally, J., & Devine, D. 1994, ApJ, 428, 65

Bally, J., Devine, D., & Alten, V. 1996, ApJ, 473, 921

Bally, J., Devine, D., Alten, V., & Sutherland, R. S. 1997, ApJ, 478, 603

Bally, J., Devine, D., Hereld, M., & Rauscher, B. J. 1993, ApJ, 418, 75

Bally, J., Devine, D., Reipurth, B. 1996, ApJ, 473, 49

Bally, J., Lada, E. A., & Lane, A. P. 1993, ApJ, 418, 322

Bally, J., & Reipurth, B. 2001, ApJ, 546, 299

Barranco, J. A., & Goodman, A. A. 1998, ApJ, 504, 207

Barsony, M., Ward-Thompson, D., André, P., & O'Linger, J. 1998, ApJ, 509, 733

Basu, S. & Mouschovias, T. Ch. 1994, ApJ, 432, 720

Beckwith, S. V. W. & Sargent, A. I. 1991, ApJ, 381, 250

Beichman, C. A., Jennings, R. E., Emerson, J. P., Baud, B., Harris, S., Rowan-Robinson, M., Aumann, H. H., Gauttier, T. N., Gillett, F. C., Habing, H. J., Marsden, P. L., Neugebauer, G., & Young, E. 1984, ApJ, 278, 45

Benson, P. J., Caselli, P., & Myers, P. C. 1998, ApJ, 506, 743

Benson, P. J., & Myers, P. C. 1989, ApJS, 71, 89

Bergin, E. A., Alves, J., Huard, T., & Lada, C. J. 2002, 570, 101

Bergin, E. A., Ciardi, D. R., Lada, C. J., Alves, J., & Lada, E. A. 2001, ApJ, 557,

209

Bergin, E. A., Goldsmith, P. F., Snell, R. L., & Langer, W. D. 1997, ApJ, 482, 285

Bergin, E. A., & Langer, W. D. 1997, ApJ, 486, 316

Blake, G. A. 1997, IAU Symposium 178, Molecules in Astrophysics: Probes and Processes, ed. E. F. van Dishoeck, (Dordrecht: Kluwer), 31

Blake, G. A., Sandell, G., van Dishoeck, E. F., Groesbeck, T. D., Mundy, L. G., & Aspin, C. 1995, ApJ, 441, 689

Bodenheimer, P., Burkert, A., Klein, R. I., & Boss, A. P. 2000, Protostars and Planets IV, ed. V. Mannings, A. P. Boss, & S. S. Russell (Tucson: University of Arizona), 675

Bonnor, W. B. 1956, MNRAS, 116, 351

Bontemps, S., André, P., Terebey, S., & Cabrit, S. 1996, A&A, 311, 858

Boss, A. P. 1997, ApJ, 483, 309

Boss, A. P. 1999, ApJ, 520, 744

Briggs, D. S., Schwab, F. R., & Sramek, R. A. 1999, Synthesis Imaging in Radio Astronomy II, ed. G. B. Taylor, C. L. Carilli, & R. A. Perley (San Francisco: ASP), 127

Burkert, A., Bate, M. R., & Bodenheimer, P. 1997, MNRAS, 289, 497

Burkert, A., & Bodenheimer, P. 2000, ApJ, 543, 822

Caselli, P., Benson, P. J., Myers, P. C., & Tafalla, M. 2002, ApJ, 572, 238

Caselli, P., Walmsley, C. M., Tafalla, M., Dore, L., & Myers, P. C. 1999, ApJ, 523, 165

Caselli, P., Walmsley, C. M., Zucconi, A., Tafalla, M., Dore, L., & Myers, P. C. 2002, ApJ, 565, 331

Caselli, P., Walmsley, C. M., Zucconi, A., Tafalla, M., Dore, L., & Myers, P. C. 2002, ApJ, 565, 344

Cernicharo, J., & Bachiller, R. 1984, A&A, 58, 327

Cernicharo, J., Bachiller, R., & Duvert, G. 1985, A&A, 149, 273

Černis. K. 1990, Ap&SS, 166, 315

Cesaroni, R., Palagi, F., Felli, M., Catarzi, M., Comoretto, G., di Franco, S., Giovanardi, C., & Palla, F. 1988, A&AS, 76, 445

Chandrasekhar, S. 1949, ApJ, 110, 329

Choi, M. 2001, ApJ, 553, 219

Choi, M., Panis, J.-F., & Evans, N. J., II 1999, ApJS, 122, 519

Clark, F. O. 1991, ApJS, 75, 611

Clarke, C. J., Bonnell, I. A., & Hillenbrand, L. A. 2000, in Protostars and Planets IV, ed. V. Mannings, A. P. Boss, & S. S. Russell (Tucson: University of Arizona), 151

Cohen, M. 1980, AJ, 85, 29

Cohen, M., & Kuhi, L. V. 1979, ApJS, 41, 743

Cohen, M. & Schwartz, R. D. 1980, MNRAS, 191, 165

Cohen, M. & Schwartz, R. D. 1983, ApJ, 265, 877

Curiel, S., Raymond, J. C., Rodríguez, L. F., Canto, J., & Moran, J. M. 1990, ApJ, 265, L85

Curiel, S., Torelles, J. M., Rodríguez, L. F., Gómez, J. F., & Anglada, G. 1999, ApJ, 527, 310

Davidson, J. A., & Jaffe, D. T. 1984, ApJ, 277, 13

Davis, C. J., Dent, W. R. F., Matthews, H. E., Aspin, C., & Lightfoot, J. F. 1994, MNRAS, 266, 933

Davis, C. J. & Smith, M. D. 1996, A&A, 309, 929

Davis, C. J. & Smith, M. D. 1995, ApJ, 443, L41

Dickel, H. R., & Auer, L. H. 1994, ApJ, 437, 222

DiFrancesco, J., Myers, P. C., Wilner, D. J., Ohashi, N., and Mardones, D. 2001, ApJ, 562, 770

Draine, B. T. & Lee, H. M. 1984, ApJ, 285, 89

Dutrey, A., Guilloteau, S., & Bachiller, R. 1997, A&A, 325, 758

Ebert, R. 1955, Zeitschrift für Astrophysik, 37, 217

Eislöffel, J. 2000, A&A, 354, 236

Elmegreen, B. G. 1979, ApJ, 232, 729

Evans, N. J., II, 1999, ARA&A, 37, 311

Evans, N. J., II, *et al.* 2003, PASP, 115, 965

Evans, N. J., II, Rawlings, J. M. C., Shirley, Y. L., & Mundy, L. G. 2001, ApJ, 557, 193

Fuller, G. A., Ladd, E. F., & Hodapp, K. W. 1996, ApJ, 463, L97

Fuller, G. A., & Myers, P. C. 1992, ApJ, 384, 523

Fuller, G. A., Myers, P. C., Welch, W. J., Goldsmith, P. F., Langer, W. D., Campbell, B. G., Guilloteau, S., & Wilson, R. W. 1991, ApJ, 376, 135

Gammie, C. F., & Ostriker, E. C. 1996, ApJ, 466, 814

Ghez, A. M., Neugebauer, G., & Matthews, K. 1993, AJ, 106, 2005

Girart, J. M., & Acord, J. M. P. 2001, ApJ, 552, L63

Goldsmith, P. F., Langer, W. D., & Wilson, R. W. 1986, ApJ, 303, 11

Goldsmith, P. F., Snell, R. L., Hemeon-Heyer, M., & Langer, W. D. 1984, ApJ, 286, 599

Goodman, A. A., Barranco, J. A., Wilner, D. W., & Heyer, M. H. 1998, ApJ, 504, 223

Goodman, A. A., Benson, P. J., Fuller, G. A., & Myers, P. C. 1993, ApJ, 406, 528

Goodwin, S. P., Whitworth, A. P., & Ward-Thompson, D. 2004, A&A, 414, 633

Greaves, J. S., & Nyman, L.-A. 1996, A&A, 305, 950

Guilloteau, S., Bachiller, R., Fuente, A., & Lucas, R. 1992, A&A, 265, L49

Hartigan, P., Edwards, S., & Ghandour, L. 1995, ApJ, 452, 736

Hartigan, P., Morse, J. A., & Raymond, J. 1994, ApJ, 436, 125

Hartmann, L. W. 2001, AJ, 121, 1030

Harvey, P. M., Wilking, B. A., & Joy, M. 1984, ApJ, 278, 156

Haschick, A. D., Moran, J. M., Rodríguez, L. F., Burke, B. F., Greenfield, P. & Garcia-Barreto, J. A. 1980, ApJ, 237, 26

Haschick, A. D., Moran, J. M., Rodríguez, L. F., & Ho, P. T. P. 1983, ApJ, 265, 281

Helfer, T. T., Thornley, M. D., Regan, M. W., Wong, T., Sheth, K., Vogel, S. N., Blitz, L., & Bock, D. C.-J. 2003, ApJS, 145, 259

Henkel, C., Haschick, A. D., & Güsten, R. 1986, A&A, 165, 197

Herbig, G. H. & Jones, B. F. 1983, AJ, 88, 104

Herbig, G. H. & Rao, N. K. 1972, ApJ, 174, 401

Heyer, M. H., Ladd, E. F., Myers, P. C., & Campbell, B. 1990, AJ, 99, 1585

Heyer, M. C., Snell, R. L., Goldsmith, P. F., Strom, S. E., & Strom, K. M. 1986, ApJ, 308, 134

Hillenbrand, L. A. 1997, AJ, 113, 1733

Hirano, N., Kamazaki, T., Mikami, H., Ohashi, N., & Umemoto, T. 1999, in *Proceedings of Star Formation 1999*, ed. T. Nakamoto, (Nagoya: Nobeyama Radio Observatory), 181

Hirano, N., Kameya, O., Mikami, H., Saito, S., Umemoto, T., & Yamamoto, S. 1997, ApJ, 478, 631

Ho, P. T. P., & Barrett, A. H. 1980, ApJ, 237, 38

Ho, P. T. P., Haschick, A. D., Moran, J. M., & Rodríguez, L. F. 1982, BAAS, 14, 927

Hodapp, K.-W., & Ladd, E. F. 1995, ApJ, 453, 715

Hogerheijde, M. R., van Dishoeck, E. F., Blake, G. A., & van Langevelde, H. J. 1998, ApJ, 502, 315

Hotzel, S., Harju, J., Juvela, M., Mattila, K., & Haikala, L. K. 2002, A&A, 391, 275

Hunter, C. 1977, ApJ, 218, 834

Irvine, W. M., Goldsmith, P. F., & Hjalmarson, A. 1987, in *Interstellar Processes*, (Dordrecht: Reidel), 561

Jeans, J. H. 1902, Phil. Trans. R. Soc. London, Ser. A, 199, 1

Jeans, J. H. 1928, Astronomy and Cosmogony, (Cambridge: Cambridge University), 340

Jennings, R. E., Cameron, D. H. M., Cudlip, W., & Hirst, C. J. 1987, MNRAS, 226, 461

Jessop, N. E., & Ward-Thompson, D. 2001, MNRAS, 323, 1025

Jijina, J., Myers, P. C., & Adams, F. C. 1999, ApJS, 125, 161

Jørgensen, J. K., Schöier, F. L., & van Dishoeck, E. F. 2002, A&A, 389, 908

Jørgensen, J. K., Schöier, F. L., & van Dishoeck, E. F. 2004, A&A, 416, 603

Juan, J., Bachiller, R., Kömpe, C., & Martín-Pintado, J. 1993, A&A, 270, 432

Klessen, R. S., & Burkert, A. 2001, ApJ, 549, 386

Klessen, R. S., Heitsch, F., & Mac Low, M. M. 2000, ApJ, 535, 887

Knee, L. B. G., & Sandell, G. 2000, A&A, 361, 671

Kolmogorov, A. N. 1941, Dokl. Akad. Nauk. SSSR, 30, 301

Kramer, C., Alves, J., Lada, C. J., Lada, E. A., Sievers, A., Ungerechts, H., & Walmsley, C. M. 1999, A&A, 342, 257

Lada, C. J. 1987, Star Forming Regions: Proc. IAU Symp. 115, ed. A. K. Dupree & M. T. V. T. Lago, (Dordrecht: Kluwer), 1

Lada, C. J. 1991, The Physics of Star Formation and Early Stellar Evolution, ed.

C. J. Lada & N. D. Kylafis (Dordrecht: Klumer), 329

Lada, C. J., Alves, J., & Lada, E. A. 1996, AJ, 111, 1964

Lada, C. J. & Lada, E. A. 2003, ARA&A, 41, 57

Ladd, E. F., Lada, E. A., & Myers, P. C. 1993, ApJ, 410, 168

Ladd, E. F., Myers, P. C., & Goodman, A. A. 1994, ApJ, 433, 117

Langer, W. D., Castets, A., & Lefloch, B. 1996, ApJ, 471, 111

Langer, W. D., Velusamy, T., & Xie, T. 1996, ApJ, 468, 41

Langer, W. D., Wilson, R. W., Goldsmith, P. F., & Beichman, C. A. 1989, ApJ, 337, 355

Larson, R. B. 1969, MNRAS, 145, 271

Larson, R. B. 1981, MNRAS, 194, 809

Larson, R. B. 1995, MNRAS, 272, 213

Lay, O. P., Carlstrom, J. E., & Hills, R. E. 1995, ApJ, 452, 73

Lefloch, B., Castets, A., Cernicharo, J., Langer, W. D., & Zylka, R. 1998, A&A, 334, 269

Lefloch, B., Castets, A., Cernicharo, J., & Loinard, L. 1998, ApJ, 504, 109

Liseau, R., Sandell, G., & Knee, L. B. G. 1988, A&A, 192, 153

Lo, K. Y., Morris, M., Moran, J. M. & Haschick, A. D. 1976, ApJ, 204, L21

Looney, L. W. 1998, Ph.D. Thesis, University of Maryland

Looney, L. W., Mundy, L. G., & Welch, W. J. 2000, ApJ, 529, 477

Looney, L. W., Mundy, L. G., & Welch, W. J. 2003, ApJ, 592, 255

Lynds, B. T. 1962, ApJS, 7, 1

Mac Low, M.-M., & Klessen, R. S. 2004, Rev. of Mod. Phys., 76, 125

Mac Low, M.-M., McKee, C. F., Klein, R. I., Stone, J. M., & Norman, M. L. 1994, ApJ, 433, 757 2004, Rev. of Mod. Phys., 76, 125

Mathieu, R. D., Ghez, A. M., Jensen, E. L. N., & Simon, M. 2000, in Protostars

and Planets IV, ed. V. Mannings, A. P. Boss, & S. S. Russell (Tucson: University of Arizona), 703

Mathis, J. S., Rumpl, W., & Nordsieck, K. H. 1977, ApJ, 217, 425

Matthews, B. C., & Wilson, C. D. 2002, ApJ, 574, 822

McKee, C. F., Zweibel, E. G., Goodman, A. A., & Heiles, C. 1993, Protostars and Planets III, ed. E. H. Levy & J. I. Lunine (Tucson: University of Arizona), 327

Miesch, M. S. & Bally, J. 1994, ApJ, 429, 645

Miesch, M. S., Scalo, J., & Bally, J. 1999, ApJ, 524, 895

Miyake, K. & Nakagawa, Y. 1993, Icarus, 106, 20

Moore, T. J. T., & Emerson, J. P. 1994, MNRAS, 271, 243

Moran, J. M. 1983, RMxAA, 7, 95

Morgan, J. A. 1995, in Astronomical Data Software and Systems IV, ed. R. A. Shaw, H. E. Payne, & J. J. E. Hayes (San Francisco: ASP), 129

Mundy, L. G., McMullin, J. P., Grossman, A. W., & Sandell, G. 1993, Icarus, 106, 11

Myers, P. C. 1983, ApJ, 270, 105

Myers, P. C., & Benson, P. J. 1983, ApJ, 266, 309

Myers, P. C., Fuller, G. A., Goodman, A. A., & Benson, P. J. 1991, ApJ, 376, 561

Myers, P. C., Fuller, G. A., Mathieu, R. D., Beichman, C. A., Benson, P. J., Schild, R. E. & Emerson, J. P. 1987, ApJ, 319, 340

Myers, P. C., & Gammie, C. F. 1999, ApJ, 522, L141

Nakamura, F. & Li, Z.-Y. 2003, ApJ, 594, 363

Nisini, B., Benedettini, M., Giannini, T., Codella, C., Lorenzetti, D., DiGiorgio, A. M., & Richer, J. S. 2000, A&A, 360, 297

O'Linger, J., Wolf-Chase, G., Barsony, M., & Ward-Thompson, D. 1999, ApJ, 515, 696

Ostriker, E. C., Stone, J. M., & Gammie, C. F. 2001, ApJ, 546, 980

Padoan, P., Bally, J., Billawala, Y., Juvela, M., & Nordlund, Å. 1999, ApJ, 525, 318

Padoan, P., Juvela, M., Goodman, A. A., & Nordlund, Å. 2001, ApJ, 553, 227

Pendleton, Y., Davidson, J., Casey, S., Harper, A., Pernic, R., & Myers, P. C. 1990, Submillimetre Astronomy, ed. G. D. Watt & A. S. Webster, (Dordrecht: Kluwer), 189

Penston, M. V. 1969, MNRAS, 145, 457

Persi, P., Palagi, F., & Felli, M. 1994, A&A, 291, 577

Preibisch, T. 1997, A&A, 324, 690

Reipurth, B., Rodríguez, L. F., Anglada, G., & Bally, J. 2002, AJ, 124, 1045

Richer, J. S., Shepherd, D. S., Cabrit, S., Bachiller, R., & Churchwell, E. 2000, Protostars and Planets IV, ed. V. Mannings, A. P. Boss, & S. S. Russell (Tucson: University of Arizona), 3

Rodríguez, L. F., Anglada, G., & Curiel, S. 1999, ApJS, 125, 427

Sandell, G., Aspin, C., Duncan, W. D., Russell, A. P. G., & Robson, E. I. 1991, ApJ, 376, 17

Sandell, G., Knee, L. B. G., Aspin, C., Robson, I. E., & Russell, A. P. G. 1994, A&A, 285, 1

Sandell, G., & Knee, L. B. G. 2001, ApJ, 546, 49

Schöier, F. L., Jørgensen, J. K., van Dishoeck, E. F., & Blake, G. A. 2004, A&A, 418, 185

Shirley, Y. L., Evans, N. J., II, Rawlings, J. M. C., & Gregersen, E. M. 2000, ApJS, 131, 249

Shu, F. H. 1977, ApJ, 214, 488

Shu, F. H. 1997, IAU Symposium 178, Molecules in Astrophysics: Probes and Processes, ed. E. F. van Dishoeck, (Dordrecht: Kluwer), 19

Shu, F. H., Adams, F. C., & Lizano, S. 1987, ARA&A, 25, 23

Smith, K. W., Bonnell, I. A., Emerson, J. P., & Jenness, T. 2000, MNRAS, 319, 991

Snell, R. L., Loren, R. B., & Plambeck, R. L. 1980, ApJ, 239, L17

Spitzer, L., Jr. 1978, Physical Processes in the Interstellar Medium, (New York: John Wiley), 287

Stanimirović, S., Staveley-Smith, L., Dickey, J. M., Sault, R. J., & Snowden, S. L. 1999, MNRAS, 302, 417

Stone, J. M., Ostriker, E. C., & Gammie, C. F. 1998, ApJ, 508, 99

Strom, S. E., Grasdalen, G. L., & Strom, K. M. 1974, ApJ, 191, 111

Strom, S. E., Vrba, F. J., & Strom, K. M. 1976, AJ, 81, 314

Sun, J., Shen, J., Zhang, Y., & Sun, J. 2000, Chinese A&A, 24, 511

Tafalla, M., Bachiller, R., Martín-Pintado, J., & Wright, M. C. H. 1993, ApJ, 415, 139

Tafalla, M., Myers, P. C., Caselli, P., Walmsley, C. M., & Comito,C. 2002, ApJ, 569, 815

Terebey, S., Chandler, C. J., & André, P. 1993, ApJ, 414, 759

Terebey, S., & Padgett, D. L. 1997, in IAU Symp. 182, Herbig-Haro Flows and the Birth of Low-Mass Stars, ed. B. Reipurth & C. Bertout (Dordrecht: Kluwer), 507

Torrelles, J. M., Ho, P. T. P., Moran, J. M., Rodríguez, L. F., & Cantó, J. 1986, ApJ, 307, 787

van Dishoeck, E. F., & Blake, G. A. 1998, ARA&A, 36, 317

Vázquez-Semadeni, E., Ostriker, E. C., Passot, T., Gammie, C. F., & Stone, J. M. 2000, Protostars and Planets IV, ed. V. Mannings, A. P. Boss, & S. S. Russell (Tucson: University of Arizona), 3

Velusamy, T. & Langer, W. D. 1998, Nature, 392, 685

Walmsley, C. M. & Menten, K. M. 1987, A&A, 179, 231

Ward-Thompson, D., & Buckley, H. D. 2001, MNRAS, 327, 955

Ward-Thompson, D., Scott, P. F., Hills, R. E., & André, P. 1994, MNRAS, 268, 276

Ward-Thompson, D., Motte, F., & André, P. 1999, MNRAS, 305, 143

Ward-Thompson, D., Buckley, H. D., Greaves, J. S., Holland, W. S., & André, P. 1996, MNRAS, 281, 53

Warin, S., Castets, A., Langer, W. D., Wilson, R. W., & Pagani, L. 1996, A&A, 306, 935

Welch, W. J., *et al.* 1996, PASP, 108, 93

White, R. J., & Ghez, A. M. 1997, ApJ, 556, 265

Whitworth, A., & Summers, D. 1985, MNRAS, 214, 1

Wilner, D. J., Myers, P. C., Mardones, D., & Tafalla, M. 2000, ApJ, 544, 69

Wilner, D. J., Welch, W. J., & Forster, J. R. 1995, ApJ, 449, L73

Wolf-Chase, G. A., Barsony, M., & O'Linger, J. 2000, AJ, 120, 1467

Wolfire, M. G. & Cassinelli, J. P. 1986, ApJ, 310, 207

Wolfire, M. G. & Churchwell, E. 1994, ApJ, 427, 889

Womack, M., Ziurys, L. M., & Wyckoff, S. 1992, ApJ, 387, 417

Yamamoto, S., Mikami, H., Saito, S., Kaifu, N., Ohishi, M., & Kawaguchi, K. 1992, PASJ, 44, 459

Yu, K. C., Billawala, Y., & Bally, J. 1999, AJ, 118, 2940